June 2001 • NREL/SR-520-30391

Subcontractor Report

Processing of $CuInSe_2$-Based Solar Cells: Characterization of Deposition Processes in Terms of Chemical Reaction Analyses

Final Report
6 May 1995—31 December 1998

T.J. Anderson and B.J. Stanbery
University of Florida
Gainesville, Florida

National Renewable Energy Laboratory

1617 Cole Boulevard
Golden, Colorado 80401-3393

NREL is a U.S. Department of Energy Laboratory
Operated by Midwest Research Institute • Battelle • Bechtel

Contract No. DE-AC36-99-GO10337

NOTICE

Available electronically at http://www.doe.gov/bridge

Available for a processing fee to U.S. Department of Energy
and its contractors, in paper, from:

U.S. Department of Energy
Office of Scientific and Technical Information
P.O. Box 62
Oak Ridge, TN 37831-0062
phone: 865.576.8401
fax: 865.576.5728
email: reports@adonis.osti.gov

Available for sale to the public, in paper, from:

U.S. Department of Commerce
National Technical Information Service
5285 Port Royal Road
Springfield, VA 22161
phone: 800.553.6847
fax: 703.605.6900
email: orders@ntis.fedworld.gov
online ordering: http://www.ntis.gov/ordering.htm

Printed on paper containing at least 50% wastepaper, including 20% postconsumer waste

June 2001 • NREL/SR-520-30391

Processing of $CuInSe_2$-Based Solar Cells: Characterization of Deposition Processes in Terms of Chemical Reaction Analyses

Final Report
6 May 1995—31 December 1998

T.J. Anderson and B.J. Stanbery
University of Florida
Gainesville, Florida

NREL Technical Monitor: Bolko von Roedern

Prepared under Subcontract No. XAF-5-14142-10

National Renewable Energy Laboratory

1617 Cole Boulevard
Golden, Colorado 80401-3393

NREL is a U.S. Department of Energy Laboratory
Operated by Midwest Research Institute • Battelle • Bechtel

Contract No. DE-AC36-99-GO10337

This Dissertation by Dr. Billy J. Stanbery describes in great detail many aspects of the research carried out by Billy Stanbery in pursuing his degree at the University of Florida (UF) under the direction of Prof. Tim Anderson.

This project was initiated after the Boeing Company decided to terminate its photovoltaic research and development efforts, and donated some research equipment to UF. Billy Stanbery, who was part of the Boeing team, decided then to enroll at UF to pursue a Ph.D degree. As such these events constituted a rare direct technology transfer from industry to a university. This helped to preserve more than the published legacy of the solar cell efforts at Boeing, and jump-started a comprehensive, multifaceted, and multidisciplinary copper indium diselenide solar cell research effort at UF.

Bolko von Roedern
Technical Monitor, May 2001

To those dedicated teachers whose encouragement enabled me and whose vision inspired me to persevere:

B. M. Stanberry
M. E. Oakes
W. T. Guy, Jr.
G. C. Hamrick
S. C. Fain
M. P. Gouterman
R. A. Mickelsen
W. S. Chen
L. E. Johns, Jr.
R. Narayanan

ACKNOWLEDGMENTS

The long voyage of discovery I have labored to share in this dissertation could not have been realized without the contributions of a multitude of others that have chosen to invest their hope and efforts in mine. My study of this subject began over two decades ago, and prior to coming to the University of Florida was conducted mostly while employed by The Boeing Company. Their generous donation to the University of the key research equipment used to conduct this research provided irreplaceable physical assets that have made it possible. This would not have happened without the advocacy within Boeing of Dr. Theodore L. Johnson, for which I am very grateful.

This research would likewise not have been possible without the financial support of the United States Department of Energy provided through contract numbers XCG–4–14194–01, XAF–5–14142–10 and XAK–8–17619–32 from the National Renewable Energy Laboratory. Although these contracts were won through competitive procurement processes, the encouragement of K. Zweibel and J. Benner, providing me hope that I might succeed (but could only if I tried), was indispensable motivation, and I thank them both.

I would like to thank my advisor, Professor T. J. Anderson, for recruiting me to the University, providing laboratory space at the University's

MicroFabritech facility, and assembling the interdisciplinary research team within which I worked over the course of this doctoral research program. Every member of that team has contributed to this work, but I must particularly thank Dr. Albert Davydov and Dr. Chih–Hung (Alex) Chang who were always available, capable, and willing to engage in the intellectual exchanges that I have found to be the most compelling fount of insight. I am also indebted to Dr. Weidong Zhuang who provided me an advanced copy of the results of the critical assessment of the binary Cu–Se system that he and Dr. Chang performed.

Those familiar with laboratory research recognize the enormous value of those who help a researcher with the essential but unglamorous and tedious tasks that actually absorb most of the time and effort required to conduct successful research of this sort. I thank W. P. Axson who helped me turn an empty space and truck full of unfinished, disassembled equipment into a productive and safe laboratory filled with operational state-of-the-art research systems, and taught me plumbing and electrical skills in the process. The control automation system that finally tamed the reactor and consolidated the data acquisition process was the work of my research assistant S. Kincal, whom I thank as well. Without his assistance the quadrapole mass spectrometric measurements could not have been performed. The EDX composition measurements vital to calibration and data interpretation were the work of my other laboratory assistant S. Kim, whom I also thank. I reaped the benefits of the support of the entire staff of MicroFabritech, especially S. Gapinski and

D. Badylak, who providing a dependable and indispensable laboratory infrastructure. I also thank the following University staff, faculty, and students who helped with advice, parts, measurements, and characterization: W. Acree, M. Davidson, D. Dishman, E. Lambers, and J. Trexler. Outside of this University, I would like to thank Dr. S. P. Ahrenkiel (NREL), who provided TEM measurements; Dr. G. Lippold (Universität Leipzig), who provided Raman measurements; and Dr. M. Klenk (Universität Konstanz), who provided XRF measurements.

I would also like to thank some of those in the scientific community at large who have shared their time and thoughts with me during the course of this graduate program: Dr. M. Al–Jassim, Dr. R. Noufi, Dr. K. Ramanathan, Prof. A. Rockett, Dr. B. von Roedern, Prof. E. Vlieg, and Prof. J. Venables.

Finally, I would like to thank Sue Wagner and my parents, Martha and Bill Stanberry, without whose faith, hope, support, help, encouragement, and love I could not have succeeded.

TABLE OF CONTENTS

page

LIST OF TABLES

LIST OF FIGURES

Abstract of Dissertation Presented to the Graduate School
of the University of Florida in Partial Fulfillment of the
Requirements for the Degree of Doctor of Philosophy

HETEROEPITAXY AND NUCLEATION CONTROL FOR THE GROWTH OF METAL CHALCOGENIDES USING ACTIVATED REACTANT SOURCES

By

Billy Jack Stanbery

May 2001

Chairman: Timothy J. Anderson
Major Department: Chemical Engineering

A novel rotating-disc reactor has been designed and built to enable modulated flux deposition of $CuInSe_2$ and its related binary compounds. The reactor incorporates both a thermally activated and a novel plasma activated sources of selenium vapor, which have been utilized for the growth of epitaxial and polycrystalline thin-film layers of $CuInSe_2$. A comparison of the different selenium reactant sources has shown evidence of increases in its incorporation when using the plasma source, but no measurable change when the thermally activated source was used. It is concluded that the chemical reactivity of

selenium vapor from the plasma source is significantly greater than that provided by the other sources studied.

Epitaxially grown $CuInSe_2$ layers on GaAs, ZnTe, and SrF_2 demonstrate the importance of nucleation effects on the morphology and crystallographic structure of the resulting materials. These studies have resulted in the first reported growth of the CuAu type-I crystallographic polytype of $CuInSe_2$, and the first reported epitaxial growth of $CuInSe_2$ on ZnTe.

Polycrystalline binary (Cu,Se) and (In,Se) thin films have been grown and the molar flux ratio of selenium to metals varied. It is shown that all of the reported binary compounds in each of the corresponding binary phase fields can be synthesized by the modulated flux deposition technique implemented in the reactor by controlling this ratio and the substrate temperature. These results were employed to deposit bilayer thin films of specific (Cu,Se) and (In,Se) compounds with low melting point temperature, which were used to verify the feasibility of synthesizing $CuInSe_2$ by subsequent rapid-thermal processing, a novel approach developed in the course of this research.

The studies of the influence of sodium during the initial stages of epitaxy have led to a new model to explain its influences based on the hypothesis that it behaves as a surfactant in the Cu–In–Se material system. This represents the first unified theory on the role of sodium that explains all of sodium's principal effects on the growth and properties of $CuInSe_2$ that have been reported in the prior scientific literature.

Finally, statistical mechanical calculations have been combined with published phase diagrams and results of *ab-initio* quantum mechanical calculations of defect formation enthalpies from the literature to develop the first free energy defect model for $CuInSe_2$ that includes the effects of defect associates (complexes). This model correctly predicts the α/β ternary phase boundary.

CHAPTER 1
REVIEW OF PRIOR RESEARCH:
CIS MATERIALS FOR PHOTOVOLTAIC DEVICES

Any legitimate review of the prior research in this long-studied field must of necessity reference a number of excellent reviews already published in the literature. Nevertheless, the field is rapidly progressing and this critical review strives to highlight from this author's perspective both some of those research results that have been previously reviewed and those too recent to have been available to prior authors. The earliest comprehensive review of chalcopyrite semiconducting materials [1] by Shay and Wernick is a classic reference in this field. It focused primarily on the physical and opto-electronic properties of the general class of I–III–VI_2 and II–IV–V_2 compound semiconductors. More recent reviews specifically oriented towards CIS materials and electronic properties [2-6] are also recommended reading for those seeking to familiarize themselves with key research results in this field.

There are also a number of excellent books and reviews on photovoltaic device physics [7,8], on the general subject of solar cells and their applications [9,10], and others specifically oriented towards thin-film solar cells [11,12], the

class to which CIS solar cells belong. Finally, a non-technical but concise and current overview of solar cell technology was recently published by Benner and Kazmerski [13].

The first solid-state photovoltaic (PV) device was demonstrated in 1876 and consisted of a sheet of selenium mechanically sandwiched between two metal electrodes [14]. The addition of copper and indium and creation of the first CIS PV device occurred almost 100 years later in 1973 [15], when a research team at Salford University annealed a single-crystal of the ternary compound semiconductor $CuInSe_2$ in indium. Almost all subsequent Cu–In–Se thin-film deposition process development for PV device applications have sought to make the compound $CuInSe_2$ or alloys thereof, but in fact generally result in a multiphase mixture [16], incorporating small amounts of other phases. Researchers have not always been careful to reserve the use of the compound designation $CuInSe_2$ for single-phase material of the designated stoichiometry, an imprecision that is understandable in view of the difficulty in discriminating $CuInSe_2$ from some other compounds in this material system, as will be discussed in detail elsewhere in this treatise. The compound designations such as $CuInSe_2$ will be reserved herein for reference to single-phase material of finite solid solution extent, and multiphasic or materials of indeterminate structure composed of copper, indium, and selenium will be referred to by the customary acronym, in this case CIS.

This review begins with an overview of the physical properties of the principal copper ternary chalcogenides utilized for PV devices, including their thermochemistry, crystallography, and opto-electronic properties. All state-of-the-art devices rely on alloys of these ternary compounds and employ alkali impurities, so the physical properties and effects of these additives will be presented, with an emphasis on their relevance to electronic carrier transport properties. This foundation will provide a basis from which to address the additional complexities and variability resulting from the plethora of materials processing methods and device structures which have been successfully employed to fabricate high efficiency PV devices utilizing absorbers belonging to this class of materials.

Phase Chemistry of Cu–III–VI Material Systems

Significant technological applications exist for Ag–III–VI_2 compounds as non-linear optical materials [17], but almost all PV devices being developed for solar energy conversion that utilize ternary chalcogenides are based on the Cu–III–VI material system. Although the reasons for this may have been initially historical, this review will demonstrate that fundamental physical properties of these materials render them uniquely well suited, and underlie the research community's continuing development of them, for PV applications.

The Cu–In–Se (CIS) Material System

The thermochemistry of the Cu–In–Se ternary material system has been intensely studied, but significant inconsistencies abound and the incompleteness of the extant scientific literature will become apparent to the reader. One superficial inconsistency is in the Greek letter designations employed to describe the various phases, but even today there persist more substantive disagreements, for example, on the number of phases found in the ternary phase field. To avoid confusion all discussions herein that employ Greek letter designations to identify thermodynamic phases will use the identifiers from the work by Boehnke and Kühn [18].

Experimental studies that require bulk synthesis are extraordinarily difficult because of the high vapor pressure of selenium and reactivity of copper with quartz ampoules typically used [19]. It is therefore difficult to insure that the thermodynamic system remains closed during synthesis and that the resulting constitution accurately reflects the starting material ratios. Thus it is difficult to judge whether syntheses intended to lie on the Cu_2Se – In_2Se_3 pseudobinary section remain so, hence whether that section is actually an equilibrium tie-line. Although considerable progress has been made in the bulk synthesis of these compounds [5], uncertainties such as these persist to this day in efforts to assess the phase diagram.

The earliest published study of the Cu–In–Se phase diagram [20] was restricted to a segment of the presumably pseudobinary section between the

compounds Cu_2Se and In_2Se_3, and centered on the equimolar composition corresponding to $CuInSe_2$. Several key features of Palatnik and Rogacheva's results have been confirmed in subsequent studies of this system, albeit with different values of the critical point temperature and compositions. First, congruent melting of the solid compound with a composition near that of $CuInSe_2$ at a temperature somewhat less than 1000°C (986°C) is observed. Second, a congruent first-order solid-solid (α —> δ) phase transition at a lower temperature (810°C) of that high-temperature phase *via* a crystallographic order-disorder transition between the sphalerite structure (δ phase) and the chalcopyrite structure (α phase) is observed. Third, temperature-dependent extensions of the phase homogeneity range of the chalcopyrite structure to somewhat indium-rich compositions, but none towards copper-enrichment is observed. Fourth, peritectoid decomposition of the sphalerite phase at its lowest stable temperature into the chalcopyrite and a relatively indium-rich defect-tetragonal structure is observed.

Extension of the characterization of the Cu–In–Se ternary phase field to compositions off the Cu_2Se–In_2Se_3 section was finally published in the 1980's by three groups [18,21,22] although there are significant discrepancies between them. Boehnke and Kühn find four phases on the indium-rich side of the pseudobinary section between the compositions of $CuInSe_2$ and In_2Se_3, whereas Fearheiley and coworkers report seven phases based primarily on crystallographic studies by Folmer *et al.* [23]. Bachmann and coworkers alone

find a congruently-melting copper-rich compound on this section with a composition Cu_5InSe_4 (analogous to the mineral bornite, Cu_5FeS_4), reported to be unstable at room temperature [24]. Bachmann and coworkers found two critical point compositions for congruent melting of the solid phases on the indium-rich side of this section: at 55% In_2Se_3 mole fraction (corresponding to about 22 at.% copper) and at 75% In_2Se_3 mole fraction (corresponding to the compound $CuIn_3Se_5$), whereas the others find only one. More recent study suggests that there is only one congruently melting composition on this segment of the liquidus at 52.5 mole% In_2Se_3 [25]. These and other studies have been assessed by Chang and coworkers [26] resulting in the T–X section of the phase diagram shown in Figure 1-1, which will be referenced in further discussions throughout this treatise.

Another important study has been conducted more recently which focused on a relatively restricted composition and temperature range directly relevant to typical CIS photovoltaic device materials and processing [27]. Its most important conclusions were that the composition of the α–δ congruent phase transition occurs at 24.5 at.% Cu (50.8 mole% In_2Se_3) rather than the stoichiometric composition of $CuInSe_2$, and that the Cu_2Se – $CuInSe_2$ phase boundary at room temperature corresponds to this same composition. Their data also confirm the retrograde phase boundary between the α–phase and β–phase at temperature below the α+β–>δ eutectoid transition temperature (which they find to be 550°C, near Rogacheva's but much lower than Boehnke's and Fearheiley's

results), with this boundary at room temperature at 24.0 at.% Cu (51.6 mole% In_2Se_3).

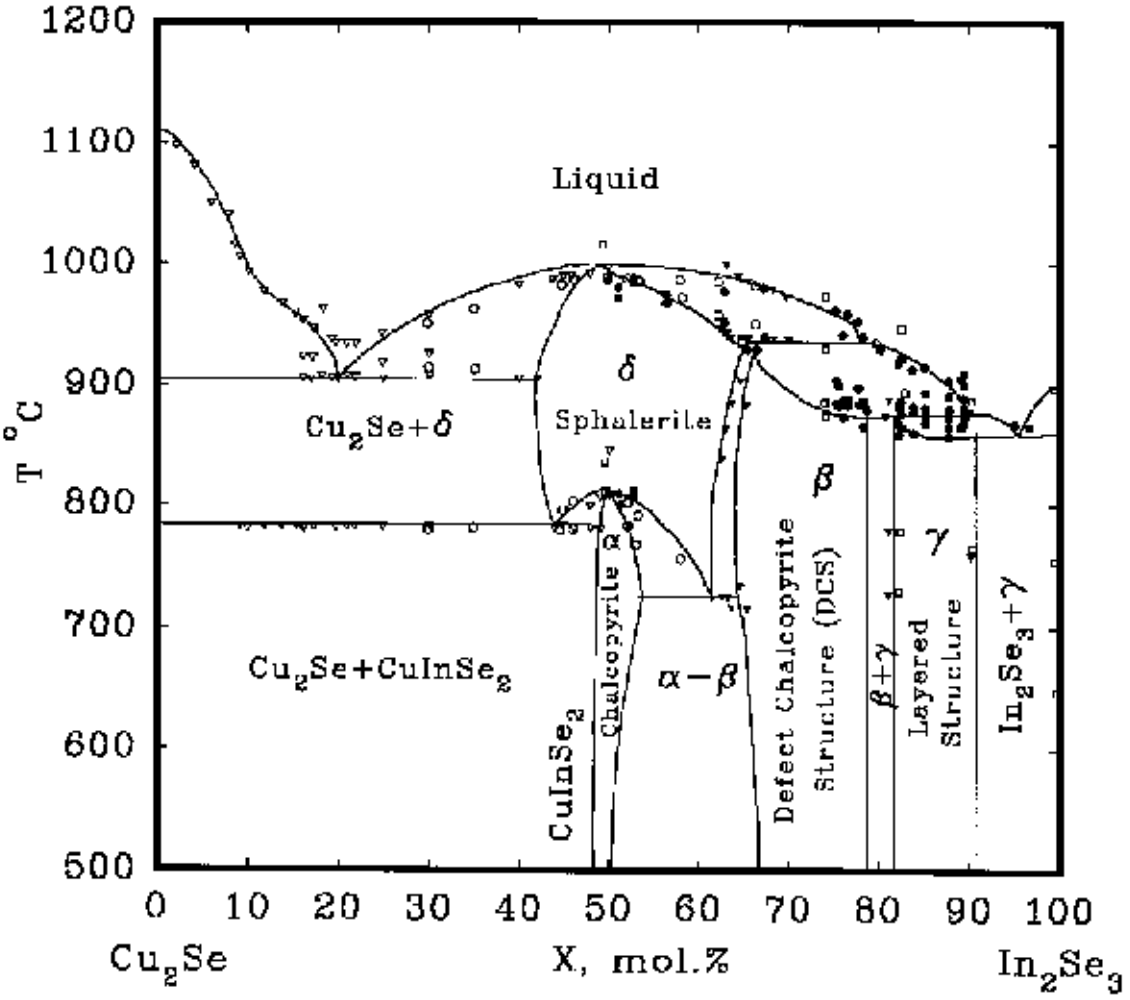

Figure 1-1 Assessed phase diagram along the Cu_2Se – In_2Se_3 pseudobinary section of the Cu–In–Se chemical system [26].

The Cu–Ga–Se (CGS) Material System

The phase diagram of the Cu–Ga–Se ternary material system remains less well-characterized and even more controversial than that of Cu–In–Se [28]. The earliest detailed phase equilibrium study [29], once again restricted to the presumably pseudobinary Cu_2Se – Ga_2Se_3 section within the ternary phase field,

reported the existence of one high-temperature disordered phase and 4 room-temperature stable phases. Two of those latter phases were solid solutions based on the terminal binary compounds, one was a phase (β) with the $CuGaSe_2$ composition as its copper-rich boundary, and the last was a relatively indium-rich phase (δ) with a layered structure. The only other comprehensive study of this ternary phase field [30] failed to confirm the existence of that δ phase or the associated compound $CuGa_5Se_8$.

Both studies, however, found that the stoichiometric compound $CuGaSe_2$ has a chalcopyrite structure and does not melt congruently, but instead undergoes peritectic decomposition at a temperature of 1050–1030°C. The earlier study by Palatnik and Belova [29] characterized the resulting gallium-rich solid, representing the copper-rich boundary of the high-temperature (γ) phase, as the compound $Cu_9Ga_{11}Se_{21}$ (55 mole% Ga_2Se_3) possessing a disordered sphalerite crystal structure. They found the associated liquid composition at the peritectic to be 38 mole% Ga_2Se_3.

A more recent study of $CuGaSe_2$ crystal growth by the gradient freeze technique [28] provides evidence contradictory to the earlier reports that the compound decomposes peritectically and suggests instead that it decomposes congruently and that the earlier studies mistook a solid-phase transformation which they find at 1045°C for peritectic decomposition. Resolution of these discrepancies will require further scientific inquiry, and a comprehensive assessment is needed.

Perhaps most importantly for photovoltaic-related process development is the consensus between both of these studies of the phase diagram that the homogeneity range of the chalcopyrite phase extends significantly to indium-rich compositions along this section as it does in $CuInSe_2$, but not measurably towards compositions more copper-rich than that of stoichiometric $CuGaSe_2$.

The Cu–In–S (CISU) Material System

Unlike the other two ternary copper chalcopyrites discussed herein, $CuInS_2$ occurs naturally, as the mineral roquesite. The earliest comprehensive study of the Cu_2S – In_2S_3 section was conducted by Binsma and coworkers [31]. They found four room-temperature phases, two corresponding to the terminal binaries and two others containing the compounds $CuInS_2$ (γ) and $CuIn_5S_8$ (ε). They did not report the low-temperature homogeneity range of these phases other than to note that for $CuInS_2$ it was below their detection limits. An earlier study, however, reported the homogeneity range of γ–$CuInS_2$ to be 50–52 mole% In_2S_3 and that of ε–$CuIn_5S_8$ from the stoichometric composition to almost 100% In_2S_3 [32]. At higher temperature, but below the chalcopyrite to sphalerite congruent solid phase order–disorder transition temperature at 980°C, Binsma found that the homogeneity range of γ–$CuInS_2$ extended to copper-rich compositions, unlike the ternary phases containing $CuInSe_2$ and $CuGaSe_2$. A third solid-phase transition of the sphalerite structure was detected at 1045°C, just below the congruent melting temperature of 1090°C.

Much of the thermochemical data published on the Cu–In–S ternary system prior to 1993 has been incorporated into an assessment published by Migge and Grzanna [33]. A more recent experimental study of the $CuInS_2$ – In_2S_3 subsection of the ternary phase field [34] found similar solid phase structures and transition temperature as those reported by Binsma, including the congruent melting of the indium-rich phase with a spinel structure and compositions around that of the compound $CuIn_5S_8$. They also found, however, an intermediate phase with a fairly narrow homogeneity range around the 62.5 mole% In_2S_3 composition of the compound $Cu_3In_5S_9$, which was reported to exhibit a monoclinic structure.

Another recent study extended the Cu–In–S ternary phase field characterization to the CuS – InS join [35], and confirmed that the Cu_2S – In_2S_3 pseudobinary section appears to be an equilibrium tie-line in this ternary phase field. They find that the room-temperature homogeneity domain for the roquesite γ–$CuInS_2$ phase is limited to 52 mole% In_2S_3 but extends towards CuS enrichment as much as six mole%. They also find that the two indium-rich ternary phases on the pseudobinary section described in the previous paragraph do not extend to this join.

Crystallographic Structure of the Ternary CIS Compounds

This section is limited to a discussion of those compounds that are stable at room temperature, with the exception of δ–CIS. This is not a particularly

serious restriction for subsequent discussions of thin film growth techniques, since all of those under development for device applications take place at temperature well below the solid-phase transition and decomposition temperature of all of these compounds, with the possible exception of the β to δ-CIS transition as discussed in the previous section.

α–CIS (Chalcopyrite $CuInSe_2$)

The crystal structure of α–CIS is well established to be chalcopyrite, corresponding to the space group $I\bar{4}2d$. It is an adamantine structure, as are δ-CIS and β-CIS, characterized by tetrahedral coordination of every lattice site to its nearest neighbors. It is distinguished from the zincblende structure of the binary Grimm-Sommerfeld compounds [36] by ordering of its *fcc* cation sublattice into two distinct sites, one occupied in the ideal structure by copper and the other by indium (Figure 1-2 (a)), and valency considerations require exactly equal numbers of each. Single-phase homogeneous crystals will for entropic reasons always exhibit some degree of disorder at room temperature irrespective of the deviation of their composition from the stoichiometric compound $CuInSe_2$, although such deviations will always increase that disorder. The chalcogenide atoms are located on another *fcc* lattice referred to as the anion sublattice. The two sublattices interpenetrate such that the four nearest neighboring sites to each cation site lie on the anion sublattice (Figure 1-2(b)) and conversely the four nearest neighboring sites to each anion site lie on the cation sublattice (Figure

1-2(c)). Each anion is surrounded by two Cu and two In site types, normally occupied by their respective atoms.

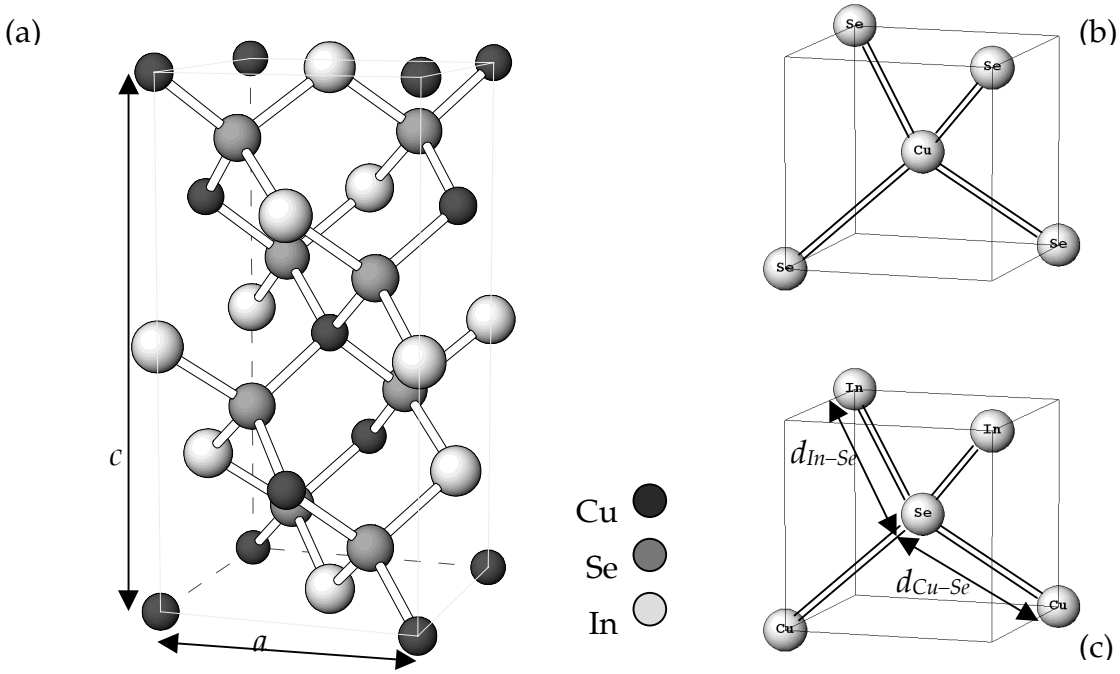

Figure 1-2 Schematic representation of $CuInSe_2$ chalcopyrite crystal structure: (a) conventional unit cell of height c, with a square base of width a; (b) cation-centered first coordination shell; (c) anion-centered first coordination shell showing bond lengths d_{Cu-Se} and d_{In-Se}.

The very different chemical nature of the copper and indium atoms result in bonds between each of them and their neighboring selenium atoms with very different ionic character and lengths [37]. This bond-length alternation has the electronic effect of reducing the bandgap energy of the compound with the chalcopyrite structure, relative to that of the ternary sphalerite structure with identical chemical composition, since the latter has a disordered cation sublattice. This bandgap reduction effect is known as optical bowing.

Bond-length alternation also has the effect of making the lattice constants of the chalcopyrite structure anisotropic in most cases. Binary compounds with the zincblende structure and the elemental compounds with a diamond structure require only one lattice constant to quantitatively characterize the crystal dimensions. The conventional unit cell of the chalcopyrite structure as shown in Figure 1-2 is equivalent to two cubic zincblende unit cells with sides of length a stacked in the c-direction and either compressed or dilated along that axis by a factor $\eta \equiv c/2a$, known as the tetragonal distortion.

The lattice constants of $CuInSe_2$ have been widely studied but the early results by Spiess and coworkers [38] are in excellent agreement with the most recent measurements of bond lengths by EXAFS [39]. Those values are a = 5.784 Å, c = 11.616 Å (and hence η = 1.004), d_{Cu-Se} = 2.484 Å, and d_{In-Se} = 2.586 Å. A more comprehensive compilation of the various reports of lattice constant measurements for $CuInSe_2$ may be found in Chang's dissertation [40].

δ–CIS (Sphalerite)

The δ–CIS phase is unstable at room temperature, and there is wide agreement that it forms from either solidification over a wide composition range of the ternary liquid or a first-order solid-phase transformation from either the α– or β–CIS phases or mixtures thereof (see Figure 1-1). The δ–CIS single-phase domain exhibits a congruent melting composition, for which the values of 1005°C at 52.5 mole% In_2Se_3 [25] are accepted here. At lower temperature the

domain of δ–CIS is limited by the eutectoid at 600°C [27] where it decomposes into a mixture of α– and β–CIS. There remains inconsistency between the various studies over the compositional range of single-phase stability in the relevant high-temperature regime. Fearheiley's phase diagram [22] posits that this phase is limited on the copper rich side by a eutectic associated with the putative compound Cu_5InSe_4, and stable to much higher In_2Se_3 mole fractions than found by Boehnke and Kühn [18], or than shown in Figure 1-1.

The congruent first-order α–δ solid phase transition at 24.5 at.% Cu (50.8 mole% In_2Se_3) and 809°C [27] corresponds to the crystallographic order/disorder transformation from the chalcopyrite to sphalerite structure. The sphalerite structure is based on the zincblende unit cell (and hence does not exhibit tetragonal distortion), with no long-range ordering of copper and indium atoms on the cation sublattice. The persistence of short-range ordering in δ–CIS, specifically the dominance of 2 In + 2 Cu tetrahedral clusters around Se anions as found in α–CIS, has been theoretically predicted [41].

β–CIS ($Cu_2In_4Se_7$ and $CuIn_3Se_5$)

It is doubtful that there is any part of the ternary Cu–In–Se phase diagram that is more controversial and simultaneously more important to understanding the operation of CIS PV devices than the indium-rich segment of the pseudobinary section containing the β–CIS phase domain shown in Figure 1-1. There is no agreement between the many studies of these relatively indium-rich materials on

the phase boundaries' compositions, the number of different phases that lie between $CuInSe_2$ and $CuIn_5Se_8$ (γ phase) or their crystallographic structure(s).

The situation in this field is very similar to that found in the study of the metal oxides, wherein there is considerable controversy as to whether nonstoichiometric phases are single phases with broad ranges of compositional stability, or a closely spaced series of ordered phases with relatively narrow ranges of stability [42, § 15.2-15.3.].

The existence of the peritectoid decomposition reaction of δ–CIS to the α phase and another In_2Se_3-rich solid phase requires that between the compositions of $CuInSe_2$ and In_2Se_3 there lies at least one other distinct phase on their tie-line to satisfy the Gibbs phase rule. A review by Chang [40] finds at least eight different compounds ($Cu_2In_4Se_7$, $Cu_1In_3Se_5$, $CuIn_5Se_8$, $Cu_8In_{18}Se_{32}$, $Cu_7In_9Se_{32}$, $Cu_{14}In_{16.7}Se_{32}$, $Cu_2In_3Se_5$, $Cu_3In_5Se_9$), and structures based on eight different space symmetry groups ($I\bar{4}$, $I\bar{4}2m$, $P23$, $Pm3$, $P432$, $P\bar{4}3m$, $Pm3m$, $P\bar{4}2c$) have been proposed for β–CIS (although not all these compounds lie on the pseudobinary). Most of these proposed structures are members of the group of adamantine superstructures derived from the cubic diamond lattice structure [43]. Recently a twinned structure that does not correspond to any of the 230 regular space groups [44,45] was also proposed.

Various nomenclatures are used by different researchers to describe the β–CIS compounds. They are sometimes referred to as P-chalcopyrite, a term coined by Hönle and coworkers when they concluded that the structure possesses $P\bar{4}2c$

symmetry [46]. These structures are also sometimes referred to generically as "Ordered Defect Compounds" (ODC's) but it is important to understand that "ordering" in the context of this terminology refers to the regular arrangement of preferred crystallographic sites on which defects are found, which alters the symmetry properties of the lattice. The defect distributions on those preferred sites in equilibrium might not have any long-range spatial order, although their statistical occupation probabilities could nevertheless be well defined.

It is beyond the scope of this review to attempt any resolution of this continuing controversy. Yet numerous studies of polycrystalline CIS [47], CISU [48], and CIGS [49] PV absorber films have shown that the composition at the surfaces of those films which ultimately yield high efficiency devices exhibits a [I]/[III] ratio of about $^1/_3$, corresponding to the compound $CuIn_3Se_5$ (except for nearly pure CGS where the ratio rises to about $^5/_6$ [49]). Resolution of these crystallographic and phase boundary uncertainties is essential to testing a recent theory that this behavior results from copper electromigration limited by the occurrence of a structural transformation at those compositions [50]. The existence of such a transformation is consistent with Fearheiley's evidence (which has not been confirmed) that the compound $CuIn_3Se_5$ melts congruently [22] and the crystallographic studies by Folmer [23] that find additional reflections in XRD spectra for pseudobinary compositions of 77 mole% In_2Se_3 or greater. The results of a recent EXAFS study directly prove that the crystallographic structure of

$CuIn_3Se_5$ (75 mole% In_2Se_3) is defect tetragonal, containing a high concentration of cation site vacancies [51].

γ–CIS ($CuIn_5Se_8$)

Folmer has pointed out [23] that the one common denominator between all of the structures found along the pseudobinary Cu_2Se–In_2Se_3 section is the persistence of a close packed lattice of selenium atoms. It is well known that different stacking sequences of such planes yields different crystallographic structures, for example the hexagonal close-packed (…ABAB…) and the face-centered cubic (…ABCABC…), and that there are an infinite number of possible stacking arrangements [52, § 4]. In cubic notation, these close-packed planes of the *fcc* structure are the {111} family (corresponding to the {221} planes of the chalcopyrite structure because of the latter's doubled periodicity along the c-axis).

Although the terminal indium binary compound In_2Se_3 on the pseudobinary section has been reported to possess several polymorphic structures, the low temperature phases are characterized by hexagonal stacking of the close-packed planes of selenium atoms on the anion sublattice [53]. Hence the existence of a structural transformation between the cubic stacking arrangement of the *fcc* anion sublattice of the chalcopyrite α–CIS structure and the hexagonal stacking of In_2Se_3 at some point along that segment of this section is reasonable. The crystallographic studies by Folmer [23] described previously

find additional reflections in XRD spectra that they index as (114) and (118), which represents evidence of at least partial hexagonal stacking of the close-packed layers of selenium anions, yielding a layered structure, presumably containing a high density of cation vacancies and antisites.

The segment on the Cu_2Se–In_2Se_3 section containing $\geq$ 77 mole% In_2Se_3 is assigned in Figure 1-1 to a single γ–CIS phase and a two-phase mixture of γ-CIS + In_2Se_3. Folmer concluded that there are three phases (excluding the terminal In_2Se_3) instead of one. Given the diversity of wurtzite-derived ternary defect adamantine structures with a hexagonal diamond structure [43] the crystallographic data do not provide clear evidence in favor of either a few distinct phases in a closely-spaced series or a pseudo-monophasic bivariant system [54] characterized by coherent intergrowth of two phases.

Metastable Crystallographic Structures — CuAu–ordering

Inasmuch as the chalcopyrite structure of α–CIS is itself an ordered variant of the sphalerite structure of δ–CIS, the issue of alternative ordering in the CIS material system has long been an active area of study. Vacancy ordering in conjunction with the indium-rich β–CIS phase has been described in an earlier section, but here alternative ordering of materials with a composition within the equilibrium stability range of α–CIS is discussed.

As early as 1992 a theoretical study by Wei and coworkers [41] of the α/δ–CIS order-disorder transition calculated that the energy of formation of the CuAu

(CA) crystallographic structure (Figure 1-3) differed by only 0.2 meV/atom from that of the chalcopyrite (CH) at T=0. In 1994 Bode [55], however, reported evidence of CuPt–ordering (CP) from TEM studies of copper-rich CIS films. CuPt–ordering of III–V alloys has been widely observed since it was first reported in the AlGaAs system [56]. In CIS the calculated formation energy difference between the CP and CH structures (at zero Kelvin) was more than 25 times greater than the difference between that of CA and CH–ordered crystals [41].

The equilibrium CH–CIS crystallographic structure shown in Figure 1-3(a) consists (in cubic notation) of alternating (201) planes of Cu and In atoms on the cation sublattice. The CA–CIS structure shown in Figure 1-3(b) consists of alternating (100) planes and CP–CIS structure consists of alternating (111) planes [57]. Consequently, each selenium atom in both the CH and CA structures is surrounded by 2 copper and 2 indium atoms in its first coordination shell whereas in the CP structure each selenium is surrounded by either (3 Cu + In) or (3 In + Cu). This variation in local atomic structure is the fundamental reason for the similar formation energies of the CH and CA structures and their mutual disparity from that of the CP structure.

The apparent doubling of the periodicity along {111} (cubic notation) planes that was observed in the study that reported CP–CIS [55] was found in polycrystalline samples made by codeposition of Cu, In, and Se with an overall composition in the mixed β-$Cu_{2-\delta}Se$ + α-$CuInSe_2$ phase domain of the equilibrium phase diagram (Figure 1-1). Their interpretation has been recently challenged

[58] based on the results of a careful study of CIS grown epitaxially on GaAs with a similar copper-rich composition, where it is shown that coherent intergrowth of a β–$Cu_{2-\delta}Se$ secondary phase can create an apparent doubling of lattice periodicity and thence of CuPt–ordering in copper-rich CIS. Coherent intergrowth of β–$Cu_{2-\delta}Se$ and $CuInSe_2$ has been suggested by other researchers to be an energetically favorable strain relief mechanism [59] since these two compounds share isomorphic, nearly identical Se sublattices.

CuAu–ordering (CA) of the Cu–III–VI_2 compounds was first detected experimentally by TEM in $CuInS_2$ [57] indium-rich MBE–grown epilayers where the formation of a secondary $Cu_{2-\delta}S$ phase is unlikely. Recently CA–ordering has been demonstrated in $CuInSe_2$ in both copper and indium–rich materials grown by Migration-Enhanced Epitaxy (MEE) [60] using XRD, TEM, and Raman scattering detection techniques [61]. Further studies of the electronic and optical properties of CA–CIS are needed to assess their impact on PV device absorber materials, which very likely contain nanoscale domains of this crystallographic polytype.

Defect Structure of α–CIS

The study of the defect structure of α–CIS has probably generated more of the literature on α–CIS than any other fundamental scientific issue. Pure α–CIS is amphoteric: its conductivity type and carrier density varies with composition. It is incorrect to say, however, that these electronic transport properties in real materials are determined by composition alone since the defect structures that

must be controlling them are empirically found to vary dramatically between compositionally indistinguishable materials.

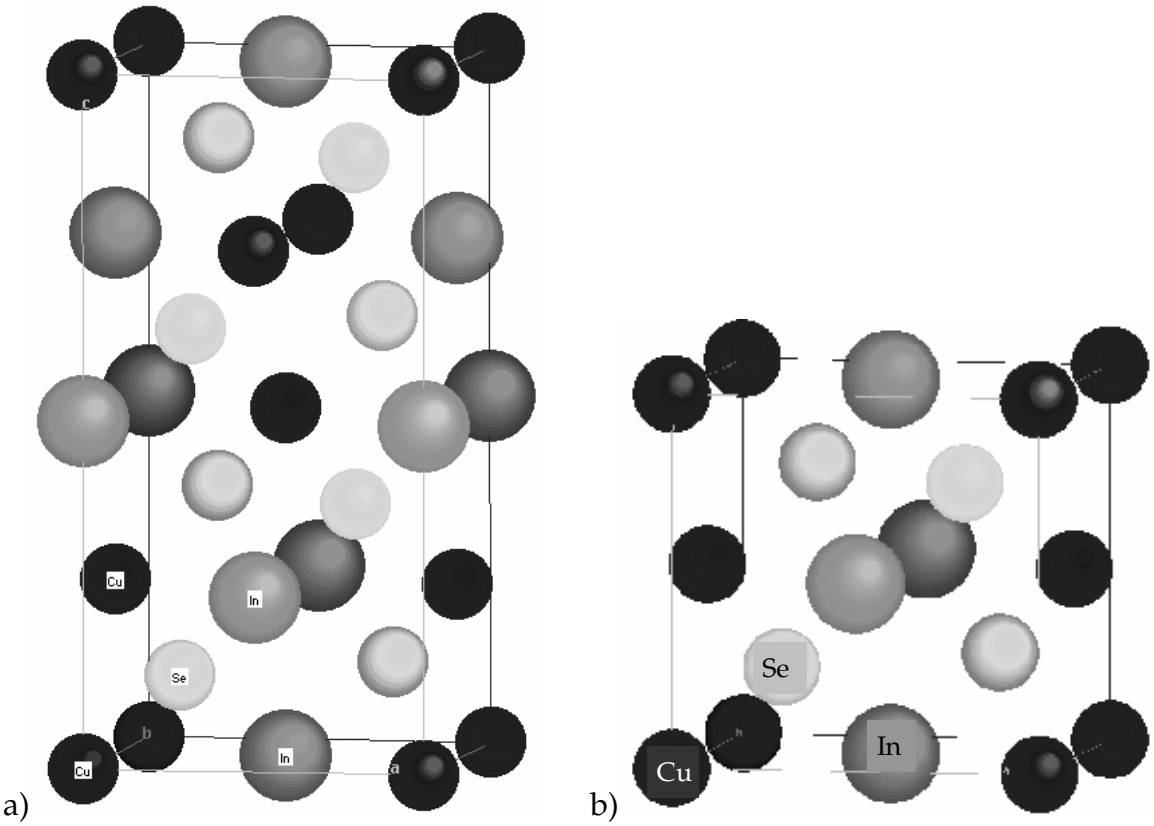

a) b)

Figure 1-3 Comparison of the crystallographic unit cells of $CuInSe_2$ polytypes: a) chalcopyrite (CH) structure, and b) CuAu (CA) structure.

Conceptually the densities of defect structures found in a single-phase material system in equilibrium must be determined uniquely by the composition, temperature, and pressure, else the Gibbs potential, a function of these variables, is not a legitimate state function for the system. The only intellectually satisfactory resolution of this conundrum is to conclude that complete thermodynamic equilibrium is not often found in real CIS materials. As described in the previous section, recent calculations and experimental results confirm

[61,62] that the free energy associated with the formation of some defect structures is so small that little increase in thermodynamic potential results, and hence there is insufficient driving force to ensure their elimination under many synthesis conditions. Furthermore, formation of many atomic defects requires bond breaking and atom transport processes. At low deposition or synthesis temperature it is expected that these processes will limit the approach to equilibrium. Comparison of theory with experiment in this field absolutely demands constant awareness of the ubiquity of metastable defects in real CIS materials and thus great caution when generalizing limited experimental data.

The starting point for atomistic analyses of the defect chemistry of $CuInSe_2$ is the paper by Groenink and Janse [63] in which they outline a generalized approach for ternary compounds based on elaboration of an earlier model developed specifically for spinels by Schmalzried [64]. The number of arbitrary combinations of possible lattice defects (vacancies, antisites, and interstitials) in a ternary system is so great that useful insight can only be gained by some approximation. Antisite defects created by putting anions on cation sites or *vice versa* are reasonably neglected because of their extremely high formation energy. The requirement that the crystal as a whole is electrically neutral also leads naturally to Schmalzried's assumption that for any given combination of the thermodynamic variables the concentrations of some pair of defects with opposite signs will be much higher than the concentrations of all other defects. Groenink and Janse referred to these as the "majority defect pairs." It is important

to note that their treatment assumes that these pairs behave as non-interacting point defects, hence in this context these are "pairs" only in the sense that they occur in roughly equal numbers. It is also significant that this pair dominance implies those conduction processes in these materials should inevitability be characterized by significant electrical compensation, deep level ionized impurity scattering, or both.

The generalized approach by Groenink and Janse was applied specifically to I–III–VI_2 compounds by Rincón and Wasim [65] who derived the proper form for the two parameters most useful for quantifying the deviation of the composition of these compounds or their alloys from their ideal stoichiometric values:

$$\Delta m = \frac{[I]}{[III]} - 1 \qquad \textit{molecularity deviation}$$

$$\Delta s = \frac{2*[VI]}{[I]+3*[III]} - 1 \qquad \textit{valence stoichiometry deviation}$$

Note that in the notation employed in these equations [I], for example, denotes the Group I atom fraction. Since [I]+[III]+[VI]=1, these two deviation variables uniquely specify the solid solution composition.

In the same way that a sum rule enables the composition of any ternary mixture to be specified completely using only two of its three fractional compositions, the composition can alternatively be specified by the two variables Δm and Δs. They are coordinates within the ternary I–III–VI composition triangle of the point corresponding to a compound's actual composition in a

coordinate system whose origin is at the point of I–III–VI_2 stoichiometry and whose axes are along (molecularity) and transverse (valency) to the I_2VI–III_2VI_3 section. Within the composition range where the I–III–VI_2 compound or alloy remains single phase, these variables may be properly viewed as analogous to the "normal coordinates" of a dynamical system in the Lagrangean formulation of the physics of motion. This coordinate system divides the ternary composition triangle into four quadrants and the analysis of Rincón and Wasim [65] shows that the 18 ionized point defects allowed in these approximations yield 81 $(= 9 * 9)$ "majority defect pairs," and which might dominate in each of the four quadrants or at their boundaries.

The merit of molecularity and valency deviations as intrinsically relevant composition measures in CIS has been empirically demonstrated by careful studies of conductivity in single crystal $CuInSe_2$ [3]. Neumann and Tomlinson demonstrated that within the range $|\Delta m| < 0.08$ and $|\Delta s| < 0.06$, p-type conductivity occurs whenever $\Delta s > 0$ (electron deficiency) whereas n-type conductivity occurs for $\Delta s < 0$ (electron surplus). Their Hall effect measurements also showed that the dominant acceptor changed in p-type CIS from shallow (20–30 meV) whenever $\Delta m > 0$ (excess copper) to deeper (78–90 meV) when $\Delta m < 0$ (indium-rich).

The actual predominance of a specific majority defect pair in any given quadrant of the molecularity *vs*. valency domain will in equilibrium be determined by whether its free energy is lower than that of the other probable

pairs. A vast amount of theoretical analysis [66-68] was directed in the 1980's towards estimation of the enthalpies of formation of the various point defects since their experimental determination is formidable. There is clear agreement among those analyses that the energy of formation for an isolated point defect is lowest for the cation antisite defects Cu_{In} and In_{Cu}. There was some disagreement as to whether the next lowest formation enthalpy values are for the copper vacancy, V_{Cu} [66,68], or selenium vacancy, V_{Se} [67].

There remained several disturbing issues with those analyses. First is the lack of the predicted correlation between the composition and net carrier concentration [3]. Second is the low level of minority carrier recombination in polycrystalline CIS PV devices, which are always made with significant negative molecularity deviation, often in the biphasic $\alpha+\beta$ domain. Recalling that the chalcopyrite unit cell contains 16 atoms, a defect concentration of little more than 6% would yield a statistical probability of one defect per unit cell if they are randomly distributed.

Defect complexes provide a resolution of these deficiencies, since all the atomistic models described above exclude defect complexes (associates) which should be anticipated given the Coulombic attraction between the oppositely charged members of these "majority defect pairs." The dominant cohesive bonding force leading to the negative contribution to enthalpy that stabilizes ionic crystals is the Madelung energy [69] resulting from precisely this Coulombic attraction, and defect clustering resulting in short-range order has

been shown essential to understanding the defect chemistry of non-stoichiometric transition metal oxide phases [54].

Theoretical *ab-initio* quantum-mechanical calculations of cation defect and defect complex formation enthalpies in $CuInSe_2$ [70] have recently provided support for these assertions. These results showed that the formation enthalpies of lattice defects depend on the chemical potential of the constituent atomic species, and in the case of charged defects, on the chemical potential for electrons (equal to the Fermi energy at T=0 K). The results showed explicitly that when the chemical potential of indium sufficiently exceeds that of copper the formation enthalpy of the $(In_{Cu}^{2+} + 2V_{Cu}^{-})^{0}$ neutral defect complex (NDC) actually becomes negative (energetically favorable). Formation of this defect requires the removal of three monovalent copper ions and substitution on one of those vacancies of the trivalent indium; hence it has no net effect on the valence stoichiometry deviation Δs. Their calculations were extended to the calculation of the energetic effects of long-range ordering of the $(In_{Cu}^{2+} + 2V_{Cu}^{-})^{0}$ complex [71]. They show that the reported compositions of indium-rich compounds ($\Delta m < 0$) on the pseudobinary section could be achieved by mathematically rational ratios of the numbers of this complex to the number of chalcopyrite unit cells, and that ordering was energetically favorable.

Additional long-range crystallographic ordering possibilities for the $(In_{Cu}^{2+} + 2V_{Cu}^{-})^{0}$ NDC have been proposed by Rockett [72] and further investigations are needed to determine the true nature and extent of NDC ordering.

Nevertheless, a recent study of the β-phase compound $CuIn_3Se_5$ (X=0.75 in Figure 1-1) [51] has shown that the EXAFS scattering spectrum of selenium in this compound is best fit by a local structure model having precisely these defect proportions in the nearest-neighbor tetrahedra surrounding Se atoms in the lattice (Figure 1-2(c)). This is strong experimental evidence that the "majority defect pair" found in indium-rich CIS compounds on the pseudobinary section is in fact this cation NDC.

Deviations from valence stoichiometry off the pseudobinary section ($\Delta s \neq 0$) cannot be caused by the $(In_{Cu}^{2+} + 2V_{Cu}^{-})^{0}$ NDC. Deviations of $\Delta s < 0$ are caused by defects which create an excess of electrons compared to those required to form the "normal valence compound" [73]. As examples, an In_{Cu} antisite defect brings two more valence electrons to that lattice site than when normally occupied by copper, Cu_{Cu}; and V_{Se} creation removes two bonding orbitals from the lattice, which would otherwise be normally occupied, thereby freeing two electrons to be donated to the conduction band by cations. Conversely, deviations of $\Delta s > 0$ are caused by defects that create a deficiency of electrons needed for the normal valence configuration (*e.g.* V_{Cu}). These considerations lead to the notation In_{Cu}^{2+}, which represents an In^{+3} ion placed at a cation antisite on the lattice that is normally occupied by Cu in its +1 oxidation state.

One of the other results from Zhang and coworkers' studies of cation defect energetics in CIS is their calculation of electronic transitions associated with the ionization of isolated point defects and clusters [70]. Their quantum-

mechanical studies show that the contrast between relative ionicity and covalency of the copper and indium bonds, respectively, result in an unexpectedly shallow acceptor level for V_{Cu} (30 meV) and unexpectedly deep donor levels (E_c-0.24 and E_c-0.59 eV) for the indium cation antisite, In_{Cu}. The shallow donor seen in α–$CuInSe_2$ with deviations of $\Delta s > 0$ had been attributed in many studies to In_{Cu} acting as a donor but these results show that both of its ionization levels are deeper than that of the $(In_{Cu}^{2+} + V_{Cu}^{-})^{+}$ part of the NDC and all were too deep to correspond to the very shallow (20–30 meV) donor seen in numerous studies [3].

One of the limitations of Zhang and coworkers' earlier studies of cation defect energetics in CIS was neglect of defects on the anion sublattice. In particular the V_{Se} is another widely suggested candidate for this shallow donor defect [3,68,74]. Investigations of vacancy defects in epitaxial $CuInSe_2$/GaAs *via* positron annihilation lifetime studies have been interpreted to suggest that the most probable defect is the $(V_{Se} + V_{Cu})$ defect [75-77]. More recent *ab-initio* quantum-mechanical calculations of the $V_{Se} \rightarrow V_{Se}^{+2}$ electronic transition energy [78] predict that significant lattice relaxation is associated with the V_{Se} ionization process, and that the energy level of the indirect (phonon-assisted) transition is E_c-0.1±0.05 eV. This represents the most shallow donor level calculated for any of the point defects investigated theoretically by that group.

The possible role of V_{Se} and cation-anion point-defect complexes in CIS with deviations from valence stoichiometry (*i.e.*, off the pseudobinary section

with $\Delta s \neq 0$) does not yet appear to have been adequately investigated. Van Vechten has argued [79] that V_{Se} is unlikely to be stable in indium-rich materials, proposing a defect annihilation mechanism when both $\Delta m < 0$ and $\Delta s < 0$ based on the quasichemical reaction:

$$2V_{Cu}^{-} + In_{In} + 2V_{Se}^{+} \rightarrow In_{Cu}^{2+} + 2e^{-} - 1 \text{ crystal unit},$$

which he suggests would be energetically favorable because of the large cohesive energy of the lattice compared to the energy of In_{Cu} formation.

Optical Properties of Ternary Cu–III–VI Materials

The focus in this section is the fundamental optical bandgaps of the α-phase compounds $CuInSe_2$, $CuInS_2$, $CuGaSe_2$, and of their associated β-phases. Discussion of the opto-electronic properties of alloys will be deferred to the following section.

Optical Properties of α–CIS and β–CIS

Early measurements of the bandgap energy of single-crystal $CuInSe_2$ exhibited nominal discrepancies [80,81], suggesting a value in the range of 1.02 to 1.04 eV. Subsequent studies [82,83] showed evidence of significant optical absorption at energies below this fundamental absorption edge. Characterization of polycrystalline CIS absorber films suitable for devices almost always indicate a significantly lower effective bandgap of ~0.90 eV [84], apparently a consequence of significant collection of carriers generated by absorption in these band-tails. It

has been suggested that the widely reported variations in the optical properties of CIS materials are a direct consequence of variations in composition [85].

The most recent published study of radiative recombination in near-stoichiometric $CuInSe_2$ epilayers on GaAs yields a value for the fundamental absorption edge of E_g = 1.046 eV at a temperature of 2 K, with a slight increase to a value of E_g = 1.048 eV at a temperature of 102 K [86]. Near room temperature, however, the temperature dependence follows the Varshni relation [87]:

$$E_g(T) = E_g(0) - \frac{\alpha T^2}{T + \beta}$$

with $\beta = 0$ and $\alpha = 1.1 \times 10^{-4} eV / K$ [85]. Anomolous low-temperature absorption edge dependency is often observed in of I–III–VI_2 semiconductors [88]. This phenomenon will be discussed in further detail in the section describing the optical properties of $CuGaSe_2$, since it has been more thoroughly investigated for that compound.

This low and high temperature data published by Nakanishi and coworkers [85] was subsequently fitted over the entire temperature range [89] to the Manoogian-Lecrerc equation [90]:

$$E_g(T) = E_g(0) - UT^s - V\left[\coth\left(\frac{\phi}{2T}\right)\right].$$

The fitting parameters $E_g(0)$, U, V, and s are temperature-independent constants, although they do have relevant physical significance. For example, the second and third terms represent the effects of lattice dilation and electron-phonon

interactions, respectively. The temperature ϕ is the Einstein temperature, related to the Debye temperature by $\phi \cong \frac{3}{4}\phi_D$ [89], and the value used in their calculations was derived from the published value of $\phi_D = 225\ [K]$ [91], yeilding $\phi = 170\ K$. The best fit to that data was found for $E_g(0) = 1.036\ [eV], U = -4.238 \times 10^{-5}\ [eV \cdot K^{-1}], V = 0.875 \times 10^{-4}\ [eV \cdot K^{-1}]$, and s = 1. The corresponding 300 K bandgap energy is 1.01 *e*V. Note the ~10 m*e*V discrepancy between this value for the bandgap at absolute zero temperature and that discussed earlier in this section [86].

The spectral dependence of the refractive index of $CuInSe_2$ has been reported for both bulk and polycrystalline [92] materials as well as epitaxial films on GaAs [93] Here too, significant discrepancies are found in the reported data.

Analogous discrepancies are found in the reported optical properties of β-CIS synthesized by different techniques. Polycrystalline films with an overall composition corresponding to the compound $CuIn_3Se_5$ are reported to exhibit a room-temperature fundamental absorption edge at 1.3 eV [47]. Optical absorption and cathodoluminescence characterization of heteroepitaxial $CuIn_3Se_5$ films on GaAs has been interpreted to indicate a bandgap of $E_g \geq 1.18$ eV at 8 K [94]. The most thorough characterization has been conducted on bulk polycrystalline samples with a nominal composition of $CuIn_3Se_5$ [95]. The temperature dependence of the absorption coefficient edge was fitted using the Manoogian-Lecrerc equation. The best fit to their data was found for

$E_g(0) = 1.25 - 1.28\ [eV]$, $U = 2.0 \times 10^{-5}\ [eV \cdot K^{-1}]$, $V = 1.2 - 1.5 \times 10^{-4}\ [eV \cdot K^{-1}]$, $\phi = 205 - 213\ [K]$, and s = 1. The corresponding 300 K bandgap energy is in the range of 1.19 to 1.21 eV. Although there are significant quantitative discrepancies between the various published data, they all agree without exception that the bandgap energy of β-CIS is substantially (0.2–0.3 *e*V) greater than that of α-CIS.

Variation of optical absorption with composition . The fundamental absorption edge for intrinsic undoped semiconductors can be determined by extrapolation of the plot of the absorption coefficient α *vs*. $\sqrt{h\upsilon}$ to $\alpha = 0$ [96]. Residual absorption at energies below the fundamental absorption edge in semiconductors which obeys the empirical relationship $d(\ln \alpha)/d(h\upsilon) = 1/k\mathrm{T}$ is referred to as an Urbach tail [97]. This is known in conventional extrinsically doped semiconductors to arise *via* the Franz-Keldysh effect produced by spatial fluctuations of the internal electrostatic field to give spatial variations in charged impurity density [98] over distances larger than the Debye screening length. Photon-assisted tunneling [99] between the resulting exponential bandtails [100] results in these characteristic exponential optical absorption tails.

The temperature and spectral dependence of the observed sub-bandgap absorption in single crystal $CuInSe_2$ has been carefully studied by Nakanishi and coworkers [101]. When they fitted their data to the conventional equation [102] of the Urbach form:

$$\alpha = \alpha_0 \exp\left[\frac{\sigma(h\upsilon - E_0)}{kT}\right],$$

where , with $\hbar\omega_p$ representing the optical phonon energy [103]:

$$\sigma = \sigma_0 \left(\frac{2kT}{\hbar\omega_p} \right) \tanh\left(\frac{\hbar\omega_p}{2kT} \right),$$

they found that unphysically large values for the optical phonon energy were required, and that they depended on composition. However, using the equation:

$$\alpha = \alpha_0 \exp\left[\frac{(h\upsilon - E_0)}{E_a(T,x)} \right],$$

they separated $E_a(T,x)$ into the sum of two terms, one linearly dependent on composition and the other a temperature dependent factor that fit the prior two equations with the reported value for the optical phonon energy. They concluded that the exponential optical absorption bandtails in $CuInSe_2$ arise both from phonon and compositional fluctuations, the latter increasing linearly with negative molecularity deviation.

Further variations in optical absorption and emission of α-CIS are associated with negative valence stoichiometry deviations ($\Delta s < 0$). Early annealing studies [74] showed a significant red-shift of photoluminescence emission when bulk samples were annealed or synthesized in excess indium vapor, and a reversible blue-shift after synthesis or annealing in excess selenium vapor. A more recent study [104] suggests the formation of an impurity (V_{Se}) subband when $\Delta s < 0.05$.

This phenomenon of strong sub-bandgap absorption in indium-rich CIS giving rise to apparent narrowing of the effective bandgap is also observed in

epitaxial films of CIS on GaAs studied by piezoelectric photoacoustic spectroscopy [105], evidence that it is a consequence of the native defect structure of these materials, and not an artifact of polycrystallinity, preparation, or measurement technique. It appears that this effect extends to the biphasic α–β composition domain, which suggests that the coexistence of these two phases is accompanied by an interaction between them that results in composition fluctuations manifested as strong band-tailing in their combined optical absorption. It is unclear whether this is an equilibrium phenomenon or related to ubiquitous metastable defect structures common to the materials investigated by so many researchers.

Optical Properties of α–CGS

The temperature dependence of the bandgap energy of $CuGaSe_2$ has been well characterized recently [89], with the data also fitted to the Manoogian-Lecrerc equation. The best fit to the data with s = 1 was found for $E_g(0) = 1.691\ [eV]$, $U = -8.82 \times 10^{-5}\ \left[eV \cdot K^{-1}\right]$, and $V = 1.6 \times 10^{-4}\ \left[eV \cdot K^{-1}\right]$, with $\phi = 189\ K$, based on the reported Debye temperature for $CuGaSe_2$ of $\phi_D = 259\ K$ [91]. The corresponding 300 K bandgap energy is 1.65 *e*V. Refractive index data for $CuGaSe_2$ over the range 0.78 to 12.0 μm has been reported by Boyd and coworkers [106].

Optical Properties of α–CISU

The most recent determination of the bandgap of α–CISU was based on bulk two-phase Cu_xS + $CuInS_2$ samples with slight negative valence stoichiometry deviations analyzed by means of photoreflectance spectroscopy, yielding a value of 1.54 eV at 80 K [107]. Earlier measurements of the bandgap varied by about 30 meV in the range of 1.52 to 1.55 eV at room temperature [108]. The relationship of the effective bandgap to composition, discussed in the preceding CIS part of this section, was studied [109], and the variance between previously published values was attributed to the same effect. In particular, a decrease in the effective bandgap was observed for negative valence stoichiometry deviations ($\Delta s < 0$).

The temperature dependence of the $CuInS_2$ bandgap is reported to exhibit anomalous low-temperature behavior, like that described for all the other Cu ternary chalcogenides discussed in this section [110,111]. Refractive index data for $CuInS_2$ over the range 0.9 to 12.0 μm has been reported by Boyd and coworkers [112].

Alloys and Dopants Employed in CIS Photovoltaic Devices

A later section of this review will describe in detail the reasons that most CIS PV devices are not made from the pure ternary compounds, but rather alloys thereof. Breifly, bandgap engineering is the principal motivation. The nomenclature might be somewhat confusing in this section unless the reader keeps clearly in mind the distinction between a compound and an alloy. $CuInSe_2$,

for example, is a ternary compound, as is $CuGaSe_2$. Both of these "compounds: show a small range of solid solution extent. An alloy of these two ternary "compounds" is a binary alloy, although it is also a quaternary material (it contains four elements). One may view this as simple mixing of Cu on the In sublattice in α-CIS. By induction, an alloy of that binary, $Cu(In,Ga)Se_2$, with the ternary compound $CuInS_2$ yields the ternary alloy $Cu(In,Ga)(S,Se)_2$, which is also a pentanary material.

Gallium Binary Alloy — CIGS

Until the very recent publication of the dissertation of Dr. Cornelia Beilharz [113] no comprehensive thermochemical study of the quaternary CIGS phase field was available. This is remarkable in view of the fact that most of the published world record thin film solar cell efficiencies since 1987 (and all since 1995) have been held by CIGS-based devices. The predominant phase fields in the pseudoternary Cu_2Se–In_2Se_3–Ga_2Se_3 composition diagram as reported in that work are shown Figure 1-4.

The most obviously important aspect of this CIGS pseudoternary predominance diagram is the monotonic broadening of the α–CIGS single-phase domain towards more Group III-rich compositions with increasing Ga. Practically speaking, this means that synthesis of single α–phase CIGS requires less precise control over the [I]/[III] ratio (molecularity) than needed for single phase α–CIS synthesis, irrespective of the technique employed. Secondly, the

appearance of a domain characterized by both α– CIGS (designated P1 in Figure 1-4) and β–CIGS (designated P2 in Figure 1-4) plus the disordered zincblende (Zb) structure, not found at room temperature in either of the pure ternary compounds. Note that the extent of this domain (designated Ch+P1+Zb in Figure 1-4) along lines of constant [In]/[Ga] molar ratio (*i.e.*, lines emanating from the Cu_2Se corner) is minimal in precisely the composition range around 25% gallium where the highest efficiency CIGS devices are fabricated [114,115].

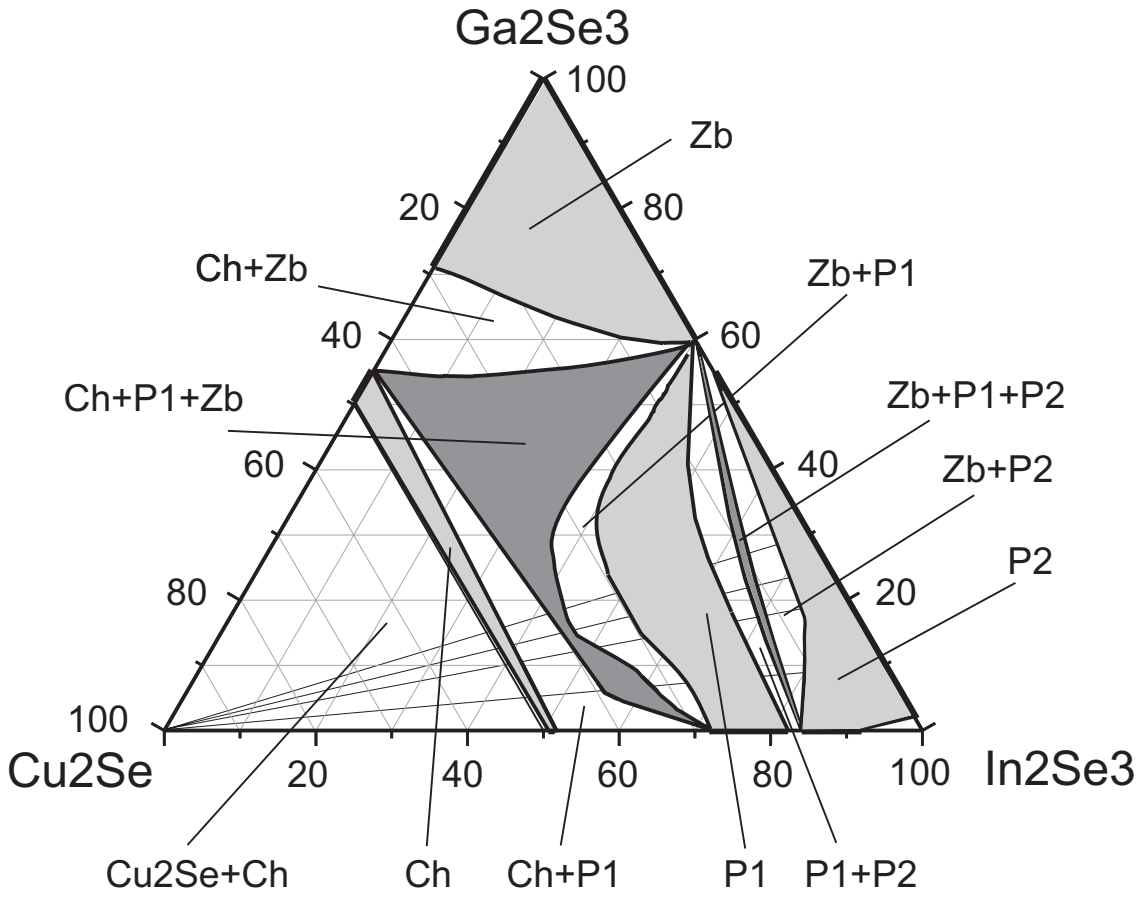

Figure 1-4 Predominance diagram for the Cu_2Se–In_2Se_3–Ga_2Se_3 pseudoternary phase field at room temperature [113]. In that author's notation, Ch is the α phase, P1 is the β phase, P2 is the γ phase, and Zb is the δ phase.

A theoretical study of the effects of gallium addition to $CuInSe_2$ provides some insight into likely atomic-scale phenomena leading to these effects [116]. First, they calculate that the energy of formation for the isolated group III cation antisite defect, Ga_{Cu}, is 0.2 to 0.9 eV greater (depending on its ionization state) than that of In_{Cu}. Second, they calculate that the donor levels for isolated Ga_{Cu}, are deeper than those of In_{Cu}, hence if present in comparable concentrations Ga_{Cu} will not thermally ionize as easily as In_{Cu}, and therefore contribute less to compensation of the acceptors which must dominate for *p*-type conductivity to prevail. This is consistent with the experimental observation that hole densities are higher in CIGS epitaxial films than in CIS epitaxial films with comparable molecularity and valence stoichiometry [117]. Finally, the $(Ga_{Cu}^{2+} + 2V_{Cu}^{-})^{0}$ Neutral Defect Complex (NDC) is calculated to require 0.4 eV more energy to form than the $(In_{Cu}^{2+} + 2V_{Cu}^{-})^{0}$ NDC, leading to 0.3 eV higher formation energy per NDC in the Ordered Defect Compounds (ODC) (*i.e.*, β or P2 phase) containing gallium. This suggests that in CIGS materials with negative molecularity deviation, under conditions where NDC aggregation can occur, ODC formation is more energetically favorable in regions where composition fluctuations have lead to a lower local gallium concentration.

Bandgap dependence on composition . Alloys of the copper ternary chalcopyrite compounds, like those of virtually all the zincblende binary alloys, are found to exhibit a sublinear dependence of their bandgap energy on alloy

composition. Their functional relationship is well approximated by the expression:

$$E_g(x) = xE_g(1) + (1-x)E_g(0) - b(1-x)x,$$

where the parameter b is referred to as the "bowing parameter." Optical bowing is now understood to be a consequence of bond alternation in the lattice [37]. Free energy minimization results in a tendency for A and B atoms to avoid each other as nearest neighbors on the cation sublattice in $A_xB_{1-x}C$ alloys, resulting in short range ordering referred to as anticlustering [118 Chapter 4.].

A very large range of bowing parameters has been reported for CIGS thin films and bulk $Cu(In,Ga)Se_2$, varying from nearly 0 to 0.025, and data on thin film CIGS absorber layers strongly supports the contention that this variability is a consequence of variations in molecularity deviation between the samples reported by various investigators [119 — and reference therein.]. Another study of combined temperature and composition dependencies of the bandgap in bulk crystalline $Cu(In,Ga)Se_2$ concluded that the bowing parameter may be temperature dependent [89]. A theoretical value of 0.21 at absolute zero has also been calculated [116]. A preponderance of the room temperature data is in the range of 0.14 [120] to 0.16 [121] so the intermediate value of $b = 0.151$ from the original work by Bodnar and coworkers is accepted here [122], leading to the following expression for α–$CuIn_{1-X}Ga_XSe_2$:

$$E_g^{CIGS}(x) = 1.65x + 1.01(1-x) - 0.151(1-x)x$$

Sulfur Binary Alloy —CISS

Woefully little thermochemical and structural data are available for the Cu–In–Se–S quaternary system. The bandgap dependence on composition has been reported by several researchers, with the reported optical bowing parameters varying from 0 to 0.88 [123-125]. There is substantially better agreement between a larger number of studies of the mixed-anion alloy $CuGa(Se_XS_{1-X})_2$ that the optical bowing parameter in that system is zero [126, and references therein]. It has been argued that the bond-alternation which leads to optical bowing in mixed-cation ternary chalcopyrite alloys does not occur in the mixed-anion alloys [127], and that the bowing parameter should therefore vanish in $CuIn(Se_XS_{1-X})_2$ as reported by Bodnar and coworkers [123]. The substantial uncertainty and disagreement amongst the published experimental results suggests that resolution of this question requires further investigation.

Alkali Impurities in CIS and Related Materials

The importance of sodium for the optimization of polycrystalline CIS thin-film solar cell absorber layers has been extensively studied since first suggested by Hedström and coworkers [128]. Their careful investigation of the serendipitous sodium "contamination" of CIS absorber films due to exchange from soda-lime glass substrates contributed to their achievement of the first CIS device with a reported efficiency exceeding 15%. Subsequent studies have concluded that whether derived from the substrate [129] or added intentionally from extrinsic sources [130-132], optimized sodium incorporation is beneficial to

device performance, and excess sodium is detrimental [133-136]. Studies of sodium's concentration and distribution in the films show it is typically present at a ~0.1 at.% concentration [137], and strongly segregates to the surface [138] and grain boundaries [139].

A plethora of mechanisms has been suggested in an effort to explain the beneficial influence of sodium, and an overview of the body of literature taken together suggests that multiple effects contribute thereto. The primary phenomenological effects in CIS and CIGS absorber materials may be summarized as:

1. An increase in *p*-type conductivity [140] due both to the elimination of deep hole traps [141], and an increase in net hole concentration resulting predominately from reduced compensation [142].

2. An increase in the (112) texture and the average grain size in polycrystalline films [143], with a concomitant reduction in surface roughness.

3. An increased range of compositions (specifically, negative molecularity deviations) that yield devices with comparable performance [144-146].

These effects have been attributed to both direct and indirect electronic effects of sodium in the resulting materials themselves, and to the dynamic effects of sodium during the synthesis process. These will be each discussed in turn, beginning with the one model that attributes the improved properties of absorbers that contain sodium on a bulk defect containing sodium.

Substitution of sodium for indium, creating residual Na_{In} antisite defect acceptors in the lattice of the resulting material, has been proposed to explain the observed increase in *p*-type conductivity [137]. Theoretical calculations predict [78] that its first ionization level, at 0.20 *e*V above the valence band edge, is shallower than that of Cu_{In}, but in typically indium-rich absorbers the formation of the Cu_{In} defect is less energetically favorable than are V_{Cu} and In_{Cu}, the structural components of the cation NDC. Furthermore, they calculate the formation enthalpy of the Na_{In} antisite defect is quite large (2.5 *e*V) when the compounds $CuInSe_2$ and $NaInSe_2$ are in thermal equilibrium.

The simplest indirect model for the sodium effect on conductivity is that the Na_{Cu} defect is more energetically favorable than the In_{Cu} defect, so it competes effectively for vacant copper sites during growth, thereby reducing the concentration of the compensating In_{Cu} antisite defect [147] in the resulting material.

A related model proposes that formation of Na_{Cu} substitutional defects in *lieu* of In_{Cu} is a transition state of the growth reaction in indium-rich materials, leading to a reduction in the final In_{Cu} antisite defect density within the bulk by inhibiting the incorporation of excess indium into the lattice [148]. In this model, sodium acts as a surfactant at the boundary between stoichiometric and indium-rich CIS, forming a two-phase $CuInSe_2$ + $NaInSe_2$ mixture or quaternary compound if sufficient sodium is available [149,150]. The advantages of this model are that it predicts a reduction in the concentration of In_{Cu} point defects

and the NDC defect complexes in the bulk [151]. This model addresses all three of the primary sodium effects: the morphological changes are a surfactant effect, and the increased tolerance to negative molecularity deviation a consequence of enhanced segregation of excess indium. This model has been developed by this author and will be described in more detail in Chapter 5.

A study of the effects of elemental sodium deposited onto $CuInSe_2$ single crystals [152] led the authors to conclude that Na atoms at the surface disrupt Cu-Se bonds, releasing Cu^+ ions. These ions subsequently diffuse into the bulk under the influence of the surface field resulting from band-bending induced by the sodium itself, thereby increasing the concentration of V_{Cu} acceptors in the near-surface region. They also suggest that Na_{Cu} substitutional defects are created during this process. For high doses of sodium, they find that this lattice disruption results in the decomposition of $CuInSe_2$, yielding metallic indium and Na_2Se, and suggest that β–phase compounds may form at the surface as intermediate reaction byproducts due to the enhanced V_{Cu} concentrations. It is difficult to understand how these effects would increase *p*-type conductivity, since the excess copper ions released from the surface and driven into the bulk would most likely recombine with the V_{Cu} shallow acceptors that make it so.

Two other models attribute the influence of sodium on electronic properties to its effects on the concentration of selenium vacancies. The first of these [146] suggests that sodium at grain boundaries catalyzes the dissociation of atmospheric O_2, creating atomic oxygen which neutralizes surface V_{Se} by

activated chemisorption, leading to the formation of a shallow acceptor [153,154]. Theoretical calculations of the bulk O_{Se} ionization energy level predict very deep levels [78], however, and studies of the electronic influence of implanted and annealed sodium in epitaxial Cu(In,Ga)Se_2 films provide evidence for substantially reduced compensation without any evidence of oxygen diffusion into the bulk [142].

The final published model for the effects of sodium attributes its influence to increased chemical activity of selenium at the film's surface during growth [155]. Strong evidence is provided that sodium polyselenides (Na_2Se_x) form on the surface during growth, and they suggest that this acts as a "reservoir" for selenium on the surface, reducing the formation of compensating V_{Se} donor defects.

Summary

The various I-III-VI_2 material systems described in the foregoing section show a great deal of similarity in the structure of their phase diagrams. The common theme among them all is the ubiquity of ordering phenomena associated with the different phases. Clearly, much more study is needed to clarify the many unknown properties of each of these material systems and provide the materials science foundation required to support their successful application to photovoltaic devices.

CHAPTER 2
CIS POINT DEFECT CHEMICAL REACTION EQUILIBRIUM MODEL

Ternary chalcopyrite I–III–VI_2 compounds such copper indium diselenide ($CuInSe_2$) differ at a fundamental level from their binary II–VI zincblende analogues because of the coexistence in the former of two distinct types of bonds. Detailed quantum-mechanical calculations [156] show that the I–VI bonds tend to be far more ionic in character than the III–VI bonds which are predominately covalent. This heterogeneity leads to extremely strong optical absorption owing to the resultant high density of unit-cell-scale local dipole fluctuations and to ionic conduction resulting from the mobility of the relatively weakly-bound group I atoms.

The point defect chemistry approach expounded by Kröger [157] is employed. The intention is to explore the consequences of the native lattice disorder (intrinsic point defects and aggregates thereof) caused by finite temperature and deviations from stoichiometry in the equilibrium α–phase of ternary Cu–In–Se, usually refered to by its ideal stoichiometric composition formula $CuInSe_2$.

Approach

An associated solution lattice defect model is developed to calculate the total Gibbs energy function $\mathcal{G}(T,P,\{N_i\})$ of a thermodynamic system comprised of a continuum of electronic states and charge carriers interacting with atoms and ions which reside on a denumerable lattice of sites. The defect chemical reactions of this model involve atomic elements and charges within the crystal which is the thermodynamic system of interest, and atoms, complexes and electrons in an outer secondary phase which constitutes the reservoir with which the crystal is in equilibrium. This approach treats specific well-defined point defects and their complexes embedded in clusters of primitive unit cells on a Bravais lattice as quasimolecular species and utilizes conventional chemical reaction equilibrium analysis [158] to calculate their equilibrium concentrations.

An activity-based formulation for the total Gibbs energy of mixing (or mixture formation) as a function of the temperature T, pressure P, and total number N_i of each component in the mixture is defined as:

$$\Delta\mathcal{G} = \mathcal{G}\,[\,T\,,P\,,\{N_i\}\,] - \sum_{j=1}^{Max(i)} N_j\ \overline{\mathcal{G}}_j^o[T,\,P,\,\{N_i^o\}]$$

where $\overline{\mathcal{G}}_j^o$ is the partial molar Gibbs energy of a specie in its reference state, according to the equations:

$$\mathcal{G}[T,P,\{N_i\}] = \sum_{j=1}^{Max(i)} N_j\Big(\overline{\mathcal{G}}_j^o[T,\,P,\,\{N_i^o\}] + \overline{\mathcal{G}}_j^{IDL}[T,\,P,\,\{N_i\}] + \overline{\mathcal{G}}_j^{XS}[T,\,P,\,\{N_i\}]\Big)$$

$$= \sum_{j=1}^{Max(i)} N_j\,(\overline{\mathcal{G}}_j^o + RT\ \ln[a_j]) = \sum_{j=1}^{Max(i)} N_j\,(\overline{\mathcal{G}}_j^o + RT\,(\ln[x_j] + \ln[\gamma_j]))$$

The relations $\Delta\mathcal{G} = \sum_{j=1}^{Max(i)} N_j\ \overline{\mathcal{G}}_j^{MIX}$ and $a_j = \exp[(RT)^{-1}\ \overline{\mathcal{G}}_j^{MIX}] = \gamma_j x_j$ have

been implicitly used, where a_j is the activity, γ_j the activity coefficient, and x_j the concentration of the "j^{th}" component. The separation of the Gibbs energy of mixing $\overline{\mathcal{G}}_j^{MIX}$ into the sum of ideal (random) and excess parts $\overline{\mathcal{G}}_j^{IDL} + \overline{\mathcal{G}}_j^{XS}$ is particularly useful when $x_j \to 1$ in the reference state since $\gamma_j = 1$ if and only if $\overline{\mathcal{G}}_j^{XS} = 0$ in that case. For these computations appropriate but different models for the partial molar total Gibbs energy of mixing ($\overline{\mathcal{G}}_j^{MIX}$) are used for each component j to solve for their concentrations, and each activity coefficient γ_j determined from the solution *via* the expression:

$$RT \ln[a_j] = \overline{\mathcal{G}}_j^{MIX} = \overline{\mathcal{G}}_j - \overline{\mathcal{G}}_j^0 \Rightarrow \gamma_j = x_j^{-1} \exp\left[\frac{\overline{\mathcal{G}}_j - \overline{\mathcal{G}}_j^0}{RT}\right].$$

The question of normalization must be addressed carefully in the transition from an extensive quantity like $\Delta\mathcal{G}$ to the intensive partial molar quantities $\overline{\mathcal{G}}_j^{XS}$. This is a particularly subtle issue in the context of a lattice model where it will sometimes be necessary to normalize the concentrations x_j with respect to the number of lattice sites. To prevent confusion a number of different concentration notations suitable for different contexts are introduced and it is simply noted here that the numerical values for activities and activity coefficients depend explicitly on the choice of concentration measure [157; §9.4, 158; §6.3].

A building units approach (which is closely related to the more common structural element approach) and the Kröger-Vink notation are used to describe the crystal lattice and its defects [157; §7.10]. Structure elements are the entities appearing at particular sites in the lattice such as a vacancy on an interstitial site $\mathcal{V}_i$, or a copper atom on its ideal lattice site $Cu_{Cu}^{\times}$, where the superscript '×' means that it

is in its normal valence state. In addition to this lattice site atom occupancy information, the change in electronic charge density surrounding a structure element compared to its normal electronic charge density distribution is of interest. Charge localization is of course an idealized concept for the fundamental structural elements of the defect-free crystal whenever covalent bonding and band formation occur. For many electronically active crystal defects on the other hand, it is reasonable to deal with the strong electronic/ionic defect interactions by treating them together as a quasiparticle. The combined defect and perturbed electronic charge density distribution are represented as a charged structure element. For example $In_{Cu}^{\bullet\bullet}$ represents a double positively charged indium atom on a lattice site normally occupied by copper, whereas $\mathcal{V}_{Cu}'$ represents a single negatively-charged copper vacancy. Note that the superscript charge notation represents the deviation of the defect's local charge distribution from that of the unperturbed lattice site.

Now that the distinction between the physical elements (*e.g.*: Cu) and structural elements (*e.g.*: $Cu_{Cu}^{\times}$) has been explicitly described, it is appropriate to introduce the notation for normalization. The notation $\|Cu_{Cu}^{\times}\|$ is used to mean the mole fraction of normal valence copper atoms on copper sites: in other words the number of moles of $Cu_{Cu}^{\times}$ structure elements divided by the total number of moles of the quasimolecular species comprised of all the elemental species in the system. Kröger used square braces [ ] to denote molar concentration, but that notation cannot be used with the *Mathematica* program employed for these calculations since it identifies and encloses therein the argument sequence of a function. The notation

$\langle Cu^{\times}_{Cu} \rangle$ is used to mean the lattice concentration, or more specifically for this example, the number of electrically neutral copper atoms on lattice sites normally occupied in the chalcopyrite lattice by Group I atoms, divided by the total number of Group I sites in the chalcopyrite lattice. Equivalently, $\langle Cu^{\times}_{Cu} \rangle$ is the probability that a Group I lattice site is occupied by a copper atom in its normal charge state. Kröger used curly braces { } but these cannot be used in *Mathematica* since they are predefined therein to identify and enclose a list.

One key requirement for the interconsistency between the physical and structural element thermochemical descriptions of phase and reaction equilibria is that the difference in their normalization changes reaction equilibrium constants differently in the two descriptions since exchange of atoms between phases may not conserve the total number of lattice sites. Strictly speaking, if the species in the model are structural elements rather than atomic or molecular species, and lattice-normalized concentrations are used in the equations given above for the Gibbs energy, the result is instead a quasichemical potential and quasichemical activities for each of them. These issues must be kept clearly in mind to avoid misapplication of the results.

This model is similar to the solution defect lattice model developed by Guggenheim [165]. Guggenheim's model employs his "quasichemical" approximation (first derived by Bethe [166]) to calculate for point defect associates (quasimolecular species) the configurational entropy contribution to $\Delta\mathcal{S}^{XS}$ in the exact relation $\Delta\mathcal{G}^{XS} = \Delta\mathcal{H}^{XS} - T\Delta\mathcal{S}^{XS}$. The essence of this approximation [159] is that

pairs of nearest-neighbor sites are treated as independent of one another, which introduces unallowable configurations into the partition function for any species that occupies more than one lattice site simultaneously. It is nevertheless superior to the assumption that $\Delta\mathcal{S}^{XS}$ vanishes (or equivalently that γ_j is unity). This is the assumption used in a regular solution lattice defect model wherein the point defects are distributed randomly on the lattice despite the existence of interaction enthalpies between the different point defect species. The introduction of correlated site distribution probabilities into the theory leads to an associated solution theory and the implicit possibility of phase segregation or long-range ordering.

The excess entropy $\Delta\mathcal{S}^{XS}$ can be partitioned into four components corresponding to electronic, internal, changes to the lattice vibrational excitations (phonons) associated with the quasimolecular species, and configurational excess entropies. These excess entropies are computed for the normal lattice constituents, point defects, and for defect associates using a cluster expansion method. These clusters are formally identical to the relative building units used by Schottky [167]. Thus strictly speaking this calculation is based on his building units approach rather than a structural element approach [157, §7.10]. The overall problem is made tractable by separating the strong short–range energetic effects due to interactions between the point defects and the normal lattice components in their immediate neighborhood into internal interactions within clusters which can then be treated as weakly-interacting. Consequently, the activity coefficients ($\boldsymbol{\gamma}$) of these clusters in their mixture corresponding to the actual state of the entire CIS lattice need only be

modified to account for the long-range Coulombic interactions between the charged species. These corrections are largely compensated by the Fermi degeneracy of the charge carriers [157, §7.11], so the activity coefficients of the clusters will be approximated as unity, yielding a simple cluster mixing model.

Prior efforts to identify the structural defects responsible for the electronic behavior in these materials [65] have relied on estimates of the enthalpy of vacancy formation by Van Vechten [168] based on a cavity model for vacancy formation energy. More recently, first principle calculations of these formation enthalpies have been conducted by Zhang and coworkers [70] which shall be used here. Their quantum-mechanical calculations provide enthalpies of isolated defect formation since they allowed for lattice relaxation and hence changes in specific volume resulting from the formation of a single defect or defect complex within an otherwise perfect lattice supercell containing 32 atoms. For the dilute point defect and quasimolecular species in this model which were considered therein, their calculated formation enthalpy is set equal to $\overline{\mathcal{H}}_j^{\mathrm{XS}} / \mathrm{N_{Av}}$. Those authors, however, estimate the uncertainty in their calculated defect formation enthalpies to be $\sim 0.2\, e\mathrm{V}$ which represents a potentially significant source of errors in the results of these calculation.

In addition to their formation enthalpy calculations for isolated defects and complexes, Zhang and coworkers calculated the enthalpies of interaction between ordered arrays of one specific defect complex, $2\,\mathrm{V_{Cu}} \oplus \mathrm{In_{Cu}}$, placed on neighboring copper sublattice sites along the (110) direction (note the infix notation '$\oplus$' is used to denote an associate or defect complex formed from the specified lattice point

defects). This neutral cation defect complex had the lowest formation enthalpy of any they considered in the dilute limit. The Madelung energy resulting from their interaction when in a dense array as described above gave an additional reduction in enthalpy that varied with their concentration. These results will be used when analyzing the defect model in the case of an overall excess of indium compared to copper in the isolated thermodynamic system.

Finally, Zhang and coworkers calculated the defect electronic transition energy levels for isolated cation point defects and complexes. In a defect chemical model these electronic transition energies correspond to the enthalpy of ionization of a neutral defect to form an ion or charge localized on a vacant lattice site (an "ionized vacancy"). Their estimated uncertainty in these electronic transition energy levels is $\pm 0.05\ eV$ for isolated point defects and ± 0.10 eV for defect pairs. This represents another potential source of errors in the results of these calculation. The entropy of ionization will be included in an approximation derived by van Vechten [169].

Formulation of the problem

The empirical observation that the compounds which form in the Cu–In–Se ternary system all exhibit wide compositional ranges of phase homogeneity is proof of a non-neglible compositional dependence of their partial molar Gibbs energies $\overline{\mathcal{G}}_j[\mathrm{T,P,}\{x_i\}]$ on the values of the component atom fractions, x_i. It has been proven that a statistical thermodynamic model can account for this variation by retaining higher order correction terms to the entropy that are usually neglected, including lattice vacancy [162] and electronic carrier band-entropy contributions [163].

This model is an adaptation of the ternary alloy model developed by Sha and Brebrick [163] to the structure of the chalcopyrite lattice, wherein there are three distinct lattice sites rather than two, as in their model. Unlike their approach, the statistical mechanics used to compute entropies is based on a cluster configuration technique. Furthermore, rather than solving the reaction equilibrium problem by the usual method of Lagrange multipliers, more recently developed matrix techniques described by Modell and Reid [158] are employed. It is assumed that:

I. The lattice structure of the α and β phases consists of four sublattices, referred to as M1, M3, X6 and $\mathcal{I}$ (interstitial). Each of the metal-sublattices (M1 and M3) has N sites and there are 2N X6-sublattice sites for a total of 4N normally-occupied lattice sites, which comprise an *fcc* Bravais lattice of N lattice unit cells. Their are eight normally-occupied lattice sites in each primitive unit cell of the chalcopyrite crystal structure, which is comprised of four lattice site tetrahedra distorted along the *c*-axis. Hence the entire ideal lattice comprises $\frac{N}{2}$ chalcopyrite primitive unit cells. In an *fcc* lattice there are a plethora of interstitial sites: eight tetrahedral, four octahedral, and thirty-two trigonal per *fcc* unit cell [172]. It is assumed that the only interstitial species included in this model, the Cu interstitial (Cu_i), occupies the tetrahedral interstitial sites only. Note that all of these tetrahedrally coordinated interstital sites are not equivalent with respect to the symmetry operations of the $I\bar{4}2d$ point group characteristic of the chalcopyrite structure (space group 122), but it is assumed nevertheless that they are statistically equivalent and energetically degenerate. There are therefore 8N total sites available

in the entire lattice including these interstitial sites, and sixteen *per* primitive unit cell cluster.

II. Each of the point defect species is distributed randomly on its respective sublattice within each cluster. Defect complexes are defined as short-range (nearest-neighbor) correlated occupancy on one or more of the sublattices. The correlation is achieved by restricting each complex to a distinguishable lattice cluster, but the distribution of those clusters over the available lattice is assumed to be random. Interactions leading to aggregation of defect complex clusters on this lattice is treated as a second phase.

III. The excess Gibbs energy of a phase is a first-degree homogeneous linear function of the numbers of clusters of each kind and the total number of clusters that comprise the lattice.

The defect structure within the α phase, and phase segregation phenomena between the α phase and any secondary phase, is analyzed in the context of this lattice model. The constituent physical elements Cu, In, and Se and charge q are distributed among the available lattice sites and between phases in accordance with the principle of minimum total Gibbs energy but the total amounts of these physical elements are strictly conserved. Hence equilibria are calculated based on the following basis set:

$$\mathrm{a} = \{\mathrm{Cu}, \mathrm{In}, \mathrm{Se}, \mathrm{q}, \mathrm{M1}, \mathrm{M3}, \mathrm{X6}, \mathcal{I}\};$$

The electrochemical state vector with respect to this basis is defined as:

$\mathbf{sN} := \{N_{Cu}, N_{In}, N_{Se}, N_q, N, N, 2N, 4N\}$

This electrochemical state vector **sN** can be transformed to express the total Cu, In, Se and charge q in terms of the reduced set of variables X, y, Z, N, and ϱ where:

$$N_{In} := y N$$
$$N_{Cu} := X y N$$
$$N_{Se} := \frac{Z y N (3 + X)}{2}$$
$$N_q := \varrho N$$

The reverse transformations are clearly (since N≠0):

$$X === \frac{N_{Cu}}{N_{In}};$$
$$y === \frac{N_{In}}{N};$$
$$Z === \frac{2 N_{Se}}{3 N_{In} + N_{Cu}};$$
$$\varrho === \frac{N_q}{N};$$

The dimensionless electrochemical state vector is now defined as:

$\mathbf{s} := \{X, y, Z, \varrho, N\}$

Conservation of mass in this chemical context where nuclear transformations between elements are inadmissable implies the conservation of N_{Cu}, N_{Se}, and N_{In} distinctly and therefore of X, Z, and y×N. When the system is closed to charge transfer, N_q is conserved and therefore ϱ×N is conserved. The importance of this transformation lies in the fact that X and Z are invariant, whereas changes in y and ϱ

can result from a change in N. It is apparent from these observations that the specification of **s** uniquely specifies **sN**. Note that both of these state vectors, **s** and **sN**, are extensive.

The significance of changes in N is apparent in a simple example where $N_{Cu} = N_{In} = \frac{N_{Se}}{2} = N$. The state vector $\mathbf{sN} \rightarrow \{N, N, 2N, N_q, N, N, 2N, 4N\}$. This represents N formula units of the compound $CuInSe_2$, N primitive unit cells of the *fcc* Bravais lattice, and a net electronic charge of N_q. Changes in N therefore represent the loss or gain of lattice sites resulting from segregation to another phase in equilibrium which has an incoherent lattice structure. "Incoherent lattice" means a lattice with a different number of crystallographically distinct sublattices, or different site ratios, or both. Any such reaction leaves X and Z unchanged but change the ratio (y) of total indium to lattice sites and the overall charge density on the lattice (ϱ). The utility of this formulation will become apparent.

The relationship of the variables in the reduced electrochemical state vector **s** to prior formulations of this problem [65] is now developed. The chemical composition of any mixture in this ternary system may be formally written as the reaction:

$$x\,Cu_2Se + (1\text{-}x)\,In_2Se_3 + \Delta s\,Se \rightharpoonup (Cu_x In_{1-x})_2 Se_{3-2x+\Delta s} \;;\; 0 \geq x \geq 1 \wedge 2x\text{-}3 \geq \Delta s.$$

It is obvious from their definitions that $X = \frac{x}{1-x} \Leftrightarrow x = \frac{X}{1+X}$ (given that $x \neq 1$) and by direct substitution (note that $\Delta s = 0 \Leftrightarrow Z = 1$):

$$Z = \frac{6-4x+2\Delta s}{2x+6(1-x)} = 1 + \frac{\Delta s}{3-2x} \Leftrightarrow \Delta s = (Z\text{-}1)(3\text{-}2x) = \frac{(Z-1)(3+X)}{1+X}$$

If phase segregation of the compound composition on the right hand side of the reaction does not occur, comparison with [63] shows that this parameter X is the "molecularity" and Z is the "valence stoichiometry" of that phase. Furthermore, $Z-1=\frac{\Delta s}{3-2x}$ is the "valence stoichiometry deviation" of the phase and $X-1=\frac{2x-1}{1-x}$ is Δx, its "molecularity deviation."

The necessary foundation has been laid to address the normalization of atom fraction and molar quantities in terms of these variables. The atom fraction corresponding to a number N_k of a given *atomic* species k is denoted x_k, and given by:

$$x_k=\frac{N_k}{N_{Cu}+N_{In}+N_{Se}}=\frac{N_k}{N\ y\times(1+X+\frac{Z\times(3+X)}{2})}=\frac{2\times N_k}{N\ y\times(2\times(1+X)+Z\times(3+X))}.$$

The mole fraction corresponding to a number N_j of any given species j is denoted $\|N_j\|$, or in the code for their computation c_j, and has been defined as the ratio of N_j to the total number of "molecules" of the hypothetical species $(Cu_x\ In_{1-x})_2\ Se_{3-2x+\Delta s}$. It is stressed that this does not necessarily imply the existence of any phase within the system with this actual composition, hence the modifier "hypothetical." Substituting for the stoichiometric coefficients from the foregoing solutions for x and Δs in terms of X and Z gives:

$$(Cu_x\ In_{1-x})_2\ Se_{3-2x+\Delta s}=\left(Cu_{\frac{X}{1+X}}\ In_{\frac{1}{1+X}}\right)_2\ Se_{3-\frac{2X}{1+X}+\frac{(Z-1)(3+X)}{1+X}}$$

$$=Cu_{\frac{2X}{1+X}}\ In_{\frac{2}{1+X}}\ Se_{\frac{Z(3+X)}{1+X}}.$$

This form of the quasimolecular species formula can be used to solve for the atom fractions x_k in terms of the variables X and Z alone:

$$x_{Cu}=\frac{2X}{2\times(1+X)+Z\times(3+X)},\ x_{In}=\frac{2}{2\times(1+X)+Z\times(3+X)},\text{ and }x_{Se}=\frac{Z\times(3+X)}{2\times(1+X)+Z\times(3+X)}.$$

Next the total number of moles, M, of this quasimolecule is sought. By the

definition of y, $N_{In} = y \times N$ and that the number of indium atoms in a mole of the quasimolecule is $\frac{2}{1+X} \times N_{Avo}$ (Avogadro's number). Hence the equation $M \times \frac{2\,N_{Avo}}{1+X} = N_{In} = y \times N$ is solved to give:

$$M = \frac{(1+X)\ \ y \times N}{2\,N_{Avo}} = \frac{N_{In} + N_{Cu}}{2\,N_{Avo}}\ \text{, and thus:}$$

$$\|N_j\| = \frac{N_j}{M \times N_{Avo}} = N_j \times \frac{2}{(1+X)\ \ y \times N}\ \text{; and } M = 1 \Rightarrow N_j = \|N_j\| \times N_{Avo}$$

Since X, Z, and the product y×N are invariants, changes in the atom fraction or molar fraction of any species, either atomic, molecular, or structural, may be due only to the change in the number of that species in the entire system.

For completeness the relatively obvious normalizations are given for the lattice site occupation probability for the species indexed by a given value of *j*:

$\langle N_j \rangle_{M1\ or\ M3} = \frac{N_j}{N}$ for the M1 or M3 (cation) sublattice;

$\langle N_j \rangle_{N} = \frac{N_j}{2N}$ for the X6 (anion) sublattice;

$\langle N_j \rangle_{\mathcal{I}} = \frac{N_j}{4N}$ for the $\mathcal{I}$ (interstitial) sublattice.

Unlike the other normalizations, however, note that these species normalizations may change *via* their explicit dependence on the unconserved quantity N.

The equilibrium associated lattice solution theory calculations will be conducted with respect to the lattice state vector, **sL**, whose components are lattice site occupation numbers and which is defined with respect to a subset of all possible lattice defects: $\{\{N_{Cu_{M1}^{q}}\}, \{N_{Cu_{M3}^{q}}\}, \{N_{Cu_{X6}^{q}}\}, \{N_{Cu_{I}^{q}}\}, \{N_{In_{M1}^{q}}\}, \{N_{In_{M3}^{q}}\}, \{N_{In_{X6}^{q}}\}, \{N_{In_{I}^{q}}\}, \{N_{Se_{M1}^{q}}\}, \{\langle N_{Se_{M3}^{q}}\}, \{N_{Se_{X6}^{q}}\}, \{N_{Se_{I}^{q}}\}, \{N_{\mathcal{V}_{M1}^{q}}\}, \{N_{\mathcal{V}_{M3}^{q}}\}, \{N_{\mathcal{V}_{X6}^{q}}\}, \{N_{\mathcal{V}_{I}^{q}}\}, \{N_{e^-}\}, \{N_{h^+}\}\}$, where the charge *q* on each of these lattice basis elements assumes all

possible values for each constituent. This complete lattice state ensemble is unnecessarily large since many configurations which are conceptually possible are so energetically unfavorable that they may be omitted without significant effects on the results. The subset chosen for these calculations will be discussed in detail at a later point. At this juncture it is only necessary to note that **sL** is constrained by sum rules that connect it to **sN** and **s**. Specifically, the sum of molar concentrations of all structural elements containing a given physical element must equal the molar concentration of that physical element in the corresponding thermochemical state vector. Similarly, the net charge on the lattice calculated from **sL** must equal the total charge, N_q. Finally, the sum of lattice site occupation probabilities must be unity for each sublattice independently.

Four independent specific variables are required to model the thermochemical reaction equilibria of a single phase, three component system. The temperature, pressure, the overall copper to indium molar ratio X, and the anion to cation ratio Z are chosen: the variable set {T, P, X, Z}. The activity of each atomic species is referenced to its standard state of pure elemental aggregation (Standard Elemental Reference, SER) at Standard Temperature and Pressure (STP is T_0 =298.15K (25°C) and P_0 =101.3 kPa = 1 atm) for which its enthalpy of formation, $\Delta\mathcal{H}_f^{\mathrm{SER}}$, is set to zero by convention. The absolute scale for entropy where $\lim_{T\to 0} S_T^o = 0$ for all elemental species is used and the changes in equilibria between phases calculated from mathematical expressions for $\mathcal{G}$ -$\Delta\mathcal{H}_f^{\mathrm{SER}}$. Furthermore the effects of pressure will not be considered and all calculations will be conducted at standard pressure, effectively reducing this

to a problem in three variables. Note that the extensive reduced electrochemical state vector **s** introduced in the preceding section contains five variables, X, y, Z, ϱ, and N. For this initial thermochemical analysis an electroneutrality constraint is imposed, hence $\varrho = 0$ (and $N_q = 0$) in this context. Note that reaction equilibria are intensive relations and that **s** may be transformed to an intensive state vector, $\bar{\mathbf{s}}$, by setting the total number of moles, M, of the quasimolecules with the formula $(Cu_x\ In_{1-x})_2\ Se_{3-2x+\Delta y}$ to unity. Using the formula derived in the prior section for M:

$$M = \frac{(1+X)\quad y \times N}{2\,N_{Avo}} = 1 \Leftrightarrow y = \frac{2}{(1+X)}\ \frac{N_{Avo}}{N}$$

This transformation from the extensive state vectors **sN** to **s** results in no loss of information regarding the state of the system assuming the ratio of sublattice site numbers remained fixed with respect to all possible reactions. The variable transformations therein for y and ϱ, however, are explicitly dependent on N *via* the physical requirement that y×N and ϱ×N remain constant. Transformation from either **sN** or **s** to the intensive molar state vector $\bar{\mathbf{s}} = \{X, y, Z, \varrho\}$ places a constraint on these products, but neither y nor ϱ independently. The choice of the independent thermodynamic variable set {T, P, X, Z} implies that equilibrium values for the state variable y (and similarly ϱ) are dependent variables calculated with the equation above (or its analog for ϱ) using the equilibrium value of N for one mole of the quasimolecular species $Cu_{\frac{2X}{1+X}}\ In_{\frac{2}{1+X}}\ Se_{\frac{Z(3+X)}{1+X}}$.

The structural element basis of the α and β phases of CIS that will be employed for these calculations consists of various clusters of the following subset of lattice species, which comprise the basis set for **sL**:

L.CIS = {{Cu^{x}_{Cu}, In^{x}_{In}, Se^{x}_{Se}, $\mathcal{V}_{i}$}, {{$\mathcal{V}^{x}_{Cu}$, $\mathcal{V}'_{Cu}$, In^{x}_{Cu}, $In^{\cdot}_{Cu}$, $In^{\cdot\cdot}_{Cu}$},
{Cu^{x}_{In}, Cu'_{In}, Cu''_{In}, $\mathcal{V}^{x}_{In}$, $\mathcal{V}^{\cdot}_{In}$, $\mathcal{V}^{\cdot\cdot}_{In}$, $\mathcal{V}^{\cdot\cdot\cdot}_{In}$}, {$\mathcal{V}^{x}_{Se}$, $\mathcal{V}^{\cdot\cdot}_{Se}$}, {$Cu^{x}_{i}$, $Cu^{\cdot}_{i}$}},
{$Cu_{i} \oplus \mathcal{V}_{Cu}$, $Cu_{In} \oplus In_{Cu}$, $\mathcal{V}_{Cu} \oplus In_{Cu}$, $(\mathcal{V}_{Cu} \oplus In_{Cu})^{\cdot}$}, {$2\,\mathcal{V}_{Cu} \oplus In_{Cu}$}};

The normal lattice constituents, the isolated point defects on each sublattice, and defect complexes on different numbers of lattice sites have each been grouped seperately in **L.CIS**. The various lattice clusters will be labeled by their characteristic point defect, except for the normal lattice constituents which combine to form the normal cluster which will be labeled simply CIS_{α}. These are grouped in the cluster basis set ***αβ*L** by the number of primitive unit cells in the structure element's cluster of lattice sites, with that corresponding number of primitive unit cells given by the ordered list **ncL**.

$\alpha\beta$L = {{CIS_{α}}, Join[Flatten[Take[L.CIS, {2, 2}]], Take[Take[L.CIS, {3, 3}]⟦1⟧, 2],
{$(2\,\mathcal{V}_{Cu} \oplus In_{Cu})_{\beta 13}$}], Join[Drop[Take[L.CIS, {3, 3}]⟦1⟧, 2],
{$(2\,\mathcal{V}_{Cu} \oplus In_{Cu})_{\alpha}$, $(2\,\mathcal{V}_{Cu} \oplus In_{Cu})_{\beta 15}$, $(2\,\mathcal{V}_{Cu} \oplus In_{Cu})_{\beta 25}$}]};

$\alpha\beta$L⟦1⟧ === {CIS_{α}}

$\alpha\beta$L⟦2⟧ === {$\mathcal{V}^{x}_{Cu}$, $\mathcal{V}'_{Cu}$, In^{x}_{Cu}, $In^{\cdot}_{Cu}$, $In^{\cdot\cdot}_{Cu}$, Cu^{x}_{In}, Cu'_{In}, Cu''_{In}, $\mathcal{V}^{x}_{In}$, $\mathcal{V}^{\cdot}_{In}$, $\mathcal{V}^{\cdot\cdot}_{In}$,
$\mathcal{V}^{\cdot\cdot\cdot}_{In}$, $\mathcal{V}^{x}_{Se}$, $\mathcal{V}^{\cdot\cdot}_{Se}$, Cu^{x}_{i}, $Cu^{\cdot}_{i}$, $Cu_{i} \oplus \mathcal{V}_{Cu}$, $Cu_{In} \oplus In_{Cu}$, $(2\,\mathcal{V}_{Cu} \oplus In_{Cu})_{\beta 13}$}

$\alpha\beta$L⟦3⟧ ===
{$\mathcal{V}_{Cu} \oplus In_{Cu}$, $(\mathcal{V}_{Cu} \oplus In_{Cu})^{\cdot}$, $(2\,\mathcal{V}_{Cu} \oplus In_{Cu})_{\alpha}$, $(2\,\mathcal{V}_{Cu} \oplus In_{Cu})_{\beta 15}$, $(2\,\mathcal{V}_{Cu} \oplus In_{Cu})_{\beta 25}$}

ncL = {1, 3, 5}; Dimensions[ncL] === Dimensions[$\alpha\beta$L]

To model solid phase equilibria the lattice building unit basis $\alpha\beta$L must be extended to quantify and characterize the transfer of physical constituents from this lattice to other phases that are in equilibrium with the lattice.

cEgrouped = {$\alpha\beta$L, {e′, h•}, ΔN, {Cu_{Cu2Se}, Cu2.δSe}};

The crystallographically incoherent secondary phase constituents which will be utilized in this model have been appended, and band-delocalized charge carriers added to construct a complete basis for the state vector, which will enable the modeling of phase segregation and electronic carrier concentrations in the equilibrium system. The basis element ΔN allows for changes of the sublattice site proportionality multiplier N independent of phase segregation processes, since vacancy generation on all sublattices (lattice expansion) is a physical mechanism whereby the total free energy of the lattice might be reduced even in the absence of a secondary phase.

The domain of this analysis is limited to the compositional range of greatest relevance to applications to photovoltaics, with Cu/In molar ratios in the range: $\frac{1}{3} \leq X \leq 1$. The case of X= 1 and Z= 1, which corresponds to the ideal stoichiometric compound $CuInSe_2$ is first analyzed. The second case will be for $\frac{1}{2} \leq X < 1-\epsilon$, corresponding to the α, β, and intermediate $\alpha + \beta$ two-phase regions [26]. Despite the present uncertainty regarding the exact crystallographic structure of the β phase, it is mostly agreed [40] that it must be closely related to the chalcopyrite structure. This structure persists between the putative α/β phase boundary composition (X=$\frac{1}{2}$), which corresponds to the compound $Cu_2In_4Se_7$, through at least those compositions corresponding to the compound $CuIn_3Se_5$ (X=$\frac{1}{3}$). Within the restricted limits of this second case the total number of lattice sites in the system (including interstitial sites) remains constant, at least in the absence of valency stoichiometry deviations from

zero. This structural coherence between the α and β phases has extremely significant ramifications which will be addressed at a later point in this treatise.

The temperature domain of these calculations is restricted to below 1048.15K (750°C) in the first case and 873.15K (600°C) for the second case. This minimizes the complications introduced by the high temperature order/disorder phase transformations of the α phase at 1083K [20] and the β phase at 873K [27].

The details of the interphase and defect equilibria calculations are included in the appendix to this dissertation, including all the *Mathematica* code required to verify the results.

Results

The results of these calculations are divided into two major subsections. The first details the predicted phase diagrams and the composition of the two different phases found in equilibrium with α–CIS over the domain of this calculation, $Cu_{2-\delta}Se$ and β–CIS. The second describes the calculated equilibrium defect concentrations within α–CIS, and their variations with composition and temperature.

Interphase Reaction Equilibria

The predicted equilibrium phase diagram for the Cu–In–Se ternary phase field along the Cu_2Se/In_2Se_3 tie-line where Z= 1 is shown below as a function of the atomic fraction of copper and temperature.

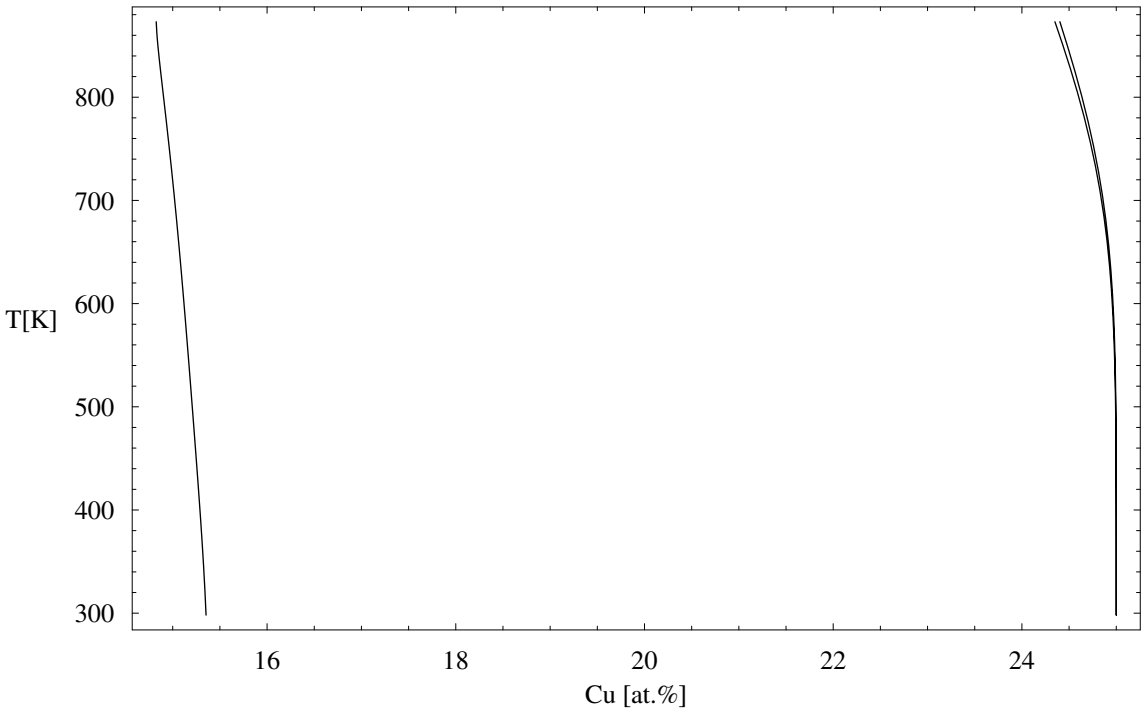

Figure 2.1 Calculated equilibrium phase diagram for the Cu–In–Se system on the Cu_2Se/In_2Se_3 section where Z= 1

Two dominant features of this model's predictions are clearly consistent with the published experimental phase diagrams. The location of the α/β–CIS two-phase boundary at STP is predicted to be at 15.35 at.% copper (X= 0.4987), corresponding almost exactly to the widely reported β–CIS compound formula $Cu_2In_4Se_7$. The curvature of the copper-rich α/β–CIS two-phase boundary towards lower copper content with increasing temperature has also often been reported, although usually to a much greater extent than found here.

The most striking inconsistency of this diagram with published data are the narrow width of the predicted single-phase α domain and curvature with increasing temperature of both the indium-rich α/β–CIS and Cu_2Se/α–CIS two-phase boundaries in the same direction, towards lower copper content.

The detailed discussion of these results in the following subsections will argue that these inconsistencies are mostly a consequence of two factors. The first is the inadequacy of the limited, four-species basis used to model the energetics of the β–CIS phase. The second is that the lowest free energy state of the system is in fact displaced from this pseudobinary section of the ternary phase field towards a small selenium enrichment ($Z \gtrsim 1$), on a scale below the resolution of current chemical composition analysis methods.

The effect of such deviations were explicitly modeled for the two-phase Cu_2Se/α–CIS boundary. Those results show a significant increase in the width of the α–CIS single-phase homogeneity range, and also imply the existence of a kinetic barrier to Cu_2Se/α–CIS equilibration at temperatures below ~100°C that would inhibit the conversion of excess Cu_2Se into α–CIS, creating an apparent shift of this boundary towards lower copper content.

Stoichiometric $CuInSe_2$ and the $Cu_{2-\delta}Se/\alpha$–CIS phase equilibrium

These $Cu_{2-\delta}Se/\alpha$–CIS equilibrium calculations have been constrained by an energy sum rule, which requires that the total Gibbs energy of any Cu–In–Se mixture with a composition corresponding to $CuInSe_2$ must at every temperature equal a reference value which has been calculated from three empirical published relations for the thermodynamic properties of $CuInSe_2$. Their values are given explicitly in the appendix and include the Gibbs energy at a reference temperature near the α/δ–CIS eutectoid [173], the standard state entropy [174], and the temperature dependence of the heat capacity [175].

A mathematical model of the Gibbs energy dependence of $Cu_{2-\delta}Se$ with composition and temperature is used, which was derived as part of a recently completed assessment of the binary Cu–Se phase diagram [176]. It is assumed here that indium is completely insoluble in Cu_2Se and that α–CIS is in equilibrium with this phase over the domain of this calculation. Consequently, the constraints on compositional variation of the non-stoichiometric compound $Cu_{2-\delta}Se$ imposed by the other binary Cu–Se phases became implicit constraints within this equilibrium calculation. This is a direct consequence of the Gibbs phase rule, as the detailed analysis in the appendix shows, which implies that any unrestricted three-phase equilibrium in a ternary phase field is confined to a single combination of temperature and composition. Thus the two-phase boundaries within the Cu–Se phase field that define limits on the value of the $Cu_{2-\delta}Se$ stoichiometry deviation parameter δ restrict its ability to accomodate stoichiometry variations in a two-phase mixture that includes indium. Over the range of this equilibrium calculation, these constraints on δ are defined by the equilibrium between $Cu_{2-\delta}Se$ and a number of different binary Cu–Se phases.

Over the entire temperature range of interest, the $Cu_{2-\delta}Se$ binary copper selenide's copper-rich single-phase domain boundary is determined by its equilibrium with *fcc* Cu with a non-vanishing solubility of selenium [176]. Thus perfectly stoichiometric Cu_2Se is not stable to decomposition in the binary model, and the $Cu_{2-\delta}Se$ binary-ternary equilibrium composition is limited by the corresponding minimum value of δ, or equivalently, this binary compound's

minimum selenium content. This effect is most significant near the Cu:Se/α–$Cu_{2-\delta}Se$/β–$Cu_{2-\delta}Se$ peritectoid temperature of 396K (123°C). The following figure shows the results of the calculated deviation of δ from that minimum value if $Cu_{2-\delta}Se$ is assumed to be in equilibrium with stoichiometric $CuInSe_2$.

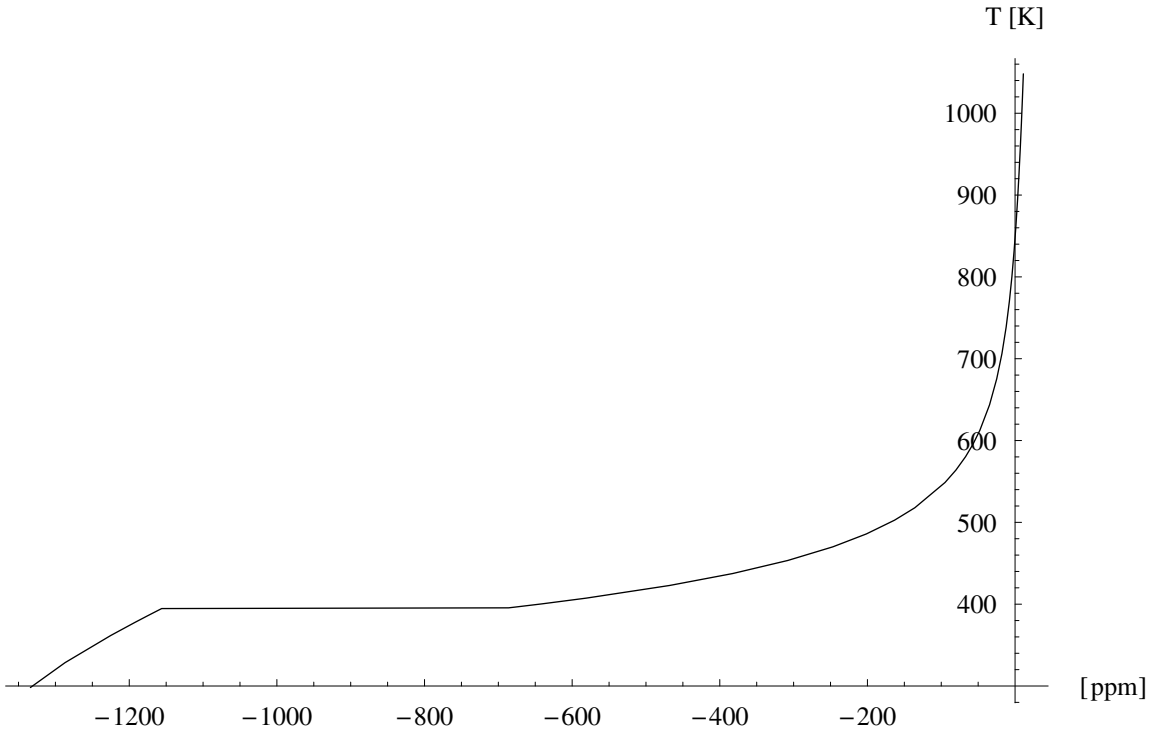

Figure 2.2 Calculated deviation of the $Cu_{2-\delta}Se$ stoichiometry parameter δ in hypothetical equilibrium with stoichiometric $CuInSe_2$

Figure 2.2 shows that without some mechanism whereby ternary α–CIS could accomodate stoichiometry variations, $Cu_{2-\delta}Se$ in equilibrium with $CuInSe_2$ would not be stable below a calculated temperature of ~850K with respect to segregation of the nearly pure metallic Cu phase found near the Cu vertex in the Cu–In–Se ternary phase triangle. Since such a three-phase equilibrium over that finite temperature range would violate the Gibbs phase rule, this cannot occur.

Figure 2.3 shows the results of the equilibrium calculation wherein the internal defect structure of the α–CIS phase, stoichiometry variation of the $Cu_{2-\delta}Se$ phase, and extent of phase segregation are varied to minimize the total Gibbs energy of the stoichiometric $CuInSe_2$ mixture. It shows that at high temperatures selenium will segregate preferentially to the binary phase, increasing δ above its minimum value. The temperature at which the equilibrium and constrained minimum values of δ are equal is lowered by the α–CIS internal defect equilibration to a value of 677K.

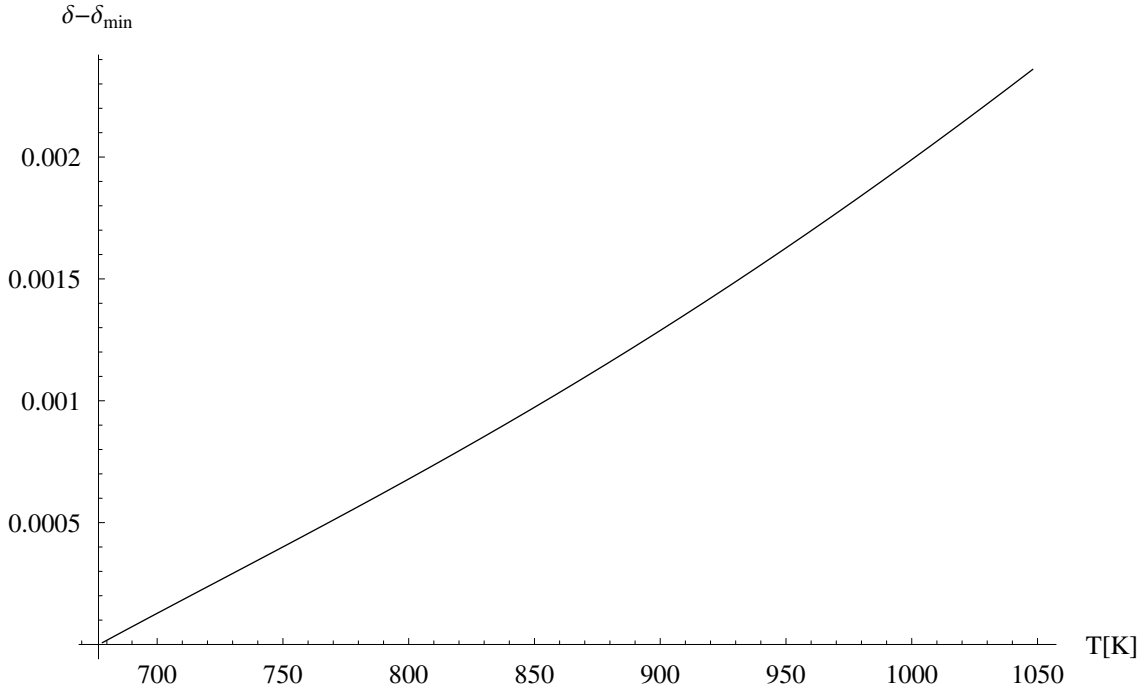

Figure 2.3 Deviation of the $Cu_{2-\delta}Se$ stoichiometry parameter δ from its minimum allowable value in equilibrium with defective ternary α–CIS in the stoichiometric $CuInSe_2$ mixture

Although this segregation of selenium in excess of its constrained minimum to the $Cu_{2-\delta}Se$ compound does not continue to lower temperatures in the stoichiometric mixture, the minimum value of the stoichiometry parameter δ_{min} is itself positive.

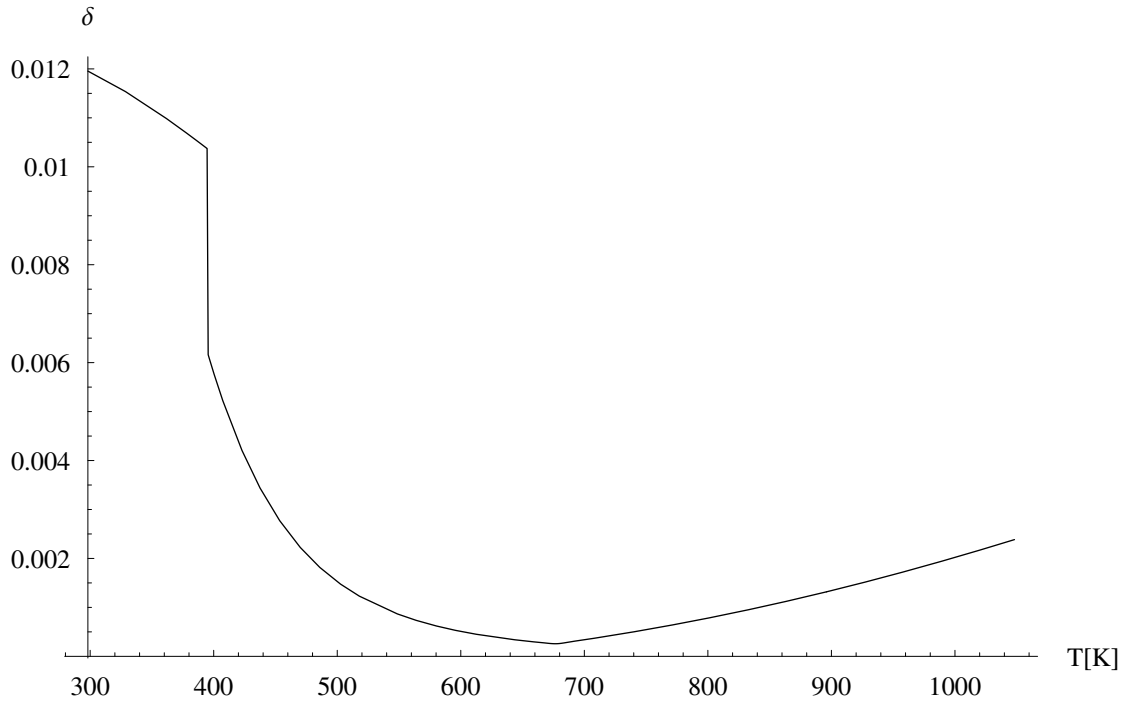

Figure 2.4 The $Cu_{2-\delta}Se$ stoichiometry parameter δ in equilibrium with α–CIS in the stoichiometric $CuInSe_2$ mixture

Figure 2.4 shows the total value of δ over the entire temperature range of this calculation. Note in particular its rapid increase in equilibrium as the temperature approaches the peritectoid from above. This also implies that the stoichiometric composition $CuInSe_2$ is not single phase at equilibrium. Figure 2.5 shows the calculated extent of phase segregation of this composition over the entire temperature range of this calculation. Clearly $Cu_{2-\delta}Se$ always segregates to some

extent, thus ideal stoichiometric ternary $CuInSe_2$ always dissociates in equilibrium to form the two-phase mixture.

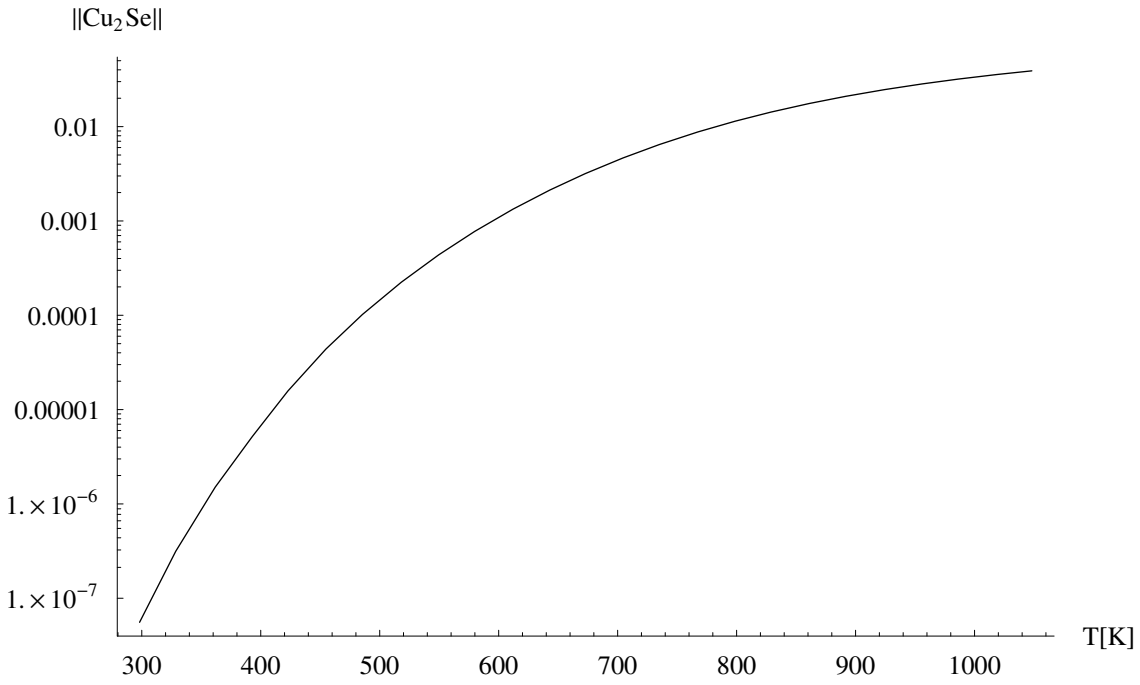

Figure 2.5 The equilibrium molar extent of binary Cu–Se phase segregation in the stoichiometric $CuInSe_2$ mixture

Since the stoichiometry deviation parameter δ of $Cu_{2-\delta}Se$ is positive, the segregation process always removes selenium from the remainder of the mixture at a rate more than half the rate at which copper is depleted. Hence this segregation process in the stoichiometric mixture creates negative valency deviation of the ternary phase in equilibrium, as shown in figure 2.6.

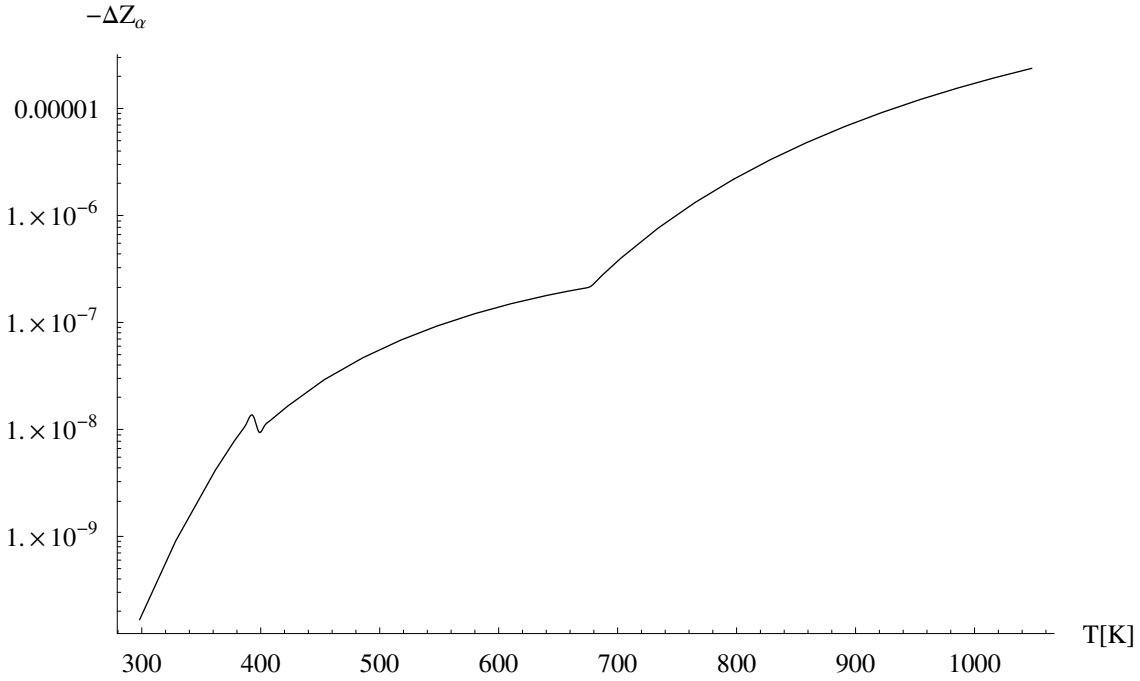

Figure 2.6 The negative valency deviation of α–CIS in equilibrium with the binary Cu–Se phase in the stoichiometric $CuInSe_2$ mixture

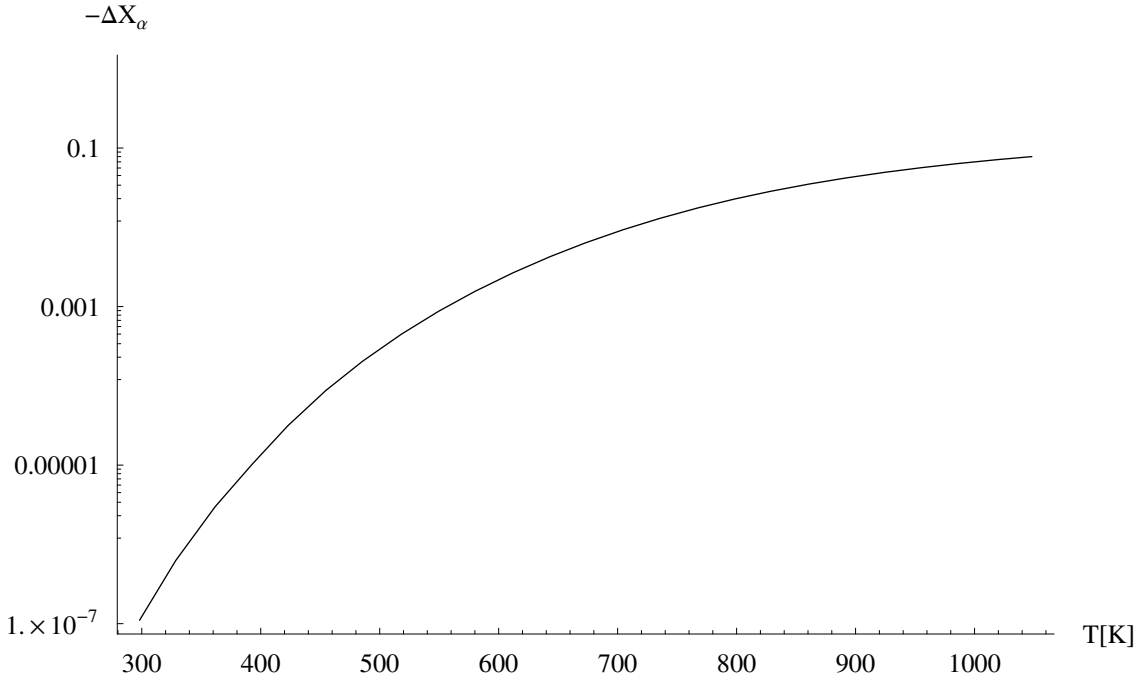

Figure 2.7 The negative molecularity deviation of α–CIS in equilibrium with the binary Cu–Se phase in the stoichiometric $CuInSe_2$ mixture

The segregation of $Cu_{2-\delta}Se$ does not remove indium from remainder of the mixture. Hence this segregation process in the stoichiometric mixture also creates negative molecularity deviation, as well as negative valency deviation of the ternary phase in equilibrium at this two-phase boundary, as shown in figure 2.7.

Two-phase regions are also present in the binary Cu–Se phase field that define an upper limit on the single-phase stability range of $Cu_{2-\delta}Se$. Over the entire temperature range, this boundary is defined by the equilibrium between $Cu_{2-\delta}Se$ and a number of different phases [176]. The maximum stoichiometry deviation of equilibrium $Cu_{2-\delta}Se$ occurs at a temperature of 650K, where its maximum selenium binary mole fraction rises to 36.8 at.%. Below that temperature it decreases monotonically, dropping to 36.0 at.% at the 291K α–$Cu_{2-\delta}Se$/β–$Cu_{2-\delta}Se$/Cu_3Se_2 eutectoid. The net result of both these upper and lower limits on δ is a significant narrowing of the homogeneity range of $Cu_{2-\delta}Se$ between 396K and 291K.

The equilibrium effects of positive valency deviation in the Cu–In–Se mixture were also modeled. As previously derived, the relationship between the valency deviation and excess selenium in the mixture is given by the relation $\Delta s = \frac{(Z-1)(3+X)}{1+X}$. All of these calculations were performed for a value of X= 1 in the mixture, so this relation reduces here to $\Delta s = 2\,\Delta Z$. The first issue of concern in these calculations was to properly include the effects of the constraints on the maximum allowable selenium content in the binary $Cu_{2-\delta}Se$ phase. It was found that the secondary phase composition first exceeds its maximum selenium content at STP when the value of ΔZ reaches about $+4.5\times10^{-6}$, as shown in figure 2.8.

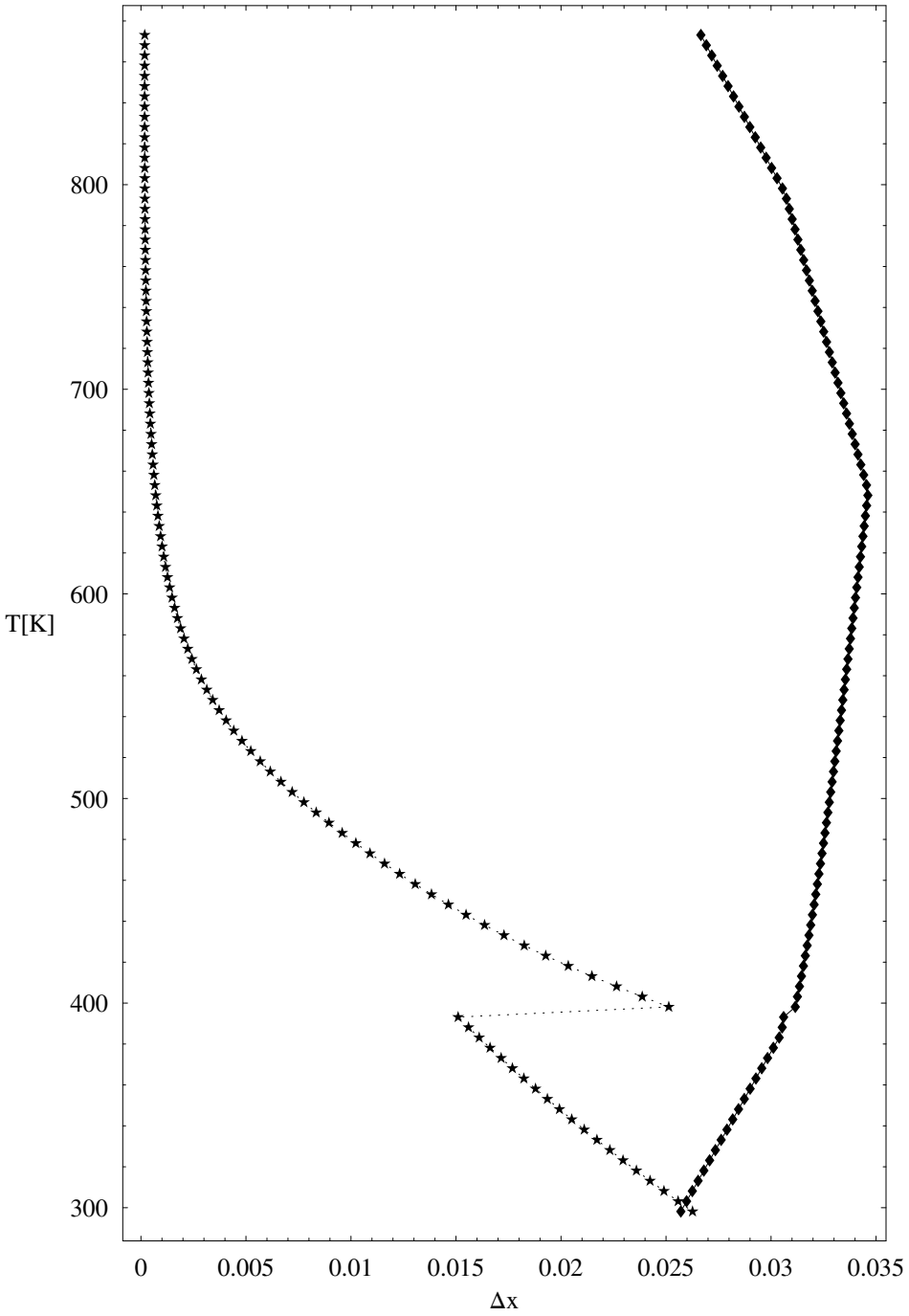

Figure 2.8 The equilibrium selenium mole fraction of the binary $Cu_x Se_{1-x}$ phase in the Cu–In–Se mixture with $\Delta X = 0$ and $\Delta Z = +4.5\times10^{-6}$ (left), and the temperature dependence of the maximum allowable selenium mole fraction (right)

Slightly greater selenium enrichment also yields a violation of this limit at the 395K Cu:Se/α–$Cu_{2-\delta}Se$/β–$Cu_{2-\delta}Se$ peritectoid. Figure 2.9 shows the specific Gibbs energy of the binary phase alone as a function of its selenium mole fraction both a few degrees above and a few below this peritectoid. The binary's composition variation with temperature in the ternary equilibrium is clearly a consequence of the energetic discontinuity at the peritectoid.

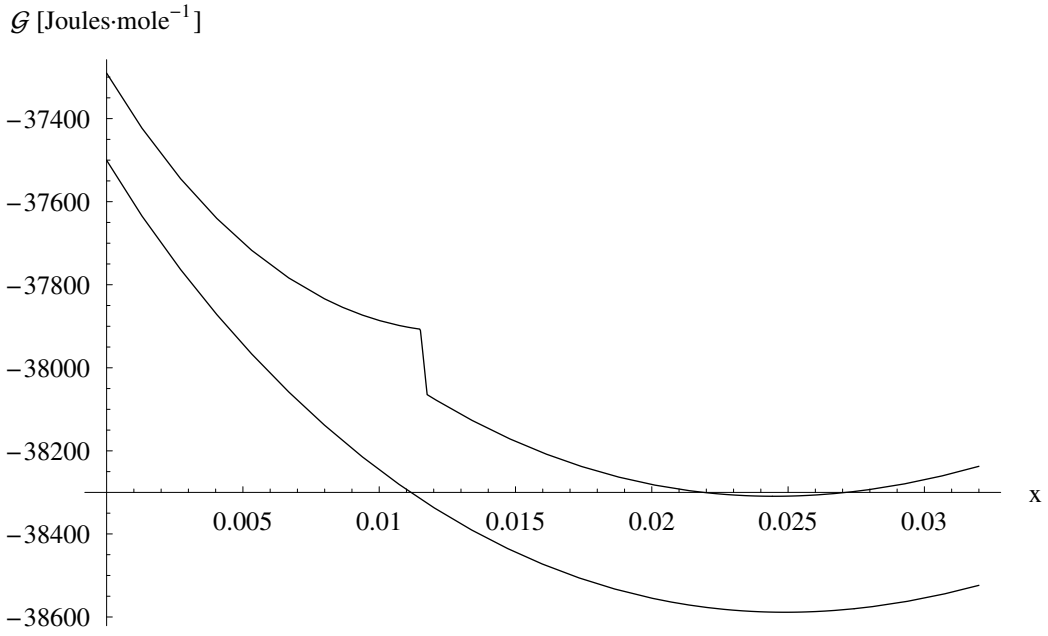

Figure 2.9 The variation of specific Gibbs energy with composition of the binary Cu_xSe_{1-x} phase at 393.15K (upper curve) and 398.15K (lower curve)

The constraint on the maximum selenium composition of the binary phase was incorporated into the calculations for all cases where $\Delta Z > 1$. The temperature at which the binary's selenium content saturates is found to increase up to $\Delta Z \simeq 0.1739$, at which point the secondary $Cu_{2-\delta}Se$ phase is found to possess its maximum selenium content over the entire temperature range from STP to the $\alpha/\beta/\delta$–CIS

eutectoid. Figure 2.10 demonstrates these results for several values of positive valency deviation.

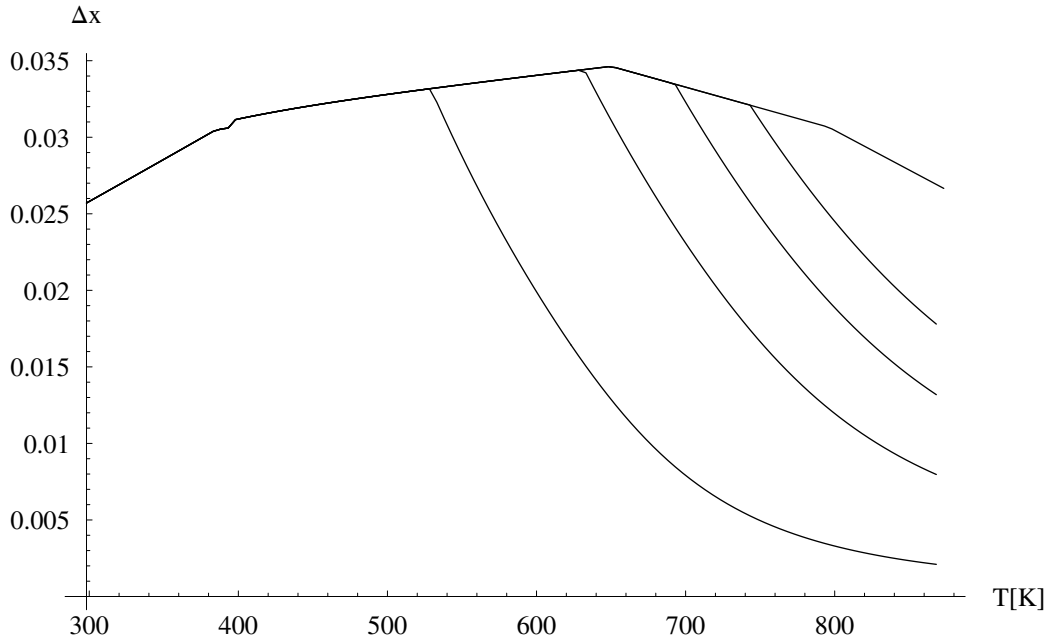

Figure 2.10 The deviation of equilibrium selenium mole fraction in the binary $Cu_x Se_{1-x}$ phase from its minimum constrained value in the Cu–In–Se mixture, with ΔX= 0 and (left to right) ΔZ= 100, 400, 700, 1000, and 1739 ($\times 10^{-6}$)

The results displayed in figure 2.5 for the calculated extent of $Cu_{2-\delta}Se$ phase segregation for the mixture with ΔZ= 0 were extended to a maximum of ΔZ= 0.22, corresponding to a selenium excess of 0.44 at.% in the two-phase mixture with X= 1. These results are displayed in figure 2.9, and clearly show a significant increase in the extent of binary segregation with increasing positive valency deviation in the mixture.

The large decrease in equilibrium solubility of the binary in the mixture with excess selenium through the final 150 degrees above STP during cool-down after synthesis may represent a significant kinetic barrier to equilibration. Either a net flux

of copper and selenium into the indium-enriched ternary or a net flux of indium out of the ternary phase into the binary is needed to effect this transformation. Since the selenium sublattices of the two phases are nearly identical and selenium interstitials and antisites so energetically unfavorable, it is unlikely to redistribute. The relative strength and covalency of the In–Se chemical bond makes indium less mobile than copper, particularly in this low temperature range. Thus synthesis under conditions of high selenium fugacity may not fully equilibrate if their composition pass through the equilibrium two-phase boundary corresponding to its composition during cool-down. Growth under conditions of indium excess may be more necessary in practice than the equilibrium phase boundaries suggest, in order to inhibit the formation of metastable binary copper selenide precipitates.

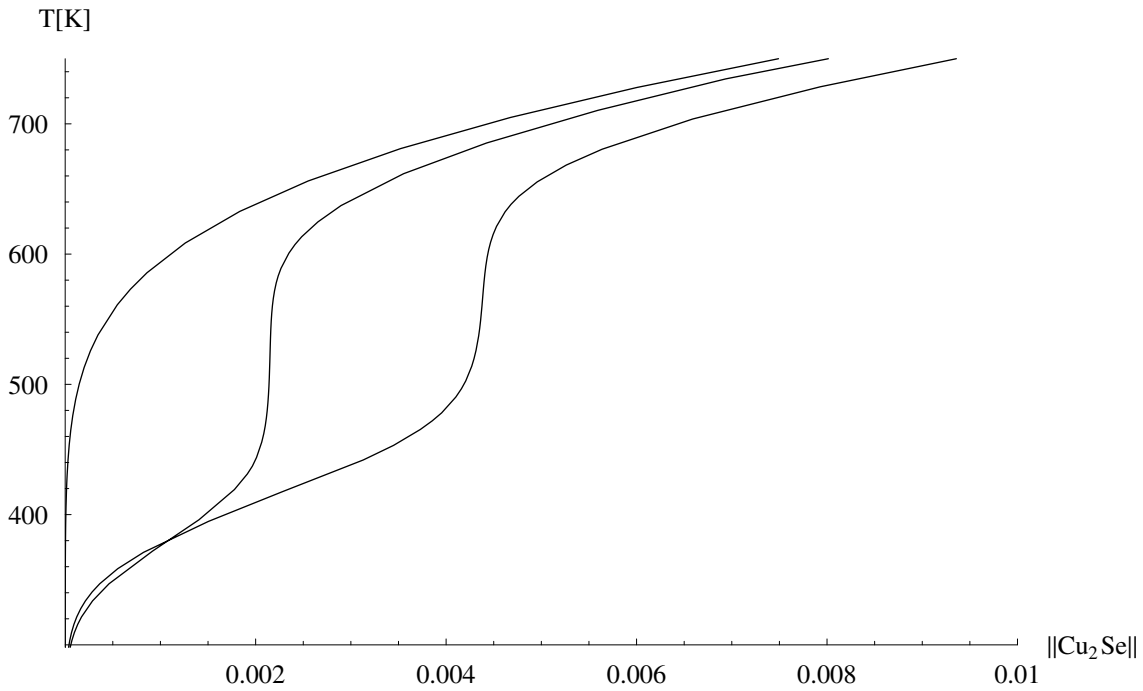

Figure 2.9 The equilibrium molar extent of $Cu_{2-\delta}Se$ phase segregation in Cu–In–Se mixtures, with $\Delta X = 0$ and (left to right) $\Delta Z = 0$, 0.11, and 0.22

This enhancement of $Cu_{2-\delta}Se$ phase segregation with increasing positive valency deviation in the two-phase mixture will exacerbate the consequent negative molecularity deviation of the α–CIS phase in equilibrium. Since the selenium content of that binary phase also increases with increasing positive valency deviation, so too the valency deviation of the ternary must decrease.

These calculations predict that a minimum of about 0.4 *ppm* excess selenium in the two-phase mixture is required to insure that the equilibrium valency deviation of the ternary α–CIS phase remains positive definite over the temperature range between STP and the peritectoid. Even more selenium is required at higher temperatures to inhibit selenium depletion of the ternary, as shown in Figure 2.10.

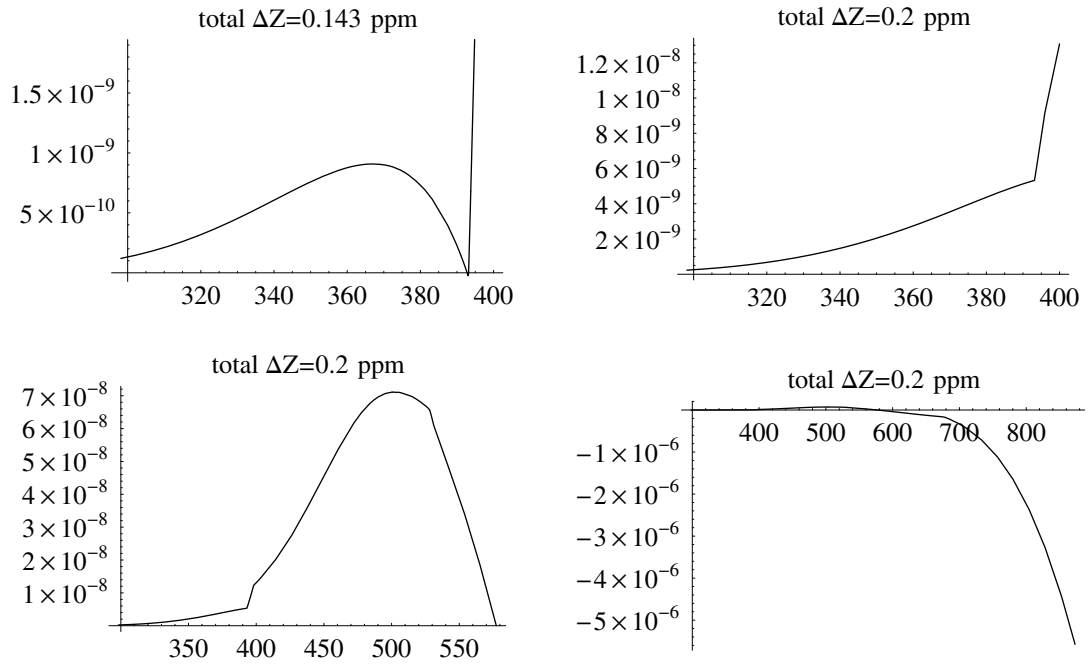

Figure 2.10 The valency deviation of α–CIS in equilibrium with $Cu_{2-\delta}Se$, with $\Delta X = 0$ and $\Delta Z = 0.143$ or 0.2 ($\times 10^{-6}$)

Although the relationships between the valency deviation of the two-phase mixture and those in each of its constituent non-stoichiometric phases are very complex, they are single-valued. Hence it was possible to invert them and calculate the valency deviation in the mixture required to yield a specified valency in its ternary α–CIS component. Figure 2.11 shows one example, demonstrating the temperature dependence of the valency deviation of the mixture with X= 1 that is required to keep the α–CIS phase valency fixed at its equilibrium value in the mixture at STP. This is equivalent to varying the two-phase mixture's values of X and Z to find those values at which the extent of $Cu_{2-\delta}Se$ phase segregation becomes infinitesimally small in equilibrium with the ternary at its specified molecularity.

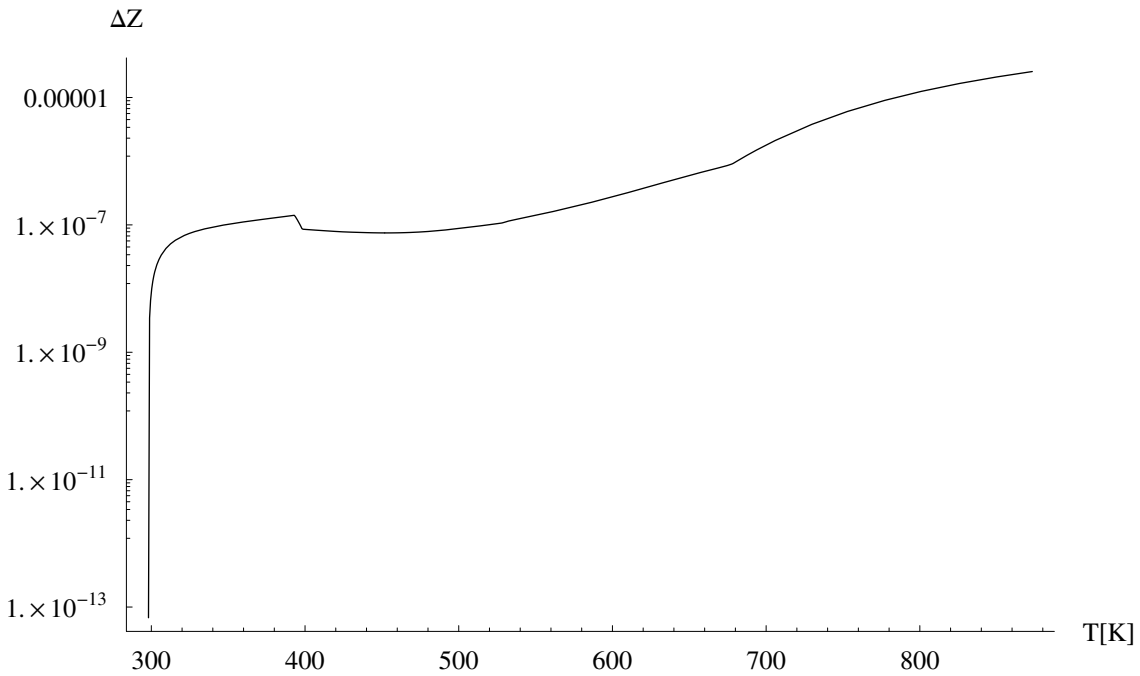

Figure 2.11 The valency deviation of the two-phase mixture with X= 1 required to maintain the valency of the α–CIS component at its STP value.

Thus the two-phase boundary value of molecularity can be determined from the two-phase equilibrium calculations at X= 1. Simplistic application of the "lever-arm rule" to this situation would give an incorrect answer, without prior knowledge of the locus of the lever's fulcrum, which effectively varies with temperature and does not lie in the T–X plane except at the phase boundary itself. This is a consequence of the non-stoichiometry of both these phases in equilibrium.

The domain over which the two-phase boundary can be calculated by this method is restricted by the range of the mapping between Z and Z_α over the domain of the two-phase calculation for X= 1. The domain of the two phase calculation between $0 \leq \Delta Z \leq 0.22\%$ maps into the range $0 \leq \Delta Z_\alpha \lesssim 0.1\%$, corresponding to a maximum excess selenium content in the single-phase ternary of about +0.2 at.%. The calculated phase boundaries both on the pseudobinary section ($\Delta Z = 0$) and in the T–X plane where $\Delta Z = +0.1\%$ are compared in figure 2.12.

Comparing the two curves in figure 2.12, the increase in valency deviation of +0.1% has yielded a shift of less than -0.01% in molecularity at STP, but a nominal shift of -0.4% in the temperature range of ~450–600K. Comparison with the extent of binary phase segregation in figure 2.9 makes it clear that this is a direct consequence of that process.

The phase boundaries shown in figure 2.12 are more easily compared to the published literature data when expressed in terms of the atomic fraction of copper, as in figure 2.13.

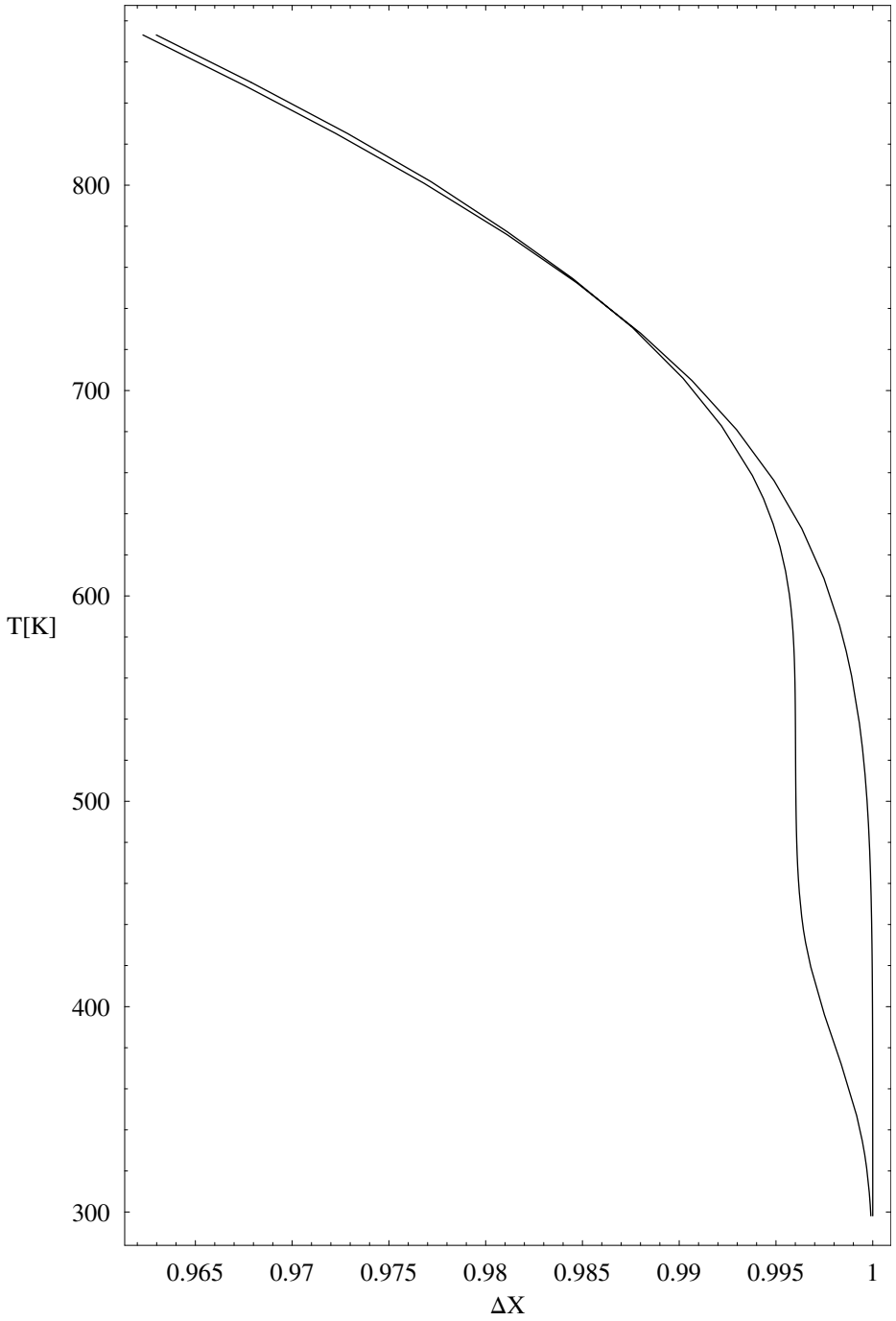

Figure 2.12 Calculated equilibrium $Cu_{2-\delta}Se/\alpha$–CIS phase boundaries in the Cu–In–Se system for ΔZ= 0 (right) and ΔZ= +0.1% (left) between STP and the $\alpha/\beta/\delta$–CIS eutectoid

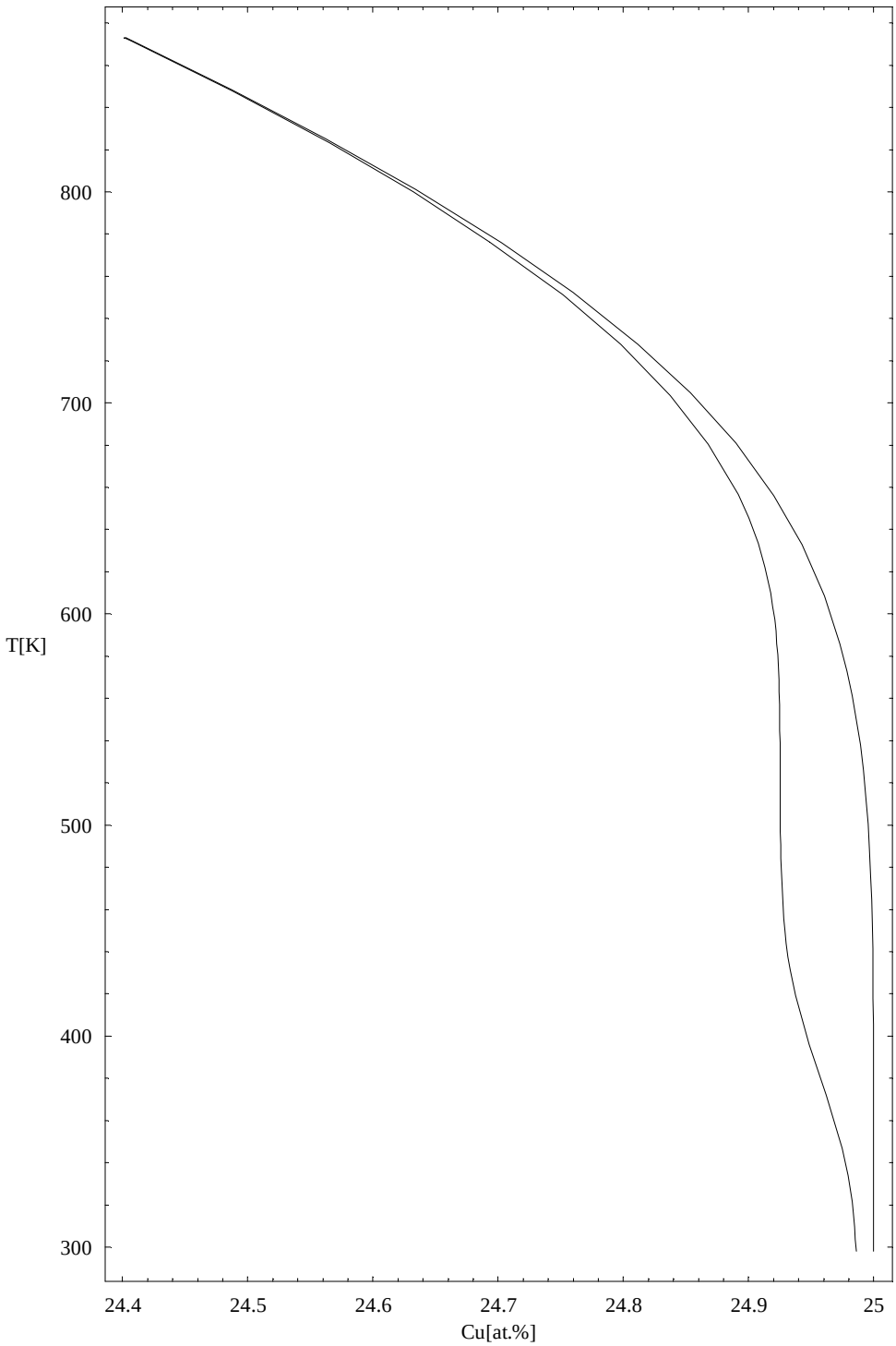

Figure 2.13 Copper composition at the equilibrium $Cu_{2-\delta}Se/\alpha$–CIS phase boundaries in the Cu–In–Se system for $\Delta Z = 0$ (right) and $\Delta Z = +0.1\%$ (left) between STP and the $\alpha/\beta/\delta$–CIS eutectoid

Figure 2.13 demonstrates that an increase in valency deviation of +0.1% yields a decrease of about three-quarters that amount in terms of the copper atomic fraction in the temperature range of ~450–600K, and less than one-fifth that amount at STP. Returning briefly to the issue of metastability, the preceding conjecture that growth under conditions of indium excess would circumvent the kinetic barrier to equilibration presented by this phase segregation process is empirically supported by comparison with the limiting composition at the eutectoid. That value does not shift with valency deviation, and is found to be 24.4 at.% copper, nearly identical to the most recently reported experimental estimate of the phase boundary [27, 277].

Finally, the solution for the internal defect equilibria within the α–CIS at the $Cu_{2-\delta}Se/\alpha$–CIS phase boundary molecularity value, and with valency deviation of up to 0.1% were computed. These are combined with the chemical potentials of the model's species to calculate the total specific Gibbs energy of α–CIS at this two-phase boundary. Figure 2.14 shows the difference between that value calculated at each temperature and valency and its value at the same temperature on the pseudobinary section.

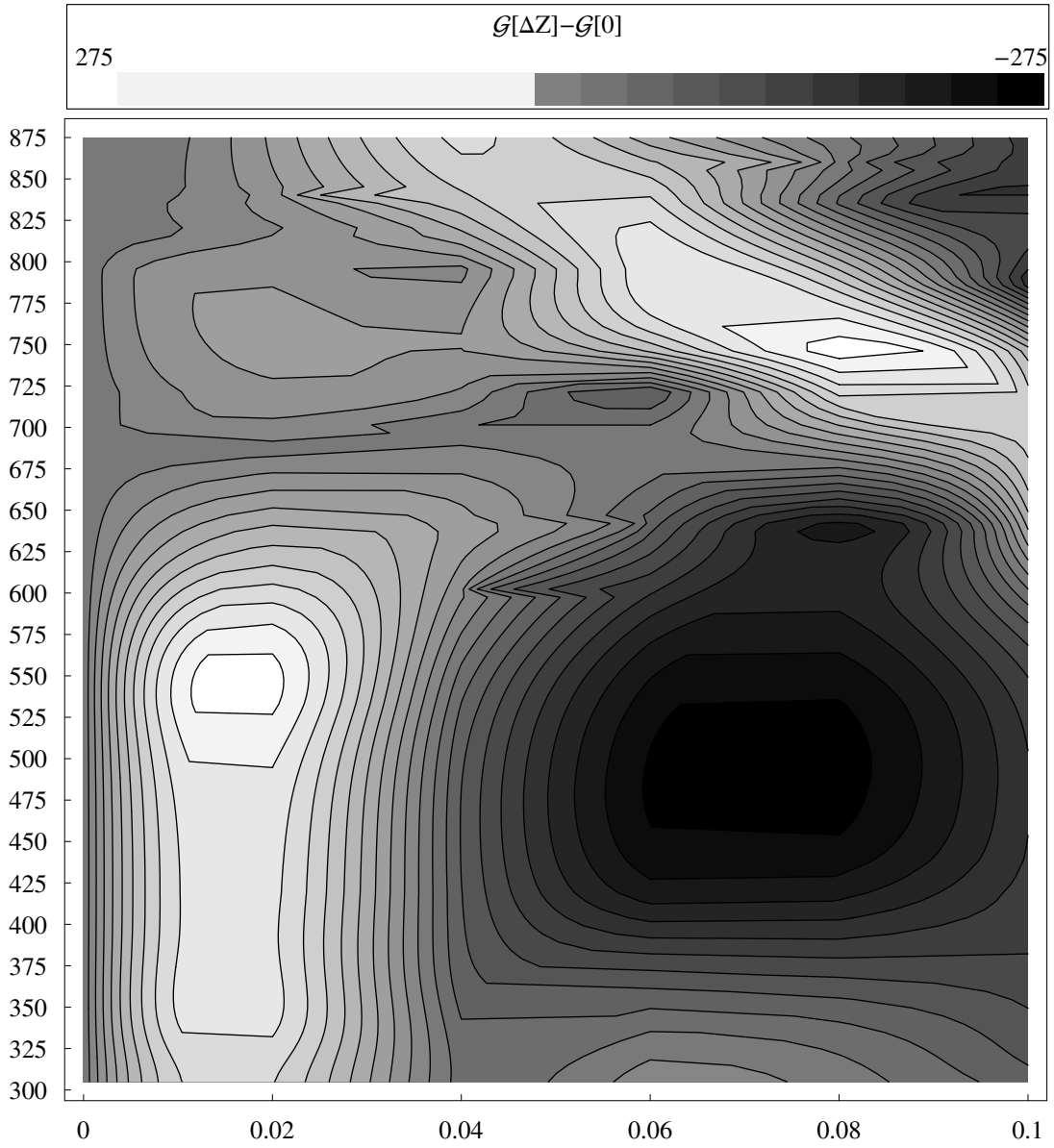

Figure 2.14 Temperature variation of the specific Gibbs energy deviation of α–CIS from its value at $\Delta Z = 0$ on the $Cu_{2-\delta}Se/\alpha$–CIS two-phase boundary. Valency deviations between $0 \leq \Delta Z_\alpha \leq 0.1\%$ and temperatures between STP and the $\alpha/\beta/\delta$–CIS eutectoid are shown.

This figure reveals a free energy barrier to the incorporation of excess selenium at temperatures below ~670K (400°C), and shows that below this temperature the minimum in total Gibbs energy lies at about $\Delta Z_\alpha \simeq 0.07 \pm 0.03\%$.

That corresponds to about 0.1–0.2% excess selenium, very near the absolute calibration and resolution limit of chemical analysis methods for the principal constituents of nonstoichiometric multinary solids. The total Gibbs energy of α–CIS is also seen to be independent of valence stoichiometry deviation at the same temperature above which the binary copper selenide phase begins to absorb selenium in excess of its constrained minimum, as previously identified in figure 2.3.

This result provides useful insight into the two-temperature processes often used for the synthesis of thin-film absorber materials for photovoltaic applications. Although CIS is rarely used for these purposes as a pure material nowadays, the earliest breakthrough in the synthesis of these films for photovoltaics [177] was based on a two-step process beginning with a two-phase copper selenide/α–CIS mixture grown at about 625K with a large [Se]/([Cu]+[In]) flux ratio, and subsequently heated to about 725K while indium was added in excess to convert the copper selenide. The defect structure of the α–CIS phase in equilibrium at this free energy minimum off the pseudobinary section at the two-phase boundary is dramatically different than its structure on the stoichiometric side of the barrier that separates them. In particular, the acceptor–donor compensation ratio is reduced from unity to almost zero at this minimum. This observation will be elaborated in the subsequent subsection on the ternary's defect structure in equilibrium.

The α–CIS/β–CIS phase equilibrium

The intent of this part of the modeling was to test the relevance of a published model for the defect structure of the β–CIS phase [70], which suggested that it is forms

as a consequence of the short-range ordering of the cation NDC. Their first-principles quantum-mechanical calculations of defect formation and ordering enthalpies were used explicitly to calculate the deviation of the enthalpies of the defect species in this model from that of the ideal chalcopyrite CIS unit cell. This model has extended those results by means of a statistical mechanical model that combines the internal entropies of those lattice point-defect and their associates within their respective clusters, with a regular solution theory for the entropy of those clusters' mixing on the lattice, to calculate the Gibbs free energy of the entire lattice. This calculation was described more fully in the introduction of this chapter and is detailed in the appendix to this dissertation.

The simplest possible model that could be used within the framework of this formalism to test that hypothesis requires a total of six independent species. Inasmuch as the α and β–CIS lattices are coherent, no quasichemical reaction between them can remove lattice sites from the system, so it is uneccessary to include lattice site multiplier in the basis. The NDC species is neutral, so charge is conserved in its exchange between the two and charge does not need to be explicitly included as a conserved quantity. Thus only three conserved quantities need to be considered, the total initial amount of the three elements copper, indium, and selenium. However, since the valency of the NDC clusters are unity the exchange of these species between the two phases cannot change the valency of either phase. Expressed differently, the exchange of selenium is independent of copper and indium exchange with only a single species that does not contain selenium, so only two parameters are required to

insure the conservation of all three species. With pressure fixed, as in all these calculations, this leaves only temperature as the other independent thermodynamic variable required to model this equilibrium, for a total of three. By using six species, three degrees of freedom remain, permitting the composition of each phase and their respective mole fractions to be determined in equilibrium.

The α–CIS phase is represented in this part of the model as a secondary phase in the same manner as Cu_2Se was in the preceding two-phase equilibrium model, with its specific Gibbs energy given by the sum of two contributions, one associated with a reference composition and the other by a species with the correct stoichiometry to quantify the exchange of conserved quantities between the two phases. In this case those species are a single formula unit of the $Cu_{\frac{2X\alpha}{1+X\alpha}}In_{\frac{2}{1+X\alpha}}Se_{\frac{Z(3+X\alpha)}{1+X\alpha}}$ quasimolecular specie with its composition equal to its solution value on the tie-line at the $Cu_{2-\delta}Se/\alpha$–CIS phase boundary, and the other species' stoichiometry given by the same formula evaluated with the molecularity value of the NDC cluster species in the building unit model for α–CIS. Neither of these are equivalent to any building unit in that former model, any more than the two species used to model the composition and temperature dependence of the binary copper selenide phase's Gibbs energy was related to the sublattice solution model employed to derive its thermodynamic properties. However, the molecularity dependence of the α–CIS phase's Gibbs energy is given here by the solution of the building unit model on the pseudobinary section.

The β–CIS phase is represented by a four-specie building unit model. The first

specie is simply the chalcopyrite unit cell, energetically identical (in its reference state) to that used to model the α–CIS phase. The second species has the same stoichiometry as the NDC cluster species used in the α–CIS phase building unit model, but is assigned a formation enthalpy of zero, based on unpublished calculations provided by S.–H. Wei, a coauthor of the original model which this calculation was intended to elaborate [70]. The other two species correspond to one or two NDC associated with different cluster sizes, both effectively more concentrated on the lattice than the stoichiometrically identical species shared by the α and β phase building unit models. The details of this formulation are given in the appendix. The salient features of this choice are that there are no implicit constraints on the composition of β–CIS between $\frac{1}{3} \leq X_\beta \leq 1$, and there are no lattice defects other than the NDC.

As described in the introductory paragraphs of this chapter, the indium-rich α/β–CIS two-phase boundary at STP is predicted to be at 15.35 at.% copper ($X = 0.4987$), corresponding almost exactly to the widely reported β–CIS compound formula $Cu_2In_4Se_7$ and the empirical two-phase boundary at STP [18,20,22,23,26,27]. This result is remarkable in view of the facts that none of the building unit species in this model obtain that characteristic composition, and no empirical data regarding the β–CIS phase is included whatsoever. The accuracy of the result of combining the quantum and statistical mechanics to model this phase equilibrium is a compelling confirmation of the hypothesis that the dominant physical process in the formation of the β phase of CIS is indeed the aggregation of the NDC.

The more detailed α–CIS phase defect model provide insight into the failure of this model to correctly predict the reported curvature of this phase boundary towards higher copper fractions with increasing temperatures. In the former case, the NDC is found to dissociate to a large extent into its constituent subspecies $\mathcal{V}'_{Cu}$ and $(\mathcal{V}_{Cu} \oplus In_{Cu})^{\bullet}$, the dominant electrically active defects. This would likely occur to some extent in a more comprehensive model of the β phase, but it raises more subtle questions about ordering and metastability regarding the experimental evidence used to identify the phase boundary itself.

If X-ray diffraction is used to characterize phase composition, it is essential that the coherence length of the order parameter in the material be at least comparable to the wavelength, else the constructive interference that contributes to the concentration of its scattering into the angles identified as peaks instead of background will be diminished. The enthalpy reduction that underlies the point defect associate formation characterized here as the NDC is a result of the Madelung interaction between the defects, a Coulombic interaction whose long-range net effective charge is null by virtue of the particular combination of 2 $\mathcal{V}'_{Cu}$ and an $In^{\bullet\bullet}_{Cu}$ in their normal valence states. The minimum correlation length implicit in this random mixing model of clusters with a maximum extent of five chalcopyrite unit cells is quite small. Those compositions within the β phase consistent with regular ordering over a shorter periodic length scale may be more apparent in XRD.

When thermal transient techniques (*e.g.*: DTA) are used to characterize this phase transformation the question of kinetic barriers to equilibration must be

addressed. Aggregates of the $2\mathcal{V}_{Cu} \oplus In_{Cu}$ complex yield a local composition fluctuation of the lattice that cannot be created simply by local depletion of copper to form $\mathcal{V}_{Cu}$ defects. The formation of In_{Cu} by a shift within neighboring coordination tetrahedra of $In_{In}^{\times}$ to occupy $\mathcal{V}_{Cu}$ leaves $\mathcal{V}_{In}$, a defect found in these equilibrium calculations to be so energetically unfavorable that it is virtually absent at all temperatures in the range of α/β–CIS two-phase equilibrium. The $\mathcal{V}_{In}$ tend to be annihilated by the formation of a common defect in the lattice equilibrium calculations, Cu_{In}, yielding $\mathcal{V}_{Cu}$ and the $In_{Cu} \oplus Cu_{In}$ complex in *lieu* of $2\mathcal{V}_{Cu} \oplus In_{Cu}$. This moderation process is mitigated in regions of the lattice wherein the spatial density of indium exceeds its stoichiometric value, but the formation of such composition fluctuations by diffusion of indium may represent a significant kinetic barrier to equilibration, given the strength and covalency of the In–Se bond.

Finally, this model has predicted that in the case of $Cu_{2-\delta}Se/\alpha$–CIS equilibrium the Gibbs energy minimum lies towards positive valency deviation at their phase boundary, and that a significant shift in the boundary results from that deviation. Calculation of the α/β–CIS equilibrium off the pseudobinary section may have an effect on the locus of this phase boundary as well, and possibly reduce the discepancy between the modeled boundary and results of experimental studies. Extension of the β–CIS defect model to incorporate species whose stoichiometry is consistent with valency deviation (unlike the NDC) would be required.

Equilibrium Defect Concentrations in the Cu–In–Se α Phase

The generation of lattice defects is a mechanism whereby the crystal can accomodate nonstoichiometry, or reduce its Gibbs energy below its value in the ideal stoichiometric crystal, a consequence of the entropic contribution to the Gibbs energy. These effects are quantified in the solution of this model for the equilibrium defect structure of the lattice. The empirical reference value of the Gibbs energy of stoichiometric $CuInSe_2$, which provided the energetic boundary condition for these calculations, was assumed to correspond to the properties of the equilibrium Cu–In–Se mixture with this stoichiometry. From the solution, the specific Gibbs energy of the hypothetical defect-free stoichiometric chalcopyrite α–$CuInSe_2$ crystal was calculated. The results shown in figure 2.15 demonstrate that the deviation of the ideal crystal's specific Gibbs energy from the reference value is positive definite, and it is therefore not the equilibrium state of the crystal.

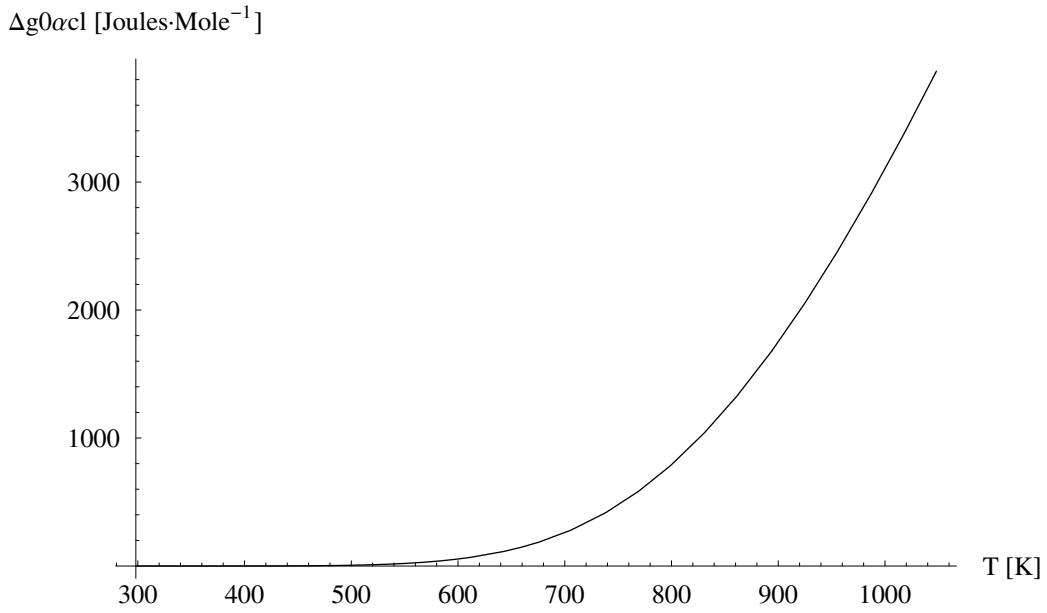

Figure 2.15 Temperature variation of the specific Gibbs energy deviation of an ideal chalcopyrite $CuInSe_2$ crystal from this model's reference value for the equilibrium stoichiometric mixture

The remainder of this section will describe the predicted equilibrium defect concentrations and their temperature dependence at three exemplary stoichiometries within the single-phase composition domain of α–CIS. These are the compositions at the phase boundary with α–CIS on the pseudobinary section, and at the phase boundary with $Cu_{2-\delta}Se$, both on the pseudobinary section, and with a positive valency deviation of 0.04. Inspection of figure 2.14 reveals that the latter two are nearly isoenergetic.

Lattice defects

The dominant lattice defects at all temperatures and molecularities within the single-phase domain on the pseudobinary section are the ionized NDC dissociation components, $\mathcal{V}'_{Cu}$ (figure 2.16) and $(\mathcal{V}_{Cu} \oplus In_{Cu})^{\bullet}$ (figure 2.17). On the pseudobinary section their concentrations are nearly equal, and they almost completely compensate one another, yielding electrically intrinsic material.

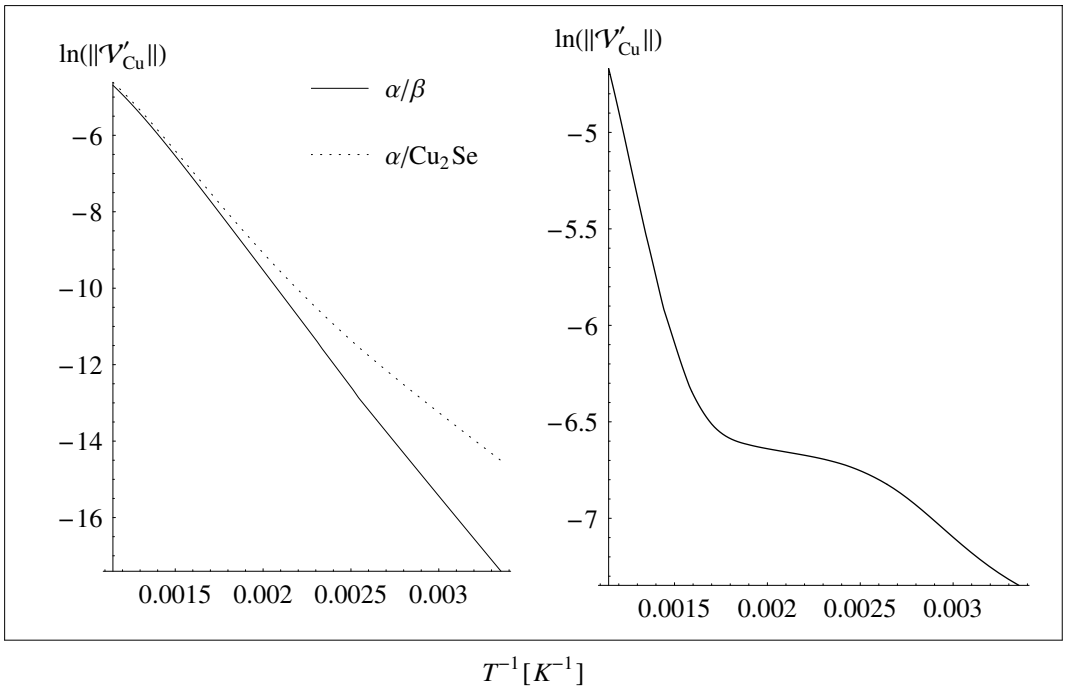

Figure 2.16 Temperature variation of the $\mathcal{V}'_{Cu}$ species mole fraction at the phase boundaries on the pseudobinary section (left) and with $\Delta Z = 4\times10^{-4}$ on the α–CIS/$Cu_{2-\delta}Se$ phase boundary (right)

The addition of about 0.08 at.% excess selenium to the α–CIS phase dramatically suppresses the formation of $(\mathcal{V}_{Cu} \oplus In_{Cu})^{\bullet}$ at temperatures below the 677K threshold where the selenium content of the binary phase drops to its minimum stable value, and as shown in figure 2.14, the specific Gibbs energy of the α phase is independent of valency deviations of this magnitude.

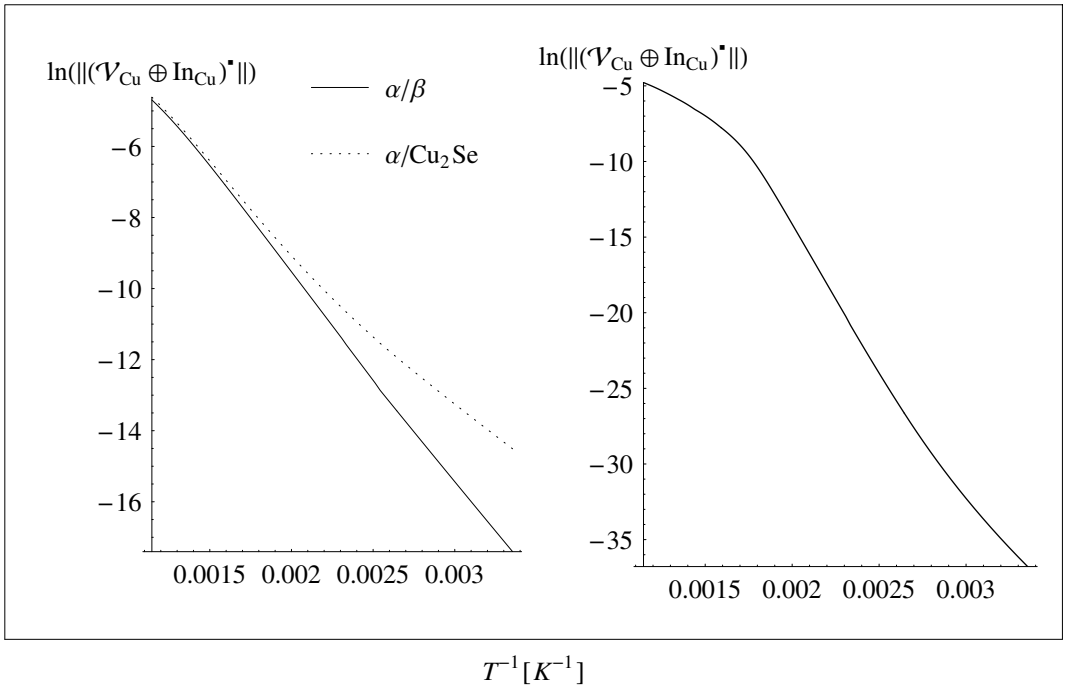

Figure 2.17 Temperature variation of the $(\mathcal{V}_{Cu} \oplus In_{Cu})^{\bullet}$ species mole fraction at the phase boundaries on the pseudobinary section (left) and with $\Delta Z = 4\times10^{-4}$ on the α–CIS/$Cu_{2-\delta}Se$ phase boundary (right)

Positive valency deviation also has a significant effect on the abundance of the NDC, as shown in figure 2.18. The similarity between the behavior of $(2\,\mathcal{V}_{Cu} \oplus In_{Cu})_{\alpha}$ and $(\mathcal{V}_{Cu} \oplus In_{Cu})^{\bullet}$ is a consequence of two phenomena. First, in equilibrium all of the In_{Cu} defects associate; the isolated defect vanishes. Second, almost all of these associates involve either one or two $\mathcal{V}_{Cu}$ defects, and their only other association option in this model is to form the antisite pair $In_{Cu} \oplus Cu_{In}$, which is relatively scarce in equilibrium. Hence the concentrations of both are dominated by the equilibrium extent of the quasichemical reaction:

$$(2\,\mathcal{V}_{Cu} \oplus In_{Cu})_{\alpha} \rightleftharpoons (\mathcal{V}_{Cu} \oplus In_{Cu})^{\bullet\square} + \mathcal{V}'_{Cu}$$

and the neutralization reactions for the partial NDC on the right-hand-side:

$$(\mathcal{V}_{Cu} \oplus In_{Cu})^{\times} \rightleftharpoons (\mathcal{V}_{Cu} \oplus In_{Cu})^{\bullet\square} + e'$$

The latter ionized dissociation reaction always goes to completion within the domain of this model, so the relative concentrations of $(2\mathcal{V}_{Cu} \oplus In_{Cu})_\alpha$ and $\mathcal{V}_{Cu} \oplus In_{Cu}$ are controlled entirely by the extent of the first reaction.

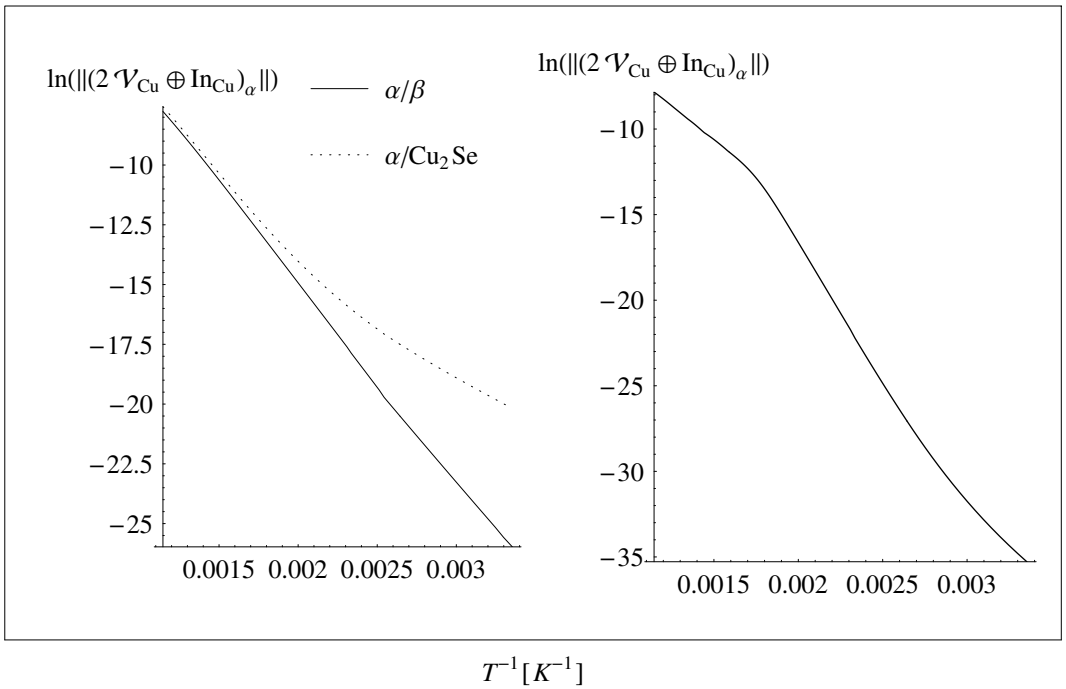

Figure 2.18 Temperature variation of the $(2\mathcal{V}_{Cu} \oplus In_{Cu})_\alpha$ species mole fraction at the phase boundaries on the pseudobinary section (left) and with $\Delta Z = 4\times10^{-4}$ on the α–CIS/$Cu_{2-\delta}Se$ phase boundary (right)

The relationship between the NDC and the $\mathcal{V}'_{Cu}$ species is not so direct, as a comparison of figures 2.16 and 2.18 shows, in spite of the symmetry between its role and that of $(\mathcal{V}_{Cu} \oplus In_{Cu})^{\bullet}$ in the NDC ionized dissociation reaction. Comparison of the ionized copper vacancy's behavior in figure 2.16 with that of the neutral shown in figure 2.19 does not clearly resolve this question.

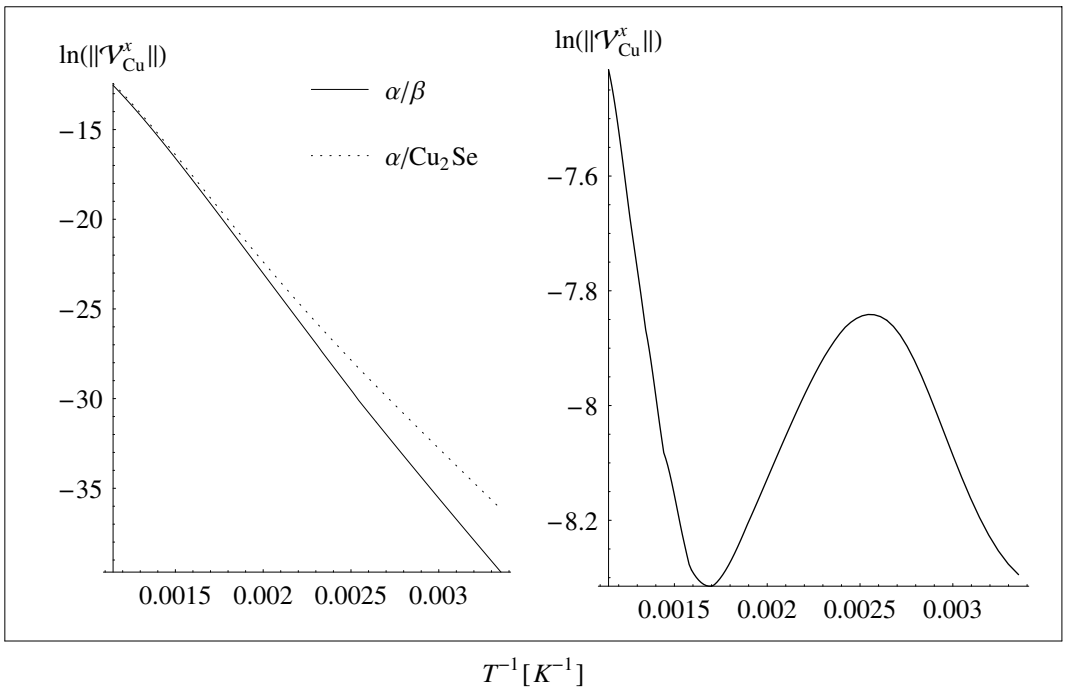

Figure 2.19 Temperature variation of the $\mathcal{V}^{\times}_{Cu}$ species mole fraction at the phase boundaries on the pseudobinary section (left) and with $\Delta Z = 4\times10^{-4}$ on the α–CIS/$Cu_{2-\delta}Se$ phase boundary (right)

Comparing figure 2.16 with figure 2.19 leads to the conclusion that the extent of the neutral copper vacancy ionization reaction:

$$\mathcal{V}^{\times}_{Cu} \rightleftharpoons \mathcal{V}'_{Cu} + h^{\bullet}$$

must vary greatly with temperature when excess selenium is incorporated into the lattice. The answer lies in the behavior of the isolated copper antisite $Cu^{\times}_{In}$, which vanishes on the pseudobinary section, but whose concentration becomes significant with positive valency deviation, as shown in figure 2.20.

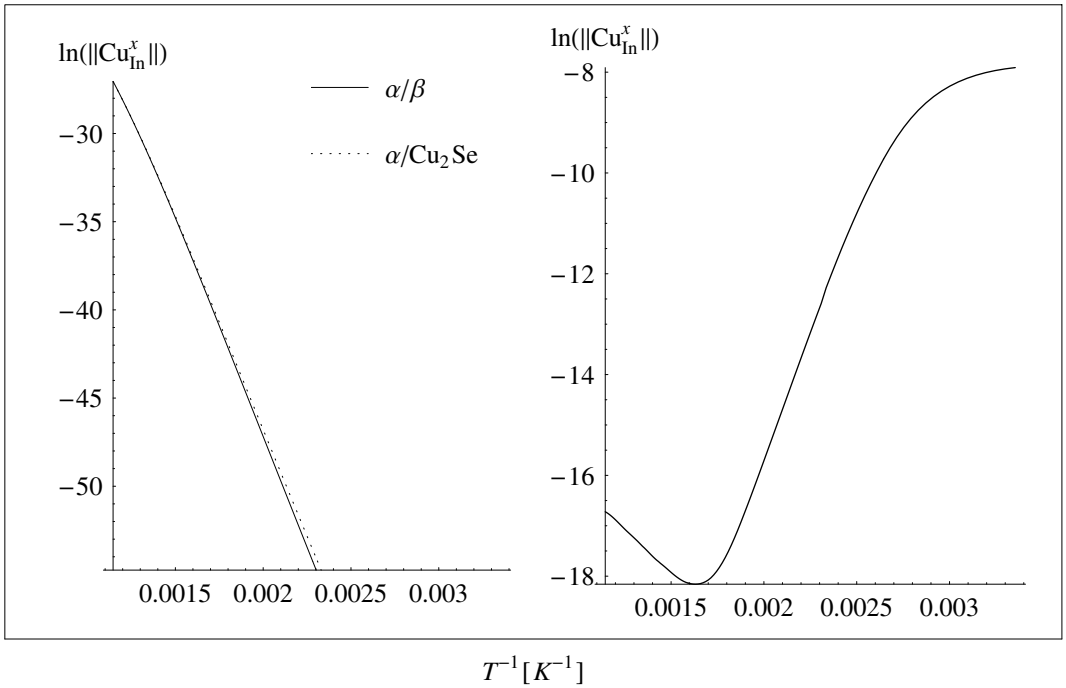

Figure 2.20 Temperature variation of the $Cu_{In}^{\times}$ species mole fraction at the phase boundaries on the pseudobinary section (left) and with $\Delta Z = 4\times10^{-4}$ on the α–CIS/$Cu_{2-\delta}Se$ phase boundary (right)

The minimum neutral $\mathcal{V}_{Cu}^{\times}$ and $Cu_{In}^{\times}$ species concentrations are found at the 677K threshold where the selenium content of the binary phase drops to its minimum stable value and the lattice is isoenergetic with respect to nominal positive valency deviations. Clearly the dominant accomodation mechanism for molecularity deviation changes upon the addition of excess selenium, from dissociation of the NDC to formation of the copper antisite.

Over the domain of this calculation the species $\mathcal{V}_{Cu}'$, $(\mathcal{V}_{Cu} \oplus In_{Cu})^{\bullet}$, $(2\mathcal{V}_{Cu} \oplus In_{Cu})_{\alpha}$, $\mathcal{V}_{Cu}^{\times}$, and $Cu_{In}^{\times}$ comprise the dominant lattice defects in single-phase α–CIS. The remaining lattice defects occur in very small concentrations in equilibrium, and only a few will be described in further detail.

The least common defect in the domain of this calculation among all those considered is the indium vacancy, in all of its ionization states. It's concentration was found to drop below one defect *per* mole over the entire range of the α/β–CIS two-phase equilibrium. The selenium vacancy was found in very low concentrations at STP, even on the pseudobinary section and effectively vanished with the addition of a few *ppm* of excess selenium. The only other species predicted to exist at equilibrium in potentially measurable quantities was the $In_{Cu} \oplus Cu_{In}$ antisite complex, whose concentrations at high temperatures as shown in figure 2.21, although in the *ppb* range, were still significantly greater than any of the other minor defects and independent of positive valency deviation.

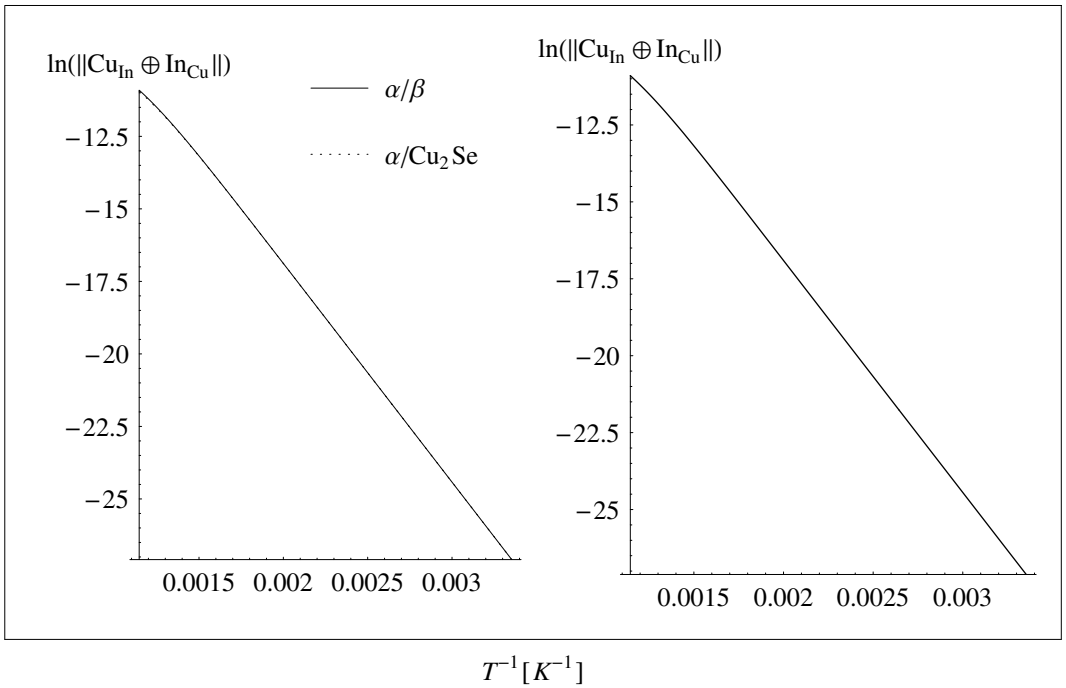

Figure 2.21 Temperature variation of the $In_{Cu} \oplus Cu_{In}$ species mole fraction at the phase boundaries on the pseudobinary section (left) and with $\Delta Z = 4\times10^{-4}$ on the α–CIS/$Cu_{2-\delta}Se$ phase boundary (right)

Electronic defects

Transport studies have shown [3] that CIS material with positive valency deviation is *p*-type at STP, but their measured carrier concentrations are considerably less than those shown in figure 2.22, which shows the hole concentration at the α–CIS/$Cu_{2-\delta}Se$ phase boundary. However, it was proposed in the preceding discussion of the interphase equilibria that essentially all experimental single-phase CIS materials are metastable, constrained by kinetic barriers when grown at compositions more copper-rich than the true equilibrium value at the α/β–CIS eutectoid of 24.4 at.% copper. Binary copper selenide is known to be strongly *p*-type and it would be quite difficult experimentally to confirm this predicted carrier concentration at their phase boundary.

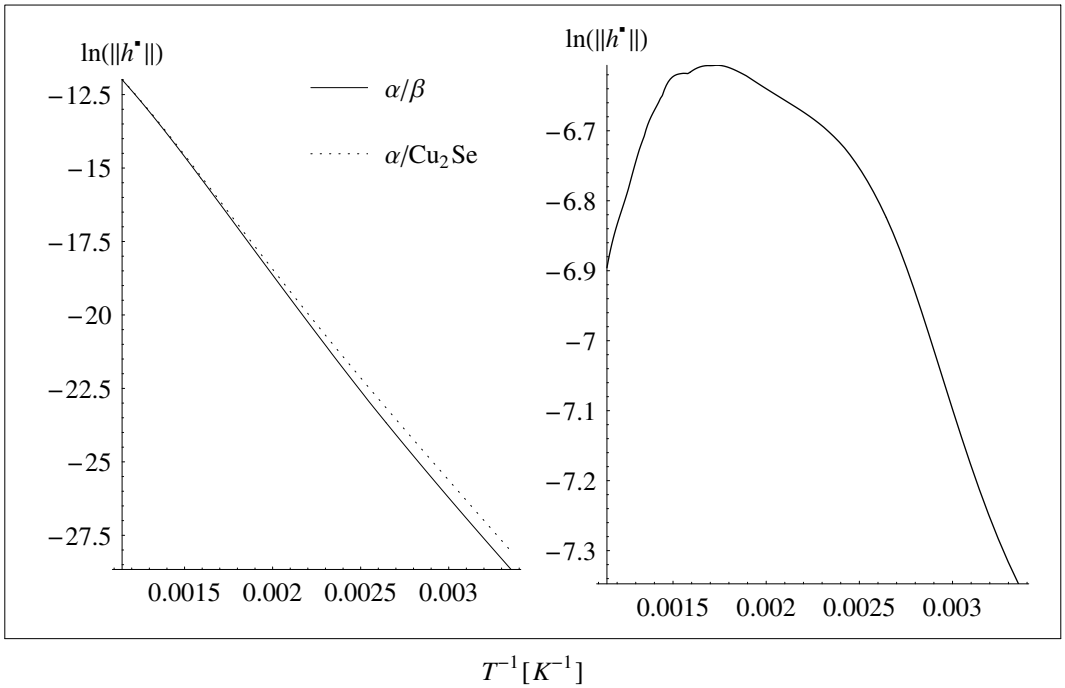

Figure 2.22 Temperature variation of the $h^{\bullet}$ species mole fraction at the phase boundaries on the pseudobinary section (left) and with $\Delta Z = 4\times10^{-4}$ on the α–CIS/$Cu_{2-\delta}Se$ phase boundary (right)

The non-degenerate approximation was used to calculate all ionization equilibria in this model. In this approximation, the Fermi-Dirac distribution is approximated by a value that is reasonably accurate whenever the electrochemical potential is far removed from a lattice defect's ionization level in the fundamental absorption gap of the semiconductor. This is sufficient for the calculations on the pseudobinary section, where as previously mentioned, the concentrations of the two dominant defects $\mathcal{V}'_{Cu}$ and $(\mathcal{V}_{Cu} \oplus In_{Cu})^{\blacksquare}$ are nearly equal and compensate one another, yielding an electrochemical potential near the middle of the fundamental absorption gap (although shifted slightly towards the valence band by a difference in the carrier mobilities).

This approximation fails with only moderate positive valency deviation, and as a consequence the carrier concentrations calculated here for those cases are erroneous. Another consequence of the non-degenerate approximation's inapplicability in this circumstance is the complementary error in the dominant ionic defect concentration. Thus the result of this calculation that the compensation ratio becomes almost zero with very small positive valency deviation cannot be taken literally without further elaboration of this model. It is nevertheless certain that this trend is correct, and that the compensation ratio is dramatically reduced in equilibrium with the addition of excess selenium to the lattice, as shown in figure 2.23.

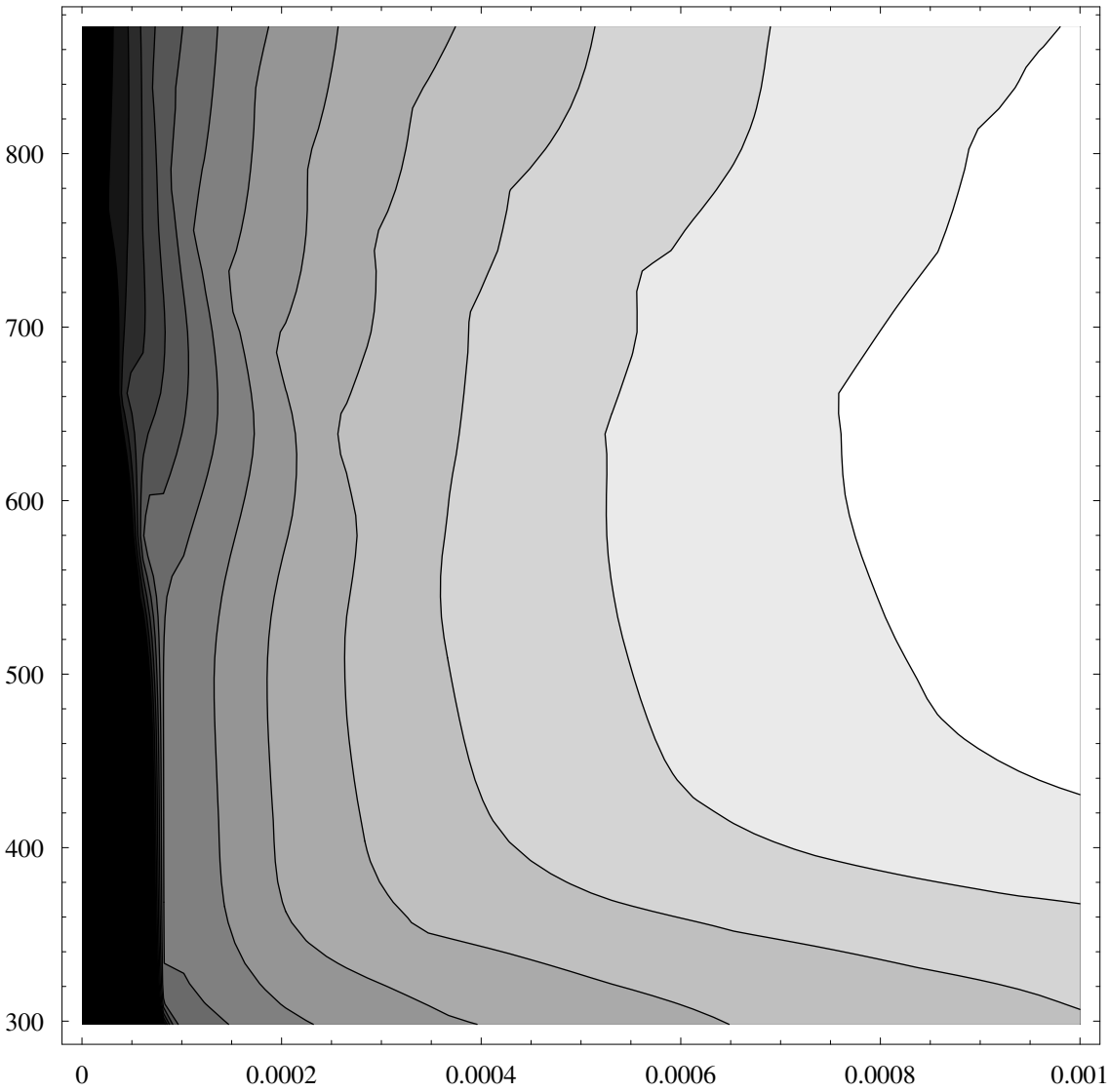

Figure 2.23 Contour map of net carrier concentrations in α–CIS in equilibrium with $Cu_{2-\delta}Se$ over the temperature range between STP and the $\alpha/\beta/\delta$–CIS eutectoid, and the valency deviation range $0 \leq \Delta Z \leq 0.1\%$. Contour intervals are $p = 2.5{\times}10^{18}$ cm^{-3} and the black region (left) is intrinsic.

Summary

The results of defect modeling presented in this chapter represent the first attempt to develop an associated solution defect model for ternary chalcopyrite compound semiconductors. The model has been used to predict the phase equilibria, compositions, and lattice defect properties of the three phases in the domain of the calculation: binary $Cu_{2-\delta}Se$, and the α and β phases of ternary copper indium selenide.

The results of modeling the binary $Cu_{2-\delta}Se/\alpha$–CIS phase equilibrium predict that the stoichiometric composition is not single phase, and that the minimum in total Gibbs energy does not lie on the pseudobinary section. The lowest Gibbs energy at this boundary is for compositions of the ternary phase that are enriched in both indium and selenium by proportions very near the resolution limits of chemical analysis methods. The discrepancies between these predictions and published experimental data are explained by the model's results themselves, which suggest the existence of significant kinetic barriers to equilibration of the lattice at low temperatures, where its equilibrium composition changes, driven by a shift in phase segregation. This is a caused by a peritectoid phase transformation in the Cu–Se system near 123 °C.

The results of modeling the α–CIS/β–CIS phase equilibrium predict experimentally reported phase boundary at STP with remarkable accuracy, using only published *ab-initio* quantum-mechanical defect formation enthalpy values for three different concentrations of a single species, the $2\mathcal{V}_{Cu} \oplus In_{Cu}$ cation neutral defect

complex, to characterize the β–CIS phase. The deviations of this model's predictions from experimental data at higher temperatures is likely due both to this severely restricted defect model, and once again, a kinetic barrier to equilibration of the lattice at low temperatures when so highly indium-enriched. Nevertheless, this result provides significant support to the model of β–CIS phase formation based on short-range ordering of the cation NDC.

Finally, a comparison was made of the calculated equilibrium defect structure of α–CIS with three different compositions within its predicted single-phase domain. It is found that the mechanism whereby the lattice accomodates excess indium is significantly different when excess selenium is introduced onto the lattice. In the absence of valency deviation the dominant defects are $\mathcal{V}'_{Cu}$ and $(\mathcal{V}_{Cu} \oplus In_{Cu})^{\bullet}$ resulting from the ionized dissociation of the NDC. The addition of excess selenium suppresses NDC formation and results in creation of the $Cu^{\times}_{In}$ defect instead, reducing the compensation of the $\mathcal{V}'_{Cu}$ acceptor and thereby increasing the net hole concentration.

CHAPTER 3
REACTOR DESIGN AND CHARACTERIZATION

Design

The growth of all semiconductor films described in this dissertation was performed in a custom-designed reactor intended specifically for this research. The system was built on the foundation provided by a commercial vacuum evaporator, a model SE-1000 from CHA Industries. The pumps and their interlocked control systems, the baseplate assembly, feedthrough ring on that baseplate, internal substrate platen support rods, and rotating shaft with its drive assembly were the only parts of the original system retained in the final system.

The principles implemented in the design of the reactor were based on careful consideration of the limitations encountered in the growth of CIS using conventional physical vapor deposition methods, and an intentional effort to explore alternative growth techniques that might be particularly suitable for heteroepitaxial growth. "Epitaxy" is the term used to describe the growth of a layer of crystalline material on a crystalline substrate in any manner such that the crystallographic axes of the film assume a well-defined geometric relationship with respect to that of the substrate upon which it is grown. This is not generally

so, and the more general case is referred to as "thin-film deposition." In either case, when the growth occurs in a reactor whose pressure is sufficiently low that the mean free path of gases and vapors is greater than the reactor's dimensions, the term "physical vapor deposition" (PVD) is used in general, and "molecular beam epitaxy" (MBE) is used when epitaxial growth results.

Conventionally, both PVD and MBE of compound semiconductors is performed with separate thermal sources for the different elemental components of the compound to be grown, heated to temperature where their vapor pressure becomes sufficiently large that the resulting fluxes can be mixed by simultaneous condensation on the substrate's surface to grow the intended compound. Under these conditions, vapor phase collisions between reactant molecules (and thus their pre-reaction) is improbable, so that the composition and internal energy of the fluxes incident on the growing surface are determined solely by those characteristics of the source's emissions.

Our understanding of the physics and chemistry of the subsequent processes is well developed [179, §1.1], but the details have been found to be highly dependent on the particular properties of the material system [180]. Nevertheless, certain elementary processes are found to occur almost universally. The flux incident on the surface may be partially reflected without coming to thermodynamic equilibrium with the surface, and thus with little or no energy exchange occurring. The remaining flux is almost always first trapped by the Van der Waals potential of the surface into a weakly bound mobile

precursor state [181], a process called physisorption first described by Langmuir [182]. Some fraction of that flux will sometimes desorb after partial or total thermal equilibration with the surface, and each of the remaining atoms or molecules (called adsorbates) will migrate across the surface until forming a chemical bond with either another adsorbed species or an energetically favorable site on the surface, a process called chemisorption [183]. Once again, some fraction of the chemisorbed species or previously bound surface atoms may desorb rather than incorporate into the growing film. The overall fraction of the incident flux that does incorporate is referred to as the accommodation coefficient. The accommodation coefficient is much easier to measure than the desorption fluxes resulting from the underlying elementary processes that determine its value, and is equivalent to the difference of the incident and all desorbed fluxes normalized to the incident flux. Its value is calculated here by measuring the incident flux, the thickness and composition of the final film, the deposition time; and then using the theoretical value for bulk density of the resulting compound to determine the rate at which each atomic species was incorporated.

As described above, two competitive processes occur among reactant molecules physisorbed into the mobile precursor state: chemisorption onto a surface site and bonding among themselves due to inelastic collisions. The bond formation occurring in the second process results in the formation of clusters with significantly lower mobilities than the independent species enjoy, thus

increasing the likelihood that the cluster will not have time to diffuse to an energetically favorable site for incorporation into the surface of the growing crystal lattice before being buried by further deposition. This can result in growth defects: kinetically stabilized non-equilibrium atomic configurations that reduce the translational symmetry of the crystal lattice and often introduce electronic defect states.

The growth of thin films on crystalline substrates is often found to exhibit three different domains determined mostly by the substrate temperature. At the lowest temperature, the films are amorphous, at intermediate temperature the films are polycrystalline and at higher temperature they grow epitaxially [184,185]. We focus here on the transition between the latter two modes of growth, which occurs for a given film material and substrate orientation at some critical temperature for epitaxy, T_c^{epi} . The explanation for this general phenomenon is based on the sensitive dependence of adatom surface mobilities on temperature, since adatom surface diffusion is a thermally activated process. The argument is that polycrystallinity in a material system (film + substrate) that can exhibit epitaxy is the manifestation of excessively high densities (above some threshold) of growth defects. These defects result in general from incomplete equilibration of the adlayer and crystal surface during growth, which in the context of the elementary kinetic processes described previously, can be due to inadequate adatom diffusion lengths.

In fact the dependency of T_c^{epi} on incident flux and substrate temperature are both consistent with this explanation. Reducing incident flux decreases T_c^{epi} by reducing the rate of bimolecular collisions that form relatively immobile clusters. This effect is particularly strong in the growth of compound semiconductors formed by the reaction of cationic and anionic species which undergo charge-exchange reactions to form a very strong bond, for example the growth of III–V, II-VI, or I–III–VI_2 compound semiconductors. Awareness of this effect led in the late 1970's to the suggestion [186] that lower epitaxial growth temperature and smoother surfaces could be achieved during compound semiconductor film growth by alternating between the cationic and anionic reactant fluxes with a flux-free pause between them to permit adatom/surface equilibration [187].

The original implementation of this approach, called Atomic Layer Epitaxy (ALE), further stipulated that a self-limiting growth mechanism involving desorption of any species in excess of that required to grow one atomic layer should desorb during the "relaxation" step between alternating flux exposures of the substrate. Such a self-regulatory mechanism is available in compounds (for example most II-VI semiconductors) wherein both cationic and anionic species are volatile at reasonable growth temperature, or in reactive growth processes that can produce volatile molecular compounds. Extension of the ALE growth technique to materials or methods where no such desorption mechanism occurs was first described by Horikoshi and coworkers in 1986 [60], a mode of MBE

growth that they refer to as Migration Enhanced Epitaxy (MEE). They reported that the MEE technique enabled them to reduce T_c^{epi} for homoepitaxial growth of GaAs to temperature as low as 200°C. Numerous other variations of this general approach have been developed, and since they are sometimes employed in the growth of non-epitaxial thin films they are collectively referred to as Modulated Flux Deposition (MFD) techniques.

The reactor designed for this research program was specifically intended and optimized for MEE growth of CIS. It has also been employed during the course of this research for the MFD growth of both CIS and its related binary (Cu,Se) and (In,Se) thin films. For compound semiconductor growth, MEE is a cyclic process divided into four component steps: cationic (metals) reactant deposition, flux-free surface equilibration, anionic (metalloid) reactant deposition, and a final flux-free equilibration step. In conventional MBE reactors this process is implemented by alternately opening the appropriate source shutters. However, this method is not very robust since it quickly leads to premature shutter failure. The first design principle for the reactor is intended to circumvent this problem by relying on substrate rotation rather than shutters to create flux modulation at the substrates' surfaces. This approach has the added benefit that films may be grown on a relatively large batch of substrates (in this case up to nine) during a single deposition run of the reactor.

The requirement for alternating exposure of the substrates to metal (Cu,In) and metalloid (Se,S) fluxes combined with the first design principle of

rotating the substrates to dictate the requirement for condensation shielding to isolate the sources into separate zones within the reactor. Since the pumping system provided with the original CHA SE–1000 deposition system employed a diffusion pump isolated from the deposition chamber by a liquid nitrogen cryotrap, the base pressure (~10^{-7} Torr) was not sufficiently low to prevent contamination of the film's growing surface by residual gases in the system. All of these problems were solved by the addition of two custom deposition shields and a liquid nitrogen cryoshroud to the system (Figure 3-1).

The liquid nitrogen cryoshroud effectively divides the reactor vertically into two zones. The pump inlet is through the baseplate at the bottom of the vacuum chamber and is blocked by the cryoshroud from direct line-of-sight exposure to the sources and substrates' surfaces. All feedthroughs above the feedthrough collar used knife-edge flanges and metal gaskets, so most steady-state permeation after bakeout comes from the lower region of the chamber, below the level of the cryoshroud. A nude ion gauge at the top of the chamber in the load-lock zone measured the same pressure ($8x10^{-8}$ Torr) as the Bayard-Alpert gauge located 6" above the baseplate on the feedthrough ring when the cryoshroud was empty, but dropped to the range of $9x10^{-10}$ to $2x10^{-9}$ Torr when the cryoshroud was filled. Thus the cryoshroud acts as a differential pump, reducing the pressure in the deposition zone between the top surface of the cryoshroud and the lower surface of the rotating substrate platen.

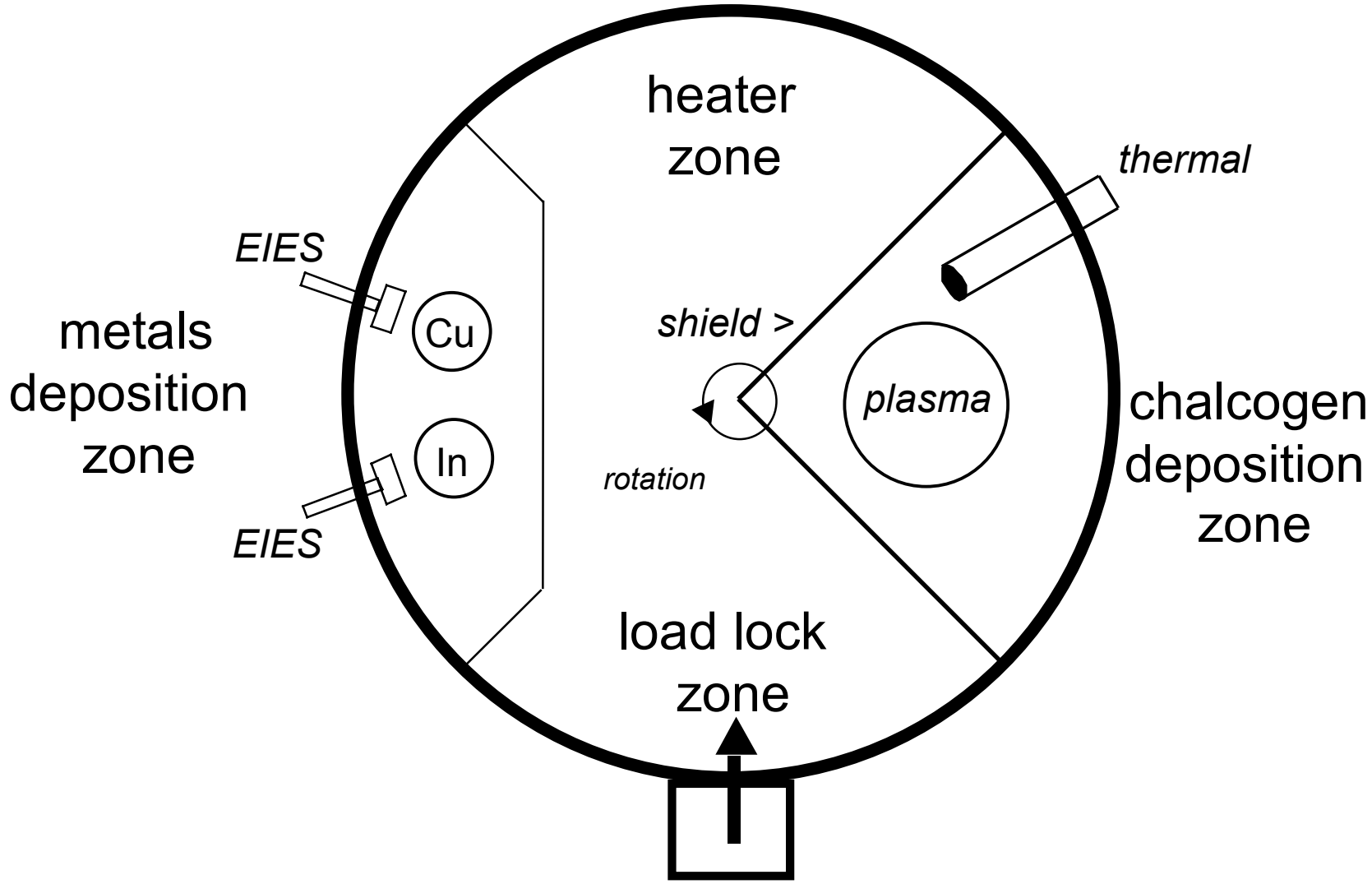

Figure 3-1 Schematic diagram of the MEE reactor showing the source and shielding configuration.

Figure 3-2 Detail of metals deposition shield with chamber removed.

The entire deposition chamber above the level of the feedthrough collar is water-cooled as are the metal deposition sources that penetrate through cylindrical apertures in the cryoshroud into the completely shielded metals deposition zone, Figure 3-2. Electron Impact Emission Spectrometry (EIES) is used

to monitor the copper and indium fluxes and the ionization head for these transducers penetrate through apertures in the metal deposition shield. Source shutters completely block the flux from the effusion cells to both the substrate and EIES sensors when closed. The rotating substrate platen blocks most of the flux by passing through a horizontal slit in the shielding, but with a wafer carrier puck removed from the platen, tubes at the top of the metal deposition shield permit cross-calibration of the EIES sensors with Quartz-Crystal Monitors (QCM) on feedthrough ports in the deposition chamber's lid.

The cryoshroud is annular but does not continue through a full 2π azimuthal angle because a $\pi/2$ sector is blocked by a full height water-cooled internal selenium condensation shield (Figure 3-3). This shield very effectively isolates the entire reactor outside the chalcogen deposition zone from the selenium source such that the background vapor pressure of selenium outside this zone of the reactor remains negligible during growth. Two sources, described in detail in the next chapter, are located within this zone: a commercial EPI–225Se double-oven thermal cracking cell passes through a port in the deposition chamber's outer wall and a unique ECR plasma cracker designed and built for this research is mounted entirely inside the zone.

A third zone lying between the metals and chalcogen deposition zones contains the backside radiant heating source that provides most of the substrate platen heating during growth. The boron nitride-encapsulated pyrolytic graphite heater uses four layers of tantalum radiant shielding and molybdenum rods as

conducting power leads. This has performed flawlessly for five years at operating temperature during growth of 1000°C. A thermocouple suspended between the heater and rotating platen provides temperature monitoring.

Figure 3-3 Detail of the chalcogen (selenium and/or sulfur) deposition zone of the reactor with the chamber outer walls removed, showing a) effusion source before the plasma cracker is mounted on the left and b) radiant heater with power leads and monitoring thermocouple at top right.

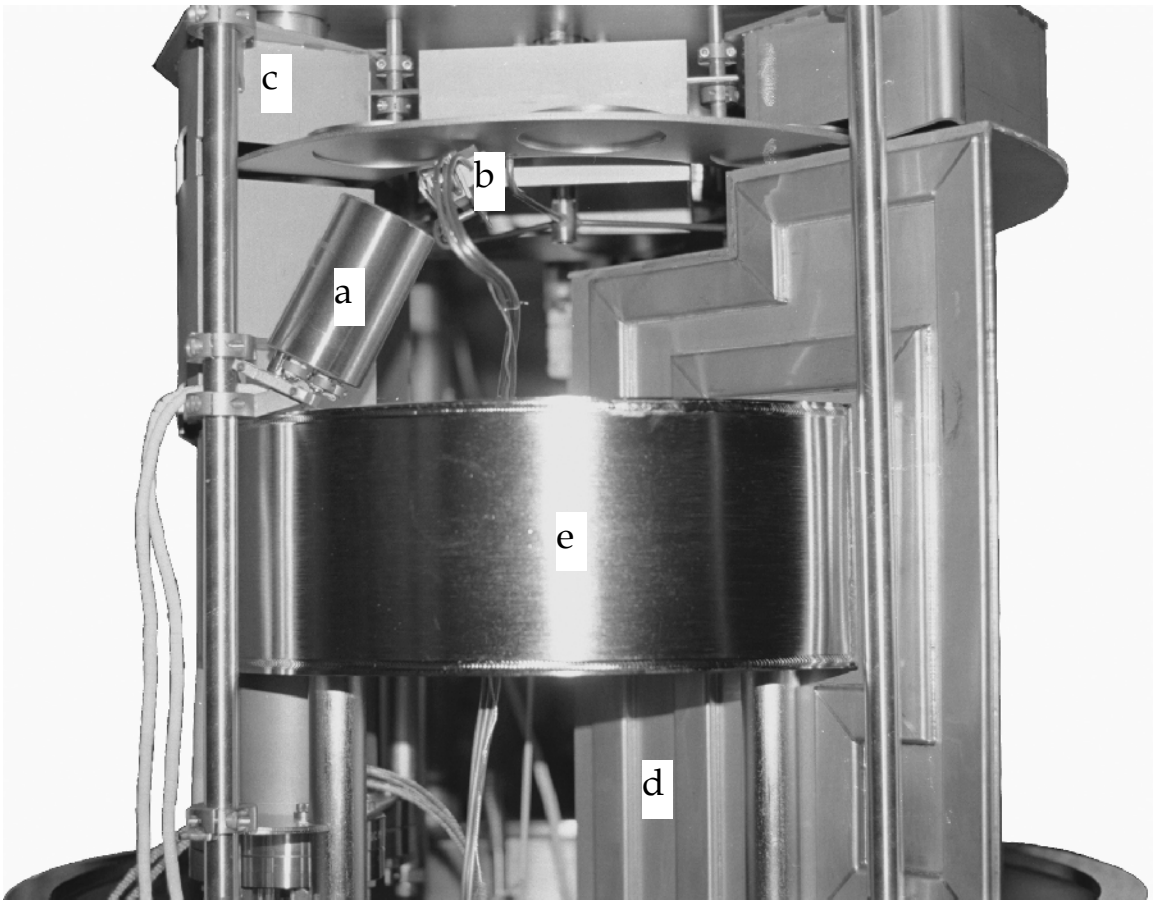

Figure 3-4 Detail of reactor viewed from the front load-lock zone with the chamber walls removed. The NaF Knudsen cell source (a) and QCM (b) are visible at upper left, in front of the metals deposition shield (c). The water-cooled selenium sector shield (d) is on the right and the annular liquid-nitrogen cryoshroud (e) at center.

A load-lock attached to a port at the substrate platen level of the deposition chamber's water-cooled cylindrical wall allows the system to remain under vacuum for months during operation. The load-lock is independently pumped with a small turbomolecular pump isolated by a gate valve from the loading chamber and equipped with a Residual Gas Analayzer (RGA) used to monitor substrate degassing in the load lock prior to transfer through the gate valve that isolates it from the deposition chamber. All chamber venting uses

argon gas and the load lock is equipped with a liquid nitrogen sorption pump for rough-pumping to the turbomolecular pump's crossover pressure of 10^{-3} Torr. A substrate and its back-side heat-spreader are placed onto a holder with a machined aperture on its bottom side, and transferred with a magnetically-coupled rod into the fourth zone of the reactor, where it is placed into one of nine recessed apertures in the rotatable carrier platen.

A Luxel Corporation 100cc effusion cell mounted in the load-lock zone of the deposition chamber is fitted with a custom-designed machined boron nitride Knudsen cell with a rate-limiting orifice and used as a sublimation source for sodium fluoride (NaF). It is monitored by both thermocouples within the source and a shuttered, water-cooled QCM suspended between the source and the substrate platen (Figure 3-4).

Operational Characteristics

Substrate Temperature Calibration

Measuring the substrate temperature in the system is complicated by the high-temperature rotating platen design. Due to the difficulty of making reliable electrical contact for thermocouple or thermistor-based temperature measurement and the problems with pyrometry presented by selenium condensation on optical ports, temperature calibration estimates were performed by *ex-situ* observation of the melting of metallic bilayer thin films at their eutectic temperature. These bilayers were deposited on molybdenum-coated soda-lime

glass substrates to mimic as nearly as possible the emissivity and thermal mass characteristics of the substrates used for *in-situ* growth of polycrystalline absorber films.

Procedurally, bilayer temperature calibration substrates were inserted into standard 2"x2" substrate holders between a $CuInSe_2$–coated alumina substrate (source side) and an uncoated alumina heat spreader (heater side). Platen rotation was then initiated and the setpoint of the substrate heater temperature controller raised slowly to a temperature where it was allowed to thermally equilibrate for at least an hour prior to a standard growth run. In this manner the calibration samples were subjected to the closest possible approximation to the conditions of the actual samples with which it was included. After the growth run, the samples were allowed to cool overnight before being removed to ascertain whether the eutectic bilayer had melted or not. After multiple repetitions of these experiments, correlations were established between the controller setpoints and the substrate temperature. The data were fitted with an equation of the form of the Stephan-Boltzman relation, $y = a*(x+b)^4$, using the two adjustable parameters a and b. The results are shown in Figure 3-5.

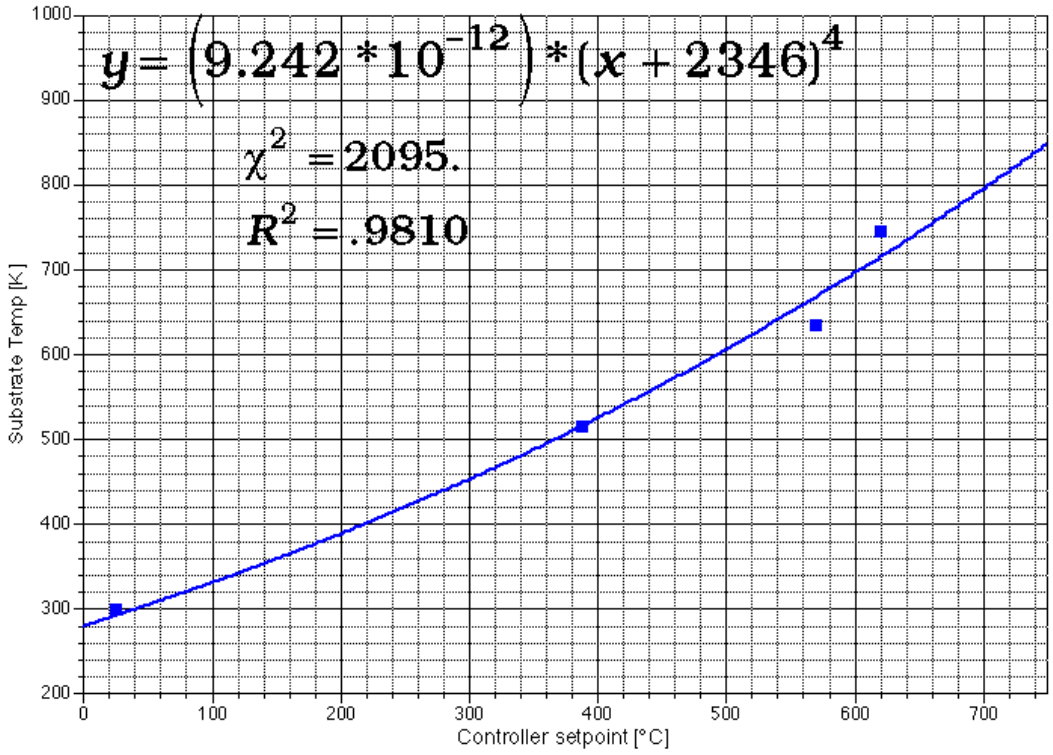

Figure 3-5 Calibration curve for substrate temperature controller

Epitaxial growth experiments were conducted at a controller setpoint temperature of 700°C, above the temperature range where empirical temperature calibration data was available. Extrapolation of the fitted expression predicts a substrate temperature of ~800K, or about 525°C, but the increasing scatter of the calibration data at higher temperature yields a ±50°C uncertainty in that temperature. At the lower setpoint temperature of 400°C typically employed for binary (Cu,Se) and (In,Se) deposition experiments, the uncertainty is much less, with a calculated substrate temperature of 250±10°C at that setpoint.

Flux Calibration

The reactor's design relies on EIES for control of the copper and indium metal evaporation sources and on temperature control for the selenium sources. Calibration of these process-monitoring measurements is essential to the goal of providing the fundamental quantitative flux data that are the inputs to the thermodynamic analysis that these experiments are intended to support.

Metal (copper and indium) sources

The reactor's design incorporates both EIES sensors for process control and QCM's with collimated shielding for each of the metal sources that permit cross-calibration and routine testing for EIES sensor calibration drift. Since these two sensors are not co-located with each other their geometric flux correction factors are different for each sensor type and both must be calibrated with respect to the flux incident on the rotating substrates. The metal deposition shielding prevents deposition on each individual substrate except during that portion of each rotation cycle of the substrate platen when it is inside the shield. The shield subtends only an 80° sector of the full circle, and the flux of each metal is not constant at the surface while each substrate is within the metals deposition zone. Therefore, an absolute flux calibration method was employed to establish ratios between the integrated sensor reading over an entire deposition cycle and the total quantity of each element measured *ex-situ* after it is deposited independently of the others.

The procedure employed for calibration was to grow a thin film of a single source material on an unheated Mo/SLG (Soda-Lime Glass) substrate. After deposition of several thousand Angstroms, the substrate was removed, *vias* etched or scraped through the film, and its thickness measured at a minimum of twelve different locations across the substrate using diamond stylus profilometry. The mean thickness data was converted into an areal molar density using the bulk mass density and molar mass of each element. The implicit assumption that the elemental film's density is the same as the bulk mass density for that element is the greatest potential source of error in this calibration procedure for copper and selenium. These films were found to be very smooth and their thickness, being very uniform across the entire substrate, was unlikely to cause a significant error.

The metallic indium films were not at all smooth, so that the uncertainty in their thickness propogated through the calculation and became the greatest source of error in its calculated calibration factor. In fact, it was found that the [Cu]/[In] ratios calculated from their absolute calibration factors differed by about 10% from those measured by EMP on codeposited CIS films grown at low temperature where the accommodation coefficients for both metals are expected from thermodynamic considerations to be unity.

Selenium sources

Absolute flux calibration was conducted only for the thermal selenium source, not the plasma selenium source. In both cases the flux was controlled by temperature control of the selenium reservoir, so the absolute flux calibration of the former required the establishment of a mathematical relationship between the temperature and calculated areal molar density derived from the thickness data measured *ex-situ* after growth, as described in the previous paragraph.

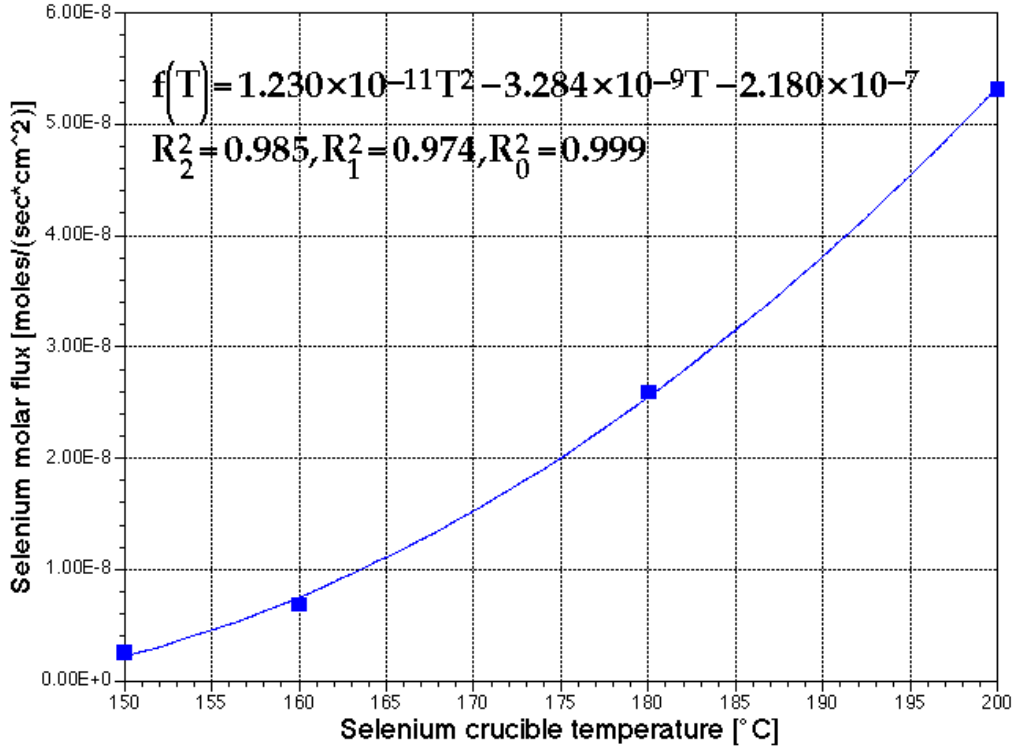

Figure 3-6 Absolute selenium molar flux calibration curve for the thermal source.

Selenium source crucible temperature between 135 and 150°C were typically used for growth of both binary and ternary thin films. Although

calibration was performed over the range 150 to 200°C, the accuracy of the data fit was extremely good and estimated uncertainty at the lower temperature used for growth is $\leq$10%.

CHAPTER 4
ACTIVATED DEPOSITION SOURCES

The history of progress in the development of semiconductor materials might be generally viewed as revolving around two fundamental issues: purity and process temperature reduction. Purity is essential due to the monotonic reduction in charge carrier mobilities, which occurs as a consequence of impurity scattering. In a few exceptional cases, semiconductor alloys such as $In_xGa_{1-x}As$ contain isoelectronic "impurities" resulting in a net increase in carrier mobility due to other effects, such as a decrease in the curvature of the conduction band dispersion relation's minima (and hence the intrinsic mobility). Even in this case, however, the total mobility is the net difference between an increase due to the latter effect, and a decrease due to the former. Process temperature reduction is inherently important for several reasons. First, low temperature are often necessary to prevent undesirable interdiffusion of component species at the interface between different materials. Second, lower crystal growth temperature to a limit usually effects a reduction in the density of point defects incorporated into the films. This empirical observation is

reasonable, even in the case of non-equilibrium growth techniques, in view of the rigorously demonstrable temperature dependence of equilibrium vacancy concentrations (Schottky disorder) [157]. The growth of II-VI compound semiconductor layers is particularly sensitive to high growth temperature due to the high volatility of *both* the group II and the group VI elements. This is distinctly different from the case of III-V compound semiconductors, where the group III element is essentially involatile, and this difference manifests itself in a fundamentally different relationship between the flux ratio and growth rate in Molecular Beam Epitaxy (MBE) [188,189]. In the CIS material system, copper has been found to be involatile, whereas indium may desorb as $InSe_2$ at temperature above ~500°C.

Examples of lower deposition temperature leading to significant advances in semiconductor device technology abound. OrganoMetallic Vapor Phase Epitaxy (OMVPE) has largely supplanted chloride and hydride-based VPE as a production process for GaAs in large part due to the fact that it results in lower deposition temperature. Plasma-Enhanced Chemical Vapor Deposition (PECVD) of silicon nitride has become a standard part of commercial silicon device fabrication technology because of the extremely high temperature required for its pyrolytic deposition.

From an economic perspective, deposition temperature reduction has a significant impact on the ultimate cost of fabricating high volumes of semiconductor materials as required for mass production of solar cells for

terrestrial applications. As processing temperature drop, the demands on system materials are reduced, enabling the use of lower cost construction materials. For example, at temperature $\leq$350°C high vacuum systems may be reliably built from aluminum, whereas at higher temperature stainless steel must be utilized, with concomitant increases in equipment cost.

It has been found in prior research that the temperature required for growth of high-quality semiconductor epilayers by MBE can be significantly reduced for some materials by thermally dissociating the polyatomic molecules characteristic of the vapor evaporating from condensed phases of most metalloids from groups V and VI of the periodic table (*e.g.*: arsenic, phosphorus, selenium, and sulfur). For example, lower defect levels are found in GaAs grown by MBE with As_2 instead of As_4 at the same growth temperature [190], and a 200°C reduction in minimum growth temperature for heteroeptiaxial ZnSe on GaAs with no loss of material quality has been reported for growth employing thermally dissociated selenium [191,192].

Plasma-enhanced deposition processes have also proven to be effective in the reduction of temperature for the epitaxy of many semiconductor materials including GaAs by Physical Vapor Deposition (PVD) [193], OMVPE [194], and Metal-Organic MBE (MOMBE) [195]; ZnSe by PVD [196] and OMVPE [197]; GaSb, InSb, and InAs by PVD [198], $Hg_xCd_{1-x}Te$ by OMVPE [199], GaN by OMVPE [200], and ZnO by OMVPE [201]. In *every* case significant reductions in the minimum

temperature required for the onset of single crystal epitaxial growth were observed, varying from 150-300°C.

One of the goals of this research has been to directly compare the efficacy of these two approaches. To that end, epitaxial growth experiments have been conducted using both thermally and plasma activated reactants. The rest of this chapter is devoted to a detailed discussion of the sources used to perform this comparison, and the experimental characterization of each source.

Thermally Activated Source and its Molecular Species Distribution

The majority of all metal chalcogenide film growth experiments reported herein were performed using a commercial thermal selenium evaporation source (model EPI–225Se from EPI). This source is a double-oven design [202] with two independent heating and thermocouple circuits, one pair for the 500cc capacity selenium reservoir, and a second pair for the baffled flux transfer tube through which the selenium vapor had to pass before exiting the source's aperture. The lower-temperature reservoir (referred to hereafter as the "selenium crucible") was equipped with a type K thermocouple and the higher-temperature downstream zone (referred to hereafter as the "selenium cracker") was equipped with a type C thermocouple. The maximum operating temperature of the selenium crucible was 250°C as discussed in the previous chapter's section on source calibration, but it was degassed at 500°C before its initial selenium charge was loaded. The selenium cracker zone was outgassed at a temperature of 1200°C prior to source

charging, and two different operating temperature for the cracker were selected for deposition experiments: 350 and 972°C.

The low-temperature cracker setpoint was slightly above the minimum temperature required to prevent condensation of selenium on the coolest parts of the cracker during extended operation. The high-temperature cracker setpoint is equivalent to 1200K and was chosen to facilitate direct comparison of experimental flux characterization data with the results of thermodynamic calculations based on a recent critical assessment of the selenium unary system [26,163]. Those theoretical calculations predict that if the source's selenium flux comes to equilibrium with the cracker at its high-temperature setpoint, the predominant molecular species would be the dimer Se_2. In contrast, those calculations indicate that the predominant molecular species at the source's low-temperature cracker setpoint would be Se_5.

The influence of cracker-zone temperature on the molecular distribution of selenium from the thermal effusion source has been studied with a Balzers QMG-420 quadrapole mass spectrometer (QMS) fitted with a cross-beam ionizer and with a mass range of 0 to 512 AMU. The QMS inserts through a port on the reactor's chamber wall at a level above the substrate platen and the ionizer's flux aperture rests directly on a hole drilled in the top surface of the selenium deposition shield. During measurement a substrate holder was removed from the platen and the resulting aperture in the platen rotated to align with the spectrometer to conduct these measurements.

QMS-based measurements of this type have been employed since the earliest days of MBE's development, but more sophisticated beam modulation methods are required unless the source flux is substantially greater than the flux of background vapor in the reactor [203]. This condition occurs at the lower cracker temperature setting (350°C), based on direct measurement of the background prior to heating the effusion cell. At the higher cracker temperature setting, the background pressure of the reactor measured by a nude ion guage outside the chalcogen deposition zone, was to 1.5×10^{-6} Torr, as compared to 1.6×10^{-7} Torr (the cryoshroud was not filled for these experiments, since it does not penetrate the selenium sector shield into the chalcogen deposition zone). Inspection of the water-cooled selenium sector shield during maintenance cleaning provides visible evidence that high-temperature cracker operation results in some sublimation of selenium on those parts nearest the cracker. However, a QMS study of the ion-energy distribution from subliming selenium [204] shows that the species Se_5, Se_6, and Se_7 dominate the vapor flux therefrom.

Two characteristics of QMS and our QMG–420's mass limitation of 512 AMU prevent a completely quantitative analysis of the data we have acquired. First, QMS do not have constant sensitivity over their whole AMU range. Their relative sensitivity S is a function of resolution and has the form $S \approx (1+x)^{-R}$ where R, the resolution, is defined as $M / \Delta M$, and x is the fractional change in sensitivity which is itself not constant over wide mass ranges [205]. The facilities required for quantitative calibration of the sensitivity were not available, so the

values of the function x(M) could not be determined, although the value of R=512/0.1=5120 is known.

The other major complication arises from the tendency of the larger selenium molecules to dissociatively ionize in the cross-beam ionizer of the QMS itself. This problem is unavoidable in the selenium molecular system since the appearance potential for positively charged ionic selenium molecules varies between 8.3 and 10.4 eV [206] and significant cross-sections for electron dissociative attachment (forming negative ions) extend to above 7 eV for Se_n when n=1,2, or 3 [207]. Even assuming prior knowledge of the dissociation pathways and probabilities for each molecular species, inversion of the measured ion currents to extract their parent molecules' distribution is not possible without data for the Se_7^+ and Se_8^+ peaks, whose most common masses are beyond the range of the QMS, at 554 and 634 AMU, respectively [204].

Table 4-1 QMS ion currents generated from the flux of selenium molecules formed from the predominant mass 80 isotope effusing from the thermal source.

a) Low Cracking Temperature
150°C on crucible, 350°C on cracker, P_{NIG} = 1.6E^{-7} Torr

	80amu	160amu	240amu	320amu	400amu	480amu
Reading	4.334	1.986	4.256	0.517	0.201	0.152
Range	9.000	9.000	12.000	12.000	12.000	12.000
Actual	4.3E-08	2.0E-08	4.3E-11	5.2E-12	2.0E-12	1.5E-12

b) High Cracking Temperature
150°C on crucible, 927°C on cracker, P_{NIG} = 1.5E^{-6} Torr

	80amu	160amu	240amu	320amu	400amu	480amu
Reading	3.583	5.533	3.286	1.535	0.367	0.218
Range	8	8	11	12	12	12
Actual	3.6E-07	5.5E-07	3.3E-10	1.5E-11	3.7E-12	2.2E-12

Keeping these limitations in mind, the selenium thermal cracker QMS characterization results shown in Table 4-1 nevertheless admit to a qualitative interpretation that indicates a significant increase in the fluxes of the lower mass species (particularly Se_2) at higher cracker temperature, as displayed in Figure 4-1. This conclusion is based on the calculated ratios of measured Beam-Equivalent Pressure (BEP) data from Table 4-1, wherein the corrections due to variations in QMS sensitivity cancel out for each distinct mass.

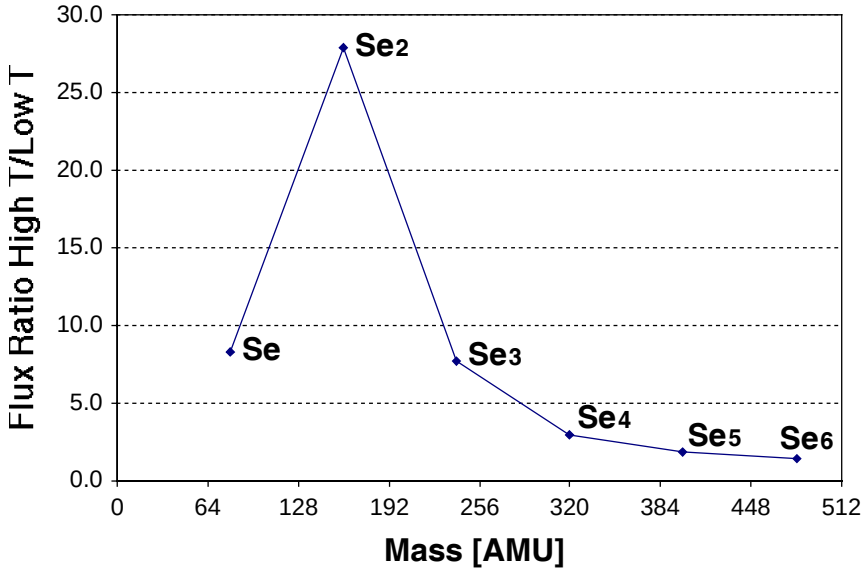

Figure 4-1 Ratio of measured ion-currents at high and low thermal source cracking zone temperature for each selenium molecular species within the mass detection range of the QMS.

Plasma Source

There are sometimes problems with plasma-activated deposition processes, mostly relating to impurity contamination and ion-bombardment

damage. The approach developed in the course of this research may make a significant contribution to low temperature CIS deposition technology by alleviating these problems through a unique approach to plasma excitation of the reactants.

This approach to lowering growth temperature could also result in a significant reduction in process equipment and facilities expenses (and hence photovoltaic costs) by pioneering a new technique for the *in-situ* generation of activated reactants. The new deposition source can significantly improve the safety of growth processes by eliminating the need for the storage or transport of large quantities (typically gas cylinders) of the hyper-toxic selenium hydride.

Several approaches to solving these safety and cost problems have been studied, including the use of non-hydride precursors. In OMVPE for example, tertiarybutylarsine has been used to replace arsine for GaAs epitaxy [208], and methylallylselenide has been used to replace hydrogen selenide for ZnSe epitaxy [209]. Problems persist in this approach, however, with residual carbon impurities and precursor costs. Another approach, for deposition processes using OM precursors, and routinely used in PVD deposition processes like MBE, is to employ an elemental source such as arsenic for GaAs epitaxy or selenium for ZnSe epitaxy. In the case of OM processes, this approach does not in itself solve the problem of residual carbon contamination.

In the case of plasma-activated PVD processes, it has been shown that the use of hydrogen provides distinctly superior results in the quality of materials

grown, when compared to argon [210]. Those results suggest that utilizing hydrogen may have beneficial results under circumstances where the reactants themselves are not sources of carbon contamination. There are several plausible mechanisms that may be suggested for this effect. First, since hydrogen atoms, radicals and ions are all powerful reducing agents, they may effectively getter oxygen or displace chemisorbed oxygen adatoms on the growth surface, increasing their desorption rate. Second, chemisorbed hydrogen may passivate dangling surface bonds, thereby reducing the binding energy of subsequently impinging species, an effect which has been shown to occur in some material systems [211]; and third, since the mass of hydrogen atoms is smaller than that of argon, momentum transfer to the lattice of the crystal, and consequently lattice displacement, is less than the argon case [212]. The approach developed in the course of this research utilizes elemental selenium buffered by argon, hydrogen, or mixtures thereof in a plasma discharge, which could be used to generate hydrogen selenide and related radical and ionic species *in-situ*.

The novel plasma-activated selenium source developed in the course of this research is significantly different than any other heretofore reported in the scientific literature of the field. It is microwave-excited, magnetically-confined helical resonator that operates under Electron Cyclotron Resonance (ECR) conditions at 2.455 GHz. This "plasma cracker" is directly coupled to the aperture of an effusion cell and evidence will be provided herein that it both excites and dissociates the vapor exiting therefrom. It can combine the effusion

cell vapor flux with a stream of hydrogen and/or inert gas at the ECR resonance point. A non-resonant, higher-pressure approach to the *in-situ* generation of arsine from elemental arsenic and hydrogen has been demonstrated in a "downstream microwave plasma" operating mode for OMCVD application [213]. All ECR sources reported in the literature, to our knowledge, utilize gas precursors (*e.g.*, hydrogen or arsine).

Thus this modified ECR source supplies plasma-activated reactants for epitaxial growth at reduced pressures utilizing elemental reactants. Furthermore, the ability to inject mixtures of hydrogen and an inert gas such as helium or argon provides another dimension of control over the relative composition of the flux generated by the source. Presumably, a lower ratio of hydrogen to selenium vapor in the plasma will reduce the steady state concentration of hydride species or shift their distribution towards greater concentrations of less completely hydrogenated species. This control over the reactant species distribution is unavailable with ECR sources that utilize hydride precursors and represents another advantage of this novel plasma source.

Conceptually, the source may be viewed as an alternative to a conventional thermal "cracker" as previously discussed, and has been utilized to convert the flux of thermally evaporated molecular species to a flux of dissociated hyperthermal molecular species which are more readily incorporated into the crystal lattice (e.g.: Se_5 to Se_2). A rendered cross-sectional CAD drawing of the final source design with a coupled effusion cell is shown in Figure 4-2.

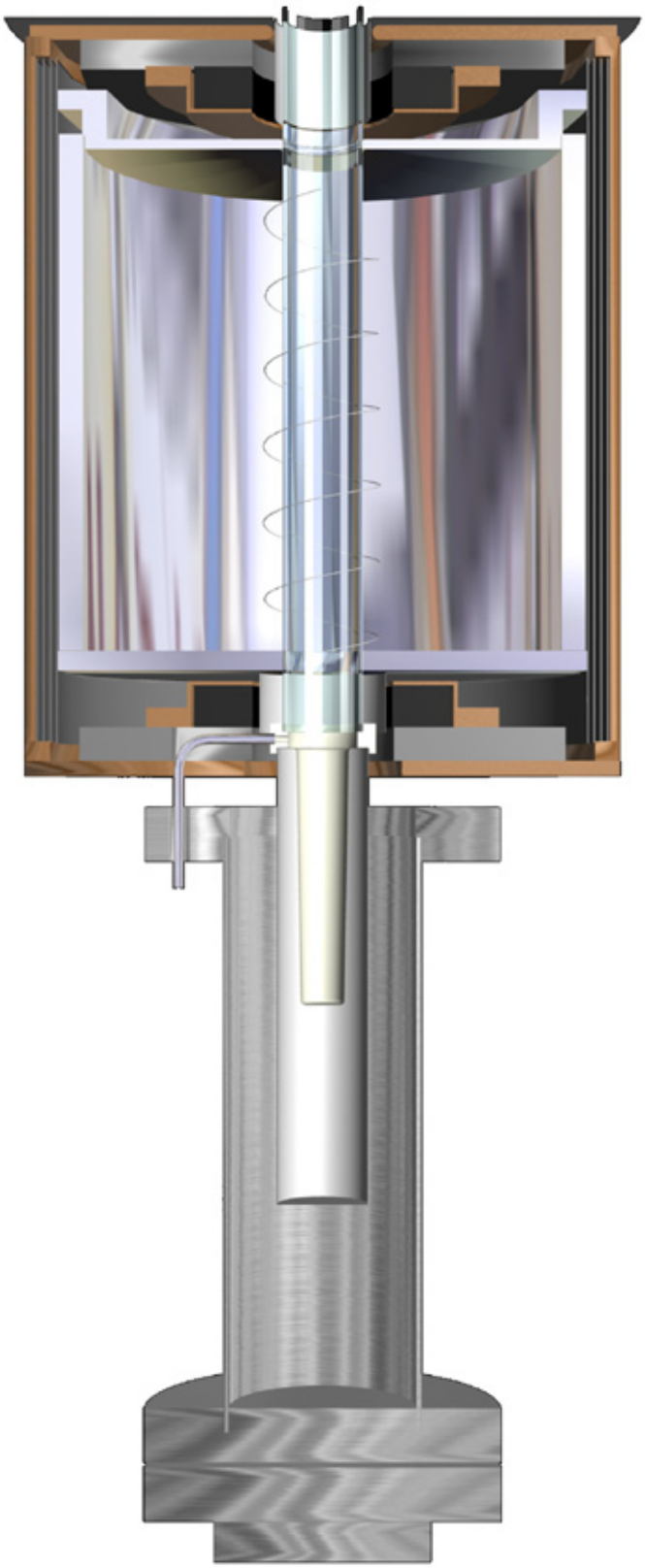

Figure 4-2 Rendered, cross-sectional CAD drawing of TE_{011} plasma cracker with coupled effusion cell.

Source Design

The ECR technique has important advantages compared to other techniques of plasma excitation, particularly for crystal growth applications. Excitation at microwave frequencies (e.g.: 2455 MHz) rather than at RF (typically 13.56 MHz) significantly reduces the average ion energies within the plasma since there is less time during which the ions can accelerate and absorb energy within each cycle before the reversal of the force on the ions due to the electromagnetic field's oscillation. Typical ion energies in microwave plasmas are tens of volts, while typical ion energies in RF plasmas are hundreds of volts.

Another related consequence of this frequency difference is that the sheath potential of a microwave plasma (*i.e.*, the potential difference between external ground and the plasma volume) is significantly lower than that of a RF plasma. The sheath potential is a consequence of the higher mobility of electrons than ions in response to the impressed electromagnetic field. Electrons tend to escape to grounded surfaces surrounding the plasma faster than ions as a consequence of their lighter mass and thus higher mobility. Hence in steady state the plasma assumes a positive electrostatic potential with respect to ground to establish a dynamic equilibrium between the electron and ion loss and generation mechanisms. Quasi-neutrality is thereby maintained in the plasma volume.

The importance of these differences for crystal growth applications is extremely significant. The value of ion bombardment of growth surfaces for increasing the surface mobility of adatoms has been clearly demonstrated [212].

It is critical for the growth of high quality crystalline materials that the energies of the incident species at the growth surface be sufficiently low to prevent ion bombardment damage, else the growth temperature (or post-growth thermal treatment temperature) must be sufficiently high to anneal the point and/or extended defects created by the bombardment.

Magnetic confinement is used in conventional RF plasmas as well as microwave plasmas. A resonance occurs when the excitation frequency coincides with the natural "cyclotron" frequency (also known as the Larmor frequency) of the electron's circular rotation around their guiding centers as they follow helical trajectories in a magnetic field, given by

$$f_{ce} = \frac{eB_0}{m_e} = B_0 * 2.8 \text{ GHz/kG}.$$

A more complete treatment [214] of the coupled electromagnetic wave and plasma system shows that the eigenmodes for the propagation of electromagnetic waves in a plasma along the direction of a static magnetic field are given by the poles of the complex index of refraction in the dispersion relation:

$$\omega = \frac{c}{\tilde{n}}\, k$$

where the complex index of refraction is given by:

$$\tilde{n}^2 = 1 - \frac{\omega_p^2/\omega^2}{1 \pm (\omega_c/\omega)}$$

with

$$\omega_p^2 = \frac{n_0 e^2}{m} \text{ and } \omega_c = 2\pi f_{ce}$$

defining the plasma and cyclotron angular frequencies respectively; m, n_0 and e are the electron mass, electron density and charge. The mode characterized by the negative sign in the denominator of this complex index of refraction is called the "whistler" mode (for historical reasons; see Chen [214] § 4.17.1) or R-wave (because it is right-hand circularly polarized), and is the relevant mode to ECR plasma excitation. Hence, unlike conventional RF magnetically confined plasmas, the magnetic field in an ECR plasma creates a resonance which dramatically increases the absorption of energy by the plasma from the power source. The result of this is that ionization efficiencies in ECR plasmas are one to two orders of magnitude higher than in conventional RF plasmas.

Another significant consequence of the stronger coupling between the excitation and plasma in ECR plasmas is that a self-sustaining discharge can be maintained at pressures one to two orders of magnitude lower than conventional RF discharges. Pressures in the 10^{-4} to 10^{-5} Torr range can be achieved, and are desirable in this and many other low-pressure techniques where long mean free paths are beneficial.

The extraction of ions from an ECR source results from divergence of the static magnetic field and the fact that ion trajectories (in the absence of collisional scattering) follow the magnetic field lines. Since the magnetic moment enclosed an ion's helical trajectory in a magnetic field is an adiabatic invariant [214] ions

gain kinetic energy when they travel from a region of higher to lower magnetic field. Hence, the energy of ions incident on the growth surface can be directly controlled (over a finite range) by controlling the relative magnetic field at the growth surface compared to the field in the source [215].

The basic source design is a 2.455 GHz resonant microwave cavity placed within a permanent magnet flux shunt assembly to create a "magnetic mirror" plasma confinement volume. Microwave power is coupled to the cavity *via* a high temperature coaxial microwave cable, and coupled within the cavity to the plasma by a helical antenna designed to couple efficiently to the R-wave eigenmode. The reactants are isolated from the cavity by a sapphire tube to prevent unwanted deposition within the source, and to insure that all of the escaping reactant flux is directed toward the substrate. Two sources have been used, a TM_{011} cavity (which is relatively small), and a TE_{011} cavity.

The combination of a helical antenna and resonant cavity is known in the modern literature as a helical resonator. It was first described in 1970 by Lisitano and coworkers [216], who built a very similar discharge source for gases, but to this author's knowledge this is the first time such a structure has been coupled to the exit orifice of an effusion cell. Although the cavity may be resonant prior to ignition of the plasma, its modes are significantly perturbed by the plasma itself, a problem previously addressed analytically by Agdur and Enander [217]. Lisitano found that very efficient non-resonant absorption was maintained in

spite of this when a helical antenna was used, so these antennas are sometimes referred to in the literature as a "Lisitano coil."

The relative advantages of ECR microwave plasmas compared to conventional and magnetically confined RF plasmas have discussed in this introduction. In summary, they are lower ion energies, control of incident ion energies *via* control of the magnetic field strength at the growth surface, higher ionization efficiency, and lower pressure operation. The advantage of this ECR source over commercial ECR sources, or conventional ECR source designs are the utilization of elemental reactants and the ability to control their hydrogenation by mixtures of hydrogen with the injected buffer gas. The results of this source development could be applicable to other material systems, such as GaAs, and other growth techniques, such as Metal-Organic MBE. Details of specific source design issues will be discussed in the following subsections.

Antenna Design

Symmetry considerations are extremely important in optimizing the design of the discharge chamber to maximize the power coupled from the power supply into the plasma. The whistler mode is a TEM-type mode propagating parallel to the external static magnetic field, hence the electric and magnetic fields oscillate in the plane perpendicular to the wave's direction of propagation. An externally impressed microwave field and cavity modes excited by that

external field can only couple to this plasma mode to the extent they share this symmetry.

Most commercial ECR sources couple microwaves into a cylindrical ionization cavity by means of an axial, end-coupled TE_{10} rectangular waveguide. This couples strongly to the cavity if it is designed to resonate in a TE mode at the oscillator's frequency, which can in turn couples strongly to the Whistler plasma mode (presuming an axial static magnetic field is used). This end-coupled waveguide, however, is completely incompatible with an end-coupled effusion cell and any other hollow waveguide coupling geometry would not efficiently couple the external power with the cavity modes.

Hence, an antenna had to be designed which would effectively couple to both a cavity TE mode and the plasma whistler mode. The choice of antenna coupling to the cavity immediately forces the use of coaxial waveguides to deliver power to the antenna. This created two challenging issues: a microwave cable and power feedthrough for the vacuum chamber. This section will discuss the significant issues and solution to each of these two problems.

Helical antennas have long been used for microwave applications since their invention in 1946, and a great deal of empirical and analytical information is available regarding their impedance and radiation characteristics in less complex applications [218]. When embedded in a resonant cavity, analytical calculation of their effective radiation impedance becomes an intractable problem, although approximation methods have been reported [219,220]. The

techniques developed for impedance matching of helical antennas to coaxial transmission lines [221] have been implemented in the final antenna design to the extent feasible given manufacturing constraints. Specifically, the antenna is peripherally fed via a bulkhead feedthrough in the base of the cavity and dielectrically isolated from the ground plane by a boron nitride disc against which it rests (pitch=0) for the first half-revolution, creating a $\lambda/2$ transmission line coupling. The pitch increases linearly over the second half-revolution to its final value determined by the radius and the "one integral wavelength per revolution" constraint described next.

One goal of the overall source design is to maximize the interaction probability to achieve the greatest possible degree of molecular dissociation, excitation and ionization. To maximize the transverse electric field strength along the central axis of the cavity a helical antenna design was selected with the helix diameter and pitch chosen to give a path length along the antenna of one wavelength at 2.455 GHz per revolution. This insures that the electric field vector in the *interior* of the helix is predominantly radial. The wavelength is fixed by the oscillator frequency at

$$\lambda_{2.455\ \mathrm{GHz}} = \frac{c}{\nu} = \frac{2.998 \times 10^{10}\ \mathrm{cm/sec}}{2.455 \times 10^{9}\ \mathrm{cyles/sec}} = \mathbf{12.21\ cm = 4.807"}$$

The general expression for the path length, s, of a helix of pitch l and with $\theta/2\pi$ rotations is:

$$s^2 = (\theta r)^2 + l^2 \leftrightarrow l = \sqrt{s^2 - (\theta r)^2}$$

Hence the maximum radius of a helical antenna at this wavelength subject to the "one integral wavelength per revolution" constraint is found by setting the pitch (l) to zero, or:

$$s^2 = (2\pi r)^2 \leftrightarrow r_{max} = \frac{12.212 \text{ cm}}{2\pi} = 1.944 \text{ cm}$$

These design choices and constraints led to the selection of a 1" outside diameter sapphire tube as the reaction vessel, when combined with the smallest physical dimensions of standard miniature microwave cable connectors (type SMA). Two antenna types were built, one with a radius of 0.6" and one wavelength pathlength; the other six wavelengths pathlength with a radius of 0.7"; for use with effusion cells with or without water cooling, respectively.

These antennas, the coaxial microwave cable and microwave vacuum power feedthroughs were custom built utilizing materials and techniques developed originally for advanced radar systems for demanding military aircraft applications. Several iterations of design were necessary to eliminate inadequacies which resulted in failure of the various components during the earlier technology development phases of this contract. Design features which were found to be important include venting of cable connectors inside the vacuum to prevent virtual leaks and localized plasma breakdown, the replacement of all brazed joints in the antenna assembly with laser welded or mechanically constrained connections to prevent thermal runaway and melting,

and the use of hermetically sealed, silica-filled high temperature stainless-clad copper coaxial conductor cables.

Cavity Design

A resonant microwave cavity load has the effect of storing electromagnetic field energy, thereby increasing the strength of the fields. It can be shown that in the absence of an interior conductor, only two types of resonant modes can be sustained in a right circular cylindrical waveguide or cavity, those with radial magnetic field vector (TM) and those with radial electric field vector (TE) [222, p. 95]. Calculating the dependence of these mode frequencies on the geometric dimensions of ideal cavities is straightforward, but provides only a first order estimate of the resonant frequencies of a practical cavity design for this application, which includes perturbations due to apertures on either end, dielectric loading (the sapphire discharge chamber tube and boron nitride insulators) and interior conductive surfaces (the helical antenna and plasma column itself during operation).

Estimation techniques for some of these perturbations have been discussed in the literature [223]. Calculating the exact magnitude of these perturbations is possible using finite-element analysis, but empirical quantification of these deviations from ideality is simpler, cheaper and quicker. The effect of the perturbations was correctly anticipated to be a reduction in the mode frequencies when compared to the idealized cavity calculations.

The procedure used to optimize a cavity was to originally construct it with a smaller inside diameter than would be calculated for the ideal mode at the pump frequency. Then microwave impedance measurements of the cavity were conducted to measure the deviations of the cavity from ideality, and then the cavities were re-machined to larger inside diameter in an iterative process which converged on the required dimensions in one or at most two iterations. Other key considerations in the choice of cavity dimensions were maximizing the frequency separation of the desired mode from competing modes (which could result in mode-hopping and instability) and maximization of the quality factor (Q) of the desired cavity mode. Resonant mode frequencies were calculated using the expression [222, p. 328]:

$$f_{\mathrm{nml}} = \left[\left(\frac{x_{\mathrm{nm}}}{a}\right)^2 + \left(\frac{l\pi}{h}\right)^2\right]^{1/2} \frac{c}{2\pi}$$

where a is the cavity radius, h is its height, c is the speed of light and for TE modes $x_{\mathrm{nm}} = p'_{\mathrm{nm}}$ (the n^{th} root of the equation $J'_m(x)=0$ where $J'_m(x)$ is the first derivative of the Bessel function $J_m(x)$) whereas for TM modes $x_{\mathrm{nm}} = p_{\mathrm{nm}}$ (the n^{th} root of the equation $J_m(x)=0$).

The initial TE_{011} mode cavity design was based on the general observation that the Q is maximal for approximately equal height and diameter, combined with a plot of "isofrequency" contours for the various neighboring modes at a frequency corrected by the loading and non-ideality shifts previously measured on a smaller cavity.

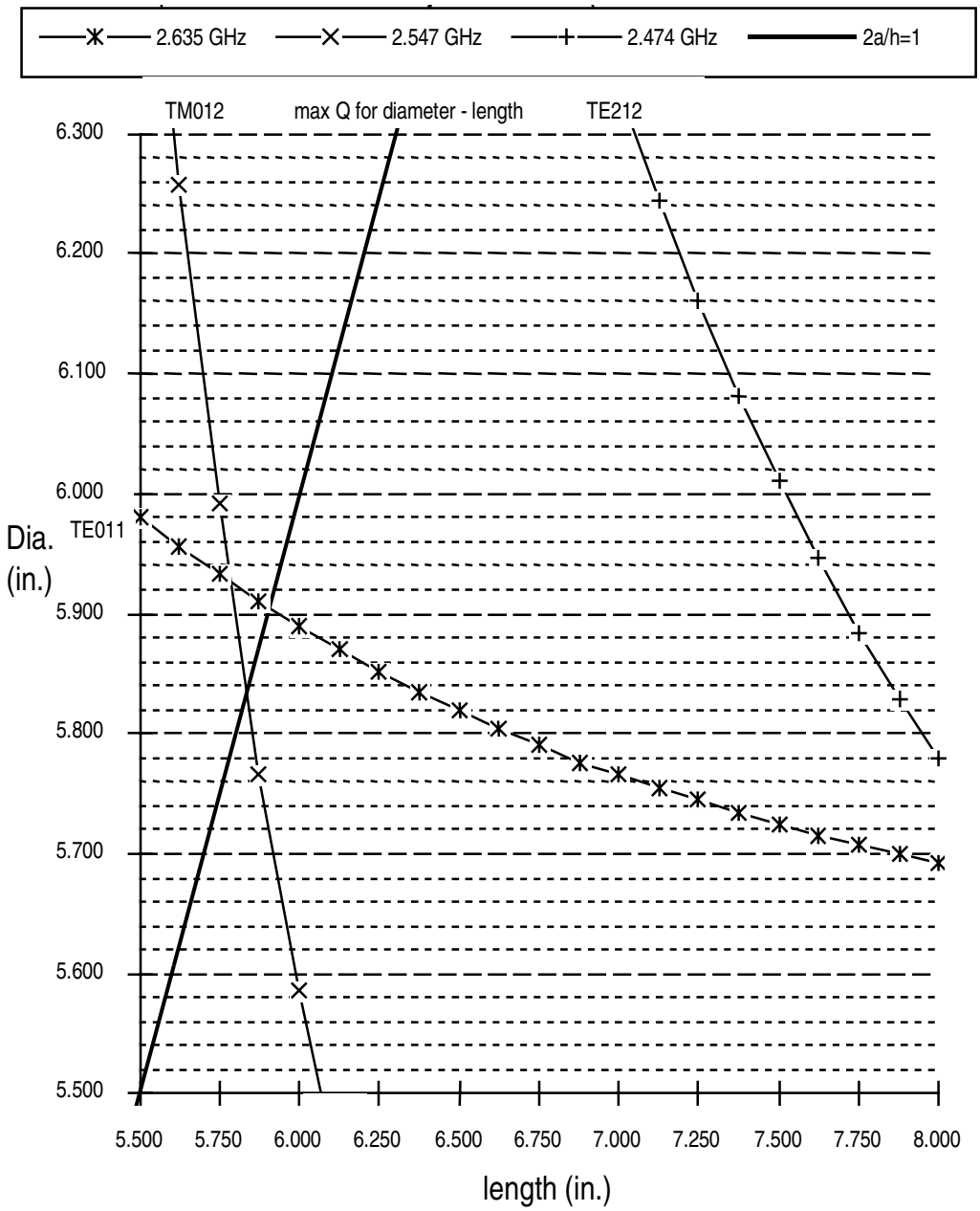

Figure 4-3 Calculated resonant frequency contours of TE_{011} and neighboring modes as a function of diameter and height of an empty ideal right circular cylindrical cavity.

In this context "unloaded" means the cavity was measured *without* the sapphire discharge tube inserted and "loaded" means measurement *with* the tube inserted (operational mode). The non-ideality shifts are the differences

between the calculated mode frequencies for an ideal cavity and those measured for the unloaded cavity, which is perturbed by the antenna, boron nitride insulators, and endface apertures. Results are shown in Figure 4-3.

Note that the total shifts of the different modes vary greatly, far more than their resonance bandwidths, as will be shown further on. Furthermore, the resonant frequency of the mode of desired symmetry, the TE_{011} mode, is relatively insensitive to the cavity length. This makes accurate tuning relatively easy but conversely requires a very careful choice of cavity diameter if the effective tuning range is to be in the frequency domain of interest.

Table 4-2 Calculated mode frequencies of semifinal TE_{011} cavity design at *minimum* tuning length limit.[a]

Character	n	m	l	Bessel root (n,m)	*f* (GHz)
TE	1	1	1	1.841	1.5380
TM	0	1	0	2.405	1.5446
TM	0	1	1	2.405	1.8312
TE	2	1	1	3.054	2.1942
TE	1	1	2	1.841	2.2952
TM	1	1	0	3.832	2.4610
TM	0	1	2	2.405	2.5011
TM	1	1	1	3.832	2.6503
TE	**0**	**1**	**1**	3.832	**2.6503**
TE	2	1	2	3.054	2.7779
TM	1	1	2	3.832	3.1506
TE	0	1	2	3.832	3.1506

[a] diameter = 5.850", length = 6.000"

Results of the ideal cavity mode analysis prior to the last design iteration of the TE_{011} cavity are shown in Table 4-2 and Table 4-3 for the upper and lower

length limits of the cavity's tuning range, respectively. Experimental data will be presented and compared with these calculations in a subsequent section.

Table 4-3 Calculated mode frequencies of semifinal TE_{011} cavity design at *maximum* tuning length limit.[b]

Character	n	m	l	Bessel root (n,m)	*f* (GHz)
TE	1	1	1	1.841	1.4994
TM	0	1	0	2.405	1.5446
TM	0	1	1	2.405	1.7989
TE	2	1	1	3.054	2.1673
TE	1	1	2	1.841	2.1907
TM	1	1	0	3.832	2.4610
TM	0	1	2	2.405	2.4056
TM	1	1	1	3.832	2.6281
TE	**0**	**1**	**1**	3.832	**2.6281**
TE	2	1	2	3.054	2.6923
TM	1	1	2	3.832	3.0754
TE	0	1	2	3.832	3.0754

[b] diameter = 5.850", length = 6.400"

Magnetic Flux Shunt Design

As described in earlier sections, one goal of the overall source design is to maximize the interaction probability to achieve the greatest possible degree of molecular dissociation, excitation and ionization. Another means of achieving this goal is to use magnetic confinement techniques to increase the residence time and thereby the steady-state concentration of ions in the plasma volume. A magnetic mirror is a field arrangement originally developed for plasma research which utilizes two annular magnets or solenoids with their magnetic fields parallel to their common axis, and creates a region of lower magnetic field flux between them. Ions generated in this lower field region will travel in helical

trajectories along the flux lines, but due once again to the adiabatic invariance of the magnetic flux enclosed in that helix they will *decelerate* as they approach the *higher* flux region, and given sufficiently high field gradients most will reflect back into the interior of the plasma volume. In the context of an ECR source, most primary ion generation will occur in the resonance field region, so it is important that this resonant field strength occur inside the microwave cavity and that higher fields exist near the entrance and exit apertures of the source.

Permanent magnets were chosen for this magnetic mirror design due to their relative compactness compared to sufficiently strong electromagnets. The tradeoff of greatest consequence was the requirement for substantial heat shielding, water cooling, and thermal isolation from the effusion cell and discharge cavity to prevent thermal demagnetization of the permanent magnets. To isolate their strong magnetic fields from the rest of the vacuum system instruments and to prevent their uncontrolled interaction with other magnetizable system components, these magnets were enclosed in a "flux shunt," an enclosure of highly susceptible magnetic materials which have the effect of "channeling" the magnetic field between the two permanent magnet annuli.

Samarium-cobalt magnets with a Sm_2Co_{17} alloy composition and 26 Oersted-Gauss B-H field energy product were chosen. The cylindrical magnetic flux shunt is comprised of end-plates fabricated from a 49% nickel, 49% cobalt, 2% vanadium alloy sold under the trade name of "2V-Permandur," connected

via a cylindrical coil of 49% iron, 49% cobalt, 2% vanadium alloy sheet metal sold under the trade name of "Permandur." These magnetic components were pre-assembled onto water-cooled copper heat spreaders, which became the primary structural components of the entire source. The exteriors of the copper components were nickel plated to prevent corrosion due to selenium vapor.

Microwave Characterization

Microwave cavity impedance measurements were conducted throughout the course of this source development effort to provide feedback to the iterative design optimization process described in a later section. All of these measurements were conducted using a Hewlett-Packard 8753 network analyzer with 8753B and 85047A modules for the measurement of forward and reflected power. The results of these measurements were plotted as reflected signal attenuation (in decibels) versus frequency. The results of one such measurement, conducted *in-situ* with the final cavity design is shown in Figure 4-4.

The assignment of modes and determination of shifts due to non-ideality were conducted by comparing the calculated and empirical data for unloaded cavities, as demonstrated with Table 4-5 for the measured data corresponding to the ideal cavity calculation results presented in Table 4-2 and Table 4-3. In general it was found that mode identification was best made on the basis of shifts in frequency accompanying changes in diameter and length of a cavity than on the basis of the absolute frequency measurement, since the frequencies of the

various modes shift by different amounts, sometimes resulting in empirically different ordering of the modes than were calculated.

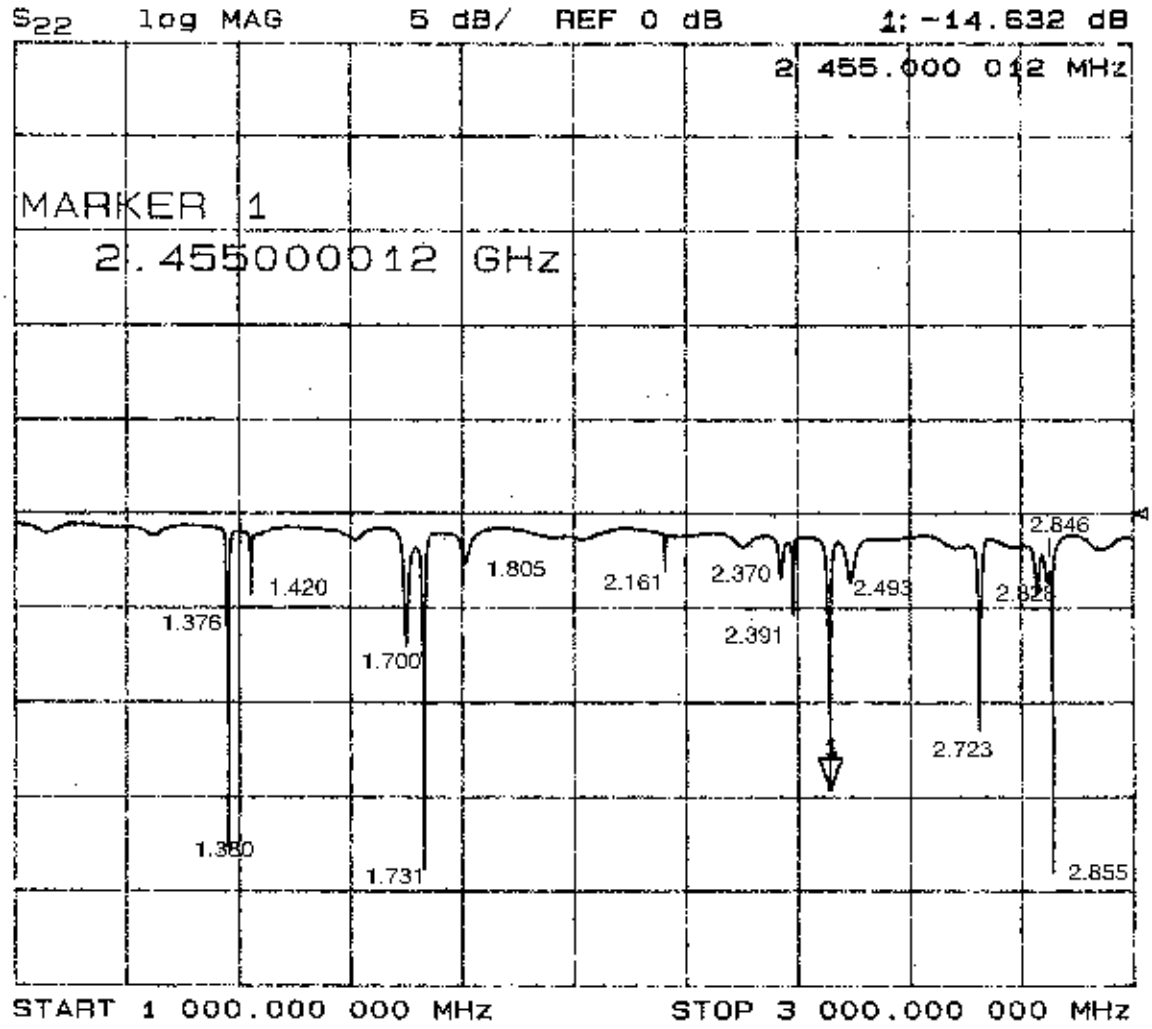

Figure 4-4 *In-situ* impedance measured over a 2GHz range of the final cavity design at its optimal tuning length for TE_{011} operation.

Note that there are more experimentally measured modes than calculated. Some of these unpredicted resonances are clearly due to splitting of degenerate modes resulting from symmetry violation. Such modes are identifiable because they nearly perfectly track one another. Another resonance, labeled "antenna" is

assigned as such because it does not shift with *any* change in cavity geometry. Finally, some of the modes may be unpredicted modes of TEM character since the introduction of the antenna in the interior of the cavity removes the previously mentioned proscription against TEM modes, which applies strictly only to cavities without interior conductors. On the other hand, no resonance was found in cavities of any dimension that correspond to the TE_{112} mode predicted by the general theory. The reason for its absence is uncertain.

The determination of shifts due to loading the cavity with the sapphire discharge chamber tube were conducted by comparing the empirical data for loaded and unloaded cavities, as shown in Table 4-4 for the TE_{011} mode. Note that the loading shift of this individual mode is quite reproducible and constant. Also, note that the lowest TE_{011} mode frequency for this semifinal cavity design, corresponding to the loaded cavity at maximum tuning length, is too high.

Table 4-4 Comparison of frequency shifts of the TE_{011} mode due to dielectric loading of the cavity[a] at several different lengths.

length (in):	loaded *f* (GHz)	Δ*f*	unloaded *f* (GHz)	Δ*f*	Loading Shift
6.0000	2.468		2.529		-0.061
		-0.008		-0.009	
~6.35	2.46		2.52		-0.06
		-0.004		-0.003	
6.4000	2.456		2.517		-0.061

[a] diameter = 5.850"

Table 4-5 Compilation of theoretical calculations and experimental data demonstrating unloaded semifinal[a] cavity mode assignments.

Cylindrical cavity calculated modes	***f* (GHz)** height= 6.0000"	height= 6.4000"	tuning shift **Δf [ideal]**	tuning shift **Δf [data]**	***f* (GHz)** height= 6.00"	height= 6.40"	**Assignment of Measured Modes**	**Non-ideality Shift** (measured-ideal) height= 6.00"	height= 6.40"
TE 111	1.5380	1.4994	0.0386	0.0260	1.3925	1.3665	TE 111	-0.14549	-0.13292
TM 010	1.5446	1.5446	0.0000	-0.0070	1.5680	1.5750	TM 010	0.02343	0.03043
TM 011	1.8312	1.7989	0.0323		1.7590				
TE 211	2.1942	2.1673	0.0269	0.0310	1.8410	1.8100			
TE 112	2.2952	2.1907	0.1045	0.0190	1.8540	1.8350	TM 011	0.02284	0.03611
TM 110	2.4610	2.4610	0.0000	0.0230	2.1730	2.1500	TE 211	-0.02119	-0.01733
TM 012	2.5011	2.4056	0.0955	0.0780	2.4970	2.4190	TM 012	-0.00411	0.0134
TM 111	2.6503	2.6281	0.0222			2.4280			
TE 011	**2.6503**	**2.6281**	**0.0222**	-0.0010	2.4350	2.4360	TM 110	-0.02603	-0.02503
TE 212	2.7779	2.6923	0.0857	0.0120	**2.5290**	**2.5170**	**TE 011**	**-0.12131**	**-0.11112**
TM 112	3.1506	3.0754	0.0753	0.0020	2.5590	2.5570	antenna		
TE 012	3.1506	3.0754	0.0753			2.6730	TE 212		-0.01925
				0.0270	2.8580	2.8310			
				0.0550	2.9100	2.8550			
				0.0490	2.9260	2.8770			

[a] diameter = 5.850"

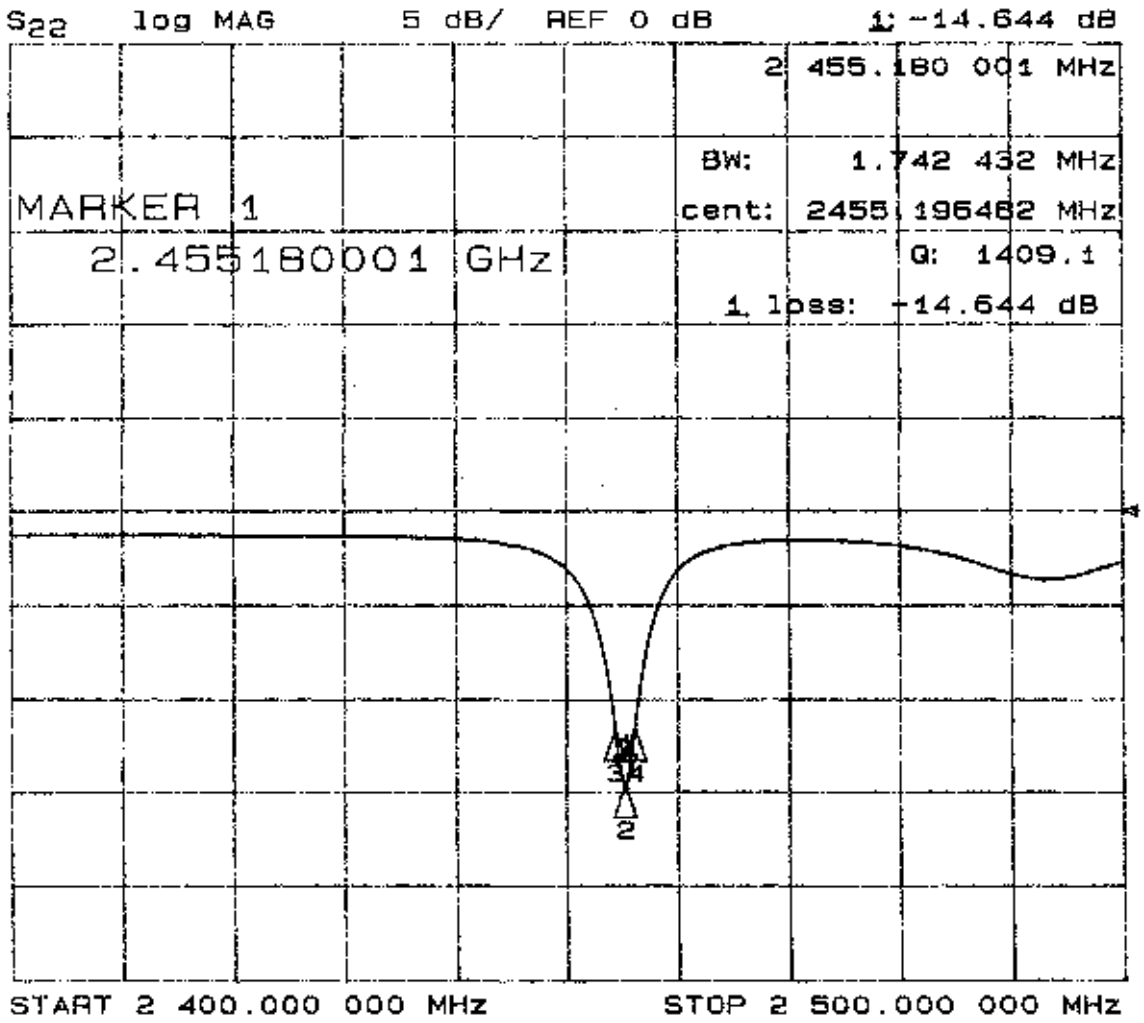

Figure 4-5 Final cavity design, tuned and fully loaded, *in-situ* TE_{011} mode impedance measurement.

The final TE_{011} cavity design, compensated for all the perturbations, loading effects, and deviations from ideality described above, has an inside diameter of 5.875" and tuned to the microwave power supply frequency at an inside length of ~6.03". Its measured microwave impedance and derived parameters are shown in Figure 4-5. Note that the bandwidth is only 1.74 MHz, quite narrow when compared to its tuning range (cf: Table 4-5) of ~12 MHz. The

quality factor (Q) of 1409 is proportional to the ratio of the time-average energy stored in the cavity to the energy loss per second, which is $Q/2\pi$ or 224 [222, p. 314]. The return loss of -14.64 dB is equivalent to an 81% attenuation of the input voltage in the reflected wave amplitude. These characteristics are quite adequate for these materials processing applications.

Magnetic Profiling

To discover whether the source design would achieve the requisite ECR resonance condition, the magnetic field strength distribution of the completed assembly was measured *in-situ*. The data were collected using a F.W. Bell Model 4048 Gaussmeter with their model A-4048-002 axial magnetic flux probe. Thus, the data compiled in Table 4-6 are a measurement of only the *axial* component of the magnetic field vector. Two sets of measurements were made, one at a radius approximately 1mm inside the sapphire discharge tube, the other along the center axis of the tube. Distances are measured from the exit aperture of the discharge tube downward toward the effusion cell. Note that both profiles achieve the critical field value of 875 Gauss for ECR resonance at 2.455 GHz outside of the interior of the resonant cavity, which begins at a distance of 4.4 cm from the exit aperture. This is not a desirable configuration since the TE_{011} mode has 0 azimuthal, 1 radial and 1 axial maxima in field strength and a transverse electric field z-dependence proportional to $\sin(\pi z/d)$. Hence, the ideal TE_{011} cavity mode transverse electric field strength falls to zero at the endplates of the

cylindrical cavity. In this configuration only fringing fields extending outside the cavity through the endplate apertures or propogated by a plasma column excited by another absorption mechanism can effectively excite the plasma in the resonance zone. Nevertheless, the source works, and Lisitano noted this same effect in the very first report of an ECR helical resonator [216].

Table 4-6 Axial magnetic field strength profiles of the final source assembly.

axial distance (cm) =	Axial Magnetic Field Strength (Gauss) at 0	0.5	1	1.5	2	2.5	3	3.5	4	4.5	5	5.5
radial distance = 0 cm	146.2	55.1	383	569	765	908	873	634	292	-370	-237	
radial distance = 1.1 cm	112.7	35	340	599	923	993	952	597	151	-197	-358	-448

Source Installation

The TE_{011}-mode cavity and flux shunt assembly described earlier in this chapter constitute the plasma "cracker" which is attached to the exit orifice of a commercial, water cooled, low temperature effusion cell, the EPI-20MLT manufactured by EPI Systems, Inc. The sapphire discharge chamber and effusion cell crucible are coupled by a small pyrolytic boron nitride disc incorporating a socket into which a $^1/_8$" stainless steel gas delivery line is inserted. Microwave power is coupled to the microwave cavity antenna bulkhead fitting by the high-temperature hermetically sealed microwave cable described previously which attaches at the opposite connection to a 1" baseplate feedthrough with

impedance-matched microwave coaxial couplers on either side of the vacuum seal. Power is provided by an Astex S-250 microwave power supply connected to the feedthrough via a circulator, water-cooled dummy load and double-slug tuner. These latter features permit tuning of the load impedance to match the source and protect the power supply from excessive reflected microwave power that might otherwise damage the klystron. The source is mounted onto a water-cooled baffle inside the reactor's chalcogen deposition zone as shown in Figure 3-3.

Source Operational Characteristics

Experiments were conducted to demonstrate operation of the source and test for microwave leakage from the system subsequent to its installation. The source was first tested using helium gas. A steady state discharge was established for ~20 minutes at a forward power of 150 watts, reflected power of 2 watts and a system background pressure of 5×10^{-5} Torr of helium (indicated pressure of 2.6×10^{-4} Torr with calibration of the vacuum gauge controller for nitrogen and a sensitivity ratio of 0.18 [224]). The strong blue emission characteristic of recombination emission from helium plasmas was clearly observable under these conditions.

Argon discharges were also established and the full operational range for this gas was studied. Steady state discharges were routinely established and maintained throughout the epitaxial growth process at a forward power of 200

watts, reflected power of 10 watts, and a system background pressure of 2×10^{-5} Torr at an argon flow of 6 sccm. A discharge could be maintained at pressures as low as 6.5×10^{-6} Torr but the 100 sccm full-range mass-flow controller used to regulate the gas flow was unstable at the lower flow setpoints required to achieve this pressure, and its fluctuations would eventually cause the discharge to extinguish. The lower first ionization potential, higher ionization cross-section, and lower mobility of argon compared to helium [225] undoubtably contribute to the lower minimum pressure for a sustained discharge in this case.

Immediately following the initial loading of the effusion cell with selenium, experiments were conducted in an effort to create a self-sustaining discharge of pure selenium, with no buffer gas flow. A discharge was successfully established on the first attempt, but all subsequent efforts to repeat that experiment were unsuccessful. A plausible conjecture is to attribute this fact to selenium contamination of the inner walls of the sapphire tube during cooldown after that first experiment. When first assembled, the sapphire tube was cleaned with a 1:1:2 mixture of hydrogen peroxide, ammonium hydroxide, and deionized water, respectively. Combined with ion bombardment from the inert gas discharges, the inner walls were uncontaminated at the commencement of the first experiment to establish a selenium discharge, and it is reasonable to argue that the recombination probability for selenium ions incident on that clean surface was significantly less than the surface once contaminated with condensed

selenium. Indeed, a semitransparent residual coating of selenium was observed on the inner surface of the tube when it was removed after a month of operation.

Insufficient plasma characterization data are available to unequivocally identify the nature of the observed discharges. Nevertheless it seems likely that the observed plasma may be sustained both by ECR coupling and a space charge wave resulting from the interaction of the plasma with charge accumulations at the surface of the sapphire discharge tube. This type of wave is not possible in the theory of idealized spatially infinite plasmas, but has been studied extensively in plasma research because of its common occurrence in practical experimental configurations, and in particular in systems with precisely this geometry. Considerable difficulty is entailed in distinguishing these space charge modes in finite plasmas bounded by dielectric surfaces from whistler-mode waves because both waves are slow and may have similar pass bands. Furthermore, nearly any antenna in a finite plasma column has fringing fields that can excite the space charge wave and both modes require close antenna coupling to the plasma [226, p. 182]. In this case the axial component of the helical antenna's interior near field is the component oriented in the direction required to couple to these space charge wave modes whereas the radial component is oriented in the direction required to couple to the whistler mode.

Molecular Species Distribution of the Plasma Source Flux

The same QMS techniques described previously in the context of thermal source flux characterization have been applied to measure the distribution of molecular species in the flux from the ECR helical resonator plasma source. The most obvious difference in the experimental conditions between the two cases was the significantly higher total background pressure in this case of 2×10^{-5} Torr, predominately due to the argon buffer gas. Nevertheless, this pressure is well below the manufacturer's claimed linearity limit of 7.5×10^{-5} Torr for the Faraday cup detector used to conduct these measurements.

The results of this experiment are shown in Figure 4-6 and Figure 4-7, which show the raw signals and calculated ratio of selenium monomer to dimer signals. Note that the signal intensities are very low (reduced by three to four orders of magnitude) compared to the data for the thermal cracking source shown in Table 4-1. These measurements of the plasma source were conducted at a selenium effusion source temperature of 200°C, and subsequent growth experiments showed that a source temperature of 300°C was required to achieve fluxes comparable to those provided by the thermal cracking source at temperature of only 150°C. Thus the absolute fluxes used for this measurement were too low for accurate determination of the relative fluxes of any of the species other than the monomer and dimer.

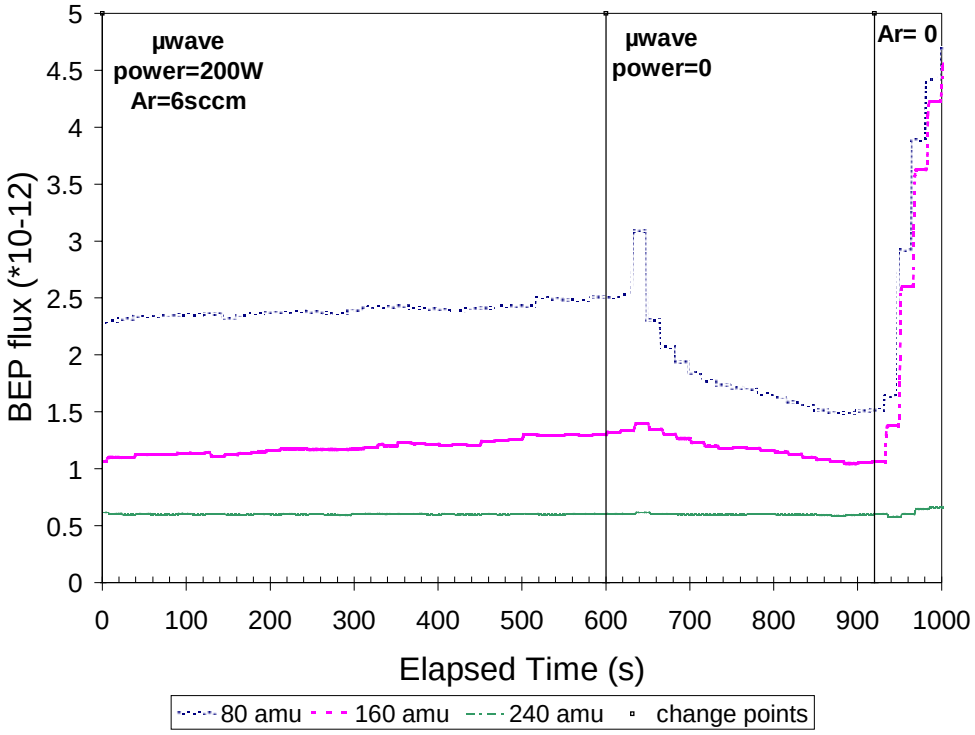

Figure 4-6 QMS ion currents generated by fluxes from the plasma source of selenium molecules formed from the predominant mass 80 isotope.

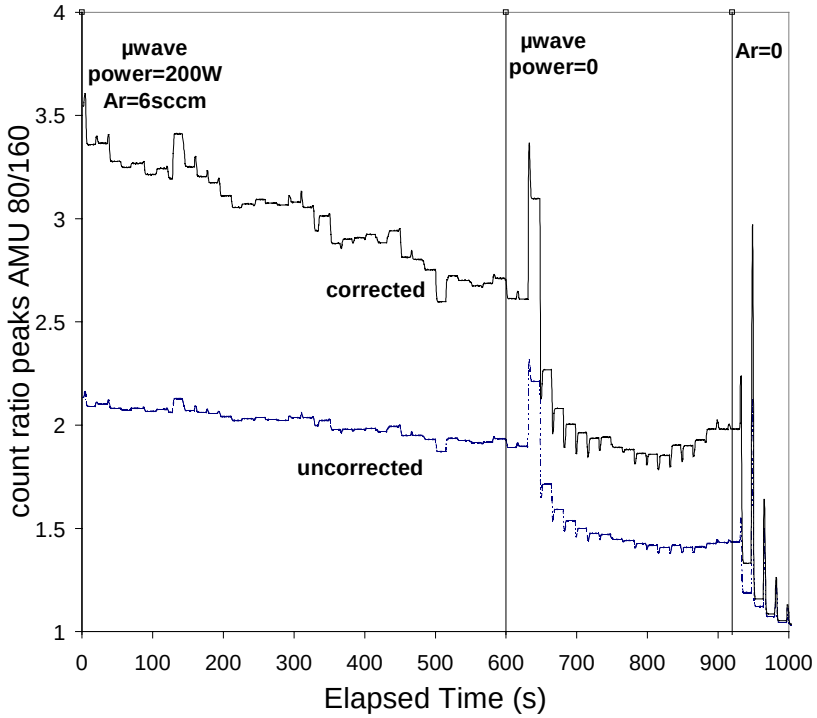

Figure 4-7 QMS ion-current ratio generated from selenium monomer and dimer fluxes from the plasma source.

Figure 4-7 shows that the uncorrected monomer/dimer ion current ratio drops from about 2 to 1.4 when the microwave power is reduced to 0. Figure 4-6 shows that the absolute magnitude of both decrease as well, but these signal intensities' declines cannot be directly analyzed quantitatively because all include too great a contribution from the noise of the detector (all higher mass peaks overlap each other thereby indicating the noise level). Thus this monomer/dimer ratio calculation provides only a lower limit. Figure 4-7 also shows the "corrected" ratio with the mean value of all higher mass peaks' signal (0.59) subtracted from both data sets before calculating the ratio. In this case the monomer/dimer ion current ratio drops from about 3 with the plasma to 2.1 without. This latter value compares favorably with that for the thermal cracker data (where the statistics are much better). The ratio from Table 4-1 is 2.15 for the low-T thermal case and decreases to 0.65 in the high-T case.

The factor of ~2 increase in absolute signal intensity when the argon flow is terminated also suggests that some gas-phase scattering occurs. Calculations of the various species' mean free path lengths were performed for the background value of pressure, and the results were all in the 100-1800 cm range (lowest for the large selenium molecules). Nevertheless, since the gas is injected a few millimeters above the effusion cell's exit orifice, the local molecular density at that point is much higher, resulting in locally reduced mean free path lengths.

Ion Flux from the Plasma Source

Considerable efforts were made to directly measure both the ion flux mass and energy distributions from the plasma source. The ion flux mass distribution measurement was attempted using the same QMS with its emission current set to zero, so that the only measurable currents would be those pre-existing in the flux from the source itself. Every experiment gave a negative result, indicating ion currents from the source could not be measured with the QMS. These experiments were conducted using the much more sensitive secondary electron multiplier as well as the Faraday cup detector but still returned a negative result.

A retarding grid ion energy analyzer was also constructed for the sole purpose of measuring the energy distribution of the ion flux, using a design published in the literature specifically optimized for the measurement of ECR plasmas. Repeated efforts to measure any ion current from the source using this instrument consistently yielded a negative result, independently verifying the results of the QMS measurements.

These results were unexpected but not inexplicable. The magnetic mirror confinement structure used to create the resonant ECR static magnetic field was originally developed as a confinement system in the course of fusion research. It was mostly abandoned for that application because of leakage from the magnetic cusps which represented an unacceptable loss in plasmas at the high densities and temperature required for fusion applications. The leakage from such a system is much less for low-temperature plasmas such as the present one.

It is likely that the dominant reason for the difference between this source and others published in the literature (some of which use magnetic mirror confinement yet nevertheless deliver measurable ion currents) is the combination of the 1 inch diameter sapphire discharge confinement tube and the divergent magnetic field within the cavity. As described earlier in this chapter, in the absence of scattering events, ions in a magnetic field follow the field lines with their gyration radius increasing as the flux density decreases, since the total flux enclosed in their trajectory is an adiabatic invariant. These effects combine to direct the vast majority of the ions generated in the plasma into a collision trajectory with the walls of the sapphire tube. This will neutralize a significant fraction of those ions that do not stick to the surface, and once neutralized their trajectories are no longer perturbed by either the static magnetic or microwave electromagnetic field. This yields a hyperthermal component in the flux from the source with energies widely distributed between ~10 m*e*V thermal energies and 10 *e*V characteristic ECR plasma energies. It probably also yields a distribution with disproportionate fractions of molecular species in excited internal vibrational states as well as molecular radicals.

Thus the experimental evidence shows that this device is most accurately described as a source that uses an ECR plasma to generate a partially dissociated hyperthermal radical beam of molecular species but which does not produce significant ion fluxes outside the source itself. The abbreviated description of the source as a "plasma cracker" is therefore more precise than reference to it as a

"plasma source." The next chapter will nevertheless demonstrate that its use for the growth of metal chalcogenides significantly changes the properties of the resulting materials, consistent with the increased selenium reactivity implied by the results of these characterization studies.

CHAPTER 5
GROWTH OF METAL CHALCOGENIDES

The reactor described in a previous chapter was applied to the growth of polycrystalline (Cu,Se) and (In,Se) thin films, polycrystalline ternary CIS thin films both with and without intentionally added sodium, and epitaxial films of CIS on GaAs, ZnTe, and SrF_2 substrates. The effects of intentionally added sodium were studied in these films, and some of the polycrystalline CIS films were processed to create photovoltaic devices. The binary selenide films were combined by sequential deposition to form bilayer structures, which were subsequently processed *ex-situ* by RTP to form single-phase chalcopyrite $CuInSe_2$. The effects of selenium reactant activation both by high-temperature thermal dissociation and by means of the ECR plasma cracker were compared in the case of epitaxial growth.

Binary Chalcogenides

The relationships between the conditions employed for growth of (Cu,Se) and (In,Se) layers on molybdenum-coated SLG and the composition and structure of the resulting polycrystalline thin films were studied. EDX and EMP composition measurements as well as XRD were used to characterize the films. These data were compared with both published crystallographic diffraction data and the

Cu–Se and In–Se binary phase diagrams, then these measured properties of the films were correlated with those of the known equilibrium phases in their respective binary phase fields. Morphology of the films was also studied both by SE-SEM imaging and Phase-Contrast Microscopy (PCM).

During the growth of polycrystalline binary chalcogenide thin films, substrate temperature during growth and the molar flux ratio of selenium to metals were varied. The full temperature range of the reactor's capability was not investigated for binary growth, however, since the goal of these studies was to determine the conditions under which (Cu,Se) and (In,Se) binary films with specific target compositions and suitable morphology could be grown for application to RTP synthesis of ternary CIS thin films. Initial experiments indicated that temperature at the lowest range available in the reactor were required for sufficient accommodation of selenium to grow any phase in the Cu–Se phase field other than the $Cu_{2-\delta}Se$ compound. Therefore all of the binary chalcogenide growth studies described below were conducted at a substrate heater control setpoint of 380-400°C, corresponding to a substrate temperature of 235-250°C.

Thermodynamic Phase Control

As previously described, substrate temperature during growth and the molar flux ratio of selenium to metals were the experimental variables amenable to control in these binary growth experiments. The relationship between these experimental variables and the fundamental thermodynamic parameters (T, P, x)

has been discussed in a published thermodynamic analysis of the results of In–Se MBE by Chatillon and coworkers [227], whose arguments are briefly recounted here.

Based on a simple calculation of supersaturation using the incident vapor fluxes and the substrate temperature MBE and related methods are sometimes thought of as highly non-equilibrium processes. However, once the typically poor accommodation of volatile species is taken into account and the thermodynamic system redefined to consider the equilibrium between the crystal bulk and the surface adlayer, thermodynamic analysis has been shown to apply remarkably well [228-230], with concomitant supersaturation pressures that are relatively small.

Deposition of (Cu,Se) polycrystalline thin films

The strategy for RTP synthesis of ternary CIS from binary precursors to be described in detail later in this chapter is based on the use of binary (Cu,Se) thin film precursors with an overall composition of not less than 52.5 mole% selenium, a composition as shown in Figure 5-1 corresponding to the two-phase CuSe + $CuSe_2$ domain at temperature below ~350°C, and also the critical point composition at the 523°C monotectic. Such films are selenium-rich compared to the compound with the highest melting temperature in the phase field, $Cu_{2-\delta}Se$.

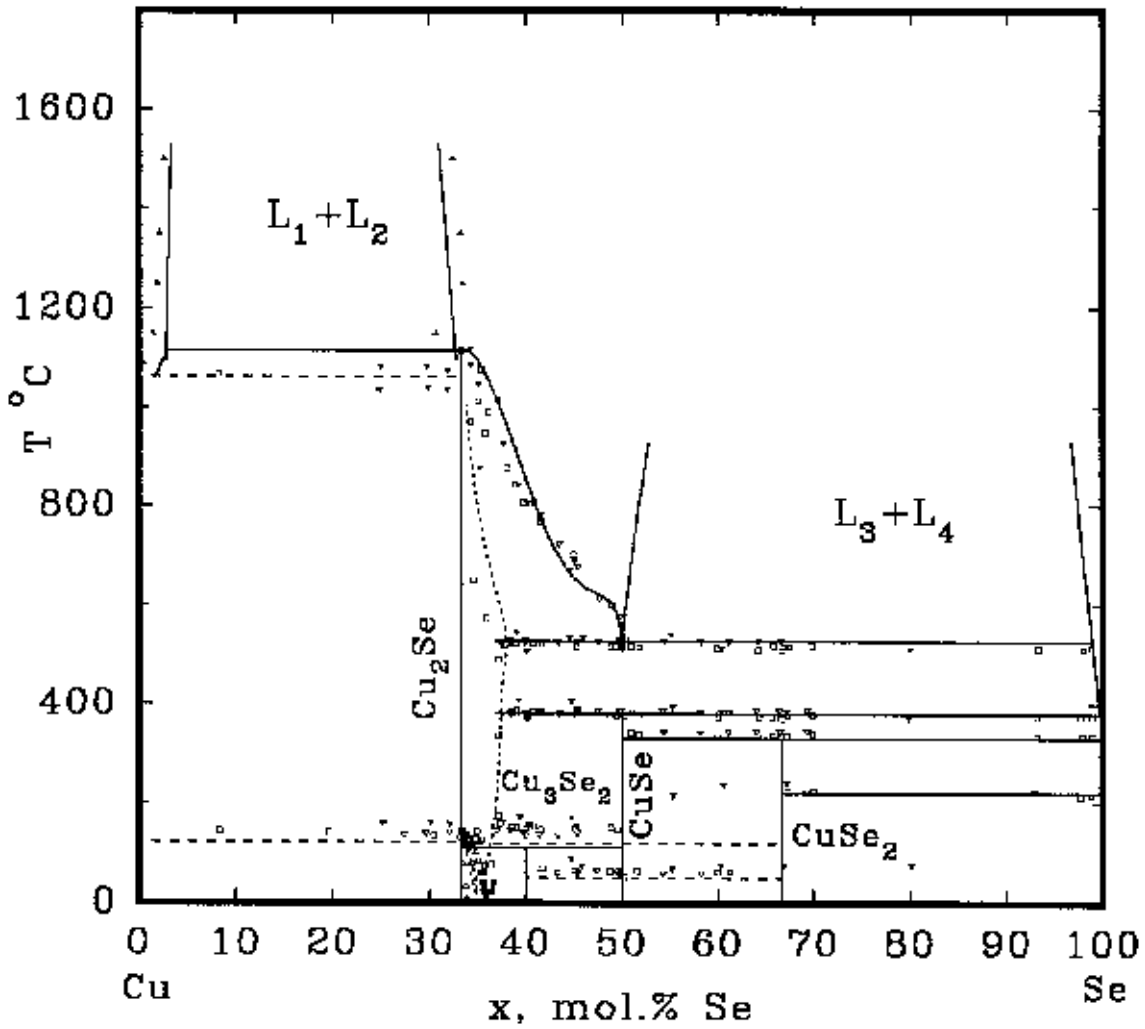

Figure 5-1 Assessed Cu–Se temperature-composition phase diagram [149].

Binary (Cu,Se) thin films with the desired composition (up to 54 at.% Se) were grown and they were found to exhibit strong diffraction spectra indicative of α–CuSe compound formation .

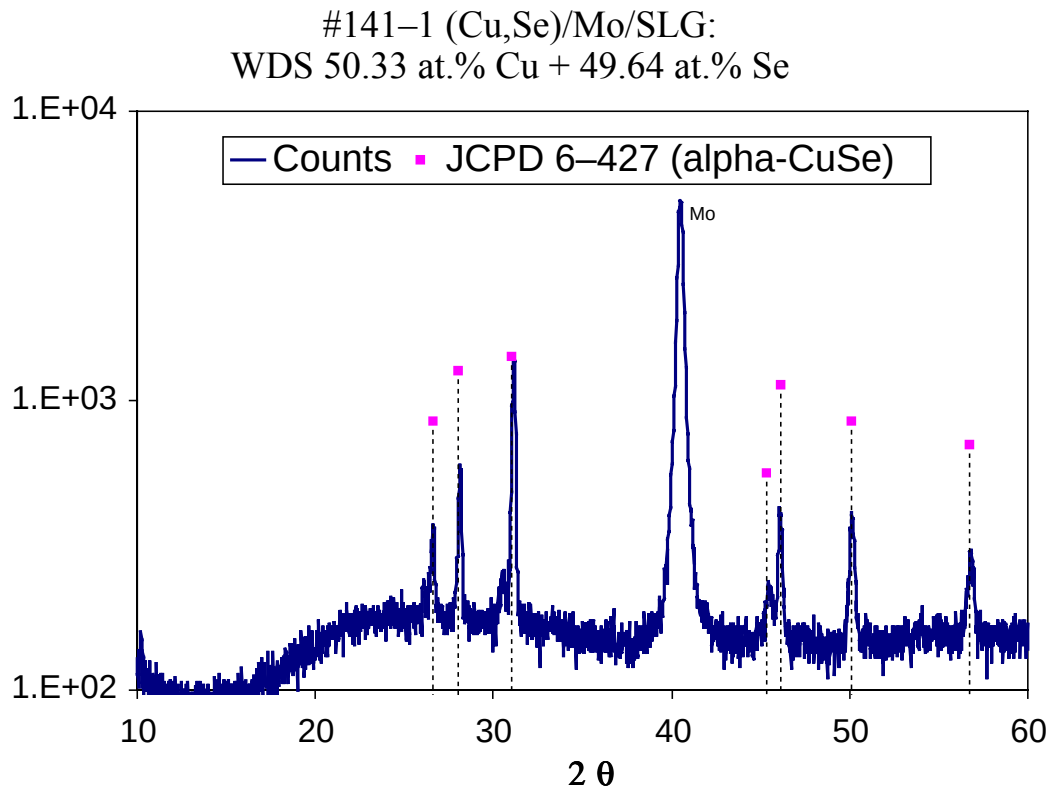

Figure 5-2 XRD θ–2θ scan of desired α–CuSe binary precursor phase for RTP. Films were grown with up to 54 at.% selenium that showed similar XRD patterns.

Deposition of (In,Se) polycrystalline thin films

This same strategy for RTP synthesis of ternary CIS from binary precursors requires binary (In,Se) thin film precursors with an overall composition of not more than 53.8 mole% selenium, a composition as shown in Figure 5-3 corresponding to the compound In_6Se_7 at temperature below ~630°C, where this compound decomposes into a two-phase mixture of In_2Se_3 and a liquid. Such films are selenium-poor compared to the compound with the highest melting temperature in the phase field, In_2Se_3.

In contrast to the (Cu,Se) precursor films grown at these low temperature, the (In,Se) thin films were found to exhibit relatively poor crystallinity, with broad peaks which could not be justifiably assigned to the published crystallographic structures of the equilibrium phases with compositions corresponding to those of these films.

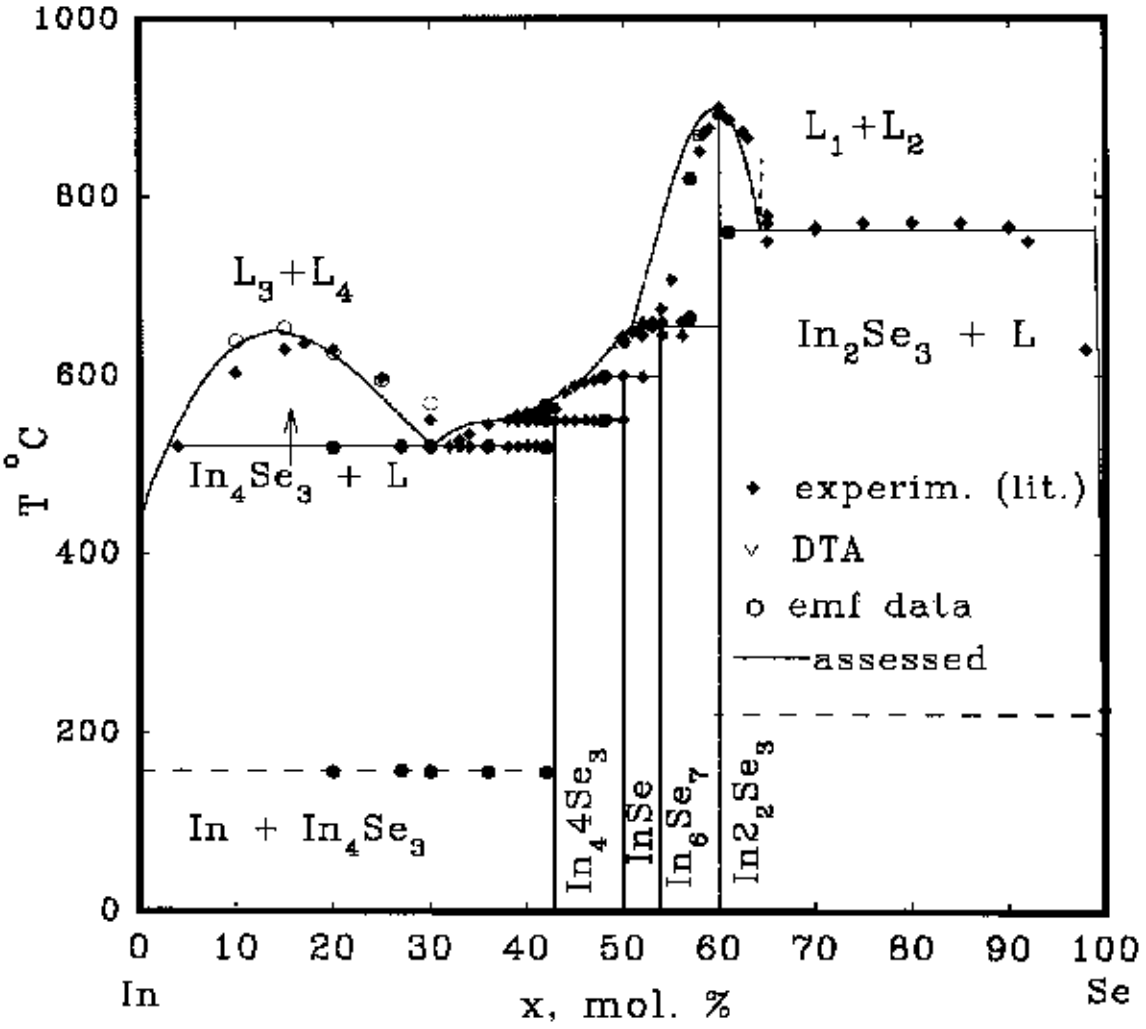

Figure 5-3 Assessed In–Se temperature-composition phase diagram [149].

Deposition of RTP Precursor Films

These foregoing results were employed to deposit bilayer thin films of specific (Cu,Se) and (In,Se) compounds with low melting point temperature, which were used to verify the feasibility of synthesizing $CuInSe_2$ by subsequent rapid-thermal processing, a novel approach developed in the course of this research. This approach is intended to realize the manufacturability benefits that RTP offers [231] whilst employing the reaction engineering flexibility provided by the use of binary precursors. The demonstrated efficacy of a liquid phase quasiepitaxial regrowth process [232] suggests that precursor melting and mixing are important components of an optimized process for CIS synthesis.

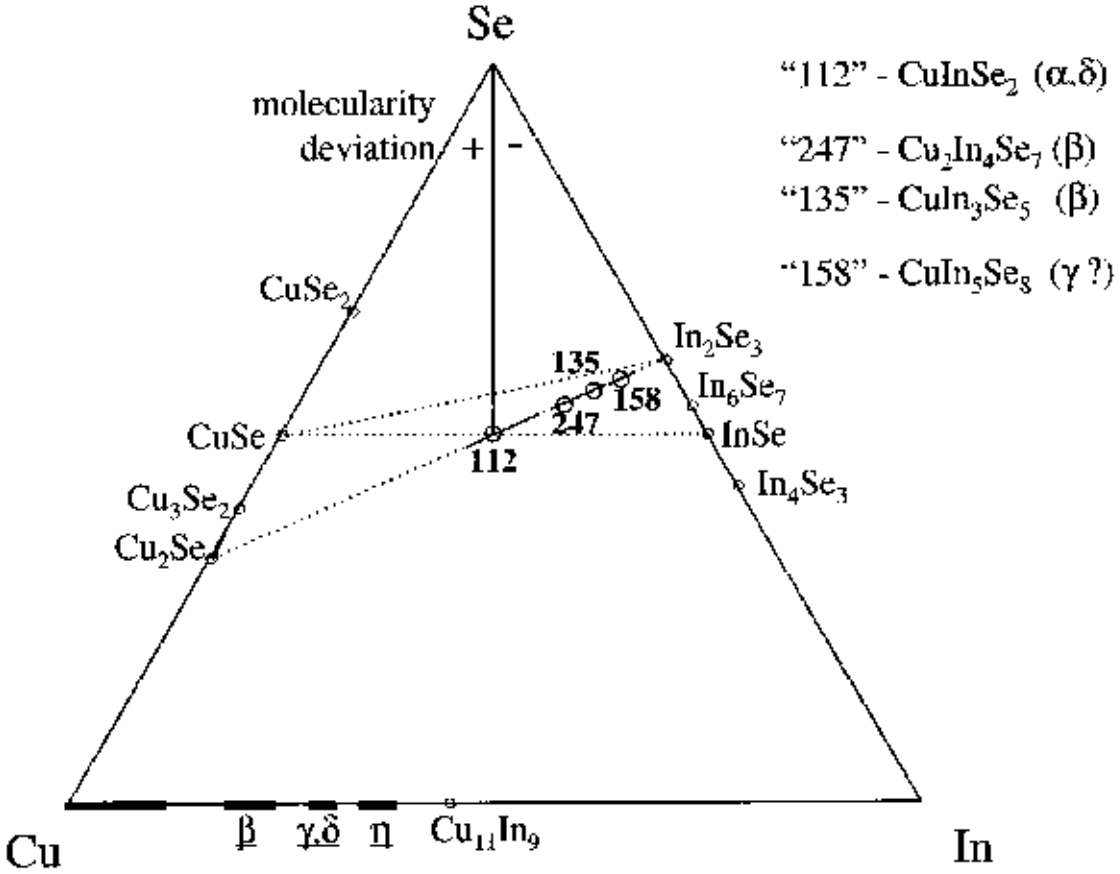

Figure 5-4 Cu–In–Se ternary composition diagram indicating compounds

Figure 5-4 is a composition diagram for the Cu-In-Se ternary system showing the accepted binary selenide compounds and several sections connecting pairs of them, including the pseudobinary section between the binary selenides with the highest melting point on each boundary (Cu_2Se and In_2Se_3). In a thermodynamic system closed to mass transfer with its environment, the overall composition of the products of any reaction two compounds must lie on the line that connects them, the exact point being determined by the reactant molar ratios and given by the inverse lever-arm rule.

Note that two of these sections pass directly through the stoichiometric α-phase composition ($CuInSe_2$), while the third, connecting the CuSe and In_2Se_3 phases, does not. This means that a reaction between the latter two binaries cannot yield only the α-phase in a closed system. Nevertheless this combination is of interest, as described below. First consider the following reaction between Cu_2Se and In_2Se_3 to form CIS:

$$Cu_2Se + In_2Se_3 \Rightarrow 2\ CuInSe_2$$

The ternary composition diagram of Figure 5-4 can be extended in the third dimension to display temperature, where phase boundaries at various temperature are represented as embedded two-dimensional manifolds. A cross-section along the line connecting the compounds Cu_2Se and In_2Se_3 through these surfaces yields the phase domains shown in a T-x diagram such as the pseudobinary $Cu_{2-\delta}Se$–In_2Se_3 section shown in Figure 1-1. The lowest temperature at which a liquid phase coexists with a solid phase in equilibrium is

the ~870°C eutectic temperature for In_2Se_3-rich compositions. This temperature is slightly less than the 885°C melting temperature of pure In_2Se_3.

The T-x diagrams for the binary selenide constituents (Figure 5-1 and Figure 5-3) represent two of the three bounding surfaces along the edges of the ternary composition diagram in Figure 5-4. Inspection of the binary diagrams show that only liquid phases persist in equilibrium above the 523°C monotectic temperature for all (Cu,Se) compositions with more than 52.5 at.% selenium. (In,Se) compositions with less selenium than that of the compound In_6Se_7 (<53.8 at.% Se) will decompose into a liquid/solid mixture at temperature above 156 to 600°C (depending on composition), but will not form the high melting temperature compound In_2Se_3 at temperature below the peritectic decomposition of In_6Se_7 at 660°C. Hence in separate closed systems at equilibrium, appropriately chosen selenium-rich copper binary precursors and selenium-poor indium binary precursors will each exist as liquids or liquid/solid mixtures at temperature above 523 to 600°C and any solid compounds would not be the highest melting-temperature ones found along each of these binary tie-lines so long as the temperature remains below 660°C.

These considerations alone do not answer the question of the reactions which would ensue upon liquid-phase mixing of such precursors. The equilibrium results of these reactions are found by re-examination of the T-x sections along this section in Figure 5-4 between the precursor reactant compositions. Views of the phase diagram along these other sections shows the

existence of a very low temperature eutectic valley for those which cross the [Cu]/[In] = 1 meridian on the selenium-rich side of the α-CIS phase, for example the reaction:

$$2\ CuSe + In_2Se_3 \Rightarrow 2\ CuInSe_2 + Se.$$

This eutectic is absent for those sections passing through the the stoichiometric α-CIS phase composition, reactions such as:

$$CuSe + InSe \Rightarrow CuInSe_2.$$

Rapid thermal processing is potentially a non-equilibrium process, which provides an additional degree of freedom for process optimization. If the heating rate of the precursors is faster than the kinetic rate of a given reaction, that reaction may not proceed to its equilibrium extent if the temperature becomes high enough that a competing reaction pathway becomes more favorable. For example, the phase Cu_3Se_2 (Figure 5-1) undergoes a peritectoid decomposition into CuSe and $Cu_{2-\delta}Se$ at a temperature of 112°C. The rate of a solid-solid phase transformation at this low temperature is expected to be very low because substantial atomic rearrangement is required to effect the solid-solid transformation and the atomic transport mechanism is diffusion. Solid state diffusion is many orders of magnitude slower than liquid phase transport processes. Sufficiently rapid heating of Cu_3Se_2 to temperature in excess of the CuSe peritectic decomposition at 377°C is expected to result in its direct decomposition into $Cu_{2-\delta}Se$ and selenium-rich liquid phase.

This strategy is supported by the results of a recently published thin-film calorimetry study of CIS ternary formation from stacked elemental layers [233]. The formation of In-selenides was shown to be controlled both by thermal activation and by the phase composition of the Cu–In alloys that form as reaction intermediates at the Cu–In interface. The reaction of elemental Cu and Se proceeds in two steps: rapid diffusion of Cu is responsible for the formation of CuSe, which is subsequently transformed to $CuSe_2$ at a significantly lower rate. At higher temperature slow interdiffusion of binary phases governs CIS formation, but it turned out that the reaction rate is increased due to the formation of liquid phases in binary peritectic transitions as previously predicted, in the first publication describing this approach [149].

These binary chalcogenide bilayer precursor structures were successfully converted to single-phase chalcopyrite $CuInSe_2$ thin films by subsequent RTP in times as short as 30 seconds [234]. Further details of the RTP process and results may be found in another dissertation [40].

Ternary Chalcogenides

Deposition of CIS Photovoltaic Absorber Films

The growth of CIS films for subsequent photovoltaic device fabrication was investigated by means of a statistical experimental design technique. An orthogonal 2-level fractional factorial design with twice repeated center points was selected to maximize the information which could be extracted from

subsequent characterization of the materials and devices derived from the 18 experimental runs required to fulfill the design requirements. Design and analysis of the experimental results were conducted using the SAS JMP software package.

These experiments implemented a single-stage [235] three-layer process [236] for the *in-situ* synthesis of CIS in our rotating-disc reactor. Growths were conducted with cycle times and metal fluxes calibrated to correspond to the growth of a single unit-cell-thick layer of $CuInSe_2$ per cycle. The first layer is grown with a constant indium flux [Se]/[In] molar flux ratio of ≈ 5, and with peak temperature slowly ramped from 200 →350°C over the entire film thickness. The second layer is grown with a constant copper flux [Se]/[Cu] molar flux ratio of ≈ 5, but with peak temperature excursions rapidly ramped from 350 →550°C after the start of copper deposition. The third and final layer is grown at 60% of the first layer indium flux and a [Se]/[Cu] molar flux ratio of ≈ 9.

The experimental design varied both the overall [Cu]/[In] molar flux ratio of the film and the ratio of indium deposited in the first layer [In_1] to that in the third layer [In_3], where [In] = [In_1] + [In_3]. The fraction of total indium deposited in the third layer varied from 2 to 8% for the subject samples in this study.

Intentional sodium doping was performed relatively rapidly and immediately at the beginning of second layer deposition. This strategy was adopted to maximize the sodium concentration at the interface between the

initial layer of indium selenide and subsequently deposited adlayers containing copper and selenium. A model of the role of sodium in the growth of CIS [148] described in detail in the next section of this chapter suggests that its efficacy as a surfactant should be enhanced when incorporated at this point rather than on the substrate prior to growth.

Device fabrication was completed at NREL, where CdS was grown on these CIS films by a Chemical Bath Deposition (CBD) process followed by deposition of a high/low resistivity ZnO bilayer film, nickel/aluminum grid deposition, and mesa isolation.

Compositional analysis by WDS, Auger depth profiling, and Secondary Ion Mass Spectrometry (SIMS) are compared and were correlated with structural properties of the films such as phase constitution, crystallinity, and texture as determined by XRD.

WDS was performed on the subject samples with two different electron beam accelerating voltages, 6 keV and 25 keV. This technique was previously reported as a means of qualitatively assessing differences between near-surface composition within the $\approx$ 100 to 200 nm penetration depth of 6 kV X-rays and the $\approx$ 2000 to 2500 nm penetration depth of 25 kV X-rays in CIS [237]. The PROZA correction algorithm employed to convert the raw X-ray intensity data to atomic composition assumes that the film is homogeneous. Otherwise, the calculated compositions are subject to significant error although the trends should be reliable to the extent that any inhomogeneous depth distributions between

samples are the same. Table 5-1 shows the [Cu]/[In] ratio of these films measured at each energy and suggests indium-enrichment of the near surface region compared to the average over a significant part of the 3.5 μm total film thickness.

Table 5-1 Composition of two samples from the CIS absorber film deposition experiments using the three-layer process showing significant variations in the extent of intermixing between the layers.

Sample	**[Cu]/[In] 6 k*e*V WDS**	**[Cu]/[In] 25 k*e*V WDS**
68	0.876	1.03
69	0.484	

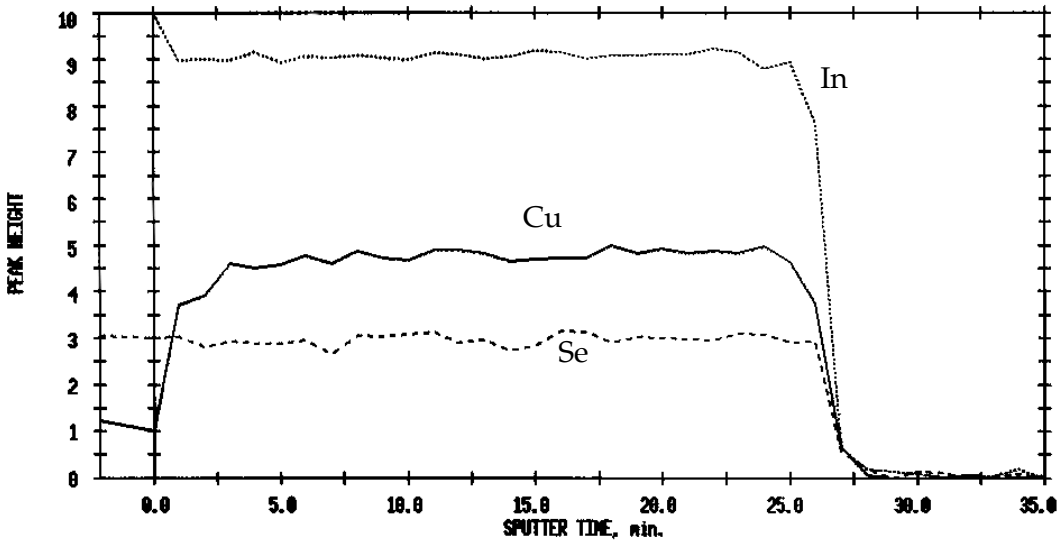

Figure 5-5 Auger depth profile of Sample 69 showing near surface indium enrichment.

Further insight into this apparent surface indium enrichment is found in Auger depth profiles. Figure 5-5 shows a profile through the entire thickness of sample 69. The constant selenium level indicates that the sputter rate was uniform throughout the sample at ≈140 nm/minute. The copper signal increases

slowly over the first ≈8 minutes of sputtering indicating enrichment in the first 1100 nm, roughly half of the thickness sampled by the 25kV WDS measurement.

Samples 70 and 71 were intentionally doped with sodium by codeposition of NaF as previously described. SIMS profiles of sample 69 provided an estimate of the background doping levels from sodium transport through the molybdenum back contact from the SLG, which has been reported to vary widely with different processing conditions. Extremely low background doping levels on the order of $\approx$ 0.1 *ppm* are found by SIMS. Sample 70 showed the same low levels throughout the bulk of the film, with the added sodium apparently segregating to the surface, where its peak concentration rose to only $\approx$ 10 ppm. Sample 71 was more heavily doped and exhibited a $\approx$ 10 ppm concentration throughout the film's thickness. Due to uncertainties in the SIMS calibration these values may be only relied upon within an order of magnitude. Even so the background doping levels appear to be an order of magnitude lower than those reported for growth on soda-lime glass [134] by conventional or RTP techniques [130] with significantly larger thermal budgets.

XRD measurements of these samples showed only those peaks associated with the α phase compound $CuInSe_2$, with no evidence of ternary β phase or binary selenide secondary phases. The crystallinity determined from diffraction peak FWHM correlated strongly with texturing. Samples #68 (the most indium rich) and #70 (low NaF doping level) exhibited broad peaks with roughly equal (112) and (024)/(220) peak intensities at 2θ values of 26.6° and 44.2°, respectively.

Samples #71 (highest copper and NaF doping level) and #69 exhibited sharp peaks with significantly reduced (112) intensity and a dominant (024)/(220) peak.

The ratio of the overlapping (024)/(220) peaks to that of the (112) peak has been recently reported to strongly correlate both with carrier concentration and efficiency [238], with the highest efficiency CIGS cells reported to date in the literature exhibiting the same preferred orientation observed here in samples #71 and #69 [239]. The empirical inverse correlation between orientation and carrier concentration reported in CIGS for polycrystalline absorber films of nominally the same composition may hold for CIS as well, and could be the reason that the highest efficiency CIS devices fabricated in these experiments was from sample #69 which is also characterized by this orientation.

The contactless Dual Beam Optical Modulation (DBOM) technique developed in our laboratory has been utilized previously to study the effects of different CdS buffer layer processing (*i.e.*, CBD, MOCVD, and sputtering) on the properties of CIS and CIGS films [240]. The results showed a significant increase in the DBOM signal ($\Delta I/I$) which is related to the free carrier absorption and excess carrier lifetimes in the absorber layer after the buffer layer deposition. An analytical model for the DBOM technique has been derived which contains the functional dependence of $\Delta I/I$ on the excess carrier lifetimes, surface/interface recombination velocities, and depletion layer width in thin film cells [241].

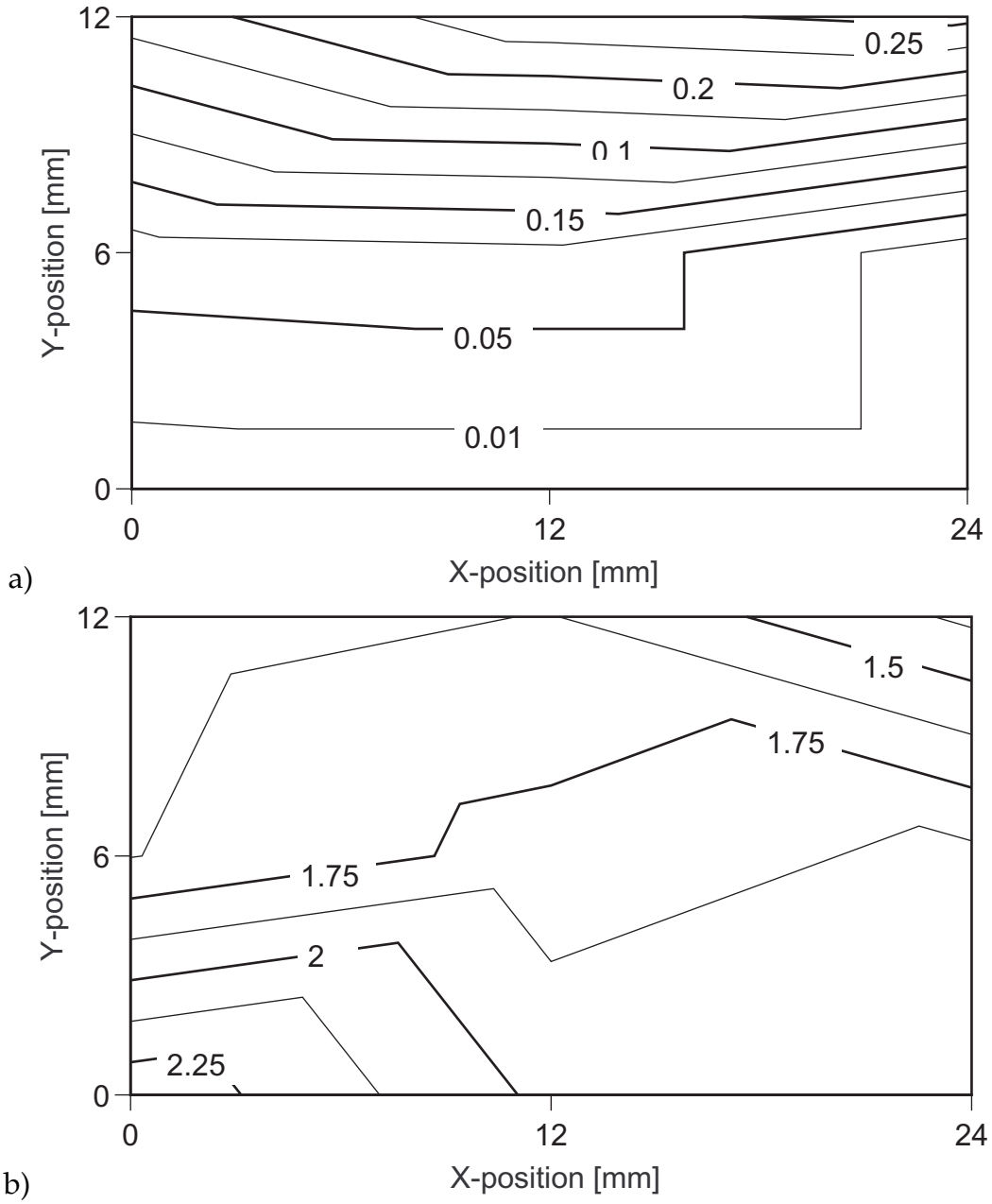

Figure 5-6 DBOM excess carrier lifetime measured on sample #70 both a) before, and b) after CBD CdS deposition.

This technique was applied to one of the subject samples previously described, and the spatial distribution of the DBOM signal intensity measured both before and after CBD of CdS. The data are analyzed as excess carrier lifetimes, based on the assumption of zero interface recombination velocity and

depletion layer width. The results shown in Figure 5-6 suggest a shorter lifetime in these samples than in those published previously for CIGS films from NREL.

Dark and illuminated I-V curves were measured at NREL for some of the samples from these experiments. The maximum efficiency observed on these samples is 7.1% as shown in Figure 5-7. A comparison shows that the light and dark I-V curves cross over one another which cannot occur for an ideal diode which obeys the superposition principle [7]. This can result from photoconductivity in one or more layers of the device structure, but insufficient data is available to determine unequivocally whether this is the cause in this case.

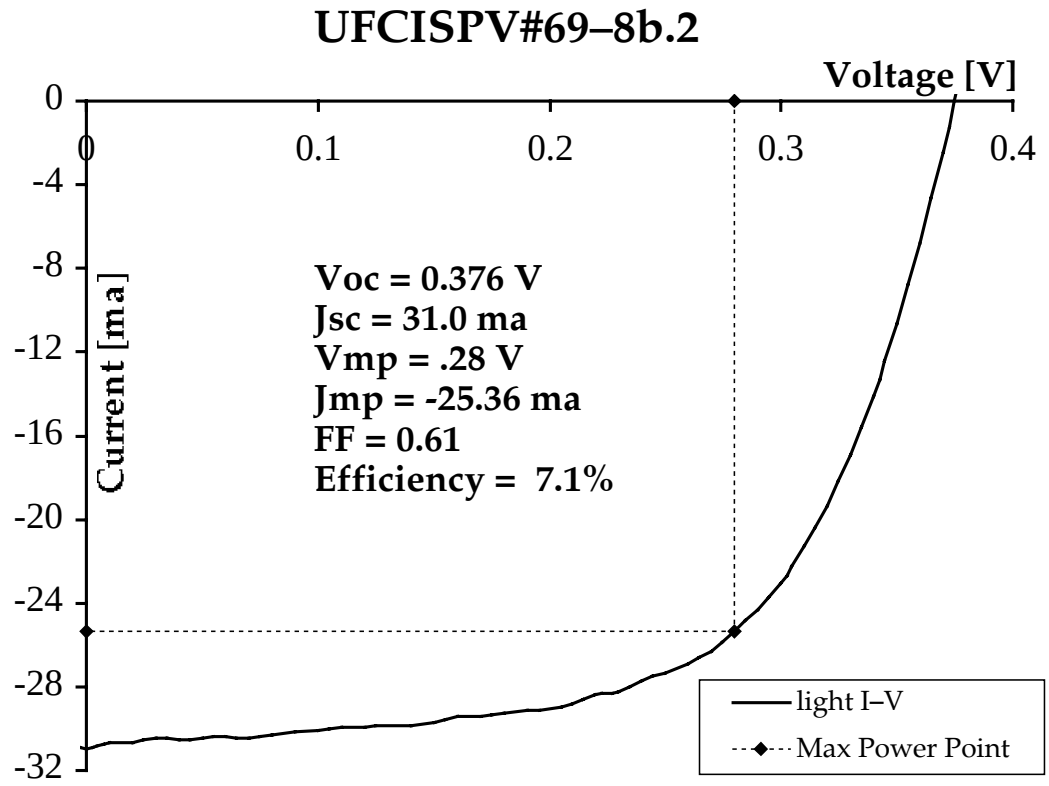

Figure 5-7 Illuminated current-voltage curve for the best CIS thin-film cell made by a three-layer codeposition process in the course of this research.

Epitaxial Growth

The epitaxial growth of CIS has been investigated to better understand the fundamental properties of these films in the absence of grain boundaries, as well as to elucidate the effects of surface reactions on their structure and morphology.

The Migration Enhanced Epitaxy (MEE) process variant [60] of molecular beam epitaxy was utilized to grow CIS epilayers on single-crystal substrates. Growth was performed in the custom rotating-disc reactor incorporating separate Langmuir effusion sources for copper and indium, (controlled by a computer using EIES sensors [242]) and selenium (under temperature control). The steady-state substrate temperature during film growth was 525±50°C. Absolute total flux calibration was employed to set the VI/(I+III) molar flux ratio to 5 and the total incident molar flux of metals (Cu+In) adjusted to provide the equivalent of 1 unit cell of chalcopyrite $CuInSe_2$ per cycle. The rotation rate of the substrate platen was 20 rpm (3 sec/cycle). Total film thicknesses were nominally 0.3 μm.

XRD data was acquired with a Philips PW3710 diffractometer using a copper anode filtered to provide predominately K_α radiation. Film compositions were measured with a JOEL electron microprobe using a 25keV beam accelerating voltage and calibrated to a single-crystal $CuInSe_2$ standard provided by NREL. TEM data were acquired at NREL using a Philips CM30 scanning microscope. Raman spectra were acquired at the University of Leipzig by Dr. Gerd Lippold

by means of confocal laser microscopy using an equipment configuration described more fully in the literature [243].

Heteroepitaxy of CIS on GaAs Substrates

Polished GaAs substrates oriented 2° off the (001) towards the nearest (110) direction were etched in a 5:1:1 solution of H_2SO_4:H_2O_2:H_2O at room temperature for 1 minute, then rinsed sequentially in H_2O and in methanol immediately prior to mounting onto the MEE system's load lock. The substrate was then heated *in-situ* to >600°C for 10 minutes before direct exposure to the selenium source flux for about a minute prior to the beginning of CIS film growth. Sodium is provided by sublimation of NaF from a Knudsen cell monitored by a QCM.

A rich diversity of atomic-scale and mesoscopic structures were found in CIS epitaxial films grown on GaAs by the MEE technique. The growth and characterization of crystallographic polytypes of the chalcopyrite structure are first discussed. Subsequently the influence of composition on film morphology and its implications for the role of defect structures in the process of island nucleation are discussed. The effects of sodium on both lattice ordering and morphology will then be described and a unified interpretation of these effects offered.

CuAu–I (CA) ordering of $CuInSe_2$ epilayers . The type-I CuAu (CA) crystal structure (space group 123) is a tetragonal distortion of the *fcc* lattice with

a c-axis only half that of the corresponding chalcopyrite (CH) structure. Its growth has been previously reported in $CuInS_2$ [57] but it has never heretofore been observed in $CuInSe_2$. The possible coexistence of the CA and CH structures in $CuInSe_2$ had been theoretically predicted [62] and it was shown that the CA structure can be derived from the CH by simply translating alternating (100)A cation planes by $a/\sqrt{2}$ in a <110> direction. Since this transformation does not change the local bonding configuration of any of the atoms, its formation enthalpy was predicted to be quite low, only 2m*e*V/atom.

A comparison of theoretical dynamical electron diffraction patterns and TEM diffraction data in Figure 5-8 show that the direction in the CuAu structure along which copper and indium form alternating cation planes is oriented parallel to the nominal (001) normal of the GaAs substrate. The CH–$CuInSe_2$ epilayers also orient with cation planes parallel to the surface but both copper and indium equally populate each. This leads to significant enhancement of the intensity of (002) and (006) peaks in the XRD spectra as shown in Figure 5-9.

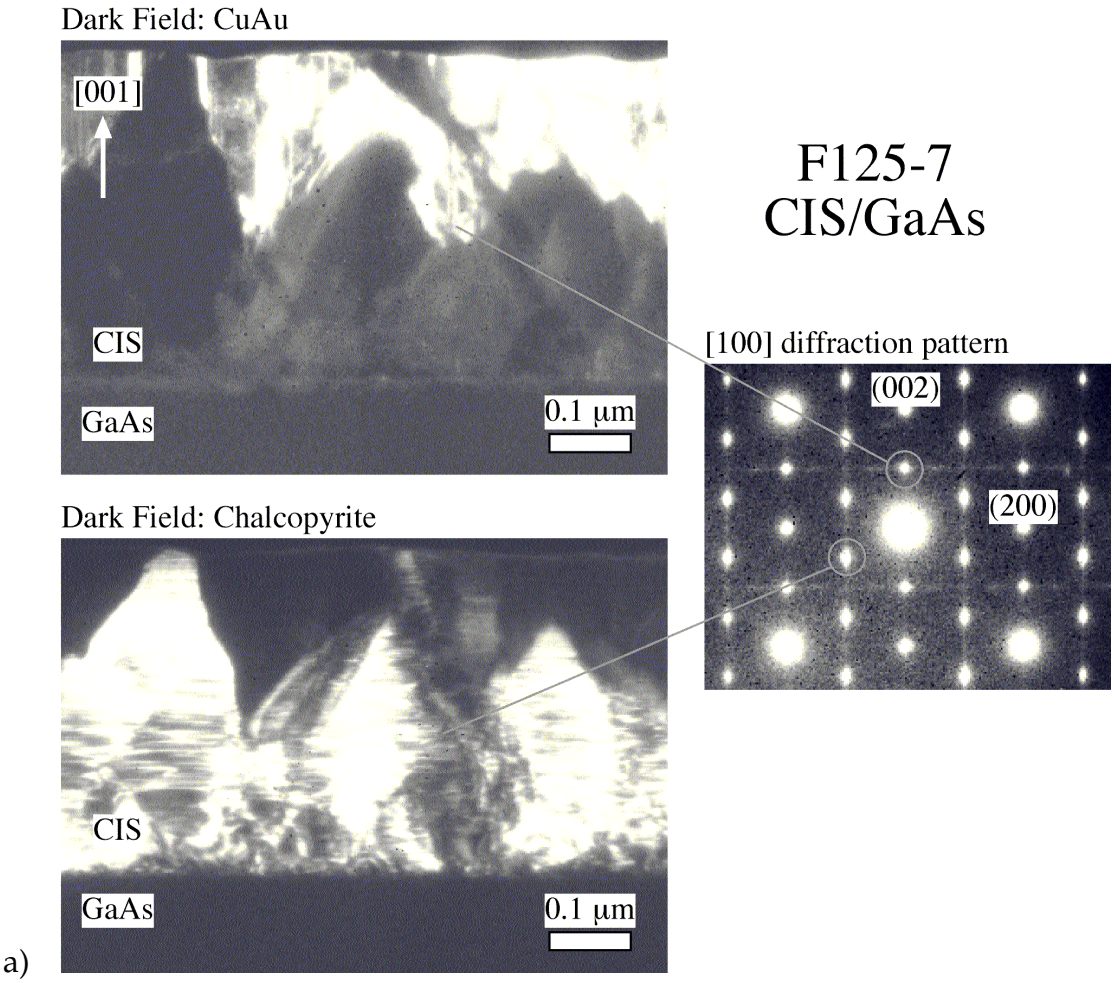

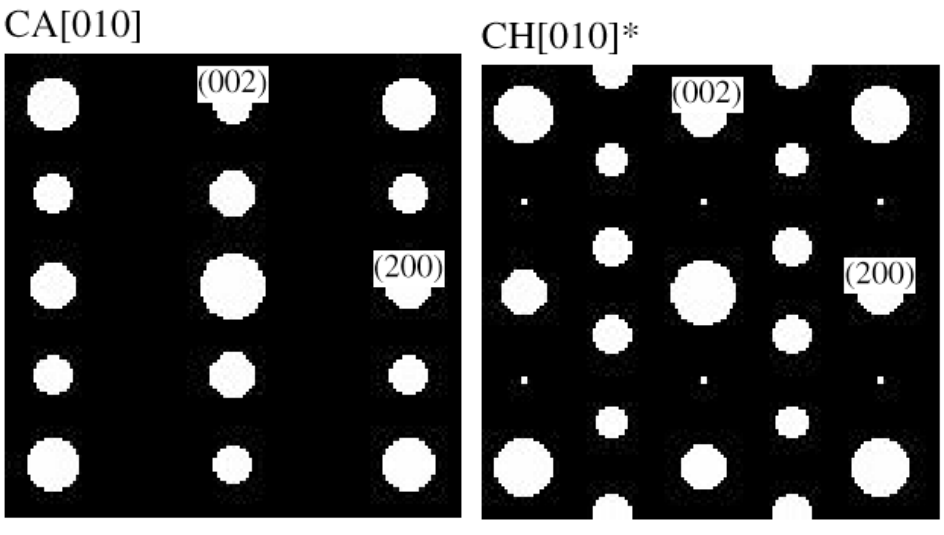

Figure 5-8 A comparison of experimental and theoretical TED data.
a) experimental dark-field cross-sections taken with intensities from the corresponding diffraction spots in the TED pattern along [010] as shown, and
b) theoretical TED patterns of CA and CH structures in $CuInSe_2$, both along [010].

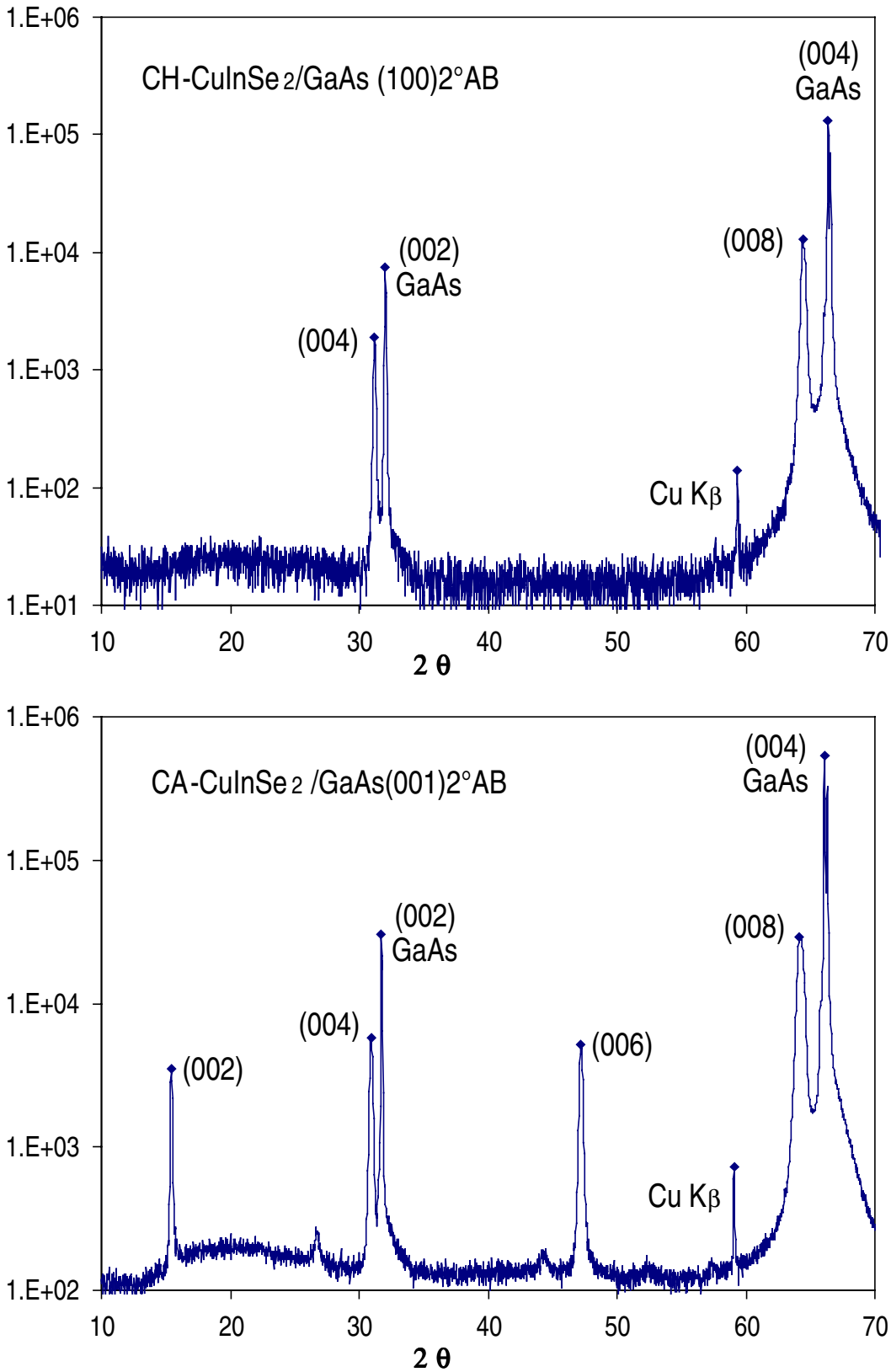

Figure 5-9 Comparison of the XRD spectra of epitaxial chalcopyrite (upper) and CuAu (lower) crystallographic polytypes of $CuInSe_2$ on (001) GaAs substrates.

The Raman spectra of CA–$CuInSe_2$ samples exhibit peaks not observed in CH– $CuInSe_2$ at 52, 186, and 462 cm^{-1}, which are labeled d, a, and c respectively in Figure 5-10. The dominant A1 mode at 175 cm^{-1} and the LO mode at 232 cm^{-1} typically observed in CH–$CuInSe_2$ are also observed.

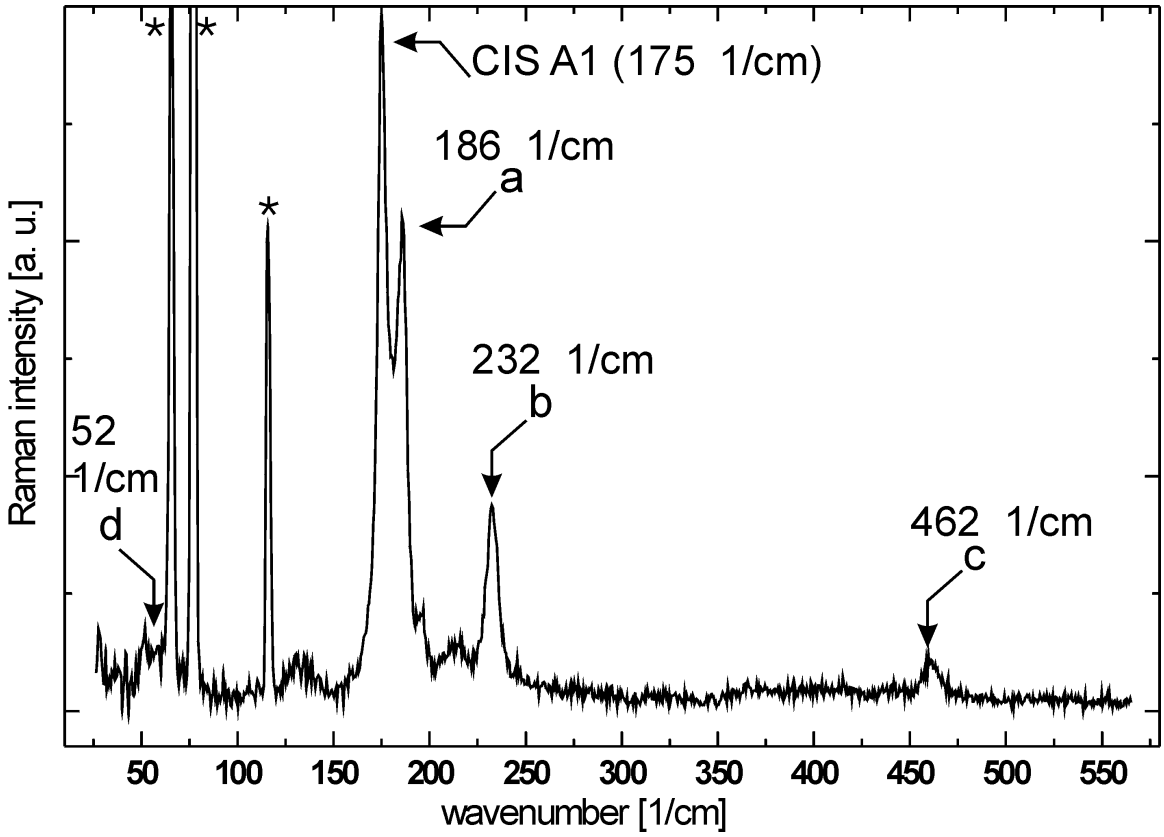

Figure 5-10 Macroscopic Raman scattering spectrum of a CA–$CuInSe_2$ epilayer on GaAs. Peaks labeled by "*" are laser plasma lines; the others are described in the text.

Peaks d and a are near the estimated acoustic and A1 optical zone boundary phonon energies, respectively, of CH–$CuInSe_2$. These modes are rendered optically active by zone-folding resulting from the halving of the unit cell in the CA–$CuInSe_2$ structure relative to that of the CH–$CuInSe_2$ structure. The

230–232 cm^{-1} E and B modes of the chalcopyrite structure exhibit little phonon dispersion and are not normally as strong as peak b in Figure 5-10. Thus the intensity observed in the signal at 232 cm^{-1} is attributed to the superposition of intensities of zone-center and folded modes, with the 462 cm^{-1} peak representing an overtone thereof.

These studies have identified XRD and Raman signatures characteristic of the CA-$CuInSe_2$ structure, identifiable by enhancement of specific peaks in the spectra. If this structure were disordered and distributed in the $CuInSe_2$ lattice on nanoscopic domain scales, it might not be clearly identifiable by these techniques since the reciprocal-space peaks would be correspondingly broad and not contribute measurably to those peaks.

Composition effects on film morphology . All of the epitaxial CIS films grown on single-crystal GaAs substrates exhibit the film + island morphology characteristic of Stranski-Krastonow mode growth, but a pronounced morphological dichotomy between indium-rich and copper-rich films is observed. A dependence on growth morphology on film molecularity is, of course, widely observed in CIS films synthesized by almost all techniques, whether epitaxial [244] or polycrystalline [144,245]. However, to the author's knowledge no previous reports of In-rich epilayers on GaAs have described epitaxial island formation.

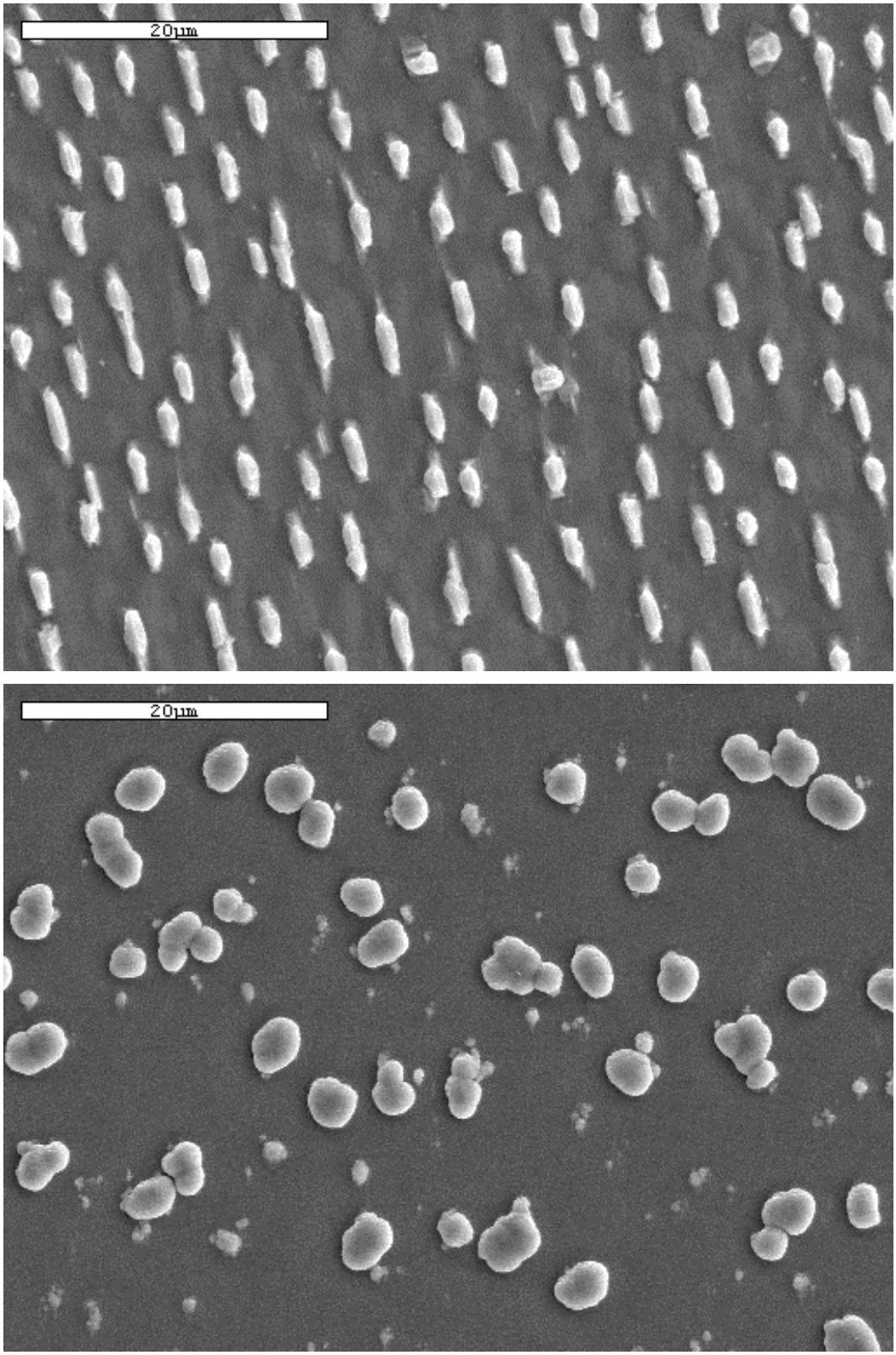

Figure 5-11 Spatial distribution and morphology of islands in copper and indium-rich cases: a) [Cu]/[In] = 1.06 and b) [Cu]/[In] = 0.99.

The lateral distribution of islands in the two cases of positive (Cu-rich) and negative (In-rich) molecularity deviation is characteristically distinct for all samples in this study. A quasiperiodic self-assembled array of similarly sized islands is observed in the case of copper excess and a spatially disordered distribution with variable island sizes in the case of indium excess. The stark contrast between them (Figure 5-11) is strong evidence that island nucleation occurs by means of fundamentally different mechanisms determined by the ratio of copper to indium in the incident flux during growth.

Similar island-distributions as shown here for the Cu-rich case have been reported for $CuInS_2$ grown epitaxially on GaAs under conditions of low sulfur partial pressure [246], where surface diffusion lengths are long, as they are in MEE. The islands in this case are highly facetted, with their longer axis oriented parallel to ripples that form on the epilayer along a {110} direction as demonstrated by the AFM images in Figure 5-12. Raman analysis shows that the copper-rich islands contain a mixture of the phases CH–$CuInSe_2$ and β-$Cu_{2-\delta}Se$. This rippling of the epilayer has been previously reported in Cu-rich CH–$CuInSe_2$ epitaxially grown on GaAs by MBE [247] and this analysis fully supports their conclusions regarding the structure of these islands.

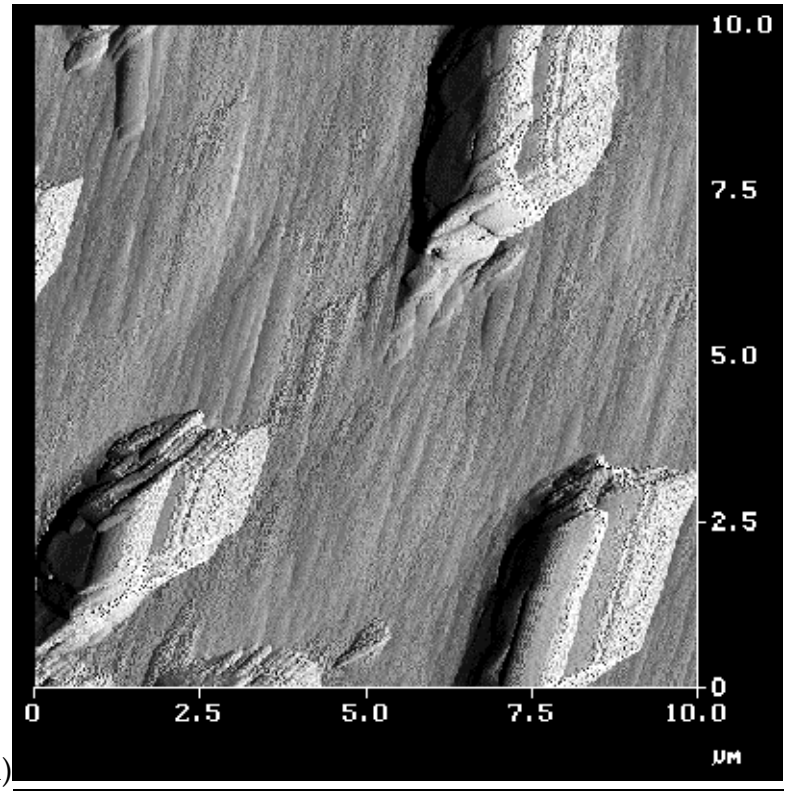

a)

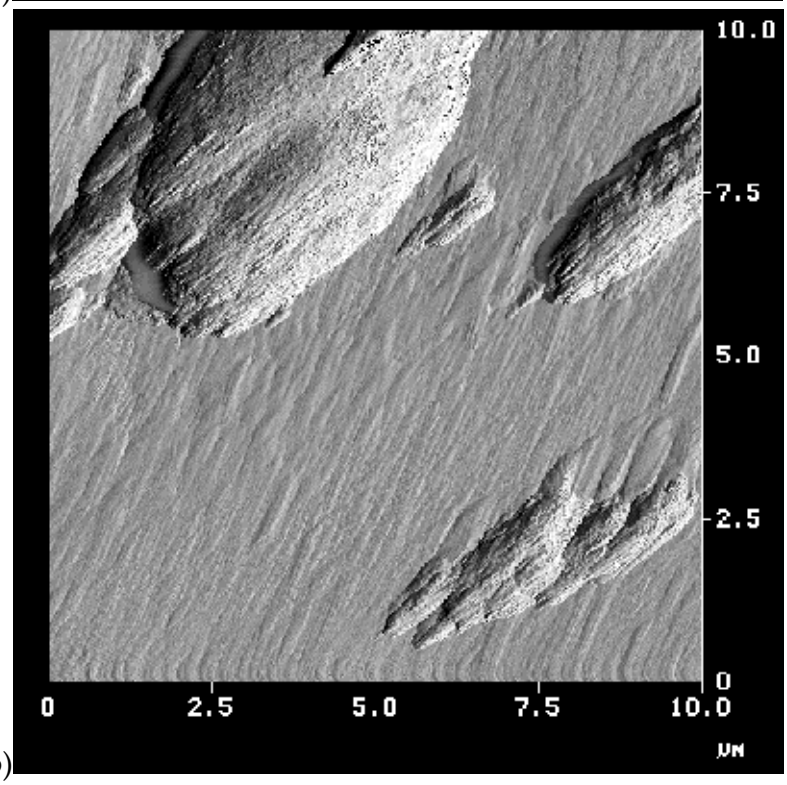

b)

Figure 5-12 AFM images of CIS islands and epilayers.
a) islands on Cu-rich films and b) islands on In-rich films.

Quasiperiodic island arrays are also observed to form on surface ripples in Si/Ge alloy epitaxy on Si. The rippling has been theoretically described as an instability phenomenon related to total free energy minimization during lattice-mismatched heteroepitaxy resulting from the interaction between the reduction of elastic strain energy and increased surface free energy [248]. The axes of the ripples are aligned along the elastically soft direction in the epilayer in this model. This locally varying strain energy density leads to a locally varying difference in chemical potential [249]. This has been shown in the SiGe case to lead directly to the evolution of ripple peaks into a quasiperiodic array of islands [250,251]. The strain field has also been shown to drive diffusion, resulting in structure-correlated composition fluctuations [252] which could, in the CIS material system, preferentially nucleate the secondary β-$Cu_{2-\delta}Se$ phase when the solubility limit for excess copper is locally exceeded in the near-surface transition layer.

Alternatively it is possible that the island orientation is a consequence of the 2°B tilt of the GaAs substrate off the singular direction. When the adatom incorporation lifetimes and mobilities enable diffusion lengths longer than the mean terrace width, anisotropic terrace or island attachment/detachment kinetics and the Ehrlich-Shwoebel barrier [253,254] at the terrace edges can result in anisotropic diffusion fluxes [255,256]. These kinetic mechanisms might contribute to the elongated growth habit we observe, as previously observed in homoepitaxial GaAs epilayers [257].

In contrast, the island morphology in the indium-rich case of MEE growth (Figure 5-11(b)) consists of rounded mounds with no clear orientation with respect to the substrate's axes or epilayer's ripples; their spatial and size distributions are relatively random compared to the copper-rich case. Epilayer rippling is still observed with AFM, although the period of the ripples is shorter than in Cu-rich epilayers, in contrast to previous reports of CIS growth by conventional MBE [247]. Despite their seeming lack of regularity, these islands in the In-rich case are in fact coherent and epitaxial (Figure 5-13).

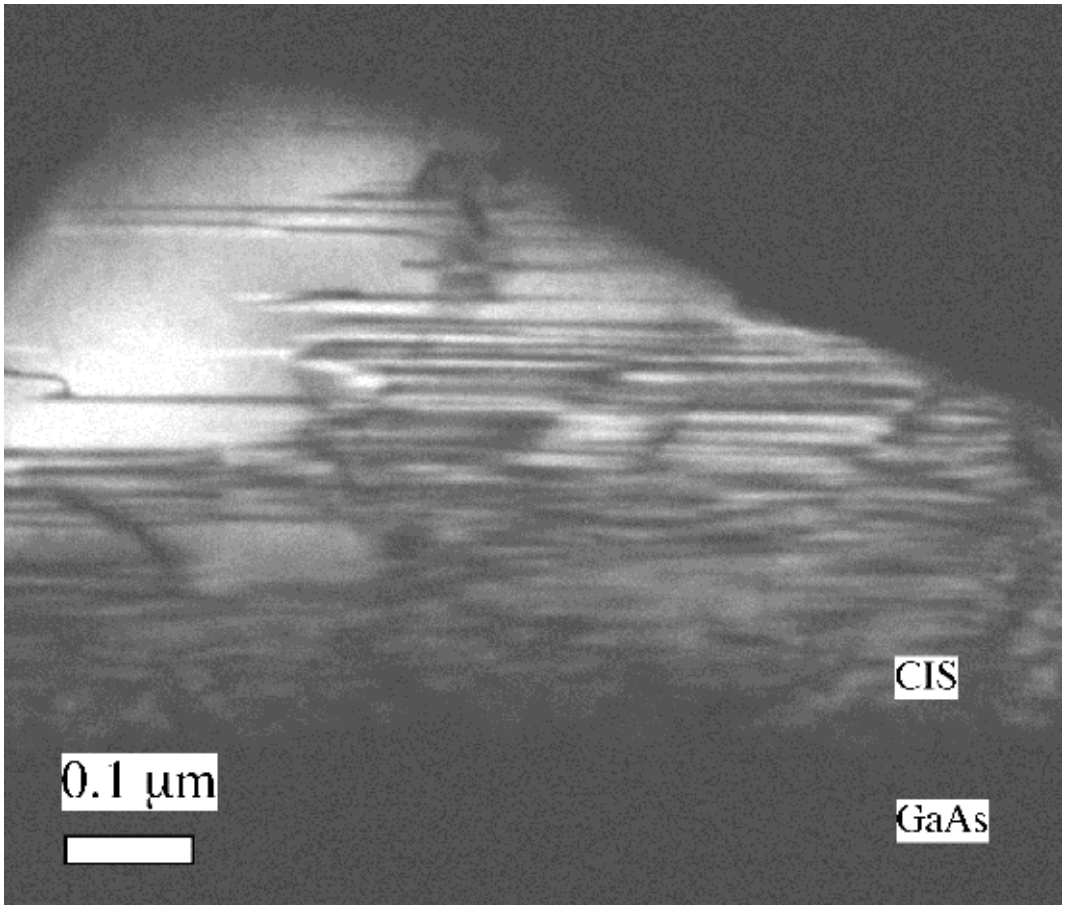

Figure 5-13 Cross-sectional TEM on [010]: dark-field using $^1/_2$ (201) spot showing CH-ordered epitaxial "island" in a sample with [Cu]/[In] = 0.97.

A simple rate-equation model has been recently developed to describe the changes in nucleation kinetics during epitaxial growth introduced by random point defects [258]. Within a mean-field approximation, and even assuming weak adatom trapping on the point defects, the model predicts a strong suppression of nucleation on terrace sites due to adatom capture by clusters nucleated on the defects [259]. As a consequence, the spatial distribution of clusters is predicted to reflect the random point defect distribution.

The process of cluster coarsening in the adlayer has been extensively studied for the case of homogeneous nucleation. Studies of silicon homoepitaxy provide the strongest experimental support [230] for thermodynamic models based on a framework of equilibrium step edge fluctuations [260] and ripening [261]. Their relevant conclusion is that the situation of a slightly supersaturated (2-D) adatom gas is very similar to that of a slightly supersaturated (3-D) vapor, for which the nucleation of droplets (2-D islands) is described by classical homogeneous nucleation theory. Thus a well-defined spatially dependent chemical potential can be defined for the adatoms, which depends not only on the incident flux but also on the surrounding topography. In regions with a high density of subcritical clusters the chemical potential is relatively high due to the inverse dependence of the chemical potential on island (droplet) radius (the Gibbs-Thompson effect).

Combining these models leads to the prediction that the distribution of 3-D islands in Stranski-Krastanov mode epitaxy on surfaces with a high density

of point defects will tend to occur where the local density of point defects is greatest. The accommodation of excess indium in the CIS lattice has been predicted theoretically [70] to occur by means of the formation of the (In_{Cu} + 2 V_{Cu}) cation neutral-defect-complex (NDC). A recent study [51] has shown that the EXAFS scattering spectrum of selenium in the compound $CuIn_3Se_5$ is best fit by a local structure model having precisely these defect proportions in the local tetrahedra surrounding Se atoms in the lattice. Further reduction in the formation enthalpy of these NDC's is predicted when they order along the [110] direction [70]. This process of NDC aggregation in the near-surface-transition layer [179] of indium-rich epilayers during growth is the proposed cause of local composition fluctuations with both a high concentration of indium and of vacancies, which are conjectured to nucleate the observed 3-D island growth. The more perfect crystallinity of copper-rich films precludes this defect-initiated nucleation mechanism.

Sodium effects on ordering and morphology. The addition of sodium to In-rich $CuInSe_2$ epilayers by dosing the surface with a few monolayers of NaF during the initial stages of growth has a dramatic effect on the film's growth morphology. Although islands still form, they are aggregated into "pools" (Figure 5-14). Electron microprobe measurements directly demonstrate that the composition of the smooth film areas is within the range of single-phase homogeneity for CH–$CuInSe_2$ but that the islands are substantially indium-enriched.

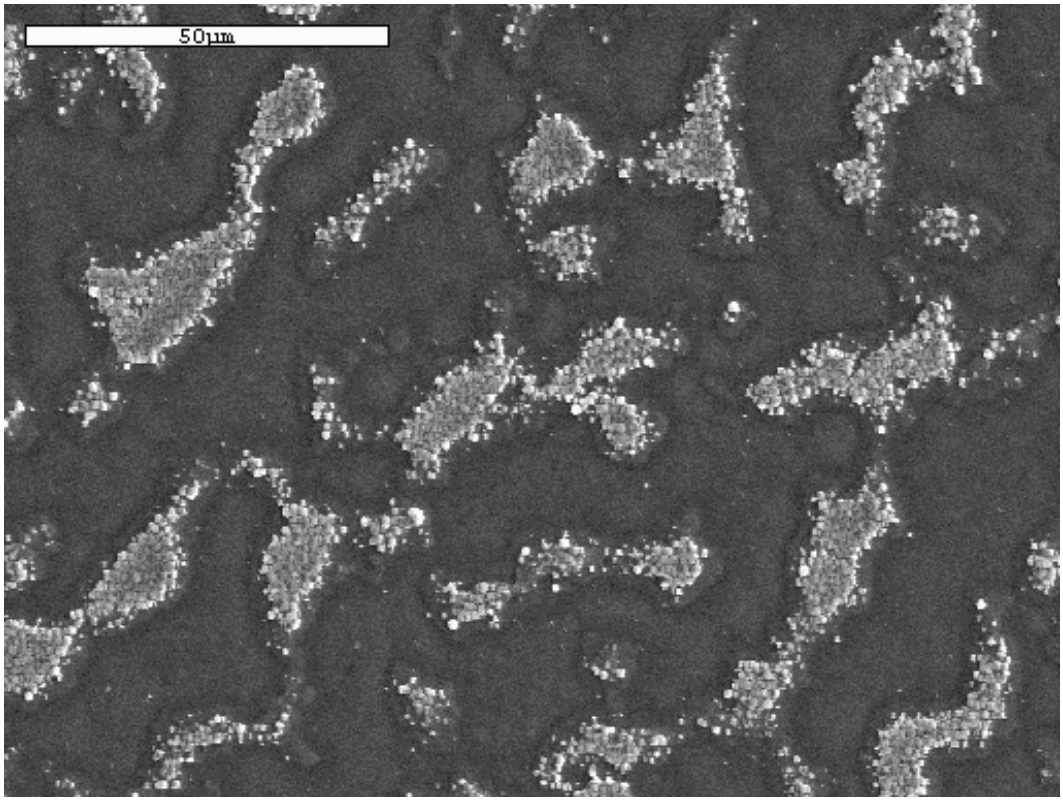

Figure 5-14 SE–SEM image of an In-rich CIS film on GaAs dosed with a few monolayers of NaF. The EMP-measured [Cu]/[In] ratios are 0.94 overall, 0.99 between the islands, and 0.81 within the island "pools."

Sodium also has a significant effect on lattice ordering of $CuInSe_2$ epilayers. Micro-Raman characterization shows that both film and island regions in Figure 5-14 are homogeneous across the samples, and that the smooth film areas exhibit less CA ordering than samples with nearly the same overall molecularity but without sodium. A comparison of the Raman spectra (Figure 5-15) of the islands on the sodium-doped sample shown in Figure 5-14 and the sodium-free sample from Figure 5-11(b) reveals no measurable difference whatsoever between them. However, the spectra are both significantly broadened and show no evidence of the Raman peak at 152 to 154 cm^{-1}

characteristic of the equilibrium indium-rich CIS β–phase [262,263]. These measured spectra can be fit with a pair of Lorentzians at 175 and 183 cm^{-1}. The former is characteristic of CH-$CuInSe_2$ which suggests that there is no significant vacancy population surrounding the selenium atoms in this structure, since it is the cation vacancies in the CIS β–phase that lead to the shift of this transition to lower energies. The broadening has been interpreted in previous studies of radiation-damaged films [264] as indicative of a loss of translational symmetry in the lattice, which implies a crystallographically disordered structure for these indium-rich islands.

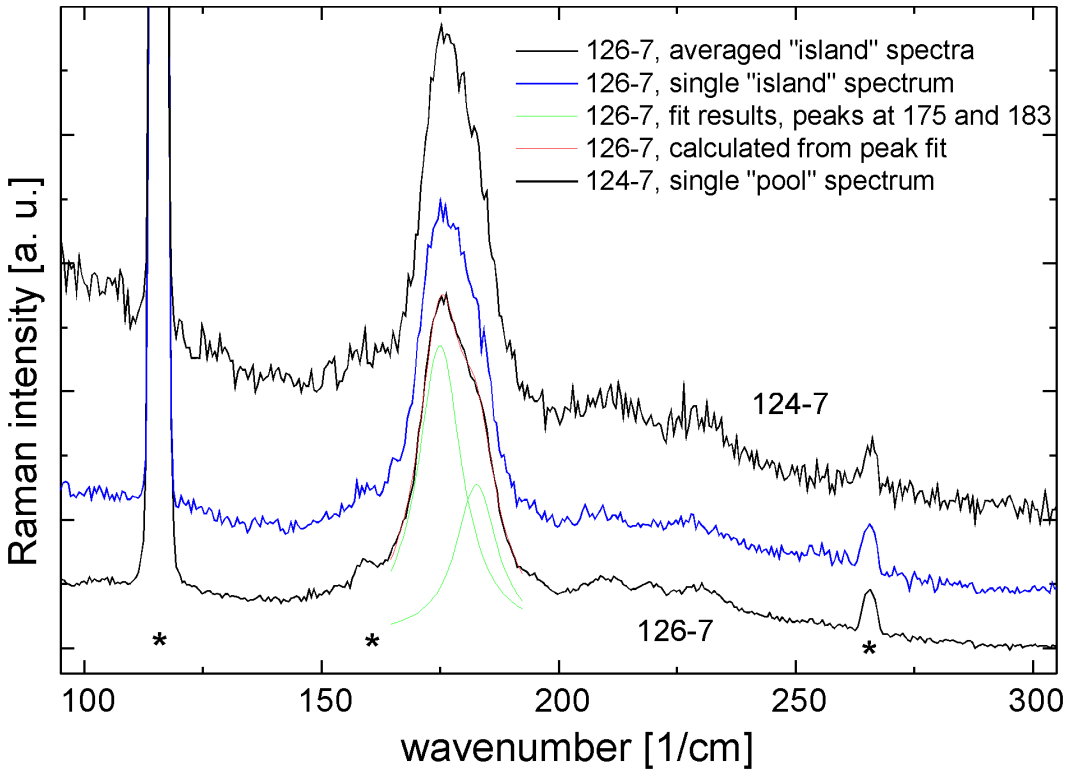

Figure 5-15 Micro-Raman scattering spectra of islands on two indium-rich CIS films grown on GaAs (100). The uppermost curve is from an island "pool" on a sodium-dosed film and the lower two are single and averaged spectra from isolated islands on the sample without sodium shown in Figure 5-11(b).

These effects can be explained within the context of the island nucleation models discussed in the previous section by the hypothesis first described in the course of this research [148] that sodium acts as a surfactant during the growth of $CuInSe_2$ by destabilizing the NDC and rejecting excess indium from the growing film. This model is consistent with that proposed by Contreras and coworkers [265], and to one proposed by Rockett [72].

Summary of sodium effects. In a traditional chemical context, a surfactant is a substance that lowers surface tension, thereby increasing spreading and wetting properties. In the context of crystal growth it is used in a broader sense as any surface-active additive that tends to flatten the surface of a growing film, since it is found that the mechanism underlying such effects is sometimes kinetic [266] rather than thermodynamic [267]. Ordering effects like the CA ordering observed here have been found in other material systems to result from surface reconstruction during growth, and surfactants have been reported to interfere with ordering in those systems [268].

These results clearly show that under our growth conditions minute quantities of sodium inhibit the incorporation of excess indium into the growing film. The island clustering exhibited in Figure 5-14 is evidence that the density of point defects capable of binding subcritical adatom clusters during the initial stages of growth is significantly reduced by sodium on the surface. A unified mechanism based on destabilization of the NDC can explain both of these effects, consistent with recent theoretical results [78]. It is possible that these two effects

have different causes: there are precedents in the literature [269] for surfactant effects resulting simply from the occupation of surface vacancies. One specific consequence of this proposed mechanism on the residual defect structures of the film bulk is to reduce the composition fluctuations therein, which may be the structural cause of the large-scale potential fluctuations which have been shown to characterize carrier transport in indium-rich CIGS thin film absorbers [270].

The addition of sodium to In-rich $CuInSe_2$ epilayers during the initial stages of epitaxy on GaAs both suppresses the formation of metastable CA–$CuInSe_2$ crystal polytypes and dramatically changes the film morphology. The suppression of CA ordering suggests a surface kinetic effect may play a role in its formation. The morphological effects on indium-rich layers are explained in the context of current island nucleation theory by the hypothesis [148] that sodium acts as a surfactant during the growth of $CuInSe_2$ by destabilizing the $(In_{Cu} + 2\ V_{Cu})$ NDC in the near-surface transition layer and rejecting excess indium from the bulk of the growing film to a second indium-rich phase. This could both reduce the In_{Cu} compensating donor density, and homogenize composition fluctuations resulting from NDC clustering, thereby improving minority carrier transport.

Heteroepitaxy on ZnTe

ZnTe is a II–VI compound semiconductor with a band-gap of 2.38 *e*V which is normally found to be a *p*-type conductor as a consequence of its native

defect structure. Extrinisic *p*-type doping has been achieved in ZnTe by the addition of both copper and Group V (*e.g.*: phosphorus) impurities, which are thought to form substitutional defects on cation or anion lattice sites, respectively. These properties have led to the suggestion that ZnTe could be useful as a heteroepitaxial back contact in device structures with Cu–III–VI_2 absorber layers [271].

Growth by the MEE process on polished zincblende ZnTe substrates 1x1cm in size and with two orientations was studied. The substrates were purchased from Eagle-Picher Research Laboratory and were either oriented 4° off the (001) towards the nearest (111) direction or were oriented on the singular (111). The quality of these substrates was quite poor, with inclusions easily visible at 100x by optical microscopy, and a dislocation density measured by cathodoluminescence at NREL of $>10^7/cm^2$.

The first growth experiments were conducted with films that were etched in a 3 vol.% solution of liquid bromine in methanol at room temperature for 1 minute, then rinsed in pure methanol and blown dry with filtered nitrogen immediately prior to mounting onto the MEE system's load lock. During a presentation at the 1999 Electronic Materials Conference, Prof. Takafumi Yao of Tohoku University presented *in-situ* surface characterization data of (001) ZnTe demonstrating that substantially better surface cleanliness and smoothness could be achieved by following the bromine/ethanol surface etch with a rinse in pure HF followed by nitrogen drying.

Epitaxial growth was not achieved in this research until that process was adopted, and was only successfully demonstrated on the (001) orientation. One sample was sent to NREL for cross-sectional TEM diffraction analysis, which verified the preliminary conclusion based on XRD diffraction data shown in Figure 5-16 that the film was epitaxial. The surface morphology of this sample was very rough. This sample was grown simultaneously with a GaAs substrate that also gave epitaxial growth, and the temperature used were significantly higher than those conventionally used for growth on ZnTe. Some dissociation of the ZnTe substrate at these high temperature may have occurred.

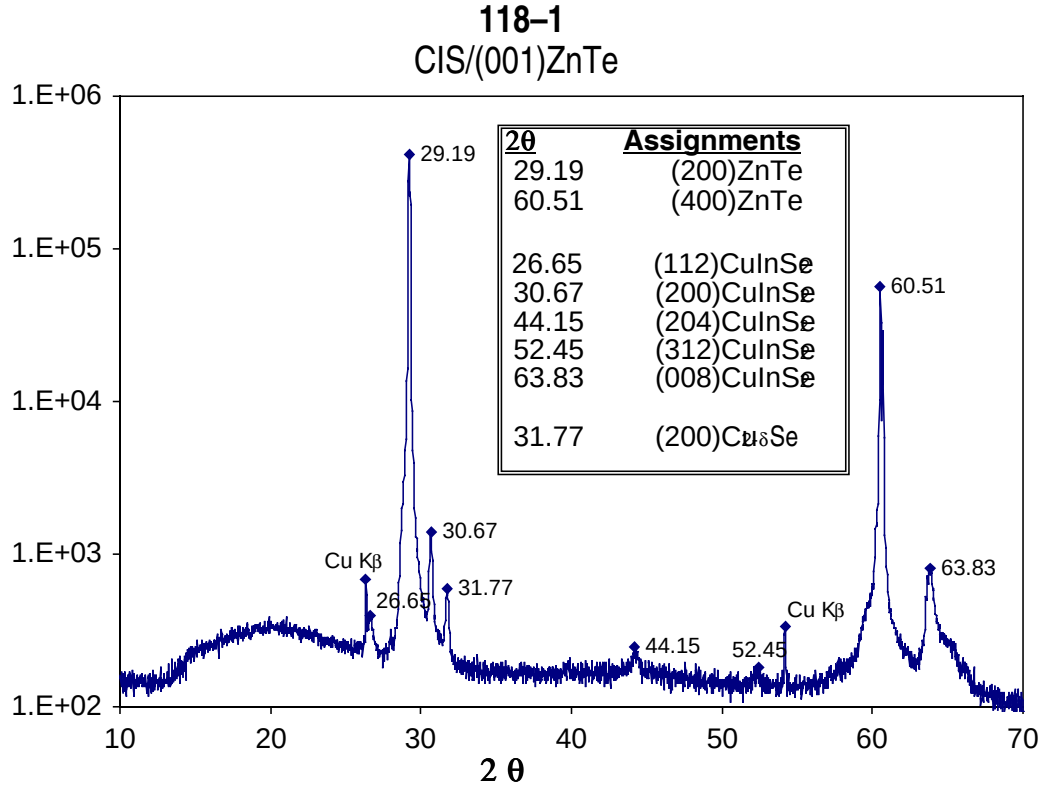

Figure 5-16 XRD θ–2θ scan of epitaxial $CuInSe_2$ on (001) ZnTe grown by MEE. The overall composition of the film was [Cu]=25.5 at.%, [In]=26.3 at.%, and [Se]=48.2 at.%.

Heteroepitaxy on SrF_2

Polished 1x1cm SrF_2 substrates oriented nominally on the singular (111) were rinsed in methanol immediately prior to mounting onto the MEE system's load lock. All growth experiments using these substrates were conducted simultaneously with GaAs samples, however they did not undergo the high temperature excursion used to desorb volatile oxides from the GaAs substrates immediately prior to the initiation of growth. This was considered unnecessary since (111) SrF_2 surfaces are terminated by fluorine [272] and hence relatively unreactive.

CIS films without sodium grown on SrF_2 substrates were without exception found to crack and peel off the substrate within about a minute of removal from the reactor's load-lock. This is of course indicative of high residual stress, but the fact that they did not peel off until removed suggests that Van der Waals forces between the film and substrate were strong enough in the absence of air or its components (*e.g.*: water vapor) to prevent this peeling. The lattice mismatch between $CuInSe_2$ and the SrF_2 substrates is actually quite small:

$$\delta a = \frac{a_{CISe} - a_{SrF_2}}{a_{SrF_2}} = -0.3\% \qquad (CuInSe_2 \ on \ SrF_2)$$

The addition of sodium during the initial stage of epitaxy allowed the growth of epilayers of $CuInSe_2$ on SrF_2 substrates that did not exhibit these adhesion problems, and which showed the narrowest linewidths and highest

peak intensities in XRD data seen from any samples grown in the course of this research as demonstrated in Figure 5-17.

In view of the hypothesis presented in this dissertation that sodium acts as a surfactant in the CIS material system, it is important to note that a similar effect is observed in Sb-mediated growth of non-lattice-matched germanium-silicon alloys on silicon substrates. It has been explicitly demonstrated in that system [273] that strain is relieved by the addition of a monolayer of antimony in the initial stages of epitaxy. The mechanism was found to be the dissociation of threading dislocations into a pair of Shockley partial dislocations at the surface, which totally relieved the misfit strain. In studies of silver homoepitaxy, the surfactant antimony has been shown to cause stacking faults to float with the growth front, preventing their incorporation into the bulk [274]. No comparable TEM data is available for the samples investigated here to conclude whether similar mechanisms might pertain in this case, but the conjecture is plausible.

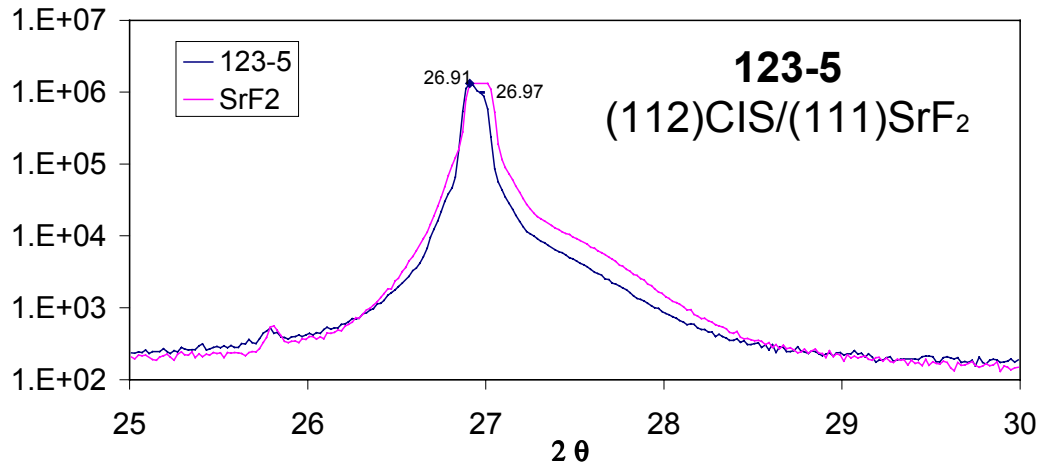

Figure 5-17 XRD θ–2θ scan of epitaxial $CuInSe_2$:Na on (111) SrF_2 grown by MEE. The overall composition of the film was [Cu]=23.4 at.%, [In]=26.3 at.%, and [Se]=50.3 at.%. The higher curve is a reference SrF_2 substrate without $CuInSe_2$.

Epitaxial Growth of CIS Using Activated Reactant Sources

Growth of CIS films using the thermal cracking source at both low (350°C) and high (928°C) cracking zone temperature and the ECR plasma cracker were compared to elucidate the effects of reactant pre-activation on the properties of the resulting films. Measured film properties included composition, XRD patterns, and morphology. Substrates included Mo/SLG, GaAs, ZnTe, and SrF_2.

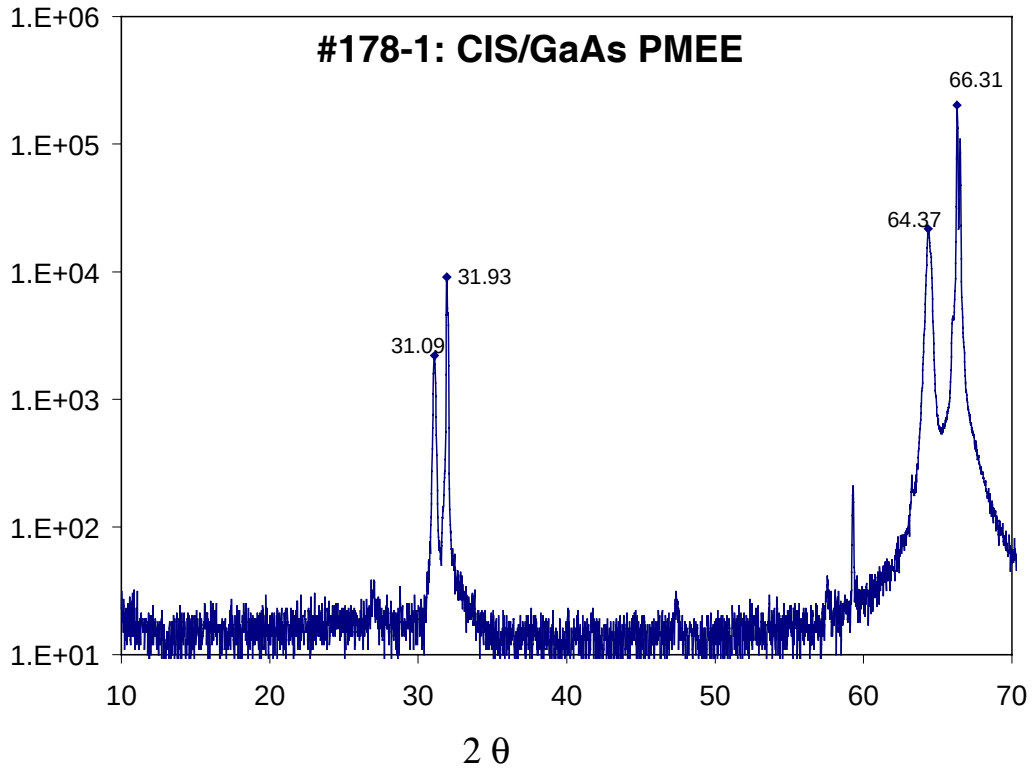

Figure 5-18 XRD θ–2θ scan of epitaxial $CuInSe_2$ on (100) GaAs grown by PMEE. The overall composition of the film was copper-rich, with [Cu]=28.1 at.%, [In]=21.1 at.%, and [Se]=50.8 at.%.

No significant and repeatable difference between the use of high and low cracking zone temperature for the thermal source was observed. On the other hand, growth using the ECR plasma cracker was characterized by a number of

significant differences from all other growth experiments conducted in this course of research, which used the thermal source. The effects on CIS/GaAs epilayer crystallinity are demonstrated in the XRD data for both copper-rich and indium-rich overall compositions in Figure 5-18 and Figure 5-19, respectively.

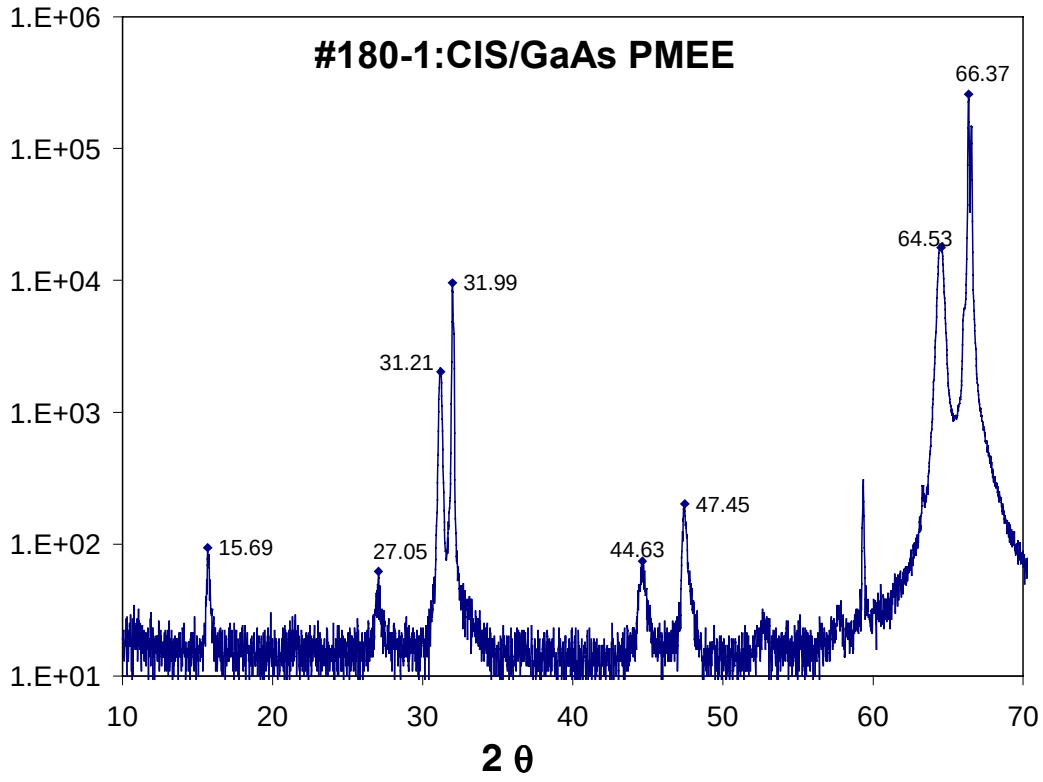

Figure 5-19 XRD θ–2θ scan of epitaxial $CuInSe_2$ on (100) GaAs grown by PMEE. The overall composition of the film was indium-rich, with [Cu]=23.1 at.%, [In]=26.3 at.%, and [Se]=50.6 at.%.

First note that irrespective of composition the background signal levels in both cases are significantly lower than measured in any sample grown with the thermal source (see for example Figure 5-9). This reduction in incoherent scattering by about one order of magnitude, particularly at low angles, is evidence that growth with the ECR plasma cracker improves epilayer crystallinity

[275]. The combination of a plasma activated source and MEE has not been heretofore reported, so this author has entitled this technique Plasma Migration-Enhanced Epitaxy, or PMEE.

In the copper-rich case shown in Figure 5-18 the composition corresponds to a valence stoichiometry deviation of +0.11, the highest ever measured in the course of this research. This directly demonstrates that the composition lies well into the selenium-rich domain of the equilibrium ternary phase field, but surprisingly there is very little indication of a diffraction peak corresponding to the $Cu_{2-\delta}Se$ binary compound expected to form in equilibrium with $CuInSe_2$ when the overall composition is so copper-rich. In contrast, such a peak is always seen in significantly copper-rich layers grown with the thermal source.

This might be consistent with coherent intergrowth of β– $Cu_{2-\delta}Se$ and $CuInSe_2$ as suggested by other researchers who have studied high-energy ion beam assisted deposition of $CuInSe_2$ [59]. They explained similar results by arguing that a non-equilibrium, selenium-enriched $Cu_{2-\delta}Se$ composition had formed because the activity of selenium is extremely high and coherent intergrowth represented an energetically favorable strain relief mechanism. However, it is also possible that these copper-rich CIS epilayers are single-phase $CuInSe_2$, which is supersaturated with copper.

The association of the anomalously high valence stoichiometry deviation with the $Cu_{2-\delta}Se$ phase in the case of overall copper-rich composition is

supported by the results for growth in the indium-rich case. The composition for the sample shown in Figure 6-19 corresponds to a valencey deviation of -0.005.

No notable effect on epilayer morphology was observed in PMEE growth of either copper or indium-rich layers on GaAs. Both ZnTe and SrF_2 substrates grown simultaneously with the GaAs epilayers described above failed to exhibit epitaxial growth. The reasons for this are uncertain, but could be related to differences in substrate preparation procedures.

CHAPTER 7
SUMMARY AND CONCLUSIONS

Published results of ternary Cu–In–Se and binary Cu–Se phase diagram studies have been combined with the published results of *ab-initio* quantum mechanical calculations of defect formation energies in $CuInSe_2$ to provide the first associated solution model for the phase equilibria and defect concentrations in -CIS. A novel method was developed to solve this problem, combining a lattice cluster expansion with the stoichiometric reaction analysis approach.

Comparison of the results of the modeling with the experimental literature suggests that crystals with metastable defect distributions are ubiquitous in this material system. Further investigation of the solubility of indium in the binary Cu_{2-} Se phase and modeling of valency deviation in the -CIS phase are recommended.

A rotating disc reactor has been designed and used to grow ternary -CIS polycrystalline thin films and many of the Cu–Se and In–Se compounds found in their respective binary phase fields. The ternary films were used to fabricate photovoltaic devices. The reactor was also used to study the migration-enhanced epitaxy of -CIS on GaAs, ZnTe, and SrF_2 single-crystal substrates. The use of this method to grow -CIS has not previously been reported in the literature. The resulting epilayers were sometimes found to exhibit CuAu (CA) ordering, rather

than the equilibrium chalcopyrite ordering. Further experimental work to determine the bandgap of CA-CIS is recommended to elucidate its possible effects on photovoltaic device performance.

A novel plasma-activated selenium source has been developed in the course of this research which is significantly different than any other heretofore reported in the scientific literature of the field. It is microwave-excited, magnetically-confined helical resonator designed to operate under Electron Cyclotron Resonance (ECR) conditions at 2.455 GHz. This source is designed to excite and dissociate the vapor exiting from the aperture of an effusion cell. It combines the effusion cell vapor flux with a stream of buffer gas injected at the resonance point. This source was also used to grow epitaxial -CIS films and their analysis indicated that plasma activation provides significantly greater selenium reactivity than effusion or double-oven (thermally activated) sources. The application of this plasma source to the growth of copper ternaries containing sulfur is recommended.

GLOSSARY

CIS	Any compound, phase, or mixture formed from the three elements copper, indium, and selenium
CGS	Any compound, phase, or mixture formed from the three elements copper, gallium, and selenium
CIS$_U$	Any compound, phase, or mixture formed from the three elements copper, indium, and sulfur
CIGS	Any compound, phase, or mixture formed from the four elements copper, indium, gallium, and selenium
CISS	Any compound, phase, or mixture formed from the four elements copper, indium, sulfur, and selenium
CIGSS	Any compound, phase, or mixture formed from the five elements copper, indium, gallium, sulfur, and selenium
ODC	An Ordered Defect Compound; a compound wherein vacancies on symmetry-distinct crystallographic lattice sites are an integral part of the crystal structure.
NDC	The Neutral Defect Complex in CIS , CGS and CIGS materials; the defect created by the following three point cation lattice defects on nearest-neighbor sites: (In_{Cu} + 2 V_{Cu}) and / or (Ga_{Cu} + 2 V_{Cu})
EXAFS	Extended X-ray Absorption Fine Structure
SEM	Scanning Electron Microscope / Microscopy
SE–SEM	Secondary Electron Scanning Electron Microscope / Microscopy
TEM	Transmission Electron Microscope / Microscopy
TED	Transmission Electron Diffraction
AFM	Atomic Force Microscope / Microscopy
XRF	X-Ray Fluorescence
PVD	Physical Vapor Deposition
MBE	Molecular Beam Epitaxy
ALE	Atomic Layer Epitaxy
MEE	Migration Enhanced Epitaxy

MFD	Modulated Flux Deposition
QCM	Quartz Crystal Monitor
RGA	Residual Gas Analayzer
SLG	Soda-Lime Glass
EMP	Electron Micro-Probe
EDX	Energy Dispersive X-ray spectrometry
QMS	Quadrapole Mass Spectrometry / Spectrometer
MOMBE	Metal-Organic Molecular Beam Epitaxy
OMVPE	OrganoMetallic Vapor Phase Epitaxy
AMU	Atomic Mass Units
BEP	Beam-Equivalent Pressure
PCM	Phase-Contrast Microscopy
CBD	Chemical Bath Deposition
SIMS	Secondary Ion Mass Spectrometry
WDS	Wavelength-Dispersive Spectroscopy

APPENDIX
CIS DEFECT AND PHASE EQUILIBRIA CALCULATIONS

The solution of quasichemical defect reaction equilibria are used to compute the defect concentrations in the α and β phases of the ternary Cu–In–Se solid system. The species in these equilbrium calculations are clusters of primitive chalcopyrite unit cells within which lattice point defects or their associates are embedded. The stoichiometric reaction formalism is employed to implement the computational solution in the *Mathematica* computer application environment. The subsequent subsections of this appendix detail the formula matrices, reaction stoichiometry matrices, and state vectors used to conduct the calculations. The mathematical solutions are constrained by boundary conditions derived in the subsection with that title. The final subsection gives the computational algorithm used to implement the solution, including select intermediate results as examples, and is written to emphasize the flow of the calculation.

Formula Matrices

Two primary species formula matrices, $\mathcal{D}$ and $\mathcal{D}\mathbf{0}$, will be used in the calculations to ensure that all denumerable conserved quantities remain invariant and to calculate changes in those which are not strictly conserved. Given the assumption that the thermodynamic system is closed, the strictly conserved quantities are the number of each type of atom and electrical charge. The "i^{th}" element of each column vector $\hat{a}_j$ within $\mathcal{D}_{ij}$ gives the stoichiometry of species (or mixture component) j with respect to the i^{th} conserved quantity.

In constructing these formula matrices, three key considerations are essential to the internal consistency of structure element-based defect reaction analysis [42; §14.3]. These are conservation of charge, conservation of mass, and maintaining fixed lattice site proportions (in this case 1:1:2:4 for the M1, M3, X6, and I sublattices, respectively). This proportionality is maintained by generating the structural species' cluster formula matrices from a lattice point defect formula matrix $\mathcal{D}\alpha\beta$ (whose basis is **sL**), an ideal (non-defective) unit cell vector, and the cluster size factors in the list **ncL**.

The function used to generate $\mathcal{D}$ and $\mathcal{D}\mathbf{0}$ from $\mathcal{D}\alpha\beta$ creates a mapping from the lattice species basis **sL** to the cluster basis set $\boldsymbol{\alpha\beta}$**L**. Since the thermodynamic functions in this model are (by assumption III in the formulation of the problem) first-degree homogeneous linear function of the numbers of defects of each kind and the number of lattice sites, a homomorphism exists between the thermodynamic functions defined with respect to these two bases. The number of species involved

permits the definition of a computationally tractable finite algebra on the cluster basis set $\boldsymbol{\alpha\beta}$**L** that yields the thermodynamic functions. This will be explicitly developed in the course of the statistical mechanics calculations employed to compute the lattice entropy.

The basis vectors for $\mathcal{D}$, $\mathcal{D}$**0**, and $\mathcal{D}\alpha\beta$ are **a** (which specifies the conserved quantities) and the building unit basis vectors **cE**, **cE0** (both derived from **cEgrouped**), and **L.CIS**, respectively. Lattice site proportionality is maintained by assigning each species to a lattice cluster which occupies an integral number of primitive unit cells. The basis vector **cE** contains all the lattice building units from the list $\boldsymbol{\alpha\beta}$**L**, whereas **cE0** removes those belonging to the secondary β–CIS phase and appends pseudo-structural element building units for the secondary $Cu_{2-\delta}Se$ phase. Conservation of the eight components of **a** is expressed with each of these formula matrices [158, §11.2] by the corresponding sum of the form $\sum_{j=1}^{32} \mathcal{D}_{ij}\,\mathrm{N}_j = \mathcal{N}_i^0$ (i=1,...,8). The formulas for the lattice-site species with respect to both its row basis **a** and column basis **L.CIS** are given by the matrix $\mathcal{D}\boldsymbol{\alpha\beta}$:

$$\mathcal{D}\boldsymbol{\alpha\beta} = \begin{pmatrix}
1 & 0 & 0 & 0 & 0 & 0 & 0 & 0 & 0 & 1 & 1 & 1 & 0 & 0 & 0 & 0 & 0 & 0 & 1 & 1 & 1 & 1 & 0 & 0 & 0 \\
0 & 1 & 0 & 0 & 0 & 0 & 1 & 1 & 1 & 0 & 0 & 0 & 0 & 0 & 0 & 0 & 0 & 0 & 0 & 0 & 0 & 1 & 1 & 1 & 1 \\
0 & 0 & 1 & 0 & 0 & 0 & 0 & 0 & 0 & 0 & 0 & 0 & 0 & 0 & 0 & 0 & 0 & 0 & 0 & 0 & 0 & 0 & 0 & 0 & 0 \\
0 & 0 & 0 & 0 & 0 & -1 & 0 & 1 & 2 & 0 & -1 & -2 & 0 & 1 & 2 & 3 & 0 & 2 & 0 & 1 & 0 & 0 & 0 & 1 & 0 \\
1 & 0 & 0 & 0 & 1 & 1 & 1 & 1 & 1 & 0 & 0 & 0 & 0 & 0 & 0 & 0 & 0 & 0 & 0 & 0 & 0 & 1 & 1 & 2 & 2 & 3 \\
0 & 1 & 0 & 0 & 0 & 0 & 0 & 0 & 0 & 1 & 1 & 1 & 1 & 1 & 1 & 1 & 0 & 0 & 0 & 0 & 0 & 1 & 0 & 0 & 0 \\
0 & 0 & 1 & 0 & 0 & 0 & 0 & 0 & 0 & 0 & 0 & 0 & 0 & 0 & 0 & 0 & 1 & 1 & 0 & 0 & 0 & 0 & 0 & 0 & 0 \\
0 & 0 & 0 & 1 & 0 & 0 & 0 & 0 & 0 & 0 & 0 & 0 & 0 & 0 & 0 & 0 & 0 & 0 & 1 & 1 & 1 & 0 & 0 & 0 & 0
\end{pmatrix};$$

These formulas may be more easily understood when conjoined with their corresponding basis vector elements:

Transpose[{Flatten[L.CIS], a .$\mathcal{D}\alpha\beta$}] // TableForm

Cu^{x}_{Cu}	Cu + M1
In^{x}_{In}	In + M3
Se^{x}_{Se}	Se + X6
$\mathcal{V}_{i}$	$\mathcal{I}$
$\mathcal{V}^{x}_{Cu}$	M1
$\mathcal{V}'_{Cu}$	M1 − q
In^{x}_{Cu}	In + M1
$In^{\cdot}_{Cu}$	In + M1 + q
$In^{\cdot\cdot}_{Cu}$	In + M1 + 2 q
Cu^{x}_{In}	Cu + M3
Cu'_{In}	Cu + M3 − q
Cu''_{In}	Cu + M3 − 2 q
$\mathcal{V}^{x}_{In}$	M3
$\mathcal{V}^{\cdot}_{In}$	M3 + q
$\mathcal{V}^{\cdot\cdot}_{In}$	M3 + 2 q
$\mathcal{V}^{\cdot\cdot\cdot}_{In}$	M3 + 3 q
$\mathcal{V}^{x}_{Se}$	X6
$\mathcal{V}^{\cdot\cdot}_{Se}$	2 q + X6
Cu^{x}_{i}	Cu + $\mathcal{I}$
$Cu^{\cdot}_{i}$	Cu + q + $\mathcal{I}$
$Cu_{i} \oplus \mathcal{V}_{Cu}$	Cu + M1 + $\mathcal{I}$
$Cu_{In} \oplus In_{Cu}$	Cu + In + M1 + M3
$\mathcal{V}_{Cu} \oplus In_{Cu}$	In + 2 M1
$(\mathcal{V}_{Cu} \oplus In_{Cu})^{\cdot}$	In + 2 M1 + q
$2\,\mathcal{V}_{Cu} \oplus In_{Cu}$	In + 3 M1

This function returns the defect's name and its formula in terms of the basis elements given the column number and name of the formula matrix:

formula[i_, $\mathcal{D}\alpha\beta$] := {Flatten[L.CIS], a .$\mathcal{D}\alpha\beta$}⟦All, i⟧

```
(* the CIS$\alpha$+CIS$\beta$ basis vector *) cE = With[{$\beta$13 = Take[cEgrouped[[1, 2]], -1][[1]]},
    Join[cEgrouped[[1, 1]], Drop[cEgrouped[[1, 2]], -1],
      Insert[cEgrouped[[1, 3]], $\beta$13, -2], cEgrouped[[2]], {cEgrouped[[3]]}]]
```

$\{CIS_\alpha, \mathcal{V}_{Cu}^{x}, \mathcal{V}'_{Cu}, In_{Cu}^{x}, In_{Cu}^{\cdot}, In_{Cu}^{\cdot\cdot}, Cu_{In}^{x}, Cu'_{In},$
$Cu''_{In}, \mathcal{V}_{In}^{x}, \mathcal{V}_{In}^{\cdot}, \mathcal{V}_{In}^{\cdot\cdot}, \mathcal{V}_{In}^{\cdot\cdot\cdot}, \mathcal{V}_{Se}^{x}, \mathcal{V}_{Se}^{\cdot\cdot}, Cu_i^{x}, Cu_i^{\cdot}, Cu_i \oplus \mathcal{V}_{Cu},$
$Cu_{In} \oplus In_{Cu}, \mathcal{V}_{Cu} \oplus In_{Cu}, (\mathcal{V}_{Cu} \oplus In_{Cu})^{\cdot}, (2\mathcal{V}_{Cu} \oplus In_{Cu})_\alpha,$
$(2\mathcal{V}_{Cu} \oplus In_{Cu})_{\beta 15}, (2\mathcal{V}_{Cu} \oplus In_{Cu})_{\beta 13}, (2\mathcal{V}_{Cu} \oplus In_{Cu})_{\beta 25}, e', h^{\cdot}, \Delta N\}$

```
Length[cE]
```

28

The formula for the ideal primitive unit cell cluster on the lattice, CIS_α, is defined as twice the sum of the normal lattice elements times their respective sublattice multiplicity, with the help of three subgroup bases corresponding to the unit lattice site cluster, the elements in ideal proportion, and the charge:

```
NL = {0, 0, 0, 0, 1, 1, 2, 4}; aL = {1, 1, 2, 0, 0, 0, 0, 0}; qL = {0, 0, 0, 1, 0, 0, 0, 0};
```

```
cL = 2 Plus @@ Array[(aL + qL + NL) $\mathcal{D}\alpha\beta$[[All, #]] &, 4]
```

{2, 2, 4, 0, 2, 2, 4, 8}

There are 8 conserved quantities and 27 distinct species in $\mathcal{D}$. Therefore a 27 species formula matrix is used, and initialized with each column given by the product of the appropriate cluster size factor and the unit cluster vector **cL**:

```
$\mathcal{D}$ = Array[cL ncL[[Position[$\alpha\beta$L, cE[[#]][[1, 1]]]]] &, 25];
$\mathcal{D}$ = Join[$\mathcal{D}$, Outer[Times, {-1, 1}, qL], {NL}];
```

Note that both charge carriers and the lattice number deviation basis vector have also been appended, expanding $\mathcal{D}$ to 27 columns in length.

These lattice cluster formulas in the column vectors of $\mathcal{D}$ are corrected by

adding two terms to the initialized matrix. The first term subtracts the normal site atoms from the sites within the cluster occupied by the defect, and the second adds the defect atoms and charge back in. Both of these terms are computed using the defect's lattice site formula from the matrix $\mathcal{D}\alpha\beta$.

```
Array[Join[Array[1 &, 4], Array[0 &, 4]]
        Plus @@ Table[𝒟αβ⟦4 + i, #⟧ 𝒟αβ⟦All, i⟧, {i, 4}] &, 25];
Array[Join[Array[1 &, 4], Array[0 &, 4]] 𝒟αβ⟦All, #⟧ &, 25] − %;
(*include β−phase dilute NDC cluster,
  with the same deviation as for the α−phase: *)
  Append[Drop[%, 4], Take[%, −1]⟦1⟧];
(*include β−phase intermediate NDC cluster,
  also with the same deviation as for the α−phase: *)Append[%, Take[%, −1]⟦1⟧];
(*include β−phase concentrated NDC cluster,
  with twice the deviation of the dilute cluster: *)Append[%, 2 Take[%, −1]⟦1⟧];
(*add zero vectors for CIS_α, e′, h•, and ΔN deviations: *)
Join[{#}, PadRight[%, 27, {#}]] &[Array[0 &, 8]];
𝒟 = Transpose[𝒟 + %];

Dimensions[𝒟]

{8, 28}
```

The representations of the building units of the α–phase lattice (the first 22 columns) and the band-delocalized electrons and holes (the two columns immediately preceding the last) with respect to the constituent basis **a** are straightforward, although the reasons for the choice of cluster sizes are not obvious. This issue will be discussed in detail when the lattice statistics are evaluated in a subsequent section.

The last column, corresponding to the basis element ΔN, allows for removal of lattice sites from the system in the proper ratios, without the transfer of any atoms.

This is necessary because the lattice sites have been effectively defined as conserved quantities so that reactions cannot change their proportions, which would violate a key requirement for validity of the structure element approach. Thus ΔN provides a mechanism for the free energy minimization procedure to adjust the total number of lattice sites over which the atoms and real lattice vacancies which have energetic costs associated with their formation are distributed. Obviously it is essential that their be no similar energetic cost directly associated with this accounting device, only the indirect effect due to the increased concentration of the energetically meaningful defects on the remaining lattice sites. This normalization effect will be made explicit in the next subsection.

The formula display function is extended to the formula matrix $\mathcal{D}$ to return the name and cluster formula associated with a given column number:

formula[i_, $\mathcal{D}$] := {cE, a .$\mathcal{D}$}[[All, i]]

The following table pairs up the column basis elements with the contraction of the row basis and species formula matrix to facilitate their direct comparison, compiling the results of the formula display function applied to the entire cluster formula matrix $\mathcal{D}$.

Transpose[{cE, a .$\mathcal{D}$}] // TableForm

CIS_{α}	$2\,Cu + 2\,In + 2\,M1 + 2\,M3 + 4\,Se + 4\,X6 + 8\,\mathcal{I}$
$\mathcal{V}_{Cu}^{x}$	$5\,Cu + 6\,In + 6\,M1 + 6\,M3 + 12\,Se + 12\,X6 + 24\,\mathcal{I}$
$\mathcal{V}_{Cu}'$	$5\,Cu + 6\,In + 6\,M1 + 6\,M3 - q + 12\,Se + 12\,X6 + 24\,\mathcal{I}$
In_{Cu}^{x}	$5\,Cu + 7\,In + 6\,M1 + 6\,M3 + 12\,Se + 12\,X6 + 24\,\mathcal{I}$
$In_{Cu}^{\bullet}$	$5\,Cu + 7\,In + 6\,M1 + 6\,M3 + q + 12\,Se + 12\,X6 + 24\,\mathcal{I}$
$In_{Cu}^{\bullet\bullet}$	$5\,Cu + 7\,In + 6\,M1 + 6\,M3 + 2\,q + 12\,Se + 12\,X6 + 24\,\mathcal{I}$
Cu_{In}^{x}	$7\,Cu + 5\,In + 6\,M1 + 6\,M3 + 12\,Se + 12\,X6 + 24\,\mathcal{I}$
Cu_{In}'	$7\,Cu + 5\,In + 6\,M1 + 6\,M3 - q + 12\,Se + 12\,X6 + 24\,\mathcal{I}$
Cu_{In}''	$7\,Cu + 5\,In + 6\,M1 + 6\,M3 - 2\,q + 12\,Se + 12\,X6 + 24\,\mathcal{I}$
$\mathcal{V}_{In}^{x}$	$6\,Cu + 5\,In + 6\,M1 + 6\,M3 + 12\,Se + 12\,X6 + 24\,\mathcal{I}$
$\mathcal{V}_{In}^{\bullet}$	$6\,Cu + 5\,In + 6\,M1 + 6\,M3 + q + 12\,Se + 12\,X6 + 24\,\mathcal{I}$
$\mathcal{V}_{In}^{\bullet\bullet}$	$6\,Cu + 5\,In + 6\,M1 + 6\,M3 + 2\,q + 12\,Se + 12\,X6 + 24\,\mathcal{I}$
$\mathcal{V}_{In}^{\bullet\bullet\bullet}$	$6\,Cu + 5\,In + 6\,M1 + 6\,M3 + 3\,q + 12\,Se + 12\,X6 + 24\,\mathcal{I}$
$\mathcal{V}_{Se}^{x}$	$6\,Cu + 6\,In + 6\,M1 + 6\,M3 + 11\,Se + 12\,X6 + 24\,\mathcal{I}$
$\mathcal{V}_{Se}^{\bullet\bullet}$	$6\,Cu + 6\,In + 6\,M1 + 6\,M3 + 2\,q + 11\,Se + 12\,X6 + 24\,\mathcal{I}$
Cu_{i}^{x}	$7\,Cu + 6\,In + 6\,M1 + 6\,M3 + 12\,Se + 12\,X6 + 24\,\mathcal{I}$
$Cu_{i}^{\bullet}$	$7\,Cu + 6\,In + 6\,M1 + 6\,M3 + q + 12\,Se + 12\,X6 + 24\,\mathcal{I}$
$Cu_{i} \oplus \mathcal{V}_{Cu}$	$6\,Cu + 6\,In + 6\,M1 + 6\,M3 + 12\,Se + 12\,X6 + 24\,\mathcal{I}$
$Cu_{In} \oplus In_{Cu}$	$6\,Cu + 6\,In + 6\,M1 + 6\,M3 + 12\,Se + 12\,X6 + 24\,\mathcal{I}$
$\mathcal{V}_{Cu} \oplus In_{Cu}$	$8\,Cu + 11\,In + 10\,M1 + 10\,M3 + 20\,Se + 20\,X6 + 40\,\mathcal{I}$
$(\mathcal{V}_{Cu} \oplus In_{Cu})^{\bullet}$	$8\,Cu + 11\,In + 10\,M1 + 10\,M3 + q + 20\,Se + 20\,X6 + 40\,\mathcal{I}$
$(2\,\mathcal{V}_{Cu} \oplus In_{Cu})_{\alpha}$	$7\,Cu + 11\,In + 10\,M1 + 10\,M3 + 20\,Se + 20\,X6 + 40\,\mathcal{I}$
$(2\,\mathcal{V}_{Cu} \oplus In_{Cu})_{\beta 15}$	$7\,Cu + 11\,In + 10\,M1 + 10\,M3 + 20\,Se + 20\,X6 + 40\,\mathcal{I}$
$(2\,\mathcal{V}_{Cu} \oplus In_{Cu})_{\beta 13}$	$3\,Cu + 7\,In + 6\,M1 + 6\,M3 + 12\,Se + 12\,X6 + 24\,\mathcal{I}$
$(2\,\mathcal{V}_{Cu} \oplus In_{Cu})_{\beta 25}$	$4\,Cu + 12\,In + 10\,M1 + 10\,M3 + 20\,Se + 20\,X6 + 40\,\mathcal{I}$
e'	$-q$
$h^{\bullet}$	q
ΔN	$M1 + M3 + 2\,X6 + 4\,\mathcal{I}$

Formation of the β phase of CIS is analyzed as a collective phenomena which occurs due to the aggregation of $(2\,\mathcal{V}_{Cu} \oplus In_{Cu})$ cation Neutral Defect Complexes (NDC) and their resulting interactions. These complexes and a part of the lattice in

their immediate neighborhood that remains unperturbed are treated here as a secondary phase, and no other defects are included in that phase. An unequivocal determination of the long-range crystallographic structure of the β–CIS phase is not yet available. The lattice entropy calculations for both the α and β phases of CIS, which will be described in a later section, employ a cluster-based approach based on a 16-site cluster of four normally-occupied tetrahedra [118, figure 4.12]. The local crystallographic structure representing the lowest-energy arrangement of the three point defects that form a single NDC [70] places them on three adjacent M1 sites along the (110) or $(1\,\bar{1}\,0)$ directions. A minimum of three 16-site clusters connected along one of these {110} diagonals is necessary to include this configuration, but an additional two clusters are required to completely internalize all these defects and their first coordination shell counterions. The resulting supercluster is shaped like a right hexagonal solid stretched along that diagonal and can be used as the basis for a Bravais lattice. Transfer of a single $(2\,\mathcal{V}_{Cu} \oplus In_{Cu})$ NDC within this supercluster from the α to the β phase results in the conversion of this portion of the lattice in the neighborhood of that defect to the β phase according to the quasichemical reaction:

$$Cu_7\ In_{11}\ Se_{20}(\beta) \rightleftharpoons (2\,\mathcal{V}_{Cu} \oplus In_{Cu})_{\alpha} + 7\ Cu^{x}_{Cu} + 10\ In^{x}_{In} + 20\ Se^{x}_{Se} + 40\ \mathcal{V}_{i}\,.$$

The primitive unit cell of the chalcopyrite lattice is included among the β–CIS phase building units so that this does not implicitly fix the stoichiometry limit of the β phase at X = $\frac{7}{11}$, as this model does the α phase.

If two NDC are transferred with the same size supercluster, they will unavoidably share counterions with neighboring superclusters and the reaction

formula becomes:

$$CuIn_3\,Se_5 \rightleftharpoons 2\,(2\,\mathcal{V}_{Cu} \oplus In_{Cu})_\alpha + 4\,Cu^x_{Cu} + 10\,In^x_{In} + 20\,Se^x_{Se} + 40\,\mathcal{V}_i\,.$$

This cluster's inclusion in the basis fulfills the requirement that the NDC are sufficiently aggregated that they interact strongly, the mechanism underlying the additional enthalpy reduction associated with their ordering [70].

The $Cu_3\,In_7\,Se_{12}$ compound ($X \simeq 0.43$) can be constructed from the previously described supercluster of three 16-site clusters connected along a common {110} diagonal in a close-packed array according to the formation reaction:

$$Cu_3\,In_7\,Se_{12} \rightleftharpoons (2\,\mathcal{V}_{Cu} \oplus In_{Cu})_\alpha + 3\,Cu^x_{Cu} + 6\,In^x_{In} + 12\,Se^x_{Se} + 24\,\mathcal{V}_i\,.$$

This is particularly intriguing since $Cu_3\,In_7\,Se_{12}$ was studied in conjunction with a published defect analysis [148] of a long-range crystallographic structure proposed [276] for the β–CIS phase based on the $I\bar{4}2m$ point group symmetry. It was found to be the only composition with no defects on one of the $I\bar{4}2m$ point group sublattices, so if that long-range structure is eventually found to apply to β–CIS, it is in a sense the stoichiometric composition of this phase. Regardless, the fact that an ordered structure can be constructed for this composition entirely as a Bravais lattice with a basis consisting simply of a linear chain of 3 primitive unit cells of the related chalcopyrite structure, each containing exactly one defect on the same site, means that it represents a composition for the non-stoichiometric β–CIS phase that could possess long-range order based on a compact unit cell. This cluster is included in the basis.

These three clusters are indexed by the number of NDC and number of

chalcopyrite unit cells from which each created. The second index is related to the second index of the pair (n,m) used in the previously published NDC ordering model [70] of the β–CIS phase by a factor of two, since there are two formula units *per* chalcopyrite primitive unit cell. These reactions combine to provide a mechanism for modeling stoichiometry variation within the CIS β phase. The overall stoichiometry in that phase is determined by the weighted average of the numbers of these three types of superclusters and chalcopyrite unit cell, which can vary throughout the $\frac{1}{3} \le X \le 1$ molecularity range limits of this calculation.

```
(* the CISα+Cu2Se basis vector *) cE0 = Flatten[
    Join[Drop[Take[Flatten[αβL], 23], {20}], RotateRight[Drop[cEgrouped, {1, 1}]]]]
```

$$\{CIS_\alpha, \mathcal{V}_{Cu}^{x}, \mathcal{V}_{Cu}', In_{Cu}^{x}, In_{Cu}^{\bullet}, In_{Cu}^{\bullet\bullet}, Cu_{In}^{x}, Cu_{In}', Cu_{In}'', \mathcal{V}_{In}^{x}, \mathcal{V}_{In}^{\bullet}, \mathcal{V}_{In}^{\bullet\bullet}, \mathcal{V}_{In}^{\bullet\bullet\bullet}, \mathcal{V}_{Se}^{x}, \mathcal{V}_{Se}^{\bullet\bullet}, Cu_i^{x}, Cu_i^{\bullet}, Cu_i \oplus \mathcal{V}_{Cu}, Cu_{In} \oplus In_{Cu}, \mathcal{V}_{Cu} \oplus In_{Cu}, (\mathcal{V}_{Cu} \oplus In_{Cu})^{\bullet}, (2\mathcal{V}_{Cu} \oplus In_{Cu})_\alpha, Cu_{Cu2Se}, Cu2\_\delta Se, e', h^{\bullet}, \Delta N\}$$

There are 8 conserved quantites and 27 distinct species in $\mathcal{D}0$. Therefore an 8×27 species formula matrix must be employed, which is derived for the secondary $Cu_{2-\delta}Se$ phase problem from $\mathcal{D}$ by dropping the β–CIS phase species and substituting two column vectors representing incremental Cu segregation to $Cu_{2-\delta}Se$ and that phase itself:

```
𝒟0 = Drop[Transpose[𝒟], {23, 25}];
𝒟0 = Insert[𝒟0, {1, 0, 0, 0, 0, 0, 0, 0}, {23}];
𝒟0 = Transpose[Insert[𝒟0, {2 – δ, 0, 1, 0, 0, 0, 0, 0}, {24} ]];
Dimensions[𝒟0]
```

```
{8, 27}
```

The secondary phase definitions are fundamentally different in this case. Unlike the preceding case, the cation sublattices of α–CIS and $Cu_{2-\delta}Se$ are

incoherent. Thus transfer of physical constituents to the secondary $Cu_{2-\delta}Se$ phase does not reassign lattice sites to it. In order to transfer physical constituents to a crystallographically incoherent secondary phase without violating the essential requirement that the site number ratios remain unchanged with respect to any allowed quasichemical reaction, the species representing the secondary phase physical constituents cannot be assigned to any of the four sublattices. In the case of transfers between the α and β phases of ternary CIS, lattice site transfer is physically meaningful since the two lattices are coherent; lattice sites are in reality neither created nor destroyed. In the case of transfers between the α and Cu_2Se phases, site numbers are not conserved: the number of lattice sites removed from the α phase is not equal to the number created in the binary phase. The formula display function can be extended to the formula matrix $\mathcal{D}\mathbf{0}$:

```
formula[i_, 𝒟0] := {cE0, a .𝒟0}⟦All, i⟧
```

All of these cluster formula are tabulated below:

Transpose[{cE0, a .$\mathcal{D}$0}] // TableForm

CIS_{α}	2 Cu + 2 In + 2 M1 + 2 M3 + 4 Se + 4 X6 + 8 $\mathcal{I}$
$\mathcal{V}^{x}_{Cu}$	5 Cu + 6 In + 6 M1 + 6 M3 + 12 Se + 12 X6 + 24 $\mathcal{I}$
$\mathcal{V}'_{Cu}$	5 Cu + 6 In + 6 M1 + 6 M3 − q + 12 Se + 12 X6 + 24 $\mathcal{I}$
In^{x}_{Cu}	5 Cu + 7 In + 6 M1 + 6 M3 + 12 Se + 12 X6 + 24 $\mathcal{I}$
$In^{\bullet}_{Cu}$	5 Cu + 7 In + 6 M1 + 6 M3 + q + 12 Se + 12 X6 + 24 $\mathcal{I}$
$In^{\bullet\bullet}_{Cu}$	5 Cu + 7 In + 6 M1 + 6 M3 + 2 q + 12 Se + 12 X6 + 24 $\mathcal{I}$
Cu^{x}_{In}	7 Cu + 5 In + 6 M1 + 6 M3 + 12 Se + 12 X6 + 24 $\mathcal{I}$
Cu'_{In}	7 Cu + 5 In + 6 M1 + 6 M3 − q + 12 Se + 12 X6 + 24 $\mathcal{I}$
Cu''_{In}	7 Cu + 5 In + 6 M1 + 6 M3 − 2 q + 12 Se + 12 X6 + 24 $\mathcal{I}$
$\mathcal{V}^{x}_{In}$	6 Cu + 5 In + 6 M1 + 6 M3 + 12 Se + 12 X6 + 24 $\mathcal{I}$
$\mathcal{V}^{\bullet}_{In}$	6 Cu + 5 In + 6 M1 + 6 M3 + q + 12 Se + 12 X6 + 24 $\mathcal{I}$
$\mathcal{V}^{\bullet\bullet}_{In}$	6 Cu + 5 In + 6 M1 + 6 M3 + 2 q + 12 Se + 12 X6 + 24 $\mathcal{I}$
$\mathcal{V}^{\bullet\bullet\bullet}_{In}$	6 Cu + 5 In + 6 M1 + 6 M3 + 3 q + 12 Se + 12 X6 + 24 $\mathcal{I}$
$\mathcal{V}^{x}_{Se}$	6 Cu + 6 In + 6 M1 + 6 M3 + 11 Se + 12 X6 + 24 $\mathcal{I}$
$\mathcal{V}^{\bullet\bullet}_{Se}$	6 Cu + 6 In + 6 M1 + 6 M3 + 2 q + 11 Se + 12 X6 + 24 $\mathcal{I}$
Cu^{x}_{i}	7 Cu + 6 In + 6 M1 + 6 M3 + 12 Se + 12 X6 + 24 $\mathcal{I}$
$Cu^{\bullet}_{i}$	7 Cu + 6 In + 6 M1 + 6 M3 + q + 12 Se + 12 X6 + 24 $\mathcal{I}$
$Cu_{i} \oplus \mathcal{V}_{Cu}$	6 Cu + 6 In + 6 M1 + 6 M3 + 12 Se + 12 X6 + 24 $\mathcal{I}$
$Cu_{In} \oplus In_{Cu}$	6 Cu + 6 In + 6 M1 + 6 M3 + 12 Se + 12 X6 + 24 $\mathcal{I}$
$\mathcal{V}_{Cu} \oplus In_{Cu}$	8 Cu + 11 In + 10 M1 + 10 M3 + 20 Se + 20 X6 + 40 $\mathcal{I}$
$(\mathcal{V}_{Cu} \oplus In_{Cu})^{\bullet}$	8 Cu + 11 In + 10 M1 + 10 M3 + q + 20 Se + 20 X6 + 40 $\mathcal{I}$
$(2\,\mathcal{V}_{Cu} \oplus In_{Cu})_{\alpha}$	7 Cu + 11 In + 10 M1 + 10 M3 + 20 Se + 20 X6 + 40 $\mathcal{I}$
Cu_{Cu2Se}	Cu
Cu2.δSe	Se + Cu $(2 - \delta)$
e′	−q
h$^{\bullet}$	q
ΔN	M1 + M3 + 2 X6 + 4 $\mathcal{I}$

Turning now to $\mathcal{D}$**0** and **cE0**, by (empirically supported) assumption, only Cu and Se (but not In) may be transferred between the α and $Cu_{2-\delta}Se$ phases, according to the reaction:

$$(2 - \delta)\ Cu^{x}_{Cu} + Se^{x}_{Se} \rightleftharpoons Cu2.\delta Se + (2 - \delta)\ \mathcal{V}^{x}_{Cu} + \mathcal{V}^{x}_{Se}\,.$$

The Cu_2Se phase has a very wide compositional range of phase stability which can extend to as much as ~36.5 at.% selenium. To model this phase properly, a mechanism must therefore be provided for independently transfering each of these components between the phases. The underlying mechanism by which stoichiometry deviations are accomodated in the crystalline structure of $Cu_{2-\delta}Se$ are discussed extensively in [160] and [176]. Its crystallographic structure is characterized by partial occupancy of the eight available tetrahedral copper sites for all compositions, including the stoichiometric where $\delta = 0$. Deviation from stoichiometry towards copper-rich compositions ($\delta < 0$) is not observed in most studies and is negligible in those where it is reported. Deviation towards selenium-rich compositions ($\delta>0$) is accomplished by an increase in copper vacancies. Hence it is the independent exchange of copper between $Cu_{2-\delta}Se$ and α-$CuInSe_2$ which must be accomodated within the formal framework of this calculation. This is accomplished by dividing the formation reaction above into two component reactions. The first:

$$(2 - \delta_{min})\, Cu^{x}_{Cu} + Se^{x}_{Se} \rightleftharpoons Cu2\_\delta_{min}\, Se + (2 - \delta_{min})\, \mathcal{V}^{x}_{Cu} + \mathcal{V}^{x}_{Se}$$

transfers both in the proportions that yield the minimum stable selenium content in the $Cu_{2-\delta}Se$ phase required to prevent formation of the copper phase as detailed in the subsequent boundary conditions section. The second:

$$Cu^{x}_{Cu} \rightleftharpoons Cu_{Cu2Se} + \mathcal{V}^{x}_{Cu}$$

permits the independent transfer of copper between the phases since their combined equilibrium could require excess segregation of copper above the minimum required for the $Cu_{2-\delta}Se$ phase's stability. These considerations lead to the

values shown in the last two (29^{th} and 30^{th}) columns of $\mathcal{D}0$. The basis elements Cu_{Cu2Se} and Cu2δSe are not actually building units (as precisely defined in the last section) of the $Cu_{2-\delta}Se$ phase, since neither of them are associated with specific lattice sites within that binary phase itself. A structural element model for $Cu_{2-\delta}Se$ will not be employed for this two-phase equilibrium calculation. Its Gibbs energy of formation and the dependence thereof on the value of δ as determined in a recent assessment of the Cu–Se binary system [176] will be utilized instead. Note, however, that this cited assessment is itself based on a sublattice solution model for the $Cu_{2-\delta}Se$ phase which will be described in detail in the subsequent boundary conditions section of this treatise. The number of lattice sites on which the model's structural elements reside is given by a sum over those elements in the α and β phases alone and that this is the number which must be employed for lattice-density normalizations of concentration, the $\langle N_j \rangle$.

Many of the defect clusters in the basis **cE0** will be found to effectively vanish in the temperature range below the α–β–δ eutectoid. The practical criterion used for this characterization is based on numerical convergence of the solution algorithm, but typically that occurs when a species has dropped to a calculated specific molar probability of substantially less than a single defect *per* mole, and has therefore effectively vanished. In anticipation of the need to eliminate those species from the basis, the subset basis **cE00** comprised of the species persisting at lower temperatures is also defined at this time. Most of the results of the defect equilibria calculations will be presented with respect to this species basis.

```
cE00 = Drop[Drop[Drop[Drop[cE0, {23}], {16, 17}], {10, 13}], {4, 6}]
```

$$\{CIS_{\alpha}, \mathcal{V}^{x}_{Cu}, \mathcal{V}'_{Cu}, Cu^{x}_{In}, Cu'_{In}, Cu''_{In}, \mathcal{V}^{x}_{Se}, \mathcal{V}^{\bullet\bullet}_{Se}, Cu_i \oplus \mathcal{V}_{Cu}, Cu_{In} \oplus In_{Cu}, \mathcal{V}_{Cu} \oplus In_{Cu}, (\mathcal{V}_{Cu} \oplus In_{Cu})^{\bullet}, (2\mathcal{V}_{Cu} \oplus In_{Cu})_{\alpha}, Cu2.\delta Se, e', h^{\bullet}, \Delta N\}$$

```
𝒟00 = Transpose[
      Drop[Drop[Drop[Drop[Transpose[𝒟0], {23}], {16, 17}], {10, 13}], {4, 6}]];
```

Finally, in preparation for the next section's development the ranks of $\mathcal{D}$ and $\mathcal{D}\mathbf{0}$ are determined:

```
rank𝒟 = Length[Transpose[𝒟]] – Length[NullSpace[𝒟]];
rank𝒟0 = Length[Transpose[𝒟0]] – Length[NullSpace[𝒟0]];
Length[𝒟] === Length[𝒟0] === 8 ⋀ rank𝒟 === rank𝒟0 === 5
```

True

Since the rank of $\mathcal{D}$ and $\mathcal{D}\mathbf{0}$ do not equal the number of their rows, this means that all of their columns are not linearly independent of one another. This is evidence that the problem has been correctly constructed to maintain lattice site proportions, since this fixed proportionality means that the lattice site numbers are not independently conserved quantities, of which there are only five. Hence the total number of independent quasichemical reactions (after eliminating those which are dependent on the remaining ones by virtue of the conservation constraints) will be reduced in both cases by the number of independent constraints to 22 (= 27 - rank$\mathcal{D}$ or rank$\mathcal{D}$0).

Reaction Stoichiometry Matrices

Next the reaction stoichiometry matrices ν and $\nu 0$, whose 22 component column vectors $\hat{\nu}_r$ correspond to the preceding reduced set of 22 independent reactions, are found by solving the matrix equation $\mathcal{D}\cdot\nu = 0$ for the unknown column vectors $\hat{\nu}_r$ which span the nullspace of $\mathcal{D}$:

ν = Transpose[NullSpace[$\mathcal{D}$]];

MatrixForm[ν]

$$\begin{pmatrix}
17 & 0 & 0 & 13 & 6 & 4 & 4 & 1 & 1 & -3 & -3 & -6 & -6 & 0 & -3 & -3 & -3 & -3 & -6 & -6 & -6 & 0 & 0 \\
-4 & -1 & 1 & -4 & -2 & -2 & -2 & -2 & -1 & 0 & 0 & 0 & 1 & -2 & -4 & -3 & -2 & -1 & 2 & 1 & 0 & -2 & -1 \\
0 & 1 & -1 & 0 & 0 & 0 & 0 & 1 & 0 & 0 & 0 & 1 & 0 & 2 & 3 & 2 & 1 & 0 & -2 & -1 & 0 & 2 & 1 \\
2 & 0 & 0 & -2 & -1 & -1 & -1 & -1 & -1 & 0 & 0 & 0 & 0 & 0 & 1 & 1 & 1 & 1 & 1 & 1 & 1 & -1 & -1 \\
0 & 0 & 0 & 0 & 0 & 0 & 0 & 0 & 0 & 0 & 0 & 0 & 0 & 0 & 0 & 0 & 0 & 0 & 0 & 0 & 0 & 0 & 1 \\
0 & 0 & 0 & 0 & 0 & 0 & 0 & 0 & 0 & 0 & 0 & 0 & 0 & 0 & 0 & 0 & 0 & 0 & 0 & 0 & 0 & 1 & 0 \\
0 & 0 & 0 & 0 & 0 & 0 & 0 & 0 & 0 & 0 & 0 & 0 & 0 & 0 & 0 & 0 & 0 & 0 & 0 & 0 & 1 & 0 & 0 \\
0 & 0 & 0 & 0 & 0 & 0 & 0 & 0 & 0 & 0 & 0 & 0 & 0 & 0 & 0 & 0 & 0 & 0 & 0 & 1 & 0 & 0 & 0 \\
0 & 0 & 0 & 0 & 0 & 0 & 0 & 0 & 0 & 0 & 0 & 0 & 0 & 0 & 0 & 0 & 0 & 0 & 1 & 0 & 0 & 0 & 0 \\
0 & 0 & 0 & 0 & 0 & 0 & 0 & 0 & 0 & 0 & 0 & 0 & 0 & 0 & 0 & 0 & 0 & 1 & 0 & 0 & 0 & 0 & 0 \\
0 & 0 & 0 & 0 & 0 & 0 & 0 & 0 & 0 & 0 & 0 & 0 & 0 & 0 & 0 & 0 & 1 & 0 & 0 & 0 & 0 & 0 & 0 \\
0 & 0 & 0 & 0 & 0 & 0 & 0 & 0 & 0 & 0 & 0 & 0 & 0 & 0 & 0 & 1 & 0 & 0 & 0 & 0 & 0 & 0 & 0 \\
0 & 0 & 0 & 0 & 0 & 0 & 0 & 0 & 0 & 0 & 0 & 0 & 0 & 0 & 1 & 0 & 0 & 0 & 0 & 0 & 0 & 0 & 0 \\
-4 & 0 & 0 & 0 & 0 & 0 & 0 & 0 & 0 & 0 & 0 & 0 & 0 & -1 & 0 & 0 & 0 & 0 & 0 & 0 & 0 & 0 & 0 \\
0 & 0 & 0 & 0 & 0 & 0 & 0 & 0 & 0 & 0 & 0 & 0 & 0 & 1 & 0 & 0 & 0 & 0 & 0 & 0 & 0 & 0 & 0 \\
0 & 0 & 0 & 0 & 0 & 0 & 0 & 0 & 0 & 0 & 0 & 0 & 1 & 0 & 0 & 0 & 0 & 0 & 0 & 0 & 0 & 0 & 0 \\
0 & 0 & 0 & 0 & 0 & 0 & 0 & 0 & 0 & 0 & 0 & 1 & 0 & 0 & 0 & 0 & 0 & 0 & 0 & 0 & 0 & 0 & 0 \\
0 & 0 & 0 & 0 & 0 & 0 & 0 & 0 & 0 & 0 & 1 & 0 & 0 & 0 & 0 & 0 & 0 & 0 & 0 & 0 & 0 & 0 & 0 \\
0 & 0 & 0 & 0 & 0 & 0 & 0 & 0 & 0 & 1 & 0 & 0 & 0 & 0 & 0 & 0 & 0 & 0 & 0 & 0 & 0 & 0 & 0 \\
0 & 0 & 0 & 0 & 0 & 0 & 0 & 0 & 1 & 0 & 0 & 0 & 0 & 0 & 0 & 0 & 0 & 0 & 0 & 0 & 0 & 0 & 0 \\
0 & 0 & 0 & 0 & 0 & 0 & 0 & 1 & 0 & 0 & 0 & 0 & 0 & 0 & 0 & 0 & 0 & 0 & 0 & 0 & 0 & 0 & 0 \\
0 & 0 & 0 & 0 & 0 & 0 & 1 & 0 & 0 & 0 & 0 & 0 & 0 & 0 & 0 & 0 & 0 & 0 & 0 & 0 & 0 & 0 & 0 \\
0 & 0 & 0 & 0 & 0 & 1 & 0 & 0 & 0 & 0 & 0 & 0 & 0 & 0 & 0 & 0 & 0 & 0 & 0 & 0 & 0 & 0 & 0 \\
0 & 0 & 0 & 0 & 1 & 0 & 0 & 0 & 0 & 0 & 0 & 0 & 0 & 0 & 0 & 0 & 0 & 0 & 0 & 0 & 0 & 0 & 0 \\
0 & 0 & 0 & 1 & 0 & 0 & 0 & 0 & 0 & 0 & 0 & 0 & 0 & 0 & 0 & 0 & 0 & 0 & 0 & 0 & 0 & 0 & 0 \\
0 & 0 & 1 & 0 & 0 & 0 & 0 & 0 & 0 & 0 & 0 & 0 & 0 & 0 & 0 & 0 & 0 & 0 & 0 & 0 & 0 & 0 & 0 \\
0 & 1 & 0 & 0 & 0 & 0 & 0 & 0 & 0 & 0 & 0 & 0 & 0 & 0 & 0 & 0 & 0 & 0 & 0 & 0 & 0 & 0 & 0 \\
2 & 0 & 0 & 0 & 0 & 0 & 0 & 0 & 0 & 0 & 0 & 0 & 0 & 0 & 0 & 0 & 0 & 0 & 0 & 0 & 0 & 0 & 0
\end{pmatrix}$$

Dimensions[ν]

{28, 23}

Any of these independent reactions may be displayed in a more readable form by taking the inner product of the corresponding column $\hat{\nu}_r$ with the basis vector, for which the following function is defined:

rxn[i_, ν] := ν[[All, i]].cE

The sixth reaction is used to demonstrate this function:

rxn[7, ν]

$$4\,\mathrm{CIS}_{\alpha} - \mathrm{In}_{\mathrm{Cu}}^{\mathrm{x}} - 2\,\mathcal{V}_{\mathrm{Cu}}^{\mathrm{x}} + (2\,\mathcal{V}_{\mathrm{Cu}} \oplus \mathrm{In}_{\mathrm{Cu}})_{\alpha}$$

The seventh reaction states that transfer of the three isolated point defects that comprise the NDC into the complex "cleans up" four unit cells of the chalcopyrite structure, consistent with the idea that to form the complex the point defects on the lattice must be more concentrated than if they are non-interacting.

ν0 = Transpose[NullSpace[$\mathcal{D}$0]];

MatrixForm[$\nu 0$]

$$\begin{pmatrix}
\frac{17}{2} & 0 & 0 & 3(-3+\delta) & -3 & 4 & 1 & 1 & -3 & -3 & -6 & -6 & 0 & -3 & -3 & -3 & -3 & -6 & -6 & -6 & 0 & 0 \\
-2 & -1 & 1 & 2-\delta & 1 & -2 & -2 & -1 & 0 & 0 & 0 & 1 & -2 & -4 & -3 & -2 & -1 & 2 & 1 & 0 & -2 & -1 \\
0 & 1 & -1 & 0 & 0 & 0 & 1 & 0 & 0 & 0 & 1 & 0 & 2 & 3 & 2 & 1 & 0 & -2 & -1 & 0 & 2 & 1 \\
1 & 0 & 0 & 0 & 0 & -1 & -1 & -1 & 0 & 0 & 0 & 0 & 0 & 1 & 1 & 1 & 1 & 1 & 1 & 1 & -1 & -1 \\
0 & 0 & 0 & 0 & 0 & 0 & 0 & 0 & 0 & 0 & 0 & 0 & 0 & 0 & 0 & 0 & 0 & 0 & 0 & 0 & 0 & 1 \\
0 & 0 & 0 & 0 & 0 & 0 & 0 & 0 & 0 & 0 & 0 & 0 & 0 & 0 & 0 & 0 & 0 & 0 & 0 & 0 & 1 & 0 \\
0 & 0 & 0 & 0 & 0 & 0 & 0 & 0 & 0 & 0 & 0 & 0 & 0 & 0 & 0 & 0 & 0 & 0 & 0 & 1 & 0 & 0 \\
0 & 0 & 0 & 0 & 0 & 0 & 0 & 0 & 0 & 0 & 0 & 0 & 0 & 0 & 0 & 0 & 0 & 0 & 1 & 0 & 0 & 0 \\
0 & 0 & 0 & 0 & 0 & 0 & 0 & 0 & 0 & 0 & 0 & 0 & 0 & 0 & 0 & 0 & 0 & 1 & 0 & 0 & 0 & 0 \\
0 & 0 & 0 & 0 & 0 & 0 & 0 & 0 & 0 & 0 & 0 & 0 & 0 & 0 & 0 & 0 & 1 & 0 & 0 & 0 & 0 & 0 \\
0 & 0 & 0 & 0 & 0 & 0 & 0 & 0 & 0 & 0 & 0 & 0 & 0 & 0 & 0 & 1 & 0 & 0 & 0 & 0 & 0 & 0 \\
0 & 0 & 0 & 0 & 0 & 0 & 0 & 0 & 0 & 0 & 0 & 0 & 0 & 0 & 1 & 0 & 0 & 0 & 0 & 0 & 0 & 0 \\
0 & 0 & 0 & 0 & 0 & 0 & 0 & 0 & 0 & 0 & 0 & 0 & 0 & 1 & 0 & 0 & 0 & 0 & 0 & 0 & 0 & 0 \\
-2 & 0 & 0 & 1 & 0 & 0 & 0 & 0 & 0 & 0 & 0 & 0 & -1 & 0 & 0 & 0 & 0 & 0 & 0 & 0 & 0 & 0 \\
0 & 0 & 0 & 0 & 0 & 0 & 0 & 0 & 0 & 0 & 0 & 0 & 1 & 0 & 0 & 0 & 0 & 0 & 0 & 0 & 0 & 0 \\
0 & 0 & 0 & 0 & 0 & 0 & 0 & 0 & 0 & 0 & 0 & 1 & 0 & 0 & 0 & 0 & 0 & 0 & 0 & 0 & 0 & 0 \\
0 & 0 & 0 & 0 & 0 & 0 & 0 & 0 & 0 & 0 & 1 & 0 & 0 & 0 & 0 & 0 & 0 & 0 & 0 & 0 & 0 & 0 \\
0 & 0 & 0 & 0 & 0 & 0 & 0 & 0 & 0 & 1 & 0 & 0 & 0 & 0 & 0 & 0 & 0 & 0 & 0 & 0 & 0 & 0 \\
0 & 0 & 0 & 0 & 0 & 0 & 0 & 0 & 1 & 0 & 0 & 0 & 0 & 0 & 0 & 0 & 0 & 0 & 0 & 0 & 0 & 0 \\
0 & 0 & 0 & 0 & 0 & 0 & 0 & 1 & 0 & 0 & 0 & 0 & 0 & 0 & 0 & 0 & 0 & 0 & 0 & 0 & 0 & 0 \\
0 & 0 & 0 & 0 & 0 & 0 & 1 & 0 & 0 & 0 & 0 & 0 & 0 & 0 & 0 & 0 & 0 & 0 & 0 & 0 & 0 & 0 \\
0 & 0 & 0 & 0 & 0 & 1 & 0 & 0 & 0 & 0 & 0 & 0 & 0 & 0 & 0 & 0 & 0 & 0 & 0 & 0 & 0 & 0 \\
0 & 0 & 0 & 0 & 1 & 0 & 0 & 0 & 0 & 0 & 0 & 0 & 0 & 0 & 0 & 0 & 0 & 0 & 0 & 0 & 0 & 0 \\
0 & 0 & 0 & 1 & 0 & 0 & 0 & 0 & 0 & 0 & 0 & 0 & 0 & 0 & 0 & 0 & 0 & 0 & 0 & 0 & 0 & 0 \\
0 & 0 & 1 & 0 & 0 & 0 & 0 & 0 & 0 & 0 & 0 & 0 & 0 & 0 & 0 & 0 & 0 & 0 & 0 & 0 & 0 & 0 \\
0 & 1 & 0 & 0 & 0 & 0 & 0 & 0 & 0 & 0 & 0 & 0 & 0 & 0 & 0 & 0 & 0 & 0 & 0 & 0 & 0 & 0 \\
1 & 0 & 0 & 0 & 0 & 0 & 0 & 0 & 0 & 0 & 0 & 0 & 0 & 0 & 0 & 0 & 0 & 0 & 0 & 0 & 0 & 0
\end{pmatrix}$$

Dimensions[$\nu 0$]

{27, 22}

The function "rxn" is extended to use the appropriate basis (**cE0**) for the reactions in ***ν*0**:

rxn[i_, $\nu 0$] := $\nu 0$[[All, i]].cE0

The thirteenth reaction is used to demonstrate this function:

rxn[13, $\nu 0$]

$$-2\,\mathcal{V}_{Cu}^{x} - \mathcal{V}_{Se}^{x} + \mathcal{V}_{Se}^{\bullet\bullet} + 2\,\mathcal{V}_{Cu}'$$

The thirteenth reaction shows that ionization of a selenium vacancy results in the ionization of two copper vacancies, without creation of any free carriers; it is an explicit example of charge exchange compensation. All of these formulas will be discussed in the results section after their equilibrium extents and stoichiometry dependence thereof are computed.

Each of the 22 column vectors $\hat{\nu_r}$ in the reduced stoichiometric reaction matrix has elements ν_{jr} which are the number of moles of species j involved in the independent reaction r (the ordering of the basis for the rows $\hat{\nu_j}$ remains the same as it is for the columns of the species formula matrix $\mathcal{D}$). Each of these independent reactions must be in equilibrium for the entire system to be in equilibrium. The mathematical formulation for these 22 equilibria in terms of the partial molar Gibbs energy $\overline{\mathcal{G}}_j$ for each species is given by the Gibbs–Duhem equation: $\sum_{j=1}^{27} \nu_{\mathrm{jr}}\, \overline{\mathcal{G}}_j = 0$. There are, however only 22 equations here and 27 unknowns (the number of each species in equilibrium, N_j). The remaining 5 equations are provided by the original conservation equations which were eliminated by transforming from the $\mathcal{D}$ matrix to the ν matrix and are $\sum_{j=1}^{27} \mathcal{D}_{ij}\, \mathrm{N}_j = \mathcal{N}_i^0$ (i=1,...,4), and for the lattice site numbers $\mathcal{N}_5^0 = \mathrm{N}_0$, $\mathcal{N}_6^0 = \mathrm{N}_0$, $\mathcal{N}_7^0 = 2\,\mathrm{N}_0$, and $\mathcal{N}_8^0 = 4\,\mathrm{N}_0$, so the conserved quantity N_0 can be calculated from any one of these. These conservation equations are easily converted to an intensive quantity based on a total of one mole of the quasimolecular species as derived previously: $\mathrm{M}=1 \Rightarrow \mathrm{N}_j = \|\mathrm{N}_j\| * \mathrm{N}_{\mathrm{Avo}}$. Dividing both sides of the conservation equation by $\mathrm{N}_{\mathrm{Avo}}$ and defining the building unit molar concentration vector **c** with respect to the basis **cE** as $\mathrm{c_j} = \|\mathrm{N}_j\|$, the set of equations $\sum_{j=1}^{27} \mathcal{D}_{ij}\, \mathrm{c}_j = \mathcal{N}_i^0 * (\mathrm{N_{Avo}})^{-1}$ is

derived, where the right hand side is the initial number of moles of the conserved quantity with index *i* in a mole of the quasimolecule.

Conservation of these five quantities and the simultaneous solution of the Gibbs-Duhem equations can be handled in a computationally efficient manner by introducing the extent of reaction variable ξ_r for each independent reaction *r*. Then the final mole fraction of each species *j* (since the total number of moles of the quasimolecule is M=1, a constant) is given by $c_j = c_j^0 + \sum_{r=1}^{22} \nu_{jr}\, \xi_r$ (where $0 \le \xi_r \le 1$). These 27 equations implicitly include the five conservation equations *via* the stoichiometry matrix *ν*, and may be combined with the 22 independent reaction equilibria equations to provide 22 relations between the 22 extents of reactions. This is accomplished by writing the partial molar Gibbs energy (the chemical potential) for each species as: $\mu_j \doteq \overline{\mathcal{G}}_j = \overline{\mathcal{G}}_j^0 + \mathrm{RT}\log[a_j] \simeq \overline{\mu}_j^0 + \mathrm{RT}\,\mathrm{Log}[c_j]$, where c_j is the mole fraction of the "j^{th}" species [15, §11.4]. Substituting this relation into the Gibbs-Duhem equation yields:

$$\sum_{j=1}^{27} \nu_{\mathrm{jr}} \left(\overline{\mu}_j^0 + \mathrm{R\,T\,Log}\left[\, c_j^0 + \sum_{r=1}^{22} \nu_{jr}\, \xi_r \right]\right) = 0.$$

This is the system of 22 simultaneous equations that must be solved to determine the equilibrium reaction extent vector $\boldsymbol{\xi}$, and therefrom the extent of phase segregation and equilibrium concentrations of defects.

Boundary Conditions

The most important information required to complete this calculation is to select the boundary conditions that will be employed to calculate the reference state chemical potential for the various building units μ_j^0. As discussed in the preceding

literature review, the structure of the relatively indium-rich CIS β–phase is controversial and there is little agreement on the phase boundary between it and α–CIS. Also, recent results [27] suggest that the composition of the CIS α–phase in equilibrium with the non-stoichiometric compound $Cu_{2-\delta}Se$ at STP is itself non-stoichiometric.

The most reliable invariant data for the ternary phase field is probably the eutectoid decomposition of the δ–CIS high-temperature sphalerite disordered phase. A recent study using the solid electrolyte EMF technique [173] includes a review of the various studies thereof. There is good agreement among these studies that the α–CIS phase in equilibrium with β–$Cu_{2-\delta}Se$ at the eutectoid temperature of 1025-1083K is stoichiometric (*i.e.*: δ=0). Furthermore, the binary Cu–Se phase diagram has been recently assessed [176], so consistent analytical expressions for the Gibbs energy of the binary Cu–Se compounds are available as functions of both temperature and composition. A reference temperature of 1048.15K is chosen near this critical point as the upper temperature limit, and the lower limit is taken to be the temperature at STP. Ternary equilibrium calculations will be restricted to temperatures less than the eutectoid decomposition of the indium-rich δ–CIS phase at 600°C.

```
tSTP = 298.15;
tRef = tSTP + 750
tMaxαβ = tSTP + 575

      1048.15
      873.15
```

Therefore the Gibbs-Duhem equations are first solved for the two-phase $Cu_{2-\delta}Se/\alpha$–$CuInSe_2$ equilibrium phase boundary using the stoichiometry matrix $\nu 0$ and corresponding state vectors. The resulting state vectors and thermodynamic potential functions define the boundary conditions for the solution of the α–CIS single phase and CIS α–β two phase equilibrium defect structure as a function of the state variables T, X, and to a limited extent Z, with P constant.

Thermodynamic Functions

The thermodynamic energy functions for each compound at its reference state (stoichiometric) composition are calculated as the inner product of a list of the coefficients for each compound and another list containing polynomial and transcendental functions of the temperature which are the same for all compounds.

```
Off[General::spell] ⋀ Off[General::spell1];

(*Avogadro' s number in units Mole^-1 *)nAvo = First[AvogadroConstant]

    6.02214 × 10^23

(*the molar gas constant in units Joules.Mole^-1.Kelvin^-1 *)rG = 8.314472145136097`;

(*the molar gas constant value built into
    Mathematica is not used because of an internal inconsistency. *)
First[MolarGasConstant] – First[AvogadroConstant] * First[BoltzmannConstant]
rG – First[AvogadroConstant] * First[BoltzmannConstant]

    −1.45136 × 10^-7
    0.

g_HSER[cThermo_, tK_] :=
  cThermo.{1, tK, tK Log[tK], tK^2, tK^-1, tK^3, tK^4, √tK, tK^7, tK^-9}
```

```
s_entropy[cThermo_, tK_] := cThermo.
    {0, -1, -1 - Log[tK], -2 tK, tK^-2, -3 tK^2, -4 tK^3, -1 / (2 Sqrt[tK]), -7 tK^6, 9 tK^-10}

h_HSER[cThermo_, tK_] :=
  cThermo.{1, 0, -tK, -tK^2, 2 tK^-1, -2 tK^3, -3 tK^4, Sqrt[tK] / 2, -6 tK^7, 10 tK^-9}

cP[cThermo_, tK_] := cThermo.
    {0, 0, -1, -2 * tK, -2 * tK^-2, -6 * tK^2, -12 * tK^3, 1 / (4 * Sqrt[tK]), -42 tK^6, -90 * tK^-10}

identity10 = Array[1 &, 10](*test value for cThermo*)
    {1, 1, 1, 1, 1, 1, 1, 1, 1, 1}

(*verify G=H-TS*)g_HSER[identity10, tK] -
    h_HSER[identity10, tK] + tK * s_entropy[identity10, tK] // Simplify
    0

(*verify ∂G/∂T =-S*)∂tK g_HSER[identity10, tK] === -s_entropy[identity10, tK]
    True

(*verify cP = ∂H/∂T *)∂tK h_HSER[identity10, tK] === cP[identity10, tK]
    True

Clear[identity10]
```

The thermodynamic coefficients for solid elemental copper [165], indium [165], and selenium [167] are:

```
cThermo_Cu[tK_] /; 1357.7 ≥ tK ≥ tSTP := {-7770.45775, 130.485222,
    -24.11239, -2.65684 * 10^-3, 0.0524778 * 10^6, 0.129222833 * 10^-6, 0, 0, 0, 0}
```

```
(*solid hexagonal @ STP, superheated solid @ tK>429.75*)
cThermo_In[tK_] /; tK ≥ tSTP ⋀ tK ≤ 429.75 := {−6978.89, 92.3338115,
    −21.8386, −5.72566 * 10^−3, −22906, −2.120321 * 10^−6, 0, 0, 0, 0}
cThermo_In[tK_] /; tK ≥ 429.75 ⋀ tK ≤ 3800 := {−7033.516, 124.476588,
    −27.4562, −0.54607 * 10^−3, −211708, −0.08367 * 10^−6, 0, 0, 0, 3.53 * 10^22}

(*superheated solid for tK>494.3*)cThermo_Se[tK_] /; 760 > tK ≥ tSTP :=
  {−6657, 92.53969, −19.14, −12.295 * 10^−3, 0, 2.677 * 10^−6, 0, 0, 0, 0}
cThermo_Se[tK_] /; 1200 ≥ tK ≥ 760 := {−9059.17, 150.33422, −28.552, 0, 0, 0, 0, 0, 0, 0}
```

Finally, a 3-element vector that will be used for computations is constructed of these three coefficient lists. Note that the ordering of these is the same as the first three elements in the vector "**a**" that specifies the conserved quantities.

```
a_thermo[tK_] := {cThermo_Cu[tK], cThermo_In[tK], cThermo_Se[tK]}
```

Compounds

Binary copper selenides

First the thermodynamic coefficients for the two phases (α and β) of $Cu_{2-\delta}Se$ [160] found in equilibrium with α–$CuInSe_2$ [27] are given. The self-consistent critical temperature for the $\alpha \rightarrow \beta$ binary phase transformation is also calculated.

```
tCrit_α2β2 = 395.000442936354;

cThermo_Cu2Se_α[tK_] /; tCrit_α2β2 ≥ tK ≥ tSTP :=
  {−80217.34, 288.16728, −59.0572, −37.5096 * 10^−3, 0, 0, 0, 0, 0, 0}
cThermo_Cu2Se_α[tK_] /; 1373 ≥ tK > tCrit_α2β2 :=
  {−98588.35, 664.34671, −120.0866, 37.85 * 10^−3, 1019900, −6.9635 * 10^−6, 0, 0, 0, 0}

cThermo_Cu2Se_β[tK_] /; tK ≥ tSTP :=
  cThermo_Cu2Se_α[tK] + {6830, −17.29114, 0, 0, 0, 0, 0, 0, 0, 0}
```

The composition dependence of the Gibbs energy of the two phases (α and β) of $Cu_{2-\delta}Se$ have been assessed on the basis of a triple sublattice model described as $(Cu, Va)_1 (Se, Va)_1 (Cu)_1$, where the subscript denotes the multiplicity of (in Kröger's notation) the M1, X, and M2 sublattices. The optimized parameters in the resulting analytical description are [176]:

```
G0α101[tK_] := 50000 + 2 g_HSER[cThermo_Cu[tK], tK]
G0α001[tK_] := 90000 + g_HSER[cThermo_Cu[tK], tK]
G0α011[tK_] :=
  40000 + g_HSER[cThermo_Cu2Se_α[tK], tK] – g_HSER[cThermo_Cu[tK], tK]
L0αi101 = 20000;
L0α10i1[tK_] := 11180 + 10 tK
L1α10i1 = −56789;

G0β101[tK_] := 50000 + 2 g_HSER[cThermo_Cu[tK], tK]
G0β001[tK_] := 80000 + 36 tK + g_HSER[cThermo_Cu[tK], tK]
G0β011[tK_] :=
  30000 + 36 tK + g_HSER[cThermo_Cu2Se_β[tK], tK] – g_HSER[cThermo_Cu[tK], tK]
L0βi101 = 20000;
L0β10i1[tK_] := −32004 + 14.0367 tK
L1β10i1[tK_] := −19864 + 11.2002 tK
```

The third (M2) sublattice in this model [176] is always completely filled with copper, and since only two species are found on each of the other two sublattices, only two parameters are required to define the state of the entire lattice. These are the lattice site occupation probability for copper on the first sublattice $\langle Cu\rangle_{M1}^{Cu2Se}$, and the lattice site occupation probability for selenium on the second sublattice $\langle Se\rangle_{X}^{Cu2Se}$. For the following calculations define y1=$\langle Cu\rangle_{M1}^{Cu2Se}$ and y2=$\langle Se\rangle_{X}^{Cu2Se}$. Thus $\langle Va\rangle_{M1}^{Cu2Se}$=1-y1 and $\langle Va\rangle_{X}^{Cu2Se}$=1-y2. The full Gibbs energy expressions in terms of y1 and y2 as given in [176] are:

```
G0α[tK_, y1_, y2_] := y1 y2 g_HSER[cThermo_Cu2Se_α[tK], tK] +
    y1 (1 − y2) G0α101[tK] + (1 − y1) y2 G0α011[tK] + (1 − y1) (1 − y2) G0α001[tK]

G_idl_α[tK_, y1_, y2_] :=
  rG tK (y1 Log[y1] + (1 − y1) Log[1 − y1] + y2 Log[y2] + (1 − y2) Log[1 − y2])
    (*/;1>y1>0/\1>y2>0*)

G_xs_α[tK_, y1_, y2_] := y1 (1 − y1) (y2 (L0α10i1[tK] + (2 y1 − 1) L1α10i1) +
          (1 − y2) (L0α10i1[tK] + (2 y1 − 1) L1α10i1)) +
    y2 (1 − y2) (y1 L0αi101 + (1 − y1) L0αi101)

G_Cu2Se_α[tK_, y1_, y2_] := G0α[tK, y1, y2] + G_idl_α[tK, y1, y2] + G_xs_α[tK, y1, y2]

G0β[tK_, y1_, y2_] := y1 y2 g_HSER[cThermo_Cu2Se_β[tK], tK] +
    y1 (1 − y2) G0β101[tK] + (1 − y1) y2 G0β011[tK] + (1 − y1) (1 − y2) G0β001[tK]

G_idl_β[tK_, y1_, y2_] :=
  rG tK (y1 Log[y1] + (1 − y1) Log[1 − y1] + y2 Log[y2] + (1 − y2) Log[1 − y2])
    (*/;1>y1>0/\1>y2>0*)

G_xs_β[tK_, y1_, y2_] := y1 (1 − y1) (y2 (L0β10i1[tK] + (2 y1 − 1) L1β10i1[tK]) +
          (1 − y2) (L0β10i1[tK] + (2 y1 − 1) L1β10i1[tK])) +
    y2 (1 − y2) (y1 L0βi101 + (1 − y1) L0βi101)
```

G_Cu2Se_β[tK_, y1_, y2_] := G0β[tK, y1, y2] + G_idl_β[tK, y1, y2] + G_xs_β[tK, y1, y2]

The calculated equilibrium specific molar values of selenium vacancy concentration (1–y2) predicted by this model [176] vary from 2.07×10^{-17} to 2.23×10^{-4}. These values are quite small compared to the variation in equilibrium values of y1. This could be approximated as zero, but the result would be divergence of the ideal mixing entropy due to the logarithmic singularity in the term (1– y2)×Log[1– y2]. Instead, it is set to 1×10^{-6} based on its nominal calculated values in the range of 800-400K.

y2 = 1 – 10^−6;

As for the case of CIS, these lattice site occupation variables y1 and y2 must be related to the overall composition of the compound $Cu_{2-\delta}Se$. The value of δ in the formula $Cu_{2-\delta}Se$ is given by the solution of $Cu_{1+y1}Se_{y2} = Cu_{2-\delta}Se$, or 2-$\delta = \frac{1+y1}{y2} \Rightarrow \delta = 2\text{-}\frac{1+y1}{y2}$. In this approximation $\delta \simeq$1-y1. Inverting the definition of the binary mole fraction variable x_Se = $\frac{y2}{1+y1+y2}$ gives:

$$y1[x\_Se\_] := \frac{y2\,(1 - x\_Se) - x\_Se}{x\_Se}$$

(* /; $\frac{1}{3} \le$ x_Se ≤ (temperature−dependent upper limit) *)

This verifies the calculated self-consistent peritectoid temperature:

G_Cu2Se_α[tK, y1[x_Se], y2] – G_Cu2Se_β[tK, y1[x_Se], y2] /.
Thread[{tK, x_Se} → {tCrit_α2β2, 1 / 3}]

$$-1.54909\times10^{-12}$$

Finally, note that in [27] it has been found that α-$CuInSe_2$ is in equilibrium with α-$Cu_{2-\delta}Se$ at room temperature and with β-$Cu_{2-\delta}Se$ at high temperature, with a transition detected by DTA between these two structures in equilibrium with α-$CuInSe_2$ at 143°C≃416K. There is an apparent inconsistency in that reported value in their discussion and the data in Figure 1 of their paper (which is lower). Another study [277] found this transition at 134°C≃405K so the value of the transition is set for these calculations at the calculated self-consistent critical point temperature, corresponding nearly to the assessed Cu/α-$Cu_{2-\delta}Se$/β-$Cu_{2-\delta}Se$ peritectoid critical point temperature of 396K. The eutectoid decomposition of β-$Cu_{2-\delta}Se$ into α-$Cu_{2-\delta}Se$ and Cu_3Se_2 at the assessed temperature [176] of 291K is included approximately by definition of a two-phase region. A single piece-wise continuous analytic function is thus defined for the computation of the Gibbs energy and partial molar properties of $Cu_{2-\delta}Se$ for all its allowable compositions and the entire temperature range between STP and the melting point of $Cu_{2-\delta}Se$, 298.15K ≤ T ≤ 1357.7K.

The Gibbs energies were derived above for $(Cu, Va)_1 (Se, Va)_1 (Cu)_1$, which contains y1+y2+1 moles of atoms. Inverting the definition of x_Se provides the required normalization:

$$x\_Se = \frac{y2}{1+y1+y2} \Rightarrow \frac{1}{1+y1+y2} = \frac{x\_Se}{y2}$$

The Gibbs energy per mole of $Cu_{1-x}Se_x$ based on the binary mole fractions of Cu (= 1– x_Se) and Se, is $\overline{\mathcal{G}}[T,x_{Se}]$ as given by the following function:

$$\text{G\_CuSeX[tK\_, x\_Se\_] /; (tSTP} - 7) \le \text{tK} < \text{tCrit\_}\alpha 2\beta 2 \bigwedge 0.346 < \text{x\_Se} \le 0.360 :=$$

$$\text{With}\left[\left\{x\beta\text{Min} = 0.360 - (0.360 - 0.346)\,\frac{\text{tK} - (\text{tSTP} - 7)}{\text{tCrit\_}\alpha 2\beta 2 - (\text{tSTP} - 7)},\right.\right.$$

$$\left.\mu\alpha = \frac{\text{x\_Se}}{\text{y2}} * \text{G\_Cu2Se\_}\alpha[\text{tK, y1[x\_Se], y2}],\ \mu\beta = \frac{\text{x\_Se}}{\text{y2}} * \text{G\_Cu2Se\_}\beta[\text{tK, y1[x\_Se], y2}]\right\},$$

$$\left(\text{UnitStep}[x\beta\text{Min} - \text{x\_Se}]\left(\frac{\mu\alpha\,(x\beta\text{Min} - \text{x\_Se}) + \mu\beta\,(\text{x\_Se} - 0.346)}{x\beta\text{Min} - 0.346}\right)\right) +$$

$$\left.(\text{UnitStep}[\text{x\_Se} - x\beta\text{Min}]\,\mu\beta)\right]$$

$$\text{G\_CuSeX[tK\_, x\_Se\_] /; tSTP} \le \text{tK} < \text{tCrit\_}\alpha 2\beta 2 \bigwedge 0.360 < \text{x\_Se} :=$$

$$\frac{\text{x\_Se}}{\text{y2}} * \text{G\_Cu2Se\_}\beta[\text{tK, y1[x\_Se], y2}]$$

$$\text{G\_CuSeX[tK\_, x\_Se\_] /; (tSTP} - 7) \le \text{tK} < \text{tCrit\_}\alpha 2\beta 2 :=$$

$$\frac{\text{x\_Se}}{\text{y2}} * \text{G\_Cu2Se\_}\alpha[\text{tK, y1[x\_Se], y2}]$$

$$\text{G\_CuSeX[tK\_, x\_Se\_] /; tCrit\_}\alpha 2\beta 2 \le \text{tK} \le \text{tMax}\alpha\beta := \frac{\text{x\_Se}}{\text{y2}} * \text{G\_Cu2Se\_}\beta[\text{tK, y1[x\_Se], y2}]$$

$$\text{G\_CuSeX[tK\_, x\_Se\_] /; tMax}\alpha\beta < \text{tK} \le 1357.7 := \frac{\text{x\_Se}}{\text{y2}} * \text{G\_Cu2Se\_}\beta[\text{tK, y1[x\_Se], y2}]$$

Boundary conditions for the solution of the ternary phase diagram based on its building unit model will be provided by this Gibbs energy function for the two binary $Cu_{2-\delta}Se$ compound components in that model whose molar concentrations enter into the Gibbs-Duhem equation, $\|Cu_{Cu2Se}\|$ and $\|Cu2\_\delta Se\|$, solved self-consistently to determine the $Cu_{2-\delta}Se/\alpha$–$CuInSe_2$ two-phase equilibrium boundary composition as a function of temperature. To do this it is useful to explicitly determine the partial molar Gibbs energy $\overline{\mathcal{G}}_j = \overline{\mathcal{G}}_j^0 + \text{RT Log}[\gamma_j c_j]$ for Cu_{Cu2Se}. The partial molar Gibbs energies for Cu and Se in $Cu_{1-x}Se_x$ are given by [158, §8.2]:

$$\overline{\mathcal{G}}_{Cu} = \overline{\mathcal{G}}[\text{T}, x_{Se}] - \text{x\_Se} \times \frac{\partial\,\overline{\mathcal{G}}[T, x_{Se}]}{\partial\,\text{x\_Se}},\ \text{and}$$

$$\overline{\mathcal{G}}_{Se} = \overline{\mathcal{G}}[\text{T}, x_{Se}] - (1 - \text{x\_Se})\,\frac{\partial\,\overline{\mathcal{G}}[T, x_{Se}]}{\partial\,\text{x\_Se}} = \overline{\mathcal{G}}[\text{T}, x_{Se}] + (1 - \text{x\_Se})\,\frac{\partial\,\overline{\mathcal{G}}[T, x_{Se}]}{\partial\,\text{x\_Se}} = \overline{\mathcal{G}}_{Cu} + \frac{\partial\,\overline{\mathcal{G}}[T, x_{Se}]}{\partial\,\text{x\_Se}}.$$

Note that $x\_Se \times \overline{\mathcal{G}}_{Se} + (1-x\_Se) \times \overline{\mathcal{G}}_{Cu} = \overline{\mathcal{G}}[T, x_{Se}]$ as required by the definition of a partial molar quantity in a binary system. The derivative $\frac{\partial \overline{\mathcal{G}}[T, x_{Se}]}{\partial x\_Se}$ can be further simplified by substituting from the functional definition of $\overline{\mathcal{G}}[T, x_{Se}] = x\_Se \times G\_Cu2Se\_\alpha\beta \times y2^{-1}$, and using the chain rule to give:

$$\frac{\partial \overline{\mathcal{G}}[T, x_{Se}]}{\partial x\_Se} = (G\_Cu2Se\_\alpha\beta + x\_Se \times \frac{\partial \overline{\mathcal{G}}[T, x_{Se}]}{\partial x\_Se}) \times y2^{-1}$$

$$\Rightarrow \overline{\mathcal{G}}_{Cu} = \overline{\mathcal{G}}[T, x_{Se}] - x\_Se \times \frac{\partial \overline{\mathcal{G}}[T, x_{Se}]}{\partial x\_Se} = -x\_Se^2 \times \frac{\partial \overline{\mathcal{G}}[T, x_{Se}]}{\partial x\_Se} \times y2^{-1}$$

$$\Rightarrow \overline{\mathcal{G}}_{Se} = \overline{\mathcal{G}}^0_{Cu} + \frac{\partial \overline{\mathcal{G}}[T, x_{Se}]}{\partial x\_Se} = (G\_Cu2Se\_\alpha\beta + (x \ (1-x) \times \frac{\partial \overline{\mathcal{G}}[T, x_{Se}]}{\partial x\_Se})) \times y2^{-1}$$

Since the defining expressions for G_Cu2Se_α and G_Cu2Se_β are in terms of the variable y1, they are most efficiently calculated using the chain rule again, giving $\frac{\partial G\_Cu2Se\_\alpha\beta}{\partial x\_Se} = \frac{\partial G\_Cu2Se\_\alpha\beta}{\partial y1} \times \frac{\partial y1}{\partial x\_Se}$. Combining these expressions to compute, the partial molar quantities are given by:

```
G_Cu_CuSeX[tK_, x_Se_] /; tSTP ≤ tK < tCrit_α2β2 :=
  −x_Se^2 ∗ ∂_y G_Cu2Se_α[tK, y, y2] ∗ ∂_x y1[x] ∗ y2^−1 /.
    Thread[{x, y} :→ {x_Se, y1[x_Se]}](∗⋀ x0_Se≤x_Se<0.346∗)
G_Cu_CuSeX[tK_, x_Se_] /; tCrit_α2β2 ≤ tK ≤ 1357.7 :=
  −x_Se^2 ∗ ∂_y G_Cu2Se_β[tK, y, y2] ∗ ∂_x y1[x] ∗ y2^−1 /.
    Thread[{x, y} :→ {x_Se, y1[x_Se]}](∗⋀ x0_Se≤x_Se<0.368∗)
G_Se_CuSeX[tK_, x_Se_] /; tSTP ≤ tK < tCrit_α2β2 :=
  (G_Cu2Se_α[tK, y1[x_Se], y2] + x_Se (1 − x_Se) ∗ ∂_y G_Cu2Se_α[tK, y, y2] ∗ ∂_x y1[x])
      y2^−1 /. Thread[{x, y} :→ {x_Se, y1[x_Se]}](∗⋀ x0_Se≤x_Se<0.346∗)
G_Se_CuSeX[tK_, x_Se_] /; tCrit_α2β2 ≤ tK ≤ 1357.7 :=
  (G_Cu2Se_β[tK, y1[x_Se], y2] + x_Se (1 − x_Se) ∗ ∂_y G_Cu2Se_β[tK, y, y2] ∗ ∂_x y1[x])
      y2^−1 /. Thread[{x, y} :→ {x_Se, y1[x_Se]}](∗⋀ x0_Se≤x_Se<0.368∗)
```

Although explicit upper limits on the range of compositional applicability of these functions have not been included in their definition, a two-phase region is present in the phase field above the upper limit of selenium that defines the single-

phase stability range of the non-stoichiometric compound $Cu_{2-\delta}Se$. Over the entire temperature range, this boundary is defined by the equilibrium between $Cu_{2-\delta}Se$ and a number of different phases. Rather than solve all these equilibria explicitly here, published solution values [176] for the relevant critical points are used to define a function which returns the approximate upper limits over the temperature range of the calculations for the α-CIS/$Cu_{2-\delta}Se$ equilibrium, the goal of these auxillary derivations.

$$\text{xMax\_Cu2Se[tK\_] /; tSTP} \le \text{tK} < 385 := 0.360 + (0.365 - 0.360)\,\frac{\text{tK} - (\text{tSTP} - 7)}{385 - (\text{tSTP} - 7)}$$

$$\text{xMax\_Cu2Se[tK\_] /; } 385 \le \text{tK} < 650 := 0.365 + (0.368 - 0.365)\,\frac{\text{tK} - 385}{650 - 385}$$

$$\text{xMax\_Cu2Se[tK\_] /; } 650 \le \text{tK} < 796 := 0.368 + (0.364 - 0.368)\,\frac{\text{tK} - 650}{796 - 650}$$

$$\text{xMax\_Cu2Se[tK\_] /; } 796 \le \text{tK} \le \text{tMax}\alpha\beta := 0.364 + (0.360 - 0.364)\,\frac{\text{tK} - 796}{\text{tMax}\alpha\beta - 796}$$

Over the entire temperature range of interest, the β–$Cu_{2-\delta}Se$ binary copper selenide's copper-rich single-phase domain boundary is determined by its equilibrium with *fcc* Cu with a finite solubility of selenium [176]. Thus perfectly stoichiometric Cu_2Se is not stable to decomposition in the binary model, and the $Cu_{2-\delta}Se$ binary-ternary equilibrium composition is limited by the minimum value of x_Se (*i.e.*: the maximum self-consistent copper composition) for which the copper partial molar Gibbs free energy (its chemical potential) is zero. A function that solves for the value of the minimum selenium content of the β–$Cu_{2-\delta}Se$ phase as a function of temperature is defined as:

```
xMin_Cu2Se[tK_?NumericQ] /; tSTP ≤ tK ≤ 1357.7 :=
  x_Se /. FindRoot[G_Cu_CuSeX[#, x_Se] == 0, {x_Se, 1/3}] &[tK]

ParametricPlot[{Evaluate[(xMin_Cu2Se[T] – 1/3) 1*^6], T},
  {T, tSTP, tRef}, AxesLabel –> {"[ppm]", "T [K]"},
  PlotLabel → "Cu2–δSe Minimum Selenium Content: Deviation from 1/3"]
```

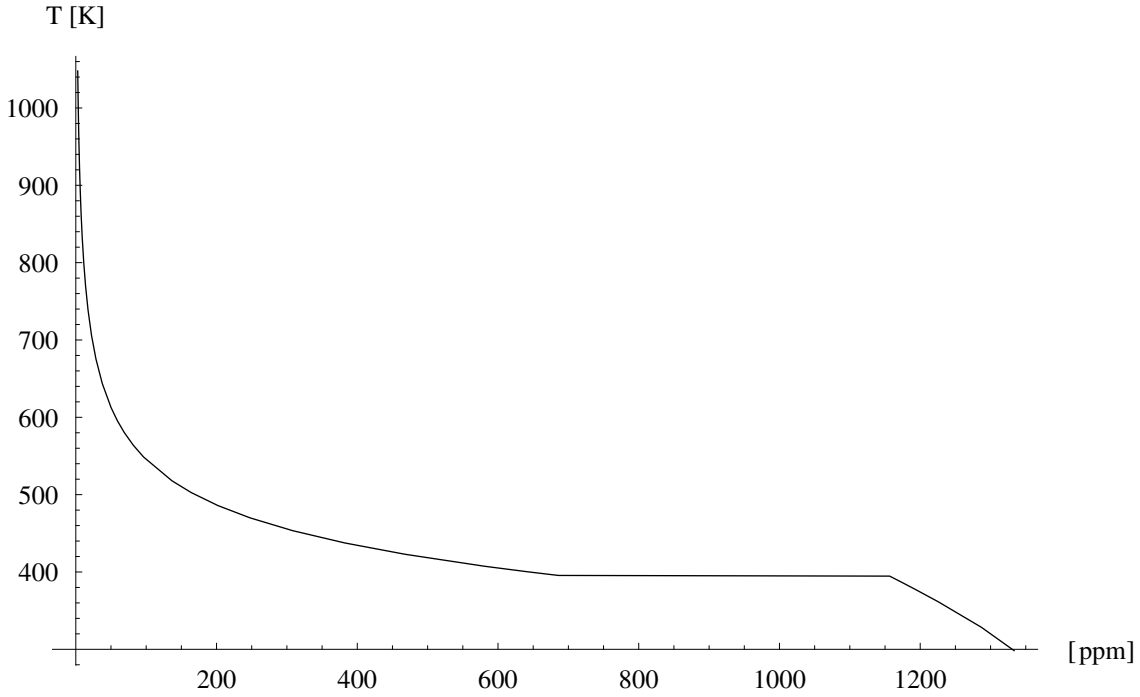

Figure A.1 Temperature dependence of the deviation from one-third of the minimum stable excess selenium content of $Cu_{2-\delta}Se$ sufficient to inhibit metallic copper phase segregation

```
(*  confirm the Cu2Se partial molar sum relation*)
x_Se × G_Se_CuSeX[tK, x_Se] + (1 – x_Se) × G_Cu_CuSeX[tK, x_Se] – G_CuSeX[tK, x_Se] /.
  Thread[{tK, x_Se} → {tRef, xMin_Cu2Se[tRef]}]

    0.
```

The foregoing development of mathematical expressions describing the energetic properties of binary copper selenide have been defined in terms of the binary mole fraction phase composition formula $Cu_{1-x}Se_x$. Subsequent interphase reactions will be analyzed in terms of the secondary phase compound's formula

$Cu_{2-\delta}Se$. For any given value of x_Se for the binary $Cu_{1-x}Se_x$ phase, the corresponding $Cu_{2-\delta}Se$ stoichiometry deviation parameter δ is determined:

```
formula[24, 𝒟0]
```

```
{Cu2_δSe, Se + Cu (2 − δ)}
```

```
part2ndΦ[𝒟0]
```

```
{{1, 2 − δ}, {0, 0}, {0, 1}, {0, 0}, {0, 0}, {0, 0}, {0, 0}, {0, 0}}
```

```
(2 − part2ndΦ[𝒟0][[1, 2]]) // Simplify
```

```
δ
```

```
formula[24, 𝒟0]
{formula[24, 𝒟0][[2, 1]] / (formula[24, 𝒟0][[2, 1]] + formula[24, 𝒟0][[2, 2]]),
    part2ndΦ[𝒟0][[3, 2]] / (part2ndΦ[𝒟0][[3, 2]] + part2ndΦ[𝒟0][[1, 2]])} // Simplify
```

```
{Cu2_δSe, Se + Cu (2 − δ)}
```

$$\left\{\frac{Se}{2\,Cu + Se - Cu\,\delta},\ \frac{1}{3-\delta}\right\}$$

The mole fraction of selenium in the secondary phase, x_Se is equivalent to $(3-\delta)^{-1}$. Whenever x_Se for the secondary $Cu_{1-x}Se_x$ phase assumes its minimum stable value, the excess copper segregation due to Cu_{Cu2Se} is zero and the corresponding $Cu_{2-\delta}Se$ stoichiometry deviation δ is given by:

```
{Solve[x == 1/(3 − δ), δ]}
```

$$\left\{\left\{\left\{\delta \to \frac{-1+3x}{x}\right\}\right\}\right\}$$

```
δmin[tK_?NumericQ] := With[{x_Se = xMin_Cu2Se[tK]}, (−1 + 3 x_Se)/x_Se]
```

```
{xMin_Cu2Se[tRef], δmin[tRef],
  {"numerical error", 1/(1 + 2 − δmin[tRef]) − xMin_Cu2Se[tRef]}}
```

{0.333336, 0.0000245812, {numerical error, 0.}}

Similarly, whenever x_Se for the secondary $Cu_{1-x}\,Se_x$ phase assumes its maximum stable value, the corresponding $Cu_{2-\delta}\,Se$ stoichiometry deviation δ is given by:

```
δmax[tK_?NumericQ] := With[{x_Se = xMax_Cu2Se[tK]}, (−1 + 3 x_Se)/x_Se]
```

```
{xMax_Cu2Se[tMaxαβ], δmax[tMaxαβ],
  {"numerical error", 1/(1 + 2 − δmax[tMaxαβ]) − xMax_Cu2Se[tMaxαβ]}}
```

{0.36, 0.222222, {numerical error, 0.}}

The minimum stable composition is nearly stoichiometric $Cu_2\,Se$ at high temperature, reflecting the limited solubility of Se in *fcc* Cu (about 3 *ppm* at this temperature). The reference state total Gibbs energy, $\overline{\mathcal{G}}^0_{Cu2Se}$, and partial molar quantities, $\overline{\mathcal{G}}^0_{Cu}$ and $\overline{\mathcal{G}}^0_{Se}$, are given by evaluating these expressions at the reference composition x_Se = xMin_Cu2Se:

```
G0_CuSeX[tK_] /; tSTP ≤ tK ≤ tRef := G_CuSeX[tK, x_Se] /. x_Se → xMin_Cu2Se[tK]

G0Cu_Cu2Se[tK_] /; tSTP ≤ tK ≤ tRef :=
  G_Cu_CuSeX[tK, x_Se] /. x_Se → xMin_Cu2Se[tK]
G0Se_Cu2Se[tK_] /; tSTP ≤ tK ≤ tRef := G_Se_CuSeX[tK, x_Se] /. x_Se → xMin_Cu2Se[tK]
```

```
(*The free energy in the binary compound in its reference state
    is associated entirely with the chemical potential of selenium *)
G0Cu_Cu2Se[tRef]
x_Se * G0Se_Cu2Se[tK] - G_CuSeX[tK, x_Se] /.
  Thread[{tK, x_Se} → {tRef, xMin_Cu2Se[tRef]}]
```

$$1.06957 \times 10^{-7}$$

$$-7.12898 \times 10^{-8}$$

The domain over which a binary Cu–Se mixture is single-phase $Cu_{2-\delta}Se$ lies between these upper and lower limits of the mixture's selenium mole fraction:

```
xRangeCu2Se = ListPlot[
    {tRef - #, xMax_Cu2Se[tRef - #] - xMin_Cu2Se[tRef - #]} & /@ Range[175, 750, 5],
    PlotJoined → True, AxesLabel → {"T[K]", "Δx"}, AxesOrigin → {tSTP, 0.0257},
    PlotLabel → " Cu2-δSe Single−phase Homogeneity Domain
        \n Cu1-xSex Binary Selenium Mole Fraction Range"]
```

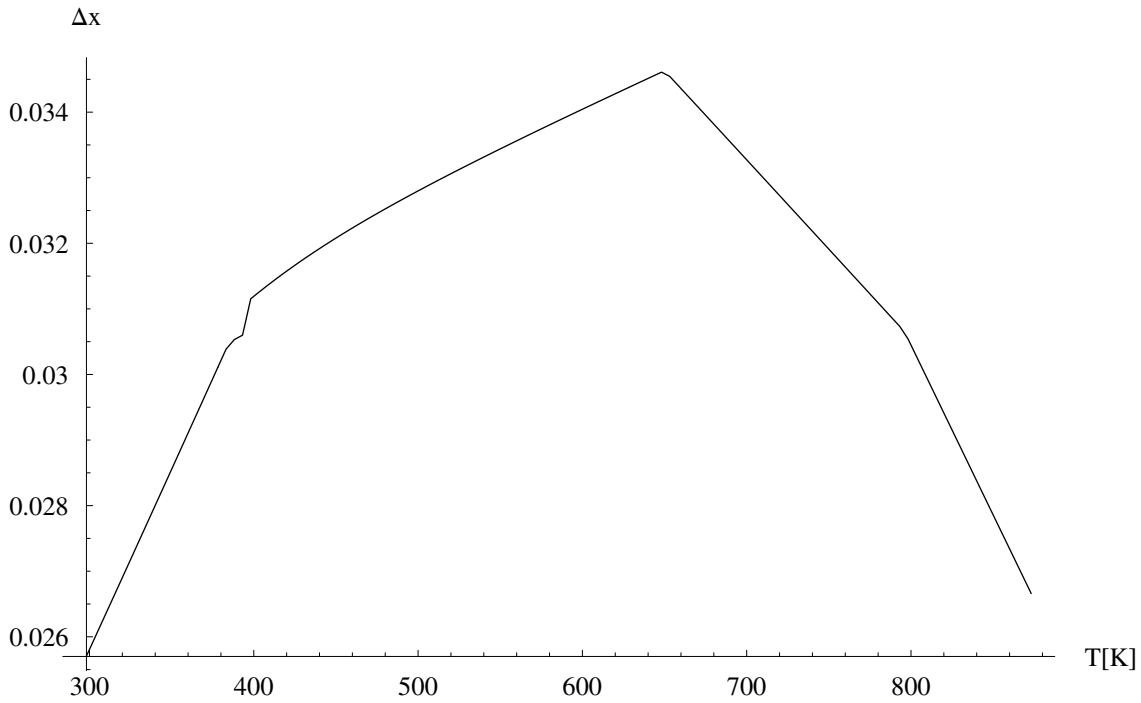

Figure A.2 Temperature dependence of the maximum selenium binary mole fraction of single-phase $Cu_{2-\delta}Se$

Now the activity coefficients can be computed. The computation is performed using the expression RT Log[$\gamma_j\ x_j$]= $\overline{\mathcal{G}}_j - \overline{\mathcal{G}}_j^0 \Rightarrow \gamma_j = x_j^{-1}\,\mathrm{Exp}\left[\frac{\overline{\mathcal{G}}_j - \overline{\mathcal{G}}_j^0}{\mathrm{RT}}\right]$:

```
γ_Cu_Cu2Se[tK_, x_Se_] /; tSTP ≤ tK ≤ 1357.7 :=
  (1 – x_Se)^-1 * Exp[(G_Cu_CuSeX[tK, x_Se] – G0Cu_Cu2Se[tK]) / (rG tK)^-1]
    (*⋀ xMin_Cu2Se≤x_Se<0.346*)
γ_Se_Cu2Se[tK_, x_Se_] /; tSTP ≤ tK ≤ 1357.7 :=
  x_Se^-1 * Exp[(G_Se_CuSeX[tK, x_Se] – G0Se_Cu2Se[tK]) / (rG tK)^-1]
    (*⋀ xMin_Cu2Se≤x_Se<0.368*)

{γ_Cu_Cu2Se[tK, x_Se], γ_Se_Cu2Se[tK, x_Se]} /.
  Thread[{tK, x_Se} → {tRef, xMin_Cu2Se[tRef]}]

    {1.50001, 2.99997}
```

Note that the asymptotic activities in the reference state are correct since the excess partial molar Gibbs energies vanish for both species:

```
{Log[(1 – x_Se) × γ_Cu_Cu2Se[tK, x_Se]], Log[x_Se × γ_Se_Cu2Se[tK, x_Se]]} /.
  Thread[{tK, x_Se} → {tRef, xMin_Cu2Se[tRef]}]

    {0., -5.07269 × 10^-7}
```

This completes the derivation of the expressions for the functional dependence of the energetics of copper and selenium in the secondary $Cu_{2-\delta}Se$ boundary phase on its temperature and composition. It remains to determine the function δ[T] (or equivalently x[T] in the molar formula $Cu_{1-x}\,Se_x$) for the $Cu_{2-\delta}Se/\alpha$–$CuInSe_2$ two-phase equilibrium boundary composition as a function of temperature. To do so requires further specification of the energetics for the elements in the ternary phase, which will be developed in the next subsection.

Ternary compound $CuInSe_2$

The standard state thermodynamic functions for the ideal stoichiometric compound $CuInSe_2$ are developed here, along with their connections to the structure element model for the ternary phase. Since the exchange of copper and selenium determine the equilibrium between $Cu_{2-\delta}Se$ and α–CIS, the partial molar Gibbs free energy of the elements Cu and Se must be the same in both at their mutual phase boundary [158, §6.6]. Thus the solutions determined in the previous section for $\overline{\mathcal{G}}_{Cu}$ and $\overline{\mathcal{G}}_{Se}$ represent constraints that may be used to determine $\overline{\mathcal{G}}_{In}$ from a knowledge of $\mathcal{G}$[T,X,Z] for the values of X and Z of the ternary in equilibrium with the binary.

As mentioned earlier, there is good agreement in the literature that the α–CIS phase formed by eutectoid decomposition of the δ–CIS sphalerite (disordered cubic) phase is stoichiometric in equilibrium at the 1025-1083K invariant temperature of the transition with β–$Cu_{2-\delta}Se$. In principle some solubility of indium in the binary copper selenide is expected, but insufficient information is available in the literature to estimate its solubility at high temperature, and at room temperature it is found to be immeasurable. Thus it is assumed that the solubility of indium in β–$Cu_{2-\delta}Se$ is negligible at all temperatures in the range of these calculations.

A recent study using the solid electrolyte EMF technique [173] directly measured this equilibrium. They found the α–δ phase transition to lie in the range of 1025-1050K, in the lower part of the range reported in the literature. They computed the molar Gibbs energy of mixing (or reaction in this case) based on the net chemical reaction $2\,Cu_2Se + In \rightleftarrows \alpha\text{–}CuInSe_2 + 3\,Cu$ in the experimental range 949-1044K, using

the Nernst equation to analyze their electrochemical data. The result was given by the expression (in J/mole) $\Delta\overline{\mathcal{G}}^{0}_{\mathrm{RXN}}$ =95760-119.80*T. They went on to calculate the standard Gibbs energy of formation for α–$CuInSe_2$ using the equation $\overline{\mathcal{G}}^{0}_{\mathrm{RXN}} = \Delta\overline{\mathcal{G}}^{f}_{\alpha} - 2\Delta\overline{\mathcal{G}}^{f}_{Cu_2Se}$, but used an expression for the standard Gibbs energy of formation for stoichiometric Cu_2Se based on older literature values. For internal consistency, $\Delta\overline{\mathcal{G}}^{f}_{\alpha}$ is recomputed using the $\Delta\overline{\mathcal{G}}^{f}_{Cu_2Se}$ calculated from the assessed values detailed in the previous section and their experimental result for $\overline{\mathcal{G}}^{0}_{\mathrm{RXN}}$ given above:

```
ΔG_CuInSe2_EMF[tK_] /; 1050 ≥ tK ≥ 949 :=
  95760 – 119.80 tK + 2 (g_HSER[cThermo_Cu2Se_β[tK], tK] –
        2 g_HSER[cThermo_Cu[tK], tK] – g_HSER[cThermo_Se[tK], tK])
```

This recomputation of the standard Gibbs energy of formation for α–$CuInSe_2$ increases its value in the range of interest by about 2.7% from that calculated using their expression of -35.6-0.1718T $kJ \cdot mole^{-1}$:

```
(*Barin & Knacke: Δg0f_Cu2Se=–65.68–.026 tK   kJ.mole^-1*)

95.76 – 0.1198 * tK + 2 * (–65.68 – .026 * tK) // Simplify

    –35.6 – 0.1718 tK

(ΔG_CuInSe2_EMF[tK] – 1000 * (–35.6 – 0.1718 tK)) /
  (1000 * (–35.6 – 0.1718 tK)) /. tK → tRef

    0.0265269

ΔG_CuInSe2_EMF[tK] /. tK → tRef

    –221393.
```

The assessed free energy expression for indium [161] can be combined with the above free energy of formation calculated for α–$CuInSe_2$ to compute the total molar Gibbs energy for the stoichiometric ternary at the reference temperature using the equation $\overline{\mathcal{G}}_{\alpha\text{–}CuInSe_2} \doteq \overline{\mathcal{G}}_{Cu}^{SER} + \overline{\mathcal{G}}_{In}^{SER} + 2\,\overline{\mathcal{G}}_{Se}^{SER} + \Delta\overline{\mathcal{G}}_{\alpha}^{f}$:

```
(*The molar Gibbs energy of stoichiometric CuInSe2 at the reference temperature *)
G0_CuInSe2_αδ = g_HSER[cThermo_Cu[tK], tK] + g_HSER[cThermo_In[tK], tK] +
     2 g_HSER[cThermo_Se[tK], tK] + ΔG_CuInSe2_EMF[tK] /. tK → tRef

−467736.
```

To provide boundary conditions over the entire range of this calculation, extension of $\Delta\overline{\mathcal{G}}_{\alpha}^{f}$ to temperatures below those experimentally accessible by the EMF method is required. Very little relevant experimental data is available in the literature. The heat capacity has been measured at low temperatures and used to calculate the standard state entropy [174], and was later measured over the range of 300-500K [175]. Combining these results to provide the temperature dependence of the thermodynamic parameters for α–$CuInSe_2$, and varying the value of $\Delta\overline{\mathcal{G}}_{\alpha}^{f}$ at absolute zero to match the value calculated from the EMF results at the reference temperature gives:

```
cThermo_CuInSe2_α(*/;tRef≥tK≥tSTP*) :=
  {−271466.0778919991, 476.405, −93.2, −14.845 * 10^−3, 95750, 0, 0, 0, 0, 0}

(*The Gibbs energy at the reference temperature
    has been fit to match the EMF results in Pankajavelli, et al. *)
  g_HSER[cThermo_CuInSe2_α, tK] − G0_CuInSe2_αδ /. tK → tRef

    0.
```

(*The heat capacity has been set to the results of Neumann, et al.*)
cP[cThermo_CuInSe2_α, tK]

$$93.2 - \frac{191500}{tK^2} + 0.02969\ tK$$

(*The standard state entropy has been set to the results of Bachmann, et al.*)
s_entropy[cThermo_CuInSe2_α, tK] /. tK → tSTP

157.74

(*The standard state enthalpy of formation is about 8 % less than
the mean of the literature values compiled in Pankajavelli et al.,
but very near the mean of their own results from EMF *)
h_HSER[cThermo_CuInSe2_α, tK] /. tK → tSTP

−241717.

For future use the excess Gibbs energy of mixing of α–$CuInSe_2$ is defined over the entire temperature range:

```
ΔG_CuInSe2_α[tK_] /; tRef ≥ tK ≥ tSTP :=
  g_HSER[cThermo_CuInSe2_α, tK] − (g_HSER[cThermo_Cu[tK], tK] +
      g_HSER[cThermo_In[tK], tK] + 2 g_HSER[cThermo_Se[tK], tK])
```

The partial molar Gibbs energy for indium (its chemical potential) in ternary α–$CuInSe_2$ in equilibrium with binary $Cu_{2-\delta}Se$ at the reference temperature of 1048.15K must be zero since it has been assumed that indium is insoluble in the binary. Using the equation:

$$\mathcal{G}_{\alpha\text{–}CuInSe_2} = \overline{\mathcal{G}}_{Cu}^{CuSe_x} + \overline{\mathcal{G}}_{In}^{\alpha\text{–}CuInSe_2} + 2\,\overline{\mathcal{G}}_{Se}^{CuSe_x} \Rightarrow \overline{\mathcal{G}}_{In}^{0} = \mathcal{G}_{\alpha\text{–}CuInSe_2} - \overline{\mathcal{G}}_{Cu}^{CuSe_x} - 2\,\overline{\mathcal{G}}_{Se}^{CuSe_x} = 0$$

, and solve for the value of x to determine the stoichiometry of the $Cu_{2-\delta}Se$ phase in equilibrium.

```
x0_Se[tK_] :=
  x_Se /. FindRoot[g_HSER[cThermo_CuInSe2_α, #] – G_Cu_CuSeX[#, x_Se] – 2
                G_Se_CuSeX[#, x_Se] == 0, {x_Se, 1 / 3}] &[tK]
```

When x_Se for the secondary $Cu_{1-x}\,Se_x$ phase assumes this value, the stoichiometry deviation parameter of the binary phase in terms of the compound formula $Cu_{2-\delta}\,Se$ is:

$$\delta 00[tK\_?NumericQ] := With\left[\{x\_Se = x0\_Se[tK]\},\ \frac{-1 + 3\,x\_Se}{x\_Se}\right]$$

$$\left\{\delta 00[tRef],\ \left\{"numerical\ error",\ \frac{1}{1 + 2 - \delta 00[tRef]} - x0\_Se[tRef]\right\}\right\}$$

```
{0.000125725, {numerical error, 0.}}
```

```
Off[FindRoot::cvnwt] ⋀ Off[FindRoot::frmp];
δx0_Se = ParametricPlot[{Evaluate[(x0_Se[T] – xMin_Cu2Se[T]) 10^6],  T},
      {T,  tSTP,  tRef}, AxesLabel → {"[ppm]", "T [K]"},
      PlotLabel → "Cu_(2–δ)Se Stoichiometry Deviation from Minimum \n if in
            Equilibrium with Stoichiometric CuInSe_2", DisplayFunction → Identity];

On[FindRoot::cvnwt] ⋀ On[FindRoot::frmp];

(x0_Se[#] – xMin_Cu2Se[#]) 10^6 &[847.431940394]
```

$$-2.09832 \times 10^{-8}$$

```
tK000 = 847.431940394;
tK000 – 273.15
```

```
574.282
```

Since the predicted equilibrium value of the $Cu_{1-x}\,Se_x$ phase's selenium content is less than the minimum required to prevent segregation of the nearly-pure *fcc* copper phase, this analysis provides the first significant result of this calculation: the prediction that below a temperature of about 847.4K (~575°C) the binary

$Cu_{1-x}Se_x$ phase cannot be in equilibrium with stoichiometric ternary α–$CuInSe_2$ alone. Since a three-phase equilibrium in a ternary system is a critical point and a two-phase equilibrium between binary copper selenide and α–CIS is known to occur, the latter must deviate from stoichiometry in equilibrium with the former at lower temperatures. To quantitatively model this predicted stoichiometry deviation of the α–CIS phase, its building unit model must be developed, which is the next task.

State Vectors

The supplementary vectors required to implement a solution to the problem are defined next. These are the reference state chemical potential vector $\boldsymbol{\mu^0}$ with 27 components μ_j^0, the reaction extent vector $\boldsymbol{\xi}$ with 22 components ξ_r, and the initial species concentration vector $\boldsymbol{c^0}$ with 27 components c_j^0. The solution concentration vector $\boldsymbol{c}$ is implicitly dependent on $\boldsymbol{\xi}$ as a consequence of the relation $c_j = c_j^0 + \sum_{r=1}^{22} \nu_{jr}\, \xi_r$.

As previously described, the two-phase $Cu_{2-\delta}Se/\alpha$–$CuInSe_2$ equilibrium values of c_j are determined first in order to provide the chemical potentials of each species *via* the relation $\overline{\mu}_j = \overline{\mu}_j^0 + RT \ln[c_j]$. These solution values become the basis for the standard state vectors, $\boldsymbol{c^0}$ and $\boldsymbol{\mu^0}$, for the solution of the α–CIS single phase and CIS α/β two phase equilibria. To avoid unnecessarily complicated notation, the initial state vectors for the first problem will be labeled with two zeros and the second by one zero in the *Mathematica* code, but distinguished in this discussion text only by context.

Initial Concentration Vector

The initial configuration must be determined by a function of the independent thermodynamic variables T, X, and Z only. The final building unit concentrations in $\boldsymbol{c}^{\mathbf{0}}$ must also correctly reflect the atomic stoichiometry. For this purpose their connection *via* sum rules with respect to the strictly conserved subset (the first four elements: Cu, In, Se, q) of the basis set **a** is developed. The function **mx**, defined below, operates on a species concentration vector and returns the quasimolecule formula numbers and charge. This list of four numbers each equals the number of moles of the corresponding atomic or electronic basis element in one mole of the quasimolecule (M=1). The elements of the list **mx**[c] are multinary generalizations of the factors y2 and 1+y1 used in the preceding sublattice solution model for the binary compound $Cu_{1+y1}\,Se_{y2}$. It will use be used to verify the internal consistency of $\boldsymbol{c}^{\mathbf{0}}$ and to switch between the partial molar and building unit normalizations as required.

mx[c_?VectorQ, $\mathcal{D}$_] /; Length[c] == Dimensions[$\mathcal{D}$][[2]] := Take[$\mathcal{D}$, 4].c

$$\text{ax[c\_?VectorQ, } \mathcal{D}\text{\_] /; Length[c] == Dimensions[}\mathcal{D}\text{][[2]] := } \frac{\text{mx[c, } \mathcal{D}\text{]}}{\text{Plus @@ mx[c, } \mathcal{D}\text{]}}$$

The atomic fraction function **ax**, also operates on a species concentration vector and for this multinary system returns the list of values corresponding to the atomic fractions x_Se and 1-x_Se, the variable(s) in the partial molar Gibbs energy functions for the binary $Cu_{1-x}\,Se_{x}$. As in the binary case, since the fractions must sum to one, the number of independent parameters in the vector **ax** is Length[**ax**]-1.

This function is distinct from the function that return the atomic fractions corresponding to the thermodynamic variables X and Z:

$$\text{xAt[X\_, Z\_] := With}\left[\{nAt = 2(1+X) + Z(3+X)\}, \left\{\frac{2X}{nAt}, \frac{2}{nAt}, \frac{Z(3+X)}{nAt}\right\}\right]$$

The atomic fraction function **xAt**, given the values of the thermodynamic variables X and Z, returns the list of values corresponding to the atomic fractions x_Se and 1– x_Se, the variable(s) in the partial molar Gibbs energy functions for the binary $Cu_{1-x}\,Se_x$. As in the binary case, since the fractions must sum to one, the number of independent parameters in the vector **xAt** is Length[**ax**]– 1.

These functions are used to define another function, which return the values of X and Z for any concentration vector supplied as its argument, although the formula matrix for that vector's species must also be specified:

$$\text{cXZ[c\_?VectorQ, } \mathcal{D}\text{\_] /; Length[c] == Dimensions[}\mathcal{D}\text{][[2]] :=}$$
$$\left\{\frac{\text{mx[c, } \mathcal{D}\text{][[1]]}}{\text{mx[c, } \mathcal{D}\text{][[2]]}}, \frac{2\,\text{mx[c, } \mathcal{D}\text{][[3]]}}{\text{mx[c, } \mathcal{D}\text{][[1]]} + 3\,\text{mx[c, } \mathcal{D}\text{][[2]]}}\right\}$$

These functions are applied to the basis set elements for the two-phase $Cu_{2-\delta}Se/\alpha$–$CuInSe_2$ equilibrium problem, **cE0**. The results are used to compute the values of X and Z for each cluster. Since every possible configuration that can be expressed in this model is a non-negative linear combination of the cluster basis elements, these results can be analyzed to determine the limits on X and Z and used to avoid evaluation of this model outside its limits of applicability.

```
clusterXZ0 = Module[{im27},  With[{im27 = IdentityMatrix[27] },
        Array[Flatten[{#, cE0[[#]], cXZ[im27[[#]], 𝒟0]}] &,  22]]];
c0Limits = Module[{x00min, x00max, z00min, z00max},  With[
      {x00min = Min[%[[All, 3]]], x00max = Max[%[[All, 3]]], z00min = Min[%[[All, 4]]],
        z00max = Max[%[[All, 4]]]}, {x00min, x00max, z00min, z00max}]]
```

$$\left\{\frac{7}{11}, \frac{7}{5}, \frac{11}{12}, \frac{8}{7}\right\}$$

It is simple to construct a list of those clusters that match these limiting values:

```
{cE0[[#]], #} & /@
    (Join[Take[(Position[clusterXZ0[[All, 3]], #] & /@ c0Limits)[[All, All, 1]], 2],
        Drop[(Position[clusterXZ0[[All, 4]], #] & /@ c0Limits)[[All, All, 1]], 2]]);
Array[FlattenAt[{c0Limits[[#]], %[[#]]}, 2] &, Length[c0Limits]] //
  TableForm(* limit   cluster       index *)
```

$\frac{7}{11}$	$(2\mathcal{V}_{Cu} \oplus In_{Cu})_{\alpha}$	22
	Cu_{In}^{x}	7
$\frac{7}{5}$	Cu_{In}'	8
	Cu_{In}''	9
	$\mathcal{V}_{Se}^{x}$	14
$\frac{11}{12}$	$\mathcal{V}_{Se}^{\cdot\cdot}$	15
	$\mathcal{V}_{In}^{x}$	10
	$\mathcal{V}_{In}^{\cdot}$	11
$\frac{8}{7}$	$\mathcal{V}_{In}^{\cdot\cdot}$	12
	$\mathcal{V}_{In}^{\cdot\cdot\cdot}$	13

The initial concentration vector $\boldsymbol{c^0}$ for any permissible X and Z values can be constructed entirely of the species $(2\mathcal{V}_{Cu} \oplus In_{Cu})_{\alpha}$, Cu_{In}, $\mathcal{V}_{Se}$, and $\mathcal{V}_{In}$. The maximum allowed value of X in the overall problem is 1, and since both Cu_{In} and $\mathcal{V}_{In}$ have $X > 0$, only the latter, which has the maximum Z value of any cluster, is required to maximize the possible range of Z for this restricted range of X. Since it is also electrically neutral, $\boldsymbol{c^0}$ will be initialized using a basis vector set that is further

restricted to include only the normal valence forms of $(2\mathcal{V}_{Cu} \oplus In_{Cu})_\alpha$, $\mathcal{V}_{Se}$, $\mathcal{V}_{In}$, and CIS_α.

```
c000basis = {1, 10, 14, 22};
clusterXZ0[[#]] & /@ c000basis // TableForm
(*index  cluster      X     Z   *)
```

1	CIS_α	1	1
10	$\mathcal{V}_{In}^{x}$	$\frac{6}{5}$	$\frac{8}{7}$
14	$\mathcal{V}_{Se}^{x}$	1	$\frac{11}{12}$
22	$(2\mathcal{V}_{Cu} \oplus In_{Cu})_\alpha$	$\frac{7}{11}$	1

Inspecting the table, it is clear that the anion/cation ratio of $\mathcal{V}_{Se}^{x}$ is Z = 11/12 and it and its ionized form are the only defect clusters with a ratio less than 1. This establishes the minimum possible value of Z in this model. Similarly, the only cluster with an X value of less than 1 is $(2\mathcal{V}_{Cu} \oplus In_{Cu})_\alpha$. The first correction to $\boldsymbol{c^0}$ will be made by combining only CIS_α and $(2\mathcal{V}_{Cu} \oplus In_{Cu})_\alpha$ to achieve the specified value of X, then Z will be adjusted by exchanging CIS_α for appropriate linear combinations of the others.

The stoichiometry matrix formalism is applicable to this solution, with the formula matrix reduced to the restricted $\boldsymbol{c^0}$ basis and the conserved quantities restricted to the first four, the set {Cu, In, Se, q}:

```
𝒟000 = Transpose[Transpose[Take[𝒟0, 4]][[#]] & /@ c000basis];
```

```
cE0[[#]] & /@ c000basis
𝒟000 // MatrixForm
```

$$\{\text{CIS}_\alpha, \mathcal{V}^{\text{x}}_{\text{In}}, \mathcal{V}^{\text{x}}_{\text{Se}}, (2\,\mathcal{V}_{\text{Cu}} \oplus \text{In}_{\text{Cu}})_\alpha\}$$

$$\begin{pmatrix} 2 & 6 & 6 & 7 \\ 2 & 5 & 6 & 11 \\ 4 & 12 & 11 & 20 \\ 0 & 0 & 0 & 0 \end{pmatrix}$$

```
formula[i_, 𝒟000] := {cE0[[#]] & /@ c000basis, Take[a, 4] .𝒟000}[[All, i]]

Array[formula[#, 𝒟000] &, Length[c000basis]] // TableForm
```

CIS_α	$2\,\text{Cu} + 2\,\text{In} + 4\,\text{Se}$
$\mathcal{V}^{\text{x}}_{\text{In}}$	$6\,\text{Cu} + 5\,\text{In} + 12\,\text{Se}$
$\mathcal{V}^{\text{x}}_{\text{Se}}$	$6\,\text{Cu} + 6\,\text{In} + 11\,\text{Se}$
$(2\,\mathcal{V}_{\text{Cu}} \oplus \text{In}_{\text{Cu}})_\alpha$	$7\,\text{Cu} + 11\,\text{In} + 20\,\text{Se}$

```
ν000 = Transpose[NullSpace[𝒟000]];

MatrixForm[ν000]
```

$$\begin{pmatrix} -67 \\ 8 \\ 12 \\ 2 \end{pmatrix}$$

```
rxn[i_, ν000] := ν000[[All, i]].(cE0[[#]] & /@ c000basis)

Array[rxn[#, ν000] &, Dimensions[ν000][[2]] // TableForm
```

$$-67\,\text{CIS}_\alpha + 8\,\mathcal{V}^{\text{x}}_{\text{In}} + 12\,\mathcal{V}^{\text{x}}_{\text{Se}} + 2\,(2\,\mathcal{V}_{\text{Cu}} \oplus \text{In}_{\text{Cu}})_\alpha$$

With 4 species and 3 nonvanishing conserved quantities, the only reaction that leaves both X and Z unchanged is the one shown above. There are also two reactions between CIS_α and the others that leave X unchanged. These are:

```
(* using c000basis→{c1,c10,c14,c22},
   are the X' s for the vectors {c1,0,0,0} and {0,0,c14,0} always equal? *)
cXZ[{c1, 0, 0, 0}, 𝒟000][[1]] === cXZ[{0, 0, c14, 0}, 𝒟000][[1]]
```

True

```
(* how does Z vary for their linear combination? *)
cXZ[{1 − c14, 0, c14, 0}, 𝒟000] // Simplify
```

$$\left\{1, \frac{4 + 7\,c14}{4 + 8\,c14}\right\}$$

```
(* what is the extremal value of Z? *) %[[2]] /. c14 → 1
```

$$\frac{11}{12}$$

```
(* does any normalized linear combination of the vectors {0,c10,0,0} and
     {0,0,0,c22} always furnish the same X value as {c1,0,0,0}? *)Solve[
   cXZ[{c1, 0, 0, 0}, 𝒟000][[1]] == cXZ[{c1 − c10 − c22, c10, 0, c22}, 𝒟000][[1]], {c22}]
```

$$\left\{\left\{c22 \to \frac{c10}{4}\right\}\right\}$$

```
(* how does Z vary for that linear combination? *)
cXZ[{1 − c10 − c22, c10, 0, c22}, 𝒟000] /. % // Simplify
```

$$\left\{\left\{1, \frac{8 + 24\,c10}{8 + 21\,c10}\right\}\right\}$$

```
(* what is the extremal value of Z for that linear combination? *) %[[1, 2]] /. c10 → 8/10
```

$$\frac{34}{31}$$

These results provide all the additional information required to correctly limit the range of X and Z, and to initialize $\boldsymbol{c^0}$. The latter is set to a linear combination of the four vectors {c1, 0, 0, 0}, {0, 0, 0, c22}, {0, 0, c14, 0}, and {0, c10, 0, c10/4} determined by the values of X and Z. The limits list is redefined so that both the minimum and maximum permissible Z values are unity at the minimum X value where the system can only consist of c22, which is $(2\,\mathcal{V}_{\mathrm{Cu}} \oplus \mathrm{In}_{\mathrm{Cu}})_{\alpha}$.

```
c0Limits = Module[{x00min, x00max, z00min, z00max},
    With[{x00min = 7/11, x00max = 1, z00min = 11/12 + 11 (1 - X)/48,
      z00max = 34/31 - 33 (1 - X)/124}, {x00min, x00max, z00min, z00max}]]
```

$$\left\{\frac{7}{11}, 1, \frac{11}{12} + \frac{11\,(1-X)}{48}, \frac{34}{31} - \frac{33\,(1-X)}{124}\right\}$$

```
(* test examples for 7/11≤X≤1 ⋀ Z≤1 *)
Solve[{X0, Z0} == cXZ[{c1 - c14, 0, c14, 1 - c1}, 𝒟000], {c1, c14}];
{cXZ[{c1 - c14, 0, c14, 1 - c1}, 𝒟000],
    mx[{c1 - c14, 0, c14, 1 - c1}, 𝒟000], {c1 - c14, 0, c14, 1 - c1}} /. %;
% /. Thread[{X0, Z0} → {1, 1}] // Simplify
%% /. Thread[{X0, Z0} → {7/11, 1}] // Simplify
%%% /. Thread[{X0, Z0} → {15/22, 1}] // Simplify
%%%% /. Thread[{X0, Z0} → {9/11, 23/24}] // Simplify
%%%%% /. Thread[{X0, Z0} → {1, 11/12}] // Simplify
(* {X,Z},{molesCu,In,Se,q},{c1,c10,c14,c22} *)
```

$$\{\{\{1, 1\}, \{2, 2, 4, 0\}, \{1, 0, 0, 0\}\}\}$$

$$\left\{\left\{\left\{\frac{7}{11}, 1\right\}, \{7, 11, 20, 0\}, \{0, 0, 0, 1\}\right\}\right\}$$

$$\left\{\left\{\left\{\frac{15}{22}, 1\right\}, \left\{\frac{24}{5}, \frac{176}{25}, \frac{324}{25}, 0\right\}, \left\{\frac{11}{25}, 0, 0, \frac{14}{25}\right\}\right\}\right\}$$

$$\left\{\left\{\left\{\frac{9}{11}, \frac{23}{24}\right\}, \left\{6, \frac{22}{3}, \frac{161}{12}, 0\right\}, \left\{\frac{1}{12}, 0, \frac{7}{12}, \frac{1}{3}\right\}\right\}\right\}$$

$$\left\{\left\{\left\{1, \frac{11}{12}\right\}, \{6, 6, 11, 0\}, \{0, 0, 1, 0\}\right\}\right\}$$

```
(* test examples for 7/11≤X≤1 ⋀ Z≥1 *)
Solve[{X0, Z0} == cXZ[{1 – 5 c10 / 4 – c22, c10, 0, c22 + c10 / 4}, 𝒟000], {c10, c22}];
{cXZ[{1 – 5 c10 / 4 – c22, c10, 0, c22 + c10 / 4}, 𝒟000],
      mx[{1 – 5 c10 / 4 – c22, c10, 0, c22 + c10 / 4}, 𝒟000],
      {1 – 5 c10 / 4 – c22, c10, 0, c22 + c10 / 4}} /. %;
% /. Thread[{X0, Z0} → {1, 1}] // Simplify
%% /. Thread[{X0, Z0} → {7 / 11, 1}] // Simplify
%%% /. Thread[{X0, Z0} → {15 / 22, 1}] // Simplify
%%%% /. Thread[{X0, Z0} → {20 / 22, 33 / 31}] // Simplify
%%%%% /. Thread[{X0, Z0} → {1, 34 / 31}] // Simplify
(*{X,Z},{molesCu,In,Se,q},{c1,c10,c14,c22} *)
```

```
{{{1, 1}, {2, 2, 4, 0}, {1, 0, 0, 0}}}
```

$$\left\{\left\{\left\{\frac{7}{11}, 1\right\}, \{7, 11, 20, 0\}, \{0, 0, 0, 1\}\right\}\right\}$$

$$\left\{\left\{\left\{\frac{15}{22}, 1\right\}, \left\{\frac{24}{5}, \frac{176}{25}, \frac{324}{25}, 0\right\}, \left\{\frac{11}{25}, 0, 0, \frac{14}{25}\right\}\right\}\right\}$$

$$\left\{\left\{\left\{\frac{10}{11}, \frac{33}{31}\right\}, \left\{\frac{2480}{483}, \frac{2728}{483}, \frac{1892}{161}, 0\right\}, \left\{\frac{403}{1449}, \frac{688}{1449}, 0, \frac{358}{1449}\right\}\right\}\right\}$$

$$\left\{\left\{\left\{1, \frac{34}{31}\right\}, \left\{\frac{31}{5}, \frac{31}{5}, \frac{68}{5}, 0\right\}, \left\{0, \frac{4}{5}, 0, \frac{1}{5}\right\}\right\}\right\}$$

The total quantities of each of the three elements and charge in one mole of the quasimolecular species $\mathrm{Cu}_{\frac{2X}{1+X}}\ \mathrm{In}_{\frac{2}{1+X}}\ \mathrm{Se}_{\frac{Z(3+X)}{1+X}}$ must be distributed among the structural species *via* the initial concentration vector. The foregoing calculations were performed on vectors normalized to unity sum, so they correctly reflect the values of X and Z as well as the corresponding proportions of the different clusters, but not this required overall normalization of $\boldsymbol{c^0}$. This can be demonstrated by comparing the mole numbers from the last example with the quasimolecule's formula coefficients for the same values of X and Z:

$$\left\{\%[\![1, 2]\!], \left\{\frac{2\,X}{1+X}, \frac{2}{1+X}, \frac{Z\,(3+X)}{(1+X)}, 0\right\}\right\} /. \text{Thread}[\{X, Z\} \to \%[\![1, 1]\!]]$$

$$\text{Array}\left[\frac{\%[\![2, \#]\!]}{\%[\![1, \#]\!]}\ \&, 3\right]$$

$$\left\{\left\{\frac{31}{5}, \frac{31}{5}, \frac{68}{5}, 0\right\}, \left\{1, 1, \frac{68}{31}, 0\right\}\right\}$$

$$\left\{\frac{5}{31}, \frac{5}{31}, \frac{5}{31}\right\}$$

Clear[X0, Z0, c1, c10, c14, c22]

The latter result above shows how the normalization factor for the cluster fraction vector can be calculated as a ratio of any one of the quasimolecule formula numbers and the atomic mole numbers for the cluster fraction vector computed using the function **mx[**c000**]**.

This completes the derivation of the mathematical expressions needed to initialize the principal components of the concentration vector $\boldsymbol{c^0}$. To avoid logarithmic divergence of the entropies associated with their chemical potentials and still approximate their infinite dilution reference state, the initial concentration of every lattice species in the full basis **cE0** must be set to at least a minute value (except ΔN, which has no entropy). The formula matrix $\mathcal{D}\mathbf{0}$ and reaction stoichiometry matrix $\boldsymbol{\nu}\mathbf{0}$ are used to distribute these. Linear combinations of any of the reactions represented by the columns of $\boldsymbol{\nu}\mathbf{0}$ may be added to the initial vector without changing any of the conserved quantities, although as derived above a limited set of reactants is available to draw upon for any permissible value of X and Z.

A particularly useful linear combination for this purpose is derived as follows:

```
Plus @@ Rest[Array[rxn[#, ν0] &, 22]] // Simplify
% – rxn[1, ν0] // Simplify
{Length[%%], Length[%]}
```

$$\begin{aligned}&\text{Cu2}\_\delta\text{Se} + \text{h}^{\bullet} + \text{Cu}_\text{i} \oplus \mathcal{V}_\text{Cu} + \text{Cu}_\text{In} \oplus \text{In}_\text{Cu} + \mathcal{V}_\text{Cu} \oplus \text{In}_\text{Cu} + \\ &\quad (\mathcal{V}_\text{Cu} \oplus \text{In}_\text{Cu})^{\bullet} - 54\,\text{CIS}_\alpha + 3\,\delta\,\text{CIS}_\alpha + \text{Cu}_\text{Cu2Se} + \text{Cu}_\text{i}^{\text{x}} + \text{Cu}_\text{i}^{\bullet} + \\ &\quad \text{Cu}_\text{In}^{\text{x}} + 2\,\text{In}_\text{Cu}^{\text{x}} + \text{In}_\text{Cu}^{\bullet} + \text{In}_\text{Cu}^{\bullet\bullet} - 13\,\mathcal{V}_\text{Cu}^{\text{x}} - \delta\,\mathcal{V}_\text{Cu}^{\text{x}} + \mathcal{V}_\text{In}^{\text{x}} + \mathcal{V}_\text{In}^{\bullet} + \\ &\quad \mathcal{V}_\text{In}^{\bullet\bullet} + \mathcal{V}_\text{In}^{\bullet\bullet\bullet} + \mathcal{V}_\text{Se}^{\bullet\bullet} + (2\,\mathcal{V}_\text{Cu} \oplus \text{In}_\text{Cu})_\alpha + \text{e}' + \text{Cu}_\text{In}' + 10\,\mathcal{V}_\text{Cu}' + \text{Cu}_\text{In}'' \\ &\text{Cu2}\_\delta\text{Se} + \text{h}^{\bullet} - \Delta\text{N} + \text{Cu}_\text{i} \oplus \mathcal{V}_\text{Cu} + \text{Cu}_\text{In} \oplus \text{In}_\text{Cu} + \mathcal{V}_\text{Cu} \oplus \text{In}_\text{Cu} + \\ &\quad (\mathcal{V}_\text{Cu} \oplus \text{In}_\text{Cu})^{\bullet} - \frac{125\,\text{CIS}_\alpha}{2} + 3\,\delta\,\text{CIS}_\alpha + \text{Cu}_\text{Cu2Se} + \text{Cu}_\text{i}^{\text{x}} + \text{Cu}_\text{i}^{\bullet} + \\ &\quad \text{Cu}_\text{In}^{\text{x}} + \text{In}_\text{Cu}^{\text{x}} + \text{In}_\text{Cu}^{\bullet} + \text{In}_\text{Cu}^{\bullet\bullet} - 11\,\mathcal{V}_\text{Cu}^{\text{x}} - \delta\,\mathcal{V}_\text{Cu}^{\text{x}} + \mathcal{V}_\text{In}^{\text{x}} + \mathcal{V}_\text{In}^{\bullet} + \mathcal{V}_\text{In}^{\bullet\bullet} + \\ &\quad \mathcal{V}_\text{In}^{\bullet\bullet\bullet} + 2\,\mathcal{V}_\text{Se}^{\text{x}} + \mathcal{V}_\text{Se}^{\bullet\bullet} + (2\,\mathcal{V}_\text{Cu} \oplus \text{In}_\text{Cu})_\alpha + \text{e}' + \text{Cu}_\text{In}' + 10\,\mathcal{V}_\text{Cu}' + \text{Cu}_\text{In}'' \\ &\{27, 29\}\end{aligned}$$

```
(* remove Cu_Cu2Se *)
Plus @@ Rest[Array[rxn[#, ν0] &, 22]] – rxn[1, ν0] + 7 rxn[4, ν0] – rxn[5, ν0] // Simplify
Length[%]
```

$$\begin{aligned}&8\,\text{Cu2}\_\delta\text{Se} + \text{h}^{\bullet} - \Delta\text{N} + \text{Cu}_\text{i} \oplus \mathcal{V}_\text{Cu} + \text{Cu}_\text{In} \oplus \text{In}_\text{Cu} + \mathcal{V}_\text{Cu} \oplus \text{In}_\text{Cu} + \\ &\quad (\mathcal{V}_\text{Cu} \oplus \text{In}_\text{Cu})^{\bullet} - \frac{245\,\text{CIS}_\alpha}{2} + 24\,\delta\,\text{CIS}_\alpha + \text{Cu}_\text{i}^{\text{x}} + \text{Cu}_\text{i}^{\bullet} + \text{Cu}_\text{In}^{\text{x}} + \\ &\quad \text{In}_\text{Cu}^{\text{x}} + \text{In}_\text{Cu}^{\bullet} + \text{In}_\text{Cu}^{\bullet\bullet} + 2\,\mathcal{V}_\text{Cu}^{\text{x}} - 8\,\delta\,\mathcal{V}_\text{Cu}^{\text{x}} + \mathcal{V}_\text{In}^{\text{x}} + \mathcal{V}_\text{In}^{\bullet} + \mathcal{V}_\text{In}^{\bullet\bullet} + \mathcal{V}_\text{In}^{\bullet\bullet\bullet} + \\ &\quad 9\,\mathcal{V}_\text{Se}^{\text{x}} + \mathcal{V}_\text{Se}^{\bullet\bullet} + (2\,\mathcal{V}_\text{Cu} \oplus \text{In}_\text{Cu})_\alpha + \text{e}' + \text{Cu}_\text{In}' + 10\,\mathcal{V}_\text{Cu}' + \text{Cu}_\text{In}'' \\ &28\end{aligned}$$

```
ξ000init = Array[1 &, 22] – 2 Array[KroneckerDelta[1, # ] &, 22] +
    7 Array[KroneckerDelta[4, # ] &, 22] – Array[KroneckerDelta[5, # ] &, 22]
```

```
{–1, 1, 1, 8, 0, 1, 1, 1, 1, 1, 1, 1, 1, 1, 1, 1, 1, 1, 1, 1, 1, 1}
```

```
Plus @@ (ξ000init Array[rxn[#, ν0] &, 22]) // Simplify
Length[%]
```

$$\begin{aligned}&8\,\text{Cu2}\_\delta\text{Se} + \text{h}^{\bullet} - \Delta\text{N} + \text{Cu}_\text{i} \oplus \mathcal{V}_\text{Cu} + \text{Cu}_\text{In} \oplus \text{In}_\text{Cu} + \mathcal{V}_\text{Cu} \oplus \text{In}_\text{Cu} + \\ &\quad (\mathcal{V}_\text{Cu} \oplus \text{In}_\text{Cu})^{\bullet} - \frac{245\,\text{CIS}_\alpha}{2} + 24\,\delta\,\text{CIS}_\alpha + \text{Cu}_\text{i}^{\text{x}} + \text{Cu}_\text{i}^{\bullet} + \text{Cu}_\text{In}^{\text{x}} + \\ &\quad \text{In}_\text{Cu}^{\text{x}} + \text{In}_\text{Cu}^{\bullet} + \text{In}_\text{Cu}^{\bullet\bullet} + 2\,\mathcal{V}_\text{Cu}^{\text{x}} - 8\,\delta\,\mathcal{V}_\text{Cu}^{\text{x}} + \mathcal{V}_\text{In}^{\text{x}} + \mathcal{V}_\text{In}^{\bullet} + \mathcal{V}_\text{In}^{\bullet\bullet} + \mathcal{V}_\text{In}^{\bullet\bullet\bullet} + \\ &\quad 9\,\mathcal{V}_\text{Se}^{\text{x}} + \mathcal{V}_\text{Se}^{\bullet\bullet} + (2\,\mathcal{V}_\text{Cu} \oplus \text{In}_\text{Cu})_\alpha + \text{e}' + \text{Cu}_\text{In}' + 10\,\mathcal{V}_\text{Cu}' + \text{Cu}_\text{In}'' \\ &28\end{aligned}$$

The final expression above shows that 26 of 27 basis elements in **cE0** are represented in the preceding expression (Cu_{Cu2Se} is omitted), which is a linear combination of all 22 reactions (except five, which generates Cu_{Cu2Se}) with extents given by the vector ξ000init, and which consumes only CIS_α and ΔN, yielding every other species in **cE0** (except Cu_{Cu2Se}) as a reaction product. By appropriately adjusting the limits on Z the distribution of initial clusters from the restricted basis set c000**basis** can be constrained to always retain enough CIS_α to permit this net reaction to proceed sufficiently to populate these "trace" species. The appearance of ΔN as a reactant is a reflection of the need to expand the lattice to accomodate the many vacancies created by this reaction. Note that the amount of Cu_{Cu2Se} is set to the minimum stable value of δ for the $Cu_{2-\delta}Se$ phase at the reference temperature, and the Cu2.δSe species will also be initialized to that composition.

The reaction extent vector ξ000init will be scaled by a factor of 1×10^{-26} so that the concentrations of the "trace" species and total quantity of CIS_α involved in those reactions correspond to less than a single cluster *per* mole. These adjustments are computed using the expression $c_j = c_j^0 + \sum_{r=1}^{22} \nu_{jr}\,\xi_r$. The foregoing results are applied to define the following function of Z, which returns the initial concentration vector $\boldsymbol{c^0}$ for X=1:

$$\text{c0Limits} = \text{Module}\Big[\{\text{x00min, x00max, z00min, z00max}\},\ \text{With}\Big[\Big\{\text{x00min} = \frac{14011}{22000},\ \text{x00max} = 1,\ \text{z00min} = \frac{11}{12} + \frac{11\,(1 - \text{X} + \frac{5}{10000})}{48},\ \text{z00max} = \frac{34}{31} - \frac{33\,(1 - \text{X} + \frac{5}{10000})}{124}\Big\},\ \{\text{x00min, x00max, z00min, z00max}\}\Big]\Big];$$

```
c0Limits /. X → c0Limits[[1]] (* no Z deviation possible in model at minimum X *)
{c0Limits[[3]], c0Limits[[4]]} /. X → 1 (* maximum Z deviation is possible for X=1 *)
```

$$\left\{\frac{14011}{22000}, 1, 1, 1\right\}$$
$$\left\{\frac{29337}{32000}, \frac{271967}{248000}\right\}$$

```
% // N (* approximate maximum limits of Z deviation *)
```

{0.916781, 1.09664}

```
Solve[{1, Z} == cXZ[{c1 − c14, 0, c14, 1 − c1}, 𝒟000], {c1, c14}];
{{c1 − c14, 0, c14, 1 − c1}, mx[{c1 − c14, 0, c14, 1 − c1}, 𝒟000][[1]]^-1} /. %
```

$$\left\{\left\{\left\{1+\frac{4(-1+Z)}{-7+8Z}, 0, -\frac{4(-1+Z)}{-7+8Z}, 0\right\}, \frac{1}{-\frac{24(-1+Z)}{-7+8Z}+2\left(1+\frac{4(-1+Z)}{-7+8Z}\right)}\right\}\right\}$$

```
Solve[{1, Z} == cXZ[{1 − 5 c10/4 − c22, c10, 0, c22 + c10/4}, 𝒟000], {c10, c22}];
{{1 − 5 c10/4 − c22, c10, 0, c22 + c10/4},
    mx[{1 − 5 c10/4 − c22, c10, 0, c22 + c10/4}, 𝒟000][[1]]^-1} /. %
```

$$\left\{\left\{\left\{1+\frac{10(-1+Z)}{3(-8+7Z)}, -\frac{8(-1+Z)}{3(-8+7Z)}, 0, -\frac{2(-1+Z)}{3(-8+7Z)}\right\},\right.\right.$$
$$\left.\left.\frac{1}{-\frac{62(-1+Z)}{3(-8+7Z)}+2\left(1+\frac{10(-1+Z)}{3(-8+7Z)}\right)}\right\}\right\}$$

```
c000[Z_] /; 29337/32000 ≤ Z ≤ 1 :=
  Module[{c000}, With[{c4Zminus = {1 + 4 (-1 + Z)/(-7 + 8 Z), 0, -4 (-1 + Z)/(-7 + 8 Z), 0},
      mCuInv1 = 1/(-24 (-1+Z)/(-7+8 Z) + 2 (1 + 4 (-1+Z)/(-7+8 Z)))}, c000 = Plus @@ MapThread[
      ReplacePart[Array[0 &, Length[cE0]], #1, #2] &, {c4Zminus, c000basis}];
    c000 = ReplacePart[c000, -δmin[tRef] ξ000init[[4]] 1*^-26, 23];
    c000 = mCuInv1 (c000 + (ν0 /. δ → δmin[tRef]).ξ000init 1*^-26);
    ReplacePart[c000, 1, 27]]]
c000[Z_, tK_] /; 1 < Z ≤ 271967/248000 := Module[{c000},
  With[{c4Zplus = {1 + 10 (-1 + Z)/(3 (-8 + 7 Z)), -8 (-1 + Z)/(3 (-8 + 7 Z)), 0, -2 (-1 + Z)/(3 (-8 + 7 Z))},
      mCuInv2 = 1/(-62 (-1+Z)/(3 (-8+7 Z)) + 2 (1 + 10 (-1+Z)/(3 (-8+7 Z))))}, c000 = Plus @@ MapThread[
      ReplacePart[Array[0 &, Length[cE0]], #1, #2] &, {c4Zplus, c000basis}];
    c000 = ReplacePart[c000, δmin[tRef] ξ000init[[4]] 2*^-26, 23];
    c000 = mCuInv2 (c000 + (ν0 /. δ → δmin[tRef]).ξ000init 1*^-26);
    ReplacePart[c000, 1, 27]]]
```

Note that the extra lattice site reservoir ΔN is set to 1 mole by this function that provides for the specified Z value (since X = 1) the initial $\boldsymbol{c^0}$ that will be used in the equation $c_j = c_j^0 + \sum_{r=1}^{22} \nu_{jr}\, \xi_r$ to solve the Gibbs-Duhem equation for the two-phase $Cu_{2-\delta}Se/\alpha$–$CuInSe_2$ equilibrium problem. For that problem X has been set to one, but once that solution is complete, many of the equations derived above will be used to derive $\boldsymbol{c^0}$ for the subsequent solution of the CIS α–β two phase equilibrium. This is an example showing the initial quasichemical species concentration vector for the mixture corresponding to exactly stoichiometric $CuInSe_2$:

c000[1] // N

$$\{0.5, 9.99902\times10^{-27}, 5.\times10^{-26}, 5.\times10^{-27}, 5.\times10^{-27}, 5.\times10^{-27}, 5.\times10^{-27},$$
$$5.\times10^{-27}, 5.\times10^{-27}, 5.\times10^{-27}, 5.\times10^{-27}, 5.\times10^{-27}, 5.\times10^{-27}, 4.5\times10^{-26},$$
$$5.\times10^{-27}, 5.\times10^{-27}, 5.\times10^{-27}, 5.\times10^{-27}, 5.\times10^{-27}, 5.\times10^{-27},$$
$$5.\times10^{-27}, 5.\times10^{-27}, -9.83246\times10^{-31}, 4.\times10^{-26}, 5.\times10^{-27}, 5.\times10^{-27}, 1.\}$$

1 / 2 – c000[1][[1]] // N (* total CIS_α deviation from 1/2 *)

0.

{1, 1} – cXZ[c000[1], $\mathcal{D}$0] /. $\delta \to 0$(* deviation from X=Z=1 *)
{1, 1} – cXZ[c000[1], $\mathcal{D}$0] /.
$\delta \to 1$(* the value of δ is irrelevant to the normalization *)

{0., 0.}
{0., 0.}

Reference State Chemical Potential Vector

The total chemical potential of a mole of the normal lattice cluster, CIS_α, is given by $\mathcal{G}^{CL}_{\alpha CIS} = \mathcal{G}^{SER}_{CuInSe2} + \Delta\mathcal{G}^{MIX}_{\alpha CIS}$. The excess Gibbs energy for the normal lattice cluster, CIS_α, is not known *a priori*, nor can it be directly computed from the boundary conditions derived previously for α–$CuInSe_2$, since those values are based on experimental data measured for the (presumably) stoichiometric compound in its defective equilibrium state. Instead this becomes a parameter which will be set by requiring that the equilibrium solution gives a predicted total Gibbs energy that matches $\mathcal{G}_{\alpha\text{–}CuInSe_2}$ when X = Z = 1. Note also that unlike every other cluster species in this model, the reference state for CIS_α is its state of pure aggregation, whereas the reference state for the other defects is their infinite dilution in a solvent lattice of CIS_α. The unknown specific molar free energy of the ideal CIS_α cluster is expressed in terms of its deviation from the empirical function for the same quantity of equilibrium (defective) α–CIS:

```
formula[1, 𝒟]
```

$$\{CIS_\alpha, 2\,Cu + 2\,In + 2\,M1 + 2\,M3 + 4\,Se + 4\,X6 + 8\,\mathcal{I}\}$$

```
g0αcl[tK_] := 2 g_HSER[cThermo_CuInSe2_α, tK] + Δg0αcl[tK]
    (* the specific molar free energy for the ideal cluster as a pure
       substance in terms of its deviation from the empirical data *)
```

The total chemical potential of a mole of each defective CIS building unit cluster is computed on the basis of its deviation from that of the same quantity of non-defective CIS, and is given by $\mathcal{G}^{CL}_j = \mathcal{G}^0_j + \Delta\mathcal{G}^{CL}_j$. The reference state free energy is $\mathcal{G}^0[m] = m * \mathcal{G}_{\alpha CIS}$, where m is the number of 16-site clusters in the given defect

cluster type j and $\mathcal{G}_{\alpha\mathrm{CIS}}$ has been computed above. Combining these expressions and separating out the effect of changing the total number of atoms yields:

$$\mathcal{G}_j^{\mathrm{CL}} = m * (\mathcal{G}_{\mathrm{CuInSe2}}^{\mathrm{SER}} + \Delta\mathcal{G}_{\alpha\mathrm{CIS}}^{\mathrm{MIX}}) + \Delta\mathcal{G}_j^{\mathrm{SER}} + \Delta\mathcal{H}_j^{\mathrm{XS}} + \Delta\mathcal{S}_j^{\mathrm{MIX}}.$$

Note that this approach insures the total Gibbs energy of any possible combination of clusters with the same total number of lattice sites is a sum of that of an equivalent number of CIS_α plus the deviation due to the defects. This satisfies assumption III in the formulation of the problem. The next task is to calculate $\Delta\mathcal{G}_j^{\mathrm{MIX}}$ for each defect cluster type j.

The first term in $\Delta\mathcal{G}_j^{\mathrm{MIX}}$ for each defect cluster type j is the deviation of the elemental contribution from $m * \mathcal{G}_{\mathrm{CuInSe2}}^{\mathrm{SER}}$, $\Delta\mathcal{G}_j^{\mathrm{SER}}$, computed as the cluster's elemental stoichiometry deviation from $m * \mathrm{CIS}_\alpha$ times the SER molar Gibbs energies of those elements. This quantity is derived for each of the lattice clusters in the basis $\boldsymbol{\alpha\beta}\mathbf{L}$. The secondary phase chemical potentials have already been derived and are not computed on the basis of this building unit model.

```
(* the list of unit cell multiplicities for each of the defect clusters *)
mcl = Array[ncL[[Position[αβL, cE[[#]]][[1, 1]]] &, 25]

    {1, 3, 3, 3, 3, 3, 3, 3, 3, 3, 3, 3, 3, 3, 3, 3, 3, 3, 5, 5, 5, 5, 3, 5}

g0cl[tK_] := mcl g0αcl[tK] ;(* the (defect−free) reference
    state free energy for the supercluster (as a pure substance)
    within which each corresponding defect will be embedded *)

Δg0cl_HSER[tK_] := (g_HSER[#, tK] & /@ a_thermo[tK]).Transpose[
      Drop[Transpose[Take[𝒟, 3]], −3] − mcl Array[Take[𝒟, 3][[All, 1]] &, 25]]
      (* (g_HSER[#,tK]&/@a_thermo[tK]).Take[𝒟,3] returns the
      length 25 vector of clusters' specific molar G0_SER's *)
```

Transpose[{Drop[cE, −3], Δg0clHSER[tSTP]}] // TableForm

CIS_{α}	0.
$\mathcal{V}_{Cu}^{x}$	9883.67
$\mathcal{V}_{Cu}^{\prime}$	9883.67
In_{Cu}^{x}	−7305.96
$In_{Cu}^{\bullet}$	−7305.96
$In_{Cu}^{\bullet\bullet}$	−7305.96
Cu_{In}^{x}	7305.96
$Cu_{In}^{\prime}$	7305.96
$Cu_{In}^{\prime\prime}$	7305.96
$\mathcal{V}_{In}^{x}$	17189.6
$\mathcal{V}_{In}^{\bullet}$	17189.6
$\mathcal{V}_{In}^{\bullet\bullet}$	17189.6
$\mathcal{V}_{In}^{\bullet\bullet\bullet}$	17189.6
$\mathcal{V}_{Se}^{x}$	12602.1
$\mathcal{V}_{Se}^{\bullet\bullet}$	12602.1
Cu_{i}^{x}	−9883.67
$Cu_{i}^{\bullet}$	−9883.67
$Cu_{i} \oplus \mathcal{V}_{Cu}$	0.
$Cu_{In} \oplus In_{Cu}$	0.
$\mathcal{V}_{Cu} \oplus In_{Cu}$	2577.71
$(\mathcal{V}_{Cu} \oplus In_{Cu})^{\bullet}$	2577.71
$(2\,\mathcal{V}_{Cu} \oplus In_{Cu})_{\alpha}$	12461.4
$(2\,\mathcal{V}_{Cu} \oplus In_{Cu})_{\beta 15}$	12461.4
$(2\,\mathcal{V}_{Cu} \oplus In_{Cu})_{\beta 13}$	12461.4
$(2\,\mathcal{V}_{Cu} \oplus In_{Cu})_{\beta 25}$	24922.8

The excess enthalpies, $\Delta\mathcal{H}_{j}^{XS}$, are derived immediately for the defect clusters by molar renormalization of the published atomic-scale formation enthalpies for individual lattice defect species calculated by *ab-initio* quantum mechanical calculations and reported in [70, Tables II and IV] and (for X6 sublattice defects) [78]. The values included for the $\mathcal{V}_{Cu} \oplus In_{Cu}$ and $(\mathcal{V}_{Cu} \oplus In_{Cu})^{\bullet}$ defects are calculated

here from unpublished calculations (S.-H. Wei) that the interaction energy for the addition of the first copper vacancy is -3.10 *e*V, much greater than that for the addition of the second that completes the NDC. This leads to a formation enthalpy value of 0.84 *e*V for $\mathcal{V}_{Cu} \oplus In_{Cu}$. Note that there is no entry in this list for the normal lattice cluster, CIS_α.

Because of their choice of the VBM as the zero of electromagnetic potential, that contribution is subtracted from the enthalpy of positively charged defects, whereas it is added to the negative defects' formation enthalpy. The energies of the delocalized charge carriers must be consistent with this choice of VBM as the potential reference. Excitation of an electron from the VB to the CB requires an amount of energy equal to the forbidden gap, and since the electron's charge is negative, the energetic contribution to its enthalpy is positive, just as with the other negatively charged species. A hole is located at the VBM so long as the carriers are under low-injection (as in equilibrium), so the electromagnetic potential contribution to its energy vanishes. Likewise since the ionization transition level of the $\mathcal{V}_{Cu} \oplus In_{Cu}$ neutral was estimated at $E_c - 0.2 = 0.84\,eV$ (exactly equal to its formation enthalpy), the reference enthalpy of $(\mathcal{V}_{Cu} \oplus In_{Cu})^{\blacksquare}$ vanishes.

```
Hf_defect_CIS := {0.6, 0.63, 3.34, 2.55, 1.85, 1.54, 1.83, 2.41, 3.04, 3.21, 3.62,
    4.29, 3.0, 2.06, 2.88, 2.04, 1.52, 0.65, 0.84, 0, 0.33, 0, −0.13, −0.12, eG, 0}

(*the conversion factor from eV → Joules*)
eV2Joule = First[Convert[1 ElectronVolt, Joule]]

    1.60218 × 10^−19

ΔhXSαβ = Join[{0}, Hf_defect_CIS * nAvo * eV2Joule];
```

Transpose[{Drop[cE, −1], ΔhXS$\alpha\beta$}] // TableForm

CIS_{α}	0
$\mathcal{V}_{\mathrm{Cu}}^{\mathrm{x}}$	57891.2
$\mathcal{V}_{\mathrm{Cu}}^{\prime}$	60785.8
$\mathrm{In}_{\mathrm{Cu}}^{\mathrm{x}}$	322261.
$\mathrm{In}_{\mathrm{Cu}}^{\bullet}$	246038.
$\mathrm{In}_{\mathrm{Cu}}^{\bullet\bullet}$	178498.
$\mathrm{Cu}_{\mathrm{In}}^{\mathrm{x}}$	148588.
$\mathrm{Cu}_{\mathrm{In}}^{\prime}$	176568.
$\mathrm{Cu}_{\mathrm{In}}^{\prime\prime}$	232530.
$\mathcal{V}_{\mathrm{In}}^{\mathrm{x}}$	293316.
$\mathcal{V}_{\mathrm{In}}^{\bullet}$	309718.
$\mathcal{V}_{\mathrm{In}}^{\bullet\bullet}$	349277.
$\mathcal{V}_{\mathrm{In}}^{\bullet\bullet\bullet}$	413922.
$\mathcal{V}_{\mathrm{Se}}^{\mathrm{x}}$	289456.
$\mathcal{V}_{\mathrm{Se}}^{\bullet\bullet}$	198760.
$\mathrm{Cu}_{\mathrm{i}}^{\mathrm{x}}$	277878.
$\mathrm{Cu}_{\mathrm{i}}^{\bullet}$	196830.
$\mathrm{Cu}_{\mathrm{i}} \oplus \mathcal{V}_{\mathrm{Cu}}$	146658.
$\mathrm{Cu}_{\mathrm{In}} \oplus \mathrm{In}_{\mathrm{Cu}}$	62715.5
$\mathcal{V}_{\mathrm{Cu}} \oplus \mathrm{In}_{\mathrm{Cu}}$	81047.7
$(\mathcal{V}_{\mathrm{Cu}} \oplus \mathrm{In}_{\mathrm{Cu}})^{\bullet}$	0
$(2\,\mathcal{V}_{\mathrm{Cu}} \oplus \mathrm{In}_{\mathrm{Cu}})_{\alpha}$	31840.2
$(2\,\mathcal{V}_{\mathrm{Cu}} \oplus \mathrm{In}_{\mathrm{Cu}})_{\beta 15}$	0
$(2\,\mathcal{V}_{\mathrm{Cu}} \oplus \mathrm{In}_{\mathrm{Cu}})_{\beta 13}$	−12543.1
$(2\,\mathcal{V}_{\mathrm{Cu}} \oplus \mathrm{In}_{\mathrm{Cu}})_{\beta 25}$	−11578.2
$\mathrm{e}^{\prime}$	96485.4 eG
$\mathrm{h}^{\bullet}$	0

The atomic species are presumed to have no internal structure that would effect their entropy other than unpaired electron spin degeneracy [278]. The configurational excess entropies are calculated using a simple mixing model incorporating Hagemark's nearest-neighbor site exclusion correction [279], adapted to

this three-sublattice model. The rationale for this is that a set of complexes has been incorporated whose interaction enthalpies have been independently calculated, so to permit point defects to occupy adjacent sites without any corresponding change in their energies due to those interactions would circumvent the value of incorporating their complexes as independent structural species. Likewise, if the exclusion zone for defect complexes is too small to incorporate all the nearest neighboring sublattice sites on which the complex resides, the statistical ensemble will include configurations that do not properly reflect the energetics.

This is implemented here by computing the configurational entropy for each lattice defect on a cluster comprised of an integral number of the 16-site (including the $\mathcal{I}$ sublattice) clusters identical to the 8-atom, 16-bond cluster used for published binary zincblende alloy cluster expansion calculations [118, figure 4.12], which in one defect-free configuration is the primitive unit cell of the chalcopyrite structure, CIS_{α}. The allowable lattice positions of a defect within its cluster are restricted to those sufficiently interior to prevent a defect on a neighboring lattice cluster from approaching close enough to interact with it in a configuration equivalent to complex formation. These are the considerations that led to the integers in the list **mcl**, which give the number of primitive unit cells in the cluster associated with the lattice site defects in the basis set $\boldsymbol{\alpha\beta}\mathbf{L}$. The total entropy of the lattice is then calculated using a cluster expansion.

The specific molar mixing entropy deviation for each cluster type, $\Delta\mathcal{S}_j^{\mathrm{MIX}}$, is initialized to zero, then the computed internal configurational entropy change for

each defect cluster is added. This is divided into two parts by $\Delta\mathcal{S}_j^{\mathrm{MIX}} = \Delta\mathcal{S}_j^{\mathrm{IDL}} + \Delta\mathcal{S}_j^{\mathrm{XS}}$. First the partition functions for the species in a normal defect-free 48-site lattice cluster are computed independently for each sublattice, because of their different multiplicities:

```
ΔsIDLcl = Array[0 &, 25];
ΔsXScl = Array[0 &, 25];
```

Surrounding every point defect on a normally-occupied site are 4 atoms in its first counterion coordination shell, and 12 in its second coordination shell (which contains only the same sublattice type: M or X) for a total of 16 atoms plus the defect. Thus if the point defect itself is restricted to a single site interior to the cluster, the 48-site exclusion zone is sufficient to guarantee that all these will be defect-free (which is not true for the next smaller 32-site, 16-atom cluster). There are six M1 and six M2 sublattice sites in each 48-site cluster. Since the metal vacancy is restricted to only one site on its sublattice within the cluster, there is no additional configurational degeneracy associated with its location. Similarly, the five remaining atoms on the same sublattice have only five lattice sites to occupy, so their is no change in the total configurational entropy. Identical arguments pertain to metal antisite defects.

The internal configurational entropy for selenium vacancy defect clusters do not vanish, however. The $\mathcal{V}_{\mathrm{Se}}$ defect is not involved in any defect complexes entering into this model, in contrast to every other point defect considered. Thus it has no exclusion zone associated with it and is permitted to occupy any X6 site in its associated cluster, of which there are 12. In the reference state there are 12 selenium

atoms to occupy those 12 sites, so there is no entropy contribution due to those selenium atoms' configuration on the X6 sublattice. The 11 selenium atoms in the cluster associated with the selenium vacancy can occupy any of the 12 sites so their configurational entropy contribution is Boltzmann's constant times the logarithm of the binomial $\binom{12}{11}$. This yields for a mole of either $\mathcal{V}_{\mathrm{Se}}^{\times}$ or $\mathcal{V}_{\mathrm{Se}}^{\bullet\bullet}$ clusters:

```
sConfig48clXV = rG Log[Binomial[12, 11]];
ΔsIDLcl = ΔsIDLcl + Plus @@
          (ReplacePart[Array[0 &, Length[ΔsIDLcl]], sConfig48clXV, #1] & /@ {14, 15});
{cE[[#]], ΔsIDLcl[[#]]} & /@ {14, 15}
```

$\{\{\mathcal{V}_{\mathrm{Se}}^{\times}, 20.6607\}, \{\mathcal{V}_{\mathrm{Se}}^{\bullet\bullet}, 20.6607\}\}$

```
(* This is equivalent to calculating the number of sites on
    which the one vacancy could be located: *) Binomial[12, 11] === 12
```

True

The internal configurational entropy for the sole interstitial point defect included in this model, Cu_i, does not vanish either. Their is an exclusion zone for the copper interstitial, unlike the selenium vacancy, since the former is component of the $\mathrm{Cu}_i \oplus \mathcal{V}_{\mathrm{Cu}}$ complex. Although there are an equal number of normally-occupied and interstitial sites in this model, their tetrahedral coordination make the four interstitials nearest to any normally-occupied site equivalent. Since the copper vacancy in the $\mathrm{Cu}_i \oplus \mathcal{V}_{\mathrm{Cu}}$ complex is restricted to a single site on the same sized cluster as the interstitital, the isolated interstitial will be allowed to occupy any of those same four in the absence of the vacancy. This yields for a mole of either $\mathrm{Cu}_i^{\times}$ or $\mathrm{Cu}_i^{\bullet}$ clusters:

```
sConfig48clCuI = rG Log[4];
ΔsIDLcl = ΔsIDLcl + Plus @@
        (ReplacePart[Array[0 &, Length[ΔsIDLcl]], sConfig48clCuI, #1] & /@ {16, 17});
{cE⟦#⟧, ΔsIDLcl⟦#⟧} & /@ {16, 17}
```

$\{\{Cu_i^x, 11.5263\}, \{Cu_i^{\bullet}, 11.5263\}\}$

The next correction is for the three defect complexes also associated with a 48-site exclusion zone cluster, $Cu_i \oplus \mathcal{V}_{Cu}$, $In_{Cu} \oplus Cu_{In}$, and $(2\mathcal{V}_{Cu} \oplus In_{Cu})_{\beta 1.3}$. The first two are restricted to nearest-neighbor site pairs. The copper interstitial/vacancy complex has exactly the same degeneracy as the lone interstitial since the vacancy is restricted to one site. The $In_{Cu} \oplus Cu_{In}$ complex occupies two sites, one on the M1 and one on the M3 sublattice, but as with the corresponding isolated point defects each is restricted to a single (but different) site on the cluster so there is no configurational entropy difference between it and its reference state. The β1.3 NDC occupies three unit cells, which collectively possess only six M1 sublattice sites. Only three of these are internal to the cluster and the component lattice point defects of the associate are restricted to these. Thus there is no internal configurational degeneracy associated with the β1.3 NDC cluster.

```
sConfig48clCuIV = rG Log[4];
ΔsIDLcl = ΔsIDLcl + Plus @@
        (ReplacePart[Array[0 &, Length[ΔsIDLcl]], sConfig48clCuIV, #1] & /@ {18});
{cE⟦#⟧, ΔsIDLcl⟦#⟧} & /@
  {18}
```

$\{\{Cu_i \oplus \mathcal{V}_{Cu}, 11.5263\}\}$

The remaining $\mathcal{V}_{Cu} \oplus In_{Cu}$, and $(2\mathcal{V}_{Cu} \oplus In_{Cu})$ defect complex cluster entropy deviations are computed using the 80-site exclusion zone (comprised of five

16-site clusters) previously described in conjunction with the NDC aggregation model of β–CIS phase formation. By using the same exclusion zone for the NDC in both α and β–CIS, the existence of a two-phase domain between them (a NDC miscibility gap) is not a presumed result of the statistical thermodynamics of this model. The neutral and ionized $\mathcal{V}_{Cu} \oplus In_{Cu}$ double-site complex is afforded the same exclusion zone as the triple-site complexes to insure a distinction in the configurational degeneracy between the combinations $2\,\mathcal{V}_{Cu} + In_{Cu}$, $\mathcal{V}_{Cu} + (\mathcal{V}_{Cu} \oplus In_{Cu})$, and $(2\,\mathcal{V}_{Cu} \oplus In_{Cu})$, which occupy nine, eight, and five 16-site clusters respectively.

The remaining corrections are for the defect complexes $(\mathcal{V}_{Cu} \oplus In_{Cu})^{\times}$, $(\mathcal{V}_{Cu} \oplus In_{Cu})^{\bullet}$, $(2\,\mathcal{V}_{Cu} \oplus In_{Cu})_{\alpha}$, $(2\,\mathcal{V}_{Cu} \oplus In_{Cu})_{\beta 1.5}$, and $(2\,\mathcal{V}_{Cu} \oplus In_{Cu})_{\beta 2.5}$. Note that their component point defects occur only on the M1 sublattice of which there are only 10 in a cluster this size. Also recall that the corresponding enthalpies are computed for the component point defects of these complexes arrayed on nearest-neighbor M1 sites along one of the two equivalent {110} directions (since tetragonal distortion makes the {101} directions inequivalent). Finally, the indium antisite must be between the two copper vacancies, further restricting the configurational degeneracy of these defect complexes on the cluster. Given these constraints the triple-defect complexes have only one possible configuration, but the double-defect clusters have a degeneracy due to the equivalence of the two sites for the $\mathcal{V}_{Cu}$.

```
sConfig80cl2M1 = rG Log[2];
ΔsIDLcl = ΔsIDLcl +
      Plus @@ (ReplacePart[Array[0 &, Length[ΔsIDLcl]], sConfig80cl2M1, #1] & /@
            {20, 21});
{cE⟦#⟧, ΔsIDLcl⟦#⟧} & /@ {20, 21}
```

$$\{\{\mathcal{V}_{Cu} \oplus In_{Cu}, 5.76315\}, \{(\mathcal{V}_{Cu} \oplus In_{Cu})^{\bullet}, 5.76315\}\}$$

```
ΔsIDLcl
```

```
{0, 0, 0, 0, 0, 0, 0, 0, 0, 0, 0, 0, 0, 20.6607, 20.6607,
  11.5263, 11.5263, 11.5263, 0, 5.76315, 5.76315, 0, 0, 0, 0}
```

The excess entropy due to two-fold electron spin degeneracy will next be added to $\Delta\mathcal{S}_j^{XS}$ for those charged defects with an unpaired electron spin [278]. The correction will be based on the assumption that they are unpaired if there are an odd-integral number of them. The correction obviously applies to electrons and holes, since they are unpaired.

```
sSpin = rG Log[2];
ΔsXScl =
    ΔsXScl + Plus @@ (ReplacePart[Array[0 &, Length[ΔsIDLcl]], sSpin, #1] & /@
            {3, 5, 8, 11, 13, 17, 21});
{cE⟦#⟧, ΔsXScl⟦#⟧} & /@ {3, 5, 8, 11, 13, 17, 21}
```

$$\{\{\mathcal{V}'_{Cu}, 5.76315\}, \{In^{\bullet}_{Cu}, 5.76315\}, \{Cu'_{In}, 5.76315\}, \{\mathcal{V}^{\bullet}_{In}, 5.76315\},$$
$$\{\mathcal{V}^{\bullet\bullet\bullet}_{In}, 5.76315\}, \{Cu^{\bullet}_{i}, 5.76315\}, \{(\mathcal{V}_{Cu} \oplus In_{Cu})^{\bullet}, 5.76315\}\}$$

The entropy of defect ionization will next be added to those cases, using an approximation due to van Vechten [168, 169] that equates these with the entropy of the forbidden gap. The latter quantity can be calculated from the coefficients of the Varshni equation, α and β, using the equation $\Delta S_g = -\partial_T E_g = \alpha T (T + 2\beta)/(T + \beta)^2$ [280]. These coefficients have been determined for CIS based on optical measurements near room temperature of single crystals by Nakanishi and coworkers [85], who

found $\beta = 0$ and $\alpha = 1.1\text{x}10^{-4}\ e\text{V}\cdot\text{K}^{-1}$. Since β vanishes, the preceding relation simplifies to $\Delta S_{cv} = \alpha$, which is added to the excess entropy of each charged defect.

```
ΔsXScl =
  ΔsXScl + Drop[(Abs[#]/Max[1, Abs[#]] & /@ 𝒟[[4]]), -3] (11*^-5) * nAvo * eV2Joule

    {0, 0, 16.3765, 0, 16.3765, 10.6134, 0, 16.3765, 10.6134, 0, 16.3765,
      10.6134, 16.3765, 0, 10.6134, 0, 16.3765, 0, 0, 0, 16.3765, 0, 0, 0, 0}
```

Although it would be appropriate to add other mixing entropy deviations like the vibrational correction for the cluster, insufficient data is available in the literature to compute the effect of the individual defects on the phonon spectrum except for the two $(2\mathcal{V}_{Cu} \oplus In_{Cu})_{\beta}$ defects. In their case it is known that the selenium A_1 breathing mode of the lattice shifts between α–CIS and β–CIS from 175 cm^{-1} to 152 cm^{-1}. The specific molar total internal mixing entropy deviations of the defect clusters from their reference states are tabulated below:

```
Transpose[{Drop[cE, −3], (ΔsIDLcl + ΔsXScl)}] // TableForm
```

CIS_{α}	0
$\mathcal{V}_{Cu}^{x}$	0
$\mathcal{V}_{Cu}^{\prime}$	16.3765
In_{Cu}^{x}	0
$In_{Cu}^{\bullet}$	16.3765
$In_{Cu}^{\bullet\bullet}$	10.6134
Cu_{In}^{x}	0
$Cu_{In}^{\prime}$	16.3765
$Cu_{In}^{\prime\prime}$	10.6134
$\mathcal{V}_{In}^{x}$	0
$\mathcal{V}_{In}^{\bullet}$	16.3765
$\mathcal{V}_{In}^{\bullet\bullet}$	10.6134
$\mathcal{V}_{In}^{\bullet\bullet\bullet}$	16.3765
$\mathcal{V}_{Se}^{x}$	20.6607
$\mathcal{V}_{Se}^{\bullet\bullet}$	31.2741
Cu_{i}^{x}	11.5263
$Cu_{i}^{\bullet}$	27.9029
$Cu_{i} \oplus \mathcal{V}_{Cu}$	11.5263
$Cu_{In} \oplus In_{Cu}$	0
$\mathcal{V}_{Cu} \oplus In_{Cu}$	5.76315
$(\mathcal{V}_{Cu} \oplus In_{Cu})^{\bullet}$	22.1397
$(2\,\mathcal{V}_{Cu} \oplus In_{Cu})_{\alpha}$	0
$(2\,\mathcal{V}_{Cu} \oplus In_{Cu})_{\beta 15}$	0
$(2\,\mathcal{V}_{Cu} \oplus In_{Cu})_{\beta 13}$	0
$(2\,\mathcal{V}_{Cu} \oplus In_{Cu})_{\beta 25}$	0

The foregoing results are combined using $\Delta\mathcal{G}_j^{CL} = \Delta\mathcal{G}_j^{SER} + \Delta\mathcal{H}_j^{XS} - T\,\Delta\mathcal{S}_j^{CL}$ to compute the specific molar free energy deviations of the defect clusters from their reference state. Since $\Delta\mathcal{H}_j^{XS}$ does not vanish for electrons, the charge carriers are added here and the bandgap energy specified. The temperature dependence of the forbidden gap is included using the Varshni equation $E_g = E_g^0 - \alpha T^2/(T+\beta)$ [87].

The reference value is taken to be 1.048 *e*V at 102K as measured by Niki and coworkers [86] on single-crystal epilayers.

```
eGα[tK_] := 1.048 − 1.1 10^−4 (tK − 102)

With[{Δs00 = Join[ΔsIDLcl + ΔsXScl, {0, 0}]},
  Δg00[tK_] := Join[Δg0clHSER[tK], {0, 0}] + (ΔhXSαβ /. eG → eGα[tK]) − tK Δs00]
```

Transpose[{Drop[cE, −1], Δg00[tSTP], Δg00[tK000], Δg00[tRef]}] // TableForm

CIS_{α}	0.	0.	0.
$\mathcal{V}^{x}_{Cu}$	67774.9	94619.5	107385.
$\mathcal{V}'_{Cu}$	65786.8	83636.	93114.1
In^{x}_{Cu}	314955.	299876.	294147.
$In^{\bullet}_{Cu}$	233849.	209774.	200758.
$In^{\bullet\bullet}_{Cu}$	168028.	147118.	139259.
Cu^{x}_{In}	155893.	170973.	176702.
Cu'_{In}	178992.	185076.	187518.
Cu''_{In}	236671.	245921.	249520.
$\mathcal{V}^{x}_{In}$	310505.	352429.	370923.
$\mathcal{V}^{\bullet}_{In}$	322025.	354954.	370161.
$\mathcal{V}^{\bullet\bullet}_{In}$	363302.	399397.	415761.
$\mathcal{V}^{\bullet\bullet\bullet\bullet}_{In}$	426229.	459158.	474365.
$\mathcal{V}^{x}_{Se}$	295898.	316743.	327421.
$\mathcal{V}^{\bullet\bullet}_{Se}$	202038.	217052.	225601.
Cu^{x}_{i}	264558.	231382.	216303.
$Cu^{\bullet}_{i}$	178627.	136456.	118090.
$Cu_{i} \oplus \mathcal{V}_{Cu}$	143221.	136890.	134577.
$Cu_{In} \oplus In_{Cu}$	62715.5	62715.5	62715.5
$\mathcal{V}_{Cu} \oplus In_{Cu}$	81907.2	90506.6	96385.9
$(\mathcal{V}_{Cu} \oplus In_{Cu})^{\bullet}$	−4023.24	−4419.18	−1826.87
$(2\,\mathcal{V}_{Cu} \oplus In_{Cu})_{\alpha}$	44301.6	82911.1	102712.
$(2\,\mathcal{V}_{Cu} \oplus In_{Cu})_{\beta 15}$	12461.4	51070.9	70872.2
$(2\,\mathcal{V}_{Cu} \oplus In_{Cu})_{\beta 13}$	−81.7145	38527.8	58329.1
$(2\,\mathcal{V}_{Cu} \oplus In_{Cu})_{\beta 25}$	13344.5	90563.6	130166.
e'	99034.9	93205.1	91074.8
$h^{\bullet}$	0	0	0

The foregoing results are combined to give the reference state specific chemical potentials of each of the basis species as given by $\mu_j^0 = \mathcal{G}^0[m] + \Delta\mathcal{G}_j$:

$\mu 00\alpha\beta$[tK_] := Join[Join[g0cl[tK], {0, 0}] + Δg00[tK], {0}]

The chemical potential of the entire CIS lattice is given by a cluster decomposition of its defect distribution with respect to the basis comprised of the clusters whose individual reference state specific free energies are given by the function above. The overall problem has now been made tractable by separating the strong short–range interactions between the point defects in the initial problem into internal interactions within clusters which can now be treated as weakly-interacting.

The chemical potentials of the delocalized charge carriers must also be corrected to account for Fermi-Dirac statistics. Rather than employ that full integral relation, an asymptotic approximation is used which has been shown to be within a factor of two over the range $n \lesssim 50\,\mathrm{N}_c$ (and presumably $p \lesssim 50\,\mathrm{N}_v$) [157, § 7.11]. With the zero of electrical potential at the VBM, the relations $n = \mathrm{N}_c\,\mathrm{Exp}\left[\frac{\eta - \mathrm{E_g}}{k\mathrm{T}}\right]$ and $p = \mathrm{N}_v\,\mathrm{Exp}\left[\frac{-\eta}{k\mathrm{T}}\right]$ approximate the Fermi-Dirac electron occupation probability of the CB and the complement of that probability for the VB, respectively. In the ideal lattice reference state there are no ionic defects so charge neutrality reduces to $n^0 = p^0$ and therefrom $\eta_0 = \frac{3\,k\,\mathrm{T}}{4}\,\mathrm{Log}\left[\frac{m_h}{m_e}\right] + \frac{\mathrm{E_g}}{2}$ [281, p. 245]. This is the value used to initialize variational free energy minima searches with ionized defects included.

The parabolic band effective-mass approximation can be applied to estimate the density of band states using $\mathrm{N}_c = 2\,g_c\left(\frac{2\pi\,m_e^*\,k\,\mathrm{T}}{h^2}\right)^{3/2}$ and $\mathrm{N}_v = 2\,g_v\left(\frac{2\pi\,m_h^*\,k\,\mathrm{T}}{h^2}\right)^{3/2}$, where g_c and g_v are the band degeneracies. These quantum mechanical density-of-states (DOS) expressions are *per* unit volume, and the concentrations in this model are molar. The conversion of units below takes the specific molar volume to be independent of composition, but uses empirical data to correct for thermal volume

expansion. The reduced mass and temperature are factored out of the expression $\left(\frac{2\pi m_e^* k}{h^2}\right)$ to give $\left(\frac{2\pi m_e k}{h^2}\right)\frac{m_e^*}{m_e}$ T and the constant prefactor converted to units of mole^{-1} of CIS.

```
(* units of cm^-3/mole *)
molVolCIScc[tK_] := With[{linTCE = 6.60 10^-6 , molVolSTP = 58.281},
    molVolSTP (1 + (tK – tSTP) linTCE)^3]
```

$$\text{Convert}\left[\left(\frac{2\pi\ \text{ElectronMass BoltzmannConstant 1 Kelvin}}{\text{PlanckConstant}^2}\right)^{3/2},\ (\text{Centi Meter})^{-3}\right]$$

$$\frac{2.41469\times 10^{15}}{\text{Centi}^3\ \text{Meter}^3}$$

```
molDOSαCIS[tK_] := With[{qmDOSfree =
    First[Convert[((2 π ElectronMass BoltzmannConstant 1 Kelvin)/PlanckConstant^2)^(3/2),
      (Centi Meter)^-3]]}, molVolCIScc[tK] 2 qmDOSfree tK^(3/2)]

cbDOSαCIS[tK_] :=
  With[{meReduced = 0.09, gCB = 1}, gCB molDOSαCIS[tK] meReduced^(3/2)]
vbDOSαCIS[tK_] := With[{mhReduced = 0.73, gVB = 1},
    gVB molDOSαCIS[tK] mhReduced^(3/2)]

{cbDOSαCIS[tRef], vbDOSαCIS[tRef]}
```

$$\{2.61728\times 10^{20},\ 6.04604\times 10^{21}\}$$

```
μF0αeV[tK_] := With[{meReduced = 0.09, mhReduced = 0.73, gCB = 1, gVB = 1,
    eVBoltzmann = First[Convert[BoltzmannConstant 1 Kelvin, ElectronVolt]]},
  1/2 (eGα[tK] + 3/2 eVBoltzmann tK Log[mhReduced/meReduced])]
```

The electrochemical potentials η_e and η_h reduce to the chemical potential μ_e and μ_h in the absence of an applied electrostatic potential since $\eta \doteq \mu + q\,\phi$. The

product of the two carrier concentrations is $np = N_c\, N_v\, \mathrm{Exp}\left[\frac{-E_g}{kT}\right]$, constant for any given temperature in this approximation. Thus neither can their concentrations nor their chemical potentials both be independent variables. This is of course a reflection of the fact that a (free) hole is an unoccupied single-electron valence band state and is thus defined implicitly as the absence of an electron. The conduction band electron concentration is taken here as the independent variable, with the hole concentration given by the expression for the *np* product given above divided by *n*. This permits both of the charge carriers' chemical potentials to be derived from the usual expressions for enthalpy plus the band entropy with only one variable, *n*.

```
npα[tK_] :=
  With[{eVBoltzmann = First[Convert[BoltzmannConstant 1 Kelvin, ElectronVolt]]},
    cbDOSαCIS[tK] vbDOSαCIS[tK] Exp[-eGα[tK] / (tK eVBoltzmann)]]

npαcc[tK_] := npα[tK] / molVolCIScc[tK]^2

(* band entropy of charge carriers in eV/carrier at the intrinsic point *)
rG tRef / nAvo eV2Joule
{Log[Sqrt[npα[tRef]] / cbDOSαCIS[tRef]], Log[Sqrt[npα[tRef]] / vbDOSαCIS[tRef]]}

{-0.330162, -0.613762}

(* Gibbs energy for charge carriers in eV/carrier at the intrinsic point *)
{eGα[tRef], 0} + %

{0.613762, -0.613762}

μF0αeV[tRef]

0.613762
```

(* the electron−hole equilibrium is satisfied *) Plus @@ %%

0.

(* Gibbs energy for charge carriers in eV/carrier *) With[{n = 3*^20},

$$\frac{\text{rG tRef}}{\text{nAvo eV2Joule}}\left\{\text{Log}[\text{n}/\text{cbDOS}\alpha\text{CIS}[\text{tRef}]],\ \text{Log}\left[\frac{\text{np}\alpha[\text{tRef}]}{\text{n}}\Big/\text{vbDOS}\alpha\text{CIS}[\text{tRef}]\right]\right\}+\{\text{eG}\alpha[\text{tRef}],\ 0\}\Big]$$

{0.95625, −0.95625}

eGα[tRef]

0.943924

(* the equilibrium electron and hole molar concentrations in intrinsic defect−free $CuInSe_2$ at tRef *)

$$\text{With}\Big[\{\text{eVBoltzmann} = \text{First}[\text{Convert}[\text{BoltzmannConstant 1 Kelvin},\ \text{ElectronVolt}]]\},\ \Big\{\text{cbDOS}\alpha\text{CIS}[\text{tRef}]\ \text{Exp}\Big[\frac{-(\text{eG}\alpha[\text{tRef}]-\mu\text{F0}\alpha\text{eV}[\text{tRef}])}{\text{tRef eVBoltzmann}}\Big],\ \text{vbDOS}\alpha\text{CIS}[\text{tRef}]\ \text{Exp}\Big[\frac{-\mu\text{F0}\alpha\text{eV}[\text{tRef}]}{\text{tRef eVBoltzmann}}\Big]\Big\}\Big]$$

$\{6.76623\times10^{18},\ 6.76623\times10^{18}\}$

The specific molar chemical potential of each type of basis cluster within their mixture that represents the actual state of the lattice is given by $\mu_j = \mu_j^0 + \Delta\mathcal{G}_j^{\text{CNFG}}$. The concentrations entering into the computation of mixing entropies must be normalized to the total of only those that are actually on the lattice, including the β–CIS building units but excluding the charge carriers and ΔN. To calculate $\Delta\mathcal{G}_j^{\text{CNFG}}$ the expression $\Delta\mathcal{G}_j^{\text{CNFG}} = \text{R T Log}[\text{n}_j]$ is used [158, §8.8]. A cluster associated with any given defect type is in a distinguishable configuration when centered on any of the unit cells in the lattice. Thus it is not the molar concentrations, the c_j, which enter into the configurational entropy calculations, but rather the number of a given cluster

type normalized to the total number of unit cells.

Inasmuch as they are confined in this model to the α–CIS phase, the charge carriers' band entropy contributions to their respective specific molar chemical potentials must use band DOS normalized to the total mole fraction of the CIS_{α} species alone. This corrects for changes in the number of band states when the number of unit cells on the lattice that form those bands change. The additive term in the electrons' chemical potential corresponds to the enthalpy of the electron, and that term vanishes for holes since the zero of potential is the VBM.

$$\mu 0\alpha\beta[c\_, tK\_] /; Length[c] == Length[cE] :=$$
$$With\Big[\{n = (mcl\,Take[c, 25])/Plus\,@@\,(mcl\,Take[c, 25]), nCIS\alpha = nAvo\,c/First[c]\},$$
$$\mu 00\alpha\beta[tK] +$$
$$rG\,tK\;Join\Big[Log[\,n], \Big\{Log\Big[\frac{nCIS\alpha[\![25]\!]}{cbDOS\alpha CIS[tK]}\Big], Log\Big[\frac{nCIS\alpha[\![26]\!]}{vbDOS\alpha CIS[tK]}\Big], 0\Big\}\Big]\Big]$$

The cluster basis set for the $Cu_{2-\delta}Se/\alpha$–CIS two-phase equilibrium problem does not include the β–CIS clusters, so a different function must be defined for the secondary phase reference state chemical potentials in that case. The corresponding species in the cluster chemical potential vector $\mu 00\alpha\beta$ are replaced by the partial molar free energy functions for binary copper selenide derived in a preceding section. The chemical potential of $Cu_{2-\delta}Se$ is related to that of $Cu_{1-x}Se_x$ by a normalization factor of $(3-\delta)$ since that secondary phase's specific molar Gibbs energy was derived for a total of one mole of its consitutent atoms. The value of δ associated with the species Cu2δSe will always be taken to correspond to its minimum stable value, given by the function δmin[T]. The specific molar Gibbs

energy associated with the species Cu_{Cu2Se} is the difference between the $Cu_{2-\delta}Se$ phase's total Gibbs energy when it's total copper content is the sum of both contributions, and its reference state (minimum selenium content) value. This formulation assures that the total Gibbs energy of the secondary phase (which is calculated as the inner product of the chemical potential and solution concentration vectors) is always equal to the product of the number of moles of Cu2.δSe and its specific Gibbs energy for the net value of δ.

The mixing entropy calculation for this problem must also include the $Cu_{2-\delta}Se$ components as a single distinct species. The mixing entropy is associated entirely with the species Cu2.δSe, since the division of that phases total copper content between the two species Cu2.δSe (with $\delta = \delta_{min}$) and Cu_{Cu2Se} is a computational construct which allows the solution algorithm to vary the secondary phase's equilibrium composition *via* an independent variable in search of the system's complete equilibrium. One consequence of this is that Cu_{Cu2Se} must be constrained to be negative.

{cE0[[23]], cE0[[24]]}

{Cu_{Cu2Se}, Cu2.δSe}

```
μ00[c_, tK_] /; Length[c] == Length[cE0] :=
  With[{n = (#/Plus @@ #) &[Join[Take[mcl Take[c, 25], 22], {c[[24]]}]],
    δm = δmin[tK], δ0 = δmin[tK] − c[[23]]/c[[24]], nCISα = nAvo c/First[c]},
   ReplacePart[ReplacePart[Drop[μ00αβ[tK], {25}], ((3 − δ0) G_CuSeX[tK, (3 − δ0)^−1] −
       (3 − δm) G_CuSeX[tK, (3 − δm)^−1]) (δm − δ0)^−1, 23],
     (3 − δm) G_CuSeX[tK, (3 − δm)^−1], 24] + rG tK Join[Log[Drop[n, −1]],
     {0, Log[Last[n]], Log[nCISα[[25]]/cbDOSαCIS[tK]], Log[nCISα[[26]]/vbDOSαCIS[tK]], 0}]]
```

Now the total free energy of the entire system in its initialized (non-equilibrium) configuration can be expressed as the weighted sum of its component species' chemical potentials.

```
g00[Z_, tK_] := c000[Z] μ00[c000[Z], tK]
```

```
g00[1, tRef] /. Δg0αcl[tRef] → 0
```

```
{−467736., −3.20483×10^−20, −1.6027×10^−19, −1.51221×10^−20,
  −1.55891×10^−20, −1.58966×10^−20, −1.57093×10^−20,
  −1.56553×10^−20, −1.53453×10^−20, −1.47382×10^−20, −1.47421×10^−20,
  −1.45141×10^−20, −1.4221×10^−20, −1.3374×10^−19, −1.54649×10^−20,
  −1.55113×10^−20, −1.60024×10^−20, −1.592×10^−20, −1.62793×10^−20,
  −2.54434×10^−20, −2.59344×10^−20, −2.54117×10^−20, 3.11054×10^−27,
  −3.03204×10^−20, −1.81597×10^−21, −2.40816×10^−21, 0}
```

```
g_HSER[cThermo_CuInSe2_α, tRef] − Plus @@ %
  (* computes the difference between the literature reference
       value and the model value for this non−equilibrium c000[Z] *)
```

```
0.
```

Reaction Extents Vector

The functional dependence of the total chemical potentials have already been computed in terms of the temperature and concentration vector, so the latter must now be connected to the reaction extents *via* the relationship $c_j = c_j^0 + \sum_{r=1}^{22} \nu_{jr}\, \xi_r$. Although the stoichiometry matrix in the Gibbs-Duhem relation $\sum_{j=1}^{27} \nu_{\mathrm{jr}}\, \mu_j = 0$ is constrained by its common basis with the chemical potential vector, the stoichiometry matrix used to calculate the concentration vector is not so limited. Since its component column vectors $\hat{\nu_r}$ form a nullspace basis for the set of all reactions that leave the conserved quantitites unchanged, homogeneous linear combinations of them may also be used to span the nullspace.

Computing the equilibrium defect cluster concentration vector by determining the reaction extents that satisfy the Gibbs-Duhem relations is facilitated by first restructuring the original reaction stoichiometry matrix ν to isolate the relatively large free energy contributions due to the reference state CIS_α clusters found in every reaction therein. Linear combinations are also chosen to eliminate the ideal CIS_α cluster from all ionization reactions, giving their ionized state energies in terms of reactions between the neutral defect and the charge carriers. The ionization equilibria can thereafter be parameterized using the electrochemical potential.

Inspection of the neutral species free energies *per* primitive unit cell at the maximum temperature of the calculation (sorted by increasing excess free energy in the table below) show that the most energetically favorable defect clusters are the NDC, its dissociation components, and the cation antisite pair $\mathrm{In_{Cu}} \oplus \mathrm{Cu_{In}}$:

```
RotateRight[Sort[
    RotateRight[Extract[Transpose[{cE, (μ00αβ[tRef] /. Δg0αcl[tRef] → 0)/Join[mcl, {1, 1, 1}]}], {{1}, {2},
        {4}, {7}, {10}, {14}, {16}, {18}, {19}, {20}, {22}}], {0, 1}]], {0, 1}] // TableForm
```

CIS_{α}	−935471.
$\mathcal{V}_{Cu} \oplus In_{Cu}$	−916194.
$(2\,\mathcal{V}_{Cu} \oplus In_{Cu})_{\alpha}$	−914929.
$Cu_{In} \oplus In_{Cu}$	−914566.
$\mathcal{V}_{Cu}^{x}$	−899676.
$Cu_{i} \oplus \mathcal{V}_{Cu}$	−890612.
Cu_{In}^{x}	−876571.
Cu_{i}^{x}	−863370.
In_{Cu}^{x}	−837422.
$\mathcal{V}_{Se}^{x}$	−826331.
$\mathcal{V}_{In}^{x}$	−811830.

This suggests that consolidating these defects into a smaller number of the basis reactions could reduce the number of reaction extents with a dominant effect on the overall equilibrium. Implementing these principles lead to the following preferred basis:

```
ν0ξ = ν0;
ν0ξ =
    Transpose[ReplacePart[Transpose[ν0ξ], ν0⟦All, 1⟧ + 2 ν0⟦All, 4⟧ + ν0⟦All, 6⟧, 1]] //
      Simplify;
ν0ξ = Transpose[ReplacePart[Transpose[ν0ξ], ν0⟦All, 3⟧ + ν0⟦All, 2⟧, 3]];
ν0ξ = Transpose[ReplacePart[Transpose[ν0ξ], −ν0⟦All, 6⟧ + ν0⟦All, 8⟧, 6]];
ν0ξ = Transpose[ReplacePart[Transpose[ν0ξ], ν0⟦All, 7⟧ + ν0⟦All, 3⟧ − ν0⟦All, 8⟧, 7]];
ν0ξ =
    Transpose[ReplacePart[Transpose[ν0ξ], ν0⟦All, 8⟧ + ν0⟦All, 12⟧ + ν0⟦All, 20⟧, 8]];
ν0ξ = Transpose[ReplacePart[Transpose[ν0ξ],
      ν0⟦All, 11⟧ + ν0⟦All, 3⟧ − ν0⟦All, 12⟧, 11]];
ν0ξ = Transpose[ReplacePart[Transpose[ν0ξ], ν0⟦All, 12⟧ − 2 ν0⟦All, 10⟧, 12]];
ν0ξ = Transpose[ReplacePart[Transpose[ν0ξ], ν0⟦All, 13⟧ + 2 ν0⟦All, 3⟧, 13]];
ν0ξ = Transpose[
      ReplacePart[Transpose[ν0ξ], ν0⟦All, 14⟧ + 3 ν0⟦All, 3⟧ − ν0⟦All, 17⟧, 14]];
ν0ξ = Transpose[ReplacePart[Transpose[ν0ξ],
        ν0⟦All, 15⟧ + 2 ν0⟦All, 3⟧ − ν0⟦All, 17⟧, 15]];
ν0ξ = Transpose[ReplacePart[Transpose[ν0ξ],
        ν0⟦All, 16⟧ + ν0⟦All, 3⟧ − ν0⟦All, 17⟧, 16]];
ν0ξ = Transpose[ReplacePart[Transpose[ν0ξ],
        ν0⟦All, 17⟧ + ν0⟦All, 12⟧ − ν0⟦All, 20⟧, 17]];
ν0ξ = Transpose[ReplacePart[Transpose[ν0ξ],
        ν0⟦All, 18⟧ + 2 ν0⟦All, 2⟧ − ν0⟦All, 20⟧, 18]];
ν0ξ = Transpose[ReplacePart[Transpose[ν0ξ],
      ν0⟦All, 19⟧ + ν0⟦All, 2⟧ − ν0⟦All, 20⟧, 19]];
ν0ξ = Transpose[ReplacePart[Transpose[ν0ξ], ν0⟦All, 20⟧ − 2 ν0⟦All, 9⟧, 20]];
ν0ξ = Transpose[ReplacePart[Transpose[ν0ξ], ν0⟦All, 21⟧ + 2 ν0⟦All, 3⟧, 21]];
ν0ξ = Transpose[ReplacePart[Transpose[ν0ξ], ν0⟦All, 22⟧ + ν0⟦All, 3⟧, 22]];

rxn[i_, ν0ξ] := ν0ξ⟦All, i⟧.cE0
```

Array[{#, rxn[#, $\nu 0\xi$]} &, 22] // TableForm

1	$2\,\text{Cu2}\_\delta\text{Se} + \Delta\text{N} + (-\frac{11}{2} + 6\,\delta)\,\text{CIS}_\alpha - 2\,\delta\,\mathcal{V}^{\text{x}}_{\text{Cu}} + (2\,\mathcal{V}_{\text{Cu}} \oplus \text{In}_{\text{Cu}})_\alpha$
2	$\text{h}^{\bullet} - \mathcal{V}^{\text{x}}_{\text{Cu}} + \mathcal{V}'_{\text{Cu}}$
3	$\text{h}^{\bullet} + \text{e}'$
4	$\text{Cu2}\_\delta\text{Se} + 3\,(-3+\delta)\,\text{CIS}_\alpha + (2-\delta)\,\mathcal{V}^{\text{x}}_{\text{Cu}} + \mathcal{V}^{\text{x}}_{\text{Se}}$
5	$-3\,\text{CIS}_\alpha + \text{Cu}_{\text{Cu2Se}} + \mathcal{V}^{\text{x}}_{\text{Cu}}$
6	$\mathcal{V}_{\text{Cu}} \oplus \text{In}_{\text{Cu}} - 3\,\text{CIS}_\alpha + \mathcal{V}^{\text{x}}_{\text{Cu}} - (2\,\mathcal{V}_{\text{Cu}} \oplus \text{In}_{\text{Cu}})_\alpha$
7	$-(\mathcal{V}_{\text{Cu}} \oplus \text{In}_{\text{Cu}}) + (\mathcal{V}_{\text{Cu}} \oplus \text{In}_{\text{Cu}})^{\bullet} + \text{e}'$
8	$\mathcal{V}_{\text{Cu}} \oplus \text{In}_{\text{Cu}} - 11\,\text{CIS}_\alpha + \text{Cu}^{\text{x}}_{\text{i}} + \text{Cu}^{\text{x}}_{\text{In}}$
9	$\text{Cu}_{\text{In}} \oplus \text{In}_{\text{Cu}} - 3\,\text{CIS}_\alpha$
10	$\text{Cu}_{\text{i}} \oplus \mathcal{V}_{\text{Cu}} - 3\,\text{CIS}_\alpha$
11	$-\text{Cu}^{\text{x}}_{\text{i}} + \text{Cu}^{\bullet}_{\text{i}} + \text{e}'$
12	$-2\,(\text{Cu}_{\text{i}} \oplus \mathcal{V}_{\text{Cu}}) + \text{Cu}^{\text{x}}_{\text{i}} + \mathcal{V}^{\text{x}}_{\text{Cu}}$
13	$-\mathcal{V}^{\text{x}}_{\text{Se}} + \mathcal{V}^{\bullet\bullet}_{\text{Se}} + 2\,\text{e}'$
14	$-\mathcal{V}^{\text{x}}_{\text{In}} + \mathcal{V}^{\bullet\bullet\bullet}_{\text{In}} + 3\,\text{e}'$
15	$-\mathcal{V}^{\text{x}}_{\text{In}} + \mathcal{V}^{\bullet\bullet}_{\text{In}} + 2\,\text{e}'$
16	$-\mathcal{V}^{\text{x}}_{\text{In}} + \mathcal{V}^{\bullet}_{\text{In}} + \text{e}'$
17	$-3\,\text{CIS}_\alpha + \text{Cu}^{\text{x}}_{\text{i}} - \text{Cu}^{\text{x}}_{\text{In}} + \mathcal{V}^{\text{x}}_{\text{In}}$
18	$2\,\text{h}^{\bullet} - \text{Cu}^{\text{x}}_{\text{In}} + \text{Cu}''_{\text{In}}$
19	$\text{h}^{\bullet} - \text{Cu}^{\text{x}}_{\text{In}} + \text{Cu}'_{\text{In}}$
20	$-2\,(\text{Cu}_{\text{In}} \oplus \text{In}_{\text{Cu}}) + \text{Cu}^{\text{x}}_{\text{In}} + \text{In}^{\text{x}}_{\text{Cu}}$
21	$-\text{In}^{\text{x}}_{\text{Cu}} + \text{In}^{\bullet\bullet}_{\text{Cu}} + 2\,\text{e}'$
22	$-\text{In}^{\text{x}}_{\text{Cu}} + \text{In}^{\bullet}_{\text{Cu}} + \text{e}'$

The chemical potential minimization procedure employed varies the values of the reaction extent vector $\boldsymbol{\xi}$'s components, with all other parameters in the equations $\sum_{j=1}^{27} \nu_{\text{jr}}\ \mu_j = \sum_{j=1}^{27} \nu_{\text{jr}}\ \left(\mu_j^0 + \text{R T Log}\left[\ \text{c}_j^0 + \sum_{r=1}^{22} \nu_{jr}\ \xi_r\right]\right) = 0$ fixed. Thus the only independent variables are the 22 components of $\boldsymbol{\xi}$.

```
ξ000 = {ξ001, ξ002, ξ003, ξ004, ξ005, ξ006, ξ007, ξ008, ξ009, ξ0010, ξ0011, ξ0012,
      ξ0013, ξ0014, ξ0015, ξ0016, ξ0017, ξ0018, ξ0019, ξ0020, ξ0021, ξ0022};
Protect[ξ000];
c0ξ[Z_, tK_] := c000[Z] + (ν0ξ /. δ → δmin[tK]).ξ000
```

Defect Quasichemical Reaction Equilibria Calculation

Solution of the Gibbs-Duhem relation $\sum_{j=1}^{27} \nu_{\mathrm{jr}}\ \mu_j = 0$ can be expedited by using a functional defined to return its left-hand-side, the list of reaction affinities [158, §11.8]:

```
gd0CIS[Z_, tK_, Δg0CISαcl_] :=
  ((μ00[c0ξ[#1, #2], #2] /. Δg0αcl[#2] → #3).(ν0 /. δ → δmin[#2])) &[Z, tK, Δg0CISαcl]
```

Computation of the solution of this complete set of simultaneous reactions is simplified by first approximately solving only the strongly-coupled neutral (charge-free) reactions, of which there are ten.

```
neutralRxns = {1, 4, 5, 6, 8, 9, 10, 12, 17, 20};
```

```
Extract[Array[{#, rxn[#, ν0ξ]} &, 22], Thread[{neutralRxns}]] // TableForm
```

1	$2\,\mathrm{Cu2}\_\delta\mathrm{Se} + \Delta\mathrm{N} + (-\frac{11}{2} + 6\,\delta)\,\mathrm{CIS}_\alpha - 2\,\delta\,\mathcal{V}^{\mathrm{x}}_{\mathrm{Cu}} + (2\,\mathcal{V}_{\mathrm{Cu}} \oplus \mathrm{In}_{\mathrm{Cu}})_\alpha$
4	$\mathrm{Cu2}\_\delta\mathrm{Se} + 3\,(-3+\delta)\,\mathrm{CIS}_\alpha + (2-\delta)\,\mathcal{V}^{\mathrm{x}}_{\mathrm{Cu}} + \mathcal{V}^{\mathrm{x}}_{\mathrm{Se}}$
5	$-3\,\mathrm{CIS}_\alpha + \mathrm{Cu}_{\mathrm{Cu2Se}} + \mathcal{V}^{\mathrm{x}}_{\mathrm{Cu}}$
6	$\mathcal{V}_{\mathrm{Cu}} \oplus \mathrm{In}_{\mathrm{Cu}} - 3\,\mathrm{CIS}_\alpha + \mathcal{V}^{\mathrm{x}}_{\mathrm{Cu}} - (2\,\mathcal{V}_{\mathrm{Cu}} \oplus \mathrm{In}_{\mathrm{Cu}})_\alpha$
8	$\mathcal{V}_{\mathrm{Cu}} \oplus \mathrm{In}_{\mathrm{Cu}} - 11\,\mathrm{CIS}_\alpha + \mathrm{Cu}^{\mathrm{x}}_{\mathrm{i}} + \mathrm{Cu}^{\mathrm{x}}_{\mathrm{In}}$
9	$\mathrm{Cu}_{\mathrm{In}} \oplus \mathrm{In}_{\mathrm{Cu}} - 3\,\mathrm{CIS}_\alpha$
10	$\mathrm{Cu}_{\mathrm{i}} \oplus \mathcal{V}_{\mathrm{Cu}} - 3\,\mathrm{CIS}_\alpha$
12	$-2\,(\mathrm{Cu}_{\mathrm{i}} \oplus \mathcal{V}_{\mathrm{Cu}}) + \mathrm{Cu}^{\mathrm{x}}_{\mathrm{i}} + \mathcal{V}^{\mathrm{x}}_{\mathrm{Cu}}$
17	$-3\,\mathrm{CIS}_\alpha + \mathrm{Cu}^{\mathrm{x}}_{\mathrm{i}} - \mathrm{Cu}^{\mathrm{x}}_{\mathrm{In}} + \mathcal{V}^{\mathrm{x}}_{\mathrm{In}}$
20	$-2\,(\mathrm{Cu}_{\mathrm{In}} \oplus \mathrm{In}_{\mathrm{Cu}}) + \mathrm{Cu}^{\mathrm{x}}_{\mathrm{In}} + \mathrm{In}^{\mathrm{x}}_{\mathrm{Cu}}$

The CIS_α cluster appears in all these reactions except 12 and 20, which couple to CIS_α *via* reactions eight, nine and ten. Since the $\mathrm{Cu}^{\mathrm{x}}_i$ and $\mathrm{Cu}^{\mathrm{x}}_{\mathrm{In}}$ species couple all these to reaction 17 but do not appear in any other neutral reactions, the complete set of neutral reactions decomposes into two subspaces coupled strongly by reactions six

and eight which both contain the dominant defect at the reference temperature, $\mathcal{V}_{Cu} \oplus In_{Cu}$. The remaining reactions all involve charged species but no CIS_{α}:

```
ionizationRxns = Complement[Array[# &, 22], neutralRxns]
```

```
{2, 3, 7, 11, 13, 14, 15, 16, 18, 19, 21, 22}
```

```
Extract[Array[{#, rxn[#, ν0ξ]} &, 22], Thread[{ionizationRxns}]] // TableForm
```

2	$h^{\bullet} - \mathcal{V}_{Cu}^{x} + \mathcal{V}'_{Cu}$
3	$h^{\bullet} + e'$
7	$-(\mathcal{V}_{Cu} \oplus In_{Cu}) + (\mathcal{V}_{Cu} \oplus In_{Cu})^{\bullet} + e'$
11	$-Cu_i^{x} + Cu_i^{\bullet} + e'$
13	$-\mathcal{V}_{Se}^{x} + \mathcal{V}_{Se}^{\bullet\bullet} + 2\,e'$
14	$-\mathcal{V}_{In}^{x} + \mathcal{V}_{In}^{\bullet\bullet\bullet} + 3\,e'$
15	$-\mathcal{V}_{In}^{x} + \mathcal{V}_{In}^{\bullet\bullet} + 2\,e'$
16	$-\mathcal{V}_{In}^{x} + \mathcal{V}_{In}^{\bullet} + e'$
18	$2\,h^{\bullet} - Cu_{In}^{x} + Cu_{In}''$
19	$h^{\bullet} - Cu_{In}^{x} + Cu_{In}'$
21	$-In_{Cu}^{x} + In_{Cu}^{\bullet\bullet} + 2\,e'$
22	$-In_{Cu}^{x} + In_{Cu}^{\bullet} + e'$

The Gibbs-Duhem functional on the neutral reaction set is defined as:

```
gd00CIS[Z_: 1, tK_, Δg0CISαcl_: 0] :=
  Extract[gd0CIS[Z, tK, Δg0CISαcl], Thread[{neutralRxns}]]
```

The initial concentration vector prior to any reactions is far from the correct solution, for which every reaction's affinity should be zero:

```
initialAffinities = gd0CIS[1, tRef, 0] /. Thread[ξ000 → Array[0 &, 22]]
```

```
{1.37837 × 10^6, −481877., −362951., −1.72105 × 10^6, −401897., 610483., 106967.,
  205424., −449442., −377581., −793044., −694587., −121457., 142199., 83838.1,
  38482.1, 39488.4, −480161., −542407., −553466., −155375., −93632.2}
```

The convergence of the solution algorithm will be characterized by the total standard deviation from zero of the calculated reaction affinities:

$$\sigma\text{SD[list\_?VectorQ]} := \text{Plus @@ } \sqrt{\text{list}^2}$$

$$\sigma\text{SD[initialAffinities]}$$

$$9.83418 \times 10^6$$

The initial solution is estimated by manual variation of the list of neutral species concentrations, with general guidance provided by the preceding compilation of their free energies *per* primitive unit cell:

```
{0.00018 , 0.3*^-11 , −1.82*^-8, 6.3*^-6 ,
    5.4*^-10, 0.000124, 3.08*^-8, −5.397*^-10, 1.*^-18, 1.5*^-16};
Fold[Insert[#, 0, #2] &, %, Thread[{Complement[Array[# &, 22], neutralRxns ]}]];
Thread[ξ000 → %];
Thread[{neutralRxns, (gd00CIS[1, tRef, 0] /. %), (gd00CIS[1, tRef, 0] /. %) /
        Extract[initialAffinities, Thread[{neutralRxns}]]}] // TableForm
{"neutral solution convergence σSD", σSD[%[[All, 2]]]}
Extract[Thread[{cE0, c000[1] + (ν0ξ /. δ → δmin[tRef]).%%%%}],
    {{1}, {2}, {4}, {7}, {10}, {14}, {16}, {18}, {19}, {20}, {22}, {23}, {24}}] // ScientificForm
```

1	198909.	0.144308
4	−168208.	0.0977357
5	13229.6	−0.032918
6	17785.9	0.0291342
8	1238.47	0.00602887
9	20.325	−0.0000452228
10	−156.002	0.000413161
12	−608.37	0.000875872
17	−950.934	−0.0240814
20	−1259.56	0.00227576

{neutral solution convergence σ_{SD}, 402367.}

{{CIS_α, 4.98619×10^{-1}}, {$\mathcal{V}^x_{Cu}$, 6.27242×10^{-6}},
 {In^x_{Cu}, 1.5×10^{-16}}, {Cu^x_{In}, 5.4×10^{-10}}, {$\mathcal{V}^x_{In}$, $1.\times10^{-18}$},
 {$\mathcal{V}^x_{Se}$, $3.\times10^{-12}$}, {Cu^x_i, 3.00001×10^{-13}}, {$Cu_i \oplus \mathcal{V}_{Cu}$, 3.18794×10^{-8}},
 {$Cu_{In} \oplus In_{Cu}$, 1.24×10^{-4}}, {$\mathcal{V}_{Cu} \oplus In_{Cu}$, 6.30054×10^{-6}},
 {$(2\,\mathcal{V}_{Cu} \oplus In_{Cu})_\alpha$, 1.737×10^{-4}}, {Cu_{Cu2Se}, -1.82×10^{-8}}, {Cu2.δSe, 3.6×10^{-4}}}

```
solvedRxns = {6, 8, 9, 10, 12, 17, 20};

Extract[Array[{#, rxn[#, ν0ξ]} &, 22], Thread[{solvedRxns}]] // TableForm
```

6	$\mathcal{V}_{Cu} \oplus In_{Cu} - 3\,CIS_\alpha + \mathcal{V}^x_{Cu} - (2\,\mathcal{V}_{Cu} \oplus In_{Cu})_\alpha$
8	$\mathcal{V}_{Cu} \oplus In_{Cu} - 11\,CIS_\alpha + Cu^x_i + Cu^x_{In}$
9	$Cu_{In} \oplus In_{Cu} - 3\,CIS_\alpha$
10	$Cu_i \oplus \mathcal{V}_{Cu} - 3\,CIS_\alpha$
12	$-2\,(Cu_i \oplus \mathcal{V}_{Cu}) + Cu^x_i + \mathcal{V}^x_{Cu}$
17	$-3\,CIS_\alpha + Cu^x_i - Cu^x_{In} + \mathcal{V}^x_{In}$
20	$-2\,(Cu_{In} \oplus In_{Cu}) + Cu^x_{In} + In^x_{Cu}$

The FindRoot functional in *Mathematica* uses a Newton-Raphson algorithm that can be used to refine the approximate solution determined above and to automate its adjustment to changes in the parameters of the equation such as Z and Δg0CISαcl.

```
Off[FindRoot::"frmp"]
{0.00018 , 0.3*^-11 , −1.82*^-8, 6.3*^-6 ,
    5.4*^-10, 0.000124, 3.08*^-8, −5.397*^-10, 1.*^-18, 1.5*^-16};
Fold[Insert[#, 0, #2] &, %, Thread[{Complement[Array[# &, 22], neutralRxns ]}]];
(FindRoot[Extract[(gd0CIS[1, tRef, 0] /. Extract[Thread[ξ000 → %],
                        Thread[{Complement[Array[# &, 22], solvedRxns ]}]]),
                Thread[{solvedRxns}]] == Array[0 &, Length[solvedRxns]], ##] & @@
       Extract[Thread[{ξ000, %}], Thread[{solvedRxns}]]);
Extract[Thread[ξ000 → %%], Thread[{Complement[neutralRxns, solvedRxns ]}]];
Extract[Thread[ξ000 → %%%], Thread[{Complement[Array[# &, 22], neutralRxns ]}]];
subspaceSoln = Join[%, %%, %%%];
Thread[{solvedRxns, Extract[(gd0CIS[1, tRef, 0] /. %), Thread[{solvedRxns}]]}] //
  TableForm
{"neutral solution convergence σSD", σSD[gd00CIS[1, tRef] /. subspaceSoln]}
On[FindRoot::"frmp"]
```

6	4.65661×10^{-10}
8	-2.26663×10^{-12}
9	0.
10	0.
12	-5.58794×10^{-9}
17	0.
20	0.

{neutral solution convergence σ_{SD}, 357436.}

The order of the solutions returned by the FindRoot code above cannot be directly put into the concentration relation $c_j = c_j^0 + \sum_{r=1}^{22} \nu_{jr}\, \xi_r$ because the order in which they are returned does not coincide with the ordering of the basis. The following function reorders the solution reaction extent vector:

```
basisOrderξ000[soln_] /; Length[soln] == Length[ξ000] :=
  Fold[ReplacePart[ #, soln⟦#2⟦2⟧⟧, #2⟦1⟧] &, Array[0 &, 22],
    MapIndexed[Flatten[{#2, Position[soln⟦All, 1⟧, #]}] &, ξ000]]
```

The unsolved neutral reactions (one, four, and five) are different from all the others, insofar as they are the only ones that involve the species that are not part of the lattice: $\mathrm{Cu}_{\mathrm{Cu2Se}}$, and Cu2.$\delta$Se. The following calculations shows that the excess Gibbs energy of the ideal lattice cluster $\Delta g0\alpha cl$ [T] does not cancel out of the total Gibbs energy calculation for these reactions.

```
Extract[Array[{#, rxn[#, ν0ξ]} &, 22],
    Thread[{Complement[neutralRxns, solvedRxns]}]] // TableForm
```

1	$2\,\mathrm{Cu2.}\delta\mathrm{Se} + \Delta N + (-\frac{11}{2} + 6\,\delta)\,\mathrm{CIS}_\alpha - 2\,\delta\,\mathcal{V}^{\mathrm{x}}_{\mathrm{Cu}} + (2\,\mathcal{V}_{\mathrm{Cu}} \oplus \mathrm{In}_{\mathrm{Cu}})_\alpha$
4	$\mathrm{Cu2.}\delta\mathrm{Se} + 3\,(-3 + \delta)\,\mathrm{CIS}_\alpha + (2 - \delta)\,\mathcal{V}^{\mathrm{x}}_{\mathrm{Cu}} + \mathcal{V}^{\mathrm{x}}_{\mathrm{Se}}$
5	$-3\,\mathrm{CIS}_\alpha + \mathrm{Cu}_{\mathrm{Cu2Se}} + \mathcal{V}^{\mathrm{x}}_{\mathrm{Cu}}$

```
Extract[
    Thread[{cE0, μ00[(c000[1] + (ν0ξ /. δ → δmin[tRef]).ξ000 /. subspaceSoln), tRef]}],
    {{1}, {2}, {14}, {22}, {23}, {24}, {27}}] // Simplify // TableForm
```

CIS_α	$-935503. + \Delta g0\alpha cl[1048.15]$
$\mathcal{V}^{\mathrm{x}}_{\mathrm{Cu}}$	$-2.77164 \times 10^6 + 3\,\Delta g0\alpha cl[1048.15]$
$\mathcal{V}^{\mathrm{x}}_{\mathrm{Se}}$	$-2.55918 \times 10^6 + 3\,\Delta g0\alpha cl[1048.15]$
$(2\,\mathcal{V}_{\mathrm{Cu}} \oplus \mathrm{In}_{\mathrm{Cu}})_\alpha$	$-4.63005 \times 10^6 + 5\,\Delta g0\alpha cl[1048.15]$
$\mathrm{Cu}_{\mathrm{Cu2Se}}$	-5280.54
Cu2.δSe	$-317070.$
ΔN	0

Thus these reactions can be simultaneously solved only by correctly determining both the extent of each reaction and the value of Δg0αcl [T]. The fourth neutral reaction is solved first among those remaining.

```
solvedRxns = Union[solvedRxns, {4}];
Complement[neutralRxns, solvedRxns]
```

```
{1, 5}
```

```
Off[FindRoot::"frmp"]
Off[FindRoot::"cvnwt"]
basisOrderξ000[subspaceSoln][[All, 2]];
(FindRoot[Extract[(gd0CIS[1, tRef, 0] /. Extract[Thread[ξ000 → %],
                        Thread[{Complement[Array[# &, 22], solvedRxns ]}]]),
                Thread[{solvedRxns}]] == Array[0 &, Length[solvedRxns]],
            ##, MaxIterations → 50] & @@
        Extract[Thread[{ξ000, %}], Thread[{solvedRxns}]]);
Extract[Thread[ξ000 → %%], Thread[{Complement[neutralRxns, solvedRxns ]}]];
Extract[Thread[ξ000 → %%%], Thread[{Complement[Array[# &, 22], neutralRxns ]}]];
subspaceSoln = Join[%, %%, %%%];
{"neutral solution convergence σSD", σSD[gd00CIS[1, tRef] /. subspaceSoln]}
On[FindRoot::"frmp"]
On[FindRoot::"cvnwt"]
```

```
{neutral solution convergence σSD, 148517.}
```

```
(* calculation of total Gibbs energy as c0ξ[Z,tK]*μ00[c0ξ[Z,tK],tK] *)
xsCISclG = 0;
{"reference value" g_HSER[cThermo_CuInSe2_α, tRef],
  "current model estimate" Plus @@ (c0ξ[1, tRef] *
            (μ00[c0ξ[1, tRef], tRef] /. Δg0αcl[tRef] → xsCISclG) /. subspaceSoln)}
"difference" (g_HSER[cThermo_CuInSe2_α, tRef] –
      Plus @@ (c0ξ[1, tRef] * (μ00[c0ξ[1, tRef], tRef] /. Δg0αcl[tRef] → xsCISclG) /.
          subspaceSoln))
```

```
{−467736. reference value, −467773. current model estimate}
37.2759 difference
```

The first reaction is solved next, using this calculated deviation of the current solution estimate's total Gibbs energy from the literature reference value as an initial estimate.

```
Extract[Array[{#, rxn[#, ν0ξ]} &, 22],
    Thread[{Complement[neutralRxns, solvedRxns]}]] // TableForm
```

1	$2\,\text{Cu2}\_\delta\text{Se} + \Delta\text{N} + (-\frac{11}{2} + 6\,\delta)\,\text{CIS}_\alpha - 2\,\delta\,\mathcal{V}^{\text{x}}_{\text{Cu}} + (2\,\mathcal{V}_{\text{Cu}} \oplus \text{In}_{\text{Cu}})_\alpha$
5	$-3\,\text{CIS}_\alpha + \text{Cu}_{\text{Cu2Se}} + \mathcal{V}^{\text{x}}_{\text{Cu}}$

```
solvedRxns = Union[solvedRxns, {1}];
Complement[neutralRxns, solvedRxns]
```

{5}

```
Off[FindRoot::"frmp"]
Off[FindRoot::"cvnwt"]
xsCISclG = 37.275884476548526`;
Extract[basisOrderξ000[subspaceSoln],  Thread[{neutralRxns }]][[All, 2]];
Fold[Insert[#, 0, #2] &, %, Thread[{Complement[Array[# &, 22], neutralRxns ]}]];
(FindRoot[Extract[(gd0CIS[1, tRef, xsCISclG] /. Extract[Thread[ξ000 → %],
                        Thread[{Complement[Array[# &, 22], solvedRxns ]}]]),
                Thread[{solvedRxns}]] == Array[0 &, Length[solvedRxns]],
            ##, MaxIterations → 25] & @@
        Extract[Thread[{ξ000, %}], Thread[{solvedRxns}]]);
Extract[Thread[ξ000 → %%], Thread[{Complement[neutralRxns, solvedRxns ]}]];
Extract[Thread[ξ000 → %%%], Thread[{Complement[Array[# &, 22], neutralRxns ]}]];
subspaceSoln = Join[%, %%, %%%];
{"neutral solution convergence σSD",
  σSD[gd00CIS[1, tRef, xsCISclG] /. subspaceSoln]}
On[FindRoot::"frmp"]
On[FindRoot::"cvnwt"]
```

{neutral solution convergence σ_{SD}, 59803.8}

```
g_HSER[cThermo_CuInSe2_α, tRef];
Plus @@
    (c0ξ[1, tRef] * (μ00[c0ξ[1, tRef], tRef] /. Δg0αcl[tRef] → xsCISclG) /. subspaceSoln);
(%% – % + xsCISclG) "new xsCISclG estimate"
```

728.347 new xsCISclG estimate

The last remaining neutral reaction is solved using the most recent estimate of the excess Gibbs energy of the ideal lattice cluster:

```
Extract[Array[{#, rxn[#, ν0ξ]} &, 22],
    Thread[{Complement[neutralRxns, solvedRxns]}]] // TableForm
```

$5 \qquad -3\,\mathrm{CIS}_{\alpha} + \mathrm{Cu}_{\mathrm{Cu2Se}} + \mathcal{V}^{x}_{\mathrm{Cu}}$

```
solvedRxns = Union[solvedRxns, {5}];

Off[FindRoot::"frmp"]
Off[FindRoot::"cvnwt"]
xsCISclG = 728.3471014881507`;
basisOrderξ000[subspaceSoln][[All, 2]];
(FindRoot[Extract[(gd0CIS[1, tRef, xsCISclG] /. Extract[Thread[ξ000 → %],
                        Thread[{Complement[Array[# &, 22], solvedRxns ]}]]),
                Thread[{solvedRxns}]] == Array[0 &, Length[solvedRxns]],
            ##, MaxIterations → 25] & @@
        Extract[Thread[{ξ000, %}], Thread[{solvedRxns}]]);
Extract[Thread[ξ000 → %%], Thread[{Complement[neutralRxns, solvedRxns ]}]];
Extract[Thread[ξ000 → %%%], Thread[{Complement[Array[# &, 22], neutralRxns ]}]];
subspaceSoln = Join[%, %%, %%%];
{"neutral solution convergence σSD",
  σSD[gd00CIS[1, tRef, xsCISclG] /. subspaceSoln]}
On[FindRoot::"frmp"]
On[FindRoot::"cvnwt"]
```

{neutral solution convergence σ_{SD}, 1.50953×10^{-9}}

```
g_HSER[cThermo_CuInSe2_α, tRef];
Plus @@
    (c0ξ[1, tRef] * (μ00[c0ξ[1, tRef], tRef] /. Δg0αcl[tRef] → xsCISclG) /. subspaceSoln);
(%% – % + xsCISclG) "new xsCISclG estimate"

    1204.98 new xsCISclG estimate
```

Since the calculated deviation of the current solution estimate's total Gibbs energy still deviates from the literature reference value, the solution algorithm is next extended to optimize all the neutral reaction variables, including xsCISclG to which Δg0αcl [tRef] will subsequently be set. The discrepancy between the reference value of the total Gibbs energy and the model's value is thereby eliminated.

```
Off[FindRoot::"frmp"]
Off[FindRoot::"cvnwt"]
Clear[xsCISclG];
basisOrderξ000[subspaceSoln][[All, 2]];
(FindRoot[Extract[(Append[gd0CIS[1, tRef, xsCISclG],
                          (Plus @@ (c0ξ[1, tRef] * μ00[c0ξ[1, tRef], tRef]) –
                              g_HSER[cThermo_CuInSe2_α, tRef])] /.
                      Append[Extract[Thread[ξ000 → %],
                          Thread[{Complement[Array[# &, 22], solvedRxns ]}]],
                      Δg0αcl[tRef] → xsCISclG]),
                  Append[Thread[{solvedRxns}], {Length[ξ000] + 1}]] ==
                Array[0 &, Length[solvedRxns] + 1],
              ##, MaxIterations → 25] & @@
        Append[Extract[Thread[{ξ000, %}],
            Thread[{solvedRxns}]],
          {xsCISclG, 1204.983835436462` }]);
Extract[Thread[ξ000 → %%], Thread[{Complement[neutralRxns, solvedRxns ]}]];
Extract[Thread[ξ000 → %%%], Thread[{Complement[Array[# &, 22], neutralRxns ]}]];
subspaceSoln = Join[%, %%, %%%];
{"neutral solution convergence σSD",
  σSD[gd00CIS[1, tRef, xsCISclG] /. subspaceSoln]}
{"model's deviation from reference specific Gibbs energy",
  (Plus @@ (c0ξ[1, tRef] * μ00[c0ξ[1, tRef], tRef]) /. Δg0αcl[tRef] → xsCISclG /.
        subspaceSoln) – g_HSER[cThermo_CuInSe2_α, tRef]}
{"xsCISclG", xsCISclG /. subspaceSoln}
c000[1] + (ν0ξ /. δ → δmin[tRef]).ξ000 /. subspaceSoln;
Extract[Thread[{cE0, %}],
    {{1}, {2}, {4}, {7}, {10}, {14}, {16}, {18}, {19}, {20}, {22}, {23}, {24}}] // ScientificForm
On[FindRoot::"frmp"]
On[FindRoot::"cvnwt"]
```

```
{neutral solution convergence σSD, 2.30182 × 10^-8}
{model's deviation from reference specific Gibbs energy, −5.82077 × 10^-11}
{xsCISclG, 1706.6}
```

$\{\{CIS_{\alpha}, 4.27298\times10^{-1}\}, \{\mathcal{V}_{Cu}^{x}, 4.70055\times10^{-5}\},$
$\{In_{Cu}^{x}, 7.63558\times10^{-16}\}, \{Cu_{In}^{x}, 4.16766\times10^{-11}\},$
$\{\mathcal{V}_{In}^{x}, 9.57397\times10^{-19}\}, \{\mathcal{V}_{Se}^{x}, 3.63289\times10^{-8}\}, \{Cu_{i}^{x}, 1.45951\times10^{-14}\},$
$\{Cu_{i}\oplus\mathcal{V}_{Cu}, 1.89245\times10^{-8}\}, \{Cu_{In}\oplus In_{Cu}, 7.21355\times10^{-5}\},$
$\{\mathcal{V}_{Cu}\oplus In_{Cu}, 2.43311\times10^{-4}\}, \{(2\,\mathcal{V}_{Cu}\oplus In_{Cu})_{\alpha}, 1.29101\times10^{-2}\},$
$\{Cu_{Cu2Se}, -1.95732\times10^{-4}\}, \{Cu2\delta Se, 2.6307\times10^{-2}\}\}$

The foregoing results will now be extended to solve the remaining (ionization) reactions. The neutral reaction solution shows that the dominant ionizable defect species in equilibrium are $\mathcal{V}'_{Cu}$ and $(\mathcal{V}_{Cu}\oplus In_{Cu})^{\bullet}$. For this problem the Fermi level is expected to be near the VBM since the secondary $Cu_{2-\delta}Se$ phase (electronic reservoir) is known to be a strongly degenerate *p*–type semiconductor [160, 176]. These observations are used only to decide that the energetics of the complete solution will likely be most influenced by the $\mathcal{V}_{Cu}^{x}$ ionization reaction, which will be solved first along with the e'–$h^{\bullet}$ equilibrium. The electron and hole concentrations in equilibrium with the defect-free lattice are related by the expression $np = N_c\,N_v\,Exp\left[\frac{-E_g}{kT}\right]$. Solving this for *p* in terms of *n* provides a dependent value for *p* which will be used as an initial estimate for the equilibrium calculation for this problem.

(∗ intrinsic ideal α–
CuInSe$_2$ charge carrier specific molar and volume concentrations ∗)

$$\left\{\frac{\sqrt{np\alpha[tRef]}}{nAvo}, \sqrt{np\alpha cc[tRef]}\right\} // \text{ScientificForm}$$

$\{1.12356\times10^{-5}, 1.1439\times10^{17}\}$

solvedRxns = neutralRxns

{1, 4, 5, 6, 8, 9, 10, 12, 17, 20}

```
Extract[Array[{#, rxn[#, ν0ξ]} &, 22], Thread[{{2, 3, 7}}]] // TableForm
```

$$\begin{array}{ll} 2 & h^{\bullet} - \mathcal{V}_{Cu}^{x} + \mathcal{V}'_{Cu} \\ 3 & h^{\bullet} + e' \\ 7 & -(\mathcal{V}_{Cu} \oplus In_{Cu}) + (\mathcal{V}_{Cu} \oplus In_{Cu})^{\bullet} + e' \end{array}$$

```
(* initializes principal ionization rxns *) nelectron = 9.73*^-6;
nsplit = 5.0*^-1;
{np α[tRef] / (nelectron nAvo^2) - nelectron, (1 - nsplit) nelectron, nsplit nelectron}
subspaceSoln =
  Insert[ReplacePart[ReplacePart[ReplacePart[basisOrderξ000[Take[neutralSoln, 22]],
      %[[1]], {2, 2}], %[[2]], {7, 2}], %[[3]], {3, 2}], neutralSoln[[23]], -1]
Clear[nsplit, nelectron]
```

$$\{3.24413 \times 10^{-6},\ 4.865 \times 10^{-6},\ 4.865 \times 10^{-6}\}$$

$$\begin{aligned} &\{\xi001 \to 0.0131535,\ \xi002 \to 3.24413 \times 10^{-6},\ \xi003 \to 4.865 \times 10^{-6},\\ &\ \ \xi004 \to 3.63289 \times 10^{-8},\ \xi005 \to -0.000195732,\ \xi006 \to 0.000243311,\\ &\ \ \xi007 \to 4.865 \times 10^{-6},\ \xi008 \to 4.16758 \times 10^{-11},\ \xi009 \to 0.0000721355,\\ &\ \ \xi0010 \to 1.88412 \times 10^{-8},\ \xi0011 \to 0,\ \xi0012 \to -4.16612 \times 10^{-11},\ \xi0013 \to 0,\\ &\ \ \xi0014 \to 0,\ \xi0015 \to 0,\ \xi0016 \to 0,\ \xi0017 \to 9.57397 \times 10^{-19},\ \xi0018 \to 0,\\ &\ \ \xi0019 \to 0,\ \xi0020 \to 7.63558 \times 10^{-16},\ \xi0021 \to 0,\ \xi0022 \to 0,\ xsCIsclG \to 1706.6\} \end{aligned}$$

```
Complement[ionizationRxns, solvedRxns]
```

$$\{2, 3, 7, 11, 13, 14, 15, 16, 18, 19, 21, 22\}$$

```
solvedRxns = Union[solvedRxns, {2, 3, 7}] ;
```

```
Off[FindRoot::"frmp"]
Off[FindRoot::"cvnwt"]
subspaceSoln = Join[Extract[basisOrderξ000[Take[subspaceSoln, 22]],
          Thread[{Complement[Array[# &, 22], solvedRxns ]}]],
        (FindRoot[Extract[(Append[gd0CIS[1, tRef, xsCIsclG],
                                  (Plus @@ (c0ξ[1, tRef] * μ00[c0ξ[1, tRef], tRef])) –
                                    g_HSER[cThermo_CuInSe2_α, tRef]] /.
                                Insert[Extract[basisOrderξ000[Take[subspaceSoln, 22]],
                                    Thread[{Complement[Array[# &, 22], solvedRxns ]}]],
                                  Δg0αcl[tRef] → xsCIsclG, −1]),
                      Insert[Thread[{solvedRxns}], {Length[ξ000] + 1}, −1]] ==
                    Array[0 &, Length[solvedRxns] + 1],
                  ##, MaxIterations → 25] & @@  Insert[
                Extract[Thread[{ξ000, basisOrderξ000[Take[subspaceSoln, 22]][[All, 2]]}],
                  Thread[{solvedRxns}]],
                {xsCIsclG, Last[subspaceSoln][[2]]}, −1])];
On[FindRoot::"frmp"]
On[FindRoot::"cvnwt"]
{"tRef solution convergence σSD", σSD[gd0CIS[1, tRef, xsCIsclG] /. subspaceSoln]}
{"model's deviation from reference specific Gibbs energy",
  Plus @@ ((c0ξ[1, tRef] * μ00[c0ξ[1, tRef], tRef]) /. Δg0αcl[tRef] → xsCIsclG /.
          subspaceSoln) – g_HSER[cThermo_CuInSe2_α, tRef]}
```

{tRef solution convergence σ_{SD}, 2.13556×10^{6}}

{model's deviation from reference specific Gibbs energy, -1.16415×10^{-10}}

```
Complement[ionizationRxns, solvedRxns]
```

{11, 13, 14, 15, 16, 18, 19, 21, 22}

```
Extract[Array[{#, rxn[#, ν0ξ]} &, 22], Thread[{{21, 22}}]] // TableForm
```

21	$-\mathrm{In}_{\mathrm{Cu}}^{\mathrm{x}} + \mathrm{In}_{\mathrm{Cu}}^{\cdot\cdot} + 2\,\mathrm{e}'$
22	$-\mathrm{In}_{\mathrm{Cu}}^{\mathrm{x}} + \mathrm{In}_{\mathrm{Cu}}^{\cdot} + \mathrm{e}'$

```
solvedRxns = Union[solvedRxns, {21, 22}] ;
```

```
Off[FindRoot::"frmp"]
Off[FindRoot::"cvnwt"]
subspaceSoln = Join[Extract[basisOrderξ000[Take[subspaceSoln, 22]],
          Thread[{Complement[Array[# &, 22], solvedRxns ]}]],
        (FindRoot[Extract[(Append[gd0CIS[1, tRef, xsCISclG],
                                  (Plus @@ (c0ξ[1, tRef] * μ00[c0ξ[1, tRef], tRef])) –
                                    g_HSER[cThermo_CuInSe2_α, tRef]] /.
                                Insert[Extract[basisOrderξ000[Take[subspaceSoln, 22]],
                                    Thread[{Complement[Array[# &, 22], solvedRxns ]}]],
                                Δg0αcl[tRef] → xsCISclG, −1]),
                      Insert[Thread[{solvedRxns}], {Length[ξ000] + 1}, −1]] ==
                    Array[0 &, Length[solvedRxns] + 1], ##] & @@ Insert[
                Extract[Thread[{ξ000, basisOrderξ000[Take[subspaceSoln, 22]][[All, 2]]}],
                  Thread[{solvedRxns}]],
                {xsCISclG, Last[subspaceSoln][[2]]}, −1])];
On[FindRoot::"frmp"]
On[FindRoot::"cvnwt"]
{"tRef solution convergence σSD", σSD[gd0CIS[1, tRef, xsCISclG] /. subspaceSoln]}
{"model's deviation from reference specific Gibbs energy",
  Plus @@ ((c0ξ[1, tRef] * μ00[c0ξ[1, tRef], tRef]) /. Δg0αcl[tRef] → xsCISclG /.
        subspaceSoln) – g_HSER[cThermo_CuInSe2_α, tRef]}
{"ideal CIS_α cluster excess Gibbs energy", xsCISclG /. subspaceSoln}
```

{tRef solution convergence σ_{SD}, 1.58539×10^{6}}
{model's deviation from reference specific Gibbs energy, 1.16415×10^{-10}}
{ideal CIS_{α} cluster excess Gibbs energy, 3865.46}

```
Complement[ionizationRxns, solvedRxns]
```

{11, 13, 14, 15, 16, 18, 19}

```
Extract[Array[{#, rxn[#, ν0ξ]} &, 22], Thread[{{11, 13}}]] // TableForm
```

11	$-Cu_i^x + Cu_i^{\bullet} + e'$
13	$-\mathcal{V}_{Se}^x + \mathcal{V}_{Se}^{\bullet\bullet} + 2\,e'$

```
solvedRxns = Union[solvedRxns, {13}] ;
```

```
Off[FindRoot::"frmp"]
Off[FindRoot::"cvnwt"]
subspaceSoln = Join[Extract[basisOrderξ000[Take[subspaceSoln, 22]],
          Thread[{Complement[Array[# &, 22], solvedRxns ]}]],
        (FindRoot[Extract[(Append[gd0CIS[1, tRef, xsCIsclG],
                                  (Plus @@ (c0ξ[1, tRef] * μ00[c0ξ[1, tRef], tRef])) –
                                    g_HSER[cThermo_CuInSe2_α, tRef]] /.
                                Insert[Extract[basisOrderξ000[Take[subspaceSoln, 22]],
                                    Thread[{Complement[Array[# &, 22], solvedRxns ]}]],
                                Δg0αcl[tRef] → xsCIsclG, −1]),
                      Insert[Thread[{solvedRxns}], {Length[ξ000] + 1}, −1]] ==
                    Array[0 &, Length[solvedRxns] + 1], ##] & @@ Insert[
                Extract[Thread[{ξ000, basisOrderξ000[Take[subspaceSoln, 22]][[All, 2]]}],
                  Thread[{solvedRxns}]],
                {xsCIsclG, Last[subspaceSoln][[2]]}, −1])];
On[FindRoot::"frmp"]
On[FindRoot::"cvnwt"]
{"tRef solution convergence σSD", σSD[gd0CIS[1, tRef, xsCIsclG] /. subspaceSoln]}
{"model's deviation from reference specific Gibbs energy",
  Plus @@ ((c0ξ[1, tRef] * μ00[c0ξ[1, tRef], tRef]) /. Δg0αcl[tRef] → xsCIsclG /.
        subspaceSoln) – g_HSER[cThermo_CuInSe2_α, tRef]}
{"ideal CIS_α cluster excess Gibbs energy", xsCIsclG /. subspaceSoln}
```

```
{tRef solution convergence σSD, 1.21328 × 10^6}
{model's deviation from reference specific Gibbs energy, 0.0000836407}
{ideal CIS_α cluster excess Gibbs energy, 3865.46}
```

```
Complement[ionizationRxns, solvedRxns]
```

```
{11, 14, 15, 16, 18, 19}
```

```
Extract[Array[{#, rxn[#, ν0ξ]} &, 22], Thread[{{11, 21, 22}}]] // TableForm
```

11	$-Cu_i^x + Cu_i^{\bullet} + e'$
21	$-In_{Cu}^x + In_{Cu}^{\bullet\bullet} + 2\,e'$
22	$-In_{Cu}^x + In_{Cu}^{\bullet} + e'$

```
solvedRxns = Union[solvedRxns, {11}] ;
```

```
Off[FindRoot::"frmp"]
Off[FindRoot::"cvnwt"]
subspaceSoln = Join[Extract[basisOrderξ000[Take[subspaceSoln, 22]],
          Thread[{Complement[Array[# &, 22], solvedRxns ]}]],
        (FindRoot[Extract[(Append[gd0CIS[1, tRef, xsCIsclG],
                                  (Plus @@ (c0ξ[1, tRef] * μ00[c0ξ[1, tRef], tRef])) –
                                    g_HSER[cThermo_CuInSe2_α, tRef]] /.
                                Insert[Extract[basisOrderξ000[Take[subspaceSoln, 22]],
                                    Thread[{Complement[Array[# &, 22], solvedRxns ]}]],
                                  Δg0αcl[tRef] → xsCIsclG, −1]),
                    Insert[Thread[{solvedRxns}], {Length[ξ000] + 1}, −1]] ==
                  Array[0 &, Length[solvedRxns] + 1], ##] & @@ Insert[
              Extract[Thread[{ξ000, basisOrderξ000[Take[subspaceSoln, 22]][[All, 2]]}],
                Thread[{solvedRxns}]],
              {xsCIsclG, Last[subspaceSoln][[2]]}, −1])];
On[FindRoot::"frmp"]
On[FindRoot::"cvnwt"]
{"tRef solution convergence σSD", σSD[gd0CIS[1, tRef, xsCIsclG] /. subspaceSoln]}
{"model's deviation from reference specific Gibbs energy",
  Plus @@ ((c0ξ[1, tRef] * μ00[c0ξ[1, tRef], tRef]) /. Δg0αcl[tRef] → xsCIsclG /.
        subspaceSoln) – g_HSER[cThermo_CuInSe2_α, tRef]}
{"ideal CIS_α cluster excess Gibbs energy", xsCIsclG /. subspaceSoln}
```

```
{tRef solution convergence σSD, 903864.}
{model's deviation from reference specific Gibbs energy, 4.65661 × 10^-10}
{ideal CIS_α cluster excess Gibbs energy, 3865.46}
```

```
Complement[ionizationRxns, solvedRxns]
```

```
{14, 15, 16, 18, 19}
```

```
Extract[Array[{#, rxn[#, ν0ξ]} &, 22], Thread[{{14, 15, 16, 18, 19}}]] // TableForm
```

14	$-\mathcal{V}_{In}^{x} + \mathcal{V}_{In}^{\bullet\bullet\bullet} + 3\,e'$
15	$-\mathcal{V}_{In}^{x} + \mathcal{V}_{In}^{\bullet\bullet} + 2\,e'$
16	$-\mathcal{V}_{In}^{x} + \mathcal{V}_{In}^{\bullet} + e'$
18	$2\,h^{\bullet} - Cu_{In}^{x} + Cu_{In}''$
19	$h^{\bullet} - Cu_{In}^{x} + Cu_{In}'$

```
solvedRxns = Union[solvedRxns, {18, 19}] ;
```

```
Off[FindRoot::"frmp"]
Off[FindRoot::"cvnwt"]
subspaceSoln = Join[Extract[basisOrderξ000[Take[subspaceSoln, 22]],
          Thread[{Complement[Array[# &, 22], solvedRxns ]}]],
        (FindRoot[Extract[(Append[gd0CIS[1, tRef, xsCIsclG],
                                  (Plus @@ (c0ξ[1, tRef] * μ00[c0ξ[1, tRef], tRef])) –
                                    g_HSER[cThermo_CuInSe2_α, tRef]] /.
                                Insert[Extract[basisOrderξ000[Take[subspaceSoln, 22]],
                                    Thread[{Complement[Array[# &, 22], solvedRxns ]}]],
                                Δg0αcl[tRef] → xsCIsclG, −1]),
                      Insert[Thread[{solvedRxns}], {Length[ξ000] + 1}, −1]] ==
                    Array[0 &, Length[solvedRxns] + 1], ##] & @@ Insert[
                Extract[Thread[{ξ000, basisOrderξ000[Take[subspaceSoln, 22]][[All, 2]]}],
                  Thread[{solvedRxns}]],
                {xsCIsclG, Last[subspaceSoln][[2]]}, −1])];
On[FindRoot::"frmp"]
On[FindRoot::"cvnwt"]
{"tRef solution convergence σSD", σSD[gd0CIS[1, tRef, xsCIsclG] /. subspaceSoln]}
{"model's deviation from reference specific Gibbs energy",
  Plus @@ ((c0ξ[1, tRef] * μ00[c0ξ[1, tRef], tRef]) /. Δg0αcl[tRef] → xsCIsclG /.
          subspaceSoln) – g_HSER[cThermo_CuInSe2_α, tRef]}
{"ideal CIS_α cluster excess Gibbs energy", xsCIsclG /. subspaceSoln}
```

```
{tRef solution convergence σSD, 231628.}
{model's deviation from reference specific Gibbs energy, 1.01188 × 10^−6}
{ideal CIS_α cluster excess Gibbs energy, 3865.46}
```

```
Complement[ionizationRxns, solvedRxns]
```

```
{14, 15, 16}
```

```
Extract[Array[{#, rxn[#, ν0ξ]} &, 22], Thread[{{14, 15, 16}}]] // TableForm
```

14	$-\mathcal{V}_{\text{In}}^{\text{x}} + \mathcal{V}_{\text{In}}^{\blacksquare\blacksquare\blacksquare} + 3\,\text{e}'$
15	$-\mathcal{V}_{\text{In}}^{\text{x}} + \mathcal{V}_{\text{In}}^{\blacksquare\blacksquare} + 2\,\text{e}'$
16	$-\mathcal{V}_{\text{In}}^{\text{x}} + \mathcal{V}_{\text{In}}^{\blacksquare} + \text{e}'$

```
solvedRxns = Union[solvedRxns, {16}] ;
```

```
Off[FindRoot::"frmp"]
Off[FindRoot::"cvnwt"]
subspaceSoln = Join[Extract[basisOrderξ000[Take[subspaceSoln, 22]],
          Thread[{Complement[Array[# &, 22], solvedRxns ]}]],
        (FindRoot[Extract[(Append[gd0CIS[1, tRef, xsCISclG],
                                  (Plus @@ (c0ξ[1, tRef] * μ00[c0ξ[1, tRef], tRef])) –
                                    g_HSER[cThermo_CuInSe2_α, tRef]] /.
                                Insert[Extract[basisOrderξ000[Take[subspaceSoln, 22]],
                                    Thread[{Complement[Array[# &, 22], solvedRxns ]}]],
                                Δg0αcl[tRef] → xsCISclG, −1]),
                      Insert[Thread[{solvedRxns}], {Length[ξ000] + 1}, −1]] ==
                    Array[0 &, Length[solvedRxns] + 1], ##] & @@ Insert[
                Extract[Thread[{ξ000, basisOrderξ000[Take[subspaceSoln, 22]][[All, 2]]}],
                  Thread[{solvedRxns}]],
                {xsCISclG, Last[subspaceSoln][[2]]}, −1])];
On[FindRoot::"frmp"]
On[FindRoot::"cvnwt"]
{"tRef solution convergence σSD", σSD[gd0CIS[1, tRef, xsCISclG] /. subspaceSoln]}
{"model's deviation from reference specific Gibbs energy",
  Plus @@ ((c0ξ[1, tRef] * μ00[c0ξ[1, tRef], tRef]) /. Δg0αcl[tRef] → xsCISclG /.
          subspaceSoln) – g_HSER[cThermo_CuInSe2_α, tRef]}
{"ideal CIS_α cluster excess Gibbs energy", xsCISclG /. subspaceSoln}
```

```
{tRef solution convergence σSD, 142870.}
{model's deviation from reference specific Gibbs energy, 5.82077 × 10^-11}
{ideal CIS_α cluster excess Gibbs energy, 3865.46}
```

```
Complement[ionizationRxns, solvedRxns]
```

```
{14, 15}
```

```
solvedRxns = Union[solvedRxns, {15}] ;
```

```
Off[FindRoot::"frmp"]
Off[FindRoot::"cvnwt"]
subspaceSoln = Join[Extract[basisOrderξ000[Take[subspaceSoln, 22]],
          Thread[{Complement[Array[# &, 22], solvedRxns ]}]],
        (FindRoot[Extract[(Append[gd0CIS[1, tRef, xsCIsclG],
                                  (Plus @@ (c0ξ[1, tRef] * μ00[c0ξ[1, tRef], tRef])) –
                                    g_HSER[cThermo_CuInSe2_α, tRef]] /.
                                Insert[Extract[basisOrderξ000[Take[subspaceSoln, 22]],
                                    Thread[{Complement[Array[# &, 22], solvedRxns ]}]],
                                Δg0αcl[tRef] → xsCIsclG, −1]),
                      Insert[Thread[{solvedRxns}], {Length[ξ000] + 1}, −1]] ==
                    Array[0 &, Length[solvedRxns] + 1], ##] & @@ Insert[
                Extract[Thread[{ξ000, basisOrderξ000[Take[subspaceSoln, 22]][[All, 2]]}],
                  Thread[{solvedRxns}]],
                {xsCIsclG, Last[subspaceSoln][[2]]}, −1])];
On[FindRoot::"frmp"]
On[FindRoot::"cvnwt"]
{"tRef solution convergence σSD", σSD[gd0CIS[1, tRef, xsCIsclG] /. subspaceSoln]}
{"model's deviation from reference specific Gibbs energy",
  Plus @@ ((c0ξ[1, tRef] * μ00[c0ξ[1, tRef], tRef]) /. Δg0αcl[tRef] → xsCIsclG /.
          subspaceSoln) – g_HSER[cThermo_CuInSe2_α, tRef]}
{"ideal CIS_α cluster excess Gibbs energy", xsCIsclG /. subspaceSoln}
```

```
{tRef solution convergence σSD, 127540.}
{model's deviation from reference specific Gibbs energy, −1.16415 × 10^−10}
{ideal CIS_α cluster excess Gibbs energy, 3865.46}
```

```
Complement[ionizationRxns, solvedRxns]
```

```
{14}
```

```
solvedRxns = Union[solvedRxns, {14}] ;
```

```
Off[FindRoot::"frmp"]
Off[FindRoot::"cvnwt"]
subspaceSoln = Join[Extract[basisOrderξ000[Take[subspaceSoln, 22]],
          Thread[{Complement[Array[# &, 22], solvedRxns ]}]],
        (FindRoot[Extract[(Append[gd0CIS[1, tRef, xsCISclG],
                                  (Plus @@ (c0ξ[1, tRef] * μ00[c0ξ[1, tRef], tRef])) –
                                    g_HSER[cThermo_CuInSe2_α, tRef]] /.
                                Insert[Extract[basisOrderξ000[Take[subspaceSoln, 22]],
                                    Thread[{Complement[Array[# &, 22], solvedRxns ]}]],
                                Δg0αcl[tRef] → xsCISclG, −1]),
                          Insert[Thread[{solvedRxns}], {Length[ξ000] + 1}, −1]] ==
                        Array[0 &, Length[solvedRxns] + 1],
                      ##, MaxIterations → 50] & @@ Insert[
                  Extract[Thread[{ξ000, basisOrderξ000[Take[subspaceSoln, 22]][[All, 2]]}],
                    Thread[{solvedRxns}]],
                  {xsCISclG, Last[subspaceSoln][[2]]}, −1])];
On[FindRoot::"frmp"]
On[FindRoot::"cvnwt"]
{"ideal CIS_α cluster excess Gibbs energy at the reference temperature",
  (xsCISclG /. subspaceSoln) "Joules"}
{"model's total deviation at the reference temperature
       from literature specific Gibbs energy value",
  (Plus @@ ((c0ξ[1, tRef] * μ00[c0ξ[1, tRef], tRef]) /. Δg0αcl[tRef] → xsCISclG /.
                subspaceSoln) – g_HSER[cThermo_CuInSe2_α, tRef]) "Joules"}
{"total RMS affinity deviation for the 23 simultaneous reaction equilibria solutions",
  σSD[gd0CIS[1, tRef, xsCISclG] /. subspaceSoln] "Joules"}
```

```
{ideal CIS_α cluster excess Gibbs energy at the reference temperature,
  3865.46 Joules}
{model's total deviation at the reference temperature
       from literature specific Gibbs energy value, 0. Joules}
{total RMS affinity deviation for the 23 simultaneous
       reaction equilibria solutions, 9.36574 × 10^−7 Joules}
```

```
solvedRxns === Array[# &, 22]
```

```
True
```

Note that the maximum deviation from complete equilibrium as exemplified in the total RMS deviation of this solution's reaction affinity values from zero is about

10^{-6} Joules, thirteen orders of magnitude less than its initial value. The following table compiles the predicted specific molar concentrations of each model species at the reference temperature:

```
Thread[{cE0, c0ξ[1, tRef] /. subspaceSoln}] // TableForm
```

CIS_{α}	0.339664
$\mathcal{V}_{Cu}^{x}$	7.30432×10^{-6}
$\mathcal{V}_{Cu}^{\prime}$	0.0176221
In_{Cu}^{x}	1.69228×10^{-15}
$In_{Cu}^{\bullet}$	1.62585×10^{-13}
$In_{Cu}^{\bullet\bullet}$	4.02263×10^{-13}
Cu_{In}^{x}	4.41121×10^{-12}
$Cu_{In}^{\prime}$	5.9826×10^{-10}
$Cu_{In}^{\prime\prime}$	2.2824×10^{-10}
$\mathcal{V}_{In}^{x}$	3.25117×10^{-20}
$\mathcal{V}_{In}^{\bullet}$	7.56345×10^{-23}
$\mathcal{V}_{In}^{\bullet\bullet}$	8.6096×10^{-28}
$\mathcal{V}_{In}^{\bullet\bullet\bullet\bullet}$	2.20373×10^{-33}
$\mathcal{V}_{Se}^{x}$	1.17317×10^{-7}
$\mathcal{V}_{Se}^{\bullet\bullet}$	6.322×10^{-8}
Cu_{i}^{x}	2.2033×10^{-14}
$Cu_{i}^{\bullet}$	3.68208×10^{-12}
$Cu_{i} \oplus \mathcal{V}_{Cu}$	9.16586×10^{-9}
$Cu_{In} \oplus In_{Cu}$	0.000034938
$\mathcal{V}_{Cu} \oplus In_{Cu}$	0.000105416
$(\mathcal{V}_{Cu} \oplus In_{Cu})^{\bullet}$	0.0176168
$(2\,\mathcal{V}_{Cu} \oplus In_{Cu})_{\alpha}$	0.00179455
Cu_{Cu2Se}	−0.0000921211
$Cu2.\delta Se$	0.0390336
$e^{\prime}$	2.00375×10^{-6}
$h^{\bullet}$	7.26855×10^{-6}
ΔN	1.01952

The calculated equilibrium selenium content of the $Cu_{2-\delta}Se$ phase exceeds the minimum required for its stability (since Cu_{Cu2Se} is negative), so this result is

consistent with the two-phase boundary condition, and is adopted as the complete solution at the reference temperature.

$\xi 00[1, \text{tRef}] = \text{subspaceSoln}$

$\{\xi 001 \to 0.0195167, \xi 002 \to 0.0176221, \xi 003 \to -0.0176149,$
$\xi 004 \to 1.80537 \times 10^{-7}, \xi 005 \to -0.0000921211, \xi 006 \to 0.0177222,$
$\xi 007 \to 0.0176168, \xi 008 \to 8.30345 \times 10^{-10}, \xi 009 \to 0.000034938,$
$\xi 0010 \to 7.51257 \times 10^{-9}, \xi 0011 \to 3.68208 \times 10^{-12}, \xi 0012 \to -8.26641 \times 10^{-10},$
$\xi 0013 \to 6.322 \times 10^{-8}, \xi 0014 \to -5. \times 10^{-27}, \xi 0015 \to -4.13904 \times 10^{-27},$
$\xi 0016 \to 7.56295 \times 10^{-23}, \xi 0017 \to 3.25874 \times 10^{-20},$
$\xi 0018 \to 2.2824 \times 10^{-10}, \xi 0019 \to 5.9826 \times 10^{-10}, \xi 0020 \to 5.6654 \times 10^{-13},$
$\xi 0021 \to 4.02263 \times 10^{-13}, \xi 0022 \to 1.62585 \times 10^{-13}, \text{xsCIsclG} \to 3865.46\}$

The solution can now be incrementally extended to lower temperatures by analytic continuation, using the same computational algorithm with the initial solution estimate taken to be the solution at the nearest temperature. For example, this solution at tRef is used as the initial estimate of the solution for a temperature of tRef–10, and that solution used as the initial estimate for tRef–20. The solution can be extended in this manner so long as the numerical algorithm continues to converge the Gibbs-Duhem equations satisfactorily.

The radius of convergence is limited by two considerations, one numerical and the other physical. The numerical limit occurs when the concentrations of the species in any single independent reaction drop to levels so small that the Newton-Raphson algorithm's incremental reaction extent step size exceeds that required to set the reactants' concentrations with sufficient precision to satisfy the the Gibbs-Duhem equation for that reaction. This difficulty can be ameliorated to some extent by increasing the WorkingPrecision option of *Mathematica*'s FindRoot function.

Eventually the increased time required to converge the solution with ever-increasing requirements for numerical precision becomes unacceptable, and it is necessary to remove those species from the basis set that have essentially vanished.

The physical limit on the radius of convergence occurs when the concentration of the Cu_{Cu2Se} species drops to zero, or as will be seen later, when it increases sufficiently (in the case where Z>1) to bring the secondary $Cu_{2-\delta}Se$ phase's composition to its maximum stable value. The mathematical formalism employed to solve this model does not incorporate these physical constraints, so it will be necessary to explicitly remove the Cu_{Cu2Se} species from the basis set when the solution reaches these points. The analysis at the end of the preceding boundary condition section estimated the lower temperature limit based on the assumption that the ternary phase was stoichiometric $CuInSe_2$. Clearly, since the overall composition of the two-phase mixture is stoichiometric and the secondary $Cu_{2-\delta}Se$ phase's composition is not, the ternary phase must also deviate from stoichiometric $CuInSe_2$, which may effect the temperature at which this limit occurs. The solution shows that the numerical convergence deteriorates even before that temperature is reached:

```
{"tRef−170", (tRef – 170) "K"}
{"tK000", tK000 "K"}
{"α−β−δ CIS eutectoid", tMaxαβ "K",
  ConvertTemperature[tMaxαβ, Kelvin, Celsius] "°C"}
{cE0⟦23⟧ "molar concentration at tRef−170 of",
  c0ξ[1, tRef – 170]⟦23⟧ /. ξ00[1, tRef – 170]}

    {tRef−170, 878.15 K}
    {tK000, 847.432 K}
```

{$\alpha-\beta-\delta$ CIS eutectoid, 873.15 K, 600. °C}
{molar concentration at tRef−170 of Cu_{Cu2Se}, −0.0000223203}

```
{"total solution affinity deviation",
  σSD[gd0CIS[1, tRef − 170, xsCISclG] /. ξ00[1, tRef − 170]] "Joules"}
{"solution affinity deviation for reaction 14",
  (gd0CIS[1, tRef − 170, xsCISclG] /. ξ00[1, tRef − 170])⟦14⟧ "Joules"}
Extract[Array[{#, rxn[#, ν0ξ]} &, 22], Thread[{{14}}]] // TableForm
```

{total solution affinity deviation, 0.58124 Joules}
{solution affinity deviation for reaction 14, −0.58124 Joules}
14 $\quad -\mathcal{V}_{In}^{x} + \mathcal{V}_{In}^{\bullet\bullet\bullet} + 3\,e'$

The concentrations of all of the $\mathcal{V}_{In}$ species have dropped to less than one atom *per* mole of CIS near the previously estimated temperature limit, and below this temperature their entropies diverge to the point that they overflow the numerical algorithms. This is already evident in the poor convergence of the solution for reaction 14. This necessitates reformulation of the underlying stoichiometry and reaction matrices to eliminate these species. Furthermore, the eutectoid decomposition temperature for δ-CIS is at about 873K, so the $\mathcal{V}_{In}$ species will be dropped from the basis below the temperature of tRef-170 = 878K. This is a numerical convergence limit, and not the physical limit, since the equilibrium value for Cu_{Cu2Se} is still negative at this temperature. Thus Cu_{Cu2Se} must remain in the basis set.

```
(* the CISα+Cu2Se basis vector without 𝒱In species *) cE0xVin = Drop[cE0, {10, 13}]
```

{CIS_α, $\mathcal{V}_{Cu}^{x}$, $\mathcal{V}_{Cu}'$, In_{Cu}^{x}, $In_{Cu}^{\bullet}$, $In_{Cu}^{\bullet\bullet}$, Cu_{In}^{x}, Cu_{In}', Cu_{In}'',
$\mathcal{V}_{Se}^{x}$, $\mathcal{V}_{Se}^{\bullet\bullet}$, Cu_i^{x}, $Cu_i^{\bullet}$, $Cu_i \oplus \mathcal{V}_{Cu}$, $Cu_{In} \oplus In_{Cu}$, $\mathcal{V}_{Cu} \oplus In_{Cu}$,
$(\mathcal{V}_{Cu} \oplus In_{Cu})^{\bullet}$, $(2\,\mathcal{V}_{Cu} \oplus In_{Cu})_\alpha$, Cu_{Cu2Se}, Cu2.δSe, e′, h•, ΔN}

```
𝒟0xVin = Transpose[Drop[Transpose[𝒟0], {10, 13}]];

formula[i_, 𝒟0xVin] := {cE0xVin, a .𝒟0xVin}⟦All, i⟧
```

```
ν0xVin = Transpose[NullSpace[𝒟0xVin]];

rxn[i_, ν0xVin] := ν0xVin⟦All, i⟧.cE0xVin

LogicalExpand[Array[rxn[#, ν0xVin] &, 13] === Array[rxn[#, ν0] &, 13]] ⋀
  LogicalExpand[
    Array[rxn[# – 4, ν0xVin] &, {5}, {18}] === Array[rxn[#, ν0] &, {5}, {18}]]

  True
```

The preceding function shows that all of the reactions in ***ν*0xVin** identically match those in ***ν*0** after those involving $\mathcal{V}_{\text{In}}$ species are deleted from the latter. Also, the linear combinations of reactions in ***ν*0** used to define the matrix ***ν*0*ξ*** only combined the deleted reactions with themselves. This substantially simplifies the extension of the previous solution to lower temperatures, which requires the definition of ***ν*0*ξ*xVin** and other analogous reformulated functions with respect to the reduced basis **cE0xVin**:

```
ν0ξxVin = Drop[Transpose[Drop[Transpose[ν0ξ], {14, 17}]], {10, 13}];

rxn[i_, ν0ξxVin] := ν0ξxVin⟦All, i⟧.cE0xVin

clusterXZ0xVin = Module[{im23},  With[{im23 = IdentityMatrix[23] },
        Array[Flatten[{#, cE0xVin⟦#⟧, cXZ[im23⟦#⟧, 𝒟0xVin]}] &,  18]]];
c0LimitsxVin = Module[{x00min, x00max, z00min, z00max},  With[
      {x00min = Min[%⟦All, 3⟧], x00max = Max[%⟦All, 3⟧], z00min = Min[%⟦All, 4⟧],
        z00max = Max[%⟦All, 4⟧]}, {x00min, x00max, z00min, z00max}]]
```

$$\left\{\frac{7}{11}, \frac{7}{5}, \frac{11}{12}, \frac{12}{11}\right\}$$

```
c00xVinbasis = {1, 10, 7, 18};
```

clusterXZ0xVin⟦#⟧ & /@ c00xVinbasis //
TableForm

(*index	cluster	X	Z *)
1	CIS_{α}	1	1
10	$\mathcal{V}_{\mathrm{Se}}^{\mathrm{x}}$	1	$\frac{11}{12}$
7	$\mathrm{Cu}_{\mathrm{In}}^{\mathrm{x}}$	$\frac{7}{5}$	$\frac{12}{11}$
18	$(2\,\mathcal{V}_{\mathrm{Cu}} \oplus \mathrm{In}_{\mathrm{Cu}})_{\alpha}$	$\frac{7}{11}$	1

$\mathcal{D}$000xVin = Transpose[Transpose[Take[$\mathcal{D}$0xVin, 4]]⟦#⟧ & /@ c00xVinbasis];

cE0xVin⟦#⟧ & /@ c00xVinbasis
$\mathcal{D}$000xVin // MatrixForm

$$\{\mathrm{CIS}_{\alpha},\ \mathcal{V}_{\mathrm{Se}}^{\mathrm{x}},\ \mathrm{Cu}_{\mathrm{In}}^{\mathrm{x}},\ (2\,\mathcal{V}_{\mathrm{Cu}} \oplus \mathrm{In}_{\mathrm{Cu}})_{\alpha}\}$$

$$\begin{pmatrix} 2 & 6 & 7 & 7 \\ 2 & 6 & 5 & 11 \\ 4 & 11 & 12 & 20 \\ 0 & 0 & 0 & 0 \end{pmatrix}$$

formula[i_, $\mathcal{D}$000xVin] := {cE0xVin⟦#⟧ & /@ c00xVinbasis, Take[a, 4].$\mathcal{D}$000xVin}⟦All, i⟧

Array[formula[#, $\mathcal{D}$000xVin] &, Length[c00xVinbasis]] // TableForm

CIS_{α}	$2\,\mathrm{Cu} + 2\,\mathrm{In} + 4\,\mathrm{Se}$
$\mathcal{V}_{\mathrm{Se}}^{\mathrm{x}}$	$6\,\mathrm{Cu} + 6\,\mathrm{In} + 11\,\mathrm{Se}$
$\mathrm{Cu}_{\mathrm{In}}^{\mathrm{x}}$	$7\,\mathrm{Cu} + 5\,\mathrm{In} + 12\,\mathrm{Se}$
$(2\,\mathcal{V}_{\mathrm{Cu}} \oplus \mathrm{In}_{\mathrm{Cu}})_{\alpha}$	$7\,\mathrm{Cu} + 11\,\mathrm{In} + 20\,\mathrm{Se}$

ν000xVin = Transpose[NullSpace[$\mathcal{D}$000xVin]];

rxn[i_, ν000xVin] := ν000xVin⟦All, i⟧.(cE0xVin⟦#⟧ & /@ c00xVinbasis)

Array[rxn[#, ν000xVin] &, Dimensions[ν000xVin][2]] // TableForm

$$-33\,\mathrm{CIS}_{\alpha} + 4\,\mathrm{Cu}_{\mathrm{In}}^{\mathrm{x}} + 4\,\mathcal{V}_{\mathrm{Se}}^{\mathrm{x}} + 2\,(2\,\mathcal{V}_{\mathrm{Cu}} \oplus \mathrm{In}_{\mathrm{Cu}})_{\alpha}$$

```
(* using c00xVinbasis→{c1,c10,c7,c18},
   are the X' s for the vectors {c1,0,0,0} and {0,c10,0,0} always equal? *)
cXZ[{c1, 0, 0, 0}, 𝒟000xVin][[1]] === cXZ[{0, c10, 0, 0}, 𝒟000xVin][[1]]
```

True

```
(* how does Z vary for their linear combination? *)
cXZ[{1 – c10, c10, 0, 0}, 𝒟000xVin] // Simplify
```

$$\left\{1, \frac{4 + 7\,c10}{4 + 8\,c10}\right\}$$

```
(* what is the extremal value of Z? *) %[[2]] /. c10 → 1
```

$$\frac{11}{12}$$

```
(* does any linear combination of the normalized vectors {0,0,c7,0} and
     {0,0,0,c18} always furnish the same X value as {c1,0,0,0}? *)Solve[
   cXZ[{c1, 0, 0, 0}, 𝒟000xVin][[1]] == cXZ[{c1 – c7 – c18, 0, c7, c18}, 𝒟000xVin][[1]], {c18
```

$$\left\{\left\{c18 \to \frac{c7}{2}\right\}\right\}$$

```
(* how does Z vary for that linear combination? *)
cXZ[{1 – c7 – c18, 0, c7, c18}, 𝒟000xVin] /. % // Simplify
```

$$\left\{\left\{1, \frac{4 + 16\,c7}{4 + 15\,c7}\right\}\right\}$$

```
(* what is the extremal value of Z for that linear combination? *) %[[1, 2]] /. c7 → 2/3
Clear[X0, Z0, c1, c10, c7, c18]
```

$$\frac{22}{21}$$

These results provide all the additional information required to correctly limit the range of X and Z, and to initialize $\boldsymbol{c^0}$. The latter is set to a linear combination of the four vectors {c1, 0, 0, 0}, {0, 0, 0, c18}, {0, c10, 0, 0}, and {0, 0, c7, c7/2} determined by the values of X and Z. The limits list is redefined so that both the minimum and

maximum permissible Z values are unity at the minimum X value where the system can only consist of c18, which is $(2\,\mathcal{V}_{\mathrm{Cu}} \oplus \mathrm{In}_{\mathrm{Cu}})_{\alpha}$ in this basis.

```
c0xVinLimits = Module[{x00min, x00max, z00min, z00max},
    With[{x00min = 7/11, x00max = 1, z00min = 11/12 + 11 (1 - X)/48,
      z00max = 12/11 - 11 (1 - X)/44}, {x00min, x00max, z00min, z00max}]]
```

$$\left\{\frac{7}{11}, 1, \frac{11}{12} + \frac{11\,(1 - X)}{48}, \frac{12}{11} + \frac{1}{4}\,(-1 + X)\right\}$$

```
ξ000xVin = Array[1 &, 18] -
    2 Array[KroneckerDelta[1, #] &, 18] - Array[KroneckerDelta[5, #] &, 18] +
    2 Array[KroneckerDelta[4, #] &, 18] + 4 Array[KroneckerDelta[16, #] &, 18]
```

```
{-1, 1, 1, 3, 0, 1, 1, 1, 1, 1, 1, 1, 1, 1, 5, 1, 1}
```

```
c0xVinLimits = Module[{x00min, x00max, z00min, z00max},
    With[{x00min = 14011/22000, x00max = 1, z00min = 11/12 + 11 (1 - X + 5/10000)/48,
      z00max = 12/11 - 11 (1 - X + 5/10000)/44}, {x00min, x00max, z00min, z00max}]];

c0xVinLimits /.
  X → c0xVinLimits[[1]] (* no Z deviation possible in model at minimum X *)
{c0xVinLimits[[3]], c0xVinLimits[[4]]} /.
  X → 1 (* maximum Z deviation is possible for X=1 *)
```

$$\left\{\frac{14011}{22000}, 1, 1, 1\right\}$$

$$\left\{\frac{29337}{32000}, \frac{95989}{88000}\right\}$$

```
% // N (* approximate maximum limits of Z deviation *)
```

```
{0.916781, 1.09078}
```

```
(* the maximum limits of Z deviation have not been significantly reduced
    by the change in basis *){c0Limits[[4]], c0xVinLimits[[4]]} /. X → 1 // N
```

```
{1.09664, 1.09078}
```

```
(* initial cluster quantities for Z <
     1 and that vector' s molar normalization factor      *)
Solve[{1, Z} == cXZ[{c1 - c10, c10, 0, 1 - c1}, 𝒟000xVin], {c1, c10}];
{{c1 - c10, c10, 0, 1 - c1}, mx[{c1 - c10, c10, 0, 1 - c1}, 𝒟000xVin][[1]]^-1} /. %
```

$$\left\{\left\{\left\{1+\frac{4(-1+Z)}{-7+8Z},-\frac{4(-1+Z)}{-7+8Z},0,0\right\},\ \frac{1}{-\frac{24(-1+Z)}{-7+8Z}+2\left(1+\frac{4(-1+Z)}{-7+8Z}\right)}\right\}\right\}$$

```
(*  initial cluster quantities for Z > 1;
   and that vector' s molar normalization factor     *)
Solve[{1, Z} == cXZ[{1 - 3 c7/2 - c18, 0, c7, c18 + c7/2}, 𝒟000xVin], {c7, c18}]
{{1 - 3 c7/2 - c18, 0, c7, c18 + c7/2},
     mx[{1 - 3 c7/2 - c18, 0, c7, c18 + c7/2}, 𝒟000xVin][[1]]^-1} /. %
```

$$\left\{\left\{c7\to-\frac{4(-1+Z)}{-16+15Z},\ c18\to 0\right\}\right\}$$

$$\left\{\left\{\left\{1+\frac{6(-1+Z)}{-16+15Z},0,-\frac{4(-1+Z)}{-16+15Z},-\frac{2(-1+Z)}{-16+15Z}\right\},\right.\right.$$
$$\left.\left.\frac{1}{-\frac{42(-1+Z)}{-16+15Z}+2\left(1+\frac{6(-1+Z)}{-16+15Z}\right)}\right\}\right\}$$

```
c00xVin[Z_] /; 29337/32000 ≤ Z ≤ 1 :=
  Module[{c00}, With[{c4Zminus = {1 + 4 (-1 + Z)/(-7 + 8 Z), -4 (-1 + Z)/(-7 + 8 Z), 0, 0},
      mCuInv1 = 1/(-24 (-1+Z)/(-7+8 Z) + 2 (1 + 4 (-1+Z)/(-7+8 Z)))},
    c00 = Plus @@ MapThread[ReplacePart[Array[0 &, Length[cE0xVin]], #1, #2] &,
        {c4Zminus, c00xVinbasis}];
    c00 = ReplacePart[c00, δmin[tRef] ξ000xVin[[4]] 2*^-26, 19];
    c00 = mCuInv1 (c00 + (ν0xVin /. δ → δmin[tRef]).ξ000xVin 1*^-26);
    ReplacePart[c00, 1, 23]]]
c00xVin[Z_] /; 1 < Z ≤ 95989/88000 := Module[{c00},
  With[{c4Zplus = {1 + 6 (-1 + Z)/(-16 + 15 Z), 0, -4 (-1 + Z)/(-16 + 15 Z), -2 (-1 + Z)/(-16 + 15 Z)},
      mCuInv2 = 1/(-42 (-1+Z)/(-16+15 Z) + 2 (1 + 6 (-1+Z)/(-16+15 Z)))},
    c00 = Plus @@ MapThread[ReplacePart[Array[0 &, Length[cE0xVin]], #1, #2] &,
        {c4Zplus, c00xVinbasis}];
    c00 = ReplacePart[c00, δmin[tRef] ξ000xVin[[4]] 2*^-26, 19];
    c00 = mCuInv2 (c00 + (ν0xVin /. δ → δmin[tRef]).ξ000xVin 1*^-26);
    ReplacePart[c00, 1, 23]]]

μ00xVin[c_, tK_] /; Length[c] === Length[cE0xVin] := With[{n = (# / Plus @@ #) &[
      Join[Take[Drop[Drop[mcl, {25}], {10, 13}] Take[c, 20], 18], {c[[20]]}]],
    δm = δmin[tK], δ0 = δmin[tK] - c[[19]] / c[[20]], nCISα = nAvo c / First[c]},
  ReplacePart[ReplacePart[Drop[Drop[μ00αβ[tK], {25}], {10, 13}],
      ((3 - δ0) G_CuSeX[tK, (3 - δ0)^-1] - (3 - δm) G_CuSeX[tK, (3 - δm)^-1])
        (δm - δ0)^-1, 19], (3 - δm) G_CuSeX[tK, (3 - δm)^-1], 20] +
  rG tK Join[Log[Drop[n, -1]], {0, Log[Last[n]], Log[nCISα[[21]] / cbDOSαCIS[tK]],
      Log[nCISα[[22]] / vbDOSαCIS[tK]], 0}]]
```

```
ξ00xVin = Drop[ξ000, {14, 17}];
c0ξxVin[Z_, tK_] := c00xVin[Z] + (ν0ξxVin /. δ → δmin[tK]).ξ00xVin
gd00xVin[Z_, tK_, Δg0CISαcl_] :=
  ((μ00xVin[c0ξxVin[#, #2], #2] /. Δg0αcl[#2] →  \#3).(ν0xVin /. δ → δmin[#2])) &[
    Z, tK, Δg0CISαcl]

(* the solution with 𝒱In defects omitted is
      virtually identical to that found previously at tRef−170 *)
"total RMS fractional difference between model species
      concentrations with old and new bases"
  With[{oldAnswer = Drop[c0ξ[1, tRef − 170] /. ξ00[1, tRef − 170], {10, 13}]},
    σSD[(c0ξxVin[1, tRef − 170] /. bridge170xVin) − oldAnswer / oldAnswer]]
```

5.68228×10^{-11} total RMS fractional difference between model species concentrations with old and new bases

The solution at the basis set cross-over temperature is virtually identical. In order to extend the solution to lower temperatures the critical temperature at which the selenium content of $Cu_{2-\delta}Se$ drops to its minimum stable value needs to be determined using this modified basis set **cE0xVin**. It is apparently below the eutectoid temperature at which indium-rich δ-CIS decomposes to form a mixture of α and β-CIS, taken here to be 600°C.

```
{"α−β−δ CIS eutectoid", tMaxαβ "K",
  ConvertTemperature[tMaxαβ, Kelvin, Celsius] "°C"}
tMaxαβ === tRef − 175
```

{α−β−δ CIS eutectoid, 873.15 K, 600. °C}
True

```
ListPlot[Thread[{tRef - Range[0, 370, 10],
    (((3 - (δmin[tRef - #] - c0ξxVin[1, tRef - #][[19]] / c0ξxVin[1, tRef - #][[20]])) /. ξ00[1, tRef - #])^-1 -
      xMin.Cu2Se[tRef - #]) & /@ Range[0, 370, 10]}],
  AxesOrigin → {tRef - 370, 0}, PlotJoined → True,
  AxesLabel → {"T[K]", "Δx"},
  PlotLabel →
    " Cu2-δSe Selenium Content in Equilibrium  at X=Z=1 with α-CIS\n  Binary
      phase composition deviation from minimum selenium mole fraction\n"];
```

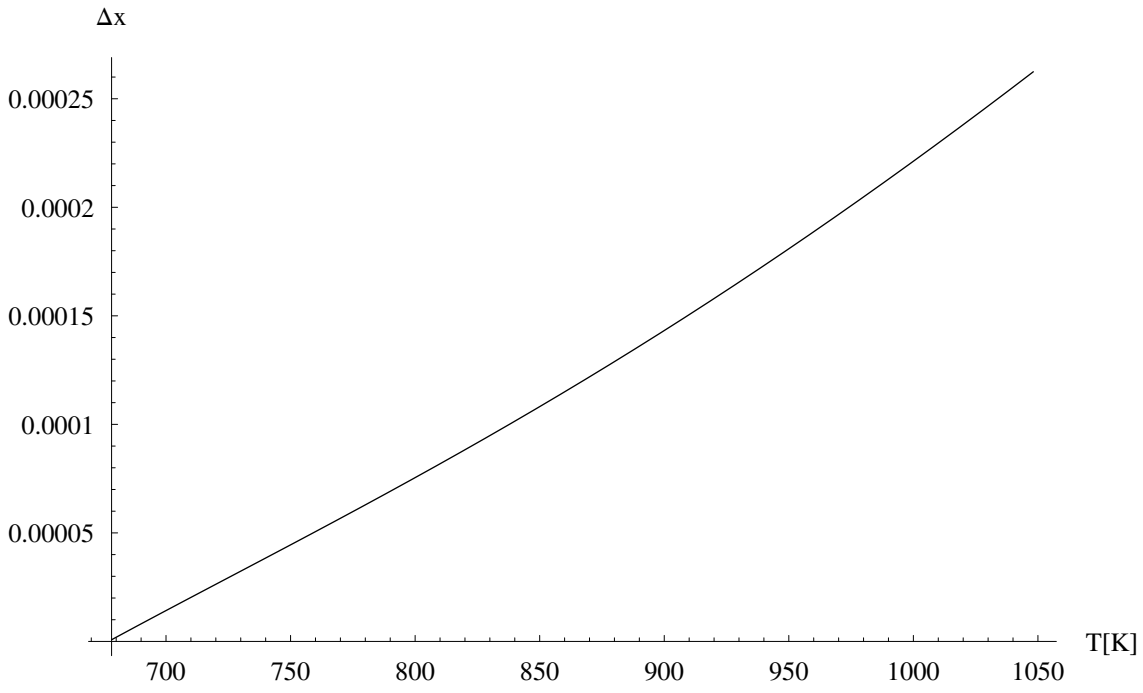

Figure A.3 Deviation of the $Cu_{2-\delta}Se$ phase's selenium content in equilibrium with α–CIS at X = Z = 1 from its minimum stable selenium mole fraction

```
tK00 = tRef - 370 - 1.4746

    676.675
```

```
(* this cell no longer executes because ξ00[1,tK00]
    was recalculated with the cE0LT basis, without Cu_Cu2Se *)
Thread[{cE0xVin, c0ξxVin[1, tK00] /. ξ00[1, tK00]}]
Positive[c0ξ[1, tK00][[23]] /. ξ00[1, tK00]]
```

$$\{\{CIS_{\alpha}, 0.4859\}, \{\mathcal{V}^{x}_{Cu}, 4.29848\times10^{-8}\}, \{\mathcal{V}'_{Cu}, 0.0016383\}, \{In^{x}_{Cu}, 2.88698\times10^{-23}\},$$
$$\{In^{\bullet}_{Cu}, 1.78049\times10^{-20}\}, \{In^{\bullet\bullet}_{Cu}, 1.63641\times10^{-19}\}, \{Cu^{x}_{In}, 3.58544\times10^{-16}\},$$
$$\{Cu'_{In}, 1.58191\times10^{-13}\}, \{Cu''_{In}, 3.36906\times10^{-14}\}, \{\mathcal{V}^{x}_{Se}, 2.54823\times10^{-10}\},$$
$$\{\mathcal{V}^{\bullet\bullet}_{Se}, 1.1571\times10^{-10}\}, \{Cu^{x}_{i}, 2.57465\times10^{-20}\}, \{Cu^{\bullet}_{i}, 3.74289\times10^{-17}\},$$
$$\{Cu_i \oplus \mathcal{V}_{Cu}, 2.8945\times10^{-12}\}, \{Cu_{In} \oplus In_{Cu}, 2.18344\times10^{-6}\},$$
$$\{\mathcal{V}_{Cu} \oplus In_{Cu}, 1.12679\times10^{-6}\}, \{(\mathcal{V}_{Cu} \oplus In_{Cu})^{\bullet}, 0.00163806\},$$
$$\{(2\,\mathcal{V}_{Cu} \oplus In_{Cu})_{\alpha}, 0.0000295799\}, \{Cu_{Cu2Se}, 4.06882\times10^{-9}\},$$
$$\{Cu2\_\delta Se, 0.00333754\}, \{e', 4.47687\times10^{-8}\}, \{h^{\bullet}, 2.82429\times10^{-7}\}, \{\Delta N, 1.00167\}\}$$

True

```
{tK00, tK00 – tK000, "critical temperature [°C]=",
  ConvertTemperature[tK00, Kelvin, Celsius]}
```

{676.675, −170.757, critical temperature [°C]=, 403.525}

This two-phase equilibrium calculation, which permits deviation of the CIS composition from that of stoichiometric $CuInSe_2$, shows that the selenium content of the $Cu_{2-\delta}Se$ phase at lower temperatures drops below the minimum required for its stability at about 400°C, if the extent of selenium and copper segregation to that phase are taken to be independent. Note that this is about 170°C below than the critical temperature calculated previously as the limiting temperature for a hypothetical equilibrium between $Cu_{2-\delta}Se$ and stoichiometric $CuInSe_2$.

This constraint must be satisfied for any solution to be valid, since it is known that along the pseudobinary section (where Z = 1) CIS is found in equilibrium with $Cu_{2-\delta}Se$ and not with the nearly pure Cu phase with which $Cu_{2-\delta}Se$ is in equilibrium when its selenium content is less than the minimum value at the two-

phase boundary between the latter two. A three-phase equilibrium between them is a thermodynamic critical point, and cannot exist at more than one point in the ternary phase field without violating the Gibbs phase rule. That point is not on the pseudobinary section.

Thus the foregoing solutions are valid only to this temperature, below which the solution algorithm must be modified to limit the segregation of excess copper. This is easily done by simply removing the species Cu_{Cu2Se}, which was included in the basis specifically to enable this segregation of excess copper to the non-stoichiometric secondary $Cu_{2-\delta}Se$ phase.

(* the CISα+Cu2Se basis vector without $\mathcal{V}_{In}$ or Cu_{Cu2Se} *)
cE0LT = Drop[cE0xVin, {19}]

$\{CIS_\alpha, \mathcal{V}^x_{Cu}, \mathcal{V}'_{Cu}, In^x_{Cu}, In^{\bullet}_{Cu}, In^{\bullet\bullet}_{Cu}, Cu^x_{In}, Cu'_{In}, Cu''_{In},$
$\mathcal{V}^x_{Se}, \mathcal{V}^{\bullet\bullet}_{Se}, Cu^x_i, Cu^{\bullet}_i, Cu_i \oplus \mathcal{V}_{Cu}, Cu_{In} \oplus In_{Cu}, \mathcal{V}_{Cu} \oplus In_{Cu},$
$(\mathcal{V}_{Cu} \oplus In_{Cu})^{\bullet}, (2\mathcal{V}_{Cu} \oplus In_{Cu})_\alpha, Cu2.\delta Se, e', h^{\bullet}, \Delta N\}$

$\mathcal{D}$0LT = Transpose[Drop[Transpose[$\mathcal{D}$0xVin], {19}]];

formula[i_, $\mathcal{D}$0LT] := {cE0LT, a .$\mathcal{D}$0LT}[[All, i]]

ν0LT = Transpose[NullSpace[$\mathcal{D}$0LT]];

rxn[i_, ν0LT] := ν0LT[[All, i]].cE0LT

$\nu 0\xi$LT = Drop[Transpose[Drop[Transpose[$\nu 0\xi$xVin], {5}]], {19}];

rxn[i_, $\nu 0\xi$LT] := $\nu 0\xi$LT[[All, i]].cE0LT

```
μ00LT[c_, tK_] /; Length[c] === Length[cE0LT] := With[
    {n = (#/Plus @@ #) &[Join[Take[Drop[Drop[mcl, {25}], {10, 13}] Take[c, 20], 18],
          {c[[19]]}]], δm = δmin[tK], nCISα = nAvo c/First[c]},
    ReplacePart[Drop[Drop[Drop[μ00αβ[tK], {25}], {10, 13}], {20}],
      (3 - δm) G_CuSeX[tK, (3 - δm)^-1], 19] + rG tK Join[Log[Drop[n, -1]],
      {Log[Last[n]], Log[nCISα[[20]]/cbDOSαCIS[tK]], Log[nCISα[[21]]/vbDOSαCIS[tK]], 0}]]

ξ000LT = Drop[ξ00xVin, {5}];
c00LT[Z_] := Drop[c00xVin[Z], {19}]
c0ξLT[Z_, tK_] := c00LT[Z] + (ν0ξLT /. δ → δmin[tK]).ξ000LT
gd00LT[Z_, tK_, Δg0CISαcl_] :=
  ((μ00LT[c0ξLT[#, #2], #2] /. Δg0αcl[#2] → \#3).(ν0LT /. δ → δmin[#2])) &[
    Z, tK, Δg0CISαcl]

(* the solution with the cE0LT basis is virtually
    identical to that found previously with cE0xVin at tK00*)
Thread[{cE0LT, c0ξLT[1, tK00] /. bridgetK00}]
"total RMS absolute difference between
      model species concentrations with old and new bases"
  With[{oldAnswer = Drop[(c0ξxVin[1, tK00] /. ξ00[1, tK00]), {19}]},
    σSD[(c0ξLT[1, tK00] /. bridgetK00) - oldAnswer]]
```

$$\{\{CIS_\alpha, 0.4859\}, \{\mathcal{V}^x_{Cu}, 4.28681\times10^{-8}\}, \{\mathcal{V}'_{Cu}, 0.0016383\}, \{In^x_{Cu}, 2.9027\times10^{-23}\},$$
$$\{In^{\bullet}_{Cu}, 1.78533\times10^{-20}\}, \{In^{\bullet\bullet}_{Cu}, 1.63642\times10^{-19}\}, \{Cu^x_{In}, 3.56602\times10^{-16}\},$$
$$\{Cu'_{In}, 1.57762\times10^{-13}\}, \{Cu''_{In}, 3.36906\times10^{-14}\}, \{\mathcal{V}^x_{Se}, 2.56211\times10^{-10}\},$$
$$\{\mathcal{V}^{\bullet\bullet}_{Se}, 1.15711\times10^{-10}\}, \{Cu^x_i, 2.58166\times10^{-20}\}, \{Cu^{\bullet}_i, 3.74289\times10^{-17}\},$$
$$\{Cu_i \oplus \mathcal{V}_{Cu}, 2.8945\times10^{-12}\}, \{Cu_{In} \oplus In_{Cu}, 2.18344\times10^{-6}\},$$
$$\{\mathcal{V}_{Cu} \oplus In_{Cu}, 1.12985\times10^{-6}\}, \{(\mathcal{V}_{Cu} \oplus In_{Cu})^{\bullet}, 0.00163806\},$$
$$\{(2\,\mathcal{V}_{Cu} \oplus In_{Cu})_\alpha, 0.0000295798\}, \{Cu2\_\delta Se, 0.00333754\},$$
$$\{e', 4.48904\times10^{-8}\}, \{h^{\bullet}, 2.81664\times10^{-7}\}, \{\Delta N, 1.00167\}\}$$
$$1.42243\times10^{-8} \text{ total RMS absolute difference between model species concentrations with old and new bases}$$

The solution concentrations with the low-temperature basis set **cE0LT** differs by at most a few *ppb* at the critical temperature, but the convergence has improved by

about four orders of magnitude. Thus the solution can be extended further over the remaining temperature range to STP:

```
tSTP + 750 === tRef
```

```
True
```

```
Thread[{cE0LT, c0ξLT[1, tRef – 750] /. ξ00[1, tRef – 750]}]
```

$$\{\{CIS_{\alpha}, 0.5\}, \{\mathcal{V}^{x}_{Cu}, 9.77066\times10^{-20}\}, \{\mathcal{V}'_{Cu}, 2.7131\times10^{-8}\}, \{In^{x}_{Cu}, 1.36318\times10^{-41}\},$$
$$\{In^{\bullet}_{Cu}, 7.17465\times10^{-42}\}, \{In^{\bullet\bullet}_{Cu}, 7.17465\times10^{-43}\}, \{Cu^{x}_{In}, 2.86986\times10^{-42}\},$$
$$\{Cu'_{In}, 1.8617\times10^{-33}\}, \{Cu''_{In}, 5.73037\times10^{-31}\}, \{\mathcal{V}^{x}_{Se}, 1.3363\times10^{-13}\},$$
$$\{\mathcal{V}^{\bullet\bullet}_{Se}, 2.41493\times10^{-22}\}, \{Cu^{x}_{i}, 5.33794\times10^{-40}\}, \{Cu^{\bullet}_{i}, 1.55161\times10^{-37}\},$$
$$\{Cu_{i}\oplus\mathcal{V}_{Cu}, 1.35084\times10^{-26}\}, \{Cu_{In}\oplus In_{Cu}, 1.71625\times10^{-12}\},$$
$$\{\mathcal{V}_{Cu}\oplus In_{Cu}, 9.5822\times10^{-11}\}, \{(\mathcal{V}_{Cu}\oplus In_{Cu})^{\bullet}, 2.76996\times10^{-8}\},$$
$$\{(2\,\mathcal{V}_{Cu}\oplus In_{Cu})_{\alpha}, 5.1677\times10^{-12}\}, \{Cu2.\delta Se, 5.56013\times10^{-8}\}, \{e', 5.68646\times10^{-10}\},$$
$$\{h^{\bullet}, 1.91401\times10^{-16}\}, \{\Delta N, 1.000000027800594754840768176 25\}\}$$

This solution shows that the In_{Cu}, Cu_{In}, and Cu_i species substantively vanish to levels of less than one defect per mole at STP in the equilibrium stoichiometric $CuInSe_2$ two-phase mixture. The dominant defects in this copper-saturated α–CIS phase at STP are the ionized cation NDC dissociation components, $\mathcal{V}'_{Cu}$ and $(\mathcal{V}_{Cu}\oplus In_{Cu})^{\bullet}$.

These results are next compiled and interpolated to define continuous solution functions, and various information functions defined.

```
solnRange = Join[Range[tRef, tRef – 170, –10],
      {tMaxαβ}, Range[tRef – 180, tRef – 745, –5], {tSTP}];
solnRangeαδ = Take[solnRange, 19];
solnRangeαβ = Reverse[Drop[solnRange, 18]];

Δg0αcl = Module[{Δg}, Δg = (Last[ξ00[1, #]][[2]]) & /@ solnRange;
      Interpolation[Thread[{solnRange, Δg}], InterpolationOrder → 4]];
```

```
c00αδ[1] =
    Module[{c, cTmin, cVin}, cVin = Interpolation[Thread[{Drop[solnRangeαδ, −1],
                  ((c0ξ[1, #] /. ξ00[1, #]) & /@ Drop[solnRangeαδ, −1])⟦All, #⟧}],
              InterpolationOrder → 4] & /@ Range[10, 13];
      Off[InterpolatingFunction::"dmval"]; cTmin =
        Drop[Flatten[Insert[c0ξxVin[1, tMaxαβ] /. ξ00[1, tMaxαβ],
            Array[cVin⟦#⟧[tMaxαβ] &, 4], 10]], {23}];
      On[InterpolatingFunction::"dmval"]; c = Append[
          Drop[(c0ξ[1, #] /. ξ00[1, #]), {23}] & /@ Drop[solnRangeαδ, −1], cTmin];
      Interpolation[Thread[{solnRangeαδ, c⟦All, #⟧}], InterpolationOrder → 4] & /@
        Range[Length[cE0] − 1]];

<< NumericalMath`SplineFit`

c00Fit[1] = Module[{c}, c = Join[(c0ξLT[1, #] /. ξ00[1, #]) & /@ Take[solnRangeαβ, 76],
          Drop[(c0ξxVin[1, #] /. ξ00[1, #]), {19}] & /@
            Take[solnRangeαβ, {77, Length[solnRangeαβ]}]]];
      SplineFit[Thread[{solnRangeαβ, c⟦All, #⟧}], Cubic] & /@ Range[Length[cE0LT]]];

cEαδ = Drop[cE0, {23}];
𝒟0αδ = Transpose[Drop[Transpose[𝒟0], {23}]];

c00[1, tK_?NumericQ] /; tMaxαβ < tK ≤ tRef :=
  Through[(c00αδ[1]⟦#⟧ & /@ Range[Length[cEαδ]])[tK]]
c00[1, tK_?NumericQ] /; tSTP ≤ tK ≤ tMaxαβ :=
  With[{T = (Length[solnRangeαβ] − 1) (tK − tSTP)/(tMaxαβ − tSTP)},
    Through[(c00Fit[1]⟦#⟧ & /@ Range[Length[cE0LT]])[T]]⟦All, 2⟧]

segCu2SeZ1[tK_?NumericQ] /; tMaxαβ < tK ≤ tRef := c00[1, tK]⟦23⟧
segCu2SeZ1[tK_?NumericQ] /; tSTP ≤ tK ≤ tMaxαβ := c00[1, tK]⟦19⟧
```

```
δ0Fit = SplineFit[Join[
          {{tRef - #, (δmin[tRef - #] - c0ξxVin[1, tRef - #][[19]] / c0ξxVin[1, tRef - #][[20]] /. ξ00[1, tRef - #])} & /@
            Range[0, 370, 10]}, {{tRef - 380, δmin[tRef - 380]}}], Cubic];

δ0[tK_?NumericQ] /; tRef - 380 ≤ tK ≤ tRef := With[{T = (tRef - tK)/10}, δ0Fit[T][[2]]]
δ0[tK_?NumericQ] /; tSTP ≤ tK < tRef - 380 :=
  With[{x_Se = xMin_Cu2Se[tK]}, (-1 + 3 x_Se)/x_Se]

mx[c00[1, tRef], 𝒟0αδ] /. δ → δ0[tRef]
mx[c00[1, tSTP], 𝒟0LT] /. δ → δ0[tSTP]

{1., 1., 2., 3.46945 × 10^-18}
{1., 1., 2., 0.}

xαZ1[tK_?NumericQ] /; tMaxαβ < tK ≤ tRef :=
  cXZ[partCIS[c00[1, tK]], partCIS[𝒟0αδ]][[1]]
xαZ1[tK_?NumericQ] /; tSTP ≤ tK ≤ tMaxαβ :=
  cXZ[partCIS[c00[1, tK]], partCIS[𝒟0LT]][[1]]

Off[General::"spell1"]
zαZ1[tK_?NumericQ] /; tMaxαβ < tK ≤ tRef :=
  cXZ[partCIS[c00[1, tK]], partCIS[𝒟0αδ]][[2]]
zαZ1[tK_?NumericQ] /; tSTP ≤ tK ≤ tMaxαβ :=
  cXZ[partCIS[c00[1, tK]], partCIS[𝒟0LT]][[2]]
```

```
Plot[Evaluate[(zαZ1[T] – 1) 1*^6], {T, tSTP, tMaxαβ},
  AxesOrigin → {tSTP, 0}, AxesLabel → {"T[K]", "ΔZ[ppm]"},
  PlotLabel → " α–CIS Phase Valency Deviation at Equilibrium
      \n with Cu2–δSe in the Stoichiometric CuInSe2 Mixture\n"]
```

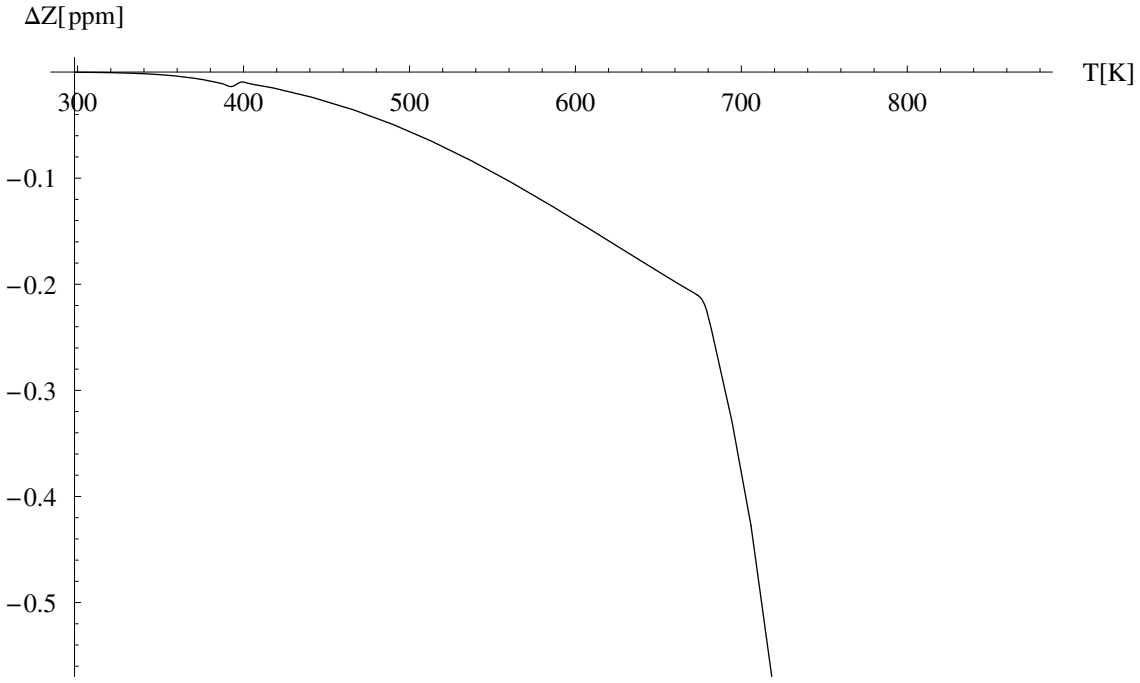

Figure A.4 Temperature dependence of the valency deviation of α–CIS in equilibrium with $Cu_{2-\delta}Se$ in the stoichiometric $CuInSe_2$ mixture

Since the excess Gibbs energy of the ideal CIS_α cluster is now determined, it may be removed from the function definitions as an independent variable, which considerably speeds the computation of the solution at other temperatures and valence stoichiometries.

```
{Last[ξ00[1, tMaxαβ]], Δg0αcl[tMaxαβ]}

    {xsCISclG → 1450.53, 1450.53}

gd0xVin[Z_, tK_] := (μ00xVin[c0ξxVin[#, #2], #2].(ν0xVin /. δ → δmin[#2])) &[Z, tK]
gd0LT[Z_, tK_] := (μ00LT[c0ξLT[#, #2], #2].(ν0LT /. δ → δmin[#2])) &[Z, tK]
```

The equilibrium solution for X = Z = 1 shows that the segregation of $Cu_{2-\delta}Se$ results in positive molecularity and valency deviations in the α-CIS phase:

" CIS valency deviation at the $\alpha/\beta/\delta-$CIS eutectoid with X=Z=1"
(cXZ[partCIS[c00[1, tMax$\alpha\beta$]], partCIS[$\mathcal{D}$0LT]][[2]] − 1)

-5.62808×10^{-6} CIS valency deviation at the $\alpha/\beta/\delta-$CIS eutectoid with X=Z=1

```
FindRoot[c00[1, T][[20]] == c00[1, T][[21]],
    {T, tSTP + 400, tSTP + 410}, AccuracyGoal → 20];
{"X=Z=1 isoelectronic temperature", T "[K]",
    "[°C]" ConvertTemperature[T, Kelvin, Celsius]} /. %
```

{X=Z=1 isoelectronic temperature, 608.563 [K], 335.413 [°C]}

```
Thread[{{cE0LT[[20]], cE0LT[[21]]}, {c00[1, tSTP][[20]], c00[1, tSTP][[21]]}}]
```

$\{\{e', 5.68646 \times 10^{-10}\}, \{h^{\blacksquare}, 1.91401 \times 10^{-16}\}\}$

The equilibrium solution for X = Z = 1 and temperatures below the δ-CIS eutectoid decomposition shows a maximum valency deviation in the α-CIS phase of less than 6 *ppm*. Deviations of this magnitude in the principal constituent compositions are considerably less than the resolution of current analytical measurement techniques. It is therefore of interest to assess the influence of introducing an excess of selenium of this same magnitude on the defect structure of the α-CIS phase, since transport studies have shown [3] that CIS material with positive valency deviation is *p*-type at STP, whereas the preceding calculation predicts that the α-CIS phase component in the precisely stoichiometric equilibrium two-phase mixture is weakly *n*-type. Experimental confirmation of this prediction might be extremely difficult since the secondary $Cu_{2-\delta}Se$ phase is always strongly *p*-type [160, 176].

A comparison of the model species' concentrations at STP, the highest temperature at which the $Cu_{2-\delta}Se$ phase's selenium content is minimal, and the $\alpha/\beta/\delta$ eutectoid shows the trends in their temperature variation:

```
"      STP   tK00    tMaxαβ"
{cE0LT⟦#⟧, c00[1, tSTP]⟦#⟧, c00[1, tK00]⟦#⟧, c00[1, tMaxαβ]⟦#⟧} & /@
  Range[Length[cE0LT]]
gd0LT[1, tSTP] /. ξ00[1, tSTP];
"Joules RMS affinity solution error at STP" σSD[%]
```

	STP	tK00	tMax$\alpha\beta$
{CIS_{α},	0.5,	0.4859,	0.421051},
{$\mathcal{V}^{x}_{Cu}$,	9.77066×10^{-20},	4.2602×10^{-8},	1.30988×10^{-6}},
{$\mathcal{V}'_{Cu}$,	2.7131×10^{-8},	0.00163829,	0.00897599},
{In^{x}_{Cu},	1.36318×10^{-41},	2.93546×10^{-23},	2.88754×10^{-18}},
{$In^{\bullet}_{Cu}$,	7.17465×10^{-42},	1.7955×10^{-20},	5.27433×10^{-16}},
{$In^{\bullet\bullet}_{Cu}$,	7.17465×10^{-43},	1.6364×10^{-19},	2.03187×10^{-15}},
{Cu^{x}_{In},	2.86986×10^{-42},	3.52425×10^{-16},	2.08787×10^{-13}},
{Cu'_{In},	1.8617×10^{-33},	1.56818×10^{-13},	4.51698×10^{-11}},
{Cu''_{In},	5.73037×10^{-31},	3.36905×10^{-14},	1.44442×10^{-11}},
{$\mathcal{V}^{x}_{Se}$,	1.3363×10^{-13},	2.59434×10^{-10},	1.73034×10^{-8}},
{$\mathcal{V}^{\bullet\bullet}_{Se}$,	2.41493×10^{-22},	1.15711×10^{-10},	8.1457×10^{-9}},
{Cu^{x}_{i},	5.33794×10^{-40},	2.59661×10^{-20},	2.2171×10^{-16}},
{$Cu^{\bullet}_{i}$,	1.55161×10^{-37},	3.74289×10^{-17},	7.87086×10^{-14}},
{$Cu_{i}\oplus\mathcal{V}_{Cu}$,	1.35084×10^{-26},	2.89449×10^{-12},	6.34405×10^{-10}},
{$Cu_{In}\oplus In_{Cu}$,	1.71625×10^{-12},	2.18344×10^{-6},	0.0000166687},
{$\mathcal{V}_{Cu}\oplus In_{Cu}$,	9.5822×10^{-11},	1.13701×10^{-6},	0.0000252791},
{$(\mathcal{V}_{Cu}\oplus In_{Cu})^{\bullet}$,	2.76996×10^{-8},	0.00163806,	0.00897427},
{$(2\,\mathcal{V}_{Cu}\oplus In_{Cu})_{\alpha}$,	5.1677×10^{-12},	0.0000295796,	0.000448909},
{Cu2.δSe,	5.56013×10^{-8},	0.00333755,	0.0188969},
{e′,	5.68646×10^{-10},	4.51775×10^{-8},	5.44693×10^{-7}},
{$h^{\bullet}$,	1.91401×10^{-16},	2.79881×10^{-7},	2.2488×10^{-6}},
{ΔN,	1.000000027800594754840768176 25,	1.00167,	1.00945}}

244981. Joules RMS affinity solution error at STP

It is apparent from the solution that defect complexes form in *lieu* of their component isolated defects in every case included in this model. The convergence of the solution at low temperatures can thus be considerably improved without the introduction of significant error by eliminating those species from the basis set. They can be reintroduced at any time if the solution in their absence shows a significant increase in the concentration of the dominant related defect associate(s). Inspection of the solution shown above at the maximum temperature of the remaining calculations reveals that the In_{Cu}, and Cu_i isolated point defect species can be removed, as the $\mathcal{V}_{In}$ defects were previously. The isolated Cu_{In} and $\mathcal{V}_{Se}$ defects must be retained because of their role in initializing the concentration vector when $Z \neq 1$, and because the latter does not form any defect associate included in this model.

(∗ the reduced CISα+Cu2Se basis vector for high temp ∗)
cE00xsδ = Drop[Drop[Drop[cE0, {16, 17}], {10, 13}], {4, 6}]

$$\{CIS_\alpha, \mathcal{V}^x_{Cu}, \mathcal{V}'_{Cu}, Cu^x_{In}, Cu'_{In}, Cu''_{In}, \mathcal{V}^x_{Se}, \mathcal{V}^{\bullet\bullet}_{Se}, Cu_i \oplus \mathcal{V}_{Cu}, Cu_{In} \oplus In_{Cu}, \mathcal{V}_{Cu} \oplus In_{Cu}, (\mathcal{V}_{Cu} \oplus In_{Cu})^\bullet, (2\mathcal{V}_{Cu} \oplus In_{Cu})_\alpha, Cu_{Cu2Se}, Cu2\_\delta Se, e', h^\bullet, \Delta N\}$$

(∗ the reduced CISα+Cu2Se basis vector for low temp ∗)cE00

$$\{CIS_\alpha, \mathcal{V}^x_{Cu}, \mathcal{V}'_{Cu}, Cu^x_{In}, Cu'_{In}, Cu''_{In}, \mathcal{V}^x_{Se}, \mathcal{V}^{\bullet\bullet}_{Se}, Cu_i \oplus \mathcal{V}_{Cu}, Cu_{In} \oplus In_{Cu}, \mathcal{V}_{Cu} \oplus In_{Cu}, (\mathcal{V}_{Cu} \oplus In_{Cu})^\bullet, (2\mathcal{V}_{Cu} \oplus In_{Cu})_\alpha, Cu2\_\delta Se, e', h^\bullet, \Delta N\}$$
$$\{CIS_\alpha, \mathcal{V}^x_{Cu}, \mathcal{V}'_{Cu}, Cu^x_{In}, Cu'_{In}, Cu''_{In}, \mathcal{V}^x_{Se}, \mathcal{V}^{\bullet\bullet}_{Se}, Cu_i \oplus \mathcal{V}_{Cu}, Cu_{In} \oplus In_{Cu}, \mathcal{V}_{Cu} \oplus In_{Cu}, (\mathcal{V}_{Cu} \oplus In_{Cu})^\bullet, (2\mathcal{V}_{Cu} \oplus In_{Cu})_\alpha, Cu2\_\delta Se, e', h^\bullet, \Delta N\}$$

$\mathcal{D}$00xsδ = Transpose[Drop[Drop[Drop[Transpose[$\mathcal{D}$0], {16, 17}], {10, 13}], {4, 6}]];

(* the stoichiometry matrix for the low temperature basis
without Cu_{Cu2Se} has been previously defined *)$\mathcal{D}$00 // MatrixForm

$$\begin{pmatrix}
2 & 5 & 5 & 7 & 7 & 7 & 6 & 6 & 6 & 6 & 8 & 8 & 7 & 2-\delta & 0 & 0 & 0 \\
2 & 6 & 6 & 5 & 5 & 5 & 6 & 6 & 6 & 6 & 11 & 11 & 11 & 0 & 0 & 0 & 0 \\
4 & 12 & 12 & 12 & 12 & 12 & 11 & 11 & 12 & 12 & 20 & 20 & 20 & 1 & 0 & 0 & 0 \\
0 & 0 & -1 & 0 & -1 & -2 & 0 & 2 & 0 & 0 & 0 & 1 & 0 & 0 & -1 & 1 & 0 \\
2 & 6 & 6 & 6 & 6 & 6 & 6 & 6 & 6 & 6 & 10 & 10 & 10 & 0 & 0 & 0 & 1 \\
2 & 6 & 6 & 6 & 6 & 6 & 6 & 6 & 6 & 6 & 10 & 10 & 10 & 0 & 0 & 0 & 1 \\
4 & 12 & 12 & 12 & 12 & 12 & 12 & 12 & 12 & 12 & 20 & 20 & 20 & 0 & 0 & 0 & 2 \\
8 & 24 & 24 & 24 & 24 & 24 & 24 & 24 & 24 & 24 & 40 & 40 & 40 & 0 & 0 & 0 & 4
\end{pmatrix}$$

```
formula[i_, 𝒟00xsδ] := {cE00xsδ, a .𝒟00xsδ}⟦All, i⟧
formula[i_, 𝒟00] := {cE00, a .𝒟00}⟦All, i⟧

ν00xsδ = Transpose[NullSpace[𝒟00xsδ]];
ν00 = Transpose[NullSpace[𝒟00]];

rxn[i_, ν00xsδ] := ν00xsδ⟦All, i⟧.cE00xsδ
rxn[i_, ν00] := ν00⟦All, i⟧.cE00

ν00ξxsδ = ν00xsδ;
ν00ξxsδ = Transpose[ReplacePart[Transpose[ν00ξxsδ],
    ν00xsδ⟦All, 1⟧ + 2 ν00xsδ⟦All, 4⟧ + ν00xsδ⟦All, 6⟧, 1]] // Simplify;
ν00ξxsδ = Transpose[ReplacePart[Transpose[ν00ξxsδ],
    ν00xsδ⟦All, 3⟧ + ν00xsδ⟦All, 2⟧, 3]];
ν00ξxsδ = Transpose[ReplacePart[Transpose[ν00ξxsδ],
    -ν00xsδ⟦All, 6⟧ + ν00xsδ⟦All, 8⟧, 6]];
ν00ξxsδ = Transpose[ReplacePart[Transpose[ν00ξxsδ],
    ν00xsδ⟦All, 7⟧ + ν00xsδ⟦All, 3⟧ - ν00xsδ⟦All, 8⟧, 7]];
ν00ξxsδ = Transpose[ReplacePart[Transpose[ν00ξxsδ],
    ν00xsδ⟦All, 11⟧ + 2 ν00xsδ⟦All, 3⟧, 11]]; ν00ξxsδ =
  Transpose[ReplacePart[Transpose[ν00ξxsδ], ν00xsδ⟦All, 12⟧ + 2 ν00xsδ⟦All, 2⟧, 12]];
ν00ξxsδ = Transpose[
    ReplacePart[Transpose[ν00ξxsδ], ν00xsδ⟦All, 13⟧ + ν00xsδ⟦All, 2⟧, 13]];

rxn[i_, ν00ξxsδ] := ν00ξxsδ⟦All, i⟧.cE00xsδ
```

```
ν00ξ = Drop[Transpose[Drop[Transpose[ν00ξxsδ], {5}]], {14}];

rxn[i_, ν00ξ] := ν00ξ⟦All, i⟧.cE00

c00xsδbasis = {1, 7, 4, 13};

cE00xsδ⟦#⟧ & /@ c00xsδbasis
```

$$\{\mathrm{CIS}_{\alpha},\ \mathcal{V}^{x}_{Se},\ \mathrm{Cu}^{x}_{In},\ (2\,\mathcal{V}_{Cu} \oplus \mathrm{In}_{Cu})_{\alpha}\}$$

```
ξ000xsδ = Array[1 &, 13] −
    2 Array[KroneckerDelta[1, # ] &, 13] − Array[KroneckerDelta[5, # ] &, 13] +
    Array[KroneckerDelta[4, # ] &, 13] + Array[KroneckerDelta[2, # ] &, 13]
```

$$\{-1, 2, 1, 2, 0, 1, 1, 1, 1, 1, 1, 1, 1\}$$

```
c00xsδ[Z_] /; 29337/32000 ≤ Z ≤ 1 :=
  Module[{c00}, With[{c4Zminus = {1 + 4 (−1 + Z)/(−7 + 8 Z), −4 (−1 + Z)/(−7 + 8 Z), 0, 0},
      mCuInv1 = 1/(−24 (−1+Z)/(−7+8 Z) + 2 (1 + 4 (−1+Z)/(−7+8 Z)))},
    c00 = Plus @@ MapThread[ReplacePart[Array[0 &, Length[cE00xsδ]], #1, #2] &,
        {c4Zminus, c00xsδbasis}];
    c00 = ReplacePart[c00, δmin[tRef] ξ000xsδ⟦4⟧ 2*^-26, 14];
    c00 = mCuInv1 (c00 + (ν00xsδ /. δ → δmin[tRef]).ξ000xsδ 1*^-26);
    ReplacePart[c00, 1, −1]]]

c00xsδ[Z_] /; 1 < Z ≤ 95989/88000 := Module[{c00},
    With[{c4Zplus = {1 + 6 (−1 + Z)/(−16 + 15 Z), 0, −4 (−1 + Z)/(−16 + 15 Z), −2 (−1 + Z)/(−16 + 15 Z)},
      mCuInv2 = 1/(−42 (−1+Z)/(−16+15 Z) + 2 (1 + 6 (−1+Z)/(−16+15 Z)))},
    c00 = Plus @@ MapThread[ReplacePart[Array[0 &, Length[cE00xsδ]], #1, #2] &,
        {c4Zplus, c00xsδbasis}];
    c00 = ReplacePart[c00, δmin[tRef] ξ000xsδ⟦4⟧ 2*^-26, 14];
    c00 = mCuInv2 (c00 + (ν00xsδ /. δ → δmin[tRef]).ξ000xsδ 1*^-26);
    ReplacePart[c00, 1, −1]]]
```

```
c00minδ[Z_] := Drop[c00xsδ[Z], {14}]

μ00xsδ[c_, tK_] /; Length[c] === Length[cE00xsδ] :=
  With[{n = (#/Plus @@ #) &[Join[Drop[Drop[Drop[Drop[Drop[mcl, {25}], {16, 17}],
                {10, 13}], {4, 6}] Take[c, 15], -2], {c[[15]]}]], δm = δmin[tK],
    δ0 = δmin[tK] - c[[14]]/c[[15]], nCISα = nAvo c/First[c]}, ReplacePart[
     ReplacePart[Drop[Drop[Drop[Drop[μ00αβ[tK], {25}], {16, 17}], {10, 13}], {4, 6}],
      ((3 - δ0) G_CuSeX[tK, (3 - δ0)^-1] - (3 - δm) G_CuSeX[tK, (3 - δm)^-1])
       (δm - δ0)^-1, 14], (3 - δm) G_CuSeX[tK, (3 - δm)^-1], 15] +
    rG tK Join[Log[Drop[n, -1]], {0, Log[Last[n]], Log[nCISα[[16]]/cbDOSαCIS[tK]],
      Log[nCISα[[17]]/vbDOSαCIS[tK]], 0}]]

μ00minδ[c_, tK_] /; Length[c] === Length[cE00] :=
  With[{n = (#/Plus @@ #) &[Join[Drop[Drop[Drop[Drop[Drop[mcl, {25}], {16, 17}],
                {10, 13}], {4, 6}] Take[c, 15], -2], {c[[14]]}]],
    δm = δmin[tK], nCISα = nAvo c/First[c]}, ReplacePart[
     Drop[Drop[Drop[Drop[Drop[μ00αβ[tK], {25}], {16, 17}], {10, 13}], {4, 6}], {15}],
     (3 - δm) G_CuSeX[tK, (3 - δm)^-1], 14] + rG tK Join[Log[Drop[n, -1]],
      {Log[Last[n]], Log[nCISα[[15]]/cbDOSαCIS[tK]], Log[nCISα[[16]]/vbDOSαCIS[tK]], 0}]]

ξ00xsδ = Drop[Drop[Take[ξ000, 19], {14, 17}], {11, 12}];
c00ξxsδ[Z_, tK_] := c00xsδ[Z] + (ν00ξxsδ /. δ → δmin[tK]).ξ00xsδ

ξ00minδ = Drop[ξ00xsδ, {5}];
c00ξminδ[Z_, tK_] := c00minδ[Z] + (ν00ξ /. δ → δmin[tK]).ξ00minδ

gd0xsδ[Z_, tK_] := (μ00xsδ[c00ξxsδ[#, #2], #2].(ν00xsδ /. δ → δmin[#2])) &[Z, tK]
gd0minδ[Z_, tK_] := (μ00minδ[c00ξminδ[#, #2], #2].(ν00 /. δ → δmin[#2])) &[Z, tK]
```

The convergence of the solution at STP with respect to the basis **cE00** is two orders of magnitude better than that of the initial solution:

gd0minδ[1, tSTP] /. ξ0[1, tSTP]
{"solution convergence σ_{SD}", σSD[%]}
Thread[{cE00, c00ξminδ[1, tSTP] /. ξ0[1, tSTP]}]

{−204.143, −0.172278, 0.172292, 0.342524, 203.454,
203.454, 203.626, 0., 0., −0.344584, −203.454, −203.626}
{solution convergence σ_{SD}, 1222.79}
{{CIS_{α}, 0.5}, {$\mathcal{V}_{Cu}^{x}$, 3.1036×10^{-21}}, {$\mathcal{V}'_{Cu}$, 2.7131×10^{-8}},
{Cu_{In}^{x}, 5.73972×10^{-42}}, {Cu'_{In}, 1.8617×10^{-33}}, {Cu''_{In}, 5.73037×10^{-31}},
{$\mathcal{V}_{Se}^{x}$, 1.3363×10^{-13}}, {$\mathcal{V}_{Se}^{\bullet\bullet}$, 2.41493×10^{-22}}, {$Cu_i \oplus \mathcal{V}_{Cu}$, 1.35084×10^{-26}},
{$Cu_{In} \oplus In_{Cu}$, 1.71625×10^{-12}}, {$\mathcal{V}_{Cu} \oplus In_{Cu}$, 9.5822×10^{-11}},
{$(\mathcal{V}_{Cu} \oplus In_{Cu})^{\bullet}$, 2.76996×10^{-8}}, {$(2\,\mathcal{V}_{Cu} \oplus In_{Cu})_{\alpha}$, 5.1677×10^{-12}},
{Cu2_δSe, 5.56013×10^{-8}}, {e′, 5.68646×10^{-10}}, {h$^{\bullet}$, 1.91401×10^{-16}}, {ΔN, 1.}}

Now that the minor isolated point defects have been removed from the basis set and the solution for Z = 1 recomputed, the Z > 1 case is considered. As previously derived, the relationship between the valency deviation and excess selenium in the mixture is given by the relation $\Delta s = \frac{(Z-1)(3+X)}{1+X}$. All of these calculations were performed for a value of X= 1 in the mixture, so this relation reduces here to $\Delta s = 2\,\Delta Z$. The solution for Z = 1 at the maximum temperature is used to initialize this calculation:

Z1plus4to5ppm = 1 + 4.5*^-6;

gd0xsδ[Z1plus4to5ppm, tMax$\alpha\beta$] /. ξ0[1, tMax$\alpha\beta$]

{−127633., 0.814731, 0.814732, 7.49127, 2.50773, 127695., 127625.,
127625., 2.50773, 2.50773, -2.32831×10^{-8}, −127621., −127621.}

gd0xsδ[Z1plus4to5ppm, tMax$\alpha\beta$] /. ξ0[Z1plus4to5ppm, tMax$\alpha\beta$]

{3.11621×10^{-6}, 1.01718×10^{-8}, -1.40135×10^{-8}, -1.76951×10^{-8}, -2.32831×10^{-9},
-3.08198×10^{-6}, -3.08082×10^{-6}, -3.09013×10^{-6}, 1.74623×10^{-10},
4.65661×10^{-10}, 1.67638×10^{-8}, 3.08198×10^{-6}, 3.09056×10^{-6}}

```
gd0xsδ[Z1plus4to5ppm, tRef – 635] /. ξ0[Z1plus4to5ppm, tRef – 635]
{"solution convergence σSD", σSD[%]}
Thread[
  {cE00xsδ, c00ξxsδ[Z1plus4to5ppm, tRef – 635] /. ξ0[Z1plus4to5ppm, tRef – 635]}]
```

$$\{0.000863334,\ 4.36557\times10^{-11},\ -0.000167168,\ -0.0000924887,\ 0.,\ -0.000678357,\ -0.000678355,\ 0.0027659,\ 0.,\ 0.,\ 0.0000924878,\ 0.000678357,\ 0.000678356\}$$

$$\{\text{solution convergence } \sigma_{SD},\ 0.0066948\}$$

$$\{\{CIS_{\alpha},\ 0.499938\},\ \{\mathcal{V}^{x}_{Cu},\ 7.14921\times10^{-8}\},\ \{\mathcal{V}'_{Cu},\ 0.0000173344\},\ \{Cu^{x}_{In},\ 2.58879\times10^{-15}\},\ \{Cu'_{In},\ 4.22824\times10^{-16}\},\ \{Cu''_{In},\ 1.39716\times10^{-21}\},\ \{\mathcal{V}^{x}_{Se},\ 1.21061\times10^{-25}\},\ \{\mathcal{V}^{\bullet\bullet}_{Se},\ 2.05823\times10^{-17}\},\ \{Cu_i\oplus\mathcal{V}_{Cu},\ 1.91485\times10^{-19}\},\ \{Cu_{In}\oplus In_{Cu},\ 1.96199\times10^{-9}\},\ \{\mathcal{V}_{Cu}\oplus In_{Cu},\ 1.06832\times10^{-15}\},\ \{(\mathcal{V}_{Cu}\oplus In_{Cu})^{\bullet},\ 1.7202\times10^{-6}\},\ \{(2\,\mathcal{V}_{Cu}\oplus In_{Cu})_{\alpha},\ 7.95252\times10^{-9}\},\ \{Cu_{Cu2Se},\ -2.2543\times10^{-6}\},\ \{Cu2.\delta Se,\ 0.0000124563\},\ \{e',\ 1.79417\times10^{-15}\},\ \{h^{\bullet},\ 0.0000156142\},\ \{\Delta N,\ 1.00001\}\}$$

$$\{tRef - 635,\ tCrit.\alpha2\beta2\}$$

$$\{413.15,\ 395.\}$$

It is not coincidental that this convergence limit is very nearly the same temperature as the the secondary $Cu_{2-\delta}Se$ phase α/β peritectoid, since the preceding boundary condition analysis showed that the deviation of the minimum selenium content from that of stoichiometric Cu_2Se increases rapidly in that temperature range. Consequently, the neutral $\mathcal{V}^{x}_{Se}$ and $(\mathcal{V}_{Cu}\oplus In_{Cu})$ species have dropped to levels where they must be removed from the basis so that these calculations for $Z > 1$ may be extended to lower temperatures.

```
(* the reduced CISα+Cu2Se basis vector for Z>1 *)
cE00xsδLT = Drop[Drop[Drop[Drop[cE0, {20}], {16, 17}], {10, 14}], {4, 6}];
{#, cE00xsδLT[[#]]} & /@ Array[# &, Length[cE00xsδLT]]
```

$$\{\{1, CIS_{\alpha}\},\ \{2, \mathcal{V}^{x}_{Cu}\},\ \{3, \mathcal{V}'_{Cu}\},\ \{4, Cu^{x}_{In}\},\ \{5, Cu'_{In}\},\ \{6, Cu''_{In}\},\ \{7, \mathcal{V}^{\bullet\bullet}_{Se}\},\ \{8, Cu_i\oplus\mathcal{V}_{Cu}\},\ \{9, Cu_{In}\oplus In_{Cu}\},\ \{10, (\mathcal{V}_{Cu}\oplus In_{Cu})^{\bullet}\},\ \{11, (2\,\mathcal{V}_{Cu}\oplus In_{Cu})_{\alpha}\},\ \{12, Cu_{Cu2Se}\},\ \{13, Cu2.\delta Se\},\ \{14, e'\},\ \{15, h^{\bullet}\},\ \{16, \Delta N\}\}$$

```
𝒟00xsδLT = Transpose[
    Drop[Drop[Drop[Drop[Transpose[𝒟0], {20}], {16, 17}], {10, 14}], {4, 6}]];

formula[i_, 𝒟00xsδLT] := {cE00xsδLT, a .𝒟00xsδLT}⟦All, i⟧

ν00xsδLT = Transpose[NullSpace[𝒟00xsδLT]];

rxn[i_, ν00xsδLT] := ν00xsδLT⟦All, i⟧.cE00xsδLT

ν00ξxsδLT = ν00xsδLT;
ν00ξxsδLT = Transpose[ReplacePart[Transpose[ν00ξxsδLT],
        ν00xsδLT⟦All, 1⟧ + 2 ν00xsδLT⟦All, 4⟧ + ν00xsδLT⟦All, 6⟧, 1]] // Simplify;
ν00ξxsδLT = Transpose[ReplacePart[Transpose[ν00ξxsδLT],
      ν00xsδLT⟦All, 3⟧ + ν00xsδLT⟦All, 2⟧, 3]];
ν00ξxsδLT = Transpose[ReplacePart[Transpose[ν00ξxsδLT],
    ν00xsδLT⟦All, 7⟧ − ν00xsδLT⟦All, 6⟧, 7]]; ν00ξxsδLT = Transpose[
  ReplacePart[Transpose[ν00ξxsδLT], ν00xsδLT⟦All, 10⟧ + 2 ν00xsδLT⟦All, 2⟧, 10]];
ν00ξxsδLT = Transpose[ReplacePart[Transpose[ν00ξxsδLT],
      ν00xsδLT⟦All, 11⟧ + ν00xsδLT⟦All, 2⟧, 11]];

rxn[i_, ν00ξxsδLT] := ν00ξxsδLT⟦All, i⟧.cE00xsδLT

ξ000xsδLT = Array[1 &, 11] − 3 Array[KroneckerDelta[1, # ] &, 11] −
  Array[KroneckerDelta[5, # ] &, 11] + 6 Array[KroneckerDelta[3, # ] &, 11]

    {−2, 1, 7, 1, 0, 1, 1, 1, 1, 1, 1}

c00Zbasis = {1, 4, 10, 11};

cE00xsδLT⟦#⟧ & /@ c00Zbasis
cE00xsδ⟦#⟧ & /@ c00xsδbasis

    {CIS_α, Cu_In^x, (𝒱_Cu ⊕ In_Cu)^▪, (2 𝒱_Cu ⊕ In_Cu)_α}
    {CIS_α, 𝒱_Se^x, Cu_In^x, (2 𝒱_Cu ⊕ In_Cu)_α}
```

```
c00xsδLT[Z_] /; 1 < Z ≤ 95989/88000 :=
  Module[{c00}, With[{c4xsδLT = {1 + 6 (-1 + Z)/(-16 + 15 Z), -4 (-1 + Z)/(-16 + 15 Z), 0, -2 (-1 + Z)/(-16 + 15 Z)},
      mCuInv2 = 1/(-42 (-1+Z)/(-16+15 Z) + 2 (1 + 6 (-1+Z)/(-16+15 Z)))}, c00 =
      Plus @@ MapThread[ReplacePart[Array[0 &, Length[cE00xsδLT]], #1, #2] &,
        {c4xsδLT, c00Zbasis}];
    c00 = ReplacePart[c00, δmin[tRef] ξ000xsδLT[[1]] 2*^-26, 12];
    c00 = mCuInv2 (c00 + (ν00xsδLT /. δ → δmin[tRef]).ξ000xsδLT 1*^-26);
    ReplacePart[c00, 1, -1]]]

μ00xsδLT[c_, tK_] /; Length[c] === Length[cE00xsδLT] :=
  With[{n = (# / Plus @@ #) &[Join[Drop[Drop[Drop[Drop[Drop[Drop[mcl, {25}], {20}],
          {16, 17}], {10, 14}], {4, 6}] Take[c, 13], -2], {c[[13]]}]],
    δm = δmin[tK], δ0 = δmin[tK] - c[[12]] / c[[13]], nCISα = nAvo c / First[c]},
   ReplacePart[ReplacePart[Drop[
      Drop[Drop[Drop[μ00αβ[tK], {25}], {20}], {16, 17}], {10, 14}], {4, 6}],
     ((3 - δ0) G_CuSeX[tK, (3 - δ0)^-1] - (3 - δm) G_CuSeX[tK, (3 - δm)^-1])
      (δm - δ0)^-1, 12], (3 - δm) G_CuSeX[tK, (3 - δm)^-1], 13] +
    rG tK Join[Log[Drop[n, -1]], {0, Log[Last[n]], Log[nCISα[[14]] / cbDOSαCIS[tK]],
      Log[nCISα[[15]] / vbDOSαCIS[tK]], 0}]]

ξ00xsδLT = Drop[Drop[Take[ξ000, 19], {11, 17}], {8}];
c00ξxsδLT[Z_, tK_] /; Z > 1 := c00xsδLT[Z] + (ν00ξxsδLT /. δ → δmin[tK]).ξ00xsδLT

gd0xsδLT[Z_, tK_] /; Z > 1 :=
  (μ00xsδLT[c00ξxsδLT[#, #2], #2].(ν00xsδLT /. δ → δmin[#2])) &[Z, tK]
```

gd0xsδLT[Z1plus4to5ppm, tSTP] /. ξ0[Z1plus4to5ppm, tSTP]
{"solution convergence σ_{SD}", σSD[%]}
Thread[{cE00xsδLT, c00ξxsδLT[Z1plus4to5ppm, tSTP] /. ξ0[Z1plus4to5ppm, tSTP]}]

$\{5.58794\times10^{-9}, 9.09495\times10^{-11}, -8.36735\times10^{-11}, 0., -2.32831\times10^{-10},$
$-0.00128309, -6.0536\times10^{-9}, 0., 0., 6.0536\times10^{-9}, 6.35555\times10^{-9}\}$
{solution convergence σ_{SD}, 0.00128312}
{{CIS_α, 0.499952}, {$\mathcal{V}^{x}_{Cu}$, 1.48949×10^{-7}}, {$\mathcal{V}'_{Cu}$, 0.0000157865},
{Cu^{x}_{In}, 1.50277×10^{-10}}, {Cu'_{In}, 6.41554×10^{-13}}, {Cu''_{In}, 2.39401×10^{-21}},
{$\mathcal{V}^{\bullet\bullet}_{Se}$, 6.41618×10^{-30}}, {$Cu_i \oplus \mathcal{V}_{Cu}$, 1.3504×10^{-26}},
{$Cu_{In} \oplus In_{Cu}$, 1.71569×10^{-12}}, {$(\mathcal{V}_{Cu} \oplus In_{Cu})^{\bullet}$, 3.85579×10^{-15}},
{$(2\,\mathcal{V}_{Cu} \oplus In_{Cu})_\alpha$, 4.18693×10^{-16}}, {Cu_{Cu2Se}, -1.95669×10^{-6}},
{Cu2δSe, 8.9997×10^{-6}}, {e′, 6.89316×10^{-21}}, {$h^{\bullet}$, 0.0000157865}, {ΔN, 1.}}

{Length[solnRange$\alpha\beta$], Length[Join[{tMax$\alpha\beta$}, Range[tRef − 180, tRef − 635, −5]]],
Length[Join[Range[tRef − 640, tRef − 745, −5], {tSTP}]]}

{116, 93, 23}

```
c00Fit[Z1plus4to5ppm] = Module[{c, cLT}, cLT =
    Insert[Insert[Drop[(c00ξxsδLT[Z1plus4to5ppm, #] /. ξ0[Z1plus4to5ppm, #]),
        {12}], e^-100, 7], e^-100, 11] & /@ Take[solnRangeαβ, 23];
  c = Join[cLT, Drop[(c00ξxsδ[Z1plus4to5ppm, #] /. ξ0[Z1plus4to5ppm, #]),
      {14}] & /@ Take[solnRangeαβ, -93]];
  SplineFit[Thread[{solnRangeαβ, c[[All, #]]}], Cubic] & /@ Range[Length[cE00]]];
```

```
c00[Z1plus4to5ppm, tK_?NumericQ] /; tSTP ≤ tK ≤ tMaxαβ :=
  With[{T = (Length[solnRangeαβ] - 1) (tK - tSTP)/(tMaxαβ - tSTP)},
   Through[(c00Fit[Z1plus4to5ppm][[#]] & /@ Range[Length[cE00]])[T]][[All, 2]]]
```

" CIS valency deviation at STP with X=1 and ΔZ=4.5 *ppm*"
(cXZ[partCIS[c00[Z1plus4to5ppm, tSTP][[#]] & /@ Range[Length[cE00]]],
partCIS[$\mathcal{D}$00xsδ]][[2]] − 1)

3.98394×10^{-6} CIS valency deviation at STP with X=1 and ΔZ=4.5 *ppm*

The calculated secondary phase composition has exceeded its maximum selenium content at STP, which is unphysical. Slightly greater selenium enrichment

would next yield a violation of this limit at the peritectoid Cu:Se/α–$Cu_{2-\delta}Se$/β–$Cu_{2-\delta}Se$ decomposition temperature. To calculate the equilibrium correctly in these regions and extend these results to further selenium enrichment, the basis needs to be modified to eliminate the additional degree of freedom associated with the non-stoichiometric $Cu_{2-\delta}Se$ phase, and to fix its composition at the maximum.

```
(* the reduced CISα+Cu2Se basis vector for Z>1 *)cE00Zplus =
    Drop[Drop[Drop[Drop[Drop[cE0, {23}], {20}], {16, 17}], {10, 14}], {4, 6}];
{#, cE00Zplus⟦#⟧} & /@ Array[# &, Length[cE00Zplus]]
```

$$\{\{1, CIS_{\alpha}\}, \{2, \mathcal{V}_{Cu}^{x}\}, \{3, \mathcal{V}_{Cu}^{\prime}\}, \{4, Cu_{In}^{x}\}, \{5, Cu_{In}^{\prime}\}, \{6, Cu_{In}^{\prime\prime}\},$$
$$\{7, \mathcal{V}_{Se}^{\bullet\bullet}\}, \{8, Cu_i \oplus \mathcal{V}_{Cu}\}, \{9, Cu_{In} \oplus In_{Cu}\}, \{10, (\mathcal{V}_{Cu} \oplus In_{Cu})^{\bullet}\},$$
$$\{11, (2\mathcal{V}_{Cu} \oplus In_{Cu})_{\alpha}\}, \{12, Cu2.\delta Se\}, \{13, e^{\prime}\}, \{14, h^{\bullet}\}, \{15, \Delta N\}\}$$

```
𝒟00Zplus = Transpose[Drop[
      Drop[Drop[Drop[Drop[Transpose[𝒟0], {23}], {20}], {16, 17}], {10, 14}], {4, 6}]];

formula[i_, 𝒟00Zplus] := {cE00Zplus, a .𝒟00Zplus}⟦All, i⟧

ν00Zplus = Transpose[NullSpace[𝒟00Zplus]];

rxn[i_, ν00Zplus] := ν00Zplus⟦All, i⟧.cE00Zplus

ν00ξZplus = ν00Zplus;
ν00ξZplus = Transpose[ReplacePart[Transpose[ν00ξZplus],
        ν00Zplus⟦All, 1⟧ + 2 ν00Zplus⟦All, 4⟧ + ν00Zplus⟦All, 5⟧, 1]] // Simplify;
ν00ξZplus = Transpose[ReplacePart[Transpose[ν00ξZplus],
      ν00Zplus⟦All, 3⟧ + ν00Zplus⟦All, 2⟧, 3]];
ν00ξZplus = Transpose[ReplacePart[Transpose[ν00ξZplus],
     ν00Zplus⟦All, 6⟧ − ν00Zplus⟦All, 5⟧, 6]]; ν00ξZplus = Transpose[
   ReplacePart[Transpose[ν00ξZplus], ν00Zplus⟦All, 9⟧ + 2 ν00Zplus⟦All, 2⟧, 9]];
ν00ξZplus = Transpose[ReplacePart[Transpose[ν00ξZplus],
      ν00Zplus⟦All, 10⟧ + ν00Zplus⟦All, 2⟧, 10]];
```

```
rxn[i_, ν00ξZplus] := ν00ξZplus⟦All, i⟧.cE00Zplus

ξ000Zplus = Array[1 &, 10] −
    3 Array[KroneckerDelta[1, # ] &, 10] + 6 Array[KroneckerDelta[3, # ] &, 10]

    {−2, 1, 7, 1, 1, 1, 1, 1, 1, 1}

cE00Zplus⟦#⟧ & /@ c00Zbasis

    {CIS_α, Cu_In^x, (V_Cu ⊕ In_Cu)•, (2 V_Cu ⊕ In_Cu)_α}

c00ΔZ[Z_] /; 1 < Z ≤ 95989/88000 :=
  Module[{c00}, With[{c4Zplus = {1 + 6 (−1 + Z)/(−16 + 15 Z), −4 (−1 + Z)/(−16 + 15 Z), 0, −2 (−1 + Z)/(−16 + 15 Z)},
      mCuInv2 = 1/(−42 (−1+Z)/(−16+15 Z) + 2 (1 + 6 (−1+Z)/(−16+15 Z)))}, c00 =
      Plus @@ MapThread[ReplacePart[Array[0 &, Length[cE00Zplus]], #1, #2] &,
        {c4Zplus, c00Zbasis}];
    c00 = mCuInv2 (c00 + (ν00Zplus /. δ → δmax[tMaxαβ]).ξ000Zplus 1*^-26);
    ReplacePart[c00, 1, −1]]]

μ00Zplus[c_, tK_] /; Length[c] === Length[cE00Zplus] :=
  With[{n = (#/Plus @@ #) &[Join[
        Drop[Drop[Drop[Drop[Drop[Drop[Drop[mcl, {25}], {23}], {20}], {16, 17}],
          {10, 14}], {4, 6}] Take[c, 12], −1], {c⟦12⟧}]],
    δm = δmax[tK], nCISα = nAvo c/First[c]}, ReplacePart[Drop[
      Drop[Drop[Drop[Drop[Drop[μ00αβ[tK], {25}], {23}], {20}], {16, 17}], {10, 14}],
      {4, 6}], (3 − δm) G.CuSeX[tK, (3 − δm)^−1], 12] + rG tK Join[Log[Drop[n, −1]],
      {Log[Last[n]], Log[nCISα⟦13⟧/cbDOSαCIS[tK]], Log[nCISα⟦14⟧/vbDOSαCIS[tK]], 0}]]

ξ00Zplus = Drop[Drop[Drop[Take[ξ000, 19], {11, 17}], {8}], {5}];
c00ξΔZ[Z_, tK_] /; Z > 1 := c00ΔZ[Z] + (ν00ξZplus /. δ → δmax[tK]).ξ00Zplus

gd0ΔZ[Z_, tK_] /; Z > 1 :=
  (μ00Zplus[c00ξΔZ[#, #2], #2].(ν00Zplus /. δ → δmax[#2])) &[Z, tK]
```

```
gd0ΔZ[Z1plus4to5ppm, tSTP] /. bridgeZ1plus4to5ppm;
{"solution convergence σSD", σSD[%]}
Thread[
  {Thread[{cE00Zplus, c00ξΔZ[Z1plus4to5ppm, tSTP] /. bridgeZ1plus4to5ppm}],
    Drop[Thread[{cE00xsδLT,
          (c00ξxsδLT[Z1plus4to5ppm, tSTP] /. ξ0[Z1plus4to5ppm, tSTP])}], {12}]}]
```

$$
\begin{aligned}
&\{\text{solution convergence } \sigma_{SD},\ 0.000620975\}\\
&\{\{\{CIS_{\alpha},\ 0.499952\},\ \{CIS_{\alpha},\ 0.499952\}\},\\
&\quad\{\{\mathcal{V}^{x}_{Cu},\ 1.49666\times10^{-7}\},\ \{\mathcal{V}^{x}_{Cu},\ 1.48949\times10^{-7}\}\},\\
&\quad\{\{\mathcal{V}'_{Cu},\ 0.0000158244\},\ \{\mathcal{V}'_{Cu},\ 0.0000157865\}\},\\
&\quad\{\{Cu^{x}_{In},\ 3.7627\times10^{-11}\},\ \{Cu^{x}_{In},\ 1.50277\times10^{-10}\}\},\\
&\quad\{\{Cu'_{In},\ 1.6025\times10^{-13}\},\ \{Cu'_{In},\ 6.41554\times10^{-13}\}\},\\
&\quad\{\{Cu''_{In},\ 5.9655\times10^{-22}\},\ \{Cu''_{In},\ 2.39401\times10^{-21}\}\},\\
&\quad\{\{\mathcal{V}^{\bullet\bullet}_{Se},\ 1.28225\times10^{-29}\},\ \{\mathcal{V}^{\bullet\bullet}_{Se},\ 6.41618\times10^{-30}\}\},\\
&\quad\{\{Cu_{i}\oplus\mathcal{V}_{Cu},\ 1.3504\times10^{-26}\},\ \{Cu_{i}\oplus\mathcal{V}_{Cu},\ 1.3504\times10^{-26}\}\},\\
&\quad\{\{Cu_{In}\oplus In_{Cu},\ 1.71569\times10^{-12}\},\ \{Cu_{In}\oplus In_{Cu},\ 1.71569\times10^{-12}\}\},\\
&\quad\{\{(\mathcal{V}_{Cu}\oplus In_{Cu})^{\bullet},\ 1.55108\times10^{-14}\},\ \{(\mathcal{V}_{Cu}\oplus In_{Cu})^{\bullet},\ 3.85579\times10^{-15}\}\},\\
&\quad\{\{(2\,\mathcal{V}_{Cu}\oplus In_{Cu})_{\alpha},\ 1.68834\times10^{-15}\},\ \{(2\,\mathcal{V}_{Cu}\oplus In_{Cu})_{\alpha},\ 4.18693\times10^{-16}\}\},\\
&\quad\{\{Cu2\delta Se,\ 8.99992\times10^{-6}\},\ \{Cu2\delta Se,\ 8.9997\times10^{-6}\}\},\\
&\quad\{\{e',\ 6.87664\times10^{-21}\},\ \{e',\ 6.89316\times10^{-21}\}\},\\
&\quad\{\{h^{\bullet},\ 0.0000158244\},\ \{h^{\bullet},\ 0.0000157865\}\},\ \{\{\Delta N,\ 1.\},\ \{\Delta N,\ 1.\}\}\}
\end{aligned}
$$

The preceding recalculation of the solution at STP for +9 *ppm* selenium excess using the basis which restricts the depletion of copper from the secondary $Cu_{2-\delta}Se$ phase so that its composition does not exceed its single-phase concentration limit demonstrates the key consequences of enforcing this restriction. These include an increase in the extent of $Cu_{2-\delta}Se$ secondary phase segregation, and increases in both the dominant ionized defects ($\mathcal{V}'_{Cu}$ and $(\mathcal{V}_{Cu}\oplus In_{Cu})^{\bullet}$) yielding a net increase in the hole concentration. These effects are subtle here, but become pronounced when the solution for $Z > 1$ is extended an order of magnitude to 100 *ppm* = 0.02% excess selenium (still well within the reported α–CIS single-phase homogeneity domain):

```
Z1plus100ppm = 1 + 1*^-4;

gd0ΔZ[Z1plus100ppm, tSTP] /. ξ0[Z1plus100ppm, tSTP];
{"solution convergence σSD", σSD[%]}
Thread[{cE00Zplus, c00ξΔZ[Z1plus100ppm, tSTP] /. ξ0[Z1plus100ppm, tSTP]}]
```

{solution convergence σ_{SD}, 0.34954}
{{CIS_{α}, 0.499019}, {$\mathcal{V}_{Cu}^{x}$, 0.0000391236}, {$\mathcal{V}'_{Cu}$, 0.000255606},
{Cu_{In}^{x}, 0.0000388661}, {Cu'_{In}, 1.02281×10^{-8}}, {Cu''_{In}, 2.35274×10^{-18}},
{$\mathcal{V}''''_{Se}$, 1.24547×10^{-32}}, {$Cu_i \oplus \mathcal{V}_{Cu}$, 1.34214×10^{-26}},
{$Cu_{In} \oplus In_{Cu}$, 1.7052×10^{-12}}, {$(\mathcal{V}_{Cu} \oplus In_{Cu})^{\bullet}$, 6.28684×10^{-17}},
{$(2\,\mathcal{V}_{Cu} \oplus In_{Cu})_{\alpha}$, 1.112×10^{-16}}, {Cu2.δSe, 0.000122247},
{e′, 4.24123×10^{-22}}, {h•, 0.000255616}, {ΔN, 1.00006}}

```
c00Fit[Z1plus100ppm] = Module[{c, cLT},
    cLT = Insert[Insert[(c00ξΔZ[Z1plus100ppm, #] /. ξ0[Z1plus100ppm, #]),
            ℯ^-100, 7], ℯ^-100, 11] & /@ Take[solnRangeαβ, 47]; c =
      Join[cLT, Drop[(c00ξxsδ[Z1plus100ppm, #] /. ξ0[Z1plus100ppm, #]), {14}] & /@
        Take[solnRangeαβ, -69]];
      SplineFit[Thread[{solnRangeαβ, c[[All, #]]}], Cubic] & /@ Range[Length[cE00]]];

c00[Z1plus100ppm, tK_?NumericQ] /; tSTP ≤ tK ≤ tMaxαβ :=
  With[{T = (Length[solnRangeαβ] - 1) (tK - tSTP)/(tMaxαβ - tSTP)},
    Through[(c00Fit[Z1plus100ppm][[#]] & /@ Range[Length[cE00]])[T]][[All, 2]]]
```

The $Z > 1$ case is extended another order of magnitude to 1000 *ppm* = 0.2% excess selenium:

```
Z1plus1000ppm = 1 + 1*^-3;
```

```
gd0xsδ[Z1plus1000ppm, tRef – 305] /. ξ0[Z1plus1000ppm, tRef – 305];
{"solution convergence σSD", σSD[%]}
Thread[
  {cE00xsδ, c00ξxsδ[Z1plus1000ppm, tRef – 305] /. ξ0[Z1plus1000ppm, tRef – 305]}]
"Cu2Se Δx deviation from maximum limit at basis crossover temperature"
```

$$\left(\left(3 - \left(\delta\text{min}[\text{tRef} - \#] - \frac{\text{c00}\xi\text{xs}\delta[\text{Z1plus1000ppm, tRef} - \#][\![14]\!]}{\text{c00}\xi\text{xs}\delta[\text{Z1plus1000ppm, tRef} - \#][\![15]\!]}\right) /. \right.\right.$$
$$\left.\left. \xi 0[\text{Z1plus1000ppm, tRef} - \#]\right)^{-1} - \text{xMax\_Cu2Se}[\text{tRef} - \#]\right) \&[305]$$

```
{solution convergence σSD, 0.0000111436}
{{CISα, 0.471367}, {V'Cu^x, 0.000510903},
  {V'Cu, 0.00413923}, {Cu'In^x, 4.70281×10^-8}, {Cu'In, 6.57222×10^-9},
  {Cu''In, 6.9176×10^-13}, {V''Se^x, 1.70226×10^-16}, {V••Se, 4.43499×10^-10},
  {Cui ⊕ VCu, 2.68302×10^-11}, {CuIn ⊕ InCu, 5.32833×10^-6},
  {VCu ⊕ InCu, 1.30894×10^-9}, {(VCu ⊕ InCu)•, 0.00258391},
  {(2 VCu ⊕ InCu)α, 0.0000826401}, {CuCu2Se, −0.00193256},
  {Cu2_δSe, 0.00733299}, {e', 5.15914×10^-11}, {h•, 0.00155533}, {ΔN, 1.00367}}
8.34265×10^-6
  Cu2Se Δx deviation from maximum limit at basis crossover temperature

gd0ΔZ[Z1plus1000ppm, tSTP] /. ξ0[Z1plus1000ppm, tSTP];
{"solution convergence σSD", σSD[%]}
Thread[{cE00Zplus, c00ξΔZ[Z1plus1000ppm, tSTP] /. ξ0[Z1plus1000ppm, tSTP]}]

{solution convergence σSD, 0.10474}
{{CISα, 0.491441}, {V'Cu^x, 0.000856105}, {V'Cu, 0.00118656}, {Cu'In^x, 0.000972414},
  {Cu'In, 5.42885×10^-8}, {Cu''In, 2.64921×10^-18}, {V••Se, 2.25432×10^-33},
  {Cui ⊕ VCu, 1.27987×10^-26}, {CuIn ⊕ InCu, 1.62609×10^-12},
  {(VCu ⊕ InCu)•, 2.39328×10^-16}, {(2 VCu ⊕ InCu)α, 2.06092×10^-15},
  {Cu2_δSe, 0.000055064}, {e', 8.8609×10^-23}, {h•, 0.00118662}, {ΔN, 1.00003}}

c00Fit[Z1plus1000ppm] = Module[{c, cLT},
    cLT = Insert[Insert[(c00ξΔZ[Z1plus1000ppm, #] /. ξ0[Z1plus1000ppm, #]),
          ℯ^-100, 7], ℯ^-100, 11] & /@ Take[solnRangeαβ, 89];
    c = Join[cLT, Drop[(c00ξxsδ[Z1plus1000ppm, #] /. ξ0[Z1plus1000ppm, #]),
          {14}] & /@ Take[solnRangeαβ, −27]];
    SplineFit[Thread[{solnRangeαβ, c[[All, #]]}], Cubic] & /@ Range[Length[cE00]]];
```

```
c00[Z1plus1000ppm, tK_?NumericQ] /; tSTP ≤ tK ≤ tMaxαβ :=
  With[{T = (Length[solnRangeαβ] − 1) (tK − tSTP)/(tMaxαβ − tSTP)},
    Through[(c00Fit[Z1plus1000ppm][#] & /@ Range[Length[cE00]])[T]][All, 2]]
```

An intermediate Z > 1 case is computed for 400 *ppm* = 0.08% excess selenium:

```
Z1plus400ppm = 1 + 4*^-4;

gd0xsδ[Z1plus400ppm, tRef − 415] /. ξ0[Z1plus400ppm, tRef − 415];
{"solution convergence σSD", σSD[%]}
Thread[
  {cE00xsδ, c00ξxsδ[Z1plus400ppm, tRef − 415] /. ξ0[Z1plus400ppm, tRef − 400]}]
"Cu2Se Δx deviation from maximum limit at basis crossover temperature"
  (((3 − (δmin[tRef − #] − c00ξxsδ[Z1plus400ppm, tRef − #][[14]]/
      c00ξxsδ[Z1plus400ppm, tRef − #][[15]]))/.
    ξ0[Z1plus400ppm, tRef − #])^-1 − xMax_Cu2Se[tRef − #]) &[415]
```

{solution convergence σ_{SD}, 0.0000811177}
{{CIS$_\alpha$, 0.49051}, {$\mathcal{V}^{x}_{Cu}$, 0.000138242}, {$\mathcal{V}'_{Cu}$, 0.00161002},
{Cu^{x}_{In}, 4.15358×10^{-9}}, {Cu'_{In}, 4.59839×10^{-10}}, {Cu''_{In}, 1.97433×10^{-14}},
{$\mathcal{V}^{x}_{Se}$, 2.39852×10^{-18}}, {$\mathcal{V}^{\bullet\bullet}_{Se}$, 2.26981×10^{-11}}, {$Cu_i \oplus \mathcal{V}_{Cu}$, 9.47524×10^{-13}},
{$Cu_{In} \oplus In_{Cu}$, 1.37826×10^{-6}}, {$\mathcal{V}_{Cu} \oplus In_{Cu}$, 8.60145×10^{-11}},
{$(\mathcal{V}_{Cu} \oplus In_{Cu})^{\bullet}$, 0.000754739}, {$(2\,\mathcal{V}_{Cu} \oplus In_{Cu})_\alpha$, 0.0000162924},
{Cu_{Cu2Se}, −0.000605599}, {Cu2.δSe, 0.00234205},
{e', 5.94538×10^{-12}}, {$h^{\bullet}$, 0.000855279}, {ΔN, 1.00117}}
−0.000226573
Cu2Se Δx deviation from maximum limit at basis crossover temperature

```
gd0ΔZ[Z1plus400ppm, tSTP] /. ξ0[Z1plus400ppm, tSTP];
{"solution convergence σSD", σSD[%]}
Thread[{cE00Zplus, c00ξΔZ[Z1plus400ppm, tSTP] /. ξ0[Z1plus400ppm, tSTP]}]
```

```
{solution convergence σSD, 0.0675196}
{{CISα, 0.496503}, {V_Cu^x, 0.000239346}, {V'_Cu, 0.000630613}, {Cu_In^x, 0.000354822},
  {Cu'_In, 3.76565×10^-8}, {Cu''_In, 3.49319×10^-18}, {V_Se^••, 3.98919×10^-33},
  {Cu_i ⊕ V_Cu, 1.32128×10^-26}, {Cu_In ⊕ In_Cu, 1.67869×10^-12},
  {(V_Cu ⊕ In_Cu)•, 1.01757×10^-16}, {(2 V_Cu ⊕ In_Cu)α, 4.51132×10^-16},
  {Cu2.δSe, 0.0000902804}, {e', 1.70177×10^-22}, {h•, 0.00063065}, {ΔN, 1.00005}}
```

```
c00Fit[Z1plus400ppm] = Module[{c, cLT},
    cLT = Insert[Insert[(c00ξΔZ[Z1plus400ppm, #] /. ξ0[Z1plus400ppm, #]),
            ℯ^-100, 7], ℯ^-100, 11] & /@ Take[solnRangeαβ, 67]; c =
      Join[cLT, Drop[(c00ξxsδ[Z1plus400ppm, #] /. ξ0[Z1plus400ppm, #]), {14}] & /@
        Take[solnRangeαβ, -49]];
      SplineFit[Thread[{solnRangeαβ, c[[All, #]]}], Cubic] & /@ Range[Length[cE00]]];
```

```
c00[Z1plus400ppm, tK_?NumericQ] /; tSTP ≤ tK ≤ tMaxαβ :=
  With[{T = (Length[solnRangeαβ] - 1) (tK - tSTP)/(tMaxαβ - tSTP)},
    Through[(c00Fit[Z1plus400ppm][[#]] & /@ Range[Length[cE00]])[T]][[All, 2]]]
```

Another intermediate $Z > 1$ case is computed for 700 *ppm* = 0.14% excess selenium:

```
Z1plus700ppm = 1 + 7*^-4;
```

gd0xsδ[Z1plus700ppm, tRef – 355] /. ξ0[Z1plus700ppm, tRef – 355];
{"solution convergence σ_{SD}", σSD[%]}
Thread[
  {cE00xsδ, c00ξxsδ[Z1plus700ppm, tRef – 355] /. ξ0[Z1plus700ppm, tRef – 355]}]
"Cu2Se Δx deviation from maximum limit at basis crossover temperature"

$$\left(\left(3-\left(\delta\text{min}[\text{tRef}-\#]-\frac{\text{c00}\xi\text{xs}\delta[\text{Z1plus700ppm, tRef}-\#][\![14]\!]}{\text{c00}\xi\text{xs}\delta[\text{Z1plus700ppm, tRef}-\#][\![15]\!]}\right)/.\right.\right.$$
$$\left.\left.\xi 0[\text{Z1plus700ppm, tRef}-\#]\right)^{-1}-\text{xMax\_Cu2Se}[\text{tRef}-\#]\right)\&[355]$$

{solution convergence σ_{SD}, 0.000037939}
{{CIS$_\alpha$, 0.483128}, {$\mathcal{V}^{x}_{Cu}$, 0.000318207}, {$\mathcal{V}'_{Cu}$, 0.00270337}, {Cu^{x}_{In}, 2.02199×10^{-8}},
  {Cu'_{In}, 2.21085×10^{-9}}, {Cu''_{In}, 1.3133×10^{-13}}, {$\mathcal{V}^{x}_{Se}$, 1.545×10^{-17}},
  {$\mathcal{V}^{\bullet\bullet}_{Se}$, 9.864×10^{-11}}, {$Cu_i \oplus \mathcal{V}_{Cu}$, 5.26525×10^{-12}}, {$Cu_{In} \oplus In_{Cu}$, 2.786×10^{-6}},
  {$\mathcal{V}_{Cu} \oplus In_{Cu}$, 2.94533×10^{-10}}, {$(\mathcal{V}_{Cu} \oplus In_{Cu})^{\bullet}$, 0.00138077},
  {$(2\,\mathcal{V}_{Cu} \oplus In_{Cu})_\alpha$, 0.0000371889}, {$Cu_{Cu2Se}$, −0.0011582},
  {Cu2_δSe, 0.00423587}, {e′, 1.56534×10^{-11}}, {h$^{\bullet}$, 0.00132261}, {ΔN, 1.00212}}
−0.0000270325
  Cu2Se Δx deviation from maximum limit at basis crossover temperature

gd0ΔZ[Z1plus700ppm, tSTP] /. ξ0[Z1plus700ppm, tSTP];
{"solution convergence σ_{SD}", σSD[%]}
Thread[{cE00Zplus, c00ξΔZ[Z1plus700ppm, tSTP] /. ξ0[Z1plus700ppm, tSTP]}]

{solution convergence σ_{SD}, 0.0435162}
{{CIS$_\alpha$, 0.493978}, {$\mathcal{V}^{x}_{Cu}$, 0.000522603}, {$\mathcal{V}'_{Cu}$, 0.00092946}, {Cu^{x}_{In}, 0.000666359},
  {Cu'_{In}, 4.77375×10^{-8}}, {Cu''_{In}, 2.98926×10^{-18}}, {$\mathcal{V}^{\bullet\bullet}_{Se}$, 2.81608×10^{-33}},
  {$Cu_i \oplus \mathcal{V}_{Cu}$, 1.30053×10^{-26}}, {$Cu_{In} \oplus In_{Cu}$, 1.65233×10^{-12}},
  {$(\mathcal{V}_{Cu} \oplus In_{Cu})^{\bullet}$, 1.7067×10^{-16}}, {$(2\,\mathcal{V}_{Cu} \oplus In_{Cu})_\alpha$, 1.13297×10^{-15}},
  {Cu2_δSe, 0.0000671862}, {e′, 1.1429×10^{-22}}, {h$^{\bullet}$, 0.000929507}, {ΔN, 1.00003}}

c00Fit[Z1plus700ppm] = Module[{c, cLT},
  cLT = Insert[Insert[(c00ξΔZ[Z1plus700ppm, #] /. ξ0[Z1plus700ppm, #]),
      e^−100, 7], e^−100, 11] & /@ Take[solnRange$\alpha\beta$, 79]; c =
   Join[cLT, Drop[(c00ξxsδ[Z1plus700ppm, #] /. ξ0[Z1plus700ppm, #]), {14}] & /@
     Take[solnRange$\alpha\beta$, −37]];
  SplineFit[Thread[{solnRange$\alpha\beta$, c[[All, #]]}], Cubic] & /@ Range[Length[cE00]]];

```
c00[Z1plus700ppm, tK_?NumericQ] /; tSTP ≤ tK ≤ tMaxαβ :=
  With[{T = (Length[solnRangeαβ] − 1) (tK − tSTP)/(tMaxαβ − tSTP)},
    Through[(c00Fit[Z1plus700ppm][#] & /@ Range[Length[cE00]])[T]][All, 2]]

{tMaxαβ, tRef − 175}

    {873.15, 873.15}
```

The $Z > 1$ case is extended to 1739 *ppm* = 0.3478% excess selenium:

```
Z1plus2Maxδ = 1 + 1739*^-6;
```

This was chosen specifically because with 0.3478% total excess selenium the secondary $Cu_{2-\delta}Se$ phase is found to possess its maximum selenium content over the entire temperature range of the α/β–CIS two-phase domain. Thus the entire equilibrium calculation for this and any greater selenium excess must be conducted using the basis **cE00**.

```
gd0ΔZ[Z1plus2Maxδ, tSTP] /. ξ0[Z1plus2Maxδ, tSTP];
{"solution convergence σSD", σSD[%]}
Thread[{cE00Zplus, c00ξΔZ[Z1plus2Maxδ, tSTP] /. ξ0[Z1plus2Maxδ, tSTP]}]

    {solution convergence σSD, 0.0423799}
    {{CIS_α, 0.485175}, {V_Cu^x, 0.00179995}, {V'_Cu, 0.00170951}, {Cu_In^x, 0.00171863},
      {Cu'_In, 6.5749×10^-8}, {Cu''_In, 2.1986×10^-18}, {V_Se^••, 1.55968×10^-33},
      {Cu_i ⊕ V_Cu, 1.22978×10^-26}, {Cu_In ⊕ In_Cu, 1.56244×10^-12},
      {(V_Cu ⊕ In_Cu)^•, 3.8854×10^-16}, {(2 V_Cu ⊕ In_Cu)_α, 5.01708×10^-15},
      {Cu2.δSe, 0.0000405995}, {e', 5.99451×10^-23}, {h^•, 0.00170958}, {ΔN, 1.00002}}

c00Fit[Z1plus2Maxδ] = Module[{cLT},
    cLT = Insert[Insert[(c00ξΔZ[Z1plus2Maxδ, #] /. ξ0[Z1plus2Maxδ, #]),
            ℯ^−100, 7], ℯ^−100, 11] & /@ solnRangeαβ;
    SplineFit[Thread[{solnRangeαβ, cLT[All, #]}], Cubic] & /@
      Range[Length[cE00]]];
```

```
c00[Z1plus2Maxδ, tK_?NumericQ] /; tSTP ≤ tK ≤ tMaxαβ :=
  With[{T = (Length[solnRangeαβ] − 1) (tK − tSTP)/(tMaxαβ − tSTP)},
    Through[(c00Fit[Z1plus2Maxδ][[#]] & /@ Range[Length[cE00]])[T]][[All, 2]]]
```

The $Z > 1$ case is extended to 2000 *ppm* = 0.40% excess selenium:

```
Z1plus2000ppm = 1 + 20*^-4;

gd0ΔZ[Z1plus2000ppm, tSTP] /. ξ0[Z1plus2000ppm, tSTP];
{"solution convergence σSD", σSD[%]}
Thread[{cE00Zplus, c00ξΔZ[Z1plus2000ppm, tSTP] /. ξ0[Z1plus2000ppm, tSTP]}]
```

```
{solution convergence σSD, 0.0848727}
{{CIS_α, 0.48296}, {V_Cu^x, 0.00216052}, {V'_Cu, 0.00186865}, {Cu_In^x, 0.0019811},
  {Cu'_In, 6.90191×10^-8}, {Cu''_In, 2.10177×10^-18}, {V••_Se, 1.41002×10^-33},
  {Cu_i ⊕ V_Cu, 1.21239×10^-26}, {Cu_In ⊕ In_Cu, 1.54034×10^-12},
  {(V_Cu ⊕ In_Cu)•, 4.33783×10^-16}, {(2 V_Cu ⊕ In_Cu)_α, 6.21021×10^-15},
  {Cu2δSe, 0.0000376547}, {e', 5.43404×10^-23}, {h•, 0.00186872}, {ΔN, 1.00002}}
```

```
c00Fit[Z1plus2000ppm] = Module[{cLT},
    cLT = Insert[Insert[(c00ξΔZ[Z1plus2000ppm, #] /. ξ0[Z1plus2000ppm, #]),
            ℯ^−100, 7], ℯ^−100, 11] & /@ solnRangeαβ;
    SplineFit[Thread[{solnRangeαβ, cLT[[All, #]]}], Cubic] & /@
      Range[Length[cE00]]];

c00[Z1plus2000ppm, tK_?NumericQ] /; tSTP ≤ tK ≤ tMaxαβ :=
  With[{T = (Length[solnRangeαβ] − 1) (tK − tSTP)/(tMaxαβ − tSTP)},
    Through[(c00Fit[Z1plus2000ppm][[#]] & /@ Range[Length[cE00]])[T]][[All, 2]]]
```

The $Z > 1$ case is extended to 2200 *ppm* = 0.44% excess selenium:

```
Z1plus2200ppm = 1 + 22*^-4;
```

```
gd0ΔZ[Z1plus2200ppm, tSTP] /. ξ0[Z1plus2200ppm, tSTP];
{"solution convergence σSD", σSD[%]}
Thread[{cE00Zplus, c00ξΔZ[Z1plus2200ppm, tSTP] /. ξ0[Z1plus2200ppm, tSTP]}]
```

{solution convergence σ_{SD}, 0.142377}

{{CIS_{α}, 0.481262}, {$\mathcal{V}_{Cu}^{x}$, 0.00244383}, {$\mathcal{V}_{Cu}'$, 0.0019839}, {Cu_{In}^{x}, 0.00218204}, {Cu_{In}', 7.13516×10^{-8}}, {Cu_{In}'', 2.03938×10^{-18}}, {$\mathcal{V}_{Se}^{\bullet\bullet\bullet}$, 1.31305×10^{-33}}, {$Cu_i \oplus \mathcal{V}_{Cu}$, 1.19917×10^{-26}}, {$Cu_{In} \oplus In_{Cu}$, 1.52356×10^{-12}}, {$(\mathcal{V}_{Cu} \oplus In_{Cu})^{\bullet}$, 4.65972×10^{-16}}, {$(2\,\mathcal{V}_{Cu} \oplus In_{Cu})_{\alpha}$, 7.16117×10^{-15}}, {Cu2.δSe, 0.0000357852}, {e′, 5.08245×10^{-23}}, {h$^{\bullet}$, 0.00198397}, {ΔN, 1.00002}}

```
c00Fit[Z1plus2200ppm] = Module[{cLT},
    cLT = Insert[Insert[(c00ξΔZ[Z1plus2200ppm, #] /. ξ0[Z1plus2200ppm, #]),
            ℯ^-100, 7], ℯ^-100, 11] & /@ solnRangeαβ;
    SplineFit[Thread[{solnRangeαβ, cLT⟦All, #⟧}], Cubic] & /@
      Range[Length[cE00]]];

c00[Z1plus2200ppm, tK_?NumericQ] /; tSTP ≤ tK ≤ tMaxαβ :=
  With[{T = (Length[solnRangeαβ] - 1) (tK - tSTP)/(tMaxαβ - tSTP)},
    Through[(c00Fit[Z1plus2200ppm]⟦#⟧ & /@ Range[Length[cE00]])[T]]⟦All, 2⟧]
```

The initialization calculations are complete and it remains to construct an interpolation function that gives the concentrations of all significant species over the valency and temperature ranges of the α–CIS/β–CIS two phase equilibrium problem. The solutions for the discrete values of Z already calculated must be interpolated to provide a continuous solution over that variable's range, but they are given with respect to different basis sets:

```
Zdomain = {1, Z1plus100ppm, Z1plus400ppm, Z1plus700ppm,
    Z1plus1000ppm, Z1plus2Maxδ, Z1plus2000ppm, Z1plus2200ppm};
Protect[Zdomain];
```

```
Length[c00[#, tSTP]] & /@ Zdomain
```

```
{22, 17, 17, 17, 17, 17, 17, 17}
```

```
{Length[cE0LT], Length[cE00]}
```

```
{22, 17}
```

```
cE00 === Drop[Drop[cE0LT, {12, 13}], {4, 6}]
```

```
True
```

The maximum solution concentrations of the In_{Cu} and Cu_i point defects over the entire temperature range total less than 10^{-13} molar, less than any other single defect alone. Since these are the defects removed from the basis **cE0LT** to create **cE00**, the latter is selected to provide the solution concentrations for the $Cu_{2-\delta}Se/\alpha$–CIS two-phase equilibrium problem.

```
c0Fit = Module[{cLog}, With[{species = Range[Length[cE00]]}, cLog = Log[Prepend[
          Apply[c00[#, #2] &, Outer[List, Rest[Zdomain], solnRangeαβ], {2}],
          Drop[Drop[c00[1, #], {12, 13}], {4, 6}] & /@ solnRangeαβ]];
    ListInterpolation[cLog⟦All, All, #⟧, {Zdomain, solnRangeαβ},
          InterpolationOrder → {1, 1}] & /@ species]];
```

```
c0[Z_?NumericQ, tK_?NumericQ] /;
   First[Zdomain] ≤ Z ≤ Last[Zdomain] ⋀ tSTP ≤ tK ≤ tMaxαβ :=
  Abs[ℯ^Through[c0Fit[Z, tK]]] /. Indeterminate → 0
```

```
segCu2SeX1[Z_?NumericQ, tK_?NumericQ] /;
   First[Zdomain] ≤ Z ≤ Last[Zdomain] ⋀ tSTP ≤ tK ≤ tMaxαβ := c0[Z, tK]⟦14⟧
```

These variations in the secondary $Cu_{2-\delta}Se$ phase's stoichiometry and equilibrium extent of segregation for X = 1 result in shifts in the valency and molecularity of α–CIS in the mixture. The equilibrium α–CIS composition and defect concentrations at this two–phase boundary are derived next.

```
zCIS[Z_?NumericQ, tK_?NumericQ] /;
    First[Zdomain] ≤ Z ≤ Last[Zdomain] ⋀ tSTP ≤ tK ≤ tMaxαβ :=
  cXZ[partCIS[c0[Z, tK]], partCIS[𝒟00]]⟦2⟧

zαUL[tK_?NumericQ] /; tSTP ≤ tK ≤ tMaxαβ :=
  cXZ[partCIS[c0[Last[Zdomain], tK]], partCIS[𝒟00]]⟦2⟧
zαLL[tK_?NumericQ] /; tSTP ≤ tK ≤ tMaxαβ :=
  cXZ[partCIS[c0[First[Zdomain], tK]], partCIS[𝒟00]]⟦2⟧

{zαMin = zαLL[tSTP], zαMax = (1 − 1*^-7) zαUL[tMaxαβ]}

    {1., 1.00105}

zαMin − 1

    −1.66184 × 10^−10

zTotal[Zα_?NumericQ, tK_?NumericQ] /;
    zαMin ≤ Zα ≤ zαMax ⋀ tSTP ≤ tK ≤ tMaxαβ :=
  Module[{Z, zTot}, Off[FindRoot::"frsec"]; Off[FindRoot::"precw"];
    Off[FindRoot::"frnum"]; zTot = Z /. FindRoot[zCIS[Z, tK] == Zα,
        {Z, 1, 1 + (zαUL[tK] − zαLL[tK])/100}, WorkingPrecision → 30];
    On[FindRoot::"frsec"]; On[FindRoot::"precw"]; On[FindRoot::"frnum"]; zTot]

(zTotal[zαMin, tSTP] − 1)

    0. × 10^−30

zTotal[zαMax, tMaxαβ]
{zαMax, zCIS[%, tMaxαβ]}

    1.00219989641370896907573322033
    {1.00105, 1.00105}

z2Φ = FunctionInterpolation[zTotal[Zα, T], {Zα, zαMin, zαMax}, {T, tSTP, tMaxαβ}]

    InterpolatingFunction[{{1., 1.00105}, {298.15, 873.15}}, <>]
```

The foregoing inversion of the functional relating the valency of the α–CIS phase in equilibrium with a specified total excess selenium enables selection of the correct solution (which has been parameterized by the total Z of both phases combined), based on a specified value of the α–CIS phase's valency at the $Cu_{2-\delta}Se/\alpha$–CIS two-phase boundary.

The concentrations from the two-phase solution must be renormalized to one mole of the α–CIS phase alone to complete the boundary solution. The total charge is zero and in one mole of the α–CIS phase the formula $Cu_{\frac{2X}{1+X}}\ In_{\frac{2}{1+X}}\ Se_{\frac{Z(3+X)}{1+X}}$ still applies, albeit with that phases values for X and Z. Since indium is never segregated to the binary phase and exactly one mole was initially introduced into the system, the overall normalization factor is $\frac{2}{1+X}$ with X given by its equilibrium value in the α–CIS phase at the two-phase boundary. Charge neutrality is also reasserted at this point, by adjusting the relative quantities of the dominant $\mathcal{V}^{x}_{Cu}$ and $\mathcal{V}'_{Cu}$ defects to correct for cumulative numerical errors. This relative correction does not exceed 2 parts in 10^3, and is typically less than one part in 10^6. The absolute correction does not exceed 10^{-6} moles.

```
{{cE00⟦7⟧, cE00⟦8⟧}, {{cE00⟦2⟧, c0[zαMax, tMaxαβ]⟦2⟧},
   {cE00⟦3⟧, c0[zαMax, tMaxαβ]⟦3⟧}, mx[c0[zαMax, tMaxαβ], 𝒟00]⟦4⟧ "net charge"},
 "worst case relative charge neutrality correction:",
 mx[c0[zαMax, tMaxαβ], 𝒟00]⟦4⟧ / c0[zαMax, tMaxαβ]⟦3⟧}
```

$\{\{\mathcal{V}^{x}_{Se}, \mathcal{V}^{\bullet\bullet}_{Se}\}, \{\{\mathcal{V}^{x}_{Cu}, 0.000419129\}, \{\mathcal{V}'_{Cu}, 0.0091097\}, -0.0000204088 \text{ net charge}\},$
$\text{worst case relative charge neutrality correction:}, -0.00224033\}$

```
c00α[Zα_?NumericQ, tK_?NumericQ] /;
    zαMin ≤ Zα ≤ zαMax ⋀ tSTP ≤ tK ≤ tMaxαβ := Module[{cα, Xα, 𝒟, c2Φ, ρ},
    With[{c2Φ = c0[z2Φ[Zα, tK], tK], 𝒟 = partCIS[𝒟00]}, ρ = mx[c2Φ, 𝒟00][[4]];
      cα = partCIS[c2Φ]; cα = ReplacePart[ReplacePart[cα, cα[[3]] + ρ, 3], cα[[2]] − ρ, 2];
      Xα = cXZ[cα, 𝒟][[1]]; 2/(1 + Xα) Join[cα, {Last[c2Φ]}]]]

cE00[[14]]
cEα = Drop[cE00, {14}]
```

Cu2.δSe

$$\{CIS_\alpha, \mathcal{V}^{x}_{Cu}, \mathcal{V}'_{Cu}, Cu^{x}_{In}, Cu'_{In}, Cu''_{In}, \mathcal{V}^{x}_{Se}, \mathcal{V}^{\bullet\bullet}_{Se}, Cu_i \oplus \mathcal{V}_{Cu}, Cu_{In} \oplus In_{Cu}, \mathcal{V}_{Cu} \oplus In_{Cu}, (\mathcal{V}_{Cu} \oplus In_{Cu})^{\bullet}, (2\,\mathcal{V}_{Cu} \oplus In_{Cu})_\alpha, e', h^{\bullet}, \Delta N\}$$

```
Thread[{cEα, c00α[1, tMaxαβ]}]
```

$$\{\{CIS_\alpha, 0.429214\}, \{\mathcal{V}^{x}_{Cu}, 8.54015\times10^{-6}\}, \{\mathcal{V}'_{Cu}, 0.00914242\}, \{Cu^{x}_{In}, 8.42159\times10^{-13}\}, \{Cu'_{In}, 9.23817\times10^{-11}\}, \{Cu''_{In}, 1.47442\times10^{-11}\}, \{\mathcal{V}^{x}_{Se}, 4.39404\times10^{-9}\}, \{\mathcal{V}^{\bullet\bullet}_{Se}, 8.30383\times10^{-9}\}, \{Cu_i \oplus \mathcal{V}_{Cu}, 6.46845\times10^{-10}\}, \{Cu_{In} \oplus In_{Cu}, 0.0000169955\}, \{\mathcal{V}_{Cu} \oplus In_{Cu}, 0.0000128473\}, \{(\mathcal{V}_{Cu} \oplus In_{Cu})^{\bullet}, 0.00913809\}, \{(2\,\mathcal{V}_{Cu} \oplus In_{Cu})_\alpha, 0.000456919\}, \{e', 2.77129\times10^{-7}\}, \{h^{\bullet}, 4.59301\times10^{-6}\}, \{\Delta N, 1.02886\}\}$$

```
(* the α−CIS single phase solution basis *)
𝒟0α = Transpose[Drop[Transpose[𝒟00], {14}]];
𝒟0α // MatrixForm
```

$$\begin{pmatrix}
2 & 5 & 5 & 7 & 7 & 7 & 6 & 6 & 6 & 6 & 8 & 8 & 7 & 0 & 0 & 0\\
2 & 6 & 6 & 5 & 5 & 5 & 6 & 6 & 6 & 6 & 11 & 11 & 11 & 0 & 0 & 0\\
4 & 12 & 12 & 12 & 12 & 12 & 11 & 11 & 12 & 12 & 20 & 20 & 20 & 0 & 0 & 0\\
0 & 0 & -1 & 0 & -1 & -2 & 0 & 2 & 0 & 0 & 0 & 1 & 0 & -1 & 1 & 0\\
2 & 6 & 6 & 6 & 6 & 6 & 6 & 6 & 6 & 6 & 10 & 10 & 10 & 0 & 0 & 1\\
2 & 6 & 6 & 6 & 6 & 6 & 6 & 6 & 6 & 6 & 10 & 10 & 10 & 0 & 0 & 1\\
4 & 12 & 12 & 12 & 12 & 12 & 12 & 12 & 12 & 12 & 20 & 20 & 20 & 0 & 0 & 2\\
8 & 24 & 24 & 24 & 24 & 24 & 24 & 24 & 24 & 24 & 40 & 40 & 40 & 0 & 0 & 4
\end{pmatrix}$$

```
formula[i_, 𝒟0α] := {cEα, a .𝒟0α}[[All, i]]

ν0α = Transpose[NullSpace[𝒟0α]];
```

```
rxn[i_, ν0α] := ν0α⟦All, i⟧.cEα

ν0αξ = ν0α;
ν0αξ = Transpose[
         ReplacePart[Transpose[ν0αξ], (−ν0α⟦All, 1⟧ + 2 ν0α⟦All, 4⟧)/2, 1]] // Simplify;
ν0αξ = Transpose[ReplacePart[Transpose[ν0αξ], ν0α⟦All, 3⟧ + ν0α⟦All, 2⟧, 3]];
ν0αξ = Transpose[ReplacePart[Transpose[ν0αξ], −ν0α⟦All, 4⟧ + ν0α⟦All, 6⟧, 4]];
ν0αξ = Transpose[
        ReplacePart[Transpose[ν0αξ], ν0α⟦All, 5⟧ + ν0α⟦All, 3⟧ − ν0α⟦All, 6⟧, 5]];
ν0αξ = Transpose[ReplacePart[Transpose[ν0αξ], ν0α⟦All, 9⟧ + 2 ν0α⟦All, 3⟧, 9]];
ν0αξ = Transpose[ReplacePart[Transpose[ν0αξ], ν0α⟦All, 10⟧ + 2 ν0α⟦All, 2⟧, 10]];
ν0αξ = Transpose[ReplacePart[Transpose[ν0αξ], ν0α⟦All, 11⟧ + ν0α⟦All, 2⟧, 11]];

rxn[i_, ν0αξ] := ν0αξ⟦All, i⟧.cEα

xMax[Zα_?NumericQ, tK_?NumericQ] /;
    zαMin ≤ Zα ≤ zαMax ⋀ tSTP ≤ tK ≤ tMaxαβ := cXZ[c00α[Zα, tK], 𝒟0α]⟦1⟧

c000αbasis = {1, 7, 4, 13};

cEα⟦#⟧ & /@ c000αbasis

      {CIS_α, 𝒱^x_Se, Cu^x_In, (2 𝒱_Cu ⊕ In_Cu)_α}

ξ000α = Array[1 &, 11] −
    3 Array[KroneckerDelta[1, #] &, 11] + Array[KroneckerDelta[2, #] &, 11]

      {−2, 2, 1, 1, 1, 1, 1, 1, 1, 1, 1}

(* using c000αbasis→{c1,c7,c4,c13},
  does any linear combination of the normalized vectors {0,0,c4,0} and
    {0,0,0,c13} always furnish the same X value as {c1,0,0,0}? *)Solve[
  cXZ[{c1, 0, 0, 0}, 𝒟000xVin]⟦1⟧ == cXZ[{c1 − c4 − c13, 0, c4, c13}, 𝒟000xVin]⟦1⟧, {c13

      {{c13 → c4/2}}

(* how does Z vary for that linear combination? *)
cXZ[{1 − c4 − c13, 0, c4, c13}, 𝒟000xVin] /. % // Simplify

      {{1, (4 + 16 c4)/(4 + 15 c4)}}
```

(* what is the extremal value of Z for that linear combination? *) %[[1, 2]] /. c4 → 2/3

$$\frac{22}{21}$$

(* are the Z' s for the vectors {c1,0,0,0} and {0,0,0,c13} always equal? *)
cXZ[{c1, 0, 0, 0}, $\mathcal{D}$000xVin][[2]] === cXZ[{0, 0, 0, c13}, $\mathcal{D}$000xVin][[2]]

True

{formula[1, $\mathcal{D}$000xVin][[1]], formula[4, $\mathcal{D}$000xVin][[1]]}
c13 × formula[4, $\mathcal{D}$000xVin][[2]] − 5 c13 × formula[1, $\mathcal{D}$000xVin][[2]] // Simplify

$$\{\mathrm{CIS}_\alpha,\ (2\,\mathcal{V}_{\mathrm{Cu}} \oplus \mathrm{In}_{\mathrm{Cu}})_\alpha\}$$
$$\mathrm{c13}\,(-3\,\mathrm{Cu} + \mathrm{In})$$

(* Since Z is unaffected by any linear combination of c1 and c13,
and $(2\,\mathcal{V}_{\mathrm{Cu}} \oplus \mathrm{In}_{\mathrm{Cu}})_\alpha - 5\,\mathrm{CIS}_\alpha$ does not change the selenium content at all,
how does X vary for that linear combination? *)
Solve[X == cXZ[{1 − 5 c13, 0, 0, c13}, $\mathcal{D}$000xVin][[1]], {c13}]

$$\left\{\left\{\mathrm{c13} \to -\frac{2\,(-1+\mathrm{X})}{3+\mathrm{X}}\right\}\right\}$$

(* initial cluster quantities for X<1, Z>1;
and that vector' s molar normalization factor *)
Solve[{X, Z} == cXZ[{1 − (3 c4/2) − 5 c13, 0, c4, c13 + c4/2}, $\mathcal{D}$000xVin], {c4, c13}]
{1 − (3 c4/2) − 5 c13, 0, c4, c13 + c4/2} /. %
mx[{1 − (3 c4/2) − 5 c13, 0, c4, c13 + c4/2}, $\mathcal{D}$000xVin][[2]] /. %% //
Simplify(* moles of indium *)
(* solve for normalization to give $\mathrm{Cu}_{\frac{2\,X}{1+X}}\ \mathrm{In}_{\frac{2}{1+X}}\ \mathrm{Se}_{\frac{Z\,(3+X)}{1+X}}$ *)
Solve$\left[\frac{2}{1+\mathrm{X}} == \mathrm{m}\ \%[[1]], \{\mathrm{m}\}\right]$

$$\left\{\left\{\mathrm{c13} \to \frac{2\,(-1+\mathrm{X})}{(3+\mathrm{X})\,(-16+15\,\mathrm{Z})},\ \mathrm{c4} \to -\frac{4\,(-1+\mathrm{Z})}{-16+15\,\mathrm{Z}}\right\}\right\}$$
$$\left\{\left\{1 - \frac{10\,(-1+\mathrm{X})}{(3+\mathrm{X})\,(-16+15\,\mathrm{Z})} + \frac{6\,(-1+\mathrm{Z})}{-16+15\,\mathrm{Z}},\right.\right.$$
$$\left.\left.0,\ -\frac{4\,(-1+\mathrm{Z})}{-16+15\,\mathrm{Z}},\ \frac{2\,(-1+\mathrm{X})}{(3+\mathrm{X})\,(-16+15\,\mathrm{Z})} - \frac{2\,(-1+\mathrm{Z})}{-16+15\,\mathrm{Z}}\right\}\right\}$$
$$\left\{-\frac{8}{(3+\mathrm{X})\,(-16+15\,\mathrm{Z})}\right\}$$
$$\left\{\left\{\mathrm{m} \to -\frac{(3+\mathrm{X})\,(-16+15\,\mathrm{Z})}{4\,(1+\mathrm{X})}\right\}\right\}$$

```
c000α[Zα_?NumericQ, tK_?NumericQ] /;
    zαMin ≤ Zα ≤ zαMax ⋀ tSTP ≤ tK ≤ tMaxαβ :=
  Module[{c00}, With[{c4Zplus = {1 - 10 (-1 + X)/((3 + X) (-16 + 15 Zα)) + 6 (-1 + Zα)/(-16 + 15 Zα),
        0, -4 (-1 + Zα)/(-16 + 15 Zα), 2 (-1 + X)/((3 + X) (-16 + 15 Zα)) - 2 (-1 + Zα)/(-16 + 15 Zα)},
      mNormFac = -(3 + X) (-16 + 15 Zα)/(4 (1 + X))}, c00 = Plus @@ MapThread[
        ReplacePart[Array[0 &, Length[cEα]], #1, #2] &, {c4Zplus, c000αbasis}];
      c00 = mNormFac (c00 + ν0α.ξ000α 1*^-45); ReplacePart[
       c00 /. X → xMax[Zα, tK], 1, -1]]]

ξ00α = Drop[ξ00minδ, {4}];
c0α[Zα_?NumericQ, tK_?NumericQ] /;
    zαMin ≤ Zα ≤ zαMax ⋀ tSTP ≤ tK ≤ tMaxαβ := c000α[Zα, tK] + ν0αξ.ξ00α

μ0α[c_, tK_] /; Length[c] === Length[cEα] := With[
    {n = (#/Plus @@ #) &[Drop[Drop[Drop[Drop[mcl, -3], {16, 17}], {10, 13}], {4, 6}]
        Take[c, 13]], nCISα = nAvo c/First[c]},
    Drop[Drop[Drop[Drop[μ00αβ[tK], {23, 25}], {16, 17}], {10, 13}], {4, 6}] +
     rG tK Join[Log[n], {Log[nCISα⟦14⟧/cbDOSαCIS[tK]], Log[nCISα⟦15⟧/vbDOSαCIS[tK]], 0}]]

gd0α[Z_, tK_] := (μ0α[c0α[#, #2], #2].ν0α) &[Z, tK]

gd0α[1, tMaxαβ] /. Thread[ξ00α → Array[0 &, Length[ξ00α]]];
σSD[%] "Joules total RMS initial affinity deviation"
```

1.10525×10^{7} Joules total RMS initial affinity deviation

```
gd0α[1, tMaxαβ – 400] /. ξ0α[1, tMaxαβ – 400];
{"solution convergence σSD", σSD[%]}
"comparison of phase–boundary single–
    phase with nearly corresponding two–phase solution:"
Thread[{Drop[cEα, –1],
    Thread[{Drop[c0α[1, tMaxαβ – 400] /. ξ0α[1, tMaxαβ – 400], –1],
        partCIS[(c00ξminδ[1, tRef – 575] / (1 – c00ξminδ[1, tRef – 575][[14]])) /.
            ξ0[1, tRef – 575]]}]}]
```

```
{solution convergence σSD, 0.00177069}
comparison of phase–boundary single–
    phase with nearly corresponding two–phase solution:
{{CISα, {0.499725, 0.499725}}, {V_Cu^x, {2.28725×10^-11, 4.72603×10^-13}},
  {V'_Cu, {0.0000365934, 0.0000365318}}, {Cu_In^x, {1.86399×10^-22, 7.97367×10^-26}},
  {Cu'_In, {5.07145×10^-19, 1.04817×10^-20}},
  {Cu''_In, {7.84222×10^-20, 7.83115×10^-20}},
  {V_Se^x, {8.98764×10^-14, 2.1016×10^-10}}, {V_Se^••, {1.5276×10^-14, 1.53018×10^-14}},
  {Cu_i ⊕ V_Cu, {4.29359×10^-17, 4.29232×10^-17}},
  {Cu_In ⊕ In_Cu, {1.98426×10^-8, 1.98368×10^-8}},
  {V_Cu ⊕ In_Cu, {2.68474×10^-9, 1.29603×10^-7}},
  {(V_Cu ⊕ In_Cu)^•, {0.0000365907, 0.0000365592}},
  {(2 V_Cu ⊕ In_Cu)_α, {1.22827×10^-7, 1.22551×10^-7}},
  {e', {5.67604×10^-10, 2.7424×10^-8}}, {h^•, {3.22965×10^-9, 6.6845×10^-11}}}
```

```
{"temperature [K]", {tRef – 575, tMaxαβ – 400}}
{"two–phase total X,Z" ,
  cXZ[c00ξminδ[1, tRef – 575] /. ξ0[1, tRef – 575], D00] /. δ → δmin[tRef – 575]}
{"CIS phase X and Z; old solution" ,
  cXZ[partCIS[c00ξminδ[1, tRef – 575] /. ξ0[1, tRef – 575]], partCIS[D00]]}
{"CIS phase X and Z; new solution" ,
  cXZ[c0α[1, tMaxαβ – 400] /. ξ0α[1, tMaxαβ – 400], D0α]}
{"difference new–old X and Z" , %[[2]] – %%[[2]]}
```

```
{temperature [K], {473.15, 473.15}}
{two–phase total X,Z, {1., 1.}}
{CIS phase X and Z; old solution, {0.999853, 1.}}
{CIS phase X and Z; new solution, {0.999853, 1.}}
{difference new–old X and Z, {2.2338×10^-7, 3.93434×10^-8}}
```

This exemplary single phase Z= 1 solution exhibits an increase in hole concentration and shifts in ionization equilibria, which are indicative of a Fermi level shift resulting from the increase in valency required to suppress the secondary $Cu_{2-\delta}Se$ phase segregation and yield single phase α-CIS. This is also evident in the four-order-of-magnitude drop in the total concentration of $\mathcal{V}_{Se}$. Otherwise, the ternary part of the two-phase Z= 1 solution renormalized to one mole of α-CIS is virtually identical to the single-phase solution at the phase boundary where its valency Z= 1 and its molecularity parameter X assumes the maximum possible value for that Z.

```
gd0α[1, tSTP] /. ξ0α[1, tSTP];
{"solution convergence σSD", σSD[%]}
Thread[{cEα, c0α[1, tSTP] /. ξ0α[1, tSTP]}]
```

$$\{\text{solution convergence } \sigma_{SD},\ 637.156\}$$

$$\{\{CIS_{\alpha},\ 0.5\},\ \{\mathcal{V}^{x}_{Cu},\ 5.88725\times10^{-18}\},\ \{\mathcal{V}'_{Cu},\ 2.76287\times10^{-8}\},$$
$$\{Cu^{x}_{In},\ 1.80556\times10^{-35}\},\ \{Cu'_{In},\ 3.54078\times10^{-30}\},\ \{Cu''_{In},\ 5.85049\times10^{-31}\},$$
$$\{\mathcal{V}^{x}_{Se},\ 3.74234\times10^{-20}\},\ \{\mathcal{V}^{\bullet\bullet}_{Se},\ 2.34695\times10^{-22}\},\ \{Cu_i \oplus \mathcal{V}_{Cu},\ 1.35084\times10^{-26}\},$$
$$\{Cu_{In} \oplus In_{Cu},\ 1.71625\times10^{-12}\},\ \{\mathcal{V}_{Cu} \oplus In_{Cu},\ 5.13063\times10^{-14}\},$$
$$\{(\mathcal{V}_{Cu} \oplus In_{Cu})^{\bullet},\ 2.76287\times10^{-8}\},\ \{(2\,\mathcal{V}_{Cu} \oplus In_{Cu})_{\alpha},\ 5.24904\times10^{-12}\},$$
$$\{e',\ 3.05254\times10^{-13}\},\ \{h^{\bullet},\ 3.56554\times10^{-13}\},\ \{\Delta N,\ 1.\}\}$$

This completes the ternary single phase equilibrium solution at the $Cu_{2-\delta}Se/\alpha$–CIS two-phase boundary for Z = 1. This solution is next extended to Z > 1. Here the concentration vector is initialized to the solution from the two-phase problem.

```
c0αΔZ[Zα_?NumericQ, tK_?NumericQ] /;
    zαMin ≤ Zα ≤ zαMax ⋀ tSTP ≤ tK ≤ tMaxαβ := c00α[Zα, tK] + ν0αξ.ξ00α
```

```
gd0αΔZ[Zα_, tK_] := (μ0α[c0αΔZ[#, #2], #2].ν0α) &[Zα, tK]

tKdomainαβ = Reverse[(tMaxαβ − #) & /@ Range[0, 575, 5]];
First[tKdomainαβ] === tSTP
Length[tKdomainαβ]
```

```
True
116
```

$$\text{zRange}\alpha = (1 + \#)\ \&\ /@\ \frac{2\,\text{Range}[0, 5]}{10000};$$

```
zαMin ≤ First[zRangeα] ⋀ Last[zRangeα] ≤ zαMax
zRangeα // N
```

```
True
{1., 1.0002, 1.0004, 1.0006, 1.0008, 1.001}
```

```
Thread[{cEα, Thread[{c0α[1, tSTP] /. ξ0α[1, tSTP],
      c0αΔZ[Last[zRangeα], tSTP] /. ξ0α[Last[zRangeα], tSTP]}]}]
```

$$\{\{\text{CIS}_\alpha, \{0.5, 0.491365\}\}, \{\mathcal{V}^{x}_{Cu}, \{5.88725\times10^{-18}, 0.000866232\}\},$$
$$\{\mathcal{V}'_{Cu}, \{2.76287\times10^{-8}, 0.00119347\}\}, \{Cu^{x}_{In}, \{1.80556\times10^{-35}, 0.000981228\}\},$$
$$\{Cu'_{In}, \{3.54078\times10^{-30}, 5.44552\times10^{-8}\}\},$$
$$\{Cu''_{In}, \{5.85049\times10^{-31}, 2.64157\times10^{-18}\}\},$$
$$\{\mathcal{V}^{x}_{Se}, \{3.74234\times10^{-20}, 6.33766\times10^{-47}\}\},$$
$$\{\mathcal{V}^{\bullet\bullet}_{Se}, \{2.34695\times10^{-22}, 2.99438\times10^{-33}\}\},$$
$$\{Cu_i \oplus \mathcal{V}_{Cu}, \{1.35084\times10^{-26}, 1.31527\times10^{-26}\}\},$$
$$\{Cu_{In} \oplus In_{Cu}, \{1.71625\times10^{-12}, 1.63061\times10^{-12}\}\},$$
$$\{\mathcal{V}_{Cu} \oplus In_{Cu}, \{5.13063\times10^{-14}, 1.0551\times10^{-29}\}\},$$
$$\{(\mathcal{V}_{Cu} \oplus In_{Cu})^{\bullet}, \{2.76287\times10^{-8}, 2.44487\times10^{-16}\}\},$$
$$\{(2\,\mathcal{V}_{Cu} \oplus In_{Cu})_\alpha, \{5.24904\times10^{-12}, 2.09752\times10^{-15}\}\},$$
$$\{e', \{3.05254\times10^{-13}, 8.80693\times10^{-23}\}\},$$
$$\{h^{\bullet}, \{3.56554\times10^{-13}, 0.00119352\}\}, \{\Delta N, \{1., 1.00008\}\}\}$$

```
𝒢0α[Zα_?(MemberQ[{N[1], 1}, #] &), tK_?(MemberQ[tKdomainαβ, #] &)] :=
  (c0α[1, tK].μ0α[c0α[1, tK], tK]) /. ξ0α[1, tK]
𝒢0α[Zα_?(MemberQ[Rest[zRangeα], #] &), tK_?(MemberQ[tKdomainαβ, #] &)] :=
  (c0αΔZ[Zα, tK].μ0α[c0αΔZ[Zα, tK], tK]) /. ξ0α[Zα, tK]
𝒢0α[Zα_?(MemberQ[N[Rest[zRangeα]], #] &), tK_?(MemberQ[tKdomainαβ, #] &)] :=
  With[{Z = First[Select[zRangeα, (N[#] === Zα) &]]},
    (c0αΔZ[Z, tK].μ0α[c0αΔZ[Z, tK], tK]) /. ξ0α[Z, tK]]
```

```
{𝒢0α[1, tSTP + 100], 𝒢0α[zRangeα⟦2⟧, tSTP + 100], 𝒢0α[1.0004, tSTP + 100]}
```

```
{−306056., −305793., −306119.}
```

This completes the ternary single phase equilibrium solution at the $Cu_{2-\delta}Se/\alpha$–CIS two-phase boundary where the α–CIS phase assumes its maximum possible molecularity (*i.e.*: maximum copper concentration). At all temperatures from STP to the $\alpha/\beta/\delta$-CIS eutectoid decomposition temperature the molecularity deviation of the ternary phase is found to be negative in equilibrium at this two-phase boundary. Thus the ideal stoichiometric ternary composition $CuInSe_2$ always dissociates in equilibrium to form the two-phase mixture.

Before turning to consideration of the α/β-CIS phase equilibrium, it is necessary to determine the variation of Gibbs energy of the α–CIS phase with its composition, in particular its Gibbs energy variation with the molecularity X.

```
c000α[Xα_?NumericQ, Zα_?NumericQ, tK_?NumericQ] /;
    c0xVinLimits⟦1⟧ ≤ Xα < xMax[Zα, tK] ⋀
      zαMin ≤ Zα ≤ zαMax ⋀ tSTP ≤ tK ≤ tMaxαβ :=
  Module[{c00}, With[{c4Zplus = {1 - 10 (-1 + Xα)/((3 + Xα) (-16 + 15 Zα)) + 6 (-1 + Zα)/(-16 + 15 Zα),
          0, -4 (-1 + Zα)/(-16 + 15 Zα), 2 (-1 + Xα)/((3 + Xα) (-16 + 15 Zα)) - 2 (-1 + Zα)/(-16 + 15 Zα)},
        mNormFac = -(3 + Xα) (-16 + 15 Zα)/(4 (1 + Xα))}, c00 = Plus @@ MapThread[
          ReplacePart[Array[0 &, Length[cEα]], #1, #2] &, {c4Zplus, c000αbasis}];
      c00 = mNormFac (c00 + ν0α.ξ000α 1*^-45); ReplacePart[c00, 1, -1]]]

c0α[Xα_?NumericQ, Zα_?NumericQ, tK_?NumericQ] /;
    c0xVinLimits⟦1⟧ ≤ Xα < xMax[Zα, tK] ⋀ zαMin ≤ Zα ≤ zαMax ⋀
      tSTP ≤ tK ≤ tMaxαβ := c000α[Xα, Zα, tK] + ν0αξ.ξ00α

gdα[Xα_?NumericQ, Zα_?NumericQ, tK_?NumericQ] /;
    c0xVinLimits⟦1⟧ ≤ Xα < xMax[Zα, tK] ⋀ zαMin ≤ Zα ≤ zαMax ⋀
      tSTP ≤ tK ≤ tMaxαβ := (μ0α[c0α[#, #2, #3], #3].ν0α) &[Xα, Zα, tK]

xMax4TmaxαβxMax[1, tMaxαβ]

    0.96229

{"limits of X variation at α−β−δ eutectoid temperature:",
    c0xVinLimits⟦1⟧, xMax4TmaxαβxMax} // N
Subtract @@ Rest[%] "difference"

    {limits of X variation at α−β−δ eutectoid temperature:, 0.636864, 0.96229}
    −0.325426 difference
```

gdα[xMax4Tmax$\alpha\beta$ – 320 / 1000, 1, tMax$\alpha\beta$] /.
$\xi\alpha$[xMax4Tmax$\alpha\beta$ – 320 / 1000, 1, tMax$\alpha\beta$];
{"solution convergence σ_{SD}", σSD[%]}
Thread[{cEα, c0α[xMax4Tmax$\alpha\beta$ – 320 / 1000, 1, tMax$\alpha\beta$] /.
$\xi\alpha$[xMax4Tmax$\alpha\beta$ – 320 / 1000, 1, tMax$\alpha\beta$]}]
{"atom and charge fractions", ax[c0α[xMax4Tmax$\alpha\beta$ – 320 / 1000, 1, tMax$\alpha\beta$] /.
$\xi\alpha$[xMax4Tmax$\alpha\beta$ – 320 / 1000, 1, tMax$\alpha\beta$], $\mathcal{D}$0α]}

{solution convergence σ_{SD}, 4.77507×10^{-7}}
{{CIS$_\alpha$, 0.00875771}, {$\mathcal{V}^{x}_{Cu}$, 1.85156×10^{-7}}, {$\mathcal{V}'_{Cu}$, 0.00038826},
{Cu^{x}_{In}, 6.4206×10^{-21}}, {Cu'_{In}, 4.25063×10^{-19}}, {Cu''_{In}, 4.1594×10^{-20}},
{$\mathcal{V}^{x}_{Se}$, 3.12032×10^{-16}}, {$\mathcal{V}^{\bullet\bullet}_{Se}$, 1.56867×10^{-15}}, {$Cu_i \oplus \mathcal{V}_{Cu}$, 4.90932×10^{-15}},
{$Cu_{In} \oplus In_{Cu}$, 1.2899×10^{-10}}, {$\mathcal{V}_{Cu} \oplus In_{Cu}$, 3.34542×10^{-7}},
{$(\mathcal{V}_{Cu} \oplus In_{Cu})^{\bullet}$, 0.00038811}, {$(2\,\mathcal{V}_{Cu} \oplus In_{Cu})_\alpha$, 0.108518},
{e′, 3.46689×10^{-9}}, {h$^{\bullet}$, 1.52853×10^{-7}}, {ΔN, 1.}}
{atom and charge fractions, {0.185449, 0.288731, 0.52582, -1.28527×10^{-20}}}

gdα[xMax4Tmax$\alpha\beta$ – 320 / 1000, 1, tSTP] /. $\xi\alpha$[xMax4Tmax$\alpha\beta$ – 320 / 1000, 1, tSTP]
{"solution convergence σ_{SD}", σSD[%]}
Thread[{cEα, c0α[xMax4Tmax$\alpha\beta$ – 320 / 1000, 1, tSTP] /.
$\xi\alpha$[xMax4Tmax$\alpha\beta$ – 320 / 1000, 1, tSTP]}]
{"atom and charge fractions", ax[c0α[xMax4Tmax$\alpha\beta$ – 320 / 1000, 1, tSTP] /.
$\xi\alpha$[xMax4Tmax$\alpha\beta$ – 320 / 1000, 1, tSTP], $\mathcal{D}$0α]}

{−0.0000665262, −0.0000206273, −0.0113311, −0.0000462462, −0.0000462467,
−0.0000186414, 0., 0., −0.000039754, 0.0000462466, 0.0000263692}
{solution convergence σ_{SD}, 0.0116418}
{{CIS$_\alpha$, 0.00989308}, {$\mathcal{V}^{x}_{Cu}$, 9.56632×10^{-14}}, {$\mathcal{V}'_{Cu}$, 9.98791×10^{-6}},
{Cu^{x}_{In}, 7.58969×10^{-41}}, {Cu'_{In}, 3.19188×10^{-37}}, {Cu''_{In}, 1.17333×10^{-39}},
{$\mathcal{V}^{x}_{Se}$, 3.11782×10^{-34}}, {$\mathcal{V}^{\bullet\bullet}_{Se}$, 3.95047×10^{-33}}, {$Cu_i \oplus \mathcal{V}_{Cu}$, 8.5094×10^{-32}},
{$Cu_{In} \oplus In_{Cu}$, 1.08112×10^{-17}}, {$\mathcal{V}_{Cu} \oplus In_{Cu}$, 4.12636×10^{-13}},
{$(\mathcal{V}_{Cu} \oplus In_{Cu})^{\bullet}$, 9.98791×10^{-6}}, {$(2\,\mathcal{V}_{Cu} \oplus In_{Cu})_\alpha$, 0.108896},
{e′, 1.3437×10^{-16}}, {h$^{\bullet}$, 3.17107×10^{-13}}, {ΔN, 1.}}
{atom and charge fractions, {0.185449, 0.288731, 0.52582, 0.}}

```
xRangeα = (xMax4Tmaxαβ − #) & /@ 5 Range[1, 64] / 1000;
First[xRangeα] === xMax4Tmaxαβ − .005
Last[xRangeα] === xMax4Tmaxαβ − .32
```

```
True
True
```

```
Do[With[{T = tKdomainαβ⟦i⟧}, c0αFit[1, T] = Module[{cα},
        cα = Join[{c0α[1, T] /. ξ0α[1, T]}, ((c0α[#, 1, T] /. ξα[#, 1, T]) & /@ xRangeα)];
SplineFit[Thread[{Join[{xMax[1, T]}, xRangeα], cα⟦All, #⟧}], Cubic] & /@
        Range[Length[cEα]]]], {i, Length[tKdomainαβ]}];
```

```
cXα[Xα_, 1, tK_?(MemberQ[tKdomainαβ, #] &)] /;
    First[xRangeα] < Xα ≤ xMax[1, tK] := With[{X = (xMax[1, tK] − Xα) / (xMax[1, tK] − First[xRangeα])},
    Through[(c0αFit[1, tK]⟦#⟧ & /@ Range[Length[cEα]])[X]]⟦All, 2⟧]
cXα[Xα_, 1, tK_?(MemberQ[tKdomainαβ, #] &)] /;
    Last[xRangeα] ≤ Xα ≤ First[xRangeα] :=
  With[{X = 1 + (Length[xRangeα] − 1) (First[xRangeα] − Xα) / (First[xRangeα] − Last[xRangeα])},
    Through[(c0αFit[1, tK]⟦#⟧ & /@ Range[Length[cEα]])[X]]⟦All, 2⟧]
```

```
Thread[{cEα, cXα[Last[xRangeα], 1, tSTP]}]
```

$$\{\{\mathrm{CIS}_{\alpha}, 0.00989308\}, \{\mathcal{V}^{x}_{Cu}, 9.56632\times10^{-14}\}, \{\mathcal{V}'_{Cu}, 9.98791\times10^{-6}\},$$
$$\{\mathrm{Cu}^{x}_{In}, 7.58969\times10^{-41}\}, \{\mathrm{Cu}'_{In}, 3.19188\times10^{-37}\}, \{\mathrm{Cu}''_{In}, 1.17333\times10^{-39}\},$$
$$\{\mathcal{V}^{x}_{Se}, 3.11782\times10^{-34}\}, \{\mathcal{V}^{\bullet\bullet}_{Se}, 3.95047\times10^{-33}\}, \{\mathrm{Cu_i}\oplus\mathcal{V}_{Cu}, 8.5094\times10^{-32}\},$$
$$\{\mathrm{Cu_{In}}\oplus\mathrm{In_{Cu}}, 1.08112\times10^{-17}\}, \{\mathcal{V}_{Cu}\oplus\mathrm{In_{Cu}}, 4.12636\times10^{-13}\},$$
$$\{(\mathcal{V}_{Cu}\oplus\mathrm{In_{Cu}})^{\bullet}, 9.98791\times10^{-6}\}, \{(2\,\mathcal{V}_{Cu}\oplus\mathrm{In_{Cu}})_{\alpha}, 0.108896\},$$
$$\{e', 1.3437\times10^{-16}\}, \{h^{\bullet}, 3.17107\times10^{-13}\}, \{\Delta N, 1.\}\}$$

```
g0α[Xα_?NumericQ, 1, tK_?(MemberQ[tKdomainαβ, #] &)] /;
    Last[xRangeα] ≤ Xα ≤ xMax[1, tK] := cXα[Xα, 1, tK]. μ0α[cXα[Xα, 1, tK], tK]
```

```
{g0α[xMax[1, tSTP], 1, tSTP], g0α[Last[xRangeα], 1, tMaxαβ]}
```

```
{−288747., −453520.}
```

This completes the initial α–CIS ternary single phase equilibrium solution as a function of temperature and molecularity X. The α/β–CIS phase equilibrium problem is considered next. The quasichemical reactions between the β–CIS and α–CIS phases are represented in a manner analogous to that used for the prior solution of the $Cu_{2-\delta}Se/\alpha$–CIS equilibrium problem. Whereas only copper could be independently exchanged between the two phases in that problem, only the $(2\mathcal{V}_{Cu} \oplus In_{Cu})$ cation NDC complex can be independently exchanged between the β–CIS and α–CIS phases in this model. The variation of the Gibbs energy of the α–CIS phase as a function of its molecularity X_α has already been determined based on the solution of its constituent defect equilibria, and cation NDC exchange between them does not change the valency Z of either, so the internal defect structure of the α–CIS phase is otherwise irrelevant to the solution of its equilibrium with the β–CIS phase. The composition and Gibbs energy of the α–CIS phase will be computed here on the basis of the two species αNDC and αCIS.

The species αCIS is not the CIS_α cluster (the ideal chalcopyrite primitive unit cell) but rather the reference state defined by one mole of the α–CIS phase with its equilibrium internal defect structure and specific Gibbs energy given by the preceding single-phase solution, and chemical formula given by $Cu_{\frac{2X_\alpha}{1+X_\alpha}}\ In_{\frac{2}{1+X_\alpha}}\ Se_{\frac{Z(3+X_\alpha)}{1+X_\alpha}}$. Its molecularity will be fixed to the maximum equilibrium single-phase value at each temperature.

The species αNDC is not the $(2\mathcal{V}_{Cu} \oplus In_{Cu})_\alpha$ cluster, although it has the same molecularity. Its purpose is analogous to that of the Cu_{Cu2Se} specie in the preceding

two-phase problem: in the stoichiometric reaction formalism it controls the overall composition (molecularity in this case) of the secondary phase in a physically meaningful way. As a consequence, the reference state chemical potential of $(2\,\mathcal{V}_{\mathrm{Cu}} \oplus \mathrm{In}_{\mathrm{Cu}})_{\alpha}$ does not enter directly into this calculation of the α–CIS phase's Gibbs energy. Since NDC exchange between the phases cannot change the valence stoichiometry, Z is set to unity.

Since the α and β–CIS phases are coherent, all species are now part of the lattice and the sublattice site numbers are no longer needed to assure the interconsistency between the building unit and quasichemical species models, so long as the cluster multiplicity factors are retained for the mixing entropy calculation.

Because of the relatively simple four-species model employed for β–CIS and this reduction of the α–CIS phase's complex internal defect structure, there are only six species in the basis used to model the α/β-CIS phase equilibrium: CIS_{β}, $(2\,\mathcal{V}_{\mathrm{Cu}} \oplus \mathrm{In}_{\mathrm{Cu}})_{\beta 1.5}$, $(2\,\mathcal{V}_{\mathrm{Cu}} \oplus \mathrm{In}_{\mathrm{Cu}})_{\beta 1.3}$, $(2\,\mathcal{V}_{\mathrm{Cu}} \oplus \mathrm{In}_{\mathrm{Cu}})_{\beta 2.5}$, αNDC, and αCIS. All these species are neutral, so the charge element in the basis set **a** is no longer needed.

Insofar as the results of the forthcoming α/β–CIS phase equilibrium calculations predict a phase mixture thereof in *lieu* of the pure α–CIS phase for some domains of the thermodynamic parameters, the corresponding α–CIS single phase solutions already developed would represent hypothetical or non-equilibrium states of the lattice.

```
cE[[#]] & /@ {1, 23, 24, 25}
```

$$\{\mathrm{CIS}_{\alpha},\ (2\,\mathcal{V}_{\mathrm{Cu}} \oplus \mathrm{In}_{\mathrm{Cu}})_{\beta 15},\ (2\,\mathcal{V}_{\mathrm{Cu}} \oplus \mathrm{In}_{\mathrm{Cu}})_{\beta 13},\ (2\,\mathcal{V}_{\mathrm{Cu}} \oplus \mathrm{In}_{\mathrm{Cu}})_{\beta 25}\}$$

```
(* the reduced CIS$\alpha$+CIS$\beta$ basis vector *)cE$\alpha\beta$ =
  Prepend[Append[Append[Drop[Drop[cE, -3], 22], $\alpha$NDC], $\alpha$CIS], CIS$_\beta$]
Length[cE$\alpha\beta$]
```

$$\{\text{CIS}_\beta, (2\,\mathcal{V}_{\text{Cu}} \oplus \text{In}_{\text{Cu}})_{\beta 15}, (2\,\mathcal{V}_{\text{Cu}} \oplus \text{In}_{\text{Cu}})_{\beta 13}, (2\,\mathcal{V}_{\text{Cu}} \oplus \text{In}_{\text{Cu}})_{\beta 25}, \alpha\text{NDC}, \alpha\text{CIS}\}$$

$$6$$

```
$\mathcal{D}\alpha\beta$ = Transpose[Prepend[Append[
      Append[RotateRight[Drop[Drop[Transpose[Drop[$\mathcal{D}$, -5]], -3], 22], 3],
        {2 X$\alpha$/(1 + X$\alpha$), 2/(1 + X$\alpha$), (3 + X$\alpha$)/(1 + X$\alpha$)} /. X$\alpha$ -> 7/11],
        {2 X$\alpha$/(1 + X$\alpha$), 2/(1 + X$\alpha$), (3 + X$\alpha$)/(1 + X$\alpha$)}],
      First[Transpose[Drop[$\mathcal{D}$, -5]]]]];
```

```
$\mathcal{D}\alpha\beta$ // MatrixForm
```

$$\begin{pmatrix} 2 & 7 & 3 & 4 & \frac{7}{9} & \frac{2\,X\alpha}{1+X\alpha} \\ 2 & 11 & 7 & 12 & \frac{11}{9} & \frac{2}{1+X\alpha} \\ 4 & 20 & 12 & 20 & \frac{20}{9} & \frac{3+X\alpha}{1+X\alpha} \end{pmatrix}$$

```
(* cluster multiplicity factors for the $\alpha$/$\beta$-CIS problem *)
mcl$\alpha\beta$ = {1, 5, 3, 5, 1/2, 1/2};

$\mathcal{D}$0$\alpha\beta$[tK_?NumericQ] := $\mathcal{D}\alpha\beta$ /. X$\alpha$ -> xMax[1, tK];

formula[i_, $\mathcal{D}\alpha\beta$] := {cE$\alpha\beta$, a .$\mathcal{D}\alpha\beta$}[[All, i]]
formula[i_, $\mathcal{D}$0$\alpha\beta$[tK_]] := {cE$\alpha\beta$, a .$\mathcal{D}$0$\alpha\beta$[tK]}[[All, i]]

$\nu\alpha\beta$ = Transpose[NullSpace[$\mathcal{D}\alpha\beta$]];

MatrixForm[$\nu\alpha\beta$]
```

$$\begin{pmatrix} -\frac{-7+11\,X\alpha}{4\,(1+X\alpha)} & 0 & 5 & 2 \\ -\frac{1-X\alpha}{2\,(1+X\alpha)} & -\frac{1}{9} & -2 & -1 \\ 0 & 0 & 0 & 1 \\ 0 & 0 & 1 & 0 \\ 0 & 1 & 0 & 0 \\ 1 & 0 & 0 & 0 \end{pmatrix}$$

```
ν0αβ[tK_?(MemberQ[tKdomainαβ, #] &)] = ναβ /. Xα → xMax[1, tK];

rxn[i_, ναβ] := ναβ⟦All, i⟧.cEαβ
rxn[i_, νFunc_?((Dimensions[#] == {6, 4}) &)] := νFunc⟦All, i⟧.cEαβ
```

The initial composition will be set to slightly more than the lowest value solved for the single phase α–CIS model, with the β–CIS species populated and molecularity of the α–CIS phase set by a linear combination of the reactions in $\boldsymbol{\nu 0\alpha\beta}$ to the lowest value solved for the single phase α–CIS model. The subsequent solution of the Gibbs-Duhem equations will quantify the relaxation of this initial distribution to its two-phase equilibrium.

```
mxαβ[c_?VectorQ, 𝒟_] /; Length[c] == Dimensions[𝒟]⟦2⟧ := Take[𝒟, 3].c
```

$$\text{axαβ[c\_?VectorQ, 𝒟\_] /; Length[c] == Dimensions[𝒟]⟦2⟧} := \frac{\text{mxαβ[c, 𝒟]}}{\text{Plus @@ mxαβ[c, 𝒟]}}$$

$$\text{cXZαβ[c\_?VectorQ, 𝒟\_] /; Length[c] == Dimensions[𝒟]⟦2⟧} := \left\{\frac{\text{mxαβ[c, 𝒟]⟦1⟧}}{\text{mxαβ[c, 𝒟]⟦2⟧}}, \frac{2\,\text{mxαβ[c, 𝒟]⟦3⟧}}{\text{mxαβ[c, 𝒟]⟦1⟧} + 3\,\text{mxαβ[c, 𝒟]⟦2⟧}}\right\}$$

```
ξ00αβ = Array[KroneckerDelta[1, #] &, 4] − 30 Array[KroneckerDelta[2, #] &, 4] +
    Array[KroneckerDelta[3, #] &, 4] + Array[KroneckerDelta[4, #] &, 4]

  {1, −30, 1, 1}

c00αβ[tK_?(MemberQ[tKdomainαβ, #] &)] :=
 Module[{c00, x, normFac, xtnt}, With[{ν = ν0αβ[tK], 𝒟 = 𝒟0αβ[tK]},
   xtnt = x /. FindRoot[cXZαβ[partCIS[{0, 0, 0, 0, 1, 0} + x ν.ξ00αβ], partCIS[𝒟]]⟦
          1⟧ == Last[xRangeα] + 1*^-6, {x, {0, .01}}];
   c00 = {0, 0, 0, 0, 1, 1} ({0, 0, 0, 0, 1, 0} + xtnt ν.ξ00αβ); c00 = c00 + ν.ξ00αβ 1*^-45;
   normFac = 2/(mxαβ[c00, 𝒟]⟦2⟧ (1 + Last[xRangeα] + 1*^-6)); c00 = normFac c00]]
```

```
ξ0αβ = Take[ξ000, 4];
c0αβ[tK_?(MemberQ[tKdomainαβ, #] &)] := c00αβ[tK] + ν0αβ[tK].ξ0αβ;
```

The reference state chemical potentials of the species αCIS and αNDC are given by the solution function for the specific Gibbs energy of the α–CIS phase with the value of it's net molecularity X determined by the relative concentrations of each species, with each normalized by their binary mole fraction in the α phase to yield their partial molar free energies therein. The function cXZ$\alpha\beta$ and choice of basis normalization makes the implementation of this considerably simpler than in the preceding $Cu_{2-\delta}Se/\alpha$–$CuInSe_2$ equilibrium calculations. In this case the net molecularity is linear with their binary mole fractions, thus the normalization factors are both unity. Unlike the previous two-phase problem, each secondary phase species contributes to the configurational entropy of the lattice as a normal mixture component, a consequence of the coherence of the α and β lattices.

```
μαβ[c_, tK_?(MemberQ[tKdomainαβ, #] &)] /; Length[c] === Length[cEαβ] :=
  Module[{gα}, With[{n = (#/Plus @@ #) &[c mclαβ],
      Xα = cXZαβ[partCIS[c], partCIS[𝒟0αβ[tK]]][[1]], μclRef = μ00αβ[tK]},
    gα = g0α[Xα, 1, tK]; Join[Prepend[Drop[Drop[μclRef, -3], 22], First[μclRef]],
      {gα, gα}] + rG tK Log[n]]]

gd0αβ[tK_?(MemberQ[tKdomainαβ, #] &)] := (μαβ[c0αβ[#], #].ν0αβ[#]) &[tK]
```

gd0$\alpha\beta$[tMax$\alpha\beta$] /. Thread[$\xi 0\alpha\beta \to$ {0.00, 0.00, 0.00, 0.00}]
"initial total RMS convergence deviation" σSD[%]
c0$\alpha\beta$[tMax$\alpha\beta$] /. Thread[$\xi 0\alpha\beta \to$ {0.00, 0.00, 0.00, 0.00}];
Thread[{cE$\alpha\beta$, %}]
$\mathcal{D}$0$\alpha\beta$[tMax$\alpha\beta$];
{{"Xmixture", cXZ$\alpha\beta$[%%%, %][[1]]}, {"Xα", cXZ$\alpha\beta$[partCIS[%%%], partCIS[%]][[1]]},
 {"Xβ", cXZ$\alpha\beta$[part2ndΦ[%%%], part2ndΦ[%]][[1]]}}

{279803., 86033.6, -2.91331×10^{6}, -1.46809×10^{6}}
4.74724×10^{6} initial total RMS convergence deviation
{{CIS$_\beta$, 1.06666×10^{-44}}, {$(2\,\mathcal{V}_{\text{Cu}} \oplus \text{In}_{\text{Cu}})_{\beta 15}$, 5.27726×10^{-46}},
 {$(2\,\mathcal{V}_{\text{Cu}} \oplus \text{In}_{\text{Cu}})_{\beta 13}$, 1.63017×10^{-45}}, {$(2\,\mathcal{V}_{\text{Cu}} \oplus \text{In}_{\text{Cu}})_{\beta 25}$, 1.63017×10^{-45}},
 {αNDC, 0.97827}, {αCIS, 0.0217299}}
{{Xmixture, 0.642291}, {Xα, 0.642291}, {Xβ, 0.627045}}

gd0$\alpha\beta$[tMax$\alpha\beta$] /. $\xi\alpha\beta$[tMax$\alpha\beta$]
{"solution convergence σ_{SD}", σSD[%]}
c0$\alpha\beta$[tMax$\alpha\beta$] /. $\xi\alpha\beta$[tMax$\alpha\beta$];
Thread[{cE$\alpha\beta$, %}]
$\mathcal{D}$0$\alpha\beta$[tMax$\alpha\beta$];
{{"Xmixture", cXZ$\alpha\beta$[%%%, %][[1]]}, {"Xα", cXZ$\alpha\beta$[partCIS[%%%], partCIS[%]][[1]]},
 {"Xβ", cXZ$\alpha\beta$[part2ndΦ[%%%], part2ndΦ[%]][[1]]}}

{-1.74623×10^{-10}, -2.21189×10^{-9}, -4.37722×10^{-8}, -2.11876×10^{-8}}
{solution convergence σ_{SD}, 6.73463×10^{-8}}
{{CIS$_\beta$, 0.054151}, {$(2\,\mathcal{V}_{\text{Cu}} \oplus \text{In}_{\text{Cu}})_{\beta 15}$, 0.000064789},
 {$(2\,\mathcal{V}_{\text{Cu}} \oplus \text{In}_{\text{Cu}})_{\beta 13}$, 0.0632205}, {$(2\,\mathcal{V}_{\text{Cu}} \oplus \text{In}_{\text{Cu}})_{\beta 25}$, 0.0206685},
 {αNDC, 0.00341692}, {αCIS, 0.406248}}
{{Xmixture, 0.642291}, {Xα, 0.959035}, {Xβ, 0.476614}}

```
gd0αβ[tSTP] /. ξαβ[tSTP]
{"STP solution convergence σSD", σSD[%]}
c0αβ[tSTP] /. ξαβ[tSTP];
Thread[{cEαβ, %}]
𝒟0αβ[tSTP];
{{"Xmixture", cXZαβ[%%%, %][[1]]}, {"Xα", cXZαβ[partCIS[%%%], partCIS[%]][[1]]},
  {"Xβ", cXZαβ[part2ndΦ[%%%], part2ndΦ[%]][[1]]}}
```

$$\{1.16415 \times 10^{-10},\ 1.68802 \times 10^{-9},\ 1.08033 \times 10^{-7},\ 5.3551 \times 10^{-8}\}$$

$$\{\text{STP solution convergence } \sigma_{SD},\ 1.63389 \times 10^{-7}\}$$

$$\{\{\text{CIS}_{\beta},\ 0.0548707\},\ \{(2\,\mathcal{V}_{Cu} \oplus \text{In}_{Cu})_{\beta 15},\ 3.9438 \times 10^{-6}\},$$
$$\{(2\,\mathcal{V}_{Cu} \oplus \text{In}_{Cu})_{\beta 13},\ 0.105746\},\ \{(2\,\mathcal{V}_{Cu} \oplus \text{In}_{Cu})_{\beta 25},\ 0.00157752\},$$
$$\{\alpha\text{NDC},\ 1.48757 \times 10^{-6}\},\ \{\alpha\text{CIS},\ 0.348869\}\}$$

$$\{\{\text{Xmixture},\ 0.642291\},\ \{\text{X}\alpha,\ 0.999998\},\ \{\text{X}\beta,\ 0.498675\}\}$$

```
c0αβFit = Module[{cαβ}, cαβ = (c0αβ[#] /. ξαβ[#]) & /@ tKdomainαβ;
SplineFit[Thread[{tKdomainαβ, cαβ[[All, #]]}], Cubic] & /@ Range[Length[cEαβ]]];

cαβ[tK_?NumericQ] /; tSTP ≤ tK ≤ tMaxαβ :=
  With[{T = (Length[tKdomainαβ] − 1) (tK − tSTP)/(tMaxαβ − tSTP)},
    Through[(c0αβFit[[#]] & /@ Range[Length[cEαβ]])[T]][[All, 2]]]

xMin[1, tK_?NumericQ] /; tSTP ≤ tK ≤ tMaxαβ :=
  cXZαβ[partCIS[cαβ[tK]], partCIS[𝒟0αβ[tK]]][[1]]
xβMax[1, tK_?NumericQ] /; tSTP ≤ tK ≤ tMaxαβ :=
  cXZαβ[part2ndΦ[cαβ[tK]], part2ndΦ[𝒟0αβ[tK]]][[1]]
```

This completes the calculation of the α/β–CIS two-phase boundary locus on the pseudobinary section. Functions are defined next to facilitate the characterization of the of β–CIS in equilibrium with α–CIS at its upper molecularity limit. One provides the specific molar concentrations of the β–CIS model's component species, and the other provides the specific Gibbs energy of the β–CIS phase, both as functions of temperature.

cEβ = part2ndΦ[cE$\alpha\beta$]

$\{CIS_\beta, (2\mathcal{V}_{Cu} \oplus In_{Cu})_{\beta 15}, (2\mathcal{V}_{Cu} \oplus In_{Cu})_{\beta 13}, (2\mathcal{V}_{Cu} \oplus In_{Cu})_{\beta 25}\}$

$\mathcal{D}\beta$ = part2ndΦ[$\mathcal{D}\alpha\beta$];

mclβ = part2ndΦ[mcl$\alpha\beta$]

{1, 5, 3, 5}

c0β[tK_?NumericQ] /; tSTP ≤ tK ≤ tMax$\alpha\beta$:=

$$\text{With}\left[\{c\beta = \text{part2nd}\Phi[c\alpha\beta[tK]],\ x\beta = x\beta\text{Max}[1, tK]\},\ \frac{c\beta\,(3 + x\beta)}{(1 + x\beta)\,\text{mx}\alpha\beta[c\beta, \mathcal{D}\beta]\llbracket 3\rrbracket}\right]$$

Thread[{cEβ, c0β[tSTP]}]

$\{\{CIS_\beta, 0.08427\}, \{(2\mathcal{V}_{Cu} \oplus In_{Cu})_{\beta 15}, 6.05686 \times 10^{-6}\},$
$\{(2\mathcal{V}_{Cu} \oplus In_{Cu})_{\beta 13}, 0.162405\}, \{(2\mathcal{V}_{Cu} \oplus In_{Cu})_{\beta 25}, 0.00242275\}\}$

Thread[{cEβ, c0β[tMax$\alpha\beta$]}]

$\{\{CIS_\beta, 0.0917292\}, \{(2\mathcal{V}_{Cu} \oplus In_{Cu})_{\beta 15}, 0.000109749\},$
$\{(2\mathcal{V}_{Cu} \oplus In_{Cu})_{\beta 13}, 0.107092\}, \{(2\mathcal{V}_{Cu} \oplus In_{Cu})_{\beta 25}, 0.0350114\}\}$

gβ[1, tK_?NumericQ] /; tSTP ≤ tK ≤ tMax$\alpha\beta$:= c0β[tK]. part2ndΦ[$\mu\alpha\beta$[c0β[tK], tK]]

This completes the calculation of all phase equilibria on the pseudobinary section of the Cu–In–Se ternary phase field within the temperature and composition domain of this model.

LIST OF REFERENCES

1. Shay, J.L. and J.H. Wernick, *Ternary Chalcopyrite Semiconductors: Growth, Electronic Properties, and Applications*, Vol. 7, First ed. (Permagon Press, Oxford, England, 1975).

2. *Copper Indium Diselenide for Photovoltaic Applications*, edited by Coutts, T.J., L.L. Kazmerski, and S. Wagner (Elsevier Science Ltd., Amsterdam, 1986).

3. Neumann, H. and R.D. Tomlinson, Solar Cells **28,** 301 (1990).

4. Rockett, A. and R.W. Birkmire, Journal of Applied Physics **70,** 81 (1991).

5. Champness, C.H., Journal of Materials Science **10,** 605 (1999).

6. Rau, U. and H.W. Schock, Applied Physics A **69,** 131 (1999).

7. Hovel, H.J., *Solar Cells*, Vol. 11, First ed. (Academic Press, New York, NY, 1975).

8. Tsubomura, H. and H. Kobayashi, Critical Reviews in Solid State and Materials Sciences **18,** 261 (1993).

9. Green, M.A., *Solar Cells: Operating Principles, Technology, and System Applications* (University of New South Wales, Kensington, 1992).

10. *Solar Cells and their Applications*, edited by Partain, L.D. (John Wiley & Sons, Inc., New York, 1995).

11. Chopra, K.L. and S.R. Das, (Plenum Press, New York, 1983).

12. Schock, H.W., Applied Surface Science **92,** 606 (1995).

13. Benner, J.P. and L. Kazmerski, IEEE Spectrum **36**, 34 (1999).

14. Adams, W.G. and R.E. Day, Proceedings of the Royal Society A **25,** 113 (1877).

15. Parkes, J., R.D. Tomlinson, and M.J. Hampshire, Journal of Crystal Growth **20,** 315 (1973).

16. Rockett, A., F. Abou-Elfotouh, D. Albin, M. Bode, J. Ermer, R. Klenk, T. Lommasson, T.W.F. Russell, R.D. Tomlinson, J. Tuttle, L. Stolt, T. Walter, and T.M. Peterson, Thin Solid Films **237,** 1 (1994).

17. Feigelson, R.S. and R.K. Route, Optical Engineering **26,** 113 (1987).

18. Boehnke, U.C. and G. Kühn, Journal of Materials Science **22,** 1635 (1987).

19. Tomlinson, R.D., in *Ternary and Multinary Compounds, Proceedings of the 7th International Conference*, 1986 (Materials Research Society, Pittsburgh), p. 177.

20. Palatnik, L.S. and E.I. Rogacheva, Sov. Phys. Dokl. **12,** 503 (1967).

21. Koneshova, T.I., A.A. Babitsyna, and V.T. Kalinnikov, Izvestiya Akademii Nauk SSSR, Neorganicheskie Materialy **18,** 1483 (1982).

22. Fearheiley, M.L., Solar Cells **16,** 91 (1986).

23. Folmer, J.C.W., J.A. Turner, R. Noufi, and D. Cahen, Journal of the Electrochemical Society **132,** 1319 (1985).

24. Bachmann, K.J., M.I. Fearheily, Y.H. Shing, and N. Tran, Applied Physics Letters **44,** 407 (1984).

25. Hornung, M., *Ph.D. Thesis University of Freiburg* (Shaker–Verlag, Aachen, 1996).

26. Chang, C.H., A. Davydov, B.J. Stanbery, and T.J. Anderson, in *The Conference Record of the 25th IEEE Photovoltaic Specialists Conference*, 1996 (Institute of Electrical and Electronic Engineers, New York), p. 849.

27. Haalboom, T., T. Gödecke, F. Ernst, M. Rühle, R. Herbholz, H.W. Schock, C. Beilharz, and K.W. Benz, in *11th International Conference on Ternary and Multinary Compounds*, 1997 (Institute of Physics, London), p. 249.

28. Tomm, Y., S. Fiechter, and C. Fischer, in *Ternary and Multinary Compounds, Proceedings of the 11th International Conference*, 1997 (Institute of Physics, London), p. 181.

29. Palatnik, L.S. and I.K. Belova, Izvestiya Akademii Nauk SSSR, Neorganicheskie Materialy **12,** 2194 (1967).

30. Mikkelsen, J.C., Jr., Journal of Electronic Materials **10,** 541 (1981).

31. Binsma, J.J.M., L.J. Giling, and J. Bloem, Journal of Crystal Growth **50,** 429 (1980).

32. Verheijen, A.W., L.J. Giling, and J. Bloem, Materials Research Bulletin **14,** 237 (1979).

33. Migge, H. and J. Grzanna, J. Mater. Res. **9,** 125 (1994).

34. Abasova, A.Z., L.G. Gasanova, and A.G. Kyazym-zade, in *Ternary and Multinary Compounds, Proceedings of the 11th International Conference*, 1997 (Institute of Physics, London), p. 87.

35. Fiechter, S., K. Diesner, and Y. Tomm, in *Ternary and Multinary Compounds, Proceedings of the 11th International Conference*, 1997 (Institute of Physics, London), p. 27.

36. Grimm, H.G. and A. Sommerfield, Z. Phys. **36,** 439 (1926).

37. Zunger, A. and J.E. Jaffe, Physical Review Letters **51,** 662 (1983).

38. Spiess, H.W., U. Haeberlen, G. Brandt, A. Räuber, and J. Schneider, Physica Status Solidi (b) **62,** 183 (1974).

39. Chang, C.H., J.W. Johnson, B.J. Stanbery, T.J. Anderson, S.H. Wei, R.N. Battacharya, R. Duran, and G. Bunker, Journal of Applied Physics**,** submitted (2000).

40. Chang, C.-H., Dissertation, University of Florida, 1999.

41. Wei, S.-H., L.G. Ferreira, and A. Zunger, Physical Review B **45,** 2533–2536 (1992).

42. Swalin, R.A., *Thermodynamics of Solids*, 2nd ed. (John Wiley & Sons, New York, 1972).

43. Delgado, J.M., in *Ternary and Multinary Compounds, Proceedings of the 11th International Conference*, 1997 (Institute of Physics, London), p. 45.

44. Leicht, M., D. Stenkamp, H.P. Strunk, M. Hornung, C. Beilharz, and K.W. Benz, in *Ternary and Multinary Compounds, Proceedings of the 11th International Conference*, 1997 (Institute of Physics, London), p. 31.

45. Leicht, M., T. Remmelle, D. Stenkamp, and H.P. Strunk, Journal of Applied Crystallography **32,** 397 (1999).

46. Hönle, W., G. Kühn, and U.-C. Boehnke, Crystal Research and Technology **23,** 1347 (1988).

47. Schmid, D., M. Ruckh, F. Grunwald, and H.W. Schock, Journal of Applied Physics **73,** 2902 (1993).

48. Scheer, R. and H.-J. Lewerenz, Journal of Vacuum Science & Technology A **13,** 1924 (1995).

49. Schmid, D., M. Ruckh, and H.W. Schock, Applied Surface Science **103,** 409 (1996).

50. Herberholz, R., U. Rau, H.W. Schock, T. Haalboom, T. Goedecke, F. Ernst, C. Beilharz, K.W. Benz, and D. Cahen, EPJ Applied Physics **6,** 131 (1999).

51. Chang, C.H., S.H. Wei, S.P. Ahrenkiel, J.W. Johnson, B.J. Stanbery, T.J. Anderson, S.B. Zhang, M.M. Al-Jassim, G. Bunker, E.A. Payzant, and R. Duran, *II-VI Compound Semiconductor Photovoltaic Materials*, 2001 (Materials Research Society, Pittsburgh), in press.

52. Ashcroft, N.W. and N.D. Mermin, *Solid State Physics*, 1st ed. (Holt, Rinehart and Winston, New York, 1976).

53. Gödecke, T., T. Haalboom, and F. Sommer, Journal of Phase Equilibria **19,** 576 (1998).

54. Collongues, R., in *Ternary and Multinary Compounds, Proceedings of the 9th International Conference*, 1993 (Japanese Journal of Applied Physics), p. 442.

55. Bode, M.H., Journal of Applied Physics **76,** 159 (1994).

56. Kuan, T.S., T.F. Kuech, W.I. Wang, and E.L. Wilkie, Physical Review Letters **54,** 201 (1985).

57. Su, D.S., W. Neumann, R. Hunger, P. Schubert-Bischoff, M. Giersig, H.J. Lewerenz, R. Scheer, and E. Zeitler, Applied Physics Letters **73,** 785 (1998).

58. Fons, P., S. Niki, A. Yamada, D.J. Tweet, and H. Oyanagi, in *Ternary and Multinary Compounds, Proceedings of the 11th International Conference*, 1997 (Institute of Physics, London), p. 711.

59. Panchekha, P., B. Boyko, V. Novikov, and A. Chernikov, in *2nd World Conference on Photovoltaic Solar Energy Conversion*, 1998 (European Commission Joint Research Centre, Brussels), p. 485.

60. Horikoshi, Y., M. Kawashima, and Y. Yamahuchi, Japanese Journal of Applied Physics **25,** L868 (1986).

61. Stanbery, B.J., C.H. Chang, S. Kim, S. Kincal, G. Lippold, A.P. Ahrenkiel, L. Li, T.J. Anderson, and M.M. Al-Jassim, in *Self-Organized Processes in Semiconductor Alloys*, 1999 (Materials Research Society, Pittsburgh), p. 195.

62. Wei, S.-H., S.B. Zhang, and A. Zunger, Physical Review B **59,** R2478 (1999).

63. Groenink, A. and P.H. Janse, Zeitschrift für Physikalische Chemie Neue Folge **110,** 17 (1978).

64. Schmalzried, H., Progress in Solid State Chemistry **2,** 265 (1965).

65. Rincón, C. and S.M. Wasim, in *Ternary and Multinary Compounds, Proceedings of the 7th International Conference*, 1986 (Materials Research Society, Pittsburgh), p. 443.

66. Endo, S., T. Irie, and H. Nakanishi, Solar Cells **16,** 1 (1986).

67. Rincón, C. and C. Bellabarba, Physical Review B **33,** 7160 (1986).

68. Wasim, S.M., Solar Cells **16,** 289 (1986).

69. Flygare, W.H., *Molecular Structure and Dynamics*, 1st ed. (Prentice–Hall, Inc., Englewood Cliffs, NJ, 1978).

70. Zhang, S.B., S.-H. Wei, A. Zunger, and H. Katayama-Yoshida, Physical Review B **57,** 9642–9656 (1998).

71. Zhang, S.B., S.-H. Wei, and A. Zunger, Physical Review Letters **78,** 4059 (1997).

72. Rockett, A., Thin Solid Films **361-362,** 330 (2000).

73. Parthé, E., *Elements of Inorganic Structural Chemistry*, 2nd ed. (Sutter-Parthé, Petit-Lancy, Switzerland, 1996).

74. Migliorato, P., J.L. Shay, H.M. Kasper, and S. Wagner, Journal of Applied Physics **46,** 1777 (1975).

75. Niki, S., R. Suzuki, S. Ishibashi, T. Ohdaira, P.J. Fons, A. Yamada, and H. Oyanagi, in *Proceedings of the 2nd World Conference on Photovoltaic Solar Energy Conversion*, 1998 (European Commission Joint Research Centre, Brussels), p. 616.

76. Suzuki, R., T. Ohdaira, S. Ishibashi, A. Uedono, S. Niki, P.J. Fons, A. Yamada, T. Mikado, T. Yamazaki, and S. Tanigawa, in *Ternary and Multinary Compounds, Proceedings of the 11th International Conference*, 1997 (Institute of Physics, London), p. 757.

77. Suzuki, R., T. Ohdaira, S. Ishibashi, S. Niki, P.J. Fons, A. Yamada, T. Mikado, T. Yamazaki, A. Uedono, and S. Tanigawa, in *Proceedings of the 2nd World Conference on Photovoltaic Solar Energy Conversion*, 1998 (European Commission Joint Research Centre, Brussels), p. 620.

78. Wei, S.-H., S.B. Zhang, and A. Zunger, Journal of Applied Physics **85,** 7214 (1999).

79. van Vechten, J.A., in *Ternary and Multinary Compounds, Proceedings of the 7th International Conference*, 1986 (Materials Research Society, Pittsburgh), p. 423.

80. Parkes, J., R.D. Tomlinson, and M.J. Hampshire, Solid State Electronics **16,** 773 (1973).

81. Shay, J.L., B. Tell, M.K. Kasper, and L.M. Schiavone, Physical Review **7,** 4485 (1973).

82. Hörig, W., H. Neumann, and H. Sobotta, Thin Solid Films **48,** 67 (1978).

83. Rincón, C. and J. González, Physica Status Solidi (b) **118,** K21 (1983).

84. Kazmerski, L.L., F.R. White, and G.K. Morgan, Applied Physics Letters **29,** 268 (1976).

85. Nakanishi, H., S. Endo, T. Irie, and B.H. Chang, in *Ternary and Multinary Compounds, Proceedings of the 7th International Conference*, 1986 (Materials Research Society, Pittsburgh), p. 99.

86. Niki, S., H. Shibata, P.J. Fons, A. Yamada, A. Obara, Y. Makita, T. Kurafuji, S. Chichibu, and H. Nakanishi, Applied Physics Letters **67,** 1289 (1995).

87. Varshni, Y.P., Physica **34,** 149 (1967).

88. Yu, P.W., Journal of Applied Physics **47,** 677 (1976).

89. Lárez, C., C. Bellabarba, and C. Rincon, Applied Physics Letters **65,** 1650 (1994).

90. Manoogian, A. and J.C. Woolley, Canadian Journal of Physics **62,** 285 (1983).

91. Rincón, C., Physica Status Solidi (a) **134,** 383 (1992).

92. Abou-Elfotouh, F.A., H. Moutinho, A. Bakry, T.J. Coutts, and L.L. Kazmerski, Solar Cells **30,** 151 (1991).

93. Bottomley, D.J., A. Mito, S. Niki, and A. Yamada, Applied Physics Letters **82,** 817 (1997).

94. Xiao, H.Z., L.-C. Yang, and A. Rockett, Journal of Applied Physics **76,** 1503 (1994).

95. Wasim, S.M., G. Marin, C. Rincón, P. Bocaranda, C. Mazón, S.G. Pérez, A.E. Mora, M. Iqbal, and G. Bacquet, in *Ternary and Multinary Compounds, Proceedings of the 11th International Conference*, 1997 (Institute of Physics, London), p. 55.

96. Pankove, J.I., *Optical Processes in Semiconductors* (Dover Publications, Inc., New York, 1971).

97. Urbach, F., Physical Review **92,** 1324 (1953).

98. Redfield, D., Physical Review **130,** 916 (1963).

99. Redfield, D. and M.A. Afromowitz, Applied Physics Letters **11,** 138 (1967).

100. Mahan, G.D. and J.W. Conley, Applied Physics Letters **11,** 29 (1967).

101. Nakanishi, H., T. Sawaya, S. Endo, and T. Irie, Japanese Journal of Applied Physics **32–3,** 200 (1993).

102. Dow, J.D. and D. Redfield, Physical Review B **5,** 594 (1972).

103. Kurkik, M.V., Physica Status Solidi (a) **8,** 9 (1971).

104. Medvedkin, G.A. and M.A. Magomedov, Journal of Applied Physics **82,** 4013 (1997).

105. Ikari, T., K. Yoshino, T. Shimizu, A. Fukuyama, K. Maeda, P.J. Fons, A. Yamada, and S. Niki, in *Ternary and Multinary Compounds, Proceedings of the 11th International Conference*, 1997 (Institute of Physics, London), p. 511.

106. Boyd, G.D., H.M. Kasper, J.H. McFee, and F.G. Storz, IEEE Journal of Quantum Electronics **QE8,** 900 (1972).

107. Angelov, M., R. Goldhahn, G. Gobsch, M. Kanis, and S. Fiechter, Journal of Applied Physics **75,** 5361 (1994).

108. Hsu, T.M., H.Y. Chang, H.L. Hwang, and S.Y. Lee, in *Ternary and Multinary Compounds, Proceedings of the 7th International Conference*, 1986 (Materials Research Society, Pittsburgh), p. 93.

109. Hsu, T.M., Journal of Applied Physics **59,** 2538 (1986).

110. Binsma, J.J.M., L.J. Giling, and J. Bloem, Journal of Luminescence **27,** 55 (1982).

111. Hsu, T.M., J.S. Lee, and H.L. Hwang, Journal of Applied Physics **68,** 283 (1990).

112. Boyd, G.D., H.M. Kasper, and J.H. McFee, IEEE Journal of Quantum Electronics **QE7,** 563 (1971).

113. Beilharz, C., *Charakterisierung von aus der Schmelze gezüchteten Kristallen in den Systemen Kupfer–Indium–Selen und Kupfer-Indium–Gallium–Selen für photovoltaische Anwendungen* (Shaker Verlag, Aachen, 1999).

114. Herberholz, R., V. Nadenau, U. Ruhle, C. Koble, H.W. Schock, and B. Dimmler, Solar Energy Materials and Solar Cells **49,** 227 (1997).

115. Shafarman, W.N., R. Klenk, and B.E. McCandless, Journal of Applied Physics **79,** 7324 (1996).

116. Wei, S.-H., S.B. Zhang, and A. Zunger, Applied Physics Letters **72,** 3199 (1998).

117. Schroeder, D.J., J.L. Hernandez, G.D. Berry, and A.A. Rockett, Journal of Applied Physics **83,** 1519 (1998).

118. Chen, A.-B. and A. Sher, *Semiconductor Alloys: Physics and Materials Engineering* (Plenum Press, New York, 1995).

119. Albin, D.S., J.R. Tuttle, G.D. Mooney, J.J. Carapella, A. Duda, A. Mason, and R. Noufi, in *The Conference Record of the 21st IEEE Photovoltaic Specialists Conference*, 1990 (Institute of Electrical and Electronic Engineers, New York), p. 562.

120. Chen, W.S., J.M. Stewart, B.J. Stanbery, W.E. Devany, and R.A. Mickelsen, in *The Conference Record of the 19th IEEE Photovoltaic Specialists Conference*, 1987 (Institute of Electrical and Electronic Engineers, New York), p. 1445.

121. Ciszek, T.F., R. Bacewicz, J.R. Durrant, S.K. Deb, and D. Dunlavy, in *The Conference Record of the 19th IEEE Photovoltaic Specialists Conference*, 1987 (Institute of Electrical and Electronic Engineers, New York), p. 1448.

122. Bodnar, I.V., A.P. Bologa, and B.V. Korzun, Physica Status Solidi (b) **109,** K31 (1982).

123. Bodnar, I.V., B.V. Korzun, and A.J. Lakomskii, Physica Status Solidi (b) **105,** K143 (1981).

124. Miyake, H., M. Tsuda, and K. Sugiyama, in *Ternary and Multinary Compounds, Proceedings of the 11th International Conference*, 1997 (Institute of Physics, London), p. 83.

125. Neff, H., P. Lange, M.L. Fearheiley, and K.J. Bachmann, Applied Physics Letters **47,** 1089 (1985).

126. Shirakata, S., A. Ogawa, S. Isomura, and T. Kariya, in *Ternary and Multinary Compounds, Proceedings of the 9th International Conference*, 1993 (Japanese Journal of Applied Physics), p. 94.

127. Antonioli, G., S. Bini, P.P. Lottici, C. Razzetti, and G. Vlaic, in *Ternary and Multinary Compounds, Proceedings of the 7th International Conference*, 1986 (Materials Research Society, Pittsburgh), p. 149.

128. Hedström, J., H. Ohlsén, M. Bodegård, A. Kylner, L. Stolt, D. Hariskos, M. Ruckh, and H.-W. Schock, in *The Conference Record of the 23rd IEEE Photovoltaic Specialists Conference*, 1993 (Institute of Electrical and Electronic Engineers, New York), p. 364.

129. Rockett, A., K. Granath, S. Asher, M.M.A. Jassim, F. Hasoon, R. Matson, B. Basol, V. Kapur, J.S. Britt, T. Gillespie, and C. Marshall, Solar Energy Materials and Solar Cells **59,** 255 (1999).

130. Probst, V., J. Rimmasch, W. Riedl, W. Stetter, J. Holz, H. Harms, F. Karg, and H.W. Schock, in *1st World Conference on Photovoltaic Energy Conversion*, 1994 (Institute of Electrical and Electronic Engineers, New York), p. 144.

131. Bodegård, M., J. Hedström, K. Granath, A. Rockett, and L. Stolt, in *Proceedings of the 13th European Photovoltaic Solar Energy Conference*, 1995 (H.S. Stephens & Associates, Bedford), p. 2080.

132. Granath, K., M. Bodegård, and L. Stolt, Solar Energy Materials and Solar Cells **60,** 279 (1999).

133. Rau, U., M. Schmitt, D. Hilburger, F. Engelhardt, O. Seifert, and J. Parisi, in *The Conference Record of the 25th IEEE Photovoltaic Specialists Conference*, 1996 (Institute of Electrical and Electronic Engineers, New York), p. 1005.

134. Granata, J.E., J.R. Sites, S. Asher, and R.J. Matson, in *Conference Record of the 26th IEEE Photovoltaic Specialists Conference*, 1997 (Institute of Electrical and Electronic Engineers, New York), p. 387.

135. Granata, J.E. and J.R. Sites, in *2nd World Conference on Photovoltaic Solar Energy Conversion*, 1998 (European Commission Joint Research Centre, Brussels), p. 604.

136. Rau, U., M. Schmitt, F. Engelhardt, O. Seifert, J. Parisi, W. Riedl, J. Rimmasch, and F. Karg, Solid State Communications **107,** 59 (1998).

137. Niles, D.W., K. Ramanathan, F. Hasoon, R. Noufi, B.J. Tielsch, and J.E. Fulghum, Journal of Vacuum Science & Technology A **15,** 3044 (1997).

138. Rockett, A., M. Bodegård, K. Granath, and L. Stolt, in *The Conference Record of the 25th IEEE Photovoltaic Specialists Conference*, 1996 (Institute of Electrical and Electronic Engineers, New York), p. 985.

139. Niles, D.W., M. Al-Jassim, and K. Ramanathan, Journal of Vacuum Science & Technology A **17,** 291 (1999).

140. Holz, J., F. Karg, and H. von Philipsborn, in *Proceedings of the 12th European Photovoltaic Solar Energy Conference*, 1994 (H.S. Stephens & Associates, Bedford), p. 1592.

141. Keyes, B.M., F. Hasoon, P. Dippo, A. Balcioglu, and F. Abufotuh, in *Conference Record of the 26th IEEE Photovoltaic Specialists Conference*, 1997 (Institute of Electrical and Electronic Engineers, New York), p. 479.

142. Schroeder, D.J. and A.A. Rockett, Journal of Applied Physics **82,** 4982 (1997).

143. Bodegård, M., L. Stolt, and J. Hedström, in *Proceedings of the 12th European Photovoltaic Solar Energy Conference*, 1994 (H.S. Stephens & Associates, Bedford), p. 1743.

144. Basol, B.M., V.K. Kapur, C.R. Leidholm, A. Minnick, and A. Halani, in *The 1st World Conference on Photovoltaic Energy Conversion*, 1994 (Institute of Electrical and Electronic Engineers, New York), p. 147.

145. Nakada, T., H. Ohbo, M. Fukuda, and A. Kunioka, Solar Energy Materials and Solar Cells **49,** 261 (1997).

146. Ruckh, M., D. Schmid, M. Kaiser, R. Schäffler, T. Walter, and H.W. Schock, in *Proceedings of the 1st World Conference on Photovoltaic Energy Conversion*, 1994 (Institute of Electrical and Electronic Engineers, New York), p. 156.

147. Contreras, M.A., B. Egaas, P. Dippo, J. Webb, J.E. Granata, K. Ramanathan, S. Asher, A. Swartzlander, and R. Noufi, in *Conference Record of the 26th IEEE Photovoltaic Specialists Conference*, 1997 (Institute of Electrical and Electronic Engineers, New York), p. 359.

148. Stanbery, B.J., C.H. Chang, and T.J. Anderson, in *Ternary and Multinary Compounds, Proceedings of the 11th International Conference*, 1997 (Institute of Physics, London), p. 915.

149. Stanbery, B.J., A. Davydov, C.H. Chang, and T.J. Anderson, in *NREL/SNL Photovoltaics Program Review, Proceedings of the 14th Conference*, 1996 (American Institute of Physics, New York), p. 579.

150. Stanbery, B.J., E.S. Lambers, and T.J. Anderson, in *Conference Record of the 26th IEEE Photovoltaic Specialists Conference*, 1997 (Institute of Electrical and Electronic Engineers, New York), p. 499.

151. Stanbery, B.J., S. Kincal, S. Kim, T.J. Anderson, O.D. Crisalle, S.P. Ahrenkiel, and G. Lippold, in *Conference Record of the 28th IEEE Photovoltaic Specialists Conference*, 2000 (Institute of Electrical and Electronic Engineers, New York).

152. Klein, A., T. Loher, C. Pettenkofer, and W. Jaegermann, Journal of Applied Physics **80,** 5039 (1996).

153. Kronik, L., D. Cahen, and H.W. Schock, Adv. Mater. **10,** 31 (1998).

154. Kronik, L., D. Cahen, U. Rau, R. Herberholz, and H.W. Schock, in *Proceedings of the 2nd World Conference on Photovoltaic Solar Energy Conversion*, 1998 (European Commission Joint Research Centre, Brussels), p. 453.

155. Braunger, D., D. Hariskos, G. Bilger, U. Rau, and H.W. Schock, Thin Solid Films **361-362,** 161 (2000).

156. Jaffe, J.E. and A. Zunger, Physical Review B **28** (1983).

157. Kröger, F.A., *The Chemistry of Imperfect Crystals*, Vol. 2: Imperfection Chemistry of Crystalline Solids, 2nd revised ed. (North-Holland Publishing Co., Amsterdam, 1973).

158. Modell, M. and R.C. Reid, *Thermodynamics and Its Applications*, second ed. (Prentice–Hall, Inc., Englewood Cliffs, New Jersey, 1983).

159. Hill, T.L., *An Introduction to Statistical Thermodynamics*, 2nd ed. (Addison-Wesley Publishing Company, Reading, MA, 1962).

160. Chakrabarti, D.J. and D.E. Laughlin, Bulletin of Alloy Phase Diagrams **2,** 305 (1981).

161. Dinsdale, A.T., CALPHAD **15,** 317 (1991).

162. Hornung, M., K.W. Benz, L. Margulis, D. Schmid, and H.W. Schock, Journal of Crystal Growth **154,** 315–321 (1995).

163. Chang, C.H., A. Davydov, B.J. Stanbery, and T.J. Anderson, unpublished.

164. Barin, I., *Thermochemical Data of Pure Substances* (VCH, Weinheim, 1993).

165. Guggenheim, E.A., *Mixtures* (Oxford University Press, Oxford, 1952).

166. Bethe, H., Proceedings of the Royal Society A **150,** 552 (1935).

167. Schottky, W., Halbleiter Probleme **4,** 235 (1959).

168. van Vechten, J.A., *Handbook of Semiconductors*, Vol. 3 (North Holland, Amsterdam, 1980).

169. van Vechten, J.A., Journal of the Electrochemical Society **122,** 423 (1975).

170. Libowitz, G.G. and J.B. Lightstone, Journal of the Physics and Chemistry of Solids **28,** 1145 (1967).

171. Sha, Y.G. and R.F. Brebrick, Journal of Electronic Materials **18,** 421 (1989).

172. Borgoin, J.C. and J.W. Corbett, *Point Defects in Solids* (Plenum Press, London, 1975).

173. Pankajavalli, R., M. Ider, B.J. Stanbery, and T.J. Anderson, Journal of Materials Science (in preparation for submission).

174. Bachmann, K.J., F.S.L. Hsu, F.A. Thiel, and H.M. Kasper, Journal of Electronic Materials **6,** 431 (1977).

175. Neumann, H., G. Kühn, and W. Möller, Physica Status Solidi (b) **144,** 565 (1987).

176. Zhuang, W., C.-H. Chang, and T.J. Anderson, CALPHAD**,** submitted (2001).

177. Mickelsen, R.A. and W.S. Chen, in *The Conference Record of the 15th IEEE Photovoltaic Specialists Conference*, 1981 (Institute of Electrical and Electronic Engineers, New York), p. 800.

178. Schumann, B., G. Kühn, U. Boehnke, and H. Neels, Soviet Physical Crystallography **26,** 678 (1981).

179. Herman, M.A. and H. Sitter, *Molecular Beam Epitaxy: Fundamentals and Current Status*, Vol. 7 (Springer–Verlag, Berlin, 1989).

180. Weir, B.E., B.S. Freer, R.L. Headrick, and D.J. Eaglesham, Applied Physics Letters **59,** 204 (1991).

181. Barker, J.A. and D.J. Auerbach, Surface Science Reports **4,** 1 (1984).

182. Taylor, J.B. and I. Langmuir, Physical Review **44,** 423 (1933).

183. D'Evelyn, M.P. and R.J. Madix, Surface Science Reports **3,** 413 (1983).

184. Kim, S.K. and H.H. Lee, Journal of Crystal Growth **151,** 200 (1994).

185. Kim, S.K. and H.H. Lee, Journal of Applied Physics **78,** 3809 (1995).

186. Suntola, T. and M.J. Antson, U.S. Patent No. 4,058,430 (1977).

187. Goodman, C.H.L. and M.V. Pessa, Journal of Applied Physics **60,** R65 (1986).

188. Cho, A.Y. and J.R. Arthur, Progress in Solid-State Chemistry **10**, 157 (1975).

189. Zhu, Z., T. Nomura, M. Miyao, and M. Hagino, in *Workbook of the Fifth International Conference on Molecular Beam Epitaxy*, 1988 (Tokyo Institute of Technology, Tokyo), p. 290.

190. Künzel, H. and K. Ploog, Applied Physics Letters **37,** 416 (1980).

191. Cammack, D.A., K. Shahzad, and T. Marshall, Applied Physics Letters **56,** 845 (1990).

192. Cheng, H., J.M. DePuydt, M. Haase, and J.E. Potts, Applied Physics Letters **56,** 848 (1990).

193. Takenaka, K., T. Hariu, and Y. Shibata, Japanese Journal of Applied Physics **19-2,** 183 (1980).

194. Pande, K.P. and A.C. Seabaugh, Journal of the Electrochemical Society **131,** 1357 (1984).

195. Kunitsugu, Y., I. Suemune, Y. Tanaka, Y. Kan, and M. Yamanishi, in *Workbook of the Fifth International Conference on Molecular Beam Epitaxy*, 1988 (Tokyo Institute of Technology, Tokyo), p. 134.

196. Sato, H., O. Osada, K. Matsushita, T. Hariu, and Y. Shibata, Vacuum **36,** 133 (1986).

197. Oda, S., R. Kawase, T. Sato, I. Shimizu, and H. Kokado, Applied Physics Letters **48,** 33 (1986).

198. Matsushita, K., T. Hariu, S.F. Fang, K. Shida, and Q.Z. Gao, in *Materials for Infrared Detectors and Sources*, 1986 (Materials Research Society, Pittsburgh), p. 479.

199. Lu, P.-Y., L.M. Williams, C.-H. Wang, S.N.G. Chu, and M.H. Ross, in *Epitaxy of Semiconductor Layered Structures*, 1987 (Materials Research Society, Pittsburgh), p. 77.

200. Zembutsu, S. and T. Sasaki, Applied Physics Letters **48,** 870 (1986).

201. Shiosaki, T., T. Yamamoto, M. Yagi, and A. Kawabata, Applied Physics Letters **39,** 399 (1981).

202. Farrow, R.F.C., P.W. Sullivan, G.M. Williams, and C.R. Stanley, in *Collected Papers of MBE-CST-2*, 1982 (Tokyo Institute of Technology, Tokyo), p. 169.

203. Foxon, C.T., M.R. Boudry, and B.A. Joyce, Surface Science **44,** 69 (1974).

204. Fujisaki, H., J.B. Westmore, and A.W. Tickner, Canadian Journal of Chemistry **44,** 3063 (1966).

205. Foxon, C.T., B.A. Joyce, R.F.C. Farrow, and R.M. Griffiths, Journal of Physics D: Applied Physics **7,** 2422 (1974).

206. Berkowitz, J. and W.A. Chupka, Journal of Chemical Physics **45,** 4289 (1966).

207. Simon, W., International Journal of Mass Spectrometry and Ion Physics **12,** 159 (1973).

208. Hobson, W.S., in *Advanced III-V Compound Semiconductor Growth, Processing and Devices*, 1991 (Materials Research Society, Pittsburgh), p. 45.

209. Giapis, K.P., L. Da-Cheng, and K.F. Jensen, in *Chemical Perspectives of Microelectronic Materials*, 1988 (Materials Research Society, Pittsburgh), p. 63.

210. Sato, Y., K. Matsushita, T. Hariu, and Y. Shibata, Applied Physics Letters **44,** 592 (1984).

211. Lu, Z.H., T.K. Sham, and P.R. Norton, Applied Physics Letters **57,** 37 (1990).

212. Kondo, N. and M. Kawashima, in *International Symposium on GaAs and Related Compounds*, 1985 (Adam Hilger, Ltd., London), p. 97.

213. Omstead, T.R., A.V. Annapragada, and K.F. Jensen, Applied Physics Letters **57,** 2543 (1990).

214. Chen, F.F., *Introduction to Plasma Physics and Controlled Fusion*, Vol. 1, 2nd ed. (Plenum Press, New York, 1984).

215. Matsuoka, M. and K.I. Ono, Journal of Vacuum Science & Technology A **6,** 25 (1988).

216. Lisitano, G., M. Fontanesi, and E. Sindoni, Applied Physics Letters **16,** 122 (1970).

217. Agdur, B. and B. Enander, Journal of Applied Physics **33,** 575 (1961).

218. Kraus, J.D., in *Antennas*, 2nd ed. (McGraw-Hill Book Company, New York, 1988).

219. Diehl, R., D.M. Wheatley, and T.G. Castner, Review of Scientific Instruments **67,** 3904 (1996).

220. Macalpine, W.W. and R.O. Schildknecht, Proceedings of the IRE**,** 2099 (1959).

221. Kraus, J.D., IEEE Transactions on Antennas and Propagation **AP-25,** 913 (1977).

222. Collin, R.E., *Foundations for Microwave Engineering* (McGraw-Hill Book Company, New York, 1966).

223. Welton, R.F., E.W. Thomas, R.K. Feeney, and T.F. Moran, Measurement Science and Technology **2,** 242 (1991).

224. Summers, R.L., "Ionization Gauge Sensitivities as Reported in the Literature," Report No. TND 5285 (National Aeronautic and Space Administration, Washington, D.C.).

225. Brown, S.C., *Basic Data of Plasma Physics* (American Institute of Physics Press, New York, 1994).

226. Heald, M.A. and C.B. Wharton, *Plasma Diagnostics with Microwaves* (John Wiley & Sons Inc., New York, 1965).

227. Chatillon, C. and J.-Y. Emery, Journal of Crystal Growth **129,** 312 (1993).

228. Heckingbottom, R., in *Molecular Beam Epitaxy and Heterostructures*; *Vol. 87*, edited by L.L. Chang and K. Ploog (Martinus Nijhoff Publishers, Dordrecht, 1985), p. 71.

229. Shen, J. and C. Chatillon, Journal of Crystal Growth **106,** 553 (1990).

230. Theis, W. and R.M. Tromp, Physical Review Letters **76,** 2770 (1996).

231. Karg, F., V. Probst, H. Harms, J. Rimmasch, W. Riedl, J. Kotschy, J. Holz, R. Treichler, O. Eibl, A. Mitwalsky, and A. Kiendl, in *The Conference Record of the 23rd IEEE Photovoltaic Specialists Conference*, 1993 (Institute of Electrical and Electronic Engineers, New York), p. 441.

232. Tuttle, J.R., M. Contreras, A. Tennant, D. Albin, and R. Noufi, in *The Conference Record of the 23rd IEEE Photovoltaic Specialists Conference*, 1993 (Institute of Electrical and Electronic Engineers, New York), p. 415.

233. Wolf, D. and G. Muller, Thin Solid Films **361-362,** 155 (2000).

234. Chang, C.-H., B.J. Stanbery, A.A. Morrone, A. Davydov, and T.J. Anderson, in *Thin-Film Structures for Photovoltaics*, 1997 (Materials Research Society, Pittsburgh), p. 163.

235. Basol, B.M., Japanese Journal of Applied Physics **32–3,** 35 (1993).

236. Gabor, A.M., J.R. Tuttle, M. Contreras, D.S. Albin, A. Franz, D.W. Niles, and R. Noufi, in *Proceedings of the 12th European Photovoltaic Solar Energy Conference*, 1994 (H.S. Stephens & Associates, Bedford), p. 939.

237. Walter, T. and H.W. Schock, Japanese Journal of Applied Physics **32–3,** 116 (1993).

238. Contreras, M.A., B. Egaas, D. King, A. Swartzlander, and T. Dullweber, Thin Solid Films **361-362** (2000).

239. Contreras, M.A., B. Egaas, K. Ramanathan, J. Hiltner, A. Swartzlander, F. Hasoon, and R. Noufi, Progress in Photovoltaics **7,** 311 (1999).

240. Li, S.S., B.J. Stanbery, C.H. Huang, C.H. Chang, T.J. Anderson, and Y.S. Chang, in *The Conference Record of the 25th IEEE Photovoltaic Specialists Conference*, 1996 (Institute of Electrical and Electronic Engineers, New York), p. 821.

241. Huang, C.H., S.S. Li, B.J. Stanbery, C.H. Chang, and T.J. Anderson, in *Conference Record of the 26th IEEE Photovoltaic Specialists Conference*, 1997 (Institute of Electrical and Electronic Engineers, New York), p. 407.

242. Kincal, S. and O.D. Crisalle, in *Proceedings of the American Control Conference*, 2000 (American Institute of Chemical Engineers, New York), p. 4401.

243. Lippold, G., A. Eifler, M.V. Yakushev, R.D. Tomlinson, R. Klenk, H.W. Schock, and W. Grill, in *Ternary and Multinary Compounds, Proceedings of the 11th International Conference*, 1997 (Institute of Physics, London), p. 697.

244. Niki, S., Y. Makita, A. Yamada, A. Obara, S. Misawa, O. Igarashi, K. Aoki, and N. Kutsuwada, Japanese Journal of Applied Physics **32–3,** 161 (1993).

245. Dittrich, H., R. Menner, and H.W. Schock, in *The Conference Record of the 21st IEEE Photovoltaic Specialists Conference*, 1990 (Institute of Electrical and Electronic Engineers, New York), p. 787.

246. Hunger, R., M. Wilhelm, K. Diesner, J. Bruns, G. Lippold, K. Hinrichs, N. Esser, H.J. Lewerenz, and R. Scheer, in *2nd World Conference and Exhibition on Photovoltaic Solar Energy Conversion*, 1998 (European Commission Joint Research Centre, Brussels), p. 541.

247. Fons, P., S. Niki, A. Yamanda, and H. Oyanagi, Journal of Applied Physics **84,** 6926 (1998).

248. Christiansen, S., M. Albrecht, J. Michler, and H.P. Strunk, Physica Status Solidi (a) **156,** 129 (1996).

249. Albrecht, M., S. Christinsen, J. Michler, H.P. Strunk, P.O. Hansson, and E. Bauser, Journal of Crystal Growth **167,** 24 (1996).

250. Christiansen, S.H., H.P. Strunk, H. Wawra, M. Becker, and M. Albrecht, Solid State Phenomena **69,** 93 (1999).

251. Dorsch, W., B. Steiner, M. Albrecht, H.P. Strunk, H. Wawra, and G. Wagner, Journal of Crystal Growth **183,** 305 (1998).

252. Strunk, H.P., M. Albrecht, S. Christiansen, W. Dorsch, U. Hormann, B. Jahnen, and T. Remmele, Physica Status Solidi (a) **171,** 215 (1999).

253. Ehrlich, G. and F.G. Hudda, Journal of Chemical Physics **44,** 1030 (1966).

254. Schwoebel, R.L. and E.J. Shipsey, Journal of Applied Physics **37,** 3682 (1966).

255. Kajikawa, Y., M. Hata, T. Isu, and Y. Katayama, Surface Science **265,** 241 (1992).

256. Villian, J., Journal of Physics I **1,** 19 (1991).

257. Orme, C., M.D. Johnson, J.L. Sudijono, K.T. Leung, and B.G. Orr, Applied Physics Letters **64,** 860 (1993).

258. Heim, K.R., S.T. Coyle, G.G. Hembree, J.A. Venables, and M.R. Scheinfein, Journal of Applied Physics **80,** 1161 (1996).

259. Venables, J.A., Physica A **239,** 35 (1997).

260. Bartelt, N.C., R.M. Tromp, and E.D. Williams, Physical Review Letters **73,** 1656 (1994).

261. Theis, W., N.C. Bartelt, and R.M. Tromp, Physical Review Letters **75,** 3328 (1995).

262. Nelson, A.J., M. Bode, G. Horner, K. Sinha, and J. Moreland, Mat. Res. Soc.Symp.Proc. **340,** 599 (1994).

263. Tiwari, A.N., S. Blunier, M. Filzmoser, H. Zogg, D. Schmid, and H.W. Schock, Applied Physics Letters **65,** 3347 (1994).

264. Yakushev, M.V., G. Lippold, A.E. Hill, R.D. Pilkington, and R.D. Tomlinson, Crystal Research and Technology **31,** 357 (1996).

265. Contreras, M.A., B. Egaas, P. Dippo, J. Webb, S. Asher, A. Swartzlander, K. Ramanathan, F.S. Hasoon, and R. Noufi, in *Ternary and Multinary Compounds, Proceedings of the 11th International Conference*, 1997 (Institute of Physics, London), p. 333.

266. Tromp, R.M. and M.C. Reuter, Physical Review Letters **68,** 954 (1992).

267. Copel, M., M.C. Reuter, E. Kaxiras, and R.M. Tromp, Physical Review Letters **63,** 632 (1989).

268. Stringfellow, G.B., R.T. Lee, C.M. Fetzer, J.K. Shurtleff, Y. Hsu, S.W. Jun, S. Lee, and T.Y. Seong, Journal of Electronic Materials **29,** 134 (2000).

269. Vegt, H.A.v.d., M. Breeman, S. Gerrer, V.H. Etgens, X. Torrelles, P. Fajardo, and E. Vlieg, Physical Review B **51,** 14806 (1995).

270. Dirnstorfer, I., M. Wagner, D.M. Hofmann, M.D. Lampert, F. Karg, and B.K. Meyer, Physica Status Solidi (a) **168,** 163 (1998).

271. Stanbery, B.J., U.S. Patent No. 5,261,969 (1993).

272. Kahn, A., Surface Science Reports **3,** 193 (1983).

273. Hoegen, M.H.-v., F.K. LeGoues, M. Copel, M.C. Reuter, and R.M. Tromp, Physical Review Letters **67,** 1130 (1991).

274. de Vries, S.A., W.J. Huisman, P. Goedtkint, M.F. Zwanenburg, S.L. Bennett, and E. Vlieg, Physical Review Letters **81,** 381 (1998).

275. Cullity, B.D., *Elements of X-Ray Diffraction*, 3rd ed. (Addison-Wesley Publishing Co., Reading, MA, 1956).

276. Hanada, T., A. Yamana, Y. Nakamura, O. Nittono, and T. Wada, in *9th International Photovoltaic Science and Engineering Conference*, 1996, p. 595.

277. Gödecke, T., T. Haalboom, and F. Ernst, (unpublished, 1998). Cited in Beilharz, C.; *Charakterisierung von aus der Schmelze gezüchteten Kristallen in den Systemen Kupfer–Indium–Selen und Kupfer-Indium–Gallium–Selen für photovoltaische Anwendungen*, (Shaker Verlag, Aachen, 1999).

278. Franklin, A.D., in *Point Defects in Solids*; *Vol. 1*, edited by J.H. Crawford, Jr. and L.M. Slifkin (Plenum Press, New York, 1972), p. 4-80.

279. Hagemark, cited by A. D. Franklin, in *Point Defects in Solids*; *Vol. 1*, edited by J. H. Crawford, Jr. and L. M. Slifkin (Plenum Press, New York, 1972), p. 4-80.

280. Thurmond, C.D., Journal of the Electrochemical Society **122,** 1133 (1975).

281. Kubo, R., *Statistical Mechanics*, 1st ed. (North-Holland Publishing Company, Amsterdam, 1965).

BIOGRAPHICAL SKETCH

Billy Jack Stanbery was born in Nacogdoches, Texas, on December 26th, 1952, to Martha Mae Stanbery (*neé* Ellis, from Huntington, Texas) while his father, Billy Mack Stanberry (from Canton, Texas), was attending the United States Army Officer Candidate School in California. He attended twelve different schools during his elementary and secondary education, graduating in 1970 from Wagner High School, Clark Air Base, Philippines. During his final year of high school, he was elected to the National Honor Society and was a National Merit Scholarship Semifinalist, receiving an Associate National Merit Scholarship to attend college.

He was nominated to the honorary academic societies Sigma Pi Sigma (physics), Pi Mu Epsilon (mathematics), and Phi Beta Kappa while attending undergraduate school. He received two coterminal undergraduate diplomas, a Bachelor of Science with Honors in mathematics and Bachelor of Science with High Honors in physics from the University of Texas at Austin in 1977, whereupon he accepted a teaching assistanceship in physics at the University of Washington in Seattle. He began research in the field of photovoltaics in 1978 upon accepting a summer job with The Boeing Company, where he remained a full-time employee for one year before returning to graduate school.

His master's research, under Professor Martin P. Gouterman of the Department of Chemistry, involved the study of photovoltaic devices fabricated in ultra-high vacuum from organic semiconductor films using compounds from the porphyrin family. He graduated in 1982 with a master's degree in physics, returning to The Boeing Company to join a team working on $CuInSe_2$-based solar cells, headed by Drs. Reid A. Mickelsen and Wen S. Chen.

While employed at Boeing, he received seven United States Patents for photovoltaic devices and manufacturing methods, and in 1987 was awarded the Boeing Outstanding Engineer Fellowship to the Massachussetts Institute of Technology, where he studied during the 1987-1988 academic year at the Center for Advanced Engineering Studies. In 1990, he led the joint Boeing/Kopin Corporation development team to achievement of the highest confirmed efficiency for any thin-film solar cell in history (23.1% AM0 or 25.8% AM1.5G), a record that still stands today.

He left The Boeing Company to pursue a doctorate in chemical engineering from the University of Florida in 1994.

REPORT DOCUMENTATION PAGE

Form Approved
OMB NO. 0704-0188

1. AGENCY USE ONLY (Leave blank)	2. REPORT DATE	3. REPORT TYPE AND DATES COVERED
	June 2001	Final Report 6 May 1995 – 31 December 1998

4. TITLE AND SUBTITLE
Processing of $CuInSe_2$-Based Solar Cells: Characterization of Deposition Processes in Terms of Chemical Reaction Analyses, Final Report, 6 May 1995–31 December 1998

5. FUNDING NUMBERS
C: XAF-5-14142-10
TA: PVP15001

6. AUTHOR(S)
T.J. Anderson and B. J. Stanbery

7. PERFORMING ORGANIZATION NAME(S) AND ADDRESS(ES)
University of Florida
Gainesville, Florida

8. PERFORMING ORGANIZATION REPORT NUMBER

9. SPONSORING/MONITORING AGENCY NAME(S) AND ADDRESS(ES)
National Renewable Energy Laboratory
1617 Cole Blvd.
Golden, CO 80401-3393

10. SPONSORING/MONITORING AGENCY REPORT NUMBER
NREL/SR-520-30391

11. SUPPLEMENTARY NOTES
NREL Technical Monitor: Bolko von Roedern

12a. DISTRIBUTION/AVAILABILITY STATEMENT
National Technical Information Service
U.S. Department of Commerce
5285 Port Royal Road
Springfield, VA 22161

12b. DISTRIBUTION CODE

13. ABSTRACT *(Maximum 200 words)* This project describes a novel rotating-disc reactor has been designed and built to enable modulated flux deposition of $CuInSe_2$ and its related binary compounds. The reactor incorporates both a thermally activated source and a novel plasma-activated source of selenium vapor, which have been used for the growth of epitaxial and polycrystalline thin-film layers of $CuInSe_2$. A comparison of the different selenium reactant sources has shown evidence of increases in its incorporation when using the plasma source, but no measurable change when the thermally activated source was used. We concluded that the chemical reactivity of selenium vapor from the plasma source is significantly greater than that provided by the other sources studied. Epitaxially grown $CuInSe_2$ layers on GaAs, ZnTe, and SrF_2 demonstrate the importance of nucleation effects on the morphology and crystallographic structure of the resulting materials. These studies have resulted in the first reported growth of the CuAu type-I crystallographic polytype of $CuInSe_2$, and the first reported epitaxial growth of $CuInSe_2$ on ZnTe. Polycrystalline binary (Cu,Se) and (In,Se) thin films have been grown, and the molar flux ratio of selenium to metals was varied. It is shown that all of the reported binary compounds in each of the corresponding binary phase fields can be synthesized by the modulated flux deposition technique implemented in the reactor by controlling this ratio and the substrate temperature. These results were employed to deposit bilayer thin films of specific (Cu,Se) and (In,Se) compounds with low melting-point temperature, which were used to verify the feasibility of synthesizing $CuInSe_2$ by subsequent rapid-thermal processing. The studies of the influence of sodium during the initial stages of epitaxy have led to a new model to explain its influences based on the hypothesis that it behaves as a surfactant in the Cu–In–Se material system. This represents the first unified theory on the role of sodium that explains all of sodium's principal effects on the growth and properties of $CuInSe_2$ that have been reported in the prior scientific literature. Comprehensive statistical mechanical calculations have been combined with published phase diagrams and results of *ab-initio* quantum mechanical calculations of defect formation enthalpies from the literature to develop the first free-energy defect model for $CuInSe_2$ that includes the effects of defect associates (complexes). This model correctly predicts the α/β ternary phase boundary.

14. SUBJECT TERMS
PV; novel rotating-disc reactor; modulated flux deposition; binary compounds; chemical reactivity; selenium vapor; crystallographic structure; polycrystalline binary; bilayer thin films; flux deposition technique; surfactant; *ab-initio* quantum mechanics

15. NUMBER OF PAGES

16. PRICE CODE

17. SECURITY CLASSIFICATION OF REPORT	18. SECURITY CLASSIFICATION OF THIS PAGE	19. SECURITY CLASSIFICATION OF ABSTRACT	20. LIMITATION OF ABSTRACT
Unclassified	Unclassified	Unclassified	UL